

Design and exploration of small molecule modulators targeting metabolic disorders and T-cell activation

A Thesis Submitted

for the Degree of

DOCTOR OF PHILOSOPHY

In Chemistry

by

SUNNY GOON

(Index No. 67/21/Chem/27)



DEPARTMENT OF CHEMISTRY

JADAVPUR UNIVERSITY

KOLKATA – 700032

JANUARY, 2025

*Dedicated to my most loving
family and friends*



सी.एस.आई.आर.-भारतीय रासायनिक जीवविज्ञान संस्थान

वैज्ञानिक तथा औद्योगिक अनुसंधान परिषद की एक इकाई

विज्ञान एवं प्रौद्योगिकी मंत्रालय, भारत सरकार

4, राजा एस. सी. मल्लिक रोड, यादवपुर, कोलकाता - 700 032



CSIR - INDIAN INSTITUTE OF CHEMICAL BIOLOGY

A Unit of Council of Scientific & Industrial Research

Ministry of Science & Technology, Government of India

4, Raja S. C. Mullick Road, Jadavpur, Kolkata-700 032

CERTIFICATE FROM THE SUPERVISOR

This is to certify that the thesis entitled **“Design and exploration of small molecule modulators targeting metabolic disorders and T-cell activation”** submitted by **Sri Sunny Goon** who got his name registered on **06/04/2021** for the award of Ph. D. (Science) Degree of Jadavpur University, is absolutely based upon his own work under our supervisions and that neither this thesis nor any part of it has been submitted for either any degree / diploma or any other academic award anywhere before.

A. Talukdar 21/01/2025

(Signature of the Supervisor

date with official seal)

डॉ. अरिंदम तालुकदार / Dr. Arindam Talukdar
वरिष्ठ प्रधान वैज्ञानिक / Senior Principal Scientist
प्रमुख, वैश्विक संपदा प्रबंधन एवं व्यापार विकास समूह
Head, Business Development Group
सी.एस.आई.आर. - भारतीय रासायनिक जीवविज्ञान संस्थान
CSIR - Indian Institute of Chemical Biology
भारत सरकार / Government of India
४ राजा एस. सी. मल्लिक रोड / 4 Raja S.C. Mullick Rd.
यादवपुर, कोलकाता / Jadavpur, Kolkata-700 032

যাদবপুর বিশ্ববিদ্যালয়
কলকাতা - ৭০০ ০৩২, ভারত



JADAVPUR UNIVERSITY
KOLKATA-700 032, INDIA

FACULTY OF SCIENCE : DEPARTMENT OF CHEMISTRY : ORGANIC CHEMISTRY SECTION

CERTIFICATE FROM THE SUPERVISORS

This is to certify that the thesis entitled “**Design and exploration of small molecule modulators targeting metabolic disorders and T-cell activation**” submitted by **Sri Sunny Goon** who got his name registered on **06/04/2021** for the award of Ph. D. (Science) Degree of Jadavpur University, is absolutely based upon his own work under our supervisions and that neither this thesis nor any part of it has been submitted for either any degree/diploma or any other academic award anywhere before.

MA Mondal 21.01.2025
(Signature of the Supervisor)

date with official seal)

Associate Professor
Department of Chemistry
Jadavpur University
Kolkata-700 032

CANDIDATE'S DECLARATION

I hereby declare that the work contained in the thesis entitled "**Design and exploration of small molecule modulators targeting metabolic disorders and T-cell activation**" submitted for Ph.D. degree to the Jadavpur University Kolkata, India has been carried out under the joint supervision of Dr. Mohabul Alam Mondal (Assoc. Professor, Dept. of Chemistry, J.U) and Dr. Arindam Talukdar (Sr. Pr. Scientist, CSIR-IICB). The work is original and has not been submitted in part or full by me for any degree or diploma to this or any other institute.

In keeping with general practice of reporting scientific observations, due acknowledgements have been made wherever the work described is based on the findings of other investigators.

Sunny Goon

21/01/2025

Date:

Sunny Goon

Research Scholar
Department of Chemistry
Jadavpur University
Kolkata-700032, West Bengal

ACKNOWLEDGEMENT

It fills me with immense joy to reflect on the countless memorable moments and the incredible individuals who accompanied me on this long journey. Their unwavering motivation, guidance, support, and blessings at various stages have been the pillars that enabled me to reach this significant milestone in my life.

First and foremost, I would like to express my deepest gratitude to my supervisors, **Dr. Mohabul Alam Mondal**, Associate Professor, Department of Chemistry, Jadavpur University and **Dr. Arindam Talukdar**, Senior Principal Scientist, CSIR-IICB, for their invaluable guidance, constant support, and encouragement throughout all my ups and downs in my PhD journey. Their expertise, patience, and insightful feedback have been instrumental in shaping this research and my growth as a researcher.

I wish to express my deepest gratitude to my **Research Advisory Committee** (RAC) members, **Dr. Kajal Krishna Rajak**, Head, Department of Chemistry, Jadavpur university, **Prof. Rajib Kumar Goswami**, School of Chemical Sciences, Indian Association for the Cultivation of Sciences (IACS), Jadavpur, **Dr. Mohabul Alam Mondal** and **Dr. Arindam Talukdar** for your dedication to knowledge, insightful guidance, and constructive feedback that have deeply inspired and enriched my research journey, driving me to excel.

I am profoundly grateful to the esteemed faculty members of the Department of Organic Chemistry at Jadavpur University and Department of Organic and Medicinal Chemistry at CSIR-Indian Institute of Chemical Biology. Your commitment to creating an engaging academic atmosphere, together with your advice and encouragement, has greatly influenced my research path, expanded my knowledge, and motivated me to succeed.

Besides my mentor, I would also like to express my regards to my esteemed biology collaborators, **Dr. Dipyaman Ganguly**, **Dr. Partha Chakrabarti** and **Dr. Shilpak Chatterjee** and their team for their insightful thoughts and biological experiments which paved the way for construction of my research work. Special thanks goes to **Dr. Chinky Shiu Chen Liu**, **Suravi Mukherjee**, **Rituparna Jana** from **Dr. Dipyaman Ganguly's** lab; **Dr. Saheli Chowdhury**, **Abhishek Sen**, **Sujay Krishna Maiti**, **Rabin Pramanik** from **Dr. Partha Chakrabarti's** lab and **Puspendu Ghosh** from **Dr. Shilpak Chatterjee's** lab

whose timeless efforts in biological evaluations shaped my research career in a meaningful way.

I am very much thankful to the technical staff members of Central Instrumentation Facility (CIF) of Jadavpur University and CSIR-IICB for providing analytical support to complete my research work on time.

The next group of people are the ones who made this exhilarating journey with me and made this lab feel like a second home. I am thankful to my lab seniors **Dr. Ayan Mukherjee, Dr. Barnali Paul, Dr. Biswajit Kundu, Dr. Swarnali Roy, Dr. Sourav Pal** and my dear labmates **Dr. Dipayan Sarkar, Dr. Debomita Bhattacharya, Dr. Nirmal Das, Dipika Sarkar, Dr. Himadri Sekhar Sarkar, Uddipta Ghosh Dastidar, Binita Patra, Israful Hoque, Anindita Dey, Trisha Ghosh, Soupayan Pal, Rimica Das and Dipankar Das** who have showered continuous help, support, care and love throughout this challenging journey. Especially to **Sourav da, Dipayan, Nirmal, Debomita, Dipika and Uddipta da**— you have been my unwavering pillars of support, my trusted confidants, and my greatest source of strength. For your steadfast presence and encouragement, I am profoundly and eternally grateful. Without their constant support and encouragement, the journey could not be possible.

A very special thanks to my friends **Sarpita Bose, Sangeeta Dey, Kunal Paul, Sabyasachi Debnath, Gopal Bhattacharya, Avratanu Das** who were always there to back me in every possible way in this roller coaster journey.

This journey would be impossible without my strongest support system which is my family. My mother has been a friend, philosopher, and guide in all walks of my life and I would not have been what I am today without her unconditional love and support. Lastly, I must show my deepest gratitude to my loving wife cum friend **Dr. Purbita Bandopadhyay** whose constant belief in me has helped me to get beyond difficulties and hurdles. You, me and Sarpita— the trio shared each and every good or bad moments of our Ph.D. Life and made the long journey beautiful. Thanks to you all.



Sunny Goon

LIST OF FIGURES

Figure No.	Figure Details	Page No.
Chapter 1: Target based design, synthesis and development of small molecules for treatment of Non-Alcoholic Fatty Liver Disease (NAFLD)		
Figure 1	Timeline summarizing the advancements in understanding fatty liver disease	4
Figure 2	Different stages of NAFLD progression	6
Figure 3	Global prevalence of NAFLD	7
Figure 4	Overview of the mechanisms of action of emerging pharmacotherapeutics	8
Figure 5	Representative small molecules as PPAR agonists	9
Figure 6	Representative small molecules as FXR agonists	11
Figure 7	Different stages of ubiquitination and proteasomal degradation pathway	17
Figure 8	Rational design of small molecule modulators for blocking V-P recognition region in WD40 domain of COP1	26
Figure 9	Structural features of quinazolinone and quinazolinone-based small molecule modulators	28
Figure 10	Biological Validation of lead compounds by western blot analysis	44
Figure 11	Biological Validation of lead compound by Confocal Microscopy	44
Figure 12	Biological Validation of lead compound by Immunoprecipitation study	45
Figure 13	Molecular docking of the lead compound	46
Chapter 2: Design and synthesis of small molecule modulators of PPARγ in ameliorating Non-Alcoholic Fatty Liver Disease (NAFLD)		
Figure 1	Regulatory effect of PPAR gamma upon ligand activation	151
Figure 2	Examples of synthetic and natural PPAR γ and PPAR α/γ dual agonists	155
Figure 3	Overview of the ROS mediated proteotoxicity in hepatic cells	157
Figure 4	Rational design of non-TZD based pharmacophore as PPAR γ agonist	159
Figure 5	Co-crystal structure of PPAR γ with bound Rosiglitazone	159
Figure 6	Biological Validation of lead compound by Confocal Microscopy	172
Figure 7	Biological Validation of lead compound by qPCR analysis data	173
Figure 8	Biological Validation of lead compound by CETSA experiment	174

Figure No.	Figure Details	Page No.
Figure 9	Graphical representation of EC ₅₀ data of lead compound	175
Figure 10	Molecular docking of the lead compound	176
Chapter 3: Mechanistic insights into Piezo1 agonist Yaddle1 as a novel adjuvant for T cell activation		
Figure 1	Ion channels of different gating types	221
Figure 2	Mechanism of action of Piezo1 channel	226
Figure 3	Structural and topological model of mouse Piezo1	227
Figure 4	Structures of non-specific and competitive inhibitors of Piezo1	231
Figure 5	Known selective Piezo1 agonists	232
Figure 6	Proposed model for the role of Piezo1 in human T cell activation	233
Figure 7	Structure of Piezo1 agonist Yoda1	235
Figure 8	Screening and dose-response assays for potential Piezo1 agonists	236
Figure 9	Molecular Docking poses of synthesised Piezo1 agonists	247
Figure 10	Molecular Docking poses of synthesised Piezo1 agonists	252
Figure 11	DFT study analysis of synthesised Piezo1 agonists	256
Figure 12	Primary human CD4 ⁺ T cell validation of potential Piezo1 agonists	259
Figure 13	Piezo1 agonistic activity as determined by CD4 ⁺ T cell primary assay	259
Figure 14	Toxicity study of synthesised Piezo1 agonists	259

LIST OF TABLES

Table No.	Table Caption	Page No.
Chapter 1: Target based design, synthesis and development of small molecules for treatment of Non-Alcoholic Fatty Liver Disease (NAFLD)		
Table 1	Activity chart based on western blot analysis of synthesized compounds	34
Table 2	Activity chart based on western blot analysis of synthesized compounds	35
Table 3	Activity chart based on western blot analysis of synthesized compounds	37
Table 4	Activity chart based on western blot analysis of synthesized compounds	39
Table 5	in-vitro ADME studies for synthesized compounds (Log D and Aq. Solubility)	41
Table 6	in-vitro ADME studies for synthesized compounds (Plasma stability and metabolic stability)	42
Chapter 2: Design and synthesis of small molecule modulators of PPARγ in ameliorating Non-Alcoholic Fatty Liver Disease (NAFLD)		
Table 1	Activity chart based on western blot analysis of synthesized compounds	165
Table 2	Activity chart based on western blot analysis of synthesized compounds	166
Table 3	Activity chart based on western blot analysis of synthesized compounds	167
Table 4	Activity chart based on western blot analysis of synthesized compounds	167
Table 5	Activity chart based on western blot analysis of synthesized compounds	168
Table 6	Activity chart based on western blot analysis of synthesized compounds	167
Table 7	in-vitro ADME studies for synthesized compounds (Log D and Aq. Solubility)	168
Table 8	in-vitro ADME studies for synthesized compounds (Plasma stability and metabolic stability)	169
Chapter 3: Mechanistic insights into Piezo1 agonist Yaddle1 as a novel adjuvant for T cell activation		
Table 1	Dose dependency of hPiezo1 agonists: 1st stage modification	243
Table 2	Dose dependency of hPiezo1 agonists: 2nd stage modification	253
Table 3	Kinetic solubility of synthesized compounds	258

LIST OF ABBREVIATIONS

Abbreviation	Full Form
μL	microlitre
μM	micromolar
ACC1	Acetyl-coenzyme A carboxylase 1
ACN	Acetonitrile
AcOH	Acetic Acid
ACh	Acetylcholine
ADME	Absorption Distribution Metabolism Elimination
Akt	Protein kinase B
ALS	Amyotrophic lateral sclerosis
ALT	Alanine aminotransferase
AML	Acute myelogenous leukaemia
AMP	Adenosine mono phosphate
	AMPK 5'-adenosine monophosphate-activated protein kinase
anhyd.	anhydrous
APC	antigen-presenting cell
aq.	aqueous
ASK1	Apoptosis Signal-Regulating Kinase 1
Asn	Asparagine
AST	Aspartate aminotransferase
ATGL	Adipose triglyceride lipase
ATP	Adenosine triphosphate
BINAP	2,2'-bis(diphenylphosphino)-1,1'-binaphthyl)
Boc	tert-Butyloxycarbonyl
calcd	calculated
cat.	catalytic
CDCl_3	Deuterated Chloroform
CD3	Cluster of differentiation 3
CD4	Cluster of differentiation 4
CD8	Cluster of differentiation 8
CED	C-terminal extracellular domain
COP1	Constitutive of Photomorphogenesis
cLogP	Calculated Logarithm of octanol-water partition coefficient
Compd.	Compound
conc.	concentrated
CTD	C-terminal domain
D_2O	Deuterated water
DCE	1,2-Dichloroethane
DCM	Dichloromethane
DGAT	Diacylglycerol O-acyltransferase
DIPEA	N,N-Diisopropylethylamine
DMA	Dimethylacetamide
DMEM	Dulbecco's Modified Eagle's Medium
DMF	Dimethylformamide
DMSO	Dimethyl Sulphoxide
DMSO-d_6	Deuterated Dimethyl Sulphoxide
DNA	Deoxyribonucleic Acid
EC_{50}	Half maximal effective concentration

Abbreviation	Full Form
EI	Electron ionization
equiv.	equivalent
ESI	Electrospray Ionization
EtOAc	Ethyl Acetate
EtOH	Ethanol
FDA	U.S. Food and Drug Administration
FXR	Farnesoid X receptor
GABA	gamma-aminobutyric acid
HATU	1-[Bis(dimethylamino)methylene]-1H-1,2,3-triazolo[4,5-b]pyridinium 3-oxide hexafluorophosphate, Hexafluorophosphate Azabenzotriazole Tetramethyl Uronium
HDL	High-density lipoprotein
HECT	Homologous to the E6AP carboxyl terminus
HEK	Human Embryonic Kidney
hERG	Human ether-a-go-go-related gene
HPLC	High Performance Liquid Chromatography
HRMS	High Resolution Mass Spectroscopy
HTS	High-Throughput Screening
IC ₅₀	half-maximal inhibitory concentration
IFN	Interferon
K	Lysine Residue
LBD	ligand binding domain
LC	Liquid Chromatography
logD	Logarithm of the distribution coefficient
m.p.	Melting point
MAP3K	Mitogen-activated protein kinase kinase kinase
MEC ₅₀	half maximal effective concentration
MeOD	Deuterated Methanol
MeOH	Methanol
MHC	Major histocompatibility complex
MHz	Megahertz
mM	milimolar
mRNA	Messenger RNA
MS	Mass spectrometry
MW	molecular weight
NA	Not applicable
NAFL	Non-alcoholic fatty liver
NAFLD	Non-alcoholic fatty liver disease
NaOtBu	Sodium tertiary butoxide
NASH	Nonalcoholic steatohepatitis
NMR	Nuclear magnetic resonance
nM	nanomolar
NO	Nitric oxide
NRF2	Nuclear factor erythroid 2-related factor 2
p53	Tumor suppressor gene 53
PD	Parkinson's disease
Pd ₂ (dba) ₃	Tris(dibenzylideneacetone)dipalladium(0)
PDB	Protein Data Bank
POCl ₃	Phosphoryl chloride
PPAR	Peroxisome proliferator-activated receptor

Abbreviation	Full Form
PPh ₃	Triphenylphosphine
ppm	Parts per million
RING	Really Interesting New Gene
rpm	rotations per minute
RR	Ruthenium Red
rt	Room temperature
ROS	Reactive oxygen species
SalB	Salvianolic Acid B
SAR	Structure Activity Relationship
SD	Standard deviation
SEM	Standard Error of Mean
T2DM	Type 2 diabetes mellitus
TAG	Triacylglycerol
TCR	T cell receptor
TEA	Triethylamine
TFA	Trifluoroacetic Acid
THF	Tetrahydrofuran
TLC	Thin layer chromatography
TMS	Trimethyl silane
tRNA	transfer RNA
TZD	Thiazolidinediones
Ub	Ubiquitin
UPS	Ubiquitin Proteasomal System
UV	ultraviolet
VP	Valine Proline
WHO	World Health Organization

CONTENTS

Chapter 1: TARGET BASED DESIGN, SYNTHESIS AND DEVELOPMENT OF SMALL MOLECULES FOR TREATMENT OF NON-ALCOHOLIC FATTY LIVER DISEASE (NAFLD).....	2
1.1 Introduction	2
1.1.1 Brief history of NAFLD	3
1.1.2 Stages of NAFLD Progression.....	4
1.1.2.1 Simple Steatosis (NAFL)	4
1.1.2.2 Non-Alcoholic Steatohepatitis (NASH)	4
1.1.2.3 Fibrosis.....	5
1.1.2.4 Cirrhosis	5
1.1.2.5 Hepatocellular Carcinoma (HCC)	5
1.1.3 Global Prevalence	6
1.1.4 Therapeutic Approaches for NAFLD/NASH	7
1.1.5 Essential Therapeutic Targets for Mitigating NAFLD/NASH	8
1.1.5.1 Metabolic Targets:.....	9
1.1.5.1.1 Peroxisome proliferator-activated receptors (PPARs):.....	9
1.1.5.1.1.1 PPAR α (Alpha):	9
1.1.5.1.1.2 PPAR δ (Delta):.....	10
1.1.5.1.1.3 PPAR γ (Gamma):.....	10
1.1.5.1.1.4 Pan-PPAR Agonists:.....	10
1.1.5.1.2 Farnesoid X Receptor:	10
1.1.5.1.3 Thyroid Hormone Receptor β :.....	11
1.1.5.1.4 5'-Adenosine Monophosphate-Activated Protein Kinase (AMPK):	12
1.1.5.1.5 Acetyl-CoA carboxylase (ACC):.....	12
1.1.5.2 Inflammation and Fibrotic Target:	13
1.1.5.2.1 Apoptosis Signal-Regulating Kinase 1 (ASK1):	13
1.1.5.2.2 C-C Chemokine Receptor 2/5 (CCR2/CCR5):	14
1.1.5.2.3 Galectin-3:.....	14
1.1.6 COP1 E3 Ubiquitin Ligase: A Promising Therapeutic Target for NAFLD/NASH	15
1.1.6.1 Ubiquitin and Ubiquitination: Key Regulators of Cellular Homeostasis.....	16
1.1.6.2 Mechanism and Biological Significance of E3 Ubiquitin Ligases:.....	18
1.1.6.2.1 Mechanism of Action:	18
1.1.6.2.2 Biological Significance:	18
1.1.6.3 Constitutive of Photomorphogenesis (COP1).....	19
1.1.6.3.1 Role of COP1 in Cancers	20
1.1.6.3.2 Role of COP1 in Fatty Liver disease.....	21
1.2 Objective	23
1.3 Methodology	25
1.3.1 Rational Design.....	25
1.3.2 Chemistry	28
1.3.2.1 Modifications at C5 position (Set-1)	28
1.3.2.2 Modifications at C2 position (Set-2)	30
1.3.2.3 Modifications from Quinazolinone to Quinazolinedione Core (Set-3)	31
1.4 Results And Discussion	33
1.4.1 SAR development	33

1.4.1.1 Set-1 strategies	33
1.4.1.2 Set-2 strategies	36
1.4.1.3 Set-3 Strategies	37
1.4.2 Biological Discussion	44
1.4.2.1 Western Blot Experiment	44
1.4.2.2 Confocal Microscopy Studies.....	44
1.4.2.3 Immunoprecipitation Study	45
1.4.3 Molecular Docking	45
1.5 Conclusion And Outcome	47
1.6 Experimental Section.....	49
1.7 References	79
1.8 Annexure.....	86
 Chapter 2: DESIGN AND SYNTHESIS OF SMALL MOLECULE MODULATORS OF PPARγ IN AMELIORATING NON-ALCOHOLIC FATTY LIVER DISEASE (NAFLD)	
2.1 Introduction	148
2.1.1 PPAR γ and the metabolic regulation	149
2.1.2 Pharmacological Potential of PPAR.....	151
2.1.2.1 Anti-Cancer effect.....	151
2.1.2.2 Neurodegenerative Disorder.....	152
2.1.2.3 Diabetes	153
2.1.2.4 Obesity and Adipocyte differentiation	153
2.1.2.5 Non-Alcoholic Fatty Liver Disease (NAFLD)	154
2.2 Objective	156
2.3 Methodology	158
2.3.1 Rational Design.....	158
2.3.2 Chemistry	160
2.4 Results And Discussion	164
2.4.1 SAR development	164
2.4.2 Biological Discussion	171
2.4.2.1 Confocal Microscopy Studies.....	171
2.4.2.2 qPCR Studies for gene expression.....	172
2.4.2.3 Cellular thermal shift assay.....	173
2.4.2.4 Half maximal effective concentration (EC ₅₀) determination.....	175
2.4.3 Molecular Docking	175
2.5 Conclusion And Outcome	177
2.6 Experimental Section.....	178
2.7 References	189

2.8 Annexure.....	194
 Chapter 3: MECHANISTIC INSIGHTS INTO PIEZO1 AGONIST YADDLE1 AS A NOVEL ADJUVANT FOR T CELL ACTIVATION	
3.1 Brief idea about Ion-Channels	220
3.2 Structure and Mechanism of Ion Channels	220
3.3 Types of Ion Channels.....	221
3.3.1 Voltage-Gated Ion Channels.....	221
3.3.1.1 Voltage-Gated Sodium Channels (Nav).....	222
3.3.1.2 Voltage-Gated Potassium Channels (Kv)	222
3.3.1.3 Voltage-Gated Calcium Channels (Cav)	222
3.3.2. Ligand-Gated Ion Channels	222
3.3.2.1 Nicotinic Acetylcholine Receptors (nAChRs).....	223
3.3.2.2 GABA Receptors	223
3.3.3. Temperature-Gated Ion Channels	223
3.3.3.1 TRPV1 (Transient Receptor Potential Vanilloid 1)	223
3.3.3.2 TRPM8 (Transient Receptor Potential Melastatin 8).....	223
3.3.4. Mechanosensitive Ion Channels.....	224
3.3.4.1 Piezo Channels (Piezo1 and Piezo2).....	224
3.3.4.2 TREK-1 and TRAAK Channels	224
3.4 Mechanosensitive ion channels: Piezo Channels.....	224
3.4.1 Structural Determination of Piezo1	226
3.4.1.1 Pore Module and Gating Mechanism	226
3.4.1.2 Ion Pathways	226
3.4.1.3 Propeller Blade Structure	226
3.4.1.4 Membrane Dome Mechanism	227
3.4.2 Biological Function of Piezo1 Channel.....	228
3.4.2.1 Role of Piezo1 in Bone.....	228
3.4.2.2 Role of Piezo1 Channel in the Cardiovascular System	228
3.4.2.3 Role of Piezo1 Channel in Innate Immunity	229
3.4.2.4 Role of Piezo1 Channel in Human Cancer.....	229
3.4.3 Development of Piezo1 Channel Modulators.....	229
3.4.3.1 Non-specific and Competitive inhibitors of Piezo1	230
3.4.3.2 Piezo1 Channel Specific Agonists	231
3.5 Objective	233
3.6 Methodology	235
3.6.1 Rational Design.....	235
3.6.2 Chemistry	238
3.7 Results And Discussion	243
3.7.1 Solubility.....	257
3.7.2 Validation of Potential Piezo1 Agonists in Primary Human CD4+ T cells.....	258
3.7.3 Cytotoxicity Assay	260
3.8 Conclusion And Outcome	261

3.9 Experimental Section.....	262
3.10 References.....	282
3.11 Annexure	291
 List of Publications	 336
Conference Presentations	338
Copy of Publications.....	340

SYNOPSIS

Name of Research Scholar: **Mr. Sunny Goon**

Index no: **62/21/Chem/27**

Degree for which submitted: **Ph.D.**

Department: **Chemistry**

Name of the Research Guide: **Dr. Mohabul Alam Mondal, Dr. Arindam Talukdar**

Thesis Title: **Design and exploration of small molecule modulators targeting metabolic disorders and T-cell activation.**

Chapter-I:

The E3 ubiquitin ligase, Constitutive Photomorphogenic 1 (COP1), plays a critical role in lipid metabolism within hepatocytes by regulating the stability and turnover of Adipose Triglyceride Lipase (ATGL), the rate-limiting enzyme in lipolysis. Dysregulation of the COP1-ATGL axis disrupts hepatic lipid homeostasis, leading to pathological conditions such as simple steatosis. In this study, we report the design and development of quinazolinone-based modulators targeting the COP1-ATGL pathway. Comprehensive structure-activity relationship (SAR) studies guided the rational incorporation of functional groups at key positions (C2, C5 and N1) of the quinazolinone scaffold to optimize molecular interactions and bioactivity. The biological activity of the synthesized compounds was evaluated through in vitro assays, which demonstrated their efficacy in modulating ATGL stability and function. The lead compound **58**, exhibited a significant ability to enhance ATGL protein levels, inhibit ATGL ubiquitination, and reduce intracellular lipid accumulation in hepatocytes in a dose-dependent manner. Pharmacokinetic properties were further assessed through ADME profiling, confirming compound **58** as a candidate with favorable drug-like properties. This study highlights quinazolinone as a promising chemotype for the therapeutic modulation of COP1-ATGL activity. By targeting this pathway, these compounds offer a novel approach for managing lipid-related disorders, particularly in the context of non-alcoholic fatty liver disease (NAFLD) and associated metabolic syndromes.

Chapter-II:

PPAR γ plays a key role in managing non-alcoholic fatty liver disease (NAFLD) by regulating lipid metabolism, glucose homeostasis, and inflammation. It mitigates oxidative stress by enhancing antioxidant defenses, improving mitochondrial function, and upregulating enzymes like superoxide dismutase (SOD) and glutathione peroxidase.

While thiazolidinediones (TZDs) have shown efficacy as PPAR γ activators, their clinical use is limited by adverse effects. This study presents a novel purine-based PPAR γ activator, compound **30**, designed to target the PPAR γ -NRF2 pathway and reduce ROS-induced hepatocellular dysfunction. Compound **30** selectively elevated PPAR γ expression and downstream genes such as NRF2, NQO1, and SOD1. In CellRox assays, it significantly reduced ROS levels, and CETSA experiments confirmed strong binding affinity with PPAR γ . Furthermore, it demonstrated superior efficacy (EC_{50} = 214.6 nM) compared to the marketed activator rosiglitazone (EC_{50} = 257.3 nM) in PPAR γ Transcription Factor Kit assays. In summary, the purine-based compound **30** offers a promising therapeutic approach to ameliorate ROS-driven hepatocellular proteotoxicity in NAFLD.

Chapter-III:

Piezo1, a mechanosensitive ion channel, is crucial for numerous physiological functions and has garnered significant attention for its therapeutic relevance. The development of selective agonists has provided insights into how cells respond to mechanical cues, offering promising therapeutic strategies. In this work, we analyzed the structural components of Yoda1, a well-characterized Piezo1 agonist, to unravel its structure–activity relationship (SAR) and facilitate the creation of improved agonists. Using Piezo1-mCherry-transfected HEK293A cells, we conducted initial screening assays with Yoda1 serving as the reference agonist. Through these efforts, we identified a novel Piezo1 agonist, Yaddle1 (**34**), featuring a trifluoromethyl substitution. Yaddle1 exhibited potent activity with an EC_{50} of 0.40 μ M and showed marked improvements in solubility. Its kinetic solubility at physiological pH (26.72 ± 1.8 μ M at pH 7.4) was approximately 22 times greater than that of Yoda1 (1.22 ± 0.11 μ M at pH 7.4), addressing the solubility issues associated with Yoda1. Computational studies as well as density functional theory (DFT) analysis revealed that Yaddle1 leverages tetrel interactions to stabilize Piezo1's domain interface, functioning as a dynamic wedge to support its activation. Furthermore, Yaddle1 demonstrated the ability to induce calcium ion (Ca^{2+}) influx in primary human CD4 $^{+}$ T cells, highlighting its potential as a novel vaccine adjuvant to enhance T cell activation. In summary, Yaddle1 emerges as a next-generation Piezo1 agonist with superior solubility and bioactivity, providing a valuable tool for studying Piezo1-mediated functions and exploring its therapeutic applications

CHAPTER ONE

Target based design, synthesis and development of small molecules for treatment of Non-Alcoholic Fatty Liver Disease (NAFLD)

CHAPTER ONE

Target based design, synthesis and development of small molecules for treatment of Non-Alcoholic Fatty Liver Disease (NAFLD)

1.1 Introduction

Non-alcoholic fatty liver disease (NAFLD) is a chronic liver disorder characterized by the excessive accumulation of fat in the liver (steatosis) in individuals who consume little to no alcohol.^{1,2} It is the most common liver disease globally, affecting around 25-30% of adults, and its prevalence is increasing in parallel with the global rise in obesity, type 2 diabetes, and metabolic syndrome.³ NAFLD encompasses a spectrum of liver conditions, from simple fatty liver (steatosis) to more severe forms such as non-alcoholic steatohepatitis (NASH), which can progress to fibrosis, cirrhosis, liver failure, and hepatocellular carcinoma (liver cancer).^{4,5} NAFLD is strongly associated with metabolic syndrome, a cluster of conditions including obesity, insulin resistance, hypertension, and dyslipidemia.^{6,7} These risk factors lead to fat accumulation in the liver, primarily driven by insulin resistance and an imbalance in fat metabolism. The liver's inability to properly manage fat leads to a buildup of triglycerides in liver cells (hepatocytes).⁸ In its early stage, NAFLD (also called simple steatosis) may be benign, with little to no inflammation or liver damage. However, around 20-30% of individuals with NAFLD develop NASH, where fat accumulation is accompanied by inflammation and hepatocyte injury, increasing the risk of liver fibrosis.⁹ The pathogenesis of NAFLD is complex and multifactorial. Insulin resistance is considered the central mechanism, as it promotes increased fat storage in the liver and prevents its breakdown (lipolysis). Additionally, oxidative stress, inflammation, and lipotoxicity contribute to liver damage, driving the progression from simple steatosis to NASH.¹⁰ Genetic factors also play a role, with certain gene variants, such as PNPLA3 and TM6SF2, increasing susceptibility to NAFLD and its progression to more advanced liver disease.¹¹ Environmental and lifestyle factors, such as a sedentary lifestyle and a diet high in saturated fats and sugars, are major contributors to the development of NAFLD. NAFLD is often asymptomatic in its early stages, making it challenging to diagnose. Many cases are discovered incidentally through abnormal liver function tests or imaging studies. Ultrasound is the most common imaging technique

used to detect fatty liver, while more advanced methods such as transient elastography (FibroScan) or magnetic resonance imaging (MRI) can assess the degree of liver fibrosis.¹² Liver biopsy remains the gold standard for diagnosing NASH and evaluating the severity of liver damage, though it is invasive and not routinely performed.¹³ Management of NAFLD primarily involves lifestyle modifications. Weight loss through diet and exercise is the cornerstone of treatment, as even modest weight loss (5-10% of body weight) can significantly reduce liver fat and improve inflammation.¹⁴ Additionally, controlling associated metabolic conditions, such as diabetes and hyperlipidemia, is crucial.¹⁵ While there are currently no approved medications specifically for NAFLD, several drugs targeting NASH are in clinical trials, focusing on reducing liver fat, inflammation, and fibrosis. As the prevalence of obesity and type 2 diabetes continues to rise, NAFLD is increasingly recognized as a major public health concern, with significant implications for liver-related and cardiovascular morbidity and mortality.¹⁶

1.1.1 Brief history of NAFLD

Fatty degeneration of the liver was first identified as a pathological change by William Bowman in 1842 when he observed fat accumulation in human liver specimens under a microscope. For the next century, it was widely assumed that chronic alcohol consumption was the primary cause of fatty liver. However, it was later recognized that a significant number of cases occurred in obese and diabetic individuals who had no history of alcohol consumption.^{17,18} In 1980, Dr. Jurgen Ludwig coined the term “non-alcoholic steatohepatitis” (NASH), and in 1986, Dr. Fenton Schaffner proposed the idea of non-alcohol-associated fatty liver disease (NAFLD).^{19,20} They describe a liver condition that mimicked alcoholic hepatitis but occurred in non-drinkers. This marked the beginning of NAFLD as a recognized medical entity.

In the 1990s, research established NAFLD’s strong association with obesity, insulin resistance, and type 2 diabetes. It became evident that NAFLD could progress from simple steatosis (fat buildup) to NASH, fibrosis, cirrhosis, and even liver cancer. NAFLD started being viewed as the hepatic manifestation of metabolic syndrome.

By the 2000s, NAFLD had become the most common cause of liver disease worldwide, driven by rising obesity and diabetes rates. It was increasingly linked to cardiovascular disease and liver-related mortality.²¹

Currently, NAFLD impacts approximately 25-30% of the global population and is one of the leading causes of liver transplantation. Efforts are ongoing to develop treatments for NASH and to enhance non-invasive diagnostic methods. Additionally, some experts have suggested renaming NAFLD to better highlight its connection to metabolic disorders. Figure 1 provides a timeline of our evolving understanding of fatty liver.

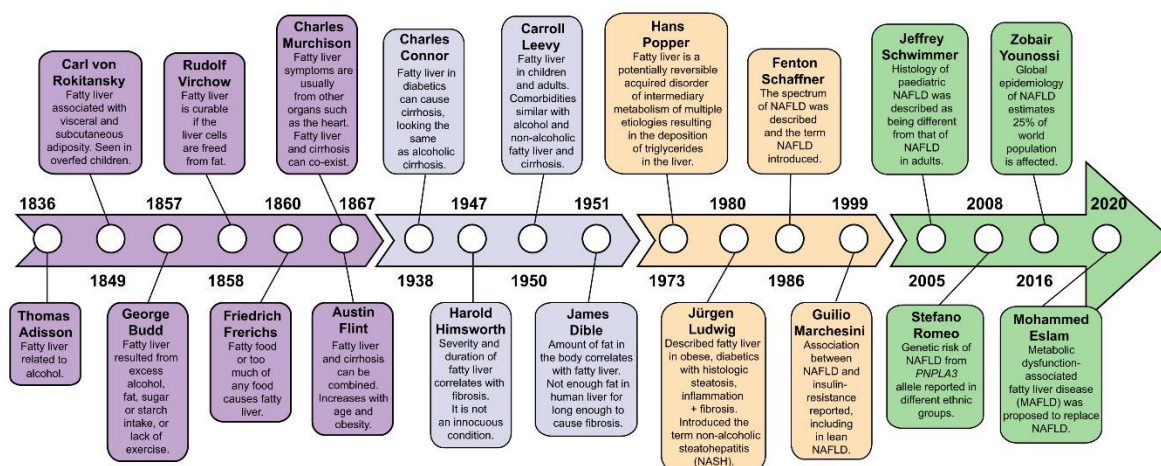


Figure 1. Timeline summarizing the advancements in understanding fatty liver disease.²²

1.1.2 Stages of NAFLD Progression

Non-alcoholic fatty liver disease (NAFLD) progresses through several distinct stages, each characterized by varying degrees of liver fat accumulation, inflammation, and fibrosis.²³ Here's a breakdown of the different stages of NAFLD:

1.1.2.1 Simple Steatosis (NAFL)

This is the earliest and mildest stage of NAFLD, characterized by the accumulation of fat (triglycerides) in liver cells without significant inflammation or damage. This is typically asymptomatic; most individuals are unaware they have this condition. It is often discovered incidentally during routine blood tests or imaging. Generally considered benign, but about 20-30% of patients may progress to NASH, especially if they have risk factors like obesity, insulin resistance, or diabetes.²⁴

1.1.2.2 Non-Alcoholic Steatohepatitis (NASH)

In this stage, fat accumulation is accompanied by inflammation and damage to liver cells (hepatocytes). NASH represents a significant progression from simple steatosis. While many individuals remain asymptomatic, some may experience fatigue, abdominal discomfort, or elevated liver enzymes in blood tests. NASH can lead to more severe liver disease, including fibrosis and cirrhosis. Approximately 15-25% of individuals with NASH may progress to advanced liver disease.²⁵

1.1.2.3 Fibrosis

Fibrosis occurs when chronic liver inflammation from NASH leads to the formation of scar tissue in the liver. The extent of fibrosis can vary from mild (limited scarring) to severe (extensive scarring). Mild fibrosis may not produce noticeable symptoms, but as it progresses, individuals might experience signs of liver dysfunction, such as fatigue and jaundice. Fibrosis is a critical marker in the progression of NAFLD. Individuals with significant fibrosis are at a higher risk of developing cirrhosis and liver-related complications.^{26,27}

1.1.2.4 Cirrhosis

Cirrhosis represents advanced scarring of the liver, resulting in a significant loss of liver function. At this stage, the liver is severely damaged and cannot effectively regenerate. Patients may experience jaundice, ascites (fluid accumulation in the abdomen), gastrointestinal bleeding, and encephalopathy (confusion or altered mental state due to liver dysfunction). Cirrhosis greatly increases the risk of liver failure and hepatocellular carcinoma (liver cancer). Management may require monitoring for complications and consideration of liver transplantation in cases of decompensated liver disease.^{28,29}

1.1.2.5 Hepatocellular Carcinoma (HCC)

HCC is a type of liver cancer that can develop in patients with advanced fibrosis or cirrhosis, particularly those with NASH. Symptoms may include unexplained weight loss, abdominal pain, jaundice, and worsening liver function. The prognosis for HCC depends on the stage at diagnosis and the patient's liver function. Early detection is crucial for successful treatment options.³⁰

The progression from NAFL to NASH and eventually to fibrosis and cirrhosis is influenced by various factors, including genetics, obesity, insulin resistance, and lifestyle choices. Not everyone with NAFLD progresses through each stage. Many individuals with simple

steatosis remain stable and do not progress to NASH or fibrosis, while others may rapidly advance due to the presence of multiple risk factors. Understanding the stages of NAFLD is essential for early detection, management, and treatment. Lifestyle modifications, such as weight loss, exercise, and dietary changes, can help prevent progression, particularly in the early stages of the disease. Regular monitoring and management of metabolic risk factors are crucial for individuals diagnosed with NAFLD to reduce the risk of progression to more severe liver disease.

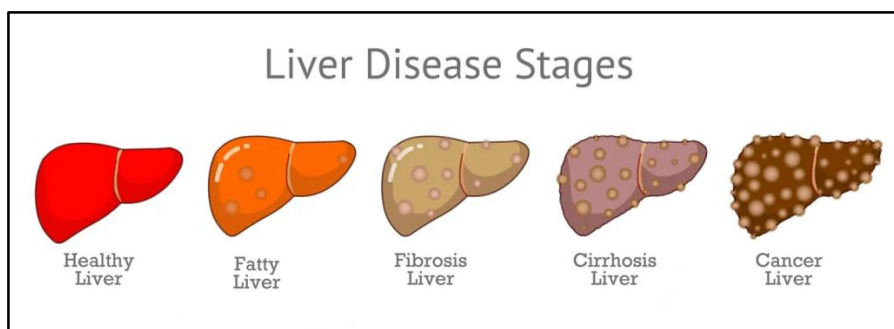


Figure 2. Different stages of NAFLD progression

1.1.3 Global Prevalence

The global prevalence of non-alcoholic fatty liver disease (NAFLD) is approximately 25% to 30% among adults, with variations across regions: around 25% to 35% in North America, 20% to 30% in Europe, and 15% to 30% in Asia, with particularly high rates in countries like Japan and China. The Middle East and Latin America also report prevalence rates between 25% to 35% and 20% to 30%, respectively (Figure 3).³¹ NAFLD is more common in middle-aged adults, particularly those aged 40 to 60, with a higher prevalence in men, although post-menopausal women may also be at increased risk. The disease is closely associated with obesity, affecting 70% to 90% of obese individuals, and type 2 diabetes, with estimates ranging from 50% to 70% in this population.³² As the global obesity epidemic continues, the prevalence of NAFLD is expected to rise, making it a significant public health concern and a leading cause of liver disease and transplantation. Despite its high prevalence, NAFLD is often underdiagnosed due to its asymptomatic nature in early stages, underscoring the need for increased awareness and improved screening methods for early detection and management.³³

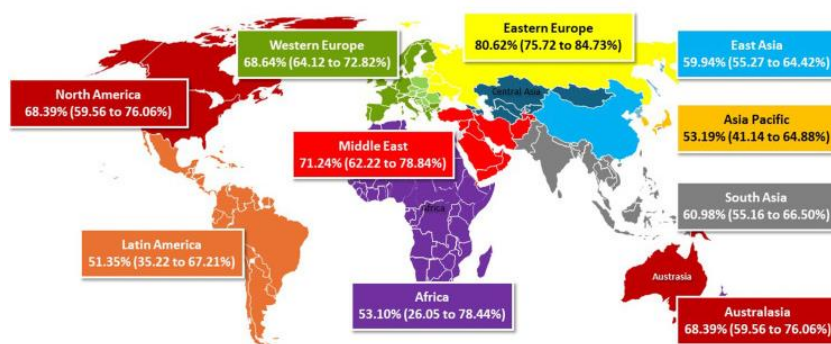


Figure 3. Global prevalence of NAFLD³⁴

1.1.4 Therapeutic Approaches for NAFLD/NASH

Nonalcoholic fatty liver disease (NAFLD) and its advanced form, nonalcoholic steatohepatitis (NASH), are widespread and pose significant global health challenges, yet there are currently no approved treatments for these conditions.³⁵ NAFLD begins with overnutrition, leading to the accumulation of fat in the liver and other tissues, insulin resistance, oxidative stress, and inflammation. This imbalance in lipid metabolism produces toxic metabolites, triggering oxidative and endoplasmic reticulum (ER) stress, lipid peroxidation, inflammasome activation, cell death, fibrosis, and tissue regeneration.⁶ The pathogenesis of NAFLD/NASH is influenced by multiple factors, including metabolic disorders, hormones, overnutrition, oxidative stress, and genetics, making the disease progression and treatment response highly heterogeneous.^{24,36}

While research into the pathophysiology of NAFLD and NASH has advanced, the development of effective therapies has been slow, despite years of study. Current medications for metabolic disorders, such as Orlistat for obesity, have shown promise in NAFLD/NASH patients, highlighting the urgent need for specific drug candidates and therapeutic targets.³⁷ Emerging treatments focus on key areas like hepatic lipid metabolism, inflammation, diabetes, and fibrosis. Moreover, signaling pathways associated with NAFLD/NASH, such as those involving extracellular vesicles (EVs) and the gut microbiota, are being explored, with hopes for more personalized therapies in the future.

Diet and lifestyle interventions remain essential in managing NAFLD. Adherence to a Mediterranean diet and calorie restriction has shown positive effects in reducing liver fat and inflammation.³⁸ Weight loss and physical activity are also vital, as they help

ameliorate hepatic steatosis and prevent NAFLD from progressing to NASH.³⁹ Although metformin, a common antihyperglycemic agent, exhibits some lipid-lowering effects, its benefits for NAFLD treatment are unproven.⁴⁰ Similarly, while statins may reduce cardiovascular risks in NASH patients, they have not been shown to improve liver histology. Bile acid metabolism offers another potential therapeutic target, with bile salt-based therapies showing promise for NASH treatment, although none are currently approved.

As understanding of NASH pathogenesis grows, novel therapeutic approaches are emerging, including metabolic regulation, antioxidants, gut microbiome modulation, microRNA targeting, inhibiting apoptosis, and stem cell-based therapies. Exosome-mediated drug delivery is also being explored for targeted treatment. Despite rapid advancements in research, NAFLD and NASH remain without approved therapies, underscoring the critical need for ongoing research into new treatments.

1.1.5 Essential Therapeutic Targets for Mitigating NAFLD/NASH

Various significant targets and pertinent therapeutics are available to mitigate liver disease, as illustrated in Figure 4. A few targets are discussed below in this section.

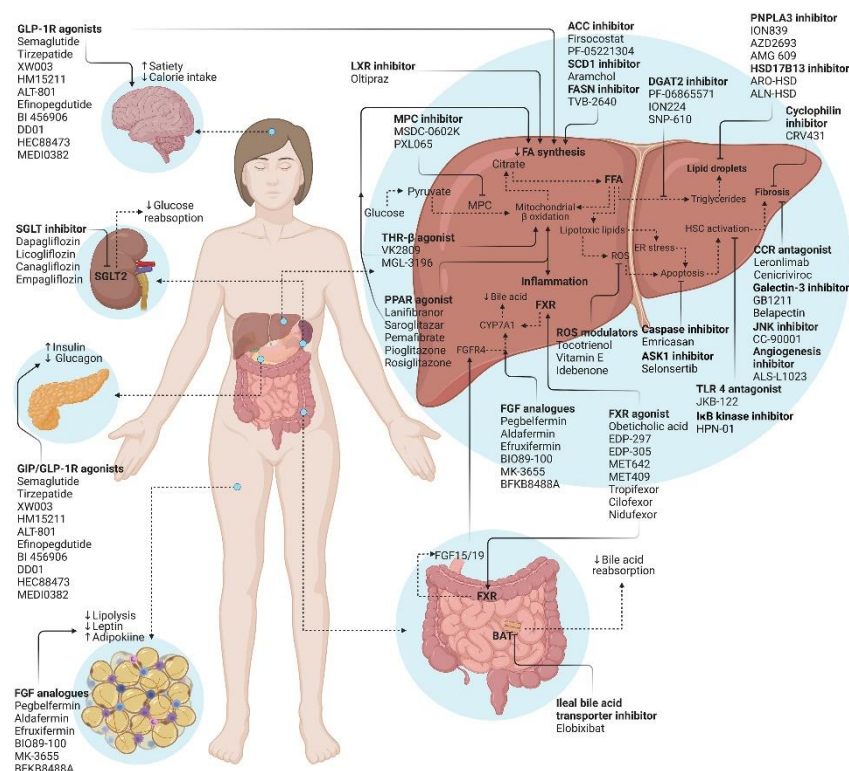


Figure 4. Overview of the mechanisms of action of emerging pharmacotherapeutics: Key targets of pharmacological interventions for NAFLD/NASH in clinical trials.⁴¹

1.1.5.1 Metabolic Targets:

NASH is typically viewed as a liver-related consequence of metabolic syndrome, with metabolic disorders playing a key role throughout its progression. Restoring and maintaining metabolic balance has been demonstrated as an effective therapeutic approach for NASH. Several treatment strategies focus on addressing the underlying metabolic dysfunctions associated with NASH. The therapies aimed at improving metabolic health are outlined below.

1.1.5.1.1 Peroxisome proliferator-activated receptors (PPARs):

Peroxisome Proliferator-Activated Receptors (PPARs) are a group of nuclear receptors that play a pivotal role in regulating lipid metabolism, glucose homeostasis, and inflammation, making them important therapeutic targets for nonalcoholic fatty liver disease (NAFLD) and its more advanced form, nonalcoholic steatohepatitis (NASH). The three major PPAR subtypes—PPAR α , PPAR δ (PPAR β), and PPAR γ —each contribute to different aspects of metabolic regulation and are being explored for their therapeutic potential in treating NAFLD.⁴²

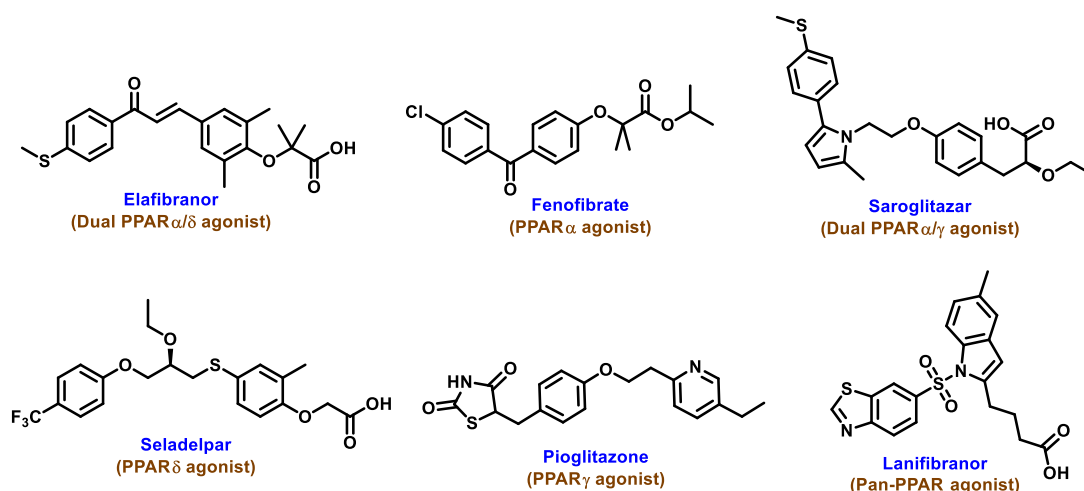


Figure 5. Representative small molecules as PPAR agonists

1.1.5.1.1.1 PPAR α (Alpha): PPAR α is highly expressed in the liver and is involved in promoting fatty acid oxidation and energy expenditure. Activation of PPAR α helps reduce hepatic lipid accumulation (steatosis) by increasing the breakdown of fatty acids. It also exerts anti-inflammatory effects. **Elafibranor**, a dual PPAR α/δ agonist, has shown potential in clinical trials by improving liver fat content, reducing inflammation, and improving liver histology in patients with NASH. Another drug, **Fenofibrate**, is primarily

used for hyperlipidemia but activates PPAR α and has been studied for its effects on liver fat reduction. **Saroglitazar**, a dual PPAR α / γ agonist developed by Zydus Cadila in India in 2001, enhances insulin sensitivity, lipid, and glycemic parameters while improving steatohepatitis and reducing lipid levels in diet-induced mice.⁴³

1.1.5.1.1.2 PPAR δ (Delta): PPAR δ is involved in fatty acid oxidation and energy metabolism in multiple tissues, including the liver and skeletal muscle. It enhances fat burning and reduces fat accumulation in the liver, while also exerting anti-inflammatory effects, making it a key target for NASH treatment. **Seladelpar**, a selective PPAR δ agonist, has demonstrated efficacy in reducing liver inflammation and fibrosis in clinical trials.⁴⁴

1.1.5.1.1.3 PPAR γ (Gamma): PPAR γ is critical for insulin sensitivity and adipogenesis. Although PPAR γ activation can reduce insulin resistance and inflammation, it can also lead to weight gain, a concern in NAFLD treatment. **Pioglitazone**, a PPAR γ agonist approved for diabetes, has shown benefits in reducing liver fat and resolving steatohepatitis, though its side effects, such as weight gain and fluid retention, limit its use.⁴⁵

1.1.5.1.1.4 Pan-PPAR Agonists: Drugs like **Lanifibranor**, a pan-PPAR agonist targeting all three subtypes (PPAR α / δ / γ), aim to balance the benefits of each receptor, showing potential in reducing steatosis, inflammation, and fibrosis in NASH patients.⁴⁵

In summary, PPAR agonists are key drug targets for NAFLD/NASH due to their multifaceted roles in improving lipid metabolism, insulin sensitivity, and reducing inflammation and fibrosis.

1.1.5.1.2 Farnesoid X Receptor:

Farnesoid X Receptor (FXR) is a nuclear receptor that plays a central role in regulating bile acid, lipid, and glucose metabolism, making it a promising therapeutic target for nonalcoholic fatty liver disease (NAFLD) and nonalcoholic steatohepatitis (NASH). FXR is predominantly expressed in the liver and intestines, where it regulates bile acid synthesis and secretion. By modulating bile acid levels, FXR also impacts lipid and glucose homeostasis, reducing fat accumulation and inflammation in the liver.

Activation of FXR helps lower hepatic steatosis (fat buildup), improve insulin sensitivity, and suppress inflammation and fibrosis—key aspects in the progression of

NAFLD/NASH. Additionally, FXR activation suppresses the production of pro-inflammatory cytokines and reduces fibrogenic pathways, preventing the transition from simple steatosis to more advanced liver disease like cirrhosis.⁴⁶

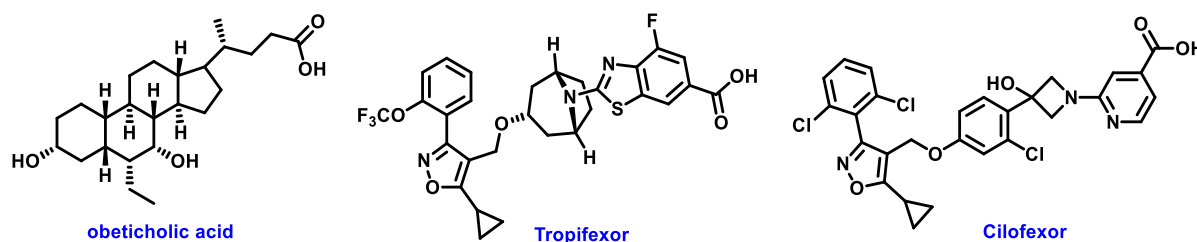


Figure 6. Representative small molecules as FXR agonists

Obeticholic acid (OCA) is the most well-known FXR agonist in clinical trials for NASH. It has shown efficacy in reducing liver fibrosis and improving histological features of NASH. However, side effects like pruritus (itching) and increased cholesterol levels are concerns with OCA.

Other FXR agonists, such as **Tropifexor** and **Cilofexor**, are in development, aiming to offer better efficacy with fewer side effects. Overall, targeting FXR holds significant potential in addressing multiple aspects of NAFLD/NASH pathogenesis, particularly in reducing liver inflammation and fibrosis.⁴⁷

1.1.5.1.3 Thyroid Hormone Receptor β :

Thyroid Hormone Receptor β (THR- β) is a promising target for the treatment of nonalcoholic fatty liver disease (NAFLD) due to its role in regulating lipid metabolism and energy expenditure in the liver. THR- β activation stimulates pathways that enhance fatty acid oxidation and reduce lipogenesis (fat production), leading to a decrease in hepatic steatosis (fat accumulation) without affecting the thyroid hormone receptor α (THR- α), which controls heart rate and other functions, minimizing the risk of cardiovascular side effects. By selectively activating THR- β in the liver, drug candidates aim to reduce liver fat and improve metabolic parameters, including cholesterol levels, without systemic hyperthyroid effects. This makes THR- β agonists particularly attractive for NAFLD and nonalcoholic steatohepatitis (NASH) treatment. **Resmetirom (MGL-3196)** is the most advanced THR- β agonist in clinical development for NAFLD/NASH. It has shown efficacy in reducing liver fat, improving liver enzymes, and reducing fibrosis progression in NASH patients, with favorable safety profiles. Other THR- β agonists, such as **VK2809**, are also

in development, showing similar potential in reducing hepatic fat and improving liver health.^{48,49}

Overall, targeting THR- β offers a promising approach to treating NAFLD by addressing key metabolic dysregulations with a lower risk of systemic side effects.

1.1.5.1. 4 5'-Adenosine Monophosphate-Activated Protein Kinase (AMPK):

5'-Adenosine Monophosphate-Activated Protein Kinase (AMPK) is a crucial energy-sensing enzyme that regulates cellular energy balance, making it an attractive therapeutic target for nonalcoholic fatty liver disease (NAFLD). AMPK activation promotes fatty acid oxidation, inhibits lipogenesis (fat production), and enhances glucose uptake, all of which are essential for reducing hepatic fat accumulation and improving insulin sensitivity.⁵⁰ In NAFLD, AMPK activity is often diminished, contributing to excessive lipid accumulation and metabolic dysfunction. Restoring AMPK activity can reverse these metabolic disturbances, reducing liver fat content and improving overall liver function. AMPK activation also has anti-inflammatory effects, which can mitigate the progression from simple steatosis to nonalcoholic steatohepatitis (NASH), where inflammation and fibrosis become dominant. **Metformin**, a commonly used drug for type 2 diabetes, indirectly activates AMPK and has shown benefits in improving liver enzymes and reducing liver fat in NAFLD patients, though its efficacy is limited in advanced NASH. Berberine, a natural compound, and AICAR, a direct AMPK activator, are also being explored for their potential to treat NAFLD by enhancing AMPK activity. In summary, targeting AMPK offers a promising approach to NAFLD treatment by improving lipid metabolism, reducing inflammation, and preventing disease progression, making it a key focus for therapeutic development.⁵¹

1.1.5.1.5 Acetyl-CoA carboxylase (ACC):

Acetyl-CoA carboxylase (ACC) plays a key role in adipogenesis by converting acetyl-CoA to malonyl-CoA, a crucial step in fat synthesis. Inhibiting ACC has shown promise in treating nonalcoholic steatohepatitis (NASH) by reducing fatty liver degeneration and improving insulin resistance.⁵² **PF-05221304**, an ACC inhibitor targeting the liver, has demonstrated the ability to alleviate inflammation and fibrosis in NASH. However, it may increase serum triglyceride levels by elevating the expression of SREBP1c and enhancing hepatic very low-density lipoprotein (VLDL) export. To address this, **PF-05221304** is

often coadministered with a diacylglycerol acyltransferase 2 (DGAT2) inhibitor. DGAT2, highly expressed in the liver and adipose tissue, catalyzes the final step of lipid synthesis by esterifying fatty acids with diacylglycerol to form triglycerides. The combination therapy of PF-05221304 and DGAT2 inhibitors significantly reduces hepatic fat content while showing good safety and tolerability. Moreover, arachidonate 12-lipoxygenase (ALOX12) has been found to protect ACC1 from lysosomal degradation, promoting the progression of NASH. IMA-1, a small molecule identified to disrupt the ALOX12–ACC1 axis by binding directly to ALOX12, prevents the progression of NASH with minimal side effects. Additionally, ACC inhibitors suppress the activation of hepatic stellate cells (HSCs), helping to reduce NASH-related fibrosis. Overall, ACC inhibition represents a multifaceted approach to tackling NASH by targeting fat synthesis, inflammation, and fibrosis.⁵³

1.1.5.2 Inflammation and Fibrotic Target:

Inflammation and fibrosis are critical components in the progression of nonalcoholic fatty liver disease (NAFLD) to its more severe form, nonalcoholic steatohepatitis (NASH). Targeting these pathways is crucial for preventing the advancement of liver damage. Several key pathways and molecular targets have been identified to manage inflammation and fibrosis in NAFLD.

1.1.5.2.1 Apoptosis Signal-Regulating Kinase 1 (ASK1):

Apoptosis Signal-Regulating Kinase 1 (ASK1) is a key regulator of stress-induced apoptosis and inflammation, making it a promising target for the treatment of nonalcoholic fatty liver disease (NAFLD) and nonalcoholic steatohepatitis (NASH). ASK1 is activated by oxidative stress and endoplasmic reticulum (ER) stress, both of which are elevated in NAFLD. Once activated, ASK1 triggers downstream signaling through the JNK and p38 MAPK pathways, leading to inflammation, apoptosis, and fibrosis in the liver. In NAFLD and NASH, the activation of ASK1 contributes to hepatocyte injury, inflammation, and the activation of hepatic stellate cells (HSCs), which are central to the development of fibrosis. By inhibiting ASK1, these harmful processes can be attenuated, reducing liver inflammation and halting the progression of fibrosis. **Selonsertib**, an ASK1 inhibitor, has been a prominent candidate in clinical trials for NASH treatment. It showed initial promise in reducing liver fibrosis and improving other liver health markers by blocking

ASK1-mediated pathways.⁵⁴ However, larger phase III trials did not meet their primary endpoints, highlighting the complexity of NASH treatment. Despite these challenges, ASK1 remains an important therapeutic target, particularly for addressing oxidative stress-induced liver injury and fibrosis in NAFLD/NASH.⁵⁵

1.1.5.2.2 C-C Chemokine Receptor 2/5 (CCR2/CCR5):

C-C Chemokine Receptors 2 and 5 (CCR2/CCR5) are key mediators of inflammation in nonalcoholic fatty liver disease (NAFLD) and its more severe form, nonalcoholic steatohepatitis (NASH). These receptors are involved in recruiting monocytes and other immune cells to the liver, which contributes to inflammation and fibrosis, two central features of NASH progression. In NAFLD, increased expression of CCR2 and CCR5 promotes the migration of inflammatory cells to the liver, where they release pro-inflammatory cytokines and activate hepatic stellate cells (HSCs). This activation of HSCs leads to extracellular matrix deposition, driving liver fibrosis. Inhibiting CCR2/CCR5 signaling can reduce the influx of these immune cells, thereby lowering inflammation and halting fibrosis progression. Cenicriviroc, a dual CCR2/CCR5 antagonist, is one of the most prominent drug candidates targeting these receptors. Clinical trials have demonstrated its potential to reduce liver fibrosis and inflammation without worsening liver steatosis. Cenicriviroc has shown promise in improving fibrosis in patients with NASH, particularly in those with more advanced disease stages. By blocking CCR2/CCR5 pathways, drugs like Cenicriviroc offer a novel therapeutic approach to mitigating the inflammatory and fibrotic processes that drive NAFLD and NASH, potentially slowing disease progression and improving liver health.⁵⁶⁻⁵⁸

1.1.5.2.3 Galectin-3:

Galectin-3 is a multifunctional protein involved in inflammation and fibrosis, making it a promising target for the treatment of nonalcoholic fatty liver disease (NAFLD) and its more severe form, nonalcoholic steatohepatitis (NASH). Galectin-3 is highly expressed in activated macrophages and hepatic stellate cells (HSCs), both of which play key roles in liver inflammation and fibrosis. In NAFLD and NASH, Galectin-3 promotes the activation of HSCs, which leads to the excessive deposition of extracellular matrix proteins, contributing to fibrosis. It also amplifies inflammatory responses by enhancing the activity of macrophages, further driving liver injury and disease progression. By inhibiting Galectin-3, it is possible to reduce both inflammation and fibrosis, two central

features of NASH progression. **Belapectin**, a Galectin-3 inhibitor, has shown potential in clinical trials by reducing liver fibrosis in NASH patients, particularly those with cirrhosis. It works by blocking the fibrogenic and pro-inflammatory effects of Galectin-3, thus preventing further liver damage. Targeting Galectin-3 offers a promising therapeutic approach to mitigating the fibrotic and inflammatory processes in NASH. By addressing both aspects, Galectin-3 inhibitors could help slow disease progression, prevent cirrhosis, and improve liver function in NAFLD patients.⁵⁹⁻⁶⁰

1.1.6 COP1 E3 Ubiquitin Ligase: A Promising Therapeutic Target for NAFLD/NASH

Proteins are large, complex molecules composed of amino acids, and they serve as essential building blocks for all living organisms. They perform a vast array of functions within cells, including catalyzing biochemical reactions (enzymes), providing structural support, facilitating communication between cells (receptors and hormones), and regulating gene expression. Each protein's specific role is determined by its unique three-dimensional structure, which is determined by the sequence of amino acids encoded by the organism's DNA.

Protein degradation is essential for maintaining cellular balance and health. It ensures the removal of damaged, misfolded, or old proteins, preventing their toxic buildup, which can disrupt cell functions. Degradation also regulates key processes such as cell division, apoptosis, and stress responses by controlling the levels of specific proteins. Additionally, it helps cells adapt to changing conditions and conserve resources. Without proper protein degradation, cells would accumulate harmful proteins, leading to diseases like cancer and neurodegenerative disorders. Therefore, protein degradation is crucial for cellular function, stability, and overall organism health. The primary mechanisms for protein breakdown are autophagy and the ubiquitin-proteasome system (UPS), both of which are essential for preserving cellular equilibrium. Autophagy is a cellular process that degrades and recycles damaged organelles, misfolded proteins, and other cellular debris by engulfing them in autophagosomes, which fuse with lysosomes for breakdown. It helps maintain cellular homeostasis and survival, especially during stress or nutrient deprivation.⁶¹

The ubiquitin-proteasome system (UPS) is a highly regulated and essential cellular mechanism responsible for the degradation of most intracellular proteins, playing a key

role in maintaining protein homeostasis. This system ensures the timely removal of misfolded, damaged, or short-lived proteins, preventing their accumulation and supporting proper cellular function.⁶² The UPS also regulates various critical processes, such as cell cycle progression, DNA repair, transcription, and immune responses. Given its central role in maintaining cellular integrity, dysregulation of the UPS has been associated with numerous diseases, including cancer, neurodegenerative disorders, and immune dysfunctions. A crucial component of the UPS is the family of enzymes known as E3 ubiquitin ligases, which confer substrate specificity to the degradation process.⁶³ The UPS operates through a cascade involving three main enzymes: ubiquitin-activating enzymes (E1s), ubiquitin-conjugating enzymes (E2s), and ubiquitin ligases (E3s). E3 ligases are responsible for recognizing target proteins and facilitating the attachment of ubiquitin molecules to these substrates, marking them for degradation by the 26S proteasome. This process, known as ubiquitination, is a vital post-translational modification that determines the fate of proteins within the cell.⁶⁴ Given their role in selectively tagging proteins for degradation, E3 ligases are key regulators of cellular protein quality control and have emerged as promising therapeutic targets in various diseases.

1.1.6.1 Ubiquitin and Ubiquitination: Key Regulators of Cellular Homeostasis

Ubiquitin, a small 76-amino-acid protein discovered 40 years ago, is essential for regulating numerous cellular processes through a modification called ubiquitination, where it marks proteins for degradation or other cellular functions. This discovery transformed cell biology, as ubiquitination is now known to regulate almost all aspects of eukaryotic biology, from yeast to humans. The ubiquitination process involves a three-step enzymatic cascade—E1, E2, and E3 enzymes—that attaches ubiquitin to lysine residues on target proteins. This modification can be reversed by deubiquitinases (DUBs), ensuring dynamic regulation.

Ubiquitination is one of the most prevalent post-translational modifications, with tens of thousands of ubiquitination sites identified on cellular proteins. It can begin with the attachment of a single ubiquitin molecule (monoubiquitination) and extend to form polymeric chains. Ubiquitin can link to itself through any of its seven lysine residues or its N-terminal methionine, resulting in eight types of homotypic polyubiquitin chains, as

well as mixed and branched chains, collectively forming the "ubiquitin code." Recent studies have revealed that these different polyubiquitin linkages act as distinct signals for regulating processes such as protein degradation via the proteasome, selective autophagy, DNA repair, cell signaling, and cell cycle control.

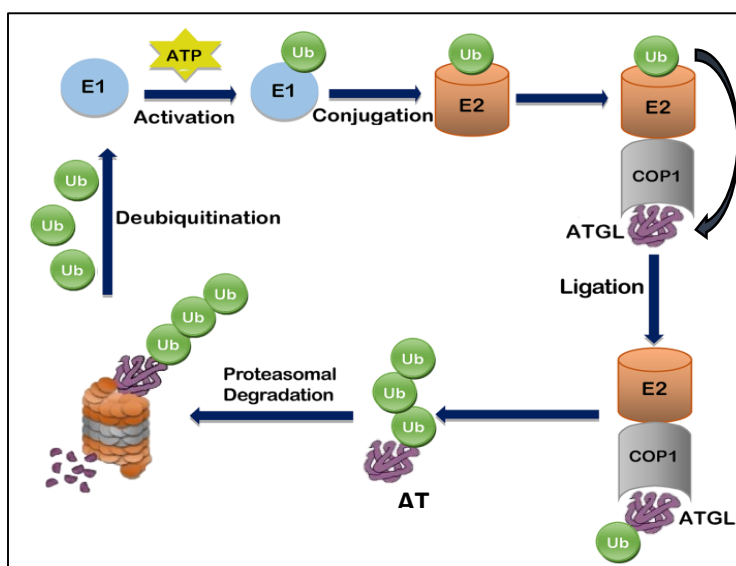


Figure 7. Different stages of ubiquitination and proteasomal degradation pathway

These discoveries, combined with advances in mass spectrometry and new tools to study specific ubiquitin modifications, have deepened our understanding of how different ubiquitin chains regulate cell function. The enzymes involved, particularly E3 ligases and DUBs, are highly specific and can control the assembly or removal of ubiquitin chains, making them crucial for maintaining cellular homeostasis. However, dysregulation of the ubiquitin system can lead to severe consequences, such as improper protein degradation, mislocalization of proteins, or aberrant signaling, contributing to diseases like cancer, neurodegenerative disorders, and immune dysfunctions. Given its widespread influence on critical cellular processes, the ubiquitin system, especially its enzymes, has become a significant target for drug development, offering therapeutic potential for a variety of diseases. As we continue to uncover the "ubiquitin code," we are getting closer to understanding how complex ubiquitin signals regulate essential biological processes, further highlighting the importance of this modification in both health and disease.

1.1.6.2 Mechanism and Biological Significance of E3 Ubiquitin Ligases:

E3 ubiquitin ligases are essential enzymes in the ubiquitin-proteasome system, a cellular pathway that regulates protein degradation and turnover. They facilitate the transfer of ubiquitin, a small regulatory protein, onto specific substrate proteins, marking them for degradation or altering their cellular functions.

1.1.6.2.1 Mechanism of Action:

The ubiquitination process involves a cascade of three main types of enzymes:

- **E1 Ubiquitin-Activating Enzyme:** This enzyme activates ubiquitin in an ATP-dependent manner, forming a high-energy thioester bond between ubiquitin and the E1 enzyme.
- **E2 Ubiquitin-Conjugating Enzyme:** The activated ubiquitin is then transferred to an E2 enzyme, which carries the ubiquitin to the E3 ligase.
- **E3 Ubiquitin Ligase:** The E3 ligase facilitates the transfer of ubiquitin from the E2 enzyme to the target substrate protein. This step is crucial for determining the specificity of substrate recognition and the type of ubiquitin linkage formed.

There are several classes of E3 ligases, each characterized by distinct structural domains and mechanisms:

- **RING (Really Interesting New Gene) E3 Ligases:** These contain a RING finger domain that mediates the interaction with E2 enzymes, positioning the ubiquitin for transfer to the substrate.
- **HECT (Homologous to E6-AP Carboxyl Terminus) E3 Ligases:** These ligases form a thioester bond with ubiquitin through a conserved cysteine residue in their HECT domain before transferring it to the substrate. This mechanism allows for the formation of polyubiquitin chains on the substrate.
- **RBR (RING-Between-RING) E3 Ligases:** These combine features of both RING and HECT ligases, possessing two RING domains that facilitate E2 recruitment and ubiquitin transfer, respectively.⁶³

1.1.6.2.2 Biological Significance:

E3 ligases play pivotal roles in various cellular processes, including:

- **Protein Degradation:** By ubiquitinating target proteins, E3 ligases mark them for degradation by the proteasome, thus regulating protein levels and function.
- **Signal Transduction:** Ubiquitination can modulate the activity of signaling proteins, thereby influencing pathways such as NF- κ B activation and DNA damage response.
- **Cell Cycle Regulation:** E3 ligases are involved in the timely degradation of cell cycle regulators, ensuring proper progression through the cell cycle.

Dysregulation of E3 ligase activity has been implicated in various diseases, including cancer, neurodegenerative disorders, and metabolic diseases. For instance, the E3 ligase Mdm2 targets the tumor suppressor p53 for degradation; overexpression of Mdm2 can lead to decreased p53 activity, contributing to tumorigenesis.

Understanding the specific modes of action of E3 ligases is crucial for developing therapeutic strategies that target aberrant ubiquitination processes in disease.

1.1.6.3 Constitutive of Photomorphogenesis (COP1)

Constitutive Photomorphogenesis 1 (COP1) plays a critical role in both plants and mammals, albeit with different biological functions due to their divergent life processes.

In plants: COP1 is a key regulator of photomorphogenesis, the light-dependent developmental process. In darkness, COP1 acts as an E3 ubiquitin ligase, targeting positive regulators of light signaling, such as HY5 (a transcription factor), for degradation, thereby suppressing light-induced development. Upon exposure to light, COP1 activity is inhibited, allowing photomorphogenesis to proceed, leading to chloroplast development, leaf expansion, and the activation of genes involved in photosynthesis. This makes COP1 essential for controlling the transition between skotomorphogenesis (dark-grown development) and photomorphogenesis (light-grown development).^{65,66}

In mammals: COP1's role extends beyond basic cellular maintenance to more complex processes involving tumor suppression, metabolic regulation, and stress responses. As an E3 ubiquitin ligase, mammalian COP1 primarily acts by targeting specific proteins for ubiquitination and subsequent degradation via the proteasome system. One of the key targets of mammalian COP1 is the tumor suppressor protein p53, which plays a central role in regulating cell cycle arrest, apoptosis, and DNA repair in response to cellular stress.

or DNA damage. By promoting the degradation of p53, COP1 can influence the balance between cell survival and apoptosis, making it a crucial regulator in cancer biology.⁶⁷

In addition to p53, COP1 also targets other transcription factors such as c-Jun and ETS family proteins, which are involved in cell proliferation, differentiation, and stress responses.⁶⁸ The ability of COP1 to regulate these transcription factors positions it as a key player in maintaining proper cellular growth and preventing hyperproliferation, a hallmark of cancer. Dysregulation of COP1, either through overexpression or mutation, has been linked to several cancers, including breast, prostate, and skin cancers, where its excessive activity leads to the degradation of tumor suppressors and unchecked cellular growth.⁶⁹

Recent studies have also shown that COP1 interacts with the circadian rhythm machinery, influencing metabolic processes by regulating the stability of clock proteins that control various metabolic pathways. This connection links COP1 to metabolic disorders, as disruptions in circadian regulation can lead to issues such as obesity and diabetes. Additionally, COP1's involvement in DNA damage responses indicates a broader role in preserving genome integrity, which is critical for preventing mutations that can lead to cancer.

Therefore, COP1 in mammals is not only a fundamental regulator of protein degradation but also a key player in maintaining cellular homeostasis, preventing tumorigenesis, and controlling metabolic and circadian processes. Its multifaceted roles make it a significant target for therapeutic interventions in cancer and metabolic diseases.

1.1.6.3.1 Role of COP1 in Cancers

COP1 (Constitutive Photomorphogenesis 1) plays a pivotal role in cancer biology, primarily through its function as an E3 ubiquitin ligase that regulates the degradation of key proteins involved in cell cycle control, tumor suppression, and stress responses. One of its most critical targets is the tumor suppressor protein p53, which is known as the "guardian of the genome" due to its role in inducing cell cycle arrest, apoptosis, and DNA repair in response to cellular damage. By promoting the ubiquitination and degradation of p53, COP1 can reduce p53 levels, diminishing the cell's ability to respond to stress and DNA damage. This mechanism can lead to uncontrolled cell proliferation, a hallmark of cancer.⁷⁰ In addition to p53, COP1 targets other proteins involved in cell growth and

differentiation, such as c-Jun, a transcription factor that regulates genes controlling proliferation and apoptosis. Through the degradation of c-Jun and other oncogenic or tumor suppressor proteins, COP1 has a dual role: while it can prevent abnormal cell growth by degrading oncogenic factors like c-Jun, it can also promote tumorigenesis by targeting tumor suppressors. Dysregulation of COP1, particularly its overexpression, has been linked to various cancers, including breast, prostate, and skin cancers. In these cases, COP1 overactivity leads to excessive degradation of tumor suppressors, tipping the balance towards oncogenesis. Research has shown that in some cancers, COP1 acts as an oncogene, while in others, it may behave as a tumor suppressor, depending on the cellular context and its interaction with other signaling pathways. Given its central role in regulating proteins involved in cancer progression, COP1 is being explored as a potential therapeutic target. Inhibiting COP1 activity could stabilize tumor suppressors like p53, providing a promising strategy for cancer treatments aimed at restoring proper cell cycle control and promoting apoptosis in cancer cells.⁷¹

1.1.6.3.2 Role of COP1 in Fatty Liver disease

Adipose triglyceride lipase (ATGL) plays a critical role in regulating hepatic lipid turnover, which is central to the development and progression of non-alcoholic fatty liver disease (NAFLD). ATGL is primarily responsible for hydrolyzing triglycerides into free fatty acids, thereby regulating lipid homeostasis in the liver. Disruption in ATGL function can lead to an accumulation of triglycerides, a key feature of NAFLD.⁷² The regulation of ATGL is complex and involves post-transcriptional modifications, particularly polyubiquitination and subsequent proteasomal degradation. The E3 ubiquitin ligase constitutive photomorphogenic 1 (COP1) is a crucial regulator of ATGL, controlling its stability and degradation. COP1 facilitates the polyubiquitination of ATGL, marking it for proteasomal degradation. Specifically, COP1 binds to ATGL through a consensus V-P (valine-proline) motif, a sequence critical for the interaction between COP1 and ATGL. Once bound, COP1 catalyzes the transfer of ubiquitin molecules to the lysine 100 (K100) residue of ATGL via K48-linked polyubiquitination, a tag that signals the protein for degradation by the proteasome. Experimental studies have demonstrated that mutation of the V-P motif of ATGL to alanine significantly impairs the binding of COP1 to ATGL. This mutation effectively blocks the ubiquitination process and inhibits the subsequent degradation of ATGL, leading to higher levels of the enzyme. The inability of COP1 to bind

and ubiquitinate ATGL in these mutant forms highlights the critical nature of the V-P motif in regulating ATGL's stability. Moreover, silencing COP1, both in vitro and in vivo, results in the loss of ATGL ubiquitination. This lack of ubiquitination prevents ATGL from being degraded, allowing for greater triglyceride breakdown. The absence of COP1 activity thus preserves ATGL levels, which in turn could enhance lipid turnover and mitigate the accumulation of hepatic fat associated with NAFLD. These findings underscore the importance of COP1 in the regulation of hepatic lipid metabolism through its control of ATGL degradation. Disrupting the COP1-ATGL interaction presents a potential therapeutic target for addressing NAFLD by preventing the degradation of ATGL, thereby promoting the breakdown of triglycerides and reducing lipid accumulation in the liver.⁷³

1.2 OBJECTIVE

The development of novel drug candidates for non-alcoholic fatty liver disease (NAFLD) aims to address its complexity and lack of effective treatments. Key objectives include targeting multiple pathways such as lipid metabolism, inflammation, and fibrosis, given that NAFLD involves diverse mechanisms like insulin resistance, oxidative stress, and progressive liver damage. A primary goal is to slow or reverse fibrosis, the key driver of disease progression, and improve liver histology and function.

Another objective is to manage metabolic comorbidities like obesity, type 2 diabetes, and cardiovascular risks, which are closely linked to NAFLD. New drugs should enhance insulin sensitivity, reduce body weight, and improve lipid profiles. Additionally, they must offer a better safety profile with fewer side effects, enabling long-term use.

Developing personalized treatment options based on patient-specific factors and genetic profiles is also crucial, as is reducing cardiovascular risks and overall healthcare costs associated with advanced liver disease. Ultimately, the aim is to improve patients' quality of life, prevent the progression to cirrhosis and liver failure, and reduce liver-related mortality and morbidity. Comprehensive and targeted therapies are essential to meet these objectives effectively.

Targeting the fibrotic stage in NASH may be less effective, as the damage at this stage is often irreversible due to collagen deposition and scar tissue formation. Instead, focusing on preventing or reversing early metabolic dysfunction could be more beneficial. Adipose triglyceride lipase (ATGL) plays a key role in regulating triacylglycerol (TAG) turnover in the liver, making it a promising drug target for addressing lipid accumulation.⁷⁴ Research in mice has shown that liver-specific ATGL knockdown leads to severe steatosis and impaired fatty acid oxidation, while overexpressing hepatic ATGL can significantly reduce lipid content in the liver. Additionally, studies indicate that ATGL expression is downregulated in NAFLD patients with insulin resistance, which further contributes to lipid buildup.^{75,76} The regulation of ATGL expression is complex and involves multiple pathways, including transcriptional regulation by FoxO1, mTORC1-Egr1, and peroxisome proliferator-activated receptor gamma (PPAR- γ). Understanding these pathways and their impact on ATGL could help in developing therapeutic strategies aimed at restoring

ATGL activity, reducing liver fat, and potentially halting the progression of NAFLD to NASH.

COP1, an ubiquitin-protein ligase initially identified in plants, plays a key role in regulating development by targeting photoreceptors and transcription factors for ubiquitination. As an E3 ligase, COP1 facilitates the degradation of several proteins, including p53, c-Jun, and ACC. In addition, COP1 significantly influences glucose homeostasis by modulating insulin secretion from pancreatic beta cells and inhibiting hepatic gluconeogenesis through the degradation of TORC2. Previous research has shown that COP1 ubiquitinates ATGL (adipose triglyceride lipase) in mammals, targeting it for proteasomal degradation in collaboration with PEDF.

In mammals, COP1 is crucial for survival, as its complete knockout results in embryonic lethality, indicating that irreversible inhibition of COP1 is not advisable. Despite its significance, there are currently no known COP1 inhibitors. Our primary objective was to design and synthesize novel small-molecule derivatives that could act as modulators within the COP1-ATGL pathway. The goal is to mitigate the ubiquitin-mediated degradation of ATGL, thereby enhancing ATGL activity and reducing triacylglycerol (TAG) levels in the liver. This approach aims to leverage the COP1-ATGL axis to address metabolic disorders associated with excessive lipid accumulation.^{77,78}

1.3 METHODOLOGY

1.3.1 Rational Design

Ghosh et. al reported that COP1 substrate ATGL contains V-P residue (Val361 and Pro362) at the substrate binding site of ATGL which is crucial for its binding with COP1 protein. When these V-P residues are mutated to alanine, the binding between ATGL and COP1 is significantly disrupted, highlighting the importance of this motif in their interaction. Moreover, it has been shown that the mutated ATGL leads to a significantly attenuated ubiquitination process, indicating that the V-P motif is crucial not only for COP1 binding but also for subsequent ubiquitination.⁷³ In a subsequent study, the co-crystal structure of human COP1 in complex with Trib1 (PDB: 5IGQ) revealed a shallow, highly conserved pocket on the COP1 surface that plays a key role in substrate recognition. The V-P (Valine-Proline) motif of Trib1 was found to be critical for this binding interaction. The substrate binding occurs through the fitting of V-P residues into this shallow pocket of COP1, which is formed by a set of specific residues: Arg515, Trp517, Asp534, Asn557, Cys559, Ala576, Lys600, Ala601, Ser603, Ser617, Thr618, Asn641, Lys643, Asn644, and Phe645. This interaction facilitates the targeted degradation of the substrate through ubiquitination by COP1 (Figure 8). However, there is no direct evidence yet to confirm the binding of ATGL by COP1. Additionally, there is no conclusive proof that Trib1 serves as a direct target for COP1-mediated ubiquitination. Nonetheless, some studies suggest that Trib1 can modulate COP1's substrate selectivity. The rationale for this study lies in the key interaction between the pseudokinase Trib1 and the WD40 domain of COP1. We hypothesized that small molecules designed to fit into the V-P binding motif of COP1 (comprising residues Arg515, Trp517, Asp534, Asn557, Cys559, Ala576, Lys600, Ala601, Ser603, Ser617, Thr618, Asn641, Lys643, Asn644, and Phe645) could mimic the peptidic interaction seen in substrate recognition. By occupying this binding pocket, these small molecules could potentially stabilize COP1, thereby preventing the ubiquitination of ATGL and ultimately stabilizing ATGL levels.

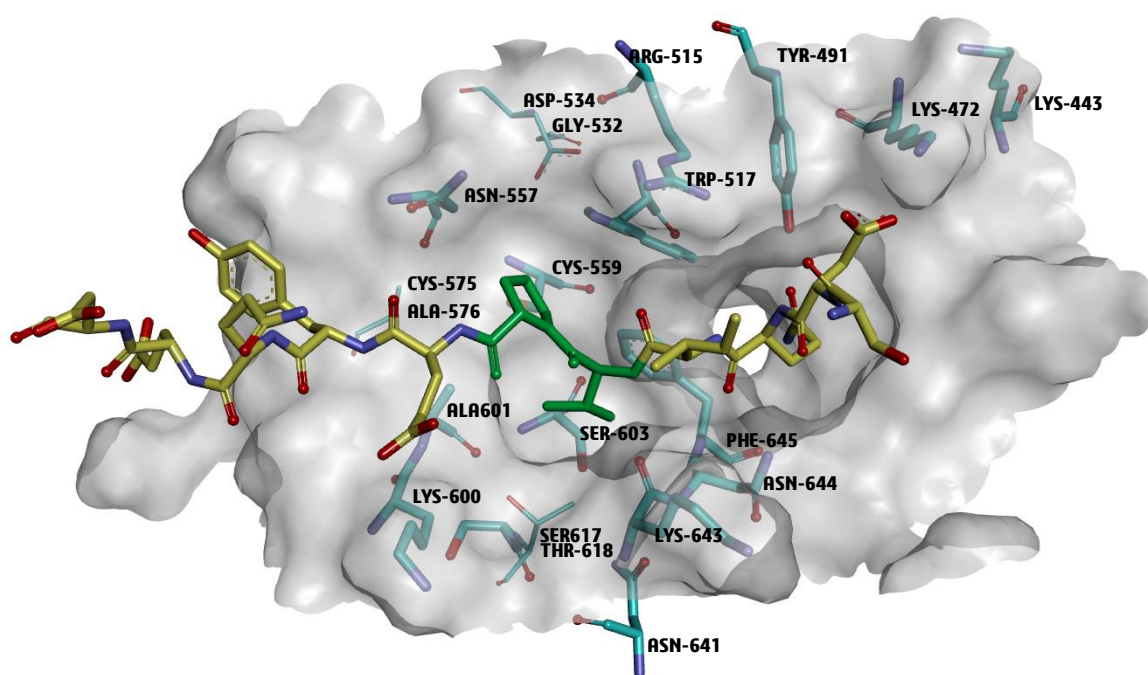


Figure 8. V-P binding pocket marked as green. The V-P pocket is consensus towards binding with different substrates. This shallow pocket comprised 15 different amino acid residues.

In our present work we report design, synthesis and evaluation of quinazolinone and quinazolinone based derivatives that can effectively occupy V-P binding site of COP1 to prevent its interaction with ATGL. By modulating COP1-ATGL pathway the synthesized small molecules can reduce ATGL ubiquitination followed by its proteasomal degradation. Thus the lipase activity of ATGL is enhanced to deplete hepatic TAG content. Developing a drug candidate involves more than just identifying biologically active compounds. Academic researchers often face limitations in accessing advanced drug development resources, like high-throughput screening (HTS), which are essential for discovering new chemotypes. To overcome these limitations, we started with a quinazolinone scaffold and utilized medicinal chemistry principles to identify the essential pharmacophoric features, thereby establishing the activity guided structure-activity relationship (SAR).

The structural optimization process began with the introduction of various linkers at the N3 position on the right-hand side (RHS), along with the concurrent incorporation of a urea linkage featuring appropriate aromatic and aliphatic substitutions at the C6 position on left hand side (LHS). The urea linkage was introduced to replicate the peptide bond

found in the substrate, which is crucial for key interactions with the COP1 substrate binding domain. **Compound A** was the first hit compound with 2-methoxy ethyl linker at N3 position (RHS) and a methoxy (-OCH₃) group at the meta position of the phenyl ring (LHS). After several modifications **compound B** with a keto-methyl group (-COCH₃) in place of methoxy (-OCH₃) group of **compound A** showed better biological results. Optimization up to this stage was done by Dr. Dipayan Sarkar (Dr. Arindam Talukdar's Lab, CSIR-IICB). Lead molecules were selected based on their ability to demonstrate dose-dependent stabilization of cellular ATGL and COP1 proteins, confirmed through western blot assays and in vitro ADME studies. Further biological validation of the lead compound was conducted by showing a reduction in the ubiquitination of ATGL and COP1 through immunoprecipitation studies. **Compound B** exhibited remarkable efficacy in stabilizing both COP1 and ATGL proteins. It can also prevent the ubiquitination process of ATGL. However, the in vitro ADME profile was not up to the mark. **Compound B** displayed very poor aqueous solubility of 2.56 µg/mL at pH 7.4 and demonstrated low plasma stability in both mouse (14.2% remaining after 2 hours) and human (16.9% remaining after 2 hours). Although its liver microsomal stability was excellent (mouse CL_{int}: 8.15 µL/min/mg protein, half-life: 86.96 min, %QH: 18.08; human CL_{int}: 5.84 µL/min/mg protein, half-life: 119.4 min, %QH: 21.26), the overall ADME profile of **Compound B** suggests it may not be suitable as a lead candidate.

In search of a better lead candidate at first, we intended to explore the chemical space around C5 position of **Compound B** with various aromatic and aliphatic functional groups keeping other parts constant (Set-1 derivatives). Next, we focused on the development of the C2 position by incorporating different aliphatic basic amine containing functional groups to get lead candidate with increased kinetic solubility (Set-2 derivatives). Furthermore, we focused on synthesizing an alternative heterocycle, quinazolinedione, to explore potential improvements (Set-3 derivatives). Lead optimization was also carried out by monitoring the ability of active compounds to suppress cellular lipid accumulation through confocal microscopy using oleate induced HepG2 cell line. The lead compound underwent further validation in mouse primary hepatocytes and was therapeutically tested in a high-fat diet (HFD)-induced NASH mouse model. To support these findings, molecular docking studies were carried out to confirm that the small molecules engage with the V-P motif of COP1, which stabilizes COP1 and prevents the ubiquitin-mediated degradation of ATGL.

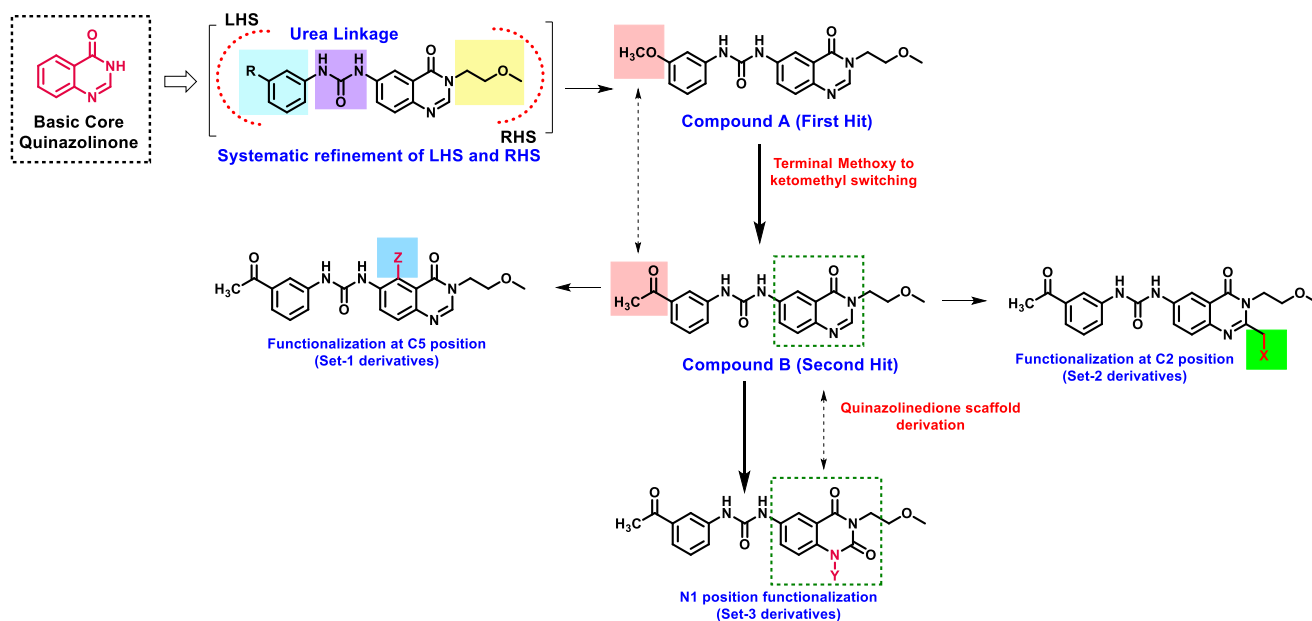


Figure 9. Structural features of quinazolinone and quinazolinone-based small molecule modulators

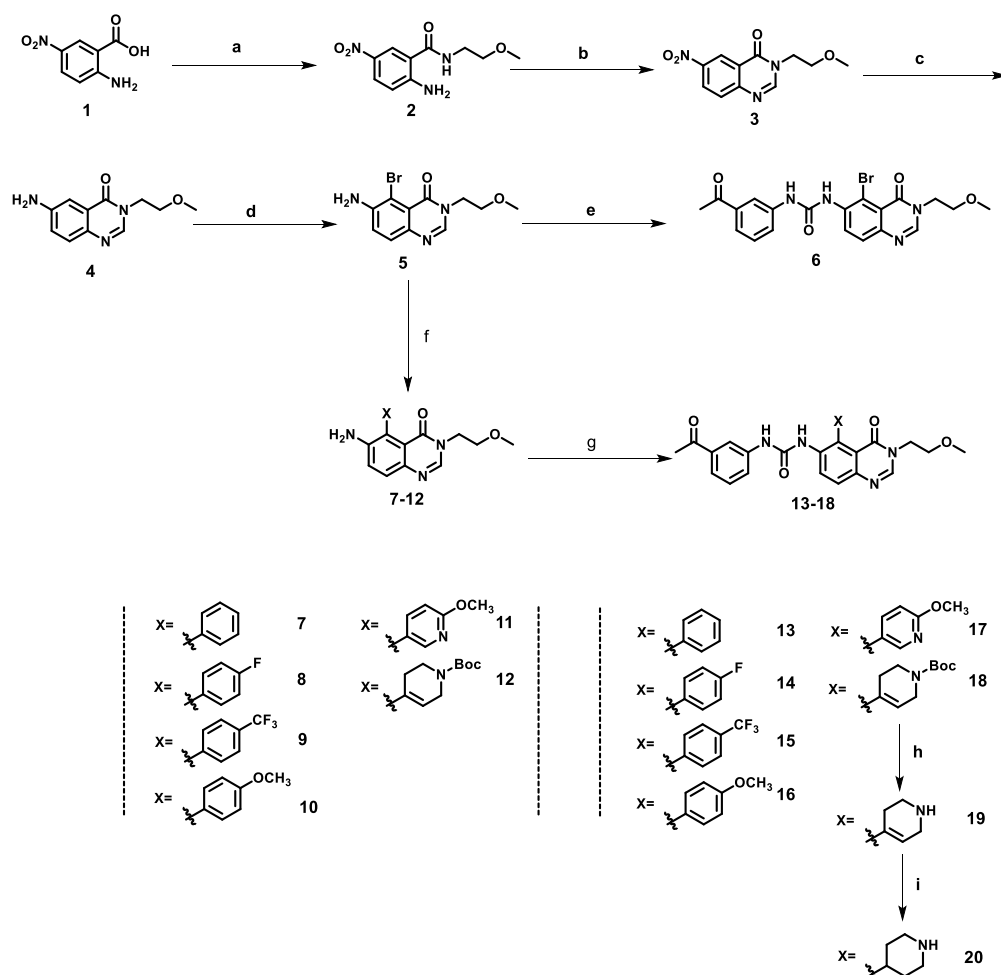
1.3.2 Chemistry

1.3.2.1 Modifications at C5 position (Set-1)

Scheme 1 describes synthetic procedures, strategies and methods for the synthesis of quinazolinone analogues with modifications at the C5 position. Reaction strategies were started by amide coupling reaction of commercially available 5-Nitroanthranilic acid (**1**) with 2-methoxyethylamine (1.2 equiv.) using HATU (1.2 equiv.) as coupling agent in dry DMF as a solvent and TEA (2.5 equiv.) as a base at room temperature (25-30 °C) for 2 hours to afford **compound 2**. Reaction progress was monitored by checking TLC. Cyclized product (**compound 3**) was obtained by reacting **compound 2** with trimethyl orthoformate at 105 °C for 12-18 hours. The nitro group (-NO₂) at the C6 position of the **compound 3** was reduced to -NH₂ by purging hydrogen gas using 10% wet palladium-charcoal (Pd/C) in methanol at room temperature (25-30 °C) for 4-8 hours to obtain **compound 4**. To incorporate a bromo group (-Br) at C5 position of **compound 4**, bromination reaction was carried out by using liq Br₂ (1.2 equiv) in dry DCM and acetic acid (AcOH) as solvent at room temperature (25-30 °C) for 3 hours to get **compound 5**. In the next step urea linkage was introduced by reacting **compound 5** with 4-nitrophenyl chloroformate (1.2 equiv) in dry THF followed by addition of 3'- aminoacetophenone (1.2 equiv), and TEA (2.5 equiv) as a base at room temperature (25-30 °C) for 4 hours to get **compound 6**. Different aromatic substitutions were inserted in C5 of **compound 5** via

C–C cross-coupling reactions (Suzuki–Miyaura coupling) using $\text{Pd}_2(\text{dba})_3$ (0.1 equiv), X-Phos (0.2 equiv) in dioxane/ H_2O (9:1 solvent ratio v/v) at 120 °C for 12–18 h in presence of Cs_2CO_3 (2 equiv) as base and various boronic acids (1.2 equiv) to obtain **7–12**.

Scheme 1^a:



Reagents and conditions: (a) HATU (1.2 equiv.), dry DMF, 2-methoxyethylamine (1.2 equiv.), TEA (2.5 equiv.) room temperature (25–30 °C), 2 h, (yield 85–90%); (b) Trimethylorthoformate (10–15 equiv.), 105 °C, 12–18 h, (yield 85–90%); (c) H_2 / Pd-C, MeOH, room temperature (25–30 °C), 4–8 h, (yield 90–95%); (d) bromine (1.2 equiv) in dry DCM, AcOH, room temperature (25–30 °C), 3 h, (yield 66%); (e) 4-nitrophenyl chloroformate (1.2 equiv), 3'-aminoacetophenone (1.2 equiv), dry THF, TEA (2.5 equiv), room temperature (25–30 °C), 4 h, (yield 42%) for **compound 6**; (f) various boronic acids (1.2 equiv), $\text{Pd}_2(\text{dba})_3$ (0.1 equiv), X-Phos (0.2 equiv), dioxane/ H_2O (9:1), Cs_2CO_3 (2 equiv), 120 °C, 12–18 h, (yield 62–72%); (g) 4-nitrophenyl chloroformate (1.2 equiv), 3'-aminoacetophenone (1.2 equiv), dry THF, TEA (2.5 equiv), room temperature (25–30 °C), 2–8 h, (yield 44–52%); (h) TFA (10 equiv), dry DCM, 0 °C to room temperature (25–30 °C), 2 h, (yield 61%) for **compound 19** (i) H_2 / Pd-C, MeOH, room temperature (25–30 °C), 4 h, (yield 42%) for **compound 20**.

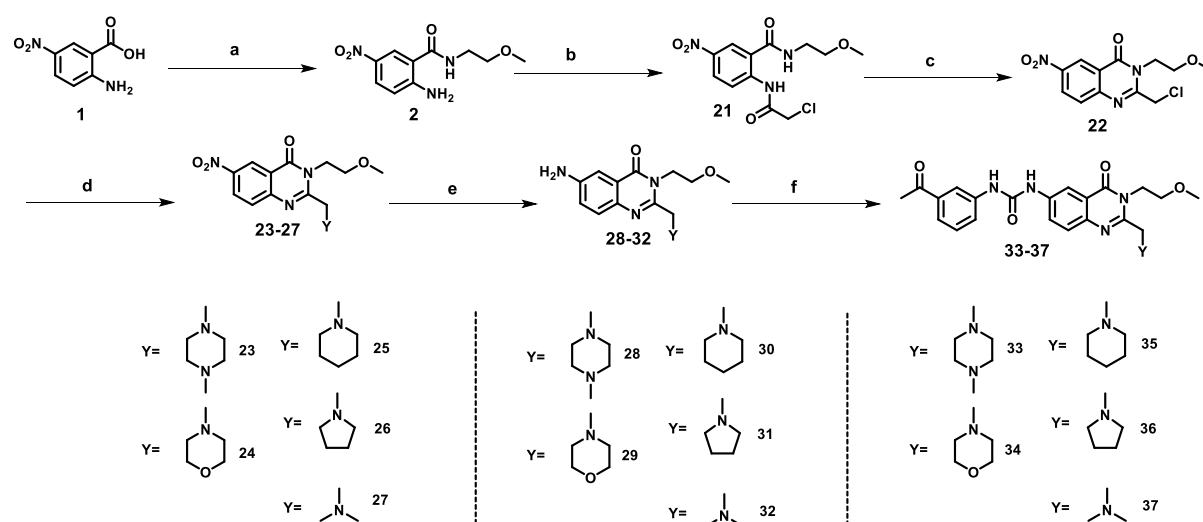
Compounds 13–18 were synthesized by following similar urea coupling reactions as mentioned before. Boc-deprotection reaction of **18** was carried out by reacting it with trifluoroacetic acid (TFA, 10 equiv) in dry DCM stirred at 0 °C to room temperature

(25–30 °C) for 2 hours to synthesise **compound 19**. Hydrogenation of **compound 19** was carried out with hydrogen gas (H₂) in the presence of 10% wet Pd/C catalyst in MeOH at room temperature (25–30 °C) for 4 hours to get **compound 20**.

1.3.2.2 Modifications at C2 position (Set-2)

Scheme 2 describes synthetic procedures, strategies and methods for the synthesis of quinazolinone analogues with modifications at the C2 position. Reaction strategies were started by amide coupling reaction of commercially available 5-Nitroanthranilic acid (**1**) with 2-methoxyethylamine (1.2 equiv.) using HATU (1.2 equiv.) as coupling agent in dry DMF as a solvent and TEA (2.5 equiv.) as a base at room temperature (25–30 °C) for 2 hours to afford **compound 2**. It was then reacted with chloroacetyl chloride in dry DCM at 120 °C for 16 h) at room temperature (25–30 °C) for 3 h to get **compound 21**. Cyclized **compound 22** was obtained by reacting **compound 21** with ZnCl₂ and HMDS at 80 °C for 1 h.

Scheme 2^a:



^aReagents and conditions: (a) HATU (1.2 equiv.), dry DMF, 2-methoxyethylamine (1.2 equiv.), TEA (2.5 equiv.) room temperature (25–30 °C), 2 h, (yield 85–90%); (b) chloroacetyl chloride (1.2 equiv.), TEA (2 equiv.), in dry DCM, room temperature (25–30 °C), 3 h, (yield 66%); (c) ZnCl₂ (4 equiv.), HMDS (8 equiv.) in dry DMF, 80 °C, 1 h, (yield 88%); (d) amines (2 equiv.) in dry Toluene, reflux, 2 hr, (yield 82%); (e) H₂/Pd-C, MeOH, room temperature (25–30 °C), 4 h, (yield 52%); (f) 4-nitrophenyl chloroformate (1.2 equiv), 3'-aminoacetophenone (1.2 equiv), dry THF, TEA (2.5 equiv), room temperature (25–30 °C), 2–8 h, (yield 42–56%).

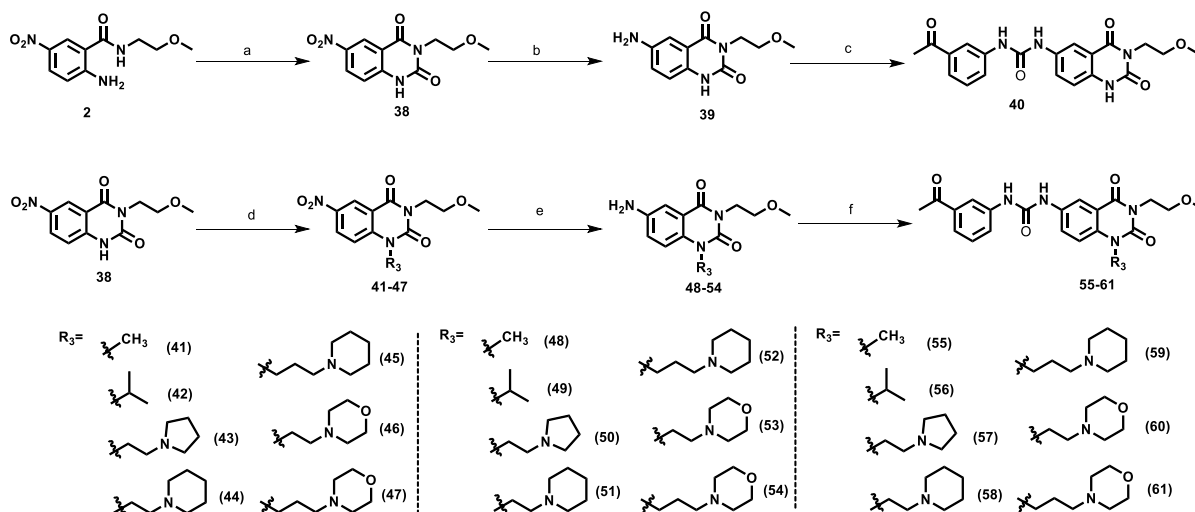
The intermediate **compound 22** was then subjected to react with different amines to get **compounds 23–24**. Reaction was done using dry toluene in refluxing condition. The nitro group (–NO₂) at the C6 position of the **compounds 23–24** was reduced to –NH₂ by purging

hydrogen gas using 10% wet palladium-charcoal (Pd/C) in methanol at room temperature (25-30 °C) for 4-8 hours to obtain **compounds 28-32**. **Compounds 33-37** were synthesized by following similar urea coupling reactions as mentioned before.

1.3.2.3 Modifications from Quinazolinone to Quinazolinedione Core (Set-3)

Scheme 3 describes synthetic procedures, strategies and methods for the synthesis of quinazolinedione analogues from quinazolinone scaffold. To prepare a new set of derivatives we intended to functionalize N1 position of quinazolinedione scaffold. Reaction scheme started with the cyclisation of previously prepared **compound 2** to get quinazolinedione scaffold (**compound 38**) using carbonyldiimidazole (CDI, 1.5 equiv) in dry DMF at 120 °C for 16 h. The nitro group (–NO₂) in **compound 38** was converted to an amino group (–NH₂) through a hydrogenation reaction. This transformation was achieved using a 10% wet palladium-charcoal (Pd/C) catalyst in methanol (MeOH) at room temperature (25–30 °C) while continuously purging with hydrogen gas (H₂) for a duration of 4 h, resulting in the formation of **compound 39**. In the next step urea linkage was introduced by reacting **compound 39** with 4-nitrophenyl chloroformate (1.2 equiv) in dry THF followed by addition of 3'- aminoacetophenone (1.2 equiv), and TEA (2.5 equiv) as a base at room temperature (25–30 °C) for 4 h to get **compound 40**. Various aliphatic and heterocyclic functionality containing flexible hydrocarbon side chains were incorporated in **compound 40** by nucleophilic substitution reactions (S_N2) using various alkyl chlorides (1.5 equiv), K₂CO₃ (2.2 equiv) as a base in dry DMF at 120 °C for 14–16 h to afford analogues **41-47**. Nitro reduction reactions of **compounds 41-47** was carried out to afford **48-54** by using 10% wet Pd-C in MeOH and charged with H₂ gas in MeOH at room temperature (25–30 °C) for 4–6 h. Final compounds (**55-61**) containing urea linkage were synthesized by following same method as described earlier.

Scheme 3^a:



^aReagents and conditions: (a) CDI (1.5 equiv), dry DMF, 120 °C, 16 h, (yield 85%); (b) H₂/ Pd-C, MeOH, room temperature (25–30 °C), 4 h, (yield 82%); (c) 4-nitrophenyl chloroformate (1.2 equiv), 3'-aminoacetophenone (1.2 equiv), dry THF, TEA (2.5 equiv), room temperature (25–30 °C), 6 h, (yield 62%); (d) various R₃-X (aliphatic alkyl chloride with different carbon chain length, 1.5 equiv), K₂CO₃ (2.2 equiv), dry DMF, 120 °C, 14–16 h; (yield 70–84%); (e) H₂/ Pd-C, MeOH, room temperature (25–30 °C), 4–6 h, (yield 90–96%) (f) p-nitrophenylchloroformate (1.2 equiv), 3'-aminoacetophenone (1.2 equiv), dry THF, TEA (2.5 equiv), room temperature (25–30 °C), 2–8 h, (yield 40–52%).

1.4 RESULTS AND DISCUSSION

We have reported previously the design, synthesis and evaluation of quinazolinone based analogues modifying at N3 and C6 positions; which yielded **compound B** as potential hit. Due to getting poor ADME results we focused on incorporating various substituted aromatic rings at C2, C5 position of quinazoline moiety followed by modifications at N1 position of quinazolinone moiety in our present study. As a preliminary screen, we chose to look at the ATGL protein levels after treatment with the given small molecules in increasing doses for 24 hours. The compounds were classified into 'active', 'moderately active' and 'inactive' based on their ability to increase ATGL protein levels in the western blot analysis. Confocal microscopy was performed to validate the reduction of lipid droplets in oleate induced HepG2 cell line. In the absence of a reporter assay to guide the progression of SAR, the newly synthesized molecules were investigated for their ability to disrupt COP1-ATGL interaction thereby obstructing the ATGL ubiquitination and increasing ATGL protein levels. The study was initiated based on a medicinal chemistry approach to identify a minimal substitution pattern around the quinazolinone and quinazolinone scaffold required to attain COP1-ATGL stabilization.

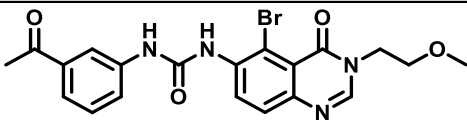
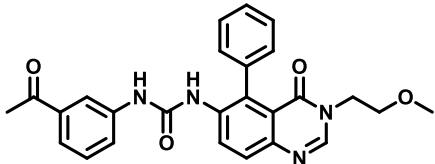
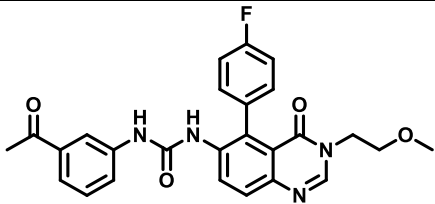
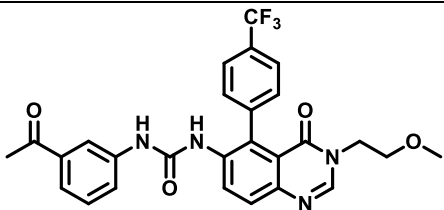
1.4.1 SAR development

1.4.1.1 Set-1 strategies

The study began with the idea of incorporating various substituted aromatic rings at C5 position of **compound B** keeping 2-methoxyethyl linker at N3 position and ketomethyl functionality containing phenyl urea linkage at the C6 position of the quinazolinone ring. At first we prepared the brominated analogue (**compound 6**) of **compound B** and checked its ability to increase ATGL protein levels dose-dependently in the western blot analysis. To our satisfaction, **compound 6** exhibited the ability to stabilize ATGL and COP1 protein, thus designated as active (Table 1). Being an E3 ligase, COP1 is responsible for the proteasomal degradation of ATGL by ubiquitinating it. The active compounds identified through the dose-dependent screening assay are anticipated to decrease ATGL ubiquitination, thereby increasing ATGL protein levels. To validate this, we conducted an immunoprecipitation assay using HepG2 cells overexpressing myc-tagged ATGL. The cells were transfected with HA-tagged ubiquitin and subsequently treated with 5 μ M of the selected compounds. Prior to harvesting, the cells were incubated with MG-132, a

proteasomal inhibitor. Immunocomplexes were pulled down using an anti-myc antibody, and immunoblotting was performed with an anti-HA antibody to detect ubiquitinated ATGL. Since the derivative **6** was showing significant activity, prompted us for further evaluation of its ability to reduce ATGL ubiquitination. The results indicated that **compound 6** effectively blocked the ubiquitination of ATGL by COP1, as shown in **Table 1**. This finding supports the potential of **compound 6** as a modulator of the COP1-ATGL axis to enhance ATGL stability. **Compound 13** containing only the phenyl ring at C5 showed modest activity in terms of protein stabilization. Subsequent validation revealed **compound 13** not being able to block the ATGL ubiquitination process. Subsequent validation experiments revealed that **compound 13** was not effective in blocking the ubiquitination of ATGL.

Table 1. Activity chart based on western blot analysis

Compound	Structure	Dose-response activity ^a	Ubiquitination Status ^b
6		++	Blocked Ubiquitination
13		+	Did not block ubiquitination
14		—	NP
15		—	NP

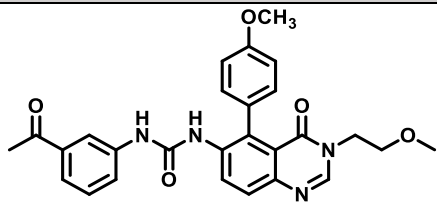
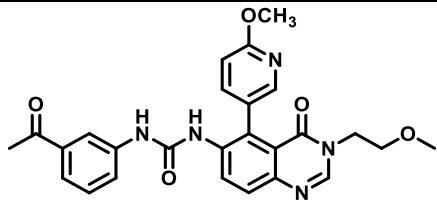
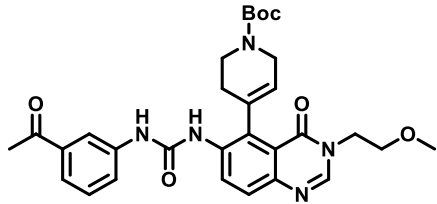
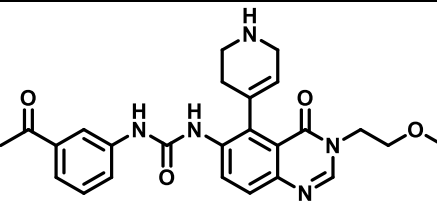
^aActivity profile: '—', not active; '+', moderately active; '++', best active. NP, not performed as molecules did not show dose dependant stabilization of COP1 and ATGL.

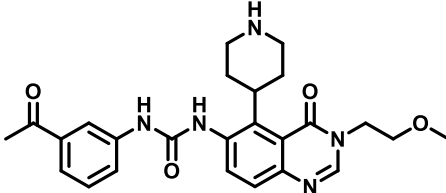
^bImmunoprecipitation studies were performed at a 5 μ M concentration of the compound.

This indicates that, unlike **compound 6**, **compound 13** lacks the ability to interfere with the COP1-mediated ubiquitination process of ATGL. Next, a couple of compounds comprising electron withdrawing fluoro (-F) (**compound 14**) and trifluoromethyl (-CF₃) functionalities were prepared (**compound 15**). Unfortunately, none of the them exhibited the ability to stabilize ATGL and COP1 proteins at 10 μ M concentration (Table 1).

To investigate further, we introduced electron donating functional groups like 4-methoxyphenyl (**16**) and 2-methoxypyridyl (**17**) groups at C5. But none of them showed activity (Table 2). Apart from aromatic substitutions at the C5 position, a few aliphatic modifications with basic nitrogen atom were inserted in **18**, **19** and **20**. Unfortunately, these replacements did not show any activity in the stabilization of both ATGL and COP1 (Table 2).

Table 2. Activity chart based on western blot analysis

Compound	Structure	Dose-response activity ^a	Ubiquitination Status ^b
16		—	NP
17		—	NP
18		—	NP
19		—	NP

Compound	Structure	Dose-response activity ^a	Ubiquitination Status ^b
20		—	NP

^aActivity profile: '-', not active; '+', moderately active; '++', best active. NP, not performed as molecules did not show dose dependant stabilization of COP1 and ATGL.

^bImmunoprecipitation studies were performed at a 5 μ M concentration of the compound.

In this series of developments, the bromo-substituted compound at the C5 position, designated as **compound 6**, showed promising results during the initial screening. Additionally, immunoprecipitation studies indicated that **compound 6** effectively reduced ATGL ubiquitination. However, despite these positive findings, **compound 6** exhibited very poor aqueous solubility of 3.4 μ g/mL at pH 7.4 (Table 5) and demonstrated low human plasma stability, with only 10.3% remaining after 2 hours (Table 6). These limitations suggest that **compound 6** lacks the essential pharmacokinetic properties required for further progression as a viable drug candidate.

1.4.1.2 Set-2 strategies

In further development we aimed to incorporate aliphatic substitutions including basic amines at C2 position to improve overall kinetic solubility. At first a couple of compounds with N-Methylpiperazine and morpholine groups followed by one carbon spacer were prepared (**compounds 33** and **34**). Both of them exhibited modest ability to stabilize ATGL and COP1 protein but they failed to block the ubiquitination of ATGL (Table 3). Then we introduced piperidine group in place of morpholine in **34** to prepare **35** which demonstrated effective stabilization of both ATGL and COP1 proteins and successfully inhibited ATGL ubiquitination (Table 3). However, despite the activity **compound 35** showed poor aqueous solubility of 2.1 μ g/mL at pH 7.4 (Table 5). Next, the piperidine in **35** was replaced with pyrrolidine and dimethylamine in **compound 36** and **37**. Both compounds demonstrated a modest ability to stabilize ATGL and COP1 proteins; however, they were unable to effectively inhibit ATGL ubiquitination. (Table 3).

Table 3. Activity chart based on western blot analysis

Compound	Structure	Dose-response activity ^a	Ubiquitination Status ^b
33		+	Did not block ubiquitination
34		+	Did not block ubiquitination
35		++	Blocked Ubiquitination
36		+	Did not block ubiquitination
37		+	Did not block ubiquitination

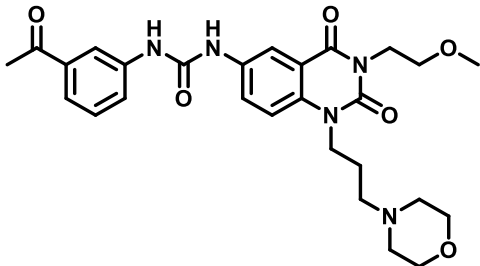
1.4.1.3 Set-3 Strategies

Variations at the C6, C5, and C2 positions of the quinazolinone moiety allowed us to identify **compounds B, 6 and 35** as potential hit compounds. However, all of them exhibited poor ADME profiles, indicating a lack of suitable drug-like properties necessary for further development as therapeutic candidates. In the next phase of development, we sought to modify the N1 position but it was conformationally locked by a double bond. We made slight modifications to the heterocyclic core by introducing a carbonyl group at the C2 position to create a cyclic amide. This strategic change led to the generation of a

new core structure, **quinazolinedione**, which aimed to enhance the compound's drug-like properties and optimize its biological activity. Quinazolinedione scaffold was found to have certain advantages in terms of better plasma stability and metabolic stability. Next, we focused on preserving the essential functionalities on both the right-hand side (RHS) and left-hand side (LHS) to retain biological activity. We then constructed a series of quinazolinedione derivatives. Leveraging our understanding of the key pharmacophoric features in the quinazolinone core, we strategically fixed the 2-methoxy ethyl linker at the N3 and a keto-methyl group (-COCH₃) at the C6 positions with suitable functionalities similar to those in **compound B** to synthesize **compound 40** to evaluate the effectiveness of the quinazolinedione scaffold in enhancing the desired biological activity. **Compound 40** demonstrated effective stabilization of both ATGL and COP1 proteins and successfully inhibited ATGL ubiquitination (Table 4). However, it showed very poor aqueous solubility, with a solubility of only 0.8 µg/mL at pH 7.4 (Table 5). On the positive side, **compound 40** displayed improved plasma stability, achieving 68.4% stability in mouse plasma and 97.4% in human plasma after 2 hours (Table 6). Additionally, the microsomal stability metrics were favorable, with mouse liver microsomes showing a clearance rate (CL_{int}) of 11.4 µL/min/mg protein, a half-life of 75.2 minutes, and %QH of 22.8. For human liver microsomes, **compound 40** exhibited a CL_{int} of 1.8 µL/min/mg protein, a half-life of 429.9 minutes, and %QH of 7.6 (Table 6). These findings indicate that the quinazolinedione scaffold holds promise, providing valuable insights for further structural modifications to improve solubility while retaining biological activity and stability.

Table 4. Activity chart based on western blot analysis

Compound	Structure	Dose-response activity ^a	Ubiquitination Status ^b
40		++	Blocked Ubiquitination
55		++	Blocked Ubiquitination
56		—	NP
57		++	Did not block ubiquitination
58		++	Blocked Ubiquitination
59		—	NP
60		—	NP

Compound	Structure	Dose-response activity ^a	Ubiquitination Status ^b
61		—	NP

^aActivity profile: '-', not active; '+', moderately active; '++', best active. NP, not performed as molecules did not show dose dependant stabilization of COP1 and ATGL.

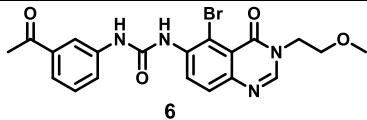
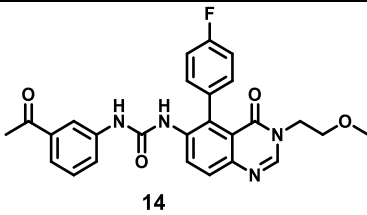
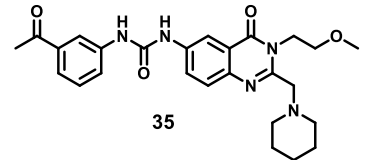
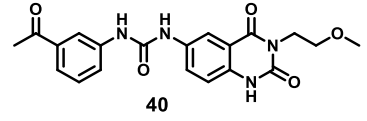
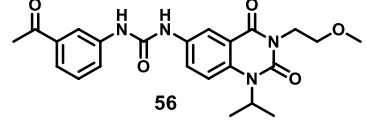
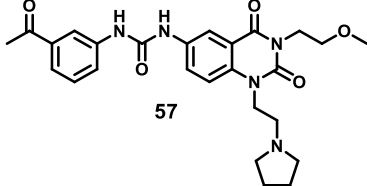
^bImmunoprecipitation studies were performed at a 5 μ M concentration of the compound.

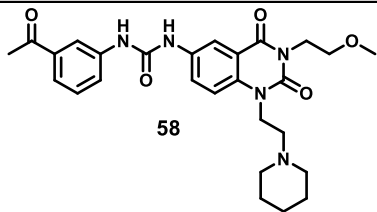
To explore the N1 position, we introduced various substituted aliphatic groups into the quinazolinone framework. Initially, we incorporated a small methyl group ($-\text{CH}_3$) in **compound 55**, which retained its activity by stabilizing both ATGL and COP1 proteins as confirmed by Western blot analysis and reducing ATGL ubiquitination (Table 4). Next, an isopropyl group was introduced to yield **compound 56**, but it failed to show the desired stabilization of ATGL and COP1 (Table 4). Despite its moderate ADME profile, **compound 56** exhibited poor solubility (2.8 $\mu\text{g/mL}$ at pH 7.4, Table 5).

To address the solubility concern, we introduced basic nitrogen substituents with various hydrocarbon chain lengths in **compounds 57-61**. **Compound 57**, featuring two hydrocarbon side chains with a pyrrolidine moiety, showed dose-dependent stabilization of ATGL and COP1 proteins (Table 4) and significantly improved solubility (124.3 $\mu\text{g/mL}$ at pH 7.4, Table 5) with a preferable log D value of 2.58 (Table 5). Although **57** exhibited enhanced metabolic stability (Table 6) with a mouse CL_{int} of 13.0 $\mu\text{L/min/mg}$ protein and half-life of 53.7 minutes, its plasma stability was suboptimal (50.3% in mouse and 32.8% in human after 2 hours). Moreover, immunoprecipitation data indicated that **57** did not effectively inhibit ATGL ubiquitination. Using a similar approach, we introduced a piperidine moiety with two hydrocarbon spacers to create **compound 58**. This compound effectively stabilized both ATGL and COP1 proteins (Table 4) and blocked the ubiquitination of both proteins, as confirmed by immunoprecipitation studies. Confocal microscopy data revealed a reduction in lipid droplets in HepG2 cells (Figure 11). **Compound 58** demonstrated high solubility (115.5 $\mu\text{g/mL}$ at pH 7.4, Table 5) and an

optimal log D value of 2.78 (Table 5). It also exhibited improved plasma stability (103.3% in mouse and 110.08% in human after 2 hours, Table 6) and acceptable metabolic stability (Table 6). To satisfy our curiosity, we intended to extend the chain length from two hydrocarbon to three hydrocarbon spacer keeping piperidine moiety as intact in **59**. However, the molecule was not active (Table 4). We also made efforts to synthesize more solubilizing components like morpholine instead of piperidine with different chain lengths. Compound **60** and **61** were made but unfortunately these analogues were inactive (Table 4). Considering these promising results, **compound 58** was identified as a potential lead candidate for in vivo studies.

Table 5. *in-vitro* ADME studies for synthesized compounds (Log D and Aq. Solubility)

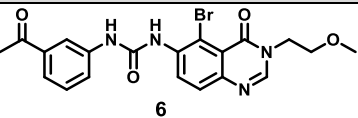
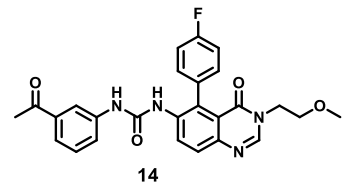
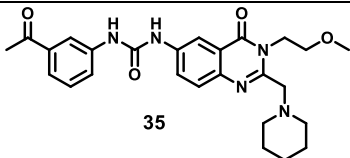
Compound	PSA ^a (Å ²)	LogD	Aq. solubility pH : 7.4 (µg / mL)
 6	100.1	1.95	3.4
 14	100.1	1.90	31.9
 35	103.34	1.60	2.1
 40	116.84	2.17	0.8
 56	108.05	2.67	2.8
 57	111.29	2.58	124.3

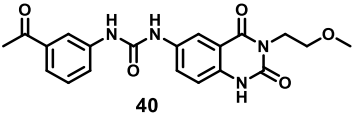
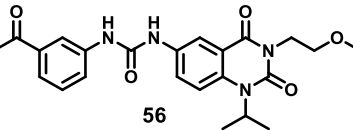
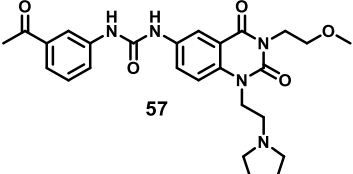
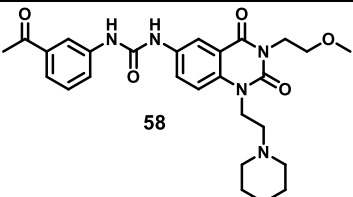
Compound	PSA ^a (Å ²)	LogD	Aq. solubility pH : 7.4 (µg / mL)
 58	111.29	2.78	115.5
Ketoconazole ^b	—	3.54	—
Metoprolol ^c	—	-0.28	—
Propanolol ^d	—	0.84	—
Albendazole ^e	—	—	2.2

^aPolar surface area. ^bKetoconazole was taken as standard for logD determination.

^cMetoprolol was taken as standard for logD determination. ^dPropanolol was taken as standard for logD determination ^eAlbendazole was taken as standard for the aqueous solubility test

Table 6. in-vitro ADME studies for synthesized compounds (Plasma stability and metabolic stability)

Compound	Plasma Stability ^f		Metabolic Stability					
	Mouse	Human	Mouse			Human		
			CL int protein (µL/min/mg)	Half-life (min)	% QH	CL int protein (µL/min/mg)	Half-life (min)	% QH
 6	NP ^g	10.3	7.5	107.0	16.7	NP ^g	NP ^g	NP ^g
 14	NP ^g	44.9	456.3	1.5	92.5	NP ^g	NP ^g	NP ^g
 35	89.4	109.6	117.3	5.9	76.1	109.1	6.4	83.5

Compound	Plasma Stability ^f		Metabolic Stability					
	Mouse	Human	Mouse			Human		
			CL int protein ($\mu\text{L}/\text{min}/\text{mg}$)	Half-life (min)	% QH	CL int protein ($\mu\text{L}/\text{min}/\text{mg}$)	Half-life (min)	% QH
 40	68.4	97.4	11.4	75.2	22.8	1.8	429.9	7.6
 56	90.7	80.8	42.6	16.3	53.6	14.6	47.6	40.3
 57	50.3	32.8	13.0	53.7	26.03	4.6	153.6	17.46
 58	103.3	110.08	56.2	12.3	60.47	28.3	24.5	56.74
Propantheline ^h	0.0	0.0	—	—	—	—	—	—
Verapamil ⁱ	—	—	318.9	2.2	89.66	248.5	2.8	92.01

^fMean% remaining after 2 h. ^gNP: Not performed. ^hPropantheline was taken as standard for human and mice plasma stability experiments. ⁱVerapamil was taken as standard for metabolic stability experiments in both humans and mice

1.4.2 Biological Discussion

1.4.2.1 Western Blot Experiment

Dose dependant western blot experiments were carried out for the validation of the stabilization of COP1 and ATGL protein. Figure 10, described the three representative compounds (**40**, **56** and **58**) which stabilized the COP1 and ATGL protein in dose dependant manner.

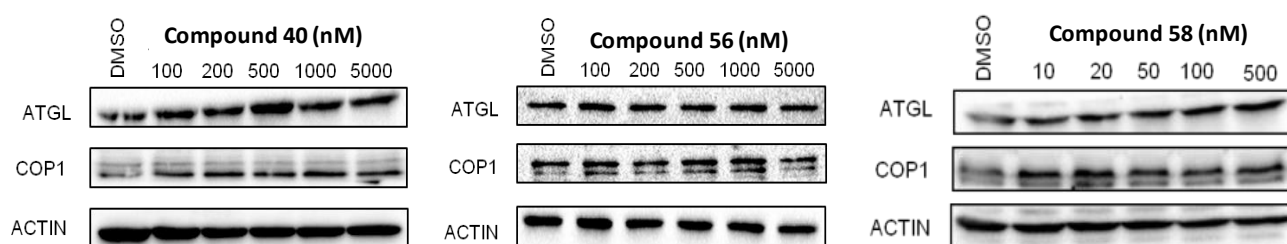


Figure 10. Dose dependant western blot analysis of **40**, **56** and **58**. Increasing intensity of black smear shows the stabilization of COP1 and ATGL protein.

1.4.2.2 Confocal Microscopy Studies

To evaluate the ability of the synthesized compounds to ameliorate lipid accumulation in hepatocytes, confocal microscopy was utilized for validation. Confluent HepG2 cells were treated with 250 μ M oleate and incubated for 24 hours. Lipid droplets and nuclei were visualized using BODIPY and Hoechst342, respectively. It was observed that synthesized **compound 58** was capable to deplete the lipid droplets at 10 μ M from oleate-induced HepG2 cells. (Figure 11)

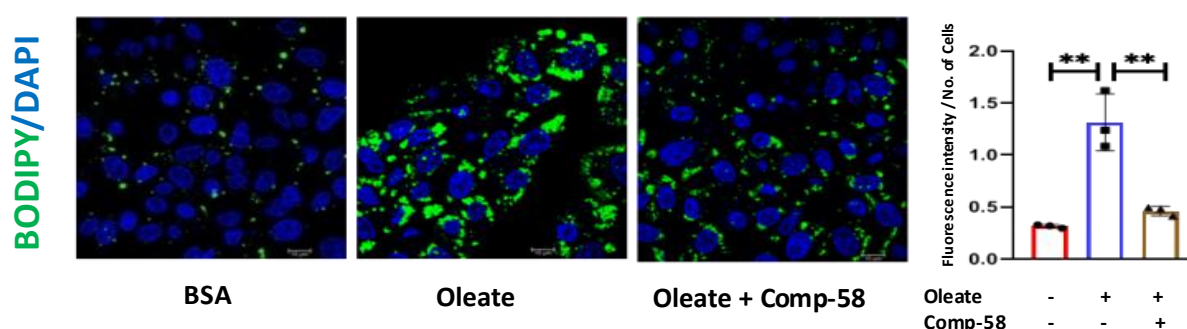


Figure 11. Confocal Microscopy data of two representative **compounds 58**. The green dot and blue dot represented the lipid droplets and nucleus.

1.4.2.3 Immunoprecipitation Study

To validate the ability of small molecules to inhibit the ubiquitination of ATGL, immunoprecipitation studies were performed. Figure 12 illustrates that **compound 58** effectively blocked ubiquitination ATGL as well as auto ubiquitination of COP1. (Figure 12)

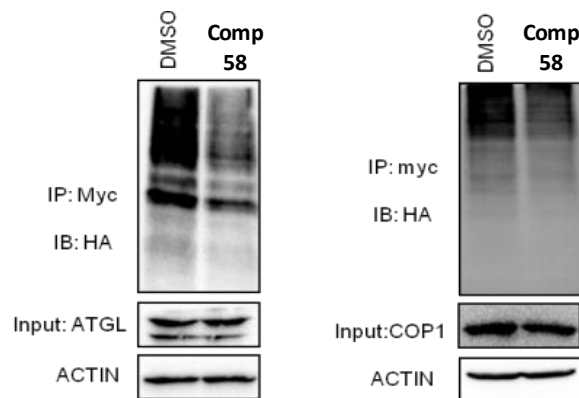


Figure 12. Immunoprecipitation studies of **58**. With respect to control, the synthesized **compounds 58** was capable of blocking the COP1-mediated ubiquitination process of ATGL and auto-ubiquitination of COP1 at 5 μ M of doses. With the treatment of compounds, it was clearly observed that the intense black smear faded due to the blocking of ATGL ubiquitination in comparison to the control.

All the biological studies and their graphical representation were conducted by Dr. Saheli Chowdhury and Abhishek Sen from Dr. Partha Chakrabarti's lab, CSIR - IICB.

1.4.3 Molecular Docking

The lead compound demonstrated a strong ability to stabilize ATGL and COP1 proteins by reducing their ubiquitination. To further understand its mechanism, docking studies were conducted to evaluate its potential interaction with the VP motif binding pockets of the WD40 domain of COP1. Computational analysis identified a plausible binding pose for **compound 58**, with a CDOCKER energy of -36.574 and a CDOCKER interaction energy of -60.318. The 3-ketomethyl phenyl group was positioned within the shallow pocket specific to the VP motif, where a hydrogen bond between its ketomethyl oxygen and Cys559 enhanced the binding affinity. Key stabilizing interactions included a π - π interaction with Trp517 and a π -cation interaction with Arg515. The ethyl piperidine group at the N1 position extended into the elongated central cavity of the WD40 domain, with the two main regions of the molecule—targeting the VP binding pocket and the central cavity—linked by a urea moiety. This linkage was stabilized by a hydrogen bond network involving Lys643 and Arg515, interacting with the nitrogen and oxygen atoms

of the urea group. At the molecule's surface-exposed region, Lys472 formed hydrogen bonds with the oxygen atoms of the C2 quinazolinedione and the 2-methoxyethyl linker. Additionally, the phenyl ring of the quinazolinone scaffold engaged in a π - π interaction with Phe699, further reinforcing its binding within the pocket (Figure 13).

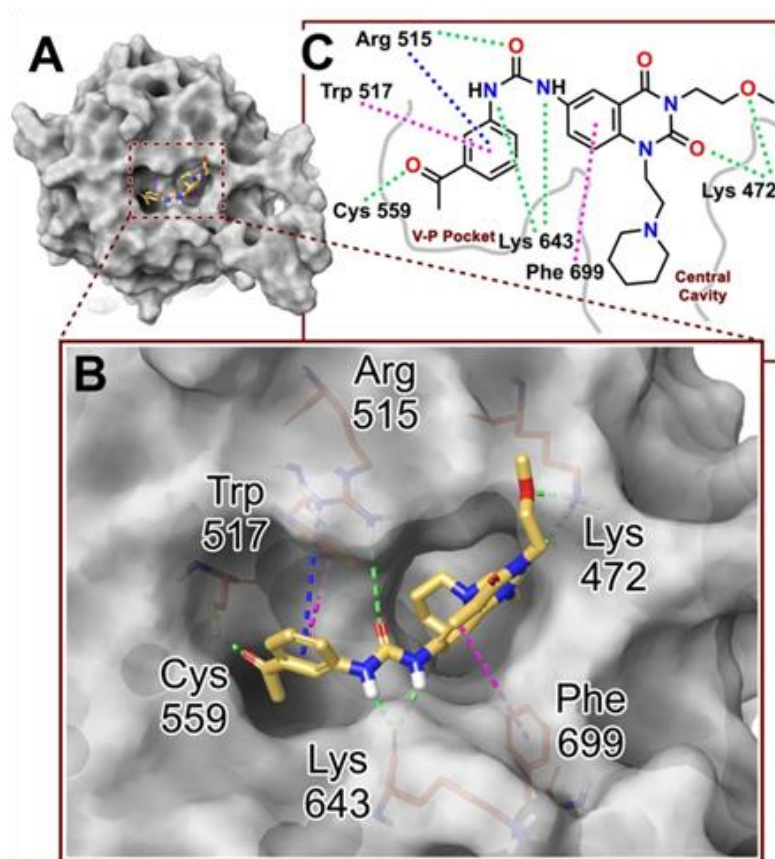


Figure 13. Molecular docking of the lead compound into V-P binding region in WD40 domain of COP1. **A.** Binding interaction of **compound 58** with COP1 WD40 domain (PDB ID: 5IGQ) showing full view of the molecule-protein complex. **B.** The zoomed view of the binding pattern. The surface view of the receptor protein is represented in grey, **compound 58** in dark yellow, and interacting residues in thin orange sticks. **C.** The 2-dimensional representation of the interaction. VP binding region and central cavity are depicted as grey colour surfaces. The green, magenta and blue dotted line represents hydrogen bonds, π - π and π -cation interactions respectively.⁷⁹

1.5 CONCLUSION AND OUTCOME

The study highlighted the development of a novel chemotype designed to effectively inhibit ATGL ubiquitination mediated by its cognate E3 ubiquitin ligase, COP1, with remarkable potency in the low nanomolar range. By curbing this ubiquitination, the chemotype prevents the degradation of ATGL, a critical enzyme responsible for lipolysis, thereby stabilizing its levels within hepatocytes. The stabilization of ATGL leads to enhanced lipolysis, promoting the breakdown of lipid stores in the liver. This mechanism addresses one of the root causes of lipid accumulation in hepatic steatosis. The investigation was started with the modification of quinazolinone pharmacophore by the addition of subsequent functional groups, required for modulating COP1 activity. The first hit molecule (**compound B**) was identified with a 2-methoxyethyl linker at the N3 position (RHS) and a keto-methyl (-COCH₃) group at the meta position of the phenyl ring (LHS). But due to its poor ADME properties we started further structural modifications to get better lead compound. In the present work, an activity guided SAR development was carried out by introducing different functional groups at C5, C2 and N1 positions of quinazolinone moiety. Though **compound 6** and **35** were able to stabilise both ATGL and COP1 proteins and halted ATGL ubiquitination; their unfavourable ADME profile impaired their drug-like nature. Finally, **compound 58** with two carbon piperidine group attached at N1 position of quinazolinone scaffold served our purpose. The compound was capable of regulating ATGL turnover and minimizing lipid droplet accumulation in both HepG2 cells and primary mouse hepatocytes without altering ATGL gene expression. Notably, it demonstrated a strong ability to reduce ATGL ubiquitination, both in cellular systems and in a cell-free in vitro ubiquitination assay. Furthermore, the lead compound significantly inhibited COP1 autoubiquitination. **Compound 58** exhibited outstanding aqueous solubility along with good to moderate plasma and microsomal stability in both mouse and human models. In a preclinical murine model of NAFLD, oral administration of **compound 58** significantly reduced fat accumulation and alleviated liver fibrosis. Additionally, it effectively decreased body weight, liver weight, serum cholesterol levels, and hepatic triglyceride content in treated mice. Given the central role of ATGL in regulating lipid metabolism, the compound offers a promising therapeutic avenue for addressing hepatic steatosis by restoring lipid homeostasis in the liver, with the potential to reverse the condition. This approach targets the molecular interaction between ATGL and COP1, providing a strong foundation for developing effective treatments for

metabolic disorders linked to lipid dysregulation. Furthermore, the results highlight quinazolinone and quinazolinedione scaffolds as promising chemotypes for creating therapeutic candidates targeting NAFLD and related conditions. The strategy outlined in this study serves as a conceptual framework for transforming basic chemical structures into potential drug candidates to combat fatty liver disease.

1.6 EXPERIMENTAL SECTION

General methods

All starting materials, reagents, and solvents were purchased from commercial suppliers and used without further purification. Dry solvents were either commercially purchased or dried using a standard protocol. Reactions that had a sensitivity toward moisture or oxygen were carried out under a dry nitrogen or argon atmosphere. All the TLC experiments were performed on silica gel plates (Merck silica gel 60, F254). The spots were visualized under UV light ($\lambda = 254$ and 365 nm) or by using the appropriate stain. Compounds were purified using a Teledyne ISCO CombiFlash Rf system using a 230–400 mesh size silica gel. ^1H NMR was recorded at 300 MHz (Bruker-DPX), 400 MHz (JEOL), and 600 MHz (Bruker AVANCE) frequencies, and ^{13}C NMR spectra were recorded at 75 MHz (Bruker-DPX), 100 MHz (JEOL), and 150 MHz (Bruker AVANCE) frequencies in CDCl_3 or CD_3OD or d_6 -DMSO using tetramethylsilane as the internal standard. The following abbreviations were used to explain multiplicities: s = singlet, d = doublet, t = triplet, q = quartet, m = multiplet, brs. = broad singlet. The coupling constant, J, was reported in the Hertz unit (Hz). High-resolution mass spectroscopy, HRMS (m/z), was carried out using ESI (Q-Tof Micro mass spectrometer), and ESI (LTQ Orbitrap XL mass spectrometer). The purity of all the compounds was determined to be >95%, analyzed using an Agilent Infinity Prep. HPLC system using a BioSuite Phenyl reverse-phase column (75×7.5 mm, $10 \mu\text{m}$ particle size, 1000 \AA pore size). Mobile phase A was composed of 0.1% TFA in water and mobile phase B of 10% water in acetonitrile for 4–6 min and a flow rate of 1 mL/min with detection at 254 nm wavelengths.

General Procedure A: Reduction. The nitro compounds (1 equiv.) was dissolved in MeOH and a pinch of 10 % wet Pd-C was added. The reaction mixture was degassed by passing nitrogen and H_2 gas was charged for $-\text{NO}_2$ functionality reduction for 4–8 h at room temperature (25 – 30°C). Consumption of starting material was confirmed by TLC. Ninhydrin stain was used to confirm the reduced ($-\text{NH}_2$ containing) compounds (purple color). Upon completion of the reaction, Pd-C was filtered through Celite bed and washed with 10% MeOH in CHCl_3 (V/V) in several times (3/4 times). Solvents were evaporated in vacuum to obtain the compounds. Column chromatography was performed

using EtOAc in Pet ether and MeOH in CHCl₃ in 230 – 400 mesh size silica gel as stationary phase to get the pure compounds with a yield of 40-96% when required.

General Procedure B: Suzuki coupling: To a stirring solution of compound **5** (1 equiv.) in dioxane and water (10-15 mL, 9:1 ratio) in a pressure tube, appropriate aliphatic and aromatic boronic acid (1.2 equiv.) and Cs₂CO₃ (2 equiv.) were added. The mixture was purged with Ar gas for 15-20 min. In next, X-Phos (0.2 equiv.) was added to the reaction mixture as a ligand and followed by the catalyst Pd₂(dba)₃ (0.1 equiv.) and the resulting reaction mixture was allowed to stir at 120 °C for 12-18 hours. The progress of the reaction was monitored by checking TLC. After reaction completion, the reaction mixture was filtered through celite bed and washed with 10% MeOH in CHCl₃ (V/V); the organic layer was washed with brine solution and dried over Na₂SO₄. The solvent was evaporated under vacuum to obtain the crude, which was then purified in flash chromatography using 230-400 mesh size silica gel and EtOAc in Pet ether and MeOH in CHCl₃ as eluent to afford pure compound with 62-72% yield.

General Procedure C: Urea derivative formation via chloroformate intermediate: To the solution of appropriate amines (1 equiv.) in dry THF, 4-nitrophenylchloroformate (1.2 equiv.) was added portion wise and reaction mixture was stirred for 0.5- 1 h at 25-30 °C till the amine got consumed. Reaction progress was monitored by checking TLC. Suitable amines (1.2 equiv.) was added to the reaction mixture followed by TEA (2.5 equiv.) and the reaction mixture was stirred well for another 1.5- 7 h at 25-30 °C. Upon completion, reaction mass was evaporated in vacuum to remove THF to afford the crude mass which was then washed with satd. NaHCO₃ solution at several times to remove *p*-Nitrophenol and extracted with EtOAc. The organic layer was dried over Na₂SO₄ and evaporated in rotary evaporator to afford sticky crude material. Flash chromatography was performed using 230-400 mesh size silica gel and EtOAc in Pet ether and MeOH in CHCl₃ as eluent to afford pure compound with 42-62% yield.

General Procedure D: 3-(2-methoxyethyl)-1-methyl-6-nitroquinazoline-2,4(1H,3H)-dione; **38** (1 equiv.) in dry DMF (5-10 mL) were taken in a pressure tube and K₂CO₃ (2.2 equiv.) was added at room temperature (25-30 °C) for 15-20 min. Suitable alkyl halide (1.5 equiv.) was then added to the reaction mixture and heated at 120 °C for 14-16 h. TLC was checked to visualize the progress of the reaction. After completion, the reaction

mixture was cooled down to room temperature (25-30 °C) and washed thoroughly with ice cold water followed by extraction with EtOAc or CHCl₃. The organic layer was dried over Na₂SO₄ and evaporated in rotary evaporator to afford sticky crude mass which was purified by flash column chromatography using 230-400 mesh size silica gel with MeOH in CHCl₃ or EtOAc in Pet ether as eluent to afford pure compound with good yield (70-84%).

Synthesis of 2-amino-N-(2-methoxyethyl)-5-nitrobenzamide (2): 5-Nitroanthranilic acid (5 g, 27.45 mmol) was taken in DMF (20 mL) and HATU (12.5 g, 32.94 mmol) was added and stirred for 30 min at room temperature (25-30 °C) to obtain a reaction mixture. 2-methoxyethylamine (2.8 mL, 32.94 mmol) was added drop wise to the reaction mixture followed by drop wise addition of TEA (9.5 mL, 68.63 mmol) and the contents of the reaction mixture were stirred for another 1.5 hours at room temperature (25-30 °C). Progress of the reaction was thoroughly monitored through TLC, and after completion of the reaction, the reaction mixture was poured into ice-cold water and extracted with EtOAc, which was then dried over Na₂SO₄. The solvent was evaporated in a rotary evaporator under reduced pressure to obtain the crude. Pure compound **2** was isolated as yellow solid (yield 90%) by column chromatography separation (Eluent: 30% EtOAc in pet ether). ¹H NMR (400 MHz, *d*₆-DMSO) δ in ppm 8.71 (t, *J*=5.2 Hz, 1H), 8.46 (d, *J*= 2.8 Hz, 1H), 7.97 (dd, *J*= 9.2 Hz, 2.4 Hz, 1H), 7.71 (brs, 2H), 6.75 (d, *J*= 9.2 Hz, 1H), 3.41 (t, *J*= 4.8 Hz, 2H), 3.36 (t, *J*= 4.8 Hz, 2H), 3.23 (s, 3H). ¹³C NMR (100 MHz, *d*₆-DMSO) δ in ppm 167.81, 155.83, 135.43, 127.90, 126.33, 116.37, 113.31, 70.79, 58.41. HRMS (ESI) *m/z* (M + H)⁺ calculated for C₁₀H₁₄N₃O₄ 240.0984; found, 240.0995. Melting point: 168 °C.

Synthesis of 3-(2-methoxyethyl)-6-nitroquinazolin-4(3H)-one (3): Compound **2** (2.6 g, 10.87 mmol) was dissolved in trimethylorthoformate (TMOF, 12 mL, 108.74 mmol) and heated at 105 °C for 12-18 h. Progress of the reaction was monitored by checking TLC. Upon completion of reaction, the reaction mixture was evaporated in rotary evaporator to remove excess TMOF. After workup column chromatography (Eluent 50% EtOAc in Pet ether) was performed for purification and compound **3** was appeared as light yellow coloured solid (yield 90%). ¹H NMR (400 MHz, *d*₆-DMSO) δ in ppm 8.78 (d, *J*= 2.4 Hz, 1H), 8.50 (dd, *J*= 9.2 Hz, 2.8 Hz, 1H), 8.45 (s, 1H), 7.82 (d, *J*= 8.8 Hz, 1H), 4.16 (t, *J*= 5.2 Hz, 2H), 3.59 (t, *J*= 5.2 Hz, 2H), 3.21 (s, 3H). ¹³C NMR (100 MHz, *d*₆-DMSO) δ in ppm 160.03, 152.54,

152.11, 145.75, 129.62, 128.82, 122.72, 122.07, 69.39, 58.67, 46.37. HRMS (ESI) m/z ($M + H$)⁺ calculated for $C_{11}H_{12}N_3O_4$ 250.0828; found, 250.0834. Melting point: 152 °C.

Synthesis of 6-amino-3-(2-methoxyethyl)quinazolin-4(3H)-one (4): Compound **3** (1 g, 4.01 mmol) was dissolved in MeOH (10 mL) and the reaction was performed by the general procedure A to afford brown coloured solid compound **4** (yield 95%). ¹H NMR (400 MHz, *d*₆-DMSO) δ in ppm 7.89 (s, 1H), 7.33 (d, *J* = 8.8 Hz, 1H), 7.17 (d, *J* = 2.4 Hz, 1H), 7.03 (dd, *J* = 8.8 Hz, 2.4 Hz, 1H), 5.59 (brs, 2H), 4.05 (t, *J* = 5.6 Hz, 2H), 3.53 (t, *J* = 5.2 Hz, 2H), 3.19 (s, 3H). ¹³C NMR (100 MHz, *d*₆-DMSO) δ in ppm 160.60, 148.64, 143.95, 139.37, 128.53, 123.13, 122.68, 106.64, 69.90, 58.61, 45.75. HRMS (ESI) m/z ($M + H$)⁺ calculated for $C_{11}H_{14}N_3O_2$ 220.1086; found, 220.1095. Melting point: 172 °C.

Synthesis of 6-amino-5-bromo-3-(2-methoxyethyl)quinazolin-4(3H)-one (5): Compound **4** (2 g, 6.73 mmol) was dissolved in acetic acid (15 mL). Bromine (Br₂) (0.56 mL, 8.07 mmol) dissolved in dry DCM (4 mL) was added to the resultant solution of **4** in a dropwise manner at 0 °C over a period of 15 min. After the complete addition of bromine, the reaction mixture was allowed to stir at room temperature for 3 h. Progress of the reaction was monitored by TLC checking. After completion of the reaction, excess bromine was removed by the addition of saturated Na₂S₂O₃ solution and the reaction mixture was washed thoroughly and partitioned with EtOAc and water. The organic layer dried over anhydrous Na₂SO₄ and concentrated in a rotary evaporator to afford a yellowish-brown coloured crude compound. Column chromatography (Silica gel, mesh size 230-400 eluting (70% EtOAc/ Pet ether, V/V) was performed to obtain compound **5** as a light brown solid (yield 66%). ¹H NMR (400 MHz, *d*₆-DMSO) δ in ppm 7.99 (s, 1H), 7.37 (d, *J* = 8.8 Hz, 1H), 7.26 (d, *J* = 8.8 Hz, 1H), 5.82 (s, 2H), 4.04 (t, *J* = 5.2 Hz, 2H), 3.54 (t, *J* = 5.6 Hz, 2H), 3.21 (s, 3H). ¹³C NMR (100 MHz, *d*₆-DMSO) δ in ppm 158.88, 146.62, 145.17, 141.52, 128.10, 122.45, 120.27, 100.98, 69.61, 58.64, 46.26. HRMS (ESI) m/z ($M + H$)⁺ calculated for $C_{11}H_{13}BrN_3O_2$ 298.0191; found, 298.0184. Melting point 134 °C.

Synthesis of 1-(3-acetylphenyl)-3-(5-bromo-3-(2-methoxyethyl)-4-oxo-3,4-dihydroquinazolin-6-yl)urea (6): Compound **5** (0.10 g, 0.33 mmol) was dissolved in dry THF (8 mL) and 4-nitrophenylchloroformate (0.08 g, 0.40 mmol) was added portion wise under nitrogen atmosphere and left for stirring for 0.5 h. 3'-aminoacetophenone (0.06 g, 0.40 mmol) was added to the reaction mixture followed by TEA (0.12 mL, 0.83 mmol) and the reaction was performed according to the general procedure C. Pure compound was

isolated by using column chromatography in 230-400 silica mesh size and with 80 % EtOAc in Pet ether (V/V) as eluent to obtain compound **6** as white solid (yield 47%). ¹H NMR (300 MHz, *d*₆-DMSO) δ in ppm 9.82 (s, 1H), 8.47 (s, 1H), 8.42 (d, *J* = 5.2 Hz, 1H), 8.21 (s, 1H), 8.05-8.04 (m, 1H), 7.68-7.65 (m, 1H), 7.61 (d, *J* = 9.2 Hz, 1H), 7.59-7.56 (m, 1H), 7.44-7.40 (m, 1H), 4.08 (t, *J* = 5.2 Hz, 2H), 3.56 (t, *J* = 5.2 Hz, 2H), 3.21 (s, 3H), 2.53 (s, 3H). ¹³C NMR (100 MHz, *d*₆-DMSO) δ in ppm 198.20, 158.90, 152.79, 148.16, 146.08, 140.32, 138.00, 137.51, 129.87, 128.52, 127.65, 123.30, 122.81, 120.04, 117.95, 110.54, 100.00, 69.47, 58.67, 46.49, 27.28. HRMS (ESI) *m/z* (M + H)⁺ calculated for C₂₀H₂₀BrN₄O₄ 459.0668; found, 459.0660. Melting Point: 204 °C. HPLC Purity: 97.89%.

Synthesis of 6-amino-3-(2-methoxyethyl)-5-phenylquinazolin-4(3H)-one (7):

Compound **5** (0.20 g, 0.67 mmol) was dissolved in dioxane/H₂O mixed solution (10 mL, 9:1 ratio). Benzene boronic acid (0.099 g, 0.80 mmol) and Cs₂CO₃ (0.44 g, 1.34 mmol) were added and the reaction mixture was purged with Ar gas for 20 min. X-phos (0.064 g, 0.13 mmol) and Pd₂(dba)₃ (0.062 g, 0.06 mmol) were added to the solution and the reaction was performed according to the general procedure B. Pure compound was isolated by column chromatography (Silica gel, mesh size 230-400 eluting (70% EtOAc/ Pet ether, V/V) to obtain **7** as a light yellow solid (yield 72%). ¹H NMR (400 MHz, CDCl₃) δ in ppm 7.88 (s, 1H), 7.55 (d, *J* = 8.8 Hz, 1H), 7.48- 7.45 (m, 2H), 7.40- 7.36 (m, 1H), 7.24- 7.22 (m, 2H), 7.15 (d, *J* = 8.4 Hz, 1H), 3.97 (t, *J* = 4.4 Hz, 2H), 3.68 (br.s., 2H), 3.49 (t, *J* = 4.4 Hz, 2H), 3.26 (s, 3H). ¹³C NMR (100 MHz, CDCl₃) δ in ppm 160.43, 144.69, 144.02, 142.04, 138.61, 128.85, 128.84, 128.31, 127.35, 124.10, 122.48, 120.60, 70.38, 58.99, 46.33. HRMS (ESI) *m/z* (M + H)⁺ calculated for C₁₇H₁₈N₃O₂ 296.1399; found, 296.1410. Melting Point: 186 °C.

Synthesis of 6-amino-5-(4-fluorophenyl)-3-(2-methoxyethyl)quinazolin-4(3H)-one (8):

Compound **5** (0.20 g, 0.67 mmol) was dissolved in dioxane/H₂O mixed solution (10 mL, 9:1 ratio). 4-fluorophenylboronic acid (0.112 g, 0.80 mmol) and Cs₂CO₃ (0.44 g, 1.34 mmol) were added and the reaction mixture was purged with Ar gas for 20 min. X-phos (0.064 g, 0.13 mmol) and Pd₂(dba)₃ (0.062 g, 0.06 mmol) were added to the solution and the reaction was performed according to the general procedure B. Pure compound was isolated by column chromatography (Silica gel, mesh size 230-400 eluting (70% EtOAc/ Pet ether, V/V) to afford **57** as yellow gummy material (yield 65%). ¹H NMR (600 MHz, *d*₆-DMSO) δ in ppm 7.93 (s, 1H), 7.42 (d, *J* = 9 Hz, 1H), 7.23 (d, *J* = 9 Hz, 1H), 7.19- 7.16 (m,

2H), 7.12- 7.09 (m, 2H), 4.77 (brs, 2H), 3.89 (t, $J = 4.8$ Hz, 2H), 3.41 (t, $J = 2.7$ Hz, 2H), 3.19 (s, 3H). ^{13}C NMR (150 MHz, DMSO) δ in ppm 162.28, 148.43, 147.04, 143.23, 137.81, 133.97, 130.71, 125.10, 123.27, 122.89, 117.97, 117.83, 72.11, 60.96, 48.08. HRMS (ESI) m/z ($M + H$)⁺ calculated for $\text{C}_{17}\text{H}_{17}\text{FN}_3\text{O}_2$ 314.1305; found, 314.1314.

Synthesis of 6-amino-3-(2-methoxyethyl)-5-(4-(trifluoromethyl)phenyl)quinazolin-4(3H)-one (9): Compound **5** (0.20 g, 0.67 mmol) was dissolved in dioxane/ H_2O mixed solution (10 mL, 9:1 ratio). 4-(trifluoromethyl)phenylboronic acid (0.153 g, 0.80 mmol) and Cs_2CO_3 (0.44 g, 1.34 mmol) were added and the reaction mixture was purged with Ar gas for 20 min. X-phos (0.064 g, 0.13 mmol) and $\text{Pd}_2(\text{dba})_3$ (0.062 g, 0.06 mmol) were added to the solution and the reaction was performed according to the general procedure B. Pure compound was isolated by column chromatography (Silica gel, mesh size 230-400 eluting (70% EtOAc/ Pet ether, V/V) to afford **9** as yellow gummy material (yield 62%). ^1H NMR (600 MHz, d_6 -DMSO) δ in ppm 7.93 (s, 1H), 7.69(d, $J = 8.0$ Hz, 2H), 7.43(d, $J = 8.8$ Hz, 2H), 7.30(d, $J = 7.6$ Hz, 2H), 7.24(d, $J = 8.8$ Hz, 1H), 4.83(s, 2H), 3.87(t, $J = 5.2$ Hz, 2H), 3.83(t, $J = 5.2$ Hz, 2H), 3.16(s, 3H). ^{13}C NMR (100 MHz, d_6 -DMSO) δ in ppm 159.91, 145.78, 144.73, 140.82, 133.77, 132.75, 132.57, 132.06, 131.96, 130.64, 129.22, 128.67, 123.08, 120.22, 69.73, 58.58, 45.73. HRMS (ESI) m/z ($M + H$)⁺ calculated for $\text{C}_{18}\text{H}_{17}\text{F}_3\text{N}_3\text{O}_2$ 364.1273; found, 364.1281.

Synthesis of 6-amino-3-(2-methoxyethyl)-5-(4-methoxyphenyl)quinazolin-4(3H)-one (10): Compound **5** (0.15 g, 0.50 mmol) was dissolved in dioxane/ H_2O mixed solution (10 mL, 9:1 ratio). 4-methoxyphenylboronic acid (0.09 g, 0.60 mmol) and Cs_2CO_3 (0.33 g, 1mmol) were added and reaction mixture was purged with Ar gas for 20 min. X-phos (0.048 g, 0.10 mmol) and $\text{Pd}_2(\text{dba})_3$ (0.048 g, 0.05 mmol) were added to the solution and the reaction was performed according to the general procedure B. Pure compound was isolated by column chromatography (Silica gel, mesh size 230-400 eluting (80% EtOAc/ Pet ether, V/V) to afford **10** as brown solid (yield 64%). ^1H NMR (600 MHz, d_6 -DMSO) δ in ppm 7.92 (s, 1H), 7.40 (d, $J = 9$ Hz, 1H), 7.22 (d, $J = 9$ Hz, 1H), 7.00 (d, $J = 9$ Hz, 2H), 6.94 (d, $J = 9$ Hz, 2H), 4.70 (t, $J = 5.4$ Hz, 2H), 3.89 (t, $J = 5.4$ Hz, 2H), 3.78 (s, 3H), 3.42 (t, $J = 5.4$ Hz, 2H), 3.19 (s, 3H). ^{13}C NMR (150 MHz, d_6 -DMSO) δ in ppm 162.27, 160.71, 148.52, 146.98, 143.30, 133.58, 133.03, 130.38, 124.86, 124.34, 123.01, 116.59, 72.13, 60.96, 57.83, 48.08, 42.83. ^{13}C NMR (150 MHz, d_6 -DMSO) δ in ppm 162.27, 160.71, 148.52, 146.98, 143.30, 133.58, 133.03, 130.38, 124.86, 124.34, 123.01, 116.59, 72.13, 60.96, 57.83,

48.08, 42.83. HRMS (ESI) m/z ($M + H$)⁺ calculated for C₁₈H₂₀N₃O₃ 326.1505; found, 326.1515. Melting Point: 204 °C.

Synthesis of 6-amino-3-(2-methoxyethyl)-5-(6-methoxypyridin-3-yl)quinazolin-4(3H)-one (11): Compound **5** (0.20 g, 0.67 mmol) was dissolved in dioxane/H₂O mixed solution (10 mL, 9:1 ratio). 2-methoxypyridine-5-boronic acid pinacol ester (0.19 g, 0.80 mmol) and Cs₂CO₃ (0.44 g, 1.34 mmol) were added and the reaction mixture was purged with Ar gas for 20 min. X-phos (0.064 g, 0.13 mmol) and Pd₂(dba)₃ (0.062 g, 0.06 mmol) were added to the solution and the reaction was performed according to the general procedure B. Pure compound was isolated by flash chromatography (Silica gel, mesh size 230-400 eluting (90% EtOAc/ Pet ether, V/V) to afford **11** as yellow gummy material (yield 62%). ¹H NMR (300 MHz, *d*₆-DMSO) δ in ppm 7.95 (s, 1H), 7.86 (d, *J* = 2.1 Hz, 1H), 7.46- 7.42 (m, 2H), 7.25 (d, *J* = 8.7 Hz, 1H), 6.83 (d, *J* = 8.4 Hz, 1H), 4.95 (s, 2H), 3.92 (t, *J* = 5.1 Hz, 2H), 3.89 (s, 3H), 3.44 (t, *J* = 5.1 Hz, 2H), 3.20 (s, 3H). ¹³C NMR (100 MHz, *d*₆-DMSO) δ in ppm 162.70, 160.10, 146.77, 144.64, 140.93, 128.62, 128.08, 122.79, 120.93, 118.00, 110.44, 69.73, 58.59, 53.48, 45.76. HRMS (ESI) m/z ($M + H$)⁺ calculated for C₁₇H₁₉N₄O₃ 327.1457; found, 327.1470.

Synthesis of tert-butyl 4-(6-amino-3-(2-methoxyethyl)-4-oxo-3,4-dihydroquinazolin-5-yl)-5,6-dihydropyridine-1(2H)-carboxylate (12): Compound **5** (0.20 g, 0.67 mmol) was dissolved in dioxane/H₂O mixed solution (10 mL, 9:1 ratio). *tert-butyl* 5-(4,4,5,5-tetramethyl-1,3,2-dioxaborolan-2-yl)-3,6-dihydropyridine-1(2H)-carboxylate (0.25 g, 0.80 mmol) and Cs₂CO₃ (0.44 g, 1.34 mmol) were added and the reaction mixture was purged with Ar gas for 20 min. X-phos (0.064 g, 0.13 mmol) and Pd₂(dba)₃ (0.062 g, 0.06 mmol) were added to the solution and the reaction was performed according to the general procedure B. Pure compound was isolated by flash chromatography (Silica gel, mesh size 230-400 eluting (90% EtOAc/ Pet ether, V/V) to afford **12** as light brown gummy material (yield 63%). ¹H NMR (300 MHz, *d*₆-DMSO) δ in ppm 7.93 (s, 1H), 7.32 (d, *J* = 8.7 Hz, 1H), 7.19 (d, *J* = 8.7 Hz, 1H), 5.36 (s, 1H), 5.18 (s, 1H), 4.12- 4.09 (m, 2H), 4.03 (t, *J* = 4.8 Hz, 2H), 3.80- 3.73 (m, 2H), 3.53 (t, *J* = 5.1 Hz, 2H), 3.23 (s, 3H), 2.82- 2.31 (m, 1H), 2.09- 2.03 (m, 1H), 1.45 (s, 9H). ¹³C NMR (100 MHz, CDCl₃) δ in ppm 160.28, 155.31, 144.50, 143.09, 141.80, 128.67, 127.64, 124.39, 122.62, 120.54, 108.74, 79.63, 70.32, 70.16, 59.07, 59.03, 46.41, 29.55, 28.60. HRMS (ESI) m/z ($M + H$)⁺ calculated for C₂₁H₂₉N₄O₄ 401.2189; found, 401.2185.

Synthesis of 1-(3-acetylphenyl)-3-(3-(2-methoxyethyl)-4-oxo-5-phenyl-3,4-dihydroquinazolin-6-yl)urea (13): 4-nitrophenylchloroformate (0.08 g, 0.40 mmol) was added portion wise to the stirring solution of compound **7** (0.1 g, 0.33 mmol) in dry THF (10 mL) under nitrogen atmosphere for 1 h. 3'-aminoacetophenone (0.06 g, 0.40 mmol) was added to the reaction mixture followed by TEA (0.12 mL, 0.84 mmol) and the reaction was performed according to the general procedure C. Pure compound was isolated by using column chromatography in 230-400 silica mesh size and with (90% EtOAc/ Pet ether, V/V) as eluent to obtain compound **13** as yellow solid (yield 45%). ¹H NMR (400 MHz, *d*₆-DMSO) δ in ppm 9.35 (s, 1H), 8.32 (d, *J* = 8.8 Hz, 1H), 8.13 (s, 1H), 7.88 (s, 1H), 7.62 (d, *J* = 8.8 Hz, 1H), 7.57 (d, *J* = 8.4 Hz, 1H), 7.50 (d, *J* = 7.6 Hz, 1H), 7.42-7.32 (m, 5H), 7.12 (s, 1H), 7.11 (s, 1H), 3.90 (t, *J* = 5.2 Hz, 2H), 3.39 (t, *J* = 5.2 Hz, 2H), 3.16 (s, 3H), 2.48 (s, 3H). ¹³C NMR (100 MHz, CDCl₃) δ in ppm 198.11, 171.38, 160.18, 152.73, 146.65, 144.99, 138.87, 137.80, 137.19, 136.12, 130.10, 129.38, 128.82, 128.65, 128.00, 127.64, 127.50, 124.74, 123.50, 120.00, 119.70, 70.03, 60.54, 58.96, 46.53, 26.77, 21.15, 14.25. HRMS (ESI) *m/z* (M + H)⁺ calculated for C₂₆H₂₅N₄O₄ 457.1876; found, 457.1876. Melting Point: 195 °C. HPLC Purity: 97.94%.

Synthesis of 1-(3-acetylphenyl)-3-(5-(4-fluorophenyl)-3-(2-methoxyethyl)-4-oxo-3,4-dihydroquinazolin-6-yl)urea (14): Compound **8** (0.15 g, 0.48 mmol) was dissolved in dry THF (8 mL) and 4-nitrophenylchloroformate (0.12 g, 0.57 mmol) was added portion wise under nitrogen atmosphere and left for stirring for 0.5 h. 3'-aminoacetophenone (0.08 g, 0.57 mmol) was added to the reaction mixture followed by TEA (0.17 mL, 1.19 mmol) and the reaction was performed according to the general procedure C. Pure compound was isolated by using column chromatography in 230-400 silica mesh size and with 80% EtOAc in Pet ether (V/V) as eluent to obtain compound **14** as white coloured solid (yield 44%). ¹H NMR (300 MHz, CDCl₃) δ in ppm 8.66 (d, *J* = 9 Hz, 1H), 8.02 (s, 1H), 7.77 (d, *J* = 9 Hz, 1H), 7.71- 7.67 (m, 2H), 7.46- 7.43 (m, 1H), 7.37- 7.32 (m, 1H), 7.13- 7.09 (m, 2H), 7.05- 6.99 (m, 2H), 6.86 (s, 1H), 6.43 (s, 1H), 3.99 (t, *J* = 4.5 Hz, 2H), 3.50 (t, *J* = 4.8 Hz, 2H), 3.28 (s, 3H), 2.58 (s, 3H). ESI- MS *m/z* 475.1 (M+H⁺). ¹³C NMR (150 MHz, *d*₆-DMSO) δ in ppm 197.66, 162.54, 160.93, 158.65, 152.44, 147.80, 139.88, 137.35, 136.49, 132.78, 131.09, 130.25, 129.23, 128.76, 125.55, 122.61, 122.02, 119.36, 117.29, 115.34, 115.20, 68.85, 58.11, 45.81, 26.74. HRMS (ESI) *m/z* (M + H)⁺ calculated for C₂₆H₂₄FN₄O₄ 475.1782; found, 475.1779. Melting Point: 218 °C. HPLC Purity: 100%.

Synthesis of 1-(3-acetylphenyl)-3-(3-(2-methoxyethyl)-4-oxo-5-(4-(trifluoromethyl)phenyl)-3,4-dihydroquinazolin-6-yl)urea (15): Compound **9** (0.10 g, 0.27 mmol) was dissolved in dry THF (8 mL) and 4-nitrophenylchloroformate (0.067 g, 0.33 mmol) was added portion wise under nitrogen atmosphere and left for stirring for 0.5 h. 3'-aminoacetophenone (0.05 g, 0.33 mmol) was added to the reaction mixture followed by TEA (0.1 mL, 0.68 mmol) and the reaction was performed according to the general procedure C. Pure compound was isolated by using column chromatography in 230-400 silica mesh size and with 80 % EtOAc in Pet ether (V/V) as eluent to obtain compound **15** as white coloured solid (yield 48%). ¹H NMR (300 MHz, *d*₆-DMSO) δ in ppm 9.29 (s, 1H), 8.37 (d, *J*= 12Hz, 1H), 8.21(s, 1H), 7.95-7.92 (m, 2H), 7.80 (d, *J*= 10.8Hz, 1H), 7.72 (d, *J*= 12Hz, 1H), 7.62-7.55 (m, 1H), 7.44-7.40 (m, 2H), 7.29-7.25 (m, 1H), 3.96 (t, *J*= 6.0Hz, 2H), 3.44 (t, *J*= 6.4Hz, 2H), 3.21 (s, 3H), 2.53 (s, 3H). ¹³C NMR (100 MHz, *d*₆-DMSO) δ in ppm 198.20, 167.40, 159.67, 153.04, 148.07, 145.62, 140.33, 137.89, 136.01, 130.64, 130.49, 129.78, 129.23, 128.13, 125.56, 122.56, 119.94, 117.87, 69.59, 58.62, 45.94, 27.25. HRMS (ESI) *m/z* (M + H)⁺ calculated for C₂₇H₂₄F₃N₄O₄ 525.1750; found, 525.1769. Melting Point: 190 °C. HPLC Purity: 98.94%.

Synthesis of 1-(3-acetylphenyl)-3-(3-(2-methoxyethyl)-5-(4-methoxyphenyl)-4-oxo-3,4-dihydroquinazolin-6-yl)urea (16): Compound **10** (0.12 g, 0.37 mmol) was dissolved in dry THF (10 mL) and 4-nitrophenylchloroformate (0.09 g, 0.44 mmol) was added portion wise under nitrogen atmosphere and left for stirring for 0.5 h. 3'-aminoacetophenone (0.06 g, 0.44 mmol) was added to the reaction mixture followed by TEA (0.13 mL, 0.92 mmol) and the reaction was performed according to the general procedure C. Pure compound was isolated by using column chromatography in 230-400 silica mesh size and with 90% EtOAc in Pet ether (V/V) as eluent to obtain compound **16** as white coloured solid (yield 52%). ¹H NMR (300 MHz, CDCl₃) δ in ppm 8.69 (d, *J*= 9 Hz, 1H), 7.99 (s, 1H), 7.74 (d, *J*= 9 Hz, 1H), 7.63 (d, *J*= 7.8 Hz, 1H), 7.49 (d, *J*= 7.8 Hz, 1H), 7.33-7.30 (m, 1H), 7.05 (d, *J*= 8.1 Hz, 3H), 6.85 (d, *J*= 8.4 Hz, 2H), 6.58 (s, 1H), 3.97 (t, *J*= 4.8 Hz, 2H), 3.76 (s, 3H), 3.49 (t, *J*= 4.8 Hz, 2H), 3.26 (s, 3H), 2.56 (s, 3H). ¹³C NMR (150 MHz, CDCl₃) δ in ppm 200.15, 162.66, 161.36, 154.88, 149.00, 147.40, 140.70, 140.36, 138.80, 132.36, 131.97, 131.28, 130.50, 129.08, 128.05, 126.53, 123.01, 122.60, 116.71, 79.68, 72.52, 61.38, 57.51, 48.86, 29.12. HRMS (ESI) *m/z* (M + H)⁺ calculated for Chemical Formula: C₂₇H₂₇N₄O₅ 487.1981; found, 487.2003. Melting Point: 192 °C. HPLC Purity: 96.82%.

Synthesis of 1-(3-acetylphenyl)-3-(3-(2-methoxyethyl)-5-(6-methoxypyridin-3-yl)-4-oxo-3,4-dihydroquinazolin-6-yl)urea (17): Compound **11** (0.15 g, 0.46 mmol) was dissolved in dry THF (10 mL) and 4-nitrophenylchloroformate (0.11 g, 0.55 mmol) was added portion wise under nitrogen atmosphere and left for stirring for 0.5 h. 3'-aminoacetophenone (0.08 g, 0.55 mmol) was added to the reaction mixture followed by TEA (0.16 mL, 1.14 mmol) and the reaction was performed according to the general procedure C. Pure compound was isolated by using column chromatography in 230-400 silica mesh size and with 90% EtOAc in Pet ether (V/V) as eluent to obtain compound **17** as light brown coloured solid (yield 48%). ¹H NMR (400 MHz, *d*₆-DMSO) δ in ppm 9.30(s, 1H), 8.41 (d, *J* = 8.8 Hz, 1H), 8.13 (s, 1H), 7.90-7.88 (m, 2H), 7.64 (d, *J* = 9.2 Hz, 1H), 7.58 (d, *J* = 6.0 Hz, 1H), 7.51 (d, *J* = 8.0 Hz, 1H), 7.46 (dd, *J* = 8.4 Hz, 1H), 7.39-7.36 (m, 2H), 6.85 (d, *J* = 8.4 Hz, 1H), 3.92 (t, *J* = 5.2 Hz, 2H), 3.88 (s, 3H), 3.40 (t, *J* = 5.2 Hz, 2H), 3.16 (s, 3H), 2.49 (s, 3H). ¹³C NMR (100 MHz, *d*₆-DMSO) δ in ppm 198.18, 163.23, 159.88, 152.93, 147.83, 146.76, 145.38, 140.68, 140.37, 137.89, 137.07, 129.77, 128.67, 127.81, 126.56, 123.14, 122.52, 120.59, 117.84, 110.61, 100.00, 69.58, 58.61, 53.57, 45.97, 27.24. HRMS (ESI) *m/z* (M + H)⁺ calculated for C₂₆H₂₆N₅O₅ 488.1934; found, 488.1919. Melting Point: 208 °C. HPLC Purity: 99.41%.

Synthesis of tert-butyl 4-(6-(3-(3-acetylphenyl)ureido)-3-(2-methoxyethyl)-4-oxo-3,4-dihydroquinazolin-5-yl)-5,6-dihydropyridine-1(2H)-carboxylate (18):

Compound **12** (0.10 g, 0.25 mmol) was dissolved in dry THF (8 mL) and 4-nitrophenylchloroformate (0.06 g, 0.30 mmol) was added portion wise under nitrogen atmosphere and left for stirring for 0.5 h. 3'-aminoacetophenone (0.04 g, 0.30 mmol) was added to the reaction mixture followed by TEA (0.09 mL, 0.62 mmol) and the reaction was performed according to the general procedure C. Pure compound was isolated by using column chromatography in 230-400 silica mesh size and with 2% MeOH in CHCl₃ (V/V) as eluent to obtain compound **18** as light brown coloured solid (yield 46%). ¹H NMR (400 MHz, CDCl₃) δ in ppm 8.55 (d, *J* = 9.2 Hz, 1H), 8.36 (brs, 1H), 8.07 (s, 1H), 8.00 (s, 1H), δ 7.71 (d, *J* = 8.4 Hz, 1H), 7.67 (d, *J* = 9.2 Hz, 1H), 7.62 (d, *J* = 6.4 Hz, 2H), 7.38 (t, *J* = 7.6 Hz, 1H), 5.55 (brs, 1H), 4.38 (d, *J* = 11.4 Hz, 1H), 4.10 (t, *J* = 4.8 Hz, 2H), 4.38 (d, *J* = 15.4 Hz, 1H), 3.61 (t, *J* = 5.2 Hz, 2H), 3.50-3.43 (m, 1H), 3.31 (s, 3H), 2.58 (s, 3H), 2.27 (brs, 3H), 1.45 (s, 9H). ¹³C NMR (150 MHz, *d*₆-DMSO) δ in ppm 197.68, 159.17, 152.69, 147.14, 139.98, 137.39, 134.72, 133.03, 131.51, 129.29, 128.79, 128.72, 126.51, 122.79, 122.07,

119.38, 117.43, 78.74, 69.17, 58.11, 45.42, 31.30, 28.19, 26.75. HRMS (ESI) m/z (M + H)⁺ calculated for C₃₀H₃₆N₅O₆ 562.2666; found 562.2667. Melting Point: 120 °C. HPLC Purity: 99.16%.

Synthesis of 1-(3-acetylphenyl)-3-(3-(2-methoxyethyl)-4-oxo-5-(1,2,3,6-tetrahydro pyridin-4-yl)-3,4-dihydroquinazolin-6-yl)urea (19):

To the stirring solution of compound **18** (0.1 g, 0.18 mmol) in dry DCM (5 mL) under ice-bath at 0 °C, trifluoroacetic acid TFA (0.14 mL, 1.8 mmol) was added dropwise over 5 min. After complete addition, ice bath was removed and reaction mixture was allowed to stir for 2 h. Progress of the reaction was monitored by checking TLC. After complete consumption of starting material, reaction mixture was poured into crushed ice and saturated NaHCO₃ solution was added to neutralize the excess TFA until pH of the solution reached to 7-8. In next, the resulting solution was partitioned between CHCl₃ and water in separating funnel to remove impurities. The organic layer was dried over Na₂SO₄ and evaporated in rotary evaporator to afford brown colored sticky crude material. Pure compound was isolated after purification in flash chromatography using 10% MeOH in CHCl₃ (V/V) to afford **19** as off-white solid (yield 61%). ¹H NMR (300 MHz, CDCl₃), δ in ppm 8.71 (d, J = 9.0 Hz, 1H), 8.10 (s, 1H), 7.94 (s, 1H), 7.68 (d, J = 8.1 Hz, 1H), 7.58 (d, J = 9.0 Hz, 1H), 7.51 (d, J = 7.5 Hz, 1H), 7.31 (d, J = 8.1 Hz, 1H), 5.52 (s, 1H), 4.02 (t, J = 4.5 Hz, 2H), 3.68-3.62 (m, 2H), 3.54 (t, J = 4.5 Hz, 2H), 3.37-3.30 (m, 2H), 3.24 (s, 3H), 2.73-2.66 (m, 1H), 2.52 (s, 3H), 2.38-2.33 (m, 1H). ¹³C NMR (150 MHz, d₆-DMSO) δ in ppm 197.36, 158.82, 152.35, 146.60, 144.11, 139.77, 137.03, 134.76, 133.25, 130.09, 128.86, 126.97, 126.19, 122.39, 121.69, 119.11, 117.00, 109.17, 68.86, 57.77, 45.06, 43.19, 41.56, 27.90, 26.39. HRMS (ESI) m/z (M + H)⁺ calculated for C₂₅H₂₈N₅O₄ 462.2141; found, 462.2142. Melting Point: 130 °C. HPLC Purity: 99.0%.

Synthesis of 1-(3-acetylphenyl)-3-(3-(2-methoxyethyl)-4-oxo-5-(piperidin-4-yl)-3,4-dihydroquinazolin-6-yl)urea (20): Compound **19** (0.12 g, 0.26 mmol) was dissolved in MeOH (8 mL) and a pinch of 10% wet Pd/C was added to the solution. H₂ gas was charged to the solution at room temperature (25-30 °C) for 4 h. Progress of the reaction was checked by TLC. After complete consumption of starting material, the reaction mixture was filtered through celite bed to remove Pd/C and washed three times (3 x 10 mL) with 10% MeOH in CHCl₃ mixture. The solution was evaporated in the rotary evaporator to obtain a light brown-coloured crude mass which was purified by flash chromatography

using 10% MeOH in CHCl₃ (V/V) as eluent to afford **20** as a white solid compound (yield 42%). ¹H NMR (300 MHz, *d*₆-DMSO) δ in ppm 8.77 (d, *J*= 9.3 Hz, 1H), 7.96 (br.s, 2H), 7.62 (d, *J*= 9.3 Hz, 1H), 7.44 (s, 1H), 7.36 (d, *J*= 8.1 Hz, 1H), 7.16- 7.10 (m, 1H), 6.79 (d, *J*= 7.5 Hz, 1H), 5.55 (s, 1H), 4.05 (t, *J*= 4.5 Hz, 2H), 3.91- 3.86 (m, 1H), 3.72-3.66 (m, 1H), 3.57 (t, *J*= 4.5 Hz, *J*= 4.5 Hz, 2H), 3.43- 3.40 (m, 2H), 3.28 (s, 3H), 3.08 (s, 3H), 3.01- 2.95 (m, 3H), 2.60- 2.43 (m, 3H). ¹³C NMR (150 MHz, *d*₆-DMSO) δ in ppm 159.24, 152.72, 146.82, 144.29, 144.20, 139.72, 135.59, 133.66, 129.63, 128.66, 127.04, 126.60, 121.47, 119.45, 117.68, 115.75, 69.22, 58.12, 45.41, 43.09, 41.62, 28.31, 15.57. HRMS (ESI) *m/z* (M + H)⁺ calculated for C₂₅H₃₀N₅O₄ 464.2298; found, 464.2289. Melting Point: 138 °C. HPLC Purity: 97.05%.

Synthesis of 2-(2-chloroacetamido)-N-(2-methoxyethyl)-5-nitrobenzamide (21):

Compound **2** (1 g, 4.18 mmol) was dissolved in dry DCM (15 mL). Chloroacetyl chloride (4mL, 5.01 mmol) and TEA (1.16 mL, 8.36 mmol) were added and the reaction mixture was allowed to stir at room temperature for 3 hours. Reaction was monitored by checking TLC. After reaction completion, the reaction mixture was worked up by using DCM and water. Pure compound was isolated after purification in flash chromatography using 20% Pet ether in EtOAc (V/V) to afford **21** as off-white solid (yield 66%). ¹H NMR (400 MHz, *d*₆-DMSO) δ in ppm 12.26 (s, 1H), 9.26-9.23 (m, 1H), 8.64-8.62 (m, 2H), 8.38-8.35 (m, 1H), 4.44 (s, 2H), 3.48-3.40 (m, 4H), 3.24 (s, 3H). ¹³C NMR (100 MHz, *d*₆-DMSO) δ in ppm 166.99, 166.44, 144.30, 142.43, 127.87, 124.53, 121.37, 121.03, 70.49, 58.45, 44.01. HRMS (ESI) *m/z* (M + H)⁺ calculated for C₁₂H₁₅ClN₃O₅ 316.0700; found, 316.0704. Melting Point: 148 °C. HPLC Purity: 97.90%.

Synthesis of 2-(chloromethyl)-3-(2-methoxyethyl)-6-nitroquinazolin-4(3H)-one (22):

Compound **21** (0.8 g, 2.53 mmol) was dissolved in dry DCM (15 mL). ZnCl₂ (1.37 g, 10.12 mmol) and HMDS (4.2 mL, 20.14 mmol) were added and the reaction mixture was stirred at 80 °C for 1 hour. Reaction was monitored by checking TLC. After reaction completion, the reaction mixture was worked up by using EtOAc and chilled water. Pure compound was isolated after purification in flash chromatography using 50% Pet ether in EtOAc (V/V) to afford **22** as off-white solid (yield 88%). ¹H NMR (400 MHz, *d*₆-DMSO) δ in ppm 8.77-8.75 (m, 1H), 8.54-8.50 (m, 1H), 7.86-7.82 (m, 1H), 4.92 (s, 2H), 4.31 (t, *J*= 2.8 Hz, 2H), 3.61 (t, *J*= 2.8 Hz, 2H), 3.20 (s, 1H). ¹³C NMR (100 MHz, *d*₆-DMSO) δ in ppm 160.87, 156.59, 150.88, 146.11, 129.67, 129.21, 122.96, 121.02, 69.63, 59.06, 44.55.

HRMS (ESI) m/z (M + H)⁺ calculated for C₁₂H₁₃ClN₃O₄ 298.0595; found, 298.0598. Melting Point: 156 °C. HPLC Purity: 98.25%.

Synthesis of 3-(2-methoxyethyl)-2-((4-methylpiperazin-1-yl)methyl)-6-nitroquinazolin-4(3H)-one (23):

Compound **22** (0.8 g, 2.69 mmol) was dissolved in dry Toluene (15 mL). 4-methylpiperazine (0.5 g, 5.38 mmol) was added and the reaction mixture was refluxed for 2 hours. Reaction was monitored by checking TLC. After reaction completion, the reaction mixture was worked up by using EtOAc and water. Pure compound was isolated after purification in flash chromatography using 80% Pet ether in EtOAc (V/V) to afford **23** as off-white solid (yield 77%). ¹H NMR (400 MHz, *d*₆-DMSO) δ in ppm 8.76 (s, 1H), 8.49-8.47 (m, 1H), 7.81-7.79 (m, 1H), 4.35 (t, *J* = 6 Hz, 2H), 3.70 (s, 2H), 3.61 (t, *J* = 6 Hz, 2H), 3.27-3.24 (m, 4H), 3.21 (s, 3H). ¹³C NMR (100 MHz, *d*₆-DMSO) δ in ppm 161.39, 158.25, 151.03, 129.54, 128.86, 122.85, 121.01, 69.92, 62.81, 58.97, 55.04, 52.99, 44.06. HRMS (ESI) m/z (M + H)⁺ calculated for C₁₇H₂₄N₅O₄ 362.1828; found, 362.1822. Melting Point: 168 °C. HPLC Purity: 98.20%.

Synthesis of 3-(2-methoxyethyl)-2-(morpholinomethyl)-6-nitroquinazolin-4(3H)-one (24): Compound **22** (0.8 g, 2.69 mmol) was dissolved in dry Toluene (15 mL). morpholine (0.46 mL, 5.38 mmol) was added and the reaction mixture was refluxed for 2 hours. Reaction was monitored by checking TLC. After reaction completion, the reaction mixture was worked up by using EtOAc and water. Pure compound was isolated after purification in flash chromatography using 80% Pet ether in EtOAc (V/V) to afford **24** as off-white solid (yield 77%). ¹H NMR (400 MHz, *d*₆-DMSO) δ in ppm 8.77 (d, *J* = 2.4 Hz, 1H), 8.49 (dd, *J* = 9.2 Hz, *j* = 2.8 Hz, 1H), 7.81 (d, *J* = 8.4 Hz, 1H), 4.60 (t, *J* = 5.6 Hz, 2H), 3.72 (s, 1H), 3.62 (t, *J* = 5.6 Hz, 2H), 3.54-3.52 (m, 4H), 3.28-3.27 (m, 4H), 3.21 (s, 3H). HRMS (ESI) m/z (M + H)⁺ calculated for C₁₆H₂₁N₄O₅ 349.1512; found, 349.1516. Melting Point: 172 °C. HPLC Purity: 97.88%.

Synthesis of 3-(2-methoxyethyl)-6-nitro-2-(piperidin-1-ylmethyl)quinazolin-4(3H)-one (25): Compound **22** (0.8 g, 2.69 mmol) was dissolved in dry Toluene (15 mL). piperidine (0.53 mL, 5.38 mmol) was added and the reaction mixture was refluxed for 2 hours. Reaction was monitored by checking TLC. After reaction completion, the reaction mixture was worked up by using EtOAc and water. Pure compound was isolated after purification in flash chromatography using 50% Pet ether in EtOAc (V/V) to afford **25** as

off-white solid (yield 80%). ^1H NMR (400 MHz, d_6 -DMSO) δ in ppm 8.76 (d, J = 2.4Hz, 1H), 8.48 (dd, J = 9.2 Hz, j = 2.8Hz, 1H), 7.80 (d, J = 8.4Hz, 1H), 4.45 (t, J = 5.6 Hz, 2H), 3.66 (s, 1H), 3.61 (t, J = 5.6 Hz, 2H), 3.21 (s, 3H), 2.42-2.37 (m, 4H), 1.48-1.42 (m, 4H), 1.37-1.30 (m, 2H). ^{13}C NMR (100 MHz, d_6 -DMSO) δ in ppm 13C NMR (101 MHz, DMSO- D_6) δ 161.40, 158.56, 151.03, 145.65, 129.51, 128.84, 122.85, 120.92, 69.95, 63.65, 58.95, 54.46, 44.06, 26.01, 24.12. HRMS (ESI) m/z ($M + H$) $^+$ calculated for $\text{C}_{17}\text{H}_{23}\text{N}_4\text{O}_4$ 347.1719; found, 347.1722 Melting Point: 170 °C. HPLC Purity: 98.62 %.

Synthesis of 3-(2-methoxyethyl)-6-nitro-2-(pyrrolidin-1-ylmethyl)quinazolin-4(3H)-one (26): Compound **22** (0.8 g, 2.69 mmol) was dissolved in dry Toluene (15 mL). pyrrolidine (0.44 mL, 5.38 mmol) was added and the reaction mixture was refluxed for 2 hours. Reaction was monitored by checking TLC. After reaction completion, the reaction mixture was worked up by using EtOAc and water. Pure compound was isolated after purification in flash chromatography using 50% Pet ether in EtOAc (V/V) to afford **26** as off-white solid (yield 60%). ^1H NMR (400 MHz, d_6 -DMSO) δ in ppm 8.76 (d, J = 2.8Hz, 1H), 8.48 (dd, J = 9.2 Hz, j = 2.8Hz, 1H), 7.80 (d, J = 8.4Hz, 1H), 4.45 (t, J = 5.6 Hz, 2H), 3.82 (s, 1H), 3.59 (t, J = 5.6 Hz, 2H), 3.20 (s, 3H), 2.54-2.49 (m, 4H), 1.69-1.64 (m, 4H). ^{13}C NMR (100 MHz, d_6 -DMSO) δ in 161.27, 159.18, 151.26, 145.63, 129.52, 128.86, 122.87, 120.91, 69.91, 60.31, 58.96, 53.93, 43.94, 23.75. HRMS (ESI) m/z ($M + H$) $^+$ calculated for $\text{C}_{16}\text{H}_{21}\text{N}_4\text{O}_4$ 333.1563; found, 333.1560. Melting Point: 188 °C. HPLC Purity: 98.62%.

Synthesis of 2-((dimethylamino)methyl)-3-(2-methoxyethyl)-6-nitroquinazolin-4(3H)-one (27): Compound **22** (0.8 g, 2.69 mmol) was dissolved in dry Toluene (15 mL). dimethylamine (0.37 mL, 5.38 mmol) was added and the reaction mixture was refluxed for 2 hours. Reaction was monitored by checking TLC. After reaction completion, the reaction mixture was worked up by using EtOAc and water. Pure compound was isolated after purification in flash chromatography using 50% Pet ether in EtOAc (V/V) to afford **27** as off-white solid (yield 72%). ^1H NMR (400 MHz, d_6 -DMSO) δ in ppm 8.77 (d, J = 2.4Hz, 1H), 8.50 (dd, J = 9.2 Hz, j = 2.8Hz, 1H), 7.82 (d, J = 8.0Hz, 1H), 4.47 (t, J = 5.6 Hz, 2H), 3.63 (s, 1H), 3.59 (t, J = 5.6 Hz, 2H), 3.20 (s, 3H), 2.20 (s, 6H). ^{13}C NMR (100 MHz, d_6 -DMSO) δ in ppm 161.32, 158.70, 151.11, 145.70, 129.56, 128.88, 122.88, 120.96, 69.93, 63.89, 58.99, 45.56, 43.98. HRMS (ESI) m/z ($M + H$) $^+$ calculated for $\text{C}_{14}\text{H}_{19}\text{N}_4\text{O}_4$ 307.1406; found, 307.1410. Melting Point: 182 °C. HPLC Purity: 99.20%.

Synthesis of 6-amino-3-(2-methoxyethyl)-2-((4-methylpiperazin-1-yl)methyl)quinazolin-4(3H)-one (28):

Compound **23** (0.5 g, 1.38 mmol) was dissolved in MeOH (8 mL) and a pinch of 10% wet Pd/C was added to the solution. H₂ gas was charged to the solution at room temperature (25-30 °C) for 4 h. Progress of the reaction was checked by TLC and the reaction procedure was followed according to general procedure C. After complete consumption of starting material, the reaction mixture was filtered through celite bed to remove Pd/C and washed three times (3 x 10 mL) with 10% MeOH in CHCl₃ mixture. The solution was evaporated in the rotary evaporator to obtain a light brown-coloured crude mass which was purified by flash chromatography using 10% MeOH in CHCl₃ (V/V) as eluent to afford **28** as a white solid compound (yield 52%). ¹H NMR (400 MHz, *d*₆-DMSO) δ in ppm 7.30 (d, *J*= 8.8Hz, 1H), 7.12 (d, *J*= 2.8Hz, 1H), 7.01 (dd, *J*= 8.8 Hz, *j*= 2.8Hz, 1H), 5.59 (s, 1H), 4.34 (t, *J*= 6.0 Hz, 2H), 3.57-3.54 (m, 4H), 3.19 (s, 3H), 2.43-2.33 (m, 4H), 2.33-2.16 (m, 4H), 2.09 (s, 3H). ¹³C NMR (100 MHz, *d*₆-DMSO) δ in ppm 161.89, 149.01, 148.64, 138.02, 128.50, 122.83, 121.92, 106.57, 70.36, 62.68, 58.92, 55.10, 52.99, 46.16, 43.34. HRMS (ESI) *m/z* (M + H)⁺ calculated for C₁₇H₂₆N₅O₂ 332.2087; found 332.2084. Melting Point: 156 °C. HPLC Purity: 98.55%.

Synthesis of 6-amino-3-(2-methoxyethyl)-2-(morpholinomethyl)quinazolin-4(3H)-one (29): Compound **24** (0.5 g, 1.43 mmol) was dissolved in MeOH (8 mL) and a pinch of 10% wet Pd/C was added to the solution. H₂ gas was charged to the solution at room temperature (25-30 °C) for 4 h. Progress of the reaction was checked by TLC and the reaction procedure was followed according to general procedure C. After complete consumption of starting material, the reaction mixture was filtered through celite bed to remove Pd/C and washed three times (3 x 10 mL) with 10% MeOH in CHCl₃ mixture. The solution was evaporated in the rotary evaporator to obtain a light brown-coloured crude mass which was purified by flash chromatography using 10% MeOH in CHCl₃ (V/V) as eluent to afford **29** as a white solid compound (yield 58%). ¹H NMR (400 MHz, *d*₆-DMSO) δ in ppm 7.30 (d, *J*= 8.8Hz, 1H), 7.12 (d, *J*= 2.8Hz, 1H), 7.01 (dd, *J*= 8.8 Hz, *j*= 2.8Hz, 1H), 5.59 (s, 1H), 4.36 (t, *J*= 6.0 Hz, 2H), 3.58-3.55 (m, 4H), 3.52-3.50 (m, 4H), 3.20 (s, 3H), 2.39-2.35 (m, 4H). ¹³C NMR (100 MHz, *d*₆-DMSO) δ in ppm 161.88, 148.67, 137.99, 128.52, 122.81, 121.96, 106.58, 70.39, 66.66, 63.03, 58.95, 53.59, 43.37. HRMS (ESI) *m/z* (M + H)⁺ calculated for C₁₆H₂₃N₄O₃ 319.1770; found, 319.1774. Melting Point: 166 °C. HPLC Purity: 97.60%.

Synthesis of 6-amino-3-(2-methoxyethyl)-2-(piperidin-1-ylmethyl)quinazolin-4(3H)-one (30): Compound **25** (0.5 g, 1.40 mmol) was dissolved in MeOH (8 mL) and a pinch of 10% wet Pd/C was added to the solution. H₂ gas was charged to the solution at room temperature (25-30 °C) for 4 h. Progress of the reaction was checked by TLC and the reaction procedure was followed according to general procedure C. After complete consumption of starting material, the reaction mixture was filtered through celite bed to remove Pd/C and washed three times (3 x 10 mL) with 10% MeOH in CHCl₃ mixture. The solution was evaporated in the rotary evaporator to obtain a light brown-coloured crude mass which was purified by flash chromatography using 10% MeOH in CHCl₃ (V/V) as eluent to afford **30** as a white solid compound (yield 66%). ¹H NMR (400 MHz, *d*₆-DMSO) δ in ppm 7.38 (d, *J* = 8.8 Hz, 1H), 7.16 (d, *J* = 2.4 Hz, 1H), 7.09 (dd, *J* = 8.8 Hz, *j* = 2.8 Hz, 1H), 5.77 (s, 2H), 4.58 (s, 2H), 4.14 (s, 2H), 3.53 (t, *J* = 5.2 Hz, 2H), 3.19 (s, 3H), 1.86-1.77 (m, 4H), 1.67-1.40 (m, 4H). ¹³C NMR (100 MHz, *d*₆-DMSO) δ in ppm 128.32, 123.07, 121.87, 106.75, 70.04, 59.06, 54.11, 43.94, 43.31, 22.54. HRMS (ESI) *m/z* (M + H)⁺ calculated for C₁₇H₂₅N₄O₂ 317.1978; found, 317.1980. Melting Point: 152 °C. HPLC Purity: 98.20%.

Synthesis of 6-amino-3-(2-methoxyethyl)-2-(pyrrolidin-1-ylmethyl)quinazolin-4(3H)-one (31): Compound **26** (0.5 g, 1.50 mmol) was dissolved in MeOH (8 mL) and a pinch of 10% wet Pd/C was added to the solution. H₂ gas was charged to the solution at room temperature (25-30 °C) for 4 h. Progress of the reaction was checked by TLC and the reaction procedure was followed according to general procedure C. After complete consumption of starting material, the reaction mixture was filtered through celite bed to remove Pd/C and washed three times (3 x 10 mL) with 10% MeOH in CHCl₃ mixture. The solution was evaporated in the rotary evaporator to obtain a light brown-coloured crude mass which was purified by flash chromatography using 10% MeOH in CHCl₃ (V/V) as eluent to afford **31** as a white solid compound (yield 68%). ¹H NMR (400 MHz, *d*₆-DMSO) δ in ppm 7.30 (d, *J* = 8.8 Hz, 1H), 7.14 (d, *J* = 2.4 Hz, 1H), 7.01 (dd, *J* = 8.4 Hz, *j* = 2.8 Hz, 1H), 5.57 (s, 2H), 4.36 (t, *J* = 5.2 Hz, 2H), 3.68 (s, 2H), 3.54 (t, *J* = 5.6 Hz, 2H), 3.18 (s, 3H), 2.45-2.42 (m, 4H), 1.67-1.62 (4H). ¹³C NMR (100 MHz, *d*₆-DMSO) δ in ppm 161.80, 150.07, 148.54, 138.22, 128.48, 122.83, 121.91, 106.64, 70.38, 60.16, 58.91, 53.87, 43.22, 23.69. HRMS (ESI) *m/z* (M + H)⁺ calculated for C₁₆H₂₃N₄O₂ 303.1821; found, 303.1825. Melting Point: 148 °C. HPLC Purity: 98.60%.

Synthesis of 6-amino-2-((dimethylamino)methyl)-3-(2-methoxyethyl)quinazolin-4(3H)-one (32): Compound **27** (0.5 g, 1.63 mmol) was dissolved in MeOH (8 mL) and a pinch of 10% wet Pd/C was added to the solution. H₂ gas was charged to the solution at room temperature (25-30 °C) for 4 h. Progress of the reaction was checked by TLC and the reaction procedure was followed according to general procedure C. After complete consumption of starting material, the reaction mixture was filtered through celite bed to remove Pd/C and washed three times (3 x 10 mL) with 10% MeOH in CHCl₃ mixture. The solution was evaporated in the rotary evaporator to obtain a light brown-coloured crude mass which was purified by flash chromatography using 10% MeOH in CHCl₃ (V/V) as eluent to afford **32** as a white solid compound (yield 68%). ¹H NMR (300 MHz, *d*₆-DMSO) δ in ppm 7.31 (d, *J* = 8.4 Hz, 1H), 7.13 (d, *J* = 2.8 Hz, 1H), 7.01 (dd, *J* = 8.4 Hz, *j* = 2.8 Hz, 1H), 5.59 (s, 2H), 4.37 (t, *J* = 5.6 Hz, 2H), 3.54 (t, *J* = 5.6 Hz, 2H), 3.49 (s, 2H), 3.18 (s, 3H), 2.15 (s, 6H). ¹³C NMR (100 MHz, *d*₆-DMSO) δ in ppm 161.83, 149.52, 148.63, 138.08, 128.52, 122.82, 121.93, 106.62, 79.70, 70.41, 63.75, 58.94, 45.40, 43.25. HRMS (ESI) *m/z* (M + H)⁺ calculated for C₁₄H₂₁N₄O₂ 277.1665; found, 277.1669. Melting Point: 178 °C. HPLC Purity: 99.60%.

Synthesis of 1-(3-acetylphenyl)-3-(3-(2-methoxyethyl)-2-((4-methylpiperazin-1-yl)methyl)-4-oxo-3,4-dihydroquinazolin-6-yl)urea (33):

Compound **28** (0.10 g, 0.30 mmol) was dissolved in dry THF (8 mL) and 4-nitrophenylchloroformate (0.07 g, 0.36 mmol) was added portion wise under nitrogen atmosphere and left for stirring for 0.5 h. 3'-aminoacetophenone (0.04 g, 0.30 mmol) was added to the reaction mixture followed by TEA (0.1 mL, 0.75 mmol) and the reaction was performed according to the general procedure E. Pure compound was isolated by using column chromatography in 230-400 silica mesh size and with 2% MeOH in CHCl₃ (V/V) as eluent to obtain compound **33** as light brown coloured solid (yield 62%). ¹H NMR (400 MHz, *d*₆-DMSO), δ in ppm 9.14 (s, 1H), 9.01 (s, 1H), 8.28 (d, *J* = 2.8 Hz, 1H), 8.05 (t, *J* = 2.0 Hz, 1H), 7.75 (dd, *J* = 8.8 Hz, *j* = 2.8 Hz, 1H), 7.68-7.64 (m, 1H), 7.58-7.54 (m, 2H), 7.44-7.38 (m, 1H), 4.44-4.37 (m, 2H), 3.63 (s, 2H), 3.61-3.58 (m, 2H), 3.21 (s, 3H), 2.53 (s, 3H), 2.44-2.38 (m, 4H), 2.36-2.19 (m, 4H), 2.11 (s, 3H). ¹³C NMR (100 MHz, *d*₆-DMSO) δ in ppm 198.27, 161.88, 153.03, 152.37, 142.12, 140.48, 139.00, 137.95, 129.72, 128.34, 126.13, 123.52, 122.64, 121.31, 118.12, 113.63, 70.25, 62.74, 58.96, 55.05, 52.96, 46.10, 43.59, 27.30. HRMS (ESI) *m/z* (M + H)⁺ calculated for C₂₆H₃₃N₆O₄ 493.2563; found, 493.2565. Melting Point: 188 °C. HPLC Purity: 99.30%.

Synthesis of 1-(3-acetylphenyl)-3-(3-(2-methoxyethyl)-2-(morpholinomethyl)-4-oxo-3,4-dihydroquinazolin-6-yl)urea (34): Compound **29** (0.10 g, 0.30 mmol) was dissolved in dry THF (8 mL) and 4-nitrophenylchloroformate (0.07 g, 0.36 mmol) was added portion wise under nitrogen atmosphere and left for stirring for 0.5 h. 3'-aminoacetophenone (0.04 g, 0.30 mmol) was added to the reaction mixture followed by TEA (0.1 mL, 0.75 mmol) and the reaction was performed according to the general procedure E. Pure compound was isolated by using column chromatography in 230-400 silica mesh size and with 2% MeOH in CHCl₃ (V/V) as eluent to obtain compound **34** as light brown coloured solid (yield 52%). ¹H NMR (400 MHz, *d*₆-DMSO), δ in ppm 9.08 (s, 1H), 8.95 (s, 1H), 8.28 (d, *J* = 2.8 Hz, 1H), 8.05 (t, *J* = 2.0 Hz, 1H), 7.75 (dd, *J* = 8.8 Hz, *j* = 2.8 Hz, 1H), 7.67-7.64 (m, 1H), 7.57-7.55 (m, 2H), 7.43-7.39 (m, 1H), 4.43-4.40 (m, 2H), 3.64 (s, 2H), 3.61-3.59 (m, 2H), 3.54-3.52 (m, 4H), 3.21 (s, 3H), 2.53 (s, 3H), 2.42-2.39 (m, 4H). ¹³C NMR (100 MHz, *d*₆-DMSO) δ in ppm 198.27, 161.87, 153.01, 152.04, 142.10, 140.44, 138.99, 137.95, 129.72, 128.34, 126.15, 123.55, 121.33, 118.15, 113.66, 70.27, 66.65, 63.08, 58.98, 53.60, 43.63, 27.30. HRMS (ESI) *m/z* (*M* + *H*)⁺ calculated for C₂₅H₃₀N₅O₅ 480.2247; found, 480.2249. Melting Point: 182 °C. HPLC Purity: 99.32%.

Synthesis of 1-(3-acetylphenyl)-3-(3-(2-methoxyethyl)-4-oxo-2-(piperidin-1-ylmethyl)-3,4-dihydroquinazolin-6-yl)urea (35): Compound **30** (0.10 g, 0.30 mmol) was dissolved in dry THF (5 mL) and 4-nitrophenylchloroformate (0.08 g, 0.38 mmol) was added portion wise under nitrogen atmosphere and left for stirring for 0.5 h. 3'-aminoacetophenone (0.06 g, 0.38 mmol) was added to the reaction mixture followed by TEA (0.1 mL, 0.75 mmol) and the reaction was performed according to the general procedure E. Pure compound was isolated by using column chromatography in 230-400 silica mesh size and with 2% MeOH in CHCl₃ (V/V) as eluent to obtain compound **35** as light brown coloured solid (yield 68%). ¹H NMR (400 MHz, *d*₆-DMSO), δ in ppm 9.08 (s, 1H), 8.95 (s, 1H), 8.28 (d, *J* = 2.8 Hz, 1H), 8.05 (t, *J* = 2.0 Hz, 1H), 7.75 (dd, *J* = 8.8 Hz, *j* = 2.8 Hz, 1H), 7.67-7.64 (m, 1H), 7.57-7.55 (m, 2H), 7.42-7.38 (m, 1H), 4.43-4.40 (m, 2H), 3.61-3.58 (m, 4H), 3.21 (s, 3H), 2.53 (s, 3H), 2.41-2.32 (m, 4H), 1.48-1.40 (m, 4H), 1.38-1.30 (m, 2H). ¹³C NMR (100 MHz, *d*₆-DMSO) δ in ppm 198.24, 161.90, 153.01, 152.67, 142.15, 140.46, 138.92, 137.95, 129.71, 128.31, 126.15, 123.53, 122.64, 121.25, 118.15, 113.66, 70.28, 63.57, 58.94, 54.44, 43.58, 27.29, 26.03, 24.22. HRMS (ESI) *m/z* (*M* + *H*)⁺ calculated for C₂₆H₃₂N₅O₄ 478.2454; found, 478.2460. Melting Point: 190 °C. HPLC Purity: 98.30%.

Synthesis of 1-(3-acetylphenyl)-3-(3-(2-methoxyethyl)-4-oxo-2-(pyrrolidin-1-yl methyl)-3,4-dihydroquinazolin-6-yl)urea (36):

Compound **31** (0.10 g, 0.33 mmol) was dissolved in dry THF (5 mL) and 4-nitrophenylchloroformate (0.08 g, 0.39 mmol) was added portion wise under nitrogen atmosphere and left for stirring for 0.5 h. 3'-aminoacetophenone (0.06 g, 0.39 mmol) was added to the reaction mixture followed by TEA (0.2 mL, 0.82 mmol) and the reaction was performed according to the general procedure E. Pure compound was isolated by using column chromatography in 230-400 silica mesh size and with 2% MeOH in CHCl₃ (V/V) as eluent to obtain compound **36** as light brown coloured solid (yield 68%). ¹H NMR (400 MHz, *d*₆-DMSO), δ in ppm 9.09 (s, 1H), 8.97 (s, 1H), 8.29 (d, *J* = 2.8 Hz, 1H), 8.05 (t, *J* = 2.0 Hz, 1H), 7.75 (dd, *J* = 8.8 Hz, *j* = 2.8 Hz, 1H), 7.67-7.64 (m, 1H), 7.57-7.55 (m, 2H), 7.43-7.39 (m, 1H), 4.43-4.40 (m, 2H), 3.76 (s, 3H), 3.59-3.56 (m, 2H), 3.20 (s, 3H), 2.53 (s, 3H), 2.50-2.47 (m, 4H), 1.69-1.64 (m, 4H). ¹³C NMR (100 MHz, *d*₆-DMSO) δ in ppm 198.26, 161.78, 153.03, 142.34, 140.47, 138.88, 137.95, 129.72, 128.32, 126.17, 123.53, 122.64, 121.28, 118.14, 113.72, 70.25, 58.95, 53.93, 43.47, 27.30, 23.72. HRMS (ESI) *m/z* (M + H)⁺ calculated for C₂₅H₃₀N₅O₄ 464.2298; found, 464.2289. Melting Point: 172 °C. HPLC Purity: 98.50%.

Synthesis of 1-(3-acetylphenyl)-3-(2-((dimethylamino)methyl)-3-(2-methoxyethyl)-4-oxo-3,4-dihydroquinazolin-6-yl)urea (37): Compound **32** (0.10 g, 0.33 mmol) was dissolved in dry THF (5 mL) and 4-nitrophenylchloroformate (0.08 g, 0.39 mmol) was added portion wise under nitrogen atmosphere and left for stirring for 0.5 h. 3'-aminoacetophenone (0.06 g, 0.39 mmol) was added to the reaction mixture followed by TEA (0.2 mL, 0.82 mmol) and the reaction was performed according to the general procedure E. Pure compound was isolated by using column chromatography in 230-400 silica mesh size and with 2% MeOH in CHCl₃ (V/V) as eluent to obtain compound **37** as light brown coloured solid (yield 70%). ¹H NMR (400 MHz, CDCl₃), δ in ppm 9.10 (s, 1H), 8.98 (s, 1H), 8.29 (d, *J* = 2.8 Hz, 1H), 8.05 (t, *J* = 2.0 Hz, 1H), 7.75 (dd, *J* = 8.8 Hz, *j* = 2.8 Hz, 1H), 7.67-7.65 (m, 1H), 7.57-7.54 (m, 2H), 7.42-7.39 (m, 1H), 4.44-4.41 (m, 2H), 3.59-3.56 (m, 2H), 3.20 (s, 3H), 2.53 (s, 3H), 2.18 (s, 6H). ¹³C NMR (100 MHz, *d*₆-DMSO) δ in ppm 198.25, 161.82, 153.02, 152.87, 142.20, 140.47, 138.97, 137.95, 129.71, 128.35, 126.18, 123.53, 122.63, 121.28, 118.14, 113.71, 100.00, 70.28, 63.81, 58.98, 45.47, 43.50, 27.30, 22.58, 21.64. HRMS (ESI) *m/z* (M + H)⁺ calculated for C₂₃H₂₈N₅O₄ 438.2141; found, 438.2144. Melting Point: 188 °C. HPLC Purity: 98.70%.

Synthesis of 3-(2-methoxyethyl)-6-nitroquinazoline-2,4(1H,3H)-dione (38):

Compound **2** (0.3 g, 1.25 mmol) was dissolved in dry DMF and CDI (0.31 g, 1.89 mmol) was added. The reaction mixture was heated at 120 °C for 16 h. Progress of the reaction was monitored by checking TLC. After reaction completion, the reaction mixture was poured into the crushed ice and extracted with EtOAc/ water in a separating funnel. The organic layer was dried over anhydrous Na₂SO₄ and evaporated in the vacuum to afford a brown-coloured crude mass. Pure compound was isolated by purification in flash chromatography using 50% EtOAc in Pet ether (V/V) as eluent to obtain compound **38** as an off-white solid (yield 85%). ¹H NMR (400MHz, *d*₆-DMSO) δ in ppm 12.08 (s, 1H), 8.64-8.60 (m, 1H), 8.49-8.45 (m, 1H), 7.32 (d, *J*= 12.0 Hz, 1H), 4.09 (t, *J*= 8.0 Hz, 2H), 3.54 (t, *J*= 8.0 Hz, 2H), 3.25 (s, 3H). ¹³C NMR (100 MHz, *d*₆-DMSO) δ in ppm 161.39, 150.31, 144.63, 142.53, 130.17, 124.10, 117.09, 114.31, 68.75, 58.44. HRMS (ESI) *m/z* (M + H)⁺ calculated for Chemical Formula: C₁₁H₁₂N₃O₅ 266.0777; found, 266.0764. Melting Point: 158°C.

Synthesis of 6-amino-3-(2-methoxyethyl)quinazoline-2,4(1H,3H)-dione (39):

Compound **38** (0.22 g, 0.83 mmol) was dissolved in MeOH (10 mL) and a pinch of 10% wet Pd/C was added to the solution. H₂ gas was charged to the solution at room temperature (25-30 °C) for 4 h. Progress of the reaction was checked by TLC and the reaction procedure was followed according to general procedure A. Pure compound was isolated by flash chromatography using 80% EtOAc in Pet ether (V/V) as eluent to afford **39** as brown solid (yield 82%). ¹H NMR (400MHz, *d*₆-DMSO) δ in ppm 11.03 (s, 1H), 7.11-7.08 (m, 1H), 6.94-6.90 (m, 2H), 5.18 (s, 2H), 4.06 (t, *J*= 8.4Hz, 2H), 3.50 (t, *J*= 8.0Hz, 2H), 3.23 (s, 3H). ¹³C NMR (100 MHz, *d*₆-DMSO) δ in ppm 162.64, 150.27, 144.72, 130.51, 123.30, 116.36, 114.85, 109.74, 69.09, 58.39. HRMS (ESI) *m/z* (M + H)⁺ calculated for Chemical Formula: C₁₁H₁₄N₃O₃ 236.1035; found, 236.1034. Melting Point: >220 °C.

Synthesis of 1-(3-acetylphenyl)-3-(3-(2-methoxyethyl)-2,4-dioxo-1,2,3,4-tetrahydroquinazolin-6-yl)urea (40):

Compound **39** (0.10 g, 0.42 mmol) was dissolved in dry THF (8 mL) and 4-nitrophenylchloroformate (0.11 g, 0.51 mmol) was added portion wise under nitrogen atmosphere and left for stirring for 1 h. 3'-aminoacetophenone (0.07 g, 0.51 mmol) was added to the reaction mixture followed by TEA (0.15 mL, 1.06 mmol) and the reaction was performed according to the general procedure C. Pure compound was isolated by using column chromatography in 230-400 silica mesh size and with 2% MeOH in CHCl₃

(V/V) as eluent to obtain compound **40** as off-white solid (yield 62%). ^1H NMR (400MHz, d_6 -DMSO) δ in ppm 11.29 (s, 1H), 8.85 (d, J = 10.8 Hz, 2H), 8.07 (d, J = 2.4 Hz, 1H), 8.04-8.02 (m, 1H), 7.64 (dd, J = 9.2 Hz, 2.8 Hz, 2H), 7.55-7.53 (m, 1H), 7.41-7.37 (m, 1H), 7.09 (d, J = 8.8 Hz, 1H), 4.05 (t, J = 6.0 Hz, 2H), 3.49 (t, J = 6.0 Hz, 2H), 3.20 (s, 3H), 2.52 (s, 3H). ^{13}C NMR (100 MHz, d_6 -DMSO) δ in ppm 198.28, 162.39, 153.16, 150.43, 140.58, 137.92, 135.11, 134.92, 129.68, 127.08, 123.44, 122.50, 118.04, 116.40, 116.19, 114.37, 69.02, 58.42, 27.28. HRMS (ESI) m/z ($M + H$) $^+$ calculated for Chemical Formula: $\text{C}_{20}\text{H}_{21}\text{N}_4\text{O}_5$ 397.1512; found, 397.1515. Melting Point: >220 °C. HPLC Purity: 98.42%.

Synthesis of 3-(2-methoxyethyl)-1-methyl-6-nitroquinazoline-2,4(1H,3H)-dione (41): Compound **38** (0.6 g, 2.26 mmol) was dissolved in dry DMF (8 mL) and K_2CO_3 (0.69 g, 4.98 mmol) was added. Methyl iodide (0.21 mL, 3.39 mmol) was added dropwise and the reaction was performed according to the general procedure D. Pure compound was isolated by purification in flash chromatography with 230-400 silica mesh size and 50% EtOAc in Pet ether (V/V) as eluent to afford **41** as yellow solid (yield 84%). ^1H NMR (400 MHz, d_6 -DMSO) δ in ppm 8.67 (d, J = 2.8 Hz, 1H), 8.50 (dd, J = 9.2 Hz, 2.8 Hz, 1H), 7.62 (d, J = 9.2 Hz, 1H), 4.11 (t, J = 6 Hz, 2H), 3.53 (s, 3H), 3.51 (t, J = 6 Hz, 2H), 3.21 (s, 3H). ^{13}C NMR (100 MHz, d_6 -DMSO) δ in ppm 160.60, 150.62, 145.41, 142.58, 130.09, 123.98, 116.90, 115.45, 68.75, 58.45, 31.91. HRMS (ESI) m/z ($M + H$) $^+$ calculated for Chemical Formula: $\text{C}_{12}\text{H}_{14}\text{N}_3\text{O}_5$ 280.0933; found, 280.0936. Melting Point: 128 °C.

Synthesis of 1-isopropyl-3-(2-methoxyethyl)-6-nitroquinazoline-2,4(1H,3H)-dione (42): Compound **38** (0.6 g, 2.26 mmol) was dissolved in dry DMF (8 mL) and K_2CO_3 (0.69 g, 4.98 mmol) was added. 2-iodopropane (0.34 mL, 3.39 mmol) was added dropwise and the reaction was performed according to the general procedure D. Pure compound was isolated by purification in flash chromatography with 230-400 silica mesh size and 60% EtOAc in Pet ether (V/V) as eluent to afford **42** as a light yellow solid (yield 70%). ^1H NMR (400 MHz, CDCl_3) δ in ppm 9.06 (d, J = 2.8 Hz, 1H), 8.42 (dd, J = 9.2 Hz, 2.58 Hz, 1H), 7.46 (d, J = 9.2 Hz, 1H), 5.17-4.99 (m, 1H), 4.30 (t, J = 6.0 Hz, 2H), 3.67 (t, J = 6.0 Hz, 2H), 3.34 (s, 3H), 1.62 (d, J = 6.8 Hz, 6H). ^{13}C NMR (100 MHz, CDCl_3) δ in ppm 160.29, 150.41, 144.16, 142.91, 129.79, 125.64, 115.89, 115.01, 69.15, 58.83, 54.38, 52.47, 43.40, 41.26, 23.62. HRMS (ESI) m/z ($M + H$) $^+$ calculated for $\text{C}_{14}\text{H}_{18}\text{N}_3\text{O}_5$ 308.1246; found 308.1246. Melting Point: 148 °C.

Synthesis of 3-(2-methoxyethyl)-6-nitro-1-(2-(pyrrolidin-1-yl)ethyl)quinazoline-2,4(1H,3H)-dione (43): Compound **38** (0.4 g, 1.50 mmol) was dissolved in dry DMF (8 mL) and K₂CO₃ (0.46 g, 3.31 mmol) was added. 1-(2-Chloroethyl)pyrrolidine hydrochloride (0.39 g, 2.26 mmol) was added and the reaction was performed according to the general procedure D. Pure compound was isolated by purification in flash chromatography with 230-400 silica mesh size and 2% MeOH in CHCl₃ (V/V) as eluent to afford **43** as a light yellow solid (yield 75%). ¹H NMR (400 MHz, CDCl₃) δ in ppm 9.04 (d, J= 2.8 Hz, 1H), 8.46 (dd, J= 9.2 Hz, 2.8 Hz, 1H), 7.46 (d, J= 9.2 Hz, 1H), 4.36-4.30 (m, 4H), 3.67 (t, J= 5.6 Hz, 2H), 3.33 (s, 3 H), 2.84-2.80 (m, 2H), 2.70-2.67 (m, 4H), 1.83-1.80 (m, 4H). ¹³C NMR (100 MHz, CDCl₃) δ in ppm 160.29, 150.41, 144.16, 142.91, 129.79, 125.64, 115.89, 115.01, 69.15, 58.83, 54.38, 52.47, 43.40, 41.26, 23.62. HRMS (ESI) *m/z* (M + H)⁺ calculated for C₁₇H₂₃N₄O₅ 363.1668; found, 363.1665. Melting Point: 172 °C.

Synthesis of 3-(2-methoxyethyl)-6-nitro-1-(2-(piperidin-1-yl)ethyl)quinazoline-2,4(1H,3H)-dione (44):

Compound **38** (0.3 g, 1.13 mmol) was dissolved in dry DMF (8 mL) and K₂CO₃ (0.34 g, 2.48 mmol) was added. 1-(2-Chloroethyl)piperidine hydrochloride (0.32 g, 1.69 mmol) was added and the reaction was performed according to the general procedure D. Pure compound was isolated by purification in flash chromatography with 230-400 silica mesh size and 90% EtOAc in Pet ether (V/V) as eluent to afford **44** as off-white solid (yield 80%). ¹H NMR (400 MHz, CDCl₃) δ in ppm 9.03 (d, J= 2.8 Hz, 1H), 8.47 (dd, J= 9.2 Hz, 2.8 Hz, 1H), 7.53 (d, J= 9.2 Hz, 1H), 4.35 (t, J= 7.2 Hz, 2H), 4.31 (t, J= 5.6 Hz, 2H), 3.67 (t, J= 5.6 Hz, 2H), 3.33 (s, 3H), 2.69 (t, J= 7.6 Hz, 2H), 2.59-2.57 (m, 4H), 1.64-1.58 (m, 4H), 1.48-1.44 (m, 2H). ¹³C NMR (100 MHz, CDCl₃) δ in ppm 160.32, 150.44, 144.25, 142.92, 129.77, 125.56, 115.83, 115.28, 69.15, 58.83, 55.07, 54.79, 41.92, 41.25, 30.74, 29.67, 25.36, 23.84. HRMS (ESI) *m/z* (M + H)⁺ calculated for C₁₈H₂₅N₄O₅ 377.1825; found, 377.1837. Melting Point: 152 °C.

Synthesis of 3-(2-methoxyethyl)-6-nitro-1-(3-(piperidin-1-yl)propyl)quinazoline-2,4(1H,3H)-dione (45): Compound **76** (0.3 g, 1.13 mmol) was dissolved in dry DMF (8 mL) and K₂CO₃ (0.34 g, 2.48 mmol) was added. 1-(3-Chloropropyl)piperidine hydrochloride (0.34 g, 1.70 mmol) was added and the reaction was performed according to the general procedure D. Pure compound was isolated by purification in flash chromatography with 230-400 silica mesh size and 90% EtOAc in Pet ether (V/V) as eluent to afford **83** as yellow solid (yield 70%). ¹H NMR (400 MHz, CDCl₃) δ in ppm 9.05

(d, J = 2.4 Hz, 1H), 8.44 (dd, J = 9.2 Hz, 3.2 Hz, 1H), 7.61 (d, J = 9.2 Hz, 1H), 4.32 (t, J = 6.0 Hz, 2H), 4.22 (t, J = 7.2 Hz, 2H), 3.67 (t, J = 6.0 Hz, 2H), 3.34 (s, 3H), 2.42-2.32 (m, 6H), 1.93-1.86 (m, 2H), 1.60-1.53 (m, 4H), 1.48-1.42 (m, 2H). ^{13}C NMR (100 MHz, CDCl_3) δ in ppm 160.44, 150.49, 144.51, 142.75, 129.51, 125.56, 115.79, 115.29, 69.17, 58.82, 55.71, 54.71, 43.16, 41.14, 26.13, 24.63, 24.40. HRMS (ESI) m/z ($M + H$)⁺ calculated for $\text{C}_{19}\text{H}_{27}\text{N}_4\text{O}_5$ 391.1981; found, 391.1978. Melting Point: 140 °C.

Synthesis of 3-(2-methoxyethyl)-1-(2-morpholinoethyl)-6-nitroquinazoline-2,4(1H,3H)-dione (46): Compound **38** (0.4 g, 1.50 mmol) was dissolved in dry DMF (8 mL) and K_2CO_3 (0.46 g, 3.31 mmol) was added. 4-(2-Chloroethyl)morpholine hydrochloride (0.42 g, 2.26 mmol) was added and the reaction was performed according to the general procedure D. Pure compound was isolated by purification in flash chromatography with 230-400 silica mesh size and 3% MeOH in CHCl_3 (V/V) as eluent to afford **46** as yellow solid (yield 72%). ^1H NMR (400 MHz, CDCl_3) δ in ppm 9.06 (d, J = 2.8 Hz, 1H), 8.47 (dd, J = 9.2 Hz, 2.4 Hz, 1H), 7.35 (d, J = 9.2 Hz, 1H), 4.34-4.29 (m, 4H), 3.69-3.65 (m, 6H), 3.34 (s, 3H), 2.66 (t, J = 6.8 Hz, 2H), 2.55-2.53 (m, 4H). ^{13}C NMR (100 MHz, CDCl_3) δ in ppm 160.27, 150.50, 144.16, 142.88, 129.64, 125.78, 115.97, 114.73, 69.18, 66.95, 58.86, 55.36, 54.04, 41.90, 41.31. HRMS (ESI) m/z ($M + H$)⁺ calculated for $\text{C}_{17}\text{H}_{23}\text{N}_4\text{O}_6$ 379.1618; found, 379.1611. Melting Point: 160 °C.

Synthesis of 3-(2-methoxyethyl)-1-(3-morpholinopropyl)-6-nitroquinazoline-2,4(1H,3H)-dione (47): Compound **38** (0.4 g, 1.50 mmol) was dissolved in dry DMF (8 mL) and K_2CO_3 (0.46 g, 3.31 mmol) was added. 4-(3-Chloropropyl)morpholine hydrochloride (0.45 g, 2.26 mmol) was added and the reaction was performed according to the general procedure D. Pure compound was isolated by purification in flash chromatography with 230-400 silica mesh size and 3% MeOH in CHCl_3 (V/V) as eluent to afford **47** as off-white solid (yield 70%). ^1H NMR (400 MHz, CDCl_3) δ in ppm 9.05 (d, J = 2.4 Hz, 1H), 8.44 (dd, J = 9.2 Hz, 2.8 Hz, 1H), 7.49 (d, J = 9.2 Hz, 1H), 4.32 (t, J = 5.6 Hz, 2H), 4.26 (t, J = 7.2 Hz, 2H), 3.70-3.66 (m, 6H), 3.34 (s, 3H), 2.46-2.41 (m, 6H), 1.92-1.87 (m, 2H). ^{13}C NMR (100 MHz, CDCl_3) δ in ppm 160.34, 150.47, 144.38, 142.78, 129.54, 125.70, 115.87, 114.82, 69.16, 67.06, 58.82, 55.61, 53.78, 43.01, 41.19, 24.20. HRMS (ESI) m/z ($M + H$)⁺ calculated for $\text{C}_{18}\text{H}_{25}\text{N}_4\text{O}_6$ 393.1774; found, 393.6787. Melting Point: 164 °C.

Synthesis of 6-amino-3-(2-methoxyethyl)-1-methylquinazoline-2,4(1H,3H)-dione (48): Compound **41** (0.40 g, 1.43 mmol) was dissolved in MeOH (8 mL) and a pinch of

10% wet Pd/C was added to the solution. H₂ gas was charged to the solution at room temperature (25-30 °C) for 4 h. Progress of the reaction was checked by TLC and the reaction procedure was followed according to general procedure A. Pure compound **48** was isolated as a light brown solid by filtration under vacuum (yield 96%). ¹H NMR (400 MHz, *d*₆-DMSO) δ in ppm 7.19(d, *J*= 2.8Hz, 1H), 7.13(d, *J*= 8.8Hz, 1H), 6.99(dd, *J*= 9.2Hz, 2.8Hz, 1H), 5.24(s, 2H), 4.07(t, *J*= 6.4Hz, 2H), 3.47(t, *J*= 6.0Hz, 2H), 3.39(s, 3H), 3.19(s, 3H). ¹³C NMR (100 MHz, *d*₆-DMSO) δ in ppm 161.77, 150.33, 145.18, 131.46, 122.74, 115.96, 115.89, 110.51, 69.09, 58.40, 30.94. HRMS (ESI) *m/z* (M + H)⁺ calculated for C₁₂H₁₆N₃O₃ 250.1192; found, 250.1181. Melting Point: 180 °C.

Synthesis of 6-amino-1-isopropyl-3-(2-methoxyethyl)quinazoline-2,4(1H,3H)-dione

(49): Compound **42** (0.40 g, 1.30 mmol) was dissolved in MeOH (8 mL) and a pinch of 10% wet Pd/C was added to the solution. H₂ gas was charged to the solution at room temperature (25-30 °C) for 4 h. Progress of the reaction was checked by TLC and the reaction procedure was followed according to general procedure A. Pure compound was isolated by purification in flash chromatography with 230-400 silica mesh size and 80% EtOAc in Pet ether(V/V) as eluent to afford **49** as light yellow gummy material (yield 92%). ¹H NMR (400 MHz, CDCl₃) δ in ppm 7.49(d, *J*= 2.8 Hz, 1H), 7.17(d, *J*= 8.8 Hz, 1H), 6.97(dd, *J*= 8.8 Hz, 2.8 Hz, 1H), 5.05-4.92 (m, 1H), 4.28(t, *J*= 6.0 Hz, 2H), 3.74(s, 2H), 3.64(t, *J*= 6.0 Hz, 2H), 3.35(s, 3H), 1.56(d, 6H). ¹³C NMR (100 MHz, CDCl₃) δ in ppm 162.03, 141.80, 122.44, 117.23, 115.52, 113.32, 69.54, 58.76, 40.47, 19.89. HRMS (ESI) *m/z* (M + H)⁺ calculated for C₁₄H₂₀N₃O₃ 278.1505; found, 278.1503.

Synthesis of 6-amino-3-(2-methoxyethyl)-1-(2-(pyrrolidin-1-yl)ethyl)quinazoline-2,4(1H,3H)-dione (50):

Compound **43** (0.50 g, 1.37 mmol) was dissolved in MeOH (10 mL) and a pinch of 10% wet Pd/C was added to the solution. H₂ gas was charged to the solution at room temperature (25-30 °C) for 6 h. Progress of the reaction was checked by TLC and the reaction procedure was followed according to general procedure A. Pure compound was isolated by purification in flash chromatography with 230-400 silica mesh size and 5% MeOH in CHCl₃(V/V) as eluent to afford **50** as brown gummy material (yield 90%). ¹H NMR (400 MHz, CDCl₃) δ in ppm 7.20 (d, *J*= 2.8Hz, 1H), 7.16 (d, *J*= 8.8Hz, 1H), 7.00 (dd, *J*= 9.2Hz, 2.8Hz, 1H), 5.27 (s, 2H), 4.19-4.06 (m, 2H), 4.07 (t, *J*= 6.0Hz, 2H), 3.47 (t, *J*= 6.4Hz, 2H), 3.19 (s, 3H), 2.86-2.52 (m, 6H), 1.74-1.63 (m, 4H). ¹³C NMR (100 MHz, CDCl₃) δ in ppm 161.62, 150.79, 143.12, 131.10, 123.93, 116.43, 115.48, 112.83, 69.48,

58.87, 53.76, 50.94, 40.92, 39.47, 23.52. HRMS (ESI) m/z (M + H)⁺ calculated for C₁₇H₂₅N₄O₃ 333.1927; found, 333.1929.

Synthesis of 6-amino-3-(2-methoxyethyl)-1-(2-(piperidin-1-yl)ethyl)quinazoline-2,4(1H,3H)-dione (51): Compound **44** (0.40 g, 1.06 mmol) was dissolved in MeOH (10 mL) and a pinch of 10% wet Pd/C was added to the solution. H₂ gas was charged to the solution at room temperature (25-30 °C) for 6 h. Progress of the reaction was checked by TLC and the reaction procedure was followed according to general procedure A. Pure compound was isolated by purification in flash chromatography with 230-400 silica mesh size and 8% MeOH in CHCl₃(V/V) as eluent to afford **51** as light brown solid (yield 93%). ¹H NMR (400 MHz, *d*₆-DMSO) δ in ppm 7.32(d, *J* = 7.2 Hz, 1H), 7.21(d, *J* = 2.8 Hz, 1H), 7.00(dd, *J* = 8.8 Hz, 1H), 5.30(s, 2H), 4.30(s, 2H), 4.07(t, *J* = 6.0 Hz, 2H), 3.47(t, *J* = 6.0 Hz, 2H), 3.20(s, 3H), 3.12-2.74(m, 6H), 1.72-1.55(m, 4H), 1.53-1.38(m, 2H). ¹³C NMR (100 MHz, *d*₆-DMSO) δ in ppm 161.71, 150.45, 145.33, 122.81, 116.36, 115.88, 110.72, 69.02, 58.42. HRMS (ESI) m/z (M + H)⁺ calculated for C₁₈H₂₇N₄O₃ 347.2083; found, 347.2078. Melting Point: 98 °C.

Synthesis of 6-amino-3-(2-methoxyethyl)-1-(3-(piperidin-1-yl)propyl)quinazoline-2,4(1H,3H)-dione (52): Compound **45** (0.50 g, 1.28 mmol) was dissolved in MeOH (10 mL) and a pinch of 10% wet Pd/C was added to the solution. H₂ gas was charged to the solution at room temperature (25-30 °C) for 6 h. Progress of the reaction was checked by TLC and reaction procedure was followed according to general procedure A. Pure compound was isolated by purification in flash chromatography with 230-400 silica mesh size and 5% MeOH in CHCl₃ (V/V) as eluent to afford **52** as light brown solid (yield 92%). ¹H NMR (400 MHz, CDCl₃) δ in ppm 7.45(d, *J* = 2.8 Hz, 1H), 7.15(d, *J* = 8.8 Hz, 1H), 6.97(dd, *J* = 8.8 Hz, 2.8 Hz, 1H), 4.28(t, *J* = 6.0 Hz, 2H), 4.09(t, *J* = 7.2 Hz, 2H), 3.76 (s, 2H), 3.64(t, *J* = 6.0 Hz, 2H), 3.33(s, 3H), 2.43-2.36 (m, 4H), 1.93-1.85 (m, 2H), 1.61-1.55(m, 4H), 1.46-1.39 (m, 2H). ¹³C NMR (100 MHz, CDCl₃) δ in ppm 161.99, 150.60, 142.17, 132.50, 123.02, 116.55, 115.16, 112.95, 69.52, 58.77, 56.06, 54.63, 42.17, 40.63, 25.85, 24.77, 24.31. HRMS (ESI) m/z (M + H)⁺ calculated for C₁₉H₂₉N₄O₃ 361.2240; found, 361.2246. Melting Point: 160 °C.

Synthesis of 6-amino-3-(2-methoxyethyl)-1-(2-morpholinoethyl)quinazoline-2,4(1H,3H)-dione (53):

Compound **46** (0.40 g, 1.05 mmol) was dissolved in MeOH (8 mL) and a pinch of 10% wet Pd/C was added to the solution. H₂ gas was charged to the solution at room temperature (25-30 °C) for 6 h. Progress of the reaction was checked by TLC and reaction procedure was followed according to general procedure A. Pure compound was isolated by purification in flash chromatography with 230-400 silica mesh size and 5% MeOH in CHCl₃ (V/V) as eluent to afford **53** as yellow solid (yield 92%). ¹H NMR (400 MHz, CDCl₃) δ in ppm 7.45 (d, *J*= 2.4Hz, 1H), 7.05-6.95 (m, 2H), 4.29 (t, *J*= 6.0Hz, 2H), 4.20 (t, *J*= 7.2Hz, 2H), 3.77 (s, 2H), 3.69-3.64 (m, 6H), 3.34 (s, 3H), 2.62 (t, *J*= 7.2Hz, 2H), 2.56-2.54 (m, 4H). ¹³C NMR (100 MHz, CDCl₃) δ in ppm 161.88, 150.62, 142.24, 132.28, 122.95, 116.68, 114.71, 113.17, 69.54, 66.99, 58.80, 55.43, 54.00, 41.05, 40.77. HRMS (ESI) *m/z* (M + H)⁺ calculated for C₁₇H₂₅N₄O₄ 349.1876; found, 349.1877. Melting Point: 180 °C.

Synthesis of 6-amino-3-(2-methoxyethyl)-1-(3-morpholinopropyl)quinazoline-2,4 (1H,3H)-dione (54):

Compound **47** (0.35 g, 0.89 mmol) was dissolved in MeOH (8 mL) and a pinch of 10% wet Pd/C was added to the solution. H₂ gas was charged to the solution at room temperature (25-30 °C) for 6 h. Progress of the reaction was checked by TLC and reaction procedure was followed according to procedure A. Pure compound was isolated by purification in flash chromatography with 230-400 silica mesh size and 8% MeOH in CHCl₃ (V/V) as eluent to afford **54** as light yellow solid (yield 94%). ¹H NMR (400 MHz, CDCl₃) δ in ppm 7.39 (d, *J*= 2.8Hz, 1H), 7.07 (d, *J*=8.8Hz, 1H), 6.98-6.95 (m, 1H), 4.23 (t, *J*= 6.0Hz, 2H), 4.06 (t, *J*= 7.2Hz, 2H), 3.65-3.63 (m, 4H), 3.59 (t, *J*= 6.0Hz, 2H), 3.29 (s, 3H), 2.42-2.37 (m, 6H), 1.87-1.79 (m, 2H). HRMS (ESI) *m/z* (M + H)⁺ calculated for C₁₈H₂₇N₄O₄ 363.2032; found, 363.5776. Melting Point: 188 °C.

Synthesis of 1-(3-acetylphenyl)-3-(3-(2-methoxyethyl)-1-methyl-2,4-dioxo-1,2,3,4-tetrahydroquinazolin-6-yl)urea (55): Compound **48** (0.12 g, 0.48 mmol) was dissolved in dry THF (8 mL) and 4-nitrophenylchloroformate (0.12 g, 0.58 mmol) was added portion wise under nitrogen atmosphere and left for stirring for 1 h. 3'-aminoacetophenone (0.08 g, 0.58 mmol) was added to the reaction mixture followed by TEA (0.17 mL, 1.21 mmol) and the reaction was performed according to the general procedure C. Pure compound was isolated by using column chromatography in 230-400 silica mesh size and with 80% EtOAc in Pet ether (V/V) as eluent to obtain compound **55** as white solid (yield 52%). ¹H NMR (400 MHz, *d*₆-DMSO) δ in ppm 8.92 (s, 1H), 8.90 (s, 1H), 8.17 (d, 2.4Hz, 1H), 8.04-8.02 (m, 1H), 7.77 (dd, *J*= 9.2Hz, 2.8Hz, 1H), 7.66-7.63 (m,

1H), 7.56-7.53 (m, 1H), 7.42-7.34 (m, 2H), 4.10 (t, J = 6.0 Hz, 2H), 3.49 (t, J = 6.0 Hz, 2H), 3.45 (s, 3H), 3.20 (s, 3H), 2.52 (s, 3H). ^{13}C NMR (100 MHz, d_6 -DMSO) δ in ppm 198.28, 162.39, 153.16, 150.43, 140.58, 137.92, 135.11, 134.92, 129.68, 127.08, 123.44, 122.50, 118.04, 116.40, 116.19, 114.37, 69.02, 58.42, 27.28. HRMS (ESI) m/z ($M + H$)⁺ calculated for $\text{C}_{21}\text{H}_{23}\text{N}_4\text{O}_5$ 411.1668; found, 411.1659. Melting Point: >220 °C. HPLC Purity: 96.52%.

Synthesis of 1-(3-acetylphenyl)-3-(1-isopropyl-3-(2-methoxyethyl)-2,4-dioxo-1,2,3,4-tetrahydroquinazolin-6-yl)urea (56):

Compound **49** (0.15 g, 0.54 mmol) was dissolved in dry THF (8 mL) and 4-nitrophenylchloroformate (0.13 g, 0.65 mmol) was added portion wise under nitrogen atmosphere and left for stirring for 1 h. 3'-aminoacetophenone (0.09 g, 0.65 mmol) was added to the reaction mixture followed by TEA (0.19 mL, 1.35 mmol) and the reaction was performed according to the general procedure C. Pure compound was isolated by using column chromatography in 230-400 silica mesh size and with 70% EtOAc in Pet ether (V/V) as eluent to obtain compound **56** as off-white solid (yield 40%). ^1H NMR (400 MHz, CDCl_3) δ in ppm 8.36 (s, 1H), 8.26 (dd, J = 9.2 Hz, 2.8 Hz, 1H), 8.17 (s, 1H), 7.92 (d, J = 2.8 Hz, 1H), 7.89-7.87 (m, 1H), 7.86-7.83 (m, 1H), 7.61-7.58 (m, 1H), 7.40-7.38 (m, 1H), 7.33 (d, J = 9.2 Hz, 1H), 5.08-4.93 (m, 1H), 4.32 (t, J = 5.6 Hz, 2H), 3.71 (t, J = 5.6 Hz, 2H), 3.29 (s, 3H), 2.60 (s, 3H), 1.56 (d, J = 6.8 Hz, 6H). ^{13}C NMR (100 MHz, CDCl_3) δ in ppm 198.89, 162.58, 153.59, 149.90, 139.51, 137.62, 135.76, 134.52, 129.44, 128.05, 124.98, 123.52, 118.97, 118.81, 116.17, 70.12, 58.97, 41.40, 26.95, 19.82. HRMS (ESI) m/z ($M + H$)⁺ calculated for $\text{C}_{23}\text{H}_{27}\text{N}_4\text{O}_5$, 439.1981; found, 439.1971. Melting Point: 170 °C. HPLC Purity: 98.94%.

Synthesis of 1-(3-acetylphenyl)-3-(3-(2-methoxyethyl)-2,4-dioxo-1-(2-(pyrrolidin-1-yl)ethyl)-1,2,3,4-tetrahydroquinazolin-6-yl)urea (57): Compound **50** (0.15 g, 0.45 mmol) was dissolved in dry THF (8 mL) and 4-nitrophenylchloroformate (0.11 g, 0.54 mmol) was added portion wise under nitrogen atmosphere and left for stirring for 1 h. 3'-aminoacetophenone (0.08 g, 0.54 mmol) was added to the reaction mixture followed by TEA (0.16 mL, 1.12 mmol) and the reaction was performed according to the general procedure C. Pure compound was isolated by using column chromatography in 230-400 silica mesh size and with 3% MeOH in CHCl_3 (V/V) as eluent to obtain compound **57** as light brown solid (yield 48%). ^1H NMR (400 MHz, CDCl_3) δ in ppm 8.74 (s, 1H), 8.50 (s, 1H), 8.02-7.99 (m, 1H), 7.87 (d, J = 2.4 Hz, 1H), 7.80-7.77 (m, 1H), 7.66-7.64 (m, 1H), 7.54-7.51 (m, 1H), 7.33-7.29 (m, 1H), 7.12-7.09 (m, 1H), 4.33 (t, J = 6.4 Hz, 2H), 4.21 (t, J = 5.2 Hz,

2H), 3.61 (t, J = 5.2 Hz, 2H), 3.28 (s, 3H), 3.16-3.13 (m, 2H), 3.04-2.98 (m, 4H), 2.55 (s, 3H), 1.94-1.89 (m, 4H). ^{13}C NMR (100 MHz, CDCl_3) δ in ppm 198.71, 161.76, 153.24, 142.50, 139.69, 137.60, 135.11, 134.41, 129.25, 127.07, 124.03, 122.92, 118.26, 117.65, 115.63, 114.43, 69.66, 58.81, 54.81, 52.89, 31.66, 26.87, 23.53, 14.19. HRMS (ESI) m/z ($M + H$)⁺ calculated for $\text{C}_{26}\text{H}_{32}\text{N}_5\text{O}_5$, 494.2403; found, 494.2403. Melting Point: 182 °C. HPLC Purity: 98.12%.

Synthesis of 1-(3-acetylphenyl)-3-(3-(2-methoxyethyl)-2,4-dioxo-1-(2-(piperidin-1-yl)ethyl)-1,2,3,4-tetrahydroquinazolin-6-yl)urea (58): Compound **51** (0.20 g, 0.58 mmol) was dissolved in dry THF (8 mL) and 4-nitrophenylchloroformate (0.14 g, 0.69 mmol) was added portion wise under nitrogen atmosphere and left for stirring for 1 h. 3'-aminoacetophenone (0.1 g, 0.69 mmol) was added to the reaction mixture followed by TEA (0.20 mL, 1.44 mmol) and the reaction was performed according to the general procedure C. Pure compound was isolated by using column chromatography in 230-400 silica mesh size and with 10% MeOH in CHCl_3 (V/V) as eluent to obtain compound **58** as off-white solid (yield 50%). ^1H NMR (400 MHz, d_6 -DMSO) δ in ppm 9.11-9.05 (m, 2H), 8.18 (d, J = 2.4 Hz, 1H), 8.04-8.03 (m, 1H), 7.76 (dd, J = 8.8 Hz, 2.4 Hz, 1H), 7.66-7.63 (m, 1H), 7.55 (d, J = 7.6 Hz, 1H), 7.41-7.38 (m, 2H), 4.24-4.19 (m, 2H), 4.10 (t, J = 6.0 Hz, 2H), 3.50 (t, J = 6.0 Hz, 2H), 3.28 (s, 6H), 3.20 (s, 3H), 2.52 (s, 3H), 1.47 (m, 4H), 1.36 (m, 2H). ^{13}C NMR (100 MHz, d_6 -DMSO) δ in ppm 198.27, 161.47, 153.19, 150.56, 140.58, 137.94, 135.49, 129.69, 126.74, 123.43, 122.55, 118.00, 116.90, 115.79, 68.98, 58.44, 27.29. HRMS (ESI) m/z ($M + H$)⁺ calculated for $\text{C}_{27}\text{H}_{34}\text{N}_5\text{O}_5$, 508.2560; found, 508.2555. Melting Point: 190 °C. HPLC Purity: 100%.

Synthesis of 1-(3-acetylphenyl)-3-(3-(2-methoxyethyl)-2,4-dioxo-1-(3-(piperidin-1-yl)propyl)-1,2,3,4-tetrahydroquinazolin-6-yl)urea (59): Compound **52** (0.15 g, 0.42 mmol) was dissolved in dry THF (8 mL) and 4-nitrophenylchloroformate (0.10 g, 0.50 mmol) was added portion wise under nitrogen atmosphere and left for stirring for 1 h. 3'-aminoacetophenone (0.07 g, 0.50 mmol) was added to the reaction mixture followed by TEA (0.15 mL, 1.04 mmol) and the reaction was performed according to the general procedure C. Pure compound was isolated by using column chromatography in 230-400 silica mesh size and with 10% MeOH in CHCl_3 (V/V) as eluent to obtain compound **59** as off-white solid (yield 46%). ^1H NMR (600 MHz, d_6 -DMSO) δ in ppm 9.08 (s, 1H), 9.04 (s, 1H), 8.22 (d, J = 1.6 Hz, 1H), 8.09-8.07 (m, 1H), 7.82-7.89 (m, 1H), 7.70-7.68 (m, 1H), 7.59

(d, J = 5.2 Hz, 1H), 7.51 (d, J = 6.0 Hz, 1H), 7.46-7.42 (m, 1H), 4.14 (t, J = 4.0 Hz, 2H), 4.11 (t, J = 4.4 Hz, 2H), 3.53 (t, J = 4.0 Hz, 2H), 3.24 (s, 3H), 2.56 (s, 3H), 2.44-2.24 (m, 6H), 1.81-1.75 (m, 2H), 1.49-1.43 (m, 4H), 1.40-1.33 (m, 2H). ^{13}C NMR (100 MHz, d_6 -DMSO) δ in ppm 198.26, 161.53, 153.19, 150.45, 140.61, 137.93, 135.37, 135.14, 129.67, 126.59, 123.47, 122.53, 118.04, 116.91, 115.71, 68.99, 58.44, 55.85, 54.38, 27.29, 25.84, 24.37. HRMS (ESI) m/z ($M + H$)⁺ calculated for $\text{C}_{28}\text{H}_{36}\text{N}_5\text{O}_5$ 522.2716; found, 522.2722. Melting Point: 175 °C. HPLC Purity: 99.28%.

Synthesis of 1-(3-acetylphenyl)-3-(3-(2-methoxyethyl)-1-(2-morpholinoethyl)-2,4-dioxo-1,2,3,4-tetrahydroquinazolin-6-yl)urea (60): Compound **53** (0.12 g, 0.34 mmol) was dissolved in dry THF (8 mL) and 4-nitrophenylchloroformate (0.09 g, 0.41 mmol) was added portion wise under nitrogen atmosphere and left for stirring for 1 h. 3'-aminoacetophenone (0.06 g, 0.41 mmol) was added to the reaction mixture followed by TEA (0.12 mL, 0.86 mmol) and the reaction was performed according to the general procedure C. Pure compound was isolated by using column chromatography in 230-400 silica mesh size and with 3% MeOH in CHCl_3 (V/V) as eluent to obtain compound **60** as off-white solid (yield 45%). ^1H NMR (400 MHz, CDCl_3) δ in ppm 8.32(s, 1H), 8.24 (dd, J = 9.2 Hz, 2.4 Hz, 1H), 8.14 (s, 1H), 7.89 (d, J = 2.8 Hz, 1H), 7.87-7.84 (m, 2H), 7.61-7.58 (m, 1H), 7.41-7.36 (m, 1H), 7.18 (d, J = 9.2 Hz, 1H), 4.32 (t, J = 5.6 Hz, 2H), 4.22 (t, J = 6.8 Hz, 2H), 3.72-3.66 (m, 6H), 3.30 (s, 3H), 2.65-2.62 (m, 2H), 2.61 (s, 3H), 2.57-2.53 (m, 4H). ^{13}C NMR (100 MHz, CDCl_3) δ in ppm 198.92, 162.31, 153.43, 150.45, 139.50, 137.60, 135.41, 134.87, 129.48, 128.27, 124.83, 123.56, 118.73, 118.59, 115.67, 114.62, 70.05, 66.95, 58.98, 55.34, 53.99, 41.53, 26.96. HRMS (ESI) m/z ($M + H$)⁺ calculated for $\text{C}_{26}\text{H}_{32}\text{N}_5\text{O}_6$ 510.2353; found, 510.2355. Melting Point: 202 °C. HPLC Purity: 100%.

Synthesis of 1-(3-acetylphenyl)-3-(3-(2-methoxyethyl)-1-(3-morpholinopropyl)-2,4-dioxo-1,2,3,4-tetrahydroquinazolin-6-yl)urea (61): Compound **54** (0.14 g, 0.39 mmol) was dissolved in dry THF (8 mL) and 4-nitrophenylchloroformate (0.1 g, 0.47 mmol) was added portion wise under nitrogen atmosphere and left for stirring for 1 h. 3'-aminoacetophenone (0.07 g, 0.47 mmol) was added to the reaction mixture followed by TEA (0.14 mL, 0.97 mmol) and the reaction was performed according to the general procedure C. Pure compound was isolated by using column chromatography in 230-400 silica mesh size and with 8% MeOH in CHCl_3 (V/V) as eluent to obtain compound **61** as off-white solid (yield 52%). ^1H NMR (400 MHz, d_6 -DMSO) δ in ppm 8.94 (s, 1H), 8.91 (s,

1H), 8.17 (d, J = 2.8Hz, 1H), 8.04-8.02 (m, 1H), 7.75 (dd, J = 8.8Hz, 2.4Hz, 1H), 7.66-7.62 (m, 1H), 7.56-7.53 (m, 1H), 7.45 (d, J = 9.2Hz, 1H), 7.39 (t, J = 7.6 Hz, 1H), 4.11-4.05 (m, 4H), 3.51-3.45 (m, 6H), 3.20 (s, 3H), 2.52 (s, 3H), 2.37-2.30 (m, 2H), 2.26 (brs, 4H), 1.78-1.70 (m, 2H). ^{13}C NMR (100 MHz, d_6 -DMSO) δ in ppm 198.25, 161.53, 153.15, 150.45, 140.55, 137.92, 135.30, 135.18, 129.67, 126.69, 123.49, 122.56, 118.07, 116.96, 115.72, 115.68, 68.99, 66.65, 58.43, 55.77, 53.76, 42.08, 27.29, 24.09. HRMS (ESI) m/z ($M + H$) $^+$ calculated for $\text{C}_{27}\text{H}_{34}\text{N}_5\text{O}_6$ 524.2509; found, 524.2511. Melting Point: 182 °C. HPLC Purity: 100%.

1.7 REFERENCES

- (1) Han, S. K.; Baik, S. K.; Kim, M. Y. Non-Alcoholic Fatty Liver Disease: Definition and Subtypes. *Clin. Mol. Hepatol.* **2023**, *29* (suppl), S5–S16. <https://doi.org/10.3350/cmh.2022.0424>.
- (2) Cotter, T. G.; Rinella, M. Nonalcoholic Fatty Liver Disease 2020: The State of the Disease. *Gastroenterology* **2020**, *158* (7), 1851–1864. <https://doi.org/https://doi.org/10.1053/j.gastro.2020.01.052>.
- (3) Shen, K.; Singh, A. D.; Modaresi Esfeh, J.; Wakim-Fleming, J. Therapies for Non-Alcoholic Fatty Liver Disease: A 2022 Update. *World J. Hepatol.* **2022**, *14* (9), 1718–1729. <https://doi.org/10.4254/wjh.v14.i9.1718>.
- (4) Chen, Y.-Y.; Yeh, M. M. Non-Alcoholic Fatty Liver Disease: A Review with Clinical and Pathological Correlation. *J. Formos. Med. Assoc.* **2021**, *120* (1 Pt 1), 68–77. <https://doi.org/10.1016/j.jfma.2020.07.006>.
- (5) Geh, D.; Manas, D. M.; Reeves, H. L. Hepatocellular Carcinoma in Non-Alcoholic Fatty Liver Disease-a Review of an Emerging Challenge Facing Clinicians. *Hepatobiliary Surg. Nutr.* **2021**, *10* (1), 59–75. <https://doi.org/10.21037/hbsn.2019.08.08>.
- (6) Buzzetti, E.; Pinzani, M.; Tsochatzis, E. A. The Multiple-Hit Pathogenesis of Non-Alcoholic Fatty Liver Disease (NAFLD). *Metabolism.* **2016**, *65* (8), 1038–1048. <https://doi.org/10.1016/j.metabol.2015.12.012>.
- (7) Glass, L. M.; Hunt, C. M.; Fuchs, M.; Su, G. L. Comorbidities and Nonalcoholic Fatty Liver Disease: The Chicken, the Egg, or Both? *Fed. Pract.* **2019**, *36* (2), 64–71.
- (8) Alves-Bezerra, M.; Cohen, D. E. Triglyceride Metabolism in the Liver. *Compr. Physiol.* **2017**, *8* (1), 1–8. <https://doi.org/10.1002/cphy.c170012>.
- (9) Mitra, S.; De, A.; Chowdhury, A. Epidemiology of Non-Alcoholic and Alcoholic Fatty Liver Diseases. *Transl. Gastroenterol. Hepatol.* **2020**, *5*, 16. <https://doi.org/10.21037/tgh.2019.09.08>.
- (10) Sanyal, A. J. Past, Present and Future Perspectives in Nonalcoholic Fatty Liver Disease. *Nat. Rev. Gastroenterol. Hepatol.* **2019**, *16* (6), 377–386. <https://doi.org/10.1038/s41575-019-0144-8>.
- (11) Mahmoudi, S. K.; Tarzamani, S.; Aghajanzadeh, T.; Kasravi, M.; Hatami, B.; Zali, M. R.; Baghaei, K. Exploring the Role of Genetic Variations in NAFLD: Implications for Disease Pathogenesis and Precision Medicine Approaches. *Eur. J. Med. Res.* **2024**, *29* (1), 190. <https://doi.org/10.1186/s40001-024-01708-8>.
- (12) Ferraioli, G.; Soares Monteiro, L. B. Ultrasound-Based Techniques for the Diagnosis of Liver Steatosis. *World J. Gastroenterol.* **2019**, *25* (40), 6053–6062. <https://doi.org/10.3748/wjg.v25.i40.6053>.
- (13) Sanai, F. M.; Keeffe, E. B. Liver Biopsy for Histological Assessment: The Case Against. *Saudi J. Gastroenterol. Off. J. Saudi Gastroenterol. Assoc.* **2010**, *16* (2), 124–132. <https://doi.org/10.4103/1319-3767.61244>.
- (14) Philip Esteban, J.; Dinani, A. Lifestyle Interventions Beyond Diet and Exercise for

- Patients With Nonalcoholic Fatty Liver Disease. *Gastroenterol. Hepatol. (N. Y.)* **2020**, *16* (3), 119–130.
- (15) Leite, N. C.; Villela-Nogueira, C. A.; Cardoso, C. R. L.; Salles, G. F. Non-Alcoholic Fatty Liver Disease and Diabetes: From Physiopathological Interplay to Diagnosis and Treatment. *World J. Gastroenterol.* **2014**, *20* (26), 8377–8392. <https://doi.org/10.3748/wjg.v20.i26.8377>.
- (16) Yang, Z.; Wang, L. Current, Emerging, and Potential Therapies for Non-Alcoholic Steatohepatitis. *Front. Pharmacol.* **2023**, *14*, 1152042. <https://doi.org/10.3389/fphar.2023.1152042>.
- (17) Xu, X.; Poulsen, K. L.; Wu, L.; Liu, S.; Miyata, T.; Song, Q.; Wei, Q.; Zhao, C.; Lin, C.; Yang, J. Targeted Therapeutics and Novel Signaling Pathways in Non-Alcohol-Associated Fatty Liver/Steatohepatitis (NAFL/NASH). *Signal Transduct. Target. Ther.* **2022**, *7* (1), 287. <https://doi.org/10.1038/s41392-022-01119-3>.
- (18) Bowman. Minute Anatomy of Fatty Degeneration of the Liver. *West. J. Med. Surg.* **1842**, *6* (2), 143–144.
- (19) Ludwig, J.; Viggiano, T. R.; McGill, D. B.; Oh, B. J. Nonalcoholic Steatohepatitis: Mayo Clinic Experiences with a Hitherto Unnamed Disease. *Mayo Clin. Proc.* **1980**, *55* (7), 434–438.
- (20) Schaffner, F.; Thaler, H. Nonalcoholic Fatty Liver Disease. *Prog. Liver Dis.* **1986**, *8*, 283–298.
- (21) Talamantes, S.; Lisjak, M.; Gilglioni, E. H.; Llamaza-Torres, C. J.; Ramos-Molina, B.; Gurzov, E. N. Non-Alcoholic Fatty Liver Disease and Diabetes Mellitus as Growing Aetiologies of Hepatocellular Carcinoma. *JHEP reports Innov. Hepatol.* **2023**, *5* (9), 100811. <https://doi.org/10.1016/j.jhepr.2023.100811>.
- (22) Ayonrinde, O. T. Historical Narrative from Fatty Liver in the Nineteenth Century to Contemporary NAFLD - Reconciling the Present with the Past. *JHEP reports Innov. Hepatol.* **2021**, *3* (3), 100261. <https://doi.org/10.1016/j.jhepr.2021.100261>.
- (23) Fernando, D. H.; Forbes, J. M.; Angus, P. W.; Herath, C. B. Development and Progression of Non-Alcoholic Fatty Liver Disease: The Role of Advanced Glycation End Products. *International Journal of Molecular Sciences*. 2019. <https://doi.org/10.3390/ijms20205037>.
- (24) Loomba, R.; Friedman, S. L.; Shulman, G. I. Mechanisms and Disease Consequences of Nonalcoholic Fatty Liver Disease. *Cell* **2021**, *184* (10), 2537–2564. <https://doi.org/10.1016/j.cell.2021.04.015>.
- (25) Sheka, A. C.; Adeyi, O.; Thompson, J.; Hameed, B.; Crawford, P. A.; Ikramuddin, S. Nonalcoholic Steatohepatitis: A Review. *JAMA* **2020**, *323* (12), 1175–1183. <https://doi.org/10.1001/jama.2020.2298>.
- (26) Younossi, Z. M.; Blissett, D.; Blissett, R.; Henry, L.; Stepanova, M.; Younossi, Y.; Racila, A.; Hunt, S.; Beckerman, R. The Economic and Clinical Burden of Nonalcoholic Fatty Liver Disease in the United States and Europe. *Hepatology* **2016**, *64* (5), 1577–1586. <https://doi.org/10.1002/hep.28785>.

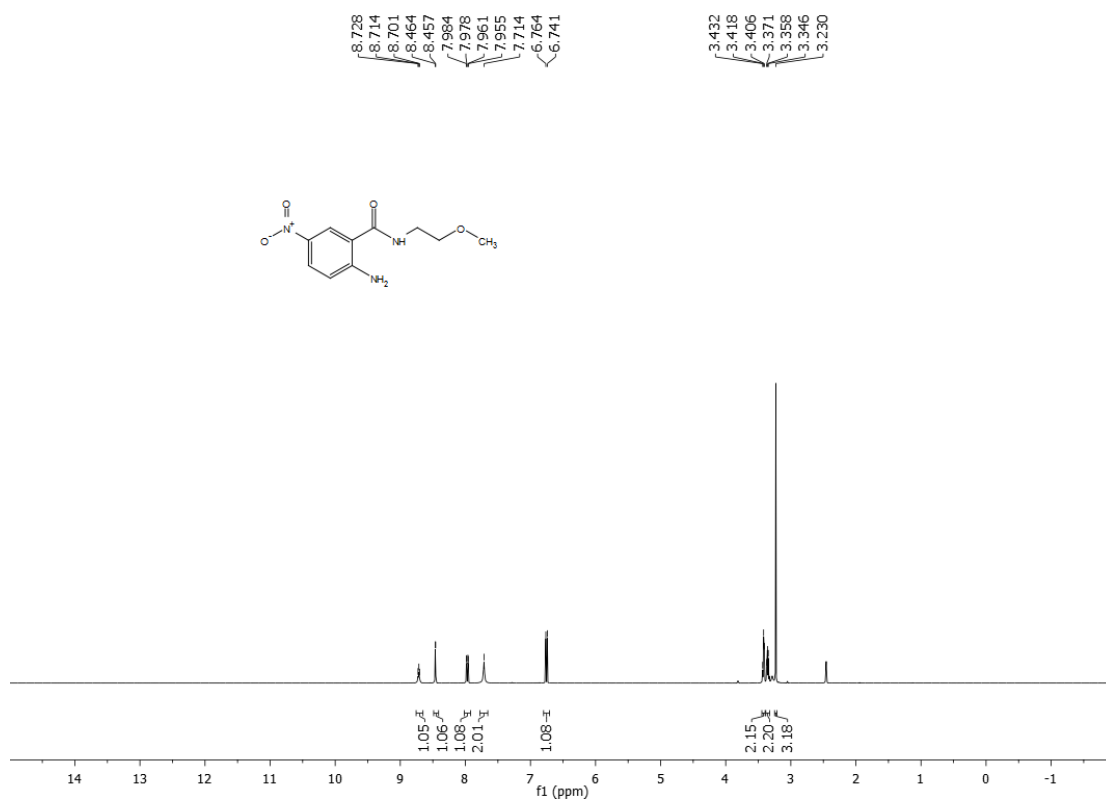
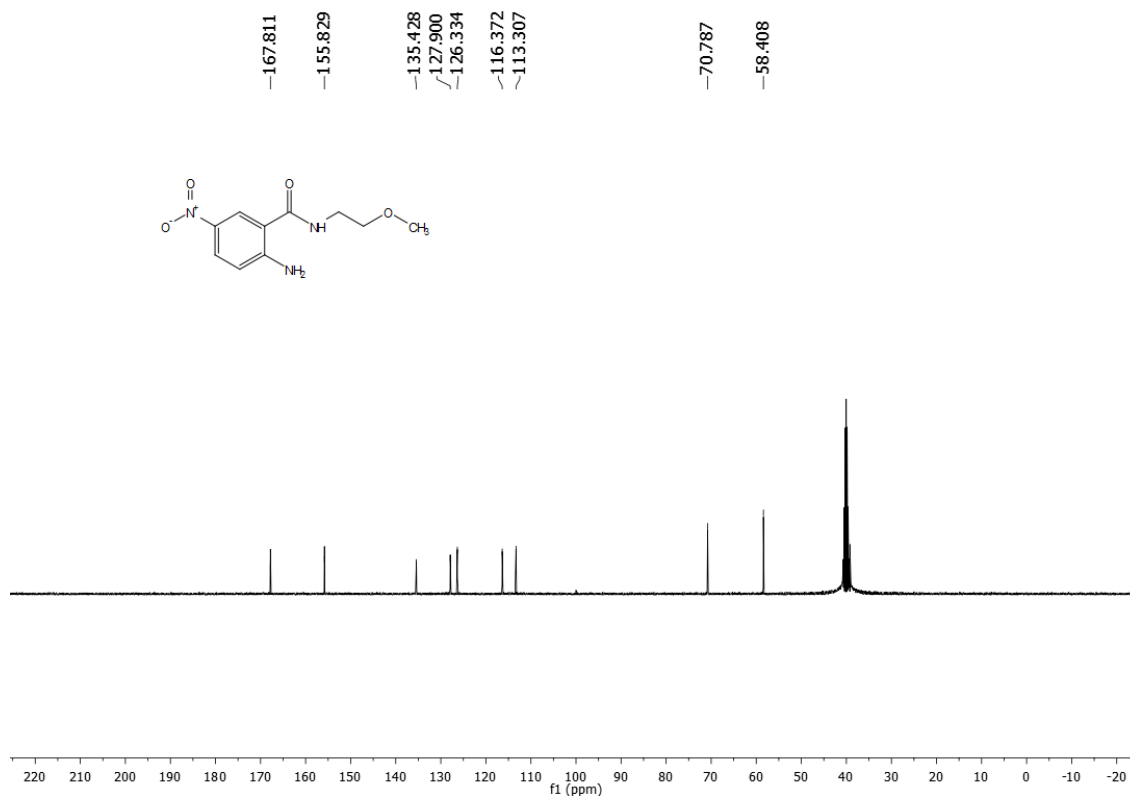
- (27) Subichin, M.; Clanton, J.; Makuszewski, M.; Bohon, A.; Zografakis, J. G.; Dan, A. Liver Disease in the Morbidly Obese: A Review of 1000 Consecutive Patients Undergoing Weight Loss Surgery. *Surg. Obes. Relat. Dis.* **2015**, *11* (1), 137–141. <https://doi.org/https://doi.org/10.1016/j.soard.2014.06.015>.
- (28) Li, B.; Zhang, C.; Zhan, Y.-T. Nonalcoholic Fatty Liver Disease Cirrhosis: A Review of Its Epidemiology, Risk Factors, Clinical Presentation, Diagnosis, Management, and Prognosis. *Can. J. Gastroenterol. Hepatol.* **2018**, *2018*, 2784537. <https://doi.org/10.1155/2018/2784537>.
- (29) Zhai, M.; Liu, Z.; Long, J.; Zhou, Q.; Yang, L.; Zhou, Q.; Liu, S.; Dai, Y. The Incidence Trends of Liver Cirrhosis Caused by Nonalcoholic Steatohepatitis via the GBD Study 2017. *Sci. Rep.* **2021**, *11* (1), 5195. <https://doi.org/10.1038/s41598-021-84577-z>.
- (30) Desai, A.; Sandhu, S.; Lai, J.-P.; Sandhu, D. S. Hepatocellular Carcinoma in Non-Cirrhotic Liver: A Comprehensive Review. *World J. Hepatol.* **2019**, *11* (1), 1–18. <https://doi.org/10.4254/wjh.v11.i1.1>.
- (31) Teng, M. L.; Ng, C. H.; Huang, D. Q.; Chan, K. E.; Tan, D. J.; Lim, W. H.; Yang, J. D.; Tan, E.; Muthiah, M. D. Global Incidence and Prevalence of Nonalcoholic Fatty Liver Disease. *Clin. Mol. Hepatol.* **2023**, *29* (Suppl), S32–S42. <https://doi.org/10.3350/cmh.2022.0365>.
- (32) Bhupathiraju, S. N.; Hu, F. B. Epidemiology of Obesity and Diabetes and Their Cardiovascular Complications. *Circ. Res.* **2016**, *118* (11), 1723–1735. <https://doi.org/10.1161/CIRCRESAHA.115.306825>.
- (33) Younossi, Z. M. Non-Alcoholic Fatty Liver Disease – A Global Public Health Perspective. *J. Hepatol.* **2019**, *70* (3), 531–544. <https://doi.org/https://doi.org/10.1016/j.jhep.2018.10.033>.
- (34) Younossi, Z. M.; Golabi, P.; Price, J. K.; Owringi, S.; Gundu-Rao, N.; Satchi, R.; Paik, J. M. The Global Epidemiology of Nonalcoholic Fatty Liver Disease and Nonalcoholic Steatohepatitis Among Patients With Type 2 Diabetes. *Clin. Gastroenterol. Hepatol. Off. Clin. Pract. J. Am. Gastroenterol. Assoc.* **2024**, *22* (10), 1999–2010.e8. <https://doi.org/10.1016/j.cgh.2024.03.006>.
- (35) Sung, K.-C.; Wild, S. H.; Byrne, C. D. Development of New Fatty Liver, or Resolution of Existing Fatty Liver, over Five Years of Follow-up, and Risk of Incident Hypertension. *J. Hepatol.* **2014**, *60* (5), 1040–1045. <https://doi.org/10.1016/j.jhep.2014.01.009>.
- (36) Han, J.; Kaufman, R. J. The Role of ER Stress in Lipid Metabolism and Lipotoxicity. *J. Lipid Res.* **2016**, *57* (8), 1329–1338. <https://doi.org/10.1194/jlr.R067595>.
- (37) Harrison, S. A.; Fecht, W.; Brunt, E. M.; Neuschwander-Tetri, B. A. Orlistat for Overweight Subjects with Nonalcoholic Steatohepatitis: A Randomized, Prospective Trial. *Hepatology* **2009**, *49* (1), 80–86. <https://doi.org/10.1002/hep.22575>.
- (38) Vachliotis, I.; Goulas, A.; Papaioannidou, P.; Polyzos, S. A. Nonalcoholic Fatty Liver Disease: Lifestyle and Quality of Life. *Hormones (Athens)*. **2022**, *21* (1), 41–49. <https://doi.org/10.1007/s42000-021-00339-6>.

- (39) Hallsworth, K.; Adams, L. A. Lifestyle Modification in NAFLD/NASH: Facts and Figures. *JHEP reports Innov. Hepatol.* **2019**, *1* (6), 468–479. <https://doi.org/10.1016/j.jhepr.2019.10.008>.
- (40) Iogna Prat, L.; Tsochatzis, E. A. The Effect of Antidiabetic Medications on Non-Alcoholic Fatty Liver Disease (NAFLD). *Hormones (Athens)*. **2018**, *17* (2), 219–229. <https://doi.org/10.1007/s42000-018-0021-9>.
- (41) Negi, C. K.; Babica, P.; Bajard, L.; Bienertova-Vasku, J.; Tarantino, G. Insights into the Molecular Targets and Emerging Pharmacotherapeutic Interventions for Nonalcoholic Fatty Liver Disease. *Metabolism* **2022**, *126*, 154925. <https://doi.org/https://doi.org/10.1016/j.metabol.2021.154925>.
- (42) Desvergne, B.; Wahli, W. Peroxisome Proliferator-Activated Receptors: Nuclear Control of Metabolism*. *Endocr. Rev.* **1999**, *20* (5), 649–688. <https://doi.org/10.1210/edrv.20.5.0380>.
- (43) Francque, S.; Verrijken, A.; Caron, S.; Prawitt, J.; Paumelle, R.; Derudas, B.; Lefebvre, P.; Taskinen, M.-R.; Van Hul, W.; Mertens, I.; Hubens, G.; Van Marck, E.; Michielsen, P.; Van Gaal, L.; Staels, B. PPAR α Gene Expression Correlates with Severity and Histological Treatment Response in Patients with Non-Alcoholic Steatohepatitis. *J. Hepatol.* **2015**, *63* (1), 164–173. <https://doi.org/https://doi.org/10.1016/j.jhep.2015.02.019>.
- (44) Liss, K. H. H.; Finck, B. N. PPARs and Nonalcoholic Fatty Liver Disease. *Biochimie* **2017**, *136*, 65–74. <https://doi.org/https://doi.org/10.1016/j.biochi.2016.11.009>.
- (45) Cooreman, M. P.; Butler, J.; Giugliano, R. P.; Zannad, F.; Dzen, L.; Huot-Marchand, P.; Baudin, M.; Beard, D. R.; Junien, J.-L.; Broqua, P.; Abdelmalek, M. F.; Francque, S. M. The Pan-PPAR Agonist Lanifibranor Improves Cardiometabolic Health in Patients with Metabolic Dysfunction-Associated Steatohepatitis. *Nat. Commun.* **2024**, *15* (1), 3962. <https://doi.org/10.1038/s41467-024-47919-9>.
- (46) Han, C. Y. Update on FXR Biology: Promising Therapeutic Target? *International Journal of Molecular Sciences*. 2018. <https://doi.org/10.3390/ijms19072069>.
- (47) Adorini, L.; Trauner, M. FXR Agonists in NASH Treatment. *J. Hepatol.* **2023**, *79* (5), 1317–1331. <https://doi.org/10.1016/j.jhep.2023.07.034>.
- (48) Li, L.; Song, Y.; Shi, Y.; Sun, L. Thyroid Hormone Receptor- β Agonists in NAFLD Therapy: Possibilities and Challenges. *J. Clin. Endocrinol. Metab.* **2023**, *108* (7), 1602–1613. <https://doi.org/10.1210/clinem/dgad072>.
- (49) Hatziagelaki, E.; Paschou, S. A.; Schön, M.; Psaltopoulou, T.; Roden, M. NAFLD and Thyroid Function: Pathophysiological and Therapeutic Considerations. *Trends Endocrinol. Metab.* **2022**, *33* (11), 755–768. <https://doi.org/10.1016/j.tem.2022.08.001>.
- (50) Krishnan U, A.; Viswanathan, P.; Venkataraman, A. C. AMPK Activation by AICAR Reduces Diet Induced Fatty Liver in C57BL/6 Mice. *Tissue Cell* **2023**, *82*, 102054. <https://doi.org/10.1016/j.tice.2023.102054>.
- (51) Zhao, P.; Saltiel, A. R. From Overnutrition to Liver Injury: AMP-Activated Protein Kinase in Nonalcoholic Fatty Liver Diseases. *J. Biol. Chem.* **2020**, *295* (34), 12279–12289. <https://doi.org/10.1074/jbc.REV120.011356>.

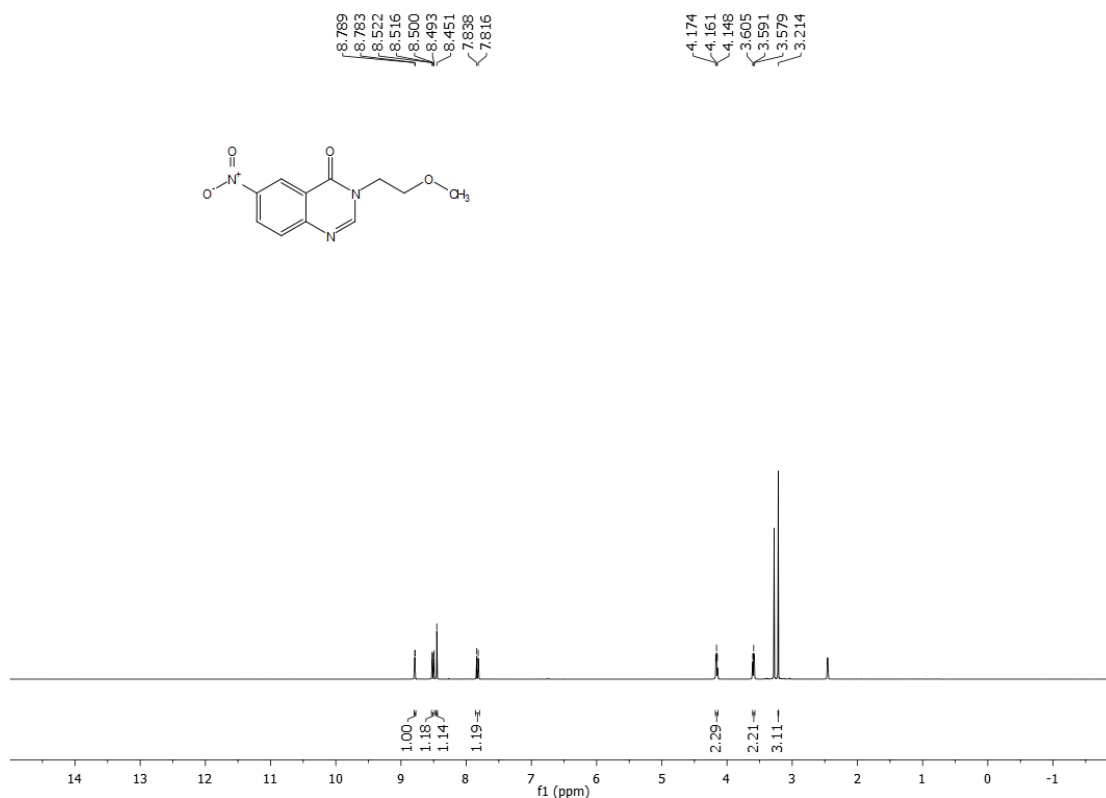
- (52) Goedeke, L.; Bates, J.; Vatner, D. F.; Perry, R. J.; Wang, T.; Ramirez, R.; Li, L.; Ellis, M. W.; Zhang, D.; Wong, K. E.; Beysen, C.; Cline, G. W.; Ray, A. S.; Shulman, G. I. Acetyl-CoA Carboxylase Inhibition Reverses NAFLD and Hepatic Insulin Resistance but Promotes Hypertriglyceridemia in Rodents. *Hepatology* **2018**, *68* (6), 2197–2211. <https://doi.org/10.1002/hep.30097>.
- (53) Wakil, S. J.; Abu-Elheiga, L. A. Fatty Acid Metabolism: Target for Metabolic Syndrome. *J. Lipid Res.* **2009**, *50*, S138–S143. <https://doi.org/10.1194/jlr.R800079-JLR200>.
- (54) Yoon, Y.-C.; Fang, Z.; Lee, J. E.; Park, J. H.; Ryu, J.-K.; Jung, K. H.; Hong, S.-S. Selonsertib Inhibits Liver Fibrosis via Downregulation of ASK1/ MAPK Pathway of Hepatic Stellate Cells. *Biomol. Ther. (Seoul)*. **2020**, *28* (6), 527–536. <https://doi.org/10.4062/biomolther.2020.016>.
- (55) Chen, Q.; Guo, J.; Qiu, T.; Zhou, J. Mechanism of ASK1 Involvement in Liver Diseases and Related Potential Therapeutic Targets: A Critical Pathway Molecule Worth Investigating. *J. Gastroenterol. Hepatol.* **2023**, *38* (3), 378–385. <https://doi.org/https://doi.org/10.1111/jgh.16087>.
- (56) Lefere, S.; Devisscher, L.; Tacke, F. Targeting CCR2/5 in the Treatment of Nonalcoholic Steatohepatitis (NASH) and Fibrosis: Opportunities and Challenges. *Expert opinion on investigational drugs*. England February 2020, pp 89–92. <https://doi.org/10.1080/13543784.2020.1718106>.
- (57) Anstee, Q. M.; Neuschwander-Tetri, B. A.; Wai-Sun Wong, V.; Abdelmalek, M. F.; Rodriguez-Araujo, G.; Landgren, H.; Park, G. S.; Bedossa, P.; Alkhouri, N.; Tacke, F.; Sanyal, A. J. Cenicriviroc Lacked Efficacy to Treat Liver Fibrosis in Nonalcoholic Steatohepatitis: AURORA Phase III Randomized Study. *Clin. Gastroenterol. Hepatol. Off. Clin. Pract. J. Am. Gastroenterol. Assoc.* **2024**, *22* (1), 124–134.e1. <https://doi.org/10.1016/j.cgh.2023.04.003>.
- (58) Li, M.; Chen, L.; Gao, Y.; Li, M.; Wang, X.; Qiang, L.; Wang, X. Recent Advances Targeting C-C Chemokine Receptor Type 2 for Liver Diseases in Monocyte/Macrophage. *Liver Int. Off. J. Int. Assoc. Study Liver* **2020**, *40* (12), 2928–2936. <https://doi.org/10.1111/liv.14687>.
- (59) Herrera-Marcos, L. V; Martínez-Beamonte, R.; Macías-Herranz, M.; Arnal, C.; Barranquero, C.; Puente-Lanzarote, J. J.; Gascón, S.; Herrero-Contiente, T.; Gonzalo-Romeo, G.; Alastrué-Vera, V.; Gutiérrez-Blázquez, D.; Lou-Bonafonte, J. M.; Surra, J. C.; Rodríguez-Yoldi, M. J.; García-Gil, A.; Güemes, A.; Osada, J. Hepatic Galectin-3 Is Associated with Lipid Droplet Area in Non-Alcoholic Steatohepatitis in a New Swine Model. *Sci. Rep.* **2022**, *12* (1), 1024. <https://doi.org/10.1038/s41598-022-04971-z>.
- (60) Yu, H.; Yang, F.; Zhong, W.; Jiang, X.; Zhang, F.; Ji, X.; Xue, M.; Qiu, Y.; Yu, J.; Hu, X.; Chen, J.; Bao, Z. Secretory Galectin-3 Promotes Hepatic Steatosis via Regulation of the PPAR γ /CD36 Signaling Pathway. *Cell. Signal.* **2021**, *84*, 110043. <https://doi.org/https://doi.org/10.1016/j.cellsig.2021.110043>.
- (61) Finley, D. Recognition and Processing of Ubiquitin-Protein Conjugates by the Proteasome. *Annu. Rev. Biochem.* **2009**, *78* (1), 477–513. <https://doi.org/10.1146/annurev.biochem.78.081507.101607>.

- (62) Tokheim, C.; Wang, X.; Timms, R. T.; Zhang, B.; Mena, E. L.; Wang, B.; Chen, C.; Ge, J.; Chu, J.; Zhang, W.; Elledge, S. J.; Brown, M.; Liu, X. S. Systematic Characterization of Mutations Altering Protein Degradation in Human Cancers. *Mol. Cell* **2021**, *81* (6), 1292-1308.e11. <https://doi.org/https://doi.org/10.1016/j.molcel.2021.01.020>.
- (63) Yang, Q.; Zhao, J.; Chen, D.; Wang, Y. E3 Ubiquitin Ligases: Styles, Structures and Functions. *Mol. Biomed.* **2021**, *2* (1), 23. <https://doi.org/10.1186/s43556-021-00043-2>.
- (64) Song, L.; Luo, Z.-Q. Post-Translational Regulation of Ubiquitin Signaling. *J. Cell Biol.* **2019**, *218* (6), 1776–1786. <https://doi.org/10.1083/jcb.201902074>.
- (65) Ang, L.-H.; Chattopadhyay, S.; Wei, N.; Oyama, T.; Okada, K.; Batschauer, A.; Deng, X.-W. Molecular Interaction between COP1 and HY5 Defines a Regulatory Switch for Light Control of Arabidopsis Development. *Mol. Cell* **1998**, *1* (2), 213–222. [https://doi.org/https://doi.org/10.1016/S1097-2765\(00\)80022-2](https://doi.org/https://doi.org/10.1016/S1097-2765(00)80022-2).
- (66) Holm, M.; Ma, L.-G.; Qu, L.-J.; Deng, X.-W. Two Interacting BZIP Proteins Are Direct Targets of COP1-Mediated Control of Light-Dependent Gene Expression in Arabidopsis. *Genes Dev.* **2002**, *16* (10), 1247–1259. <https://doi.org/10.1101/gad.969702>.
- (67) Dornan, D.; Wertz, I.; Shimizu, H.; Arnott, D.; Frantz, G. D.; Dowd, P.; O' Rourke, K.; Koeppen, H.; Dixit, V. M. The Ubiquitin Ligase COP1 Is a Critical Negative Regulator of P53. *Nature* **2004**, *429* (6987), 86–92. <https://doi.org/10.1038/nature02514>.
- (68) Migliorini, D.; Bogaerts, S.; Defever, D.; Vyas, R.; Denecker, G.; Radaelli, E.; Zwolinska, A.; Depaepe, V.; Hocheplied, T.; Skarnes, W. C.; Marine, J.-C. Cop1 Constitutively Regulates C-Jun Protein Stability and Functions as a Tumor Suppressor in Mice. *J. Clin. Invest.* **2011**, *121* (4), 1329–1343. <https://doi.org/10.1172/JCI45784>.
- (69) Choi, H. H.; Phan, L.; Chou, P.-C.; Su, C.-H.; Yeung, S.-C. J.; Chen, J.-S.; Lee, M.-H. COP1 Enhances Ubiquitin-Mediated Degradation of P27Kip1 to Promote Cancer Cell Growth. *Oncotarget* **2015**, *6* (23), 19721–19734. <https://doi.org/10.18632/oncotarget.3821>.
- (70) Song, Y.; Liu, Y.; Pan, S.; Xie, S.; Wang, Z.-W.; Zhu, X. Role of the COP1 Protein in Cancer Development and Therapy. *Semin. Cancer Biol.* **2020**, *67* (Pt 2), 43–52. <https://doi.org/10.1016/j.semcancer.2020.02.001>.
- (71) Savio, M. G.; Rotondo, G.; Maglie, S.; Rossetti, G.; Bender, J. R.; Pardi, R. COP1D, an Alternatively Spliced Constitutive Photomorphogenic-1 (COP1) Product, Stabilizes UV Stress-Induced c-Jun through Inhibition of Full-Length COP1. *Oncogene* **2008**, *27* (17), 2401–2411. <https://doi.org/10.1038/sj.onc.1210892>.
- (72) Li, T.; Guo, W.; Zhou, Z. Adipose Triglyceride Lipase in Hepatic Physiology and Pathophysiology. *Biomolecules* **2021**, *12* (1). <https://doi.org/10.3390/biom12010057>.
- (73) Ghosh, M.; Niyogi, S.; Bhattacharyya, M.; Adak, M.; Nayak, D. K.; Chakrabarti, S.; Chakrabarti, P. Ubiquitin Ligase COP1 Controls Hepatic Fat Metabolism by

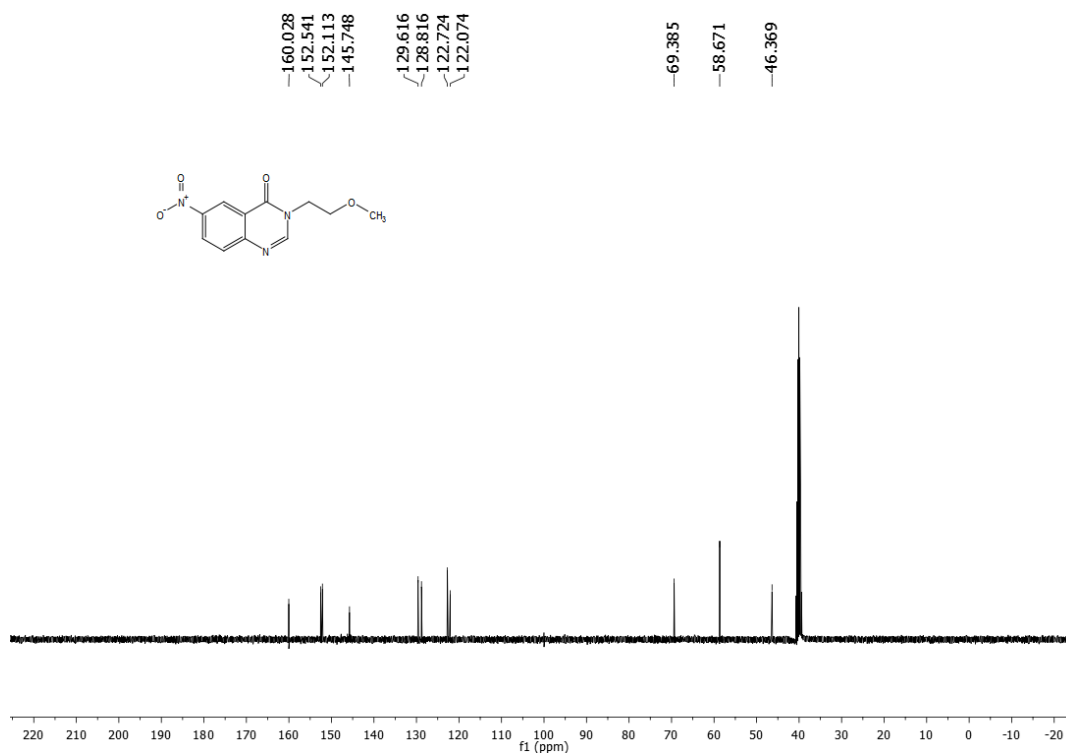
- Targeting ATGL for Degradation. *Diabetes* **2016**, 65 (12), 3561–3572.
<https://doi.org/10.2337/db16-0506>.
- (74) Ong, K. T.; Mashek, M. T.; Bu, S. Y.; Greenberg, A. S.; Mashek, D. G. Adipose Triglyceride Lipase Is a Major Hepatic Lipase That Regulates Triacylglycerol Turnover and Fatty Acid Signaling and Partitioning. *Hepatology* **2011**, 53 (1), 116–126. <https://doi.org/https://doi.org/10.1002/hep.24006>.
- (75) Wu, J. W.; Wang, S. P.; Alvarez, F.; Casavant, S.; Gauthier, N.; Abed, L.; Soni, K. G.; Yang, G.; Mitchell, G. A. Deficiency of Liver Adipose Triglyceride Lipase in Mice Causes Progressive Hepatic Steatosis. *Hepatology* **2011**, 54 (1), 122–132. <https://doi.org/https://doi.org/10.1002/hep.24338>.
- (76) Kato, M.; Higuchi, N.; Enjoji, M. Reduced Hepatic Expression of Adipose Tissue Triglyceride Lipase and CGI-58 May Contribute to the Development of Non-Alcoholic Fatty Liver Disease in Patients with Insulin Resistance. *Scand. J. Gastroenterol.* **2008**, 43 (8), 1018–1019. <https://doi.org/10.1080/00365520802008140>.
- (77) Yi, C.; Deng, X. W. COP1 – from Plant Photomorphogenesis to Mammalian Tumorigenesis. *Trends Cell Biol.* **2005**, 15 (11), 618–625. <https://doi.org/https://doi.org/10.1016/j.tcb.2005.09.007>.
- (78) Suriben, R.; Kaihara, K. A.; Paolino, M.; Reichelt, M.; Kummerfeld, S. K.; Modrusan, Z.; Dugger, D. L.; Newton, K.; Sagolla, M.; Webster, J. D.; Liu, J.; Hebrok, M.; Dixit, V. M. β -Cell Insulin Secretion Requires the Ubiquitin Ligase COP1. *Cell* **2015**, 163 (6), 1457–1467. <https://doi.org/https://doi.org/10.1016/j.cell.2015.10.076>.
- (79) Sarkar, D.; Chowdhuri, S.; Goon, S.; Sen, A. Discovery of Novel Small Molecule Derivatives for Modulating COP1- ATGL Axis in Ameliorating Non-Alcoholic Fatty Liver Disease. 1, 2–3.

1.8 ANNEXURE¹H NMR of compound **2** (400 MHz, *d*₆-DMSO):¹³C NMR of compound **2** (100 MHz, *d*₆-DMSO):

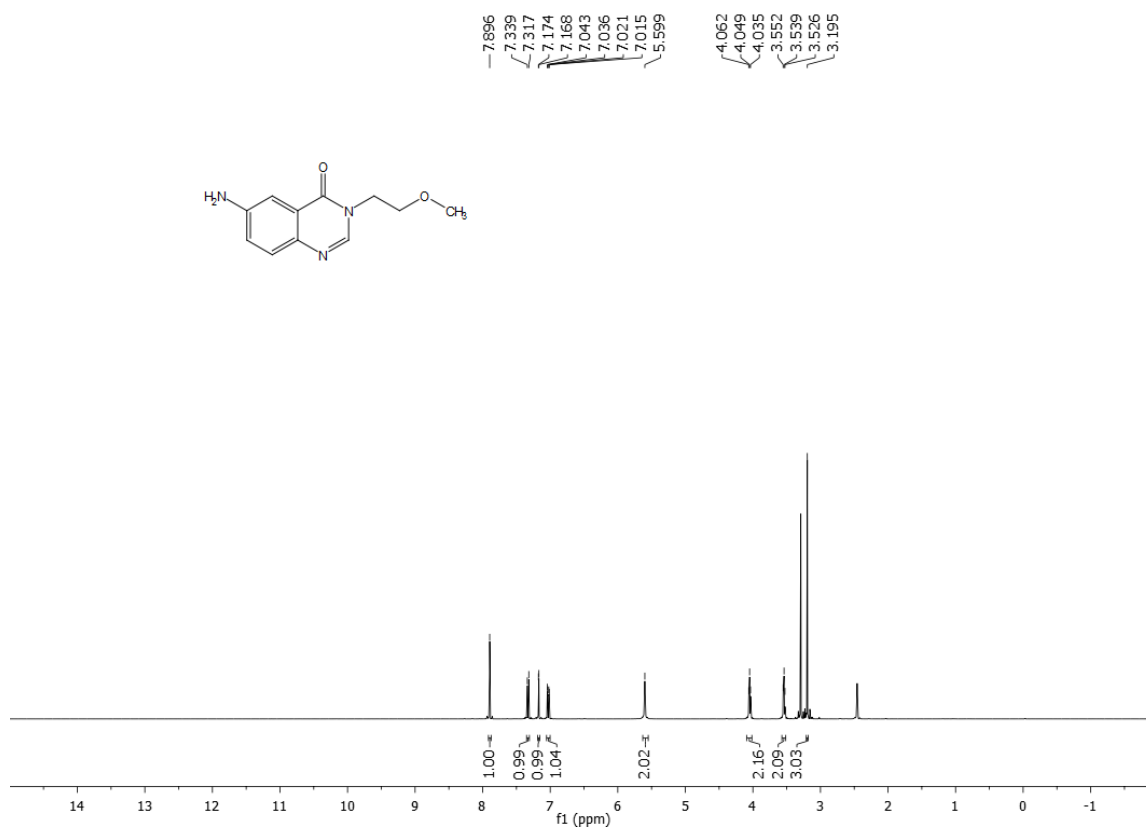
^1H NMR of compound **3** (400 MHz, d_6 -DMSO):



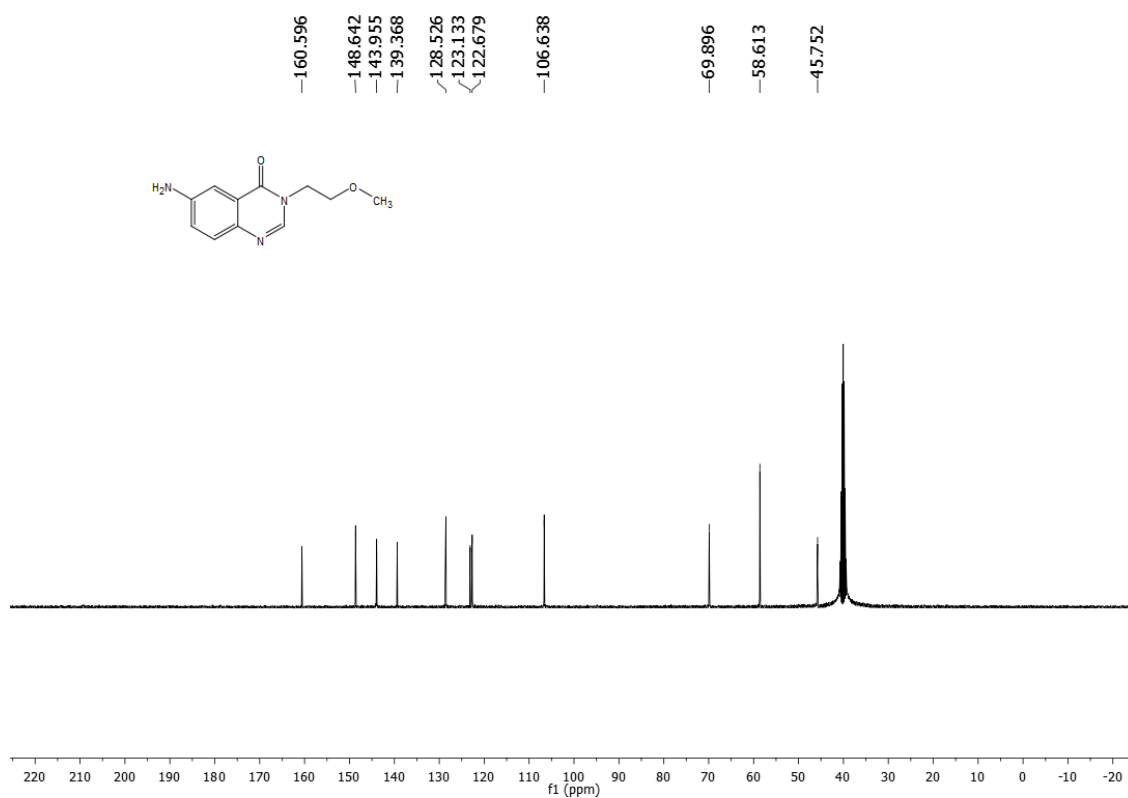
^{13}C NMR of compound **3** (100 MHz, d_6 -DMSO):



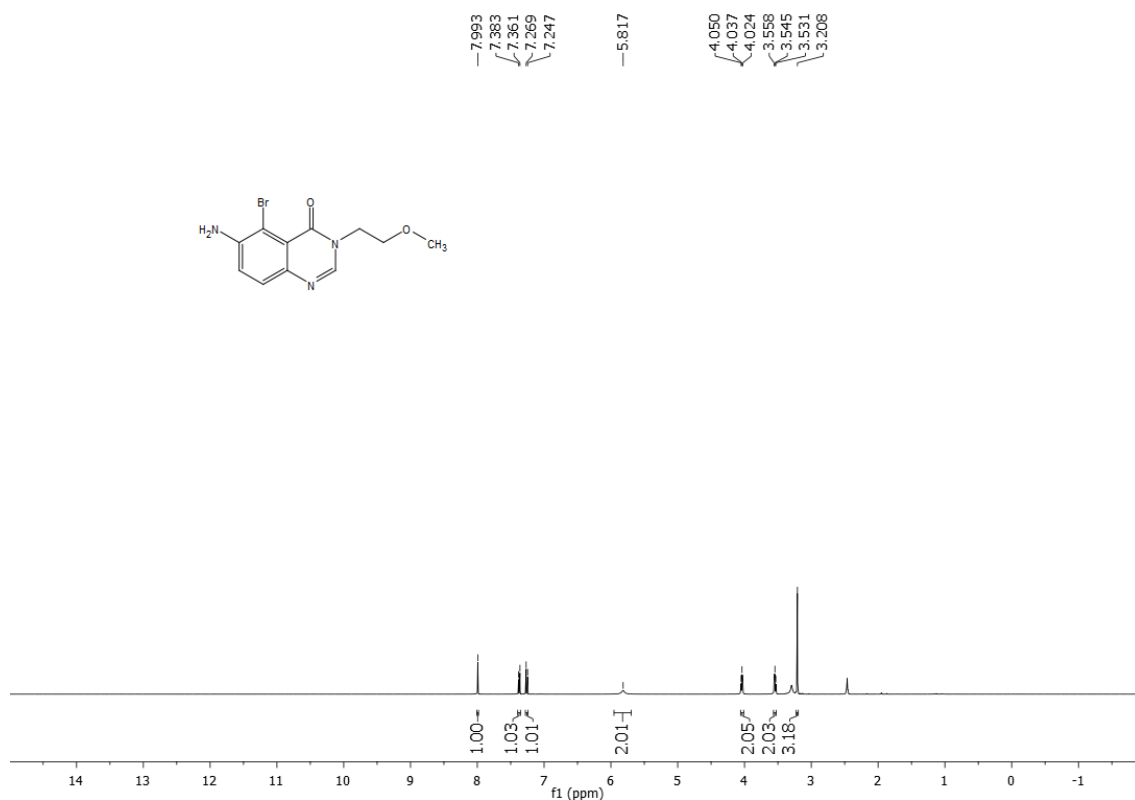
^1H NMR of compound **4** (400 MHz, d_6 -DMSO):



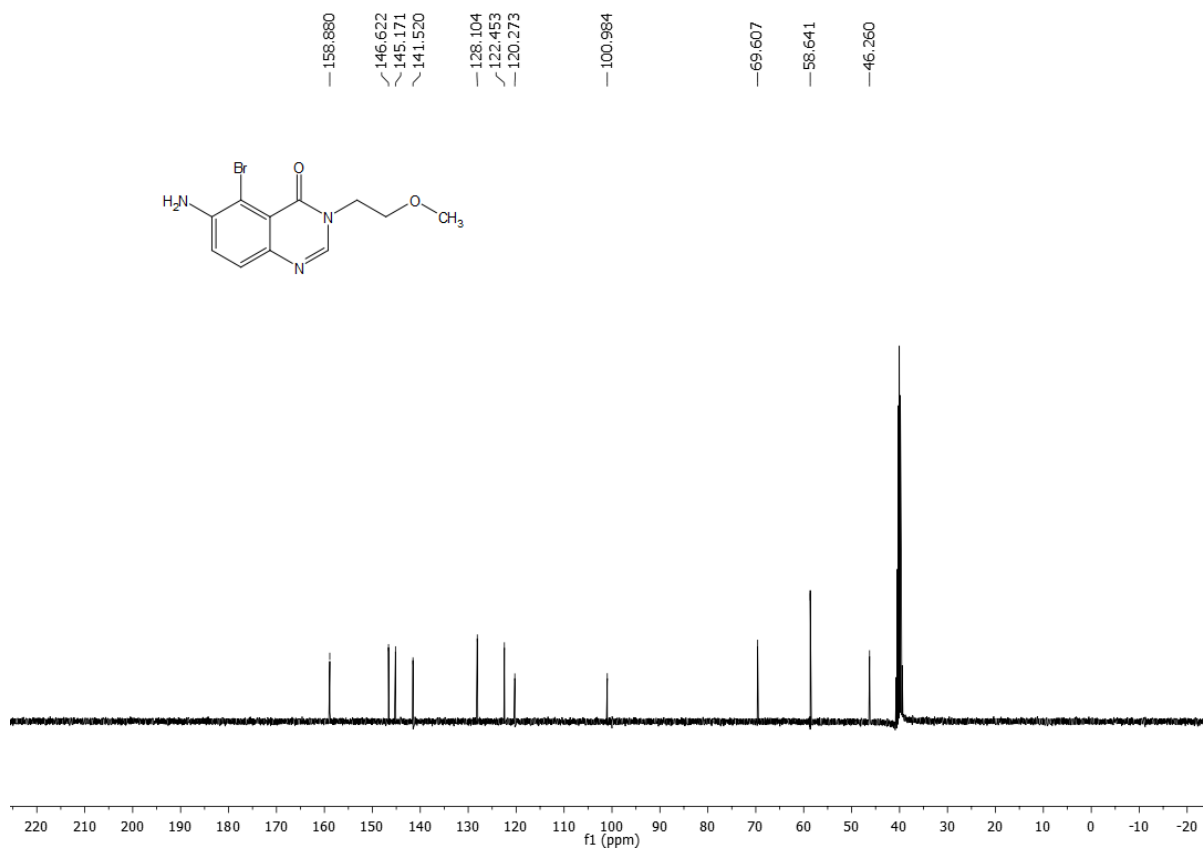
^{13}C NMR of compound **4** (100 MHz, d_6 -DMSO):



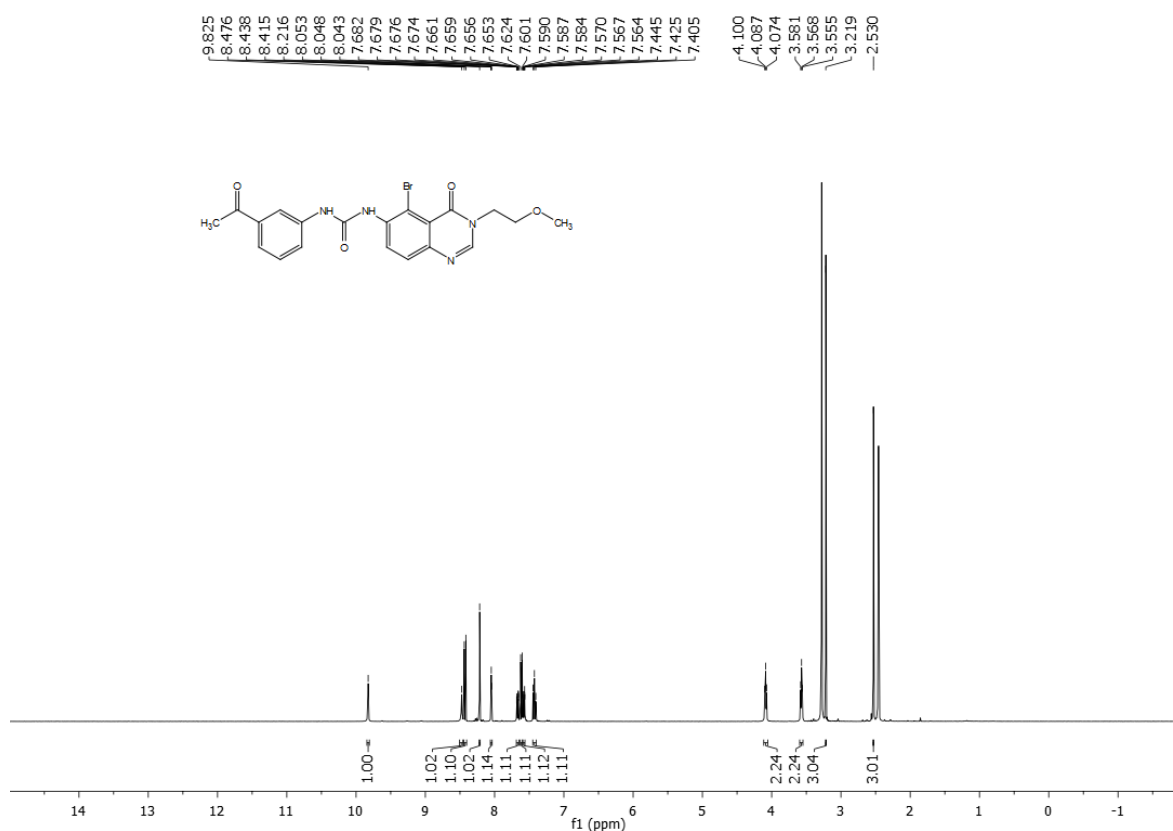
^1H NMR of compound **5** (400 MHz, d_6 -DMSO):



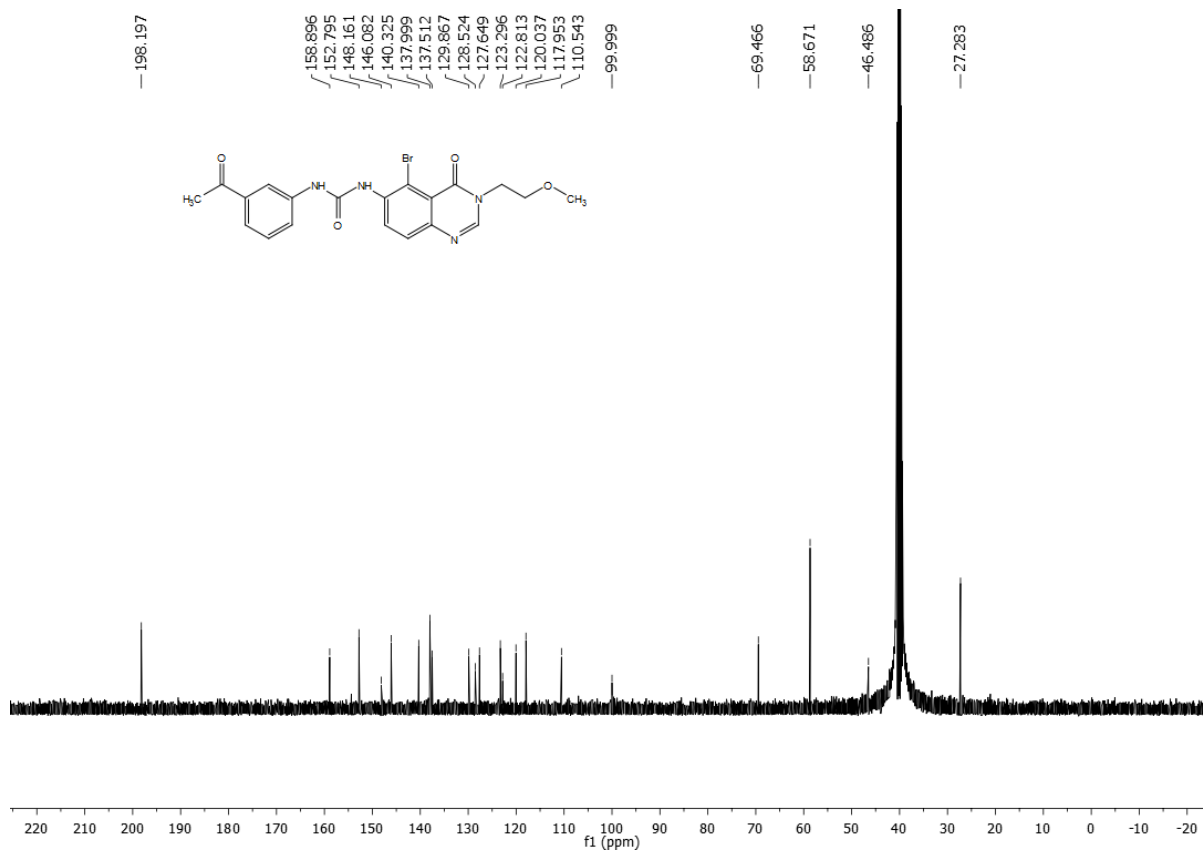
^{13}C NMR of compound **5** (100 MHz, d_6 -DMSO):



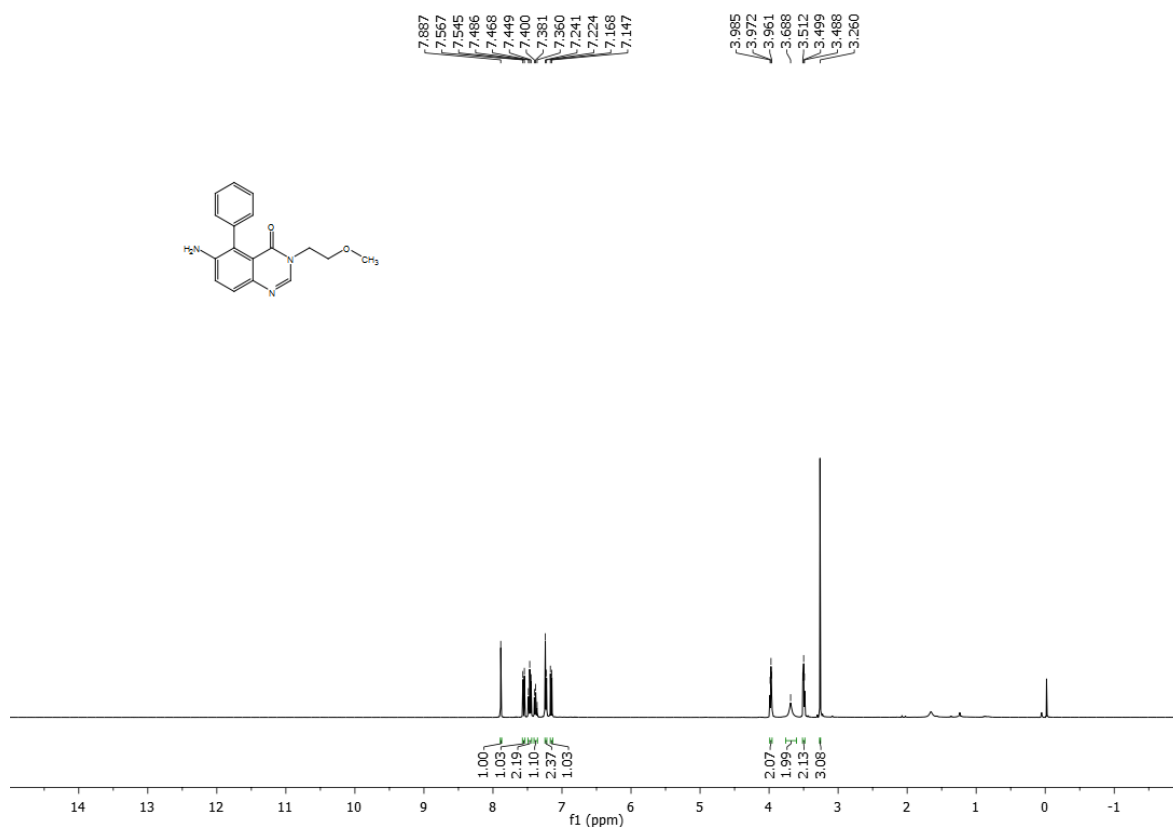
^1H NMR of compound **6** (400 MHz, d_6 -DMSO):



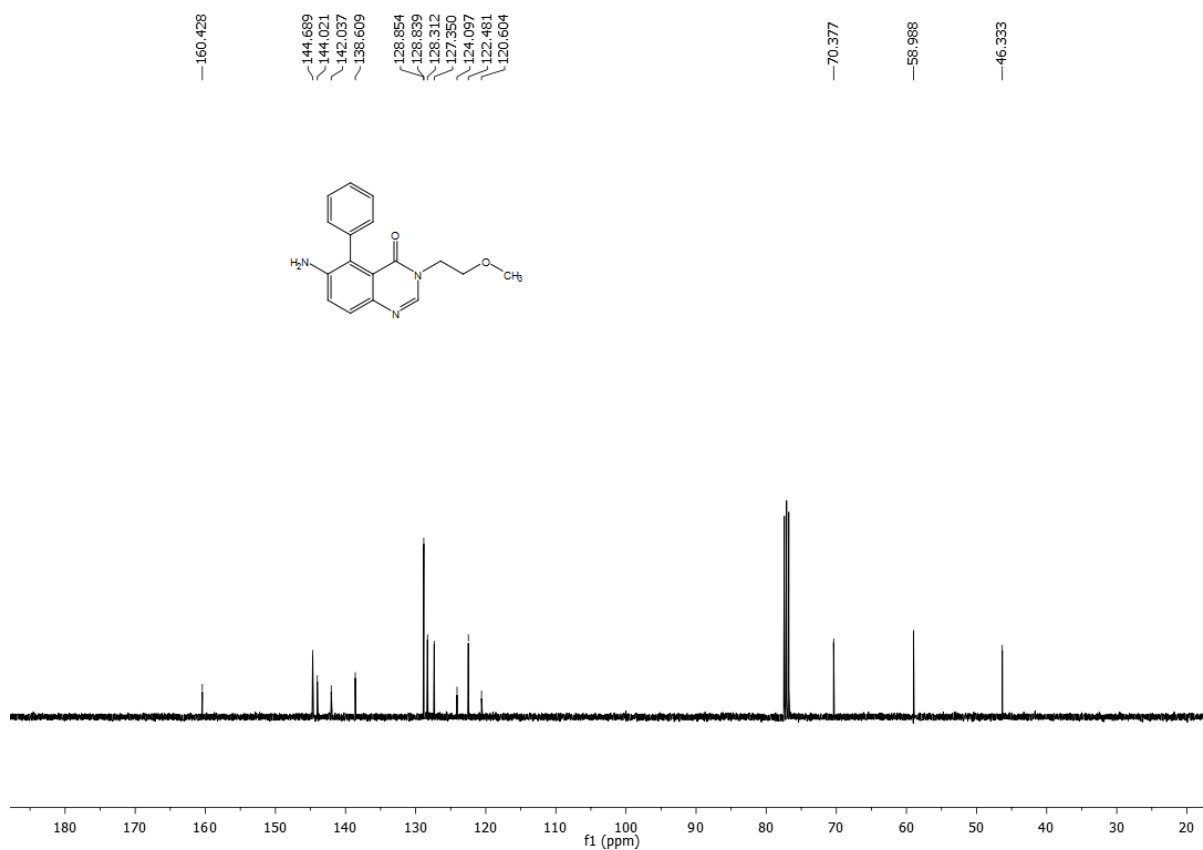
^{13}C NMR of compound **6** (100 MHz, d_6 -DMSO):



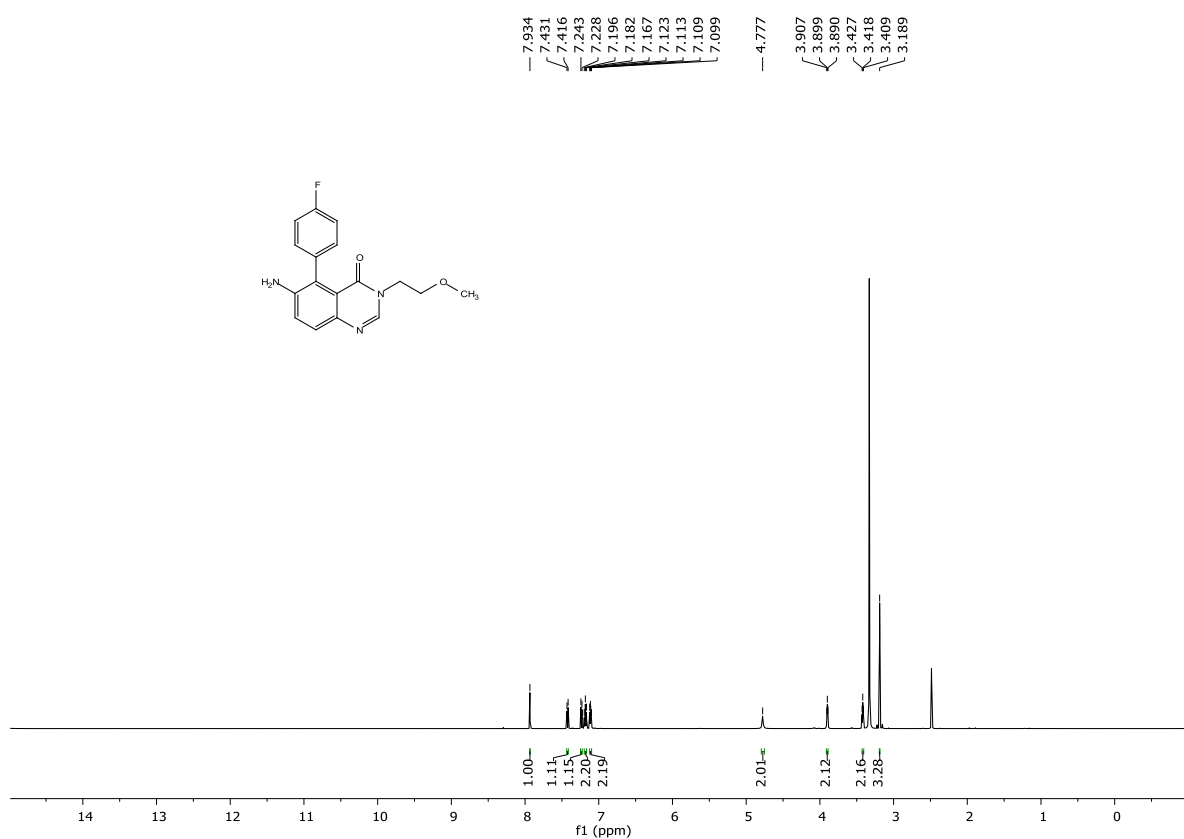
^1H NMR of compound **7** (400 MHz, d_6 -DMSO):



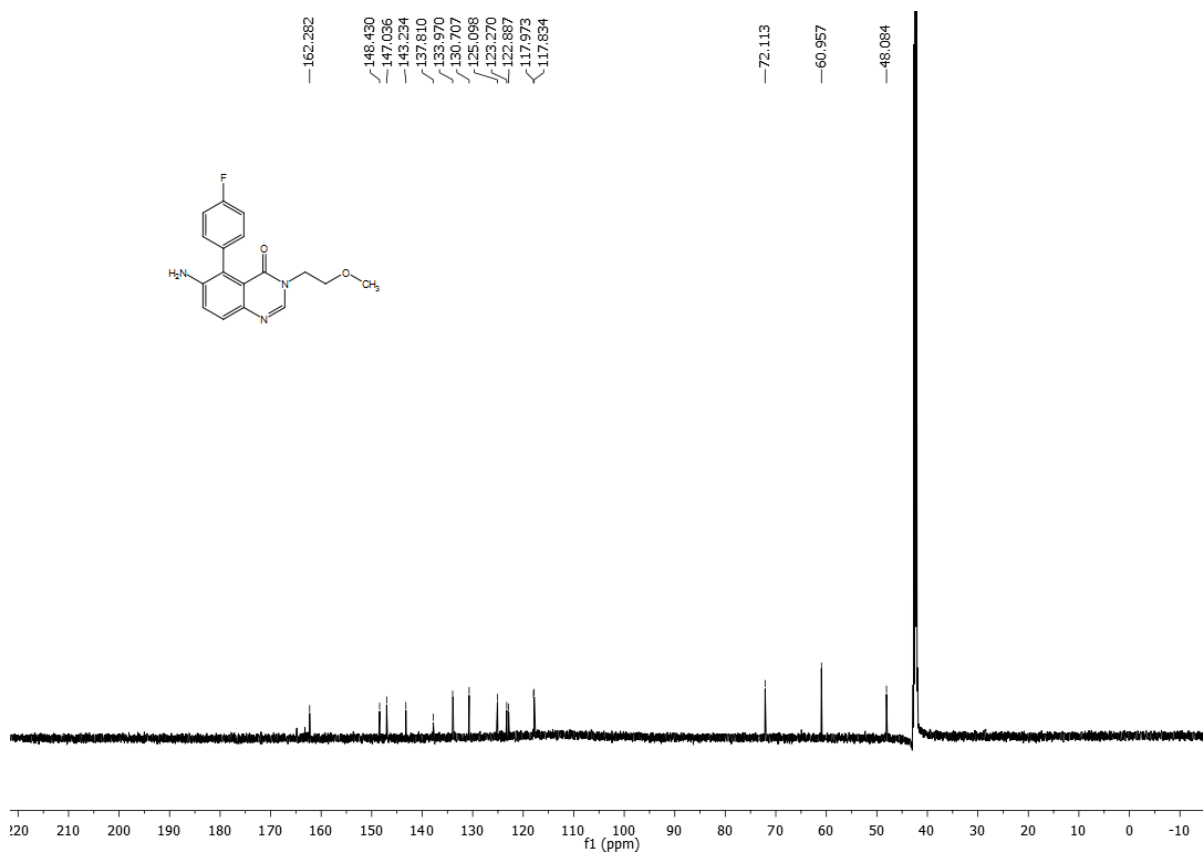
^{13}C NMR of compound **7** (100 MHz, d_6 -DMSO):



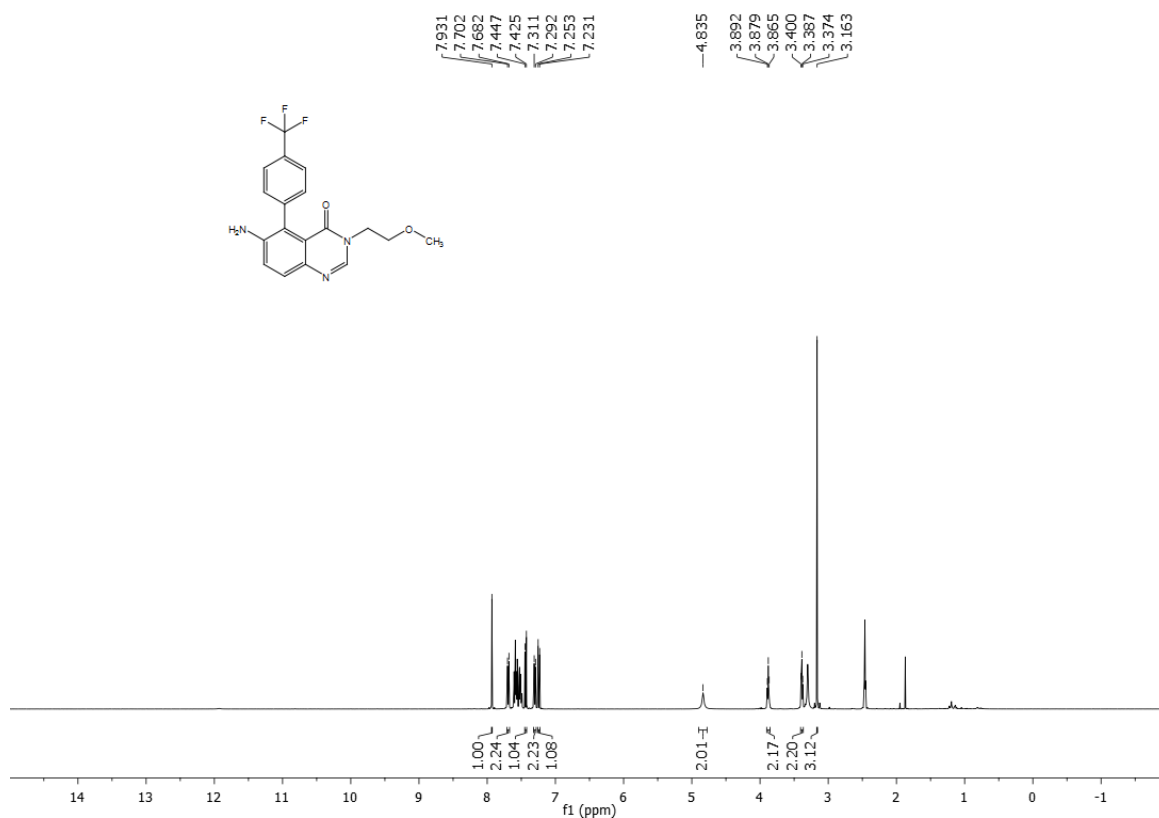
^1H NMR of compound **8** (400 MHz, d_6 -DMSO):



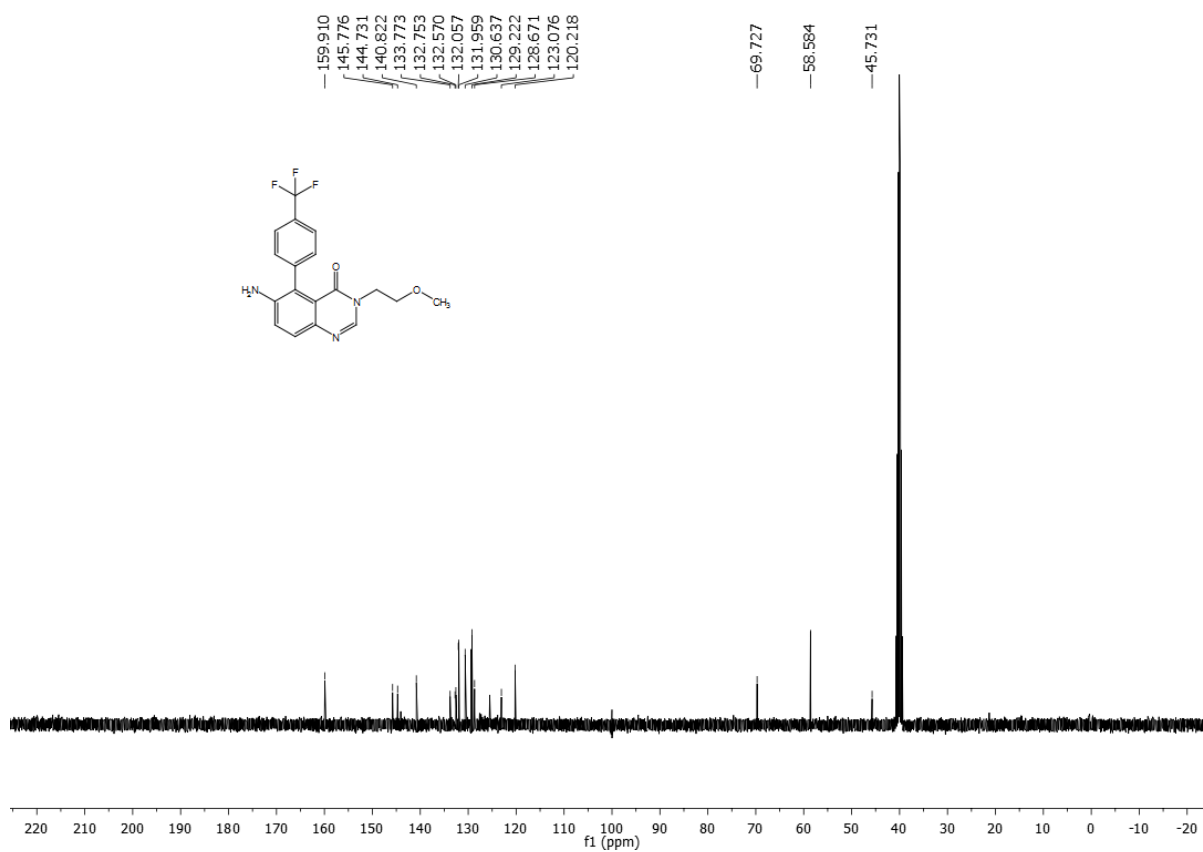
^{13}C NMR of compound **8** (100 MHz, d_6 -DMSO):



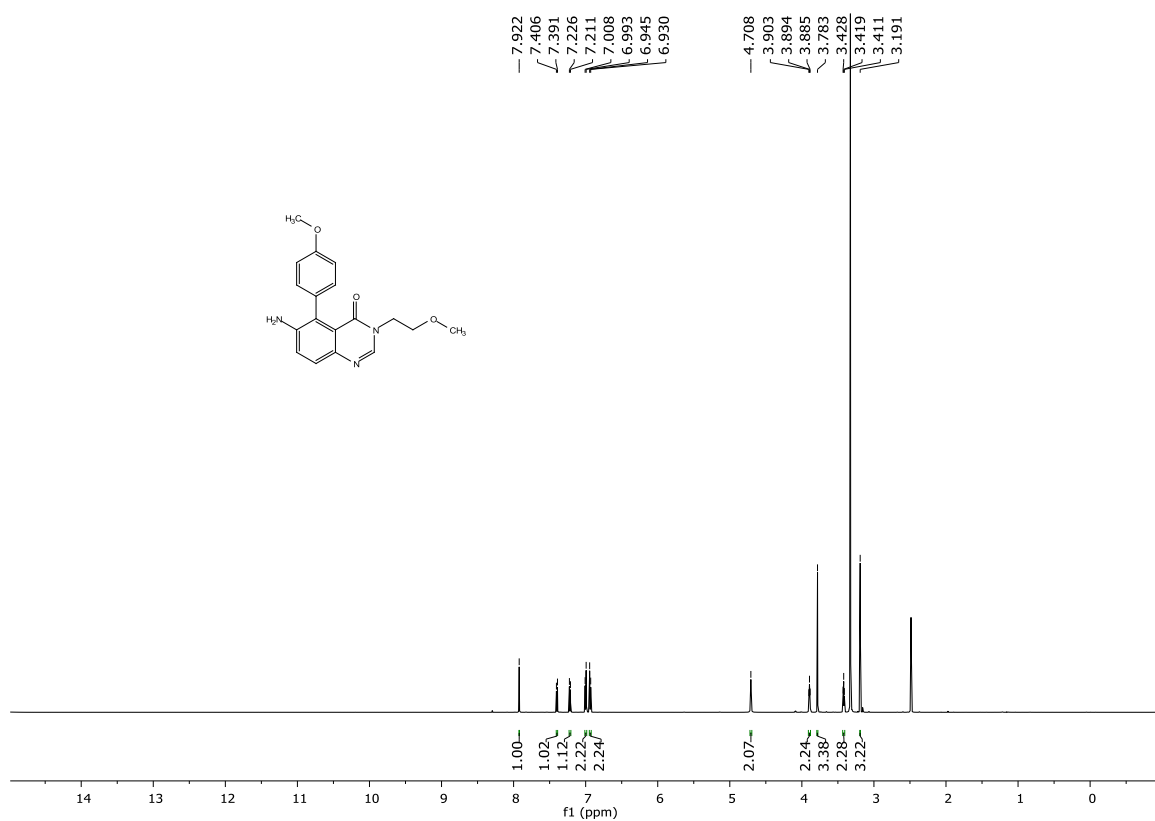
^1H NMR of compound **9** (400 MHz, d_6 -DMSO):



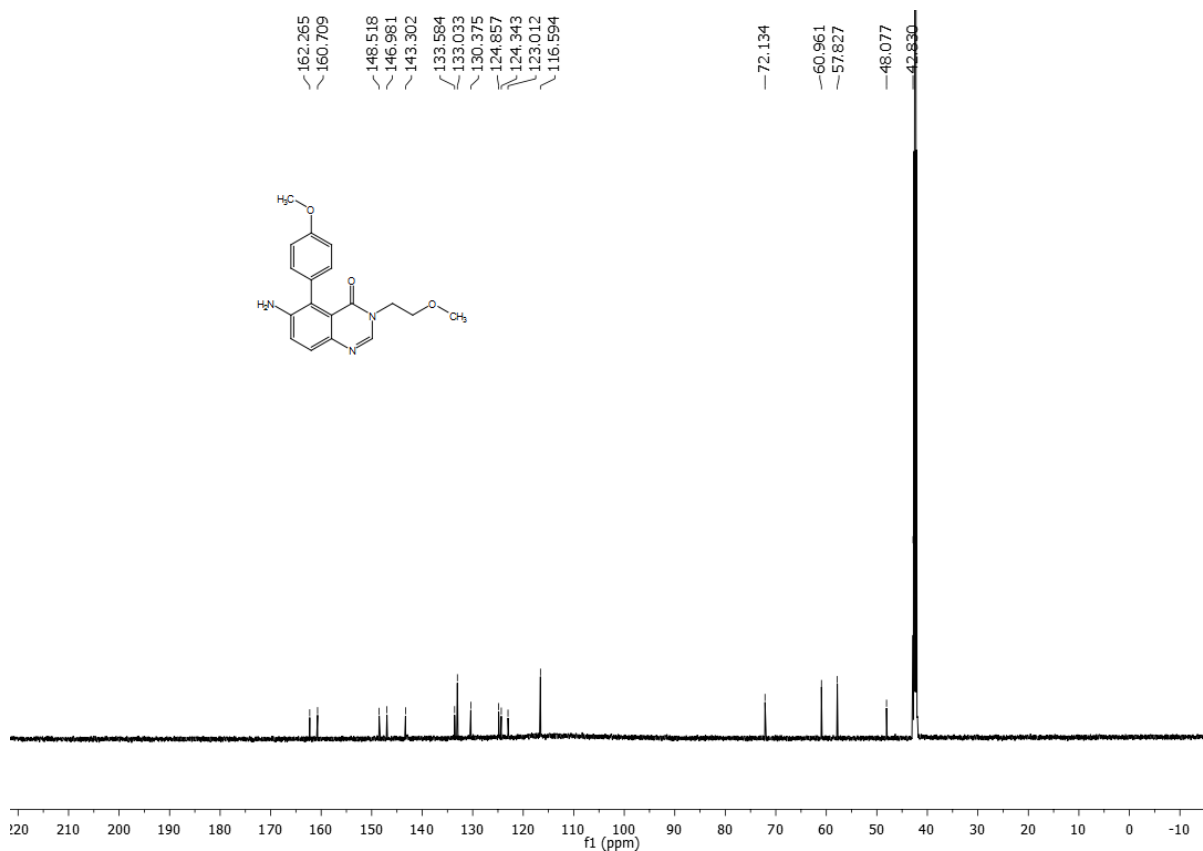
^{13}C NMR of compound **9** (100 MHz, d_6 -DMSO):



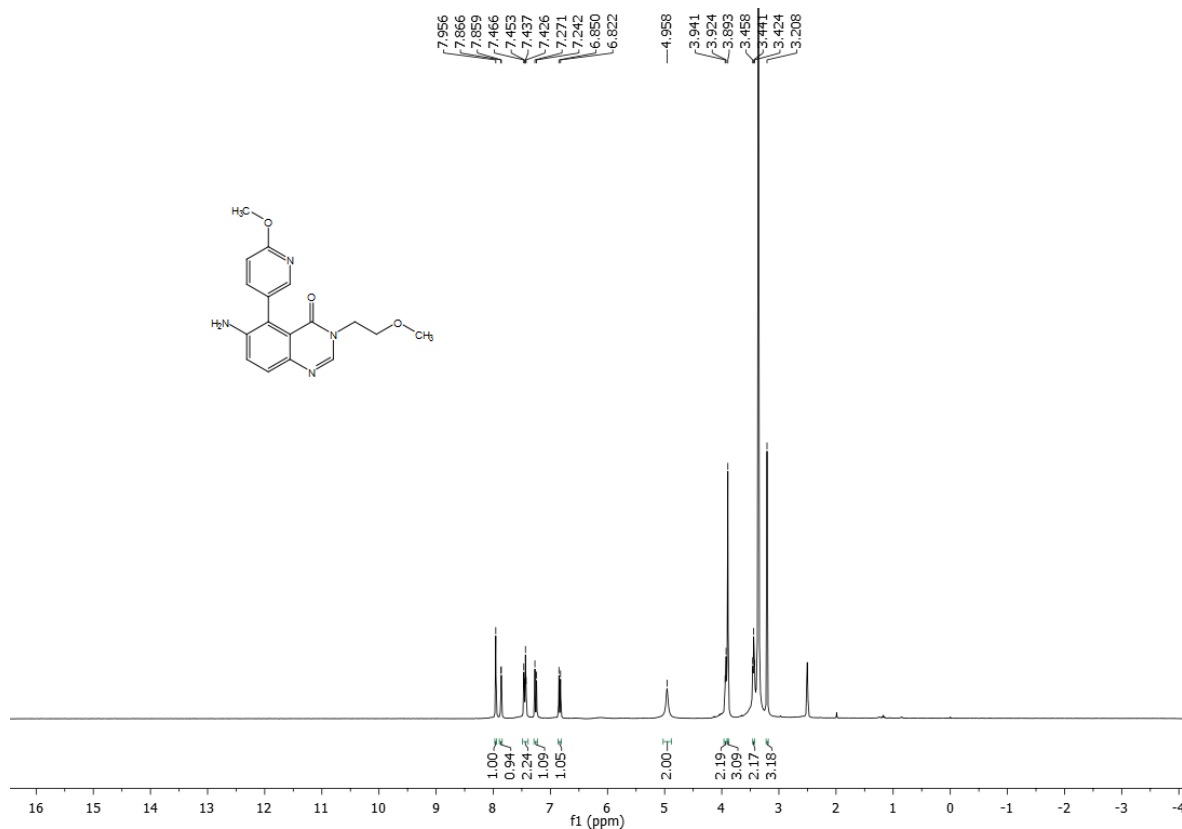
^1H NMR of compound **10** (400 MHz, d_6 -DMSO):



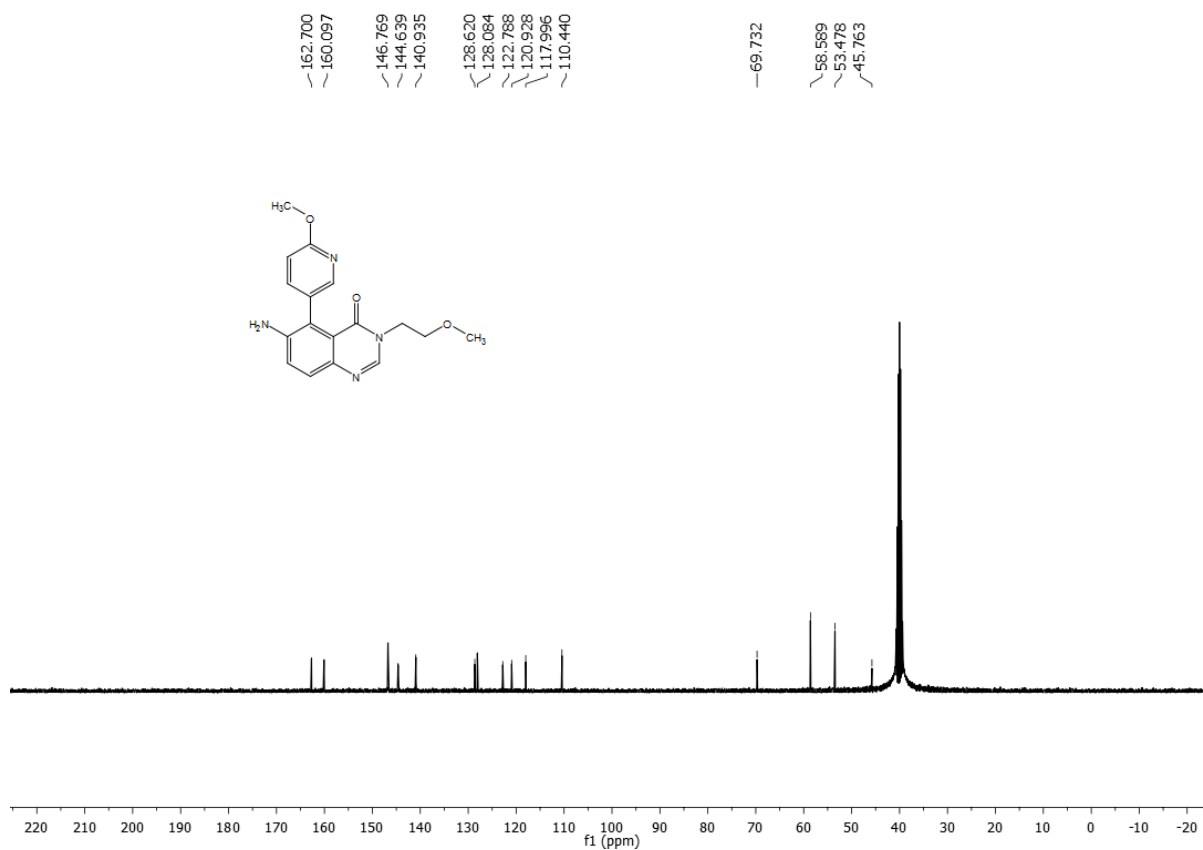
^{13}C NMR of compound **10** (100 MHz, d_6 -DMSO):



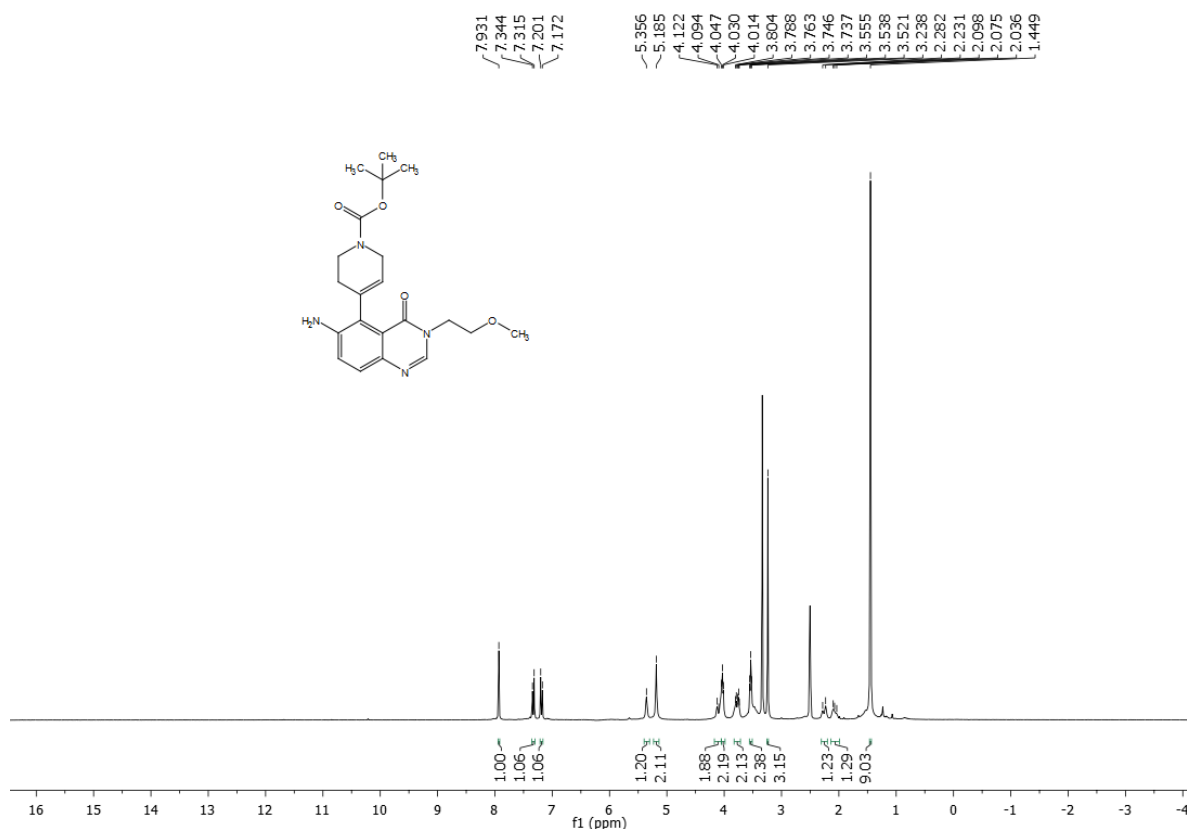
^1H NMR of compound **11** (300 MHz, d_6 -DMSO):



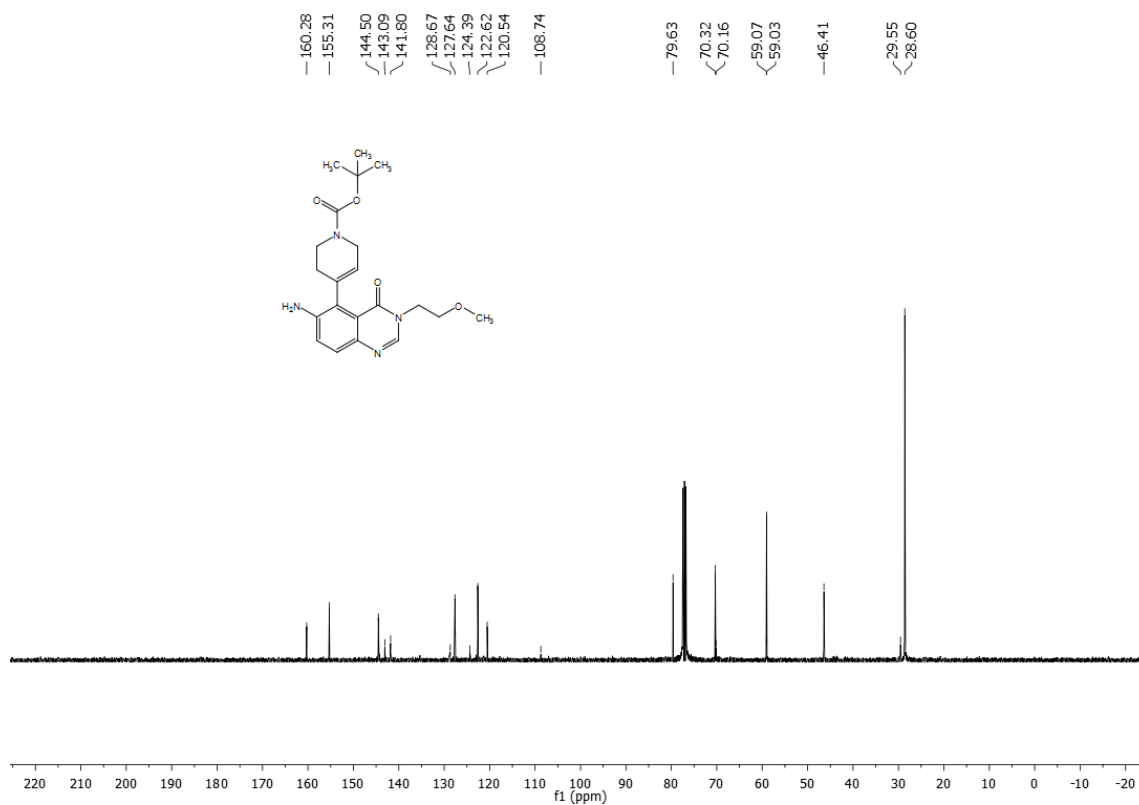
^{13}C NMR of compound **11** (100 MHz, d_6 -DMSO):



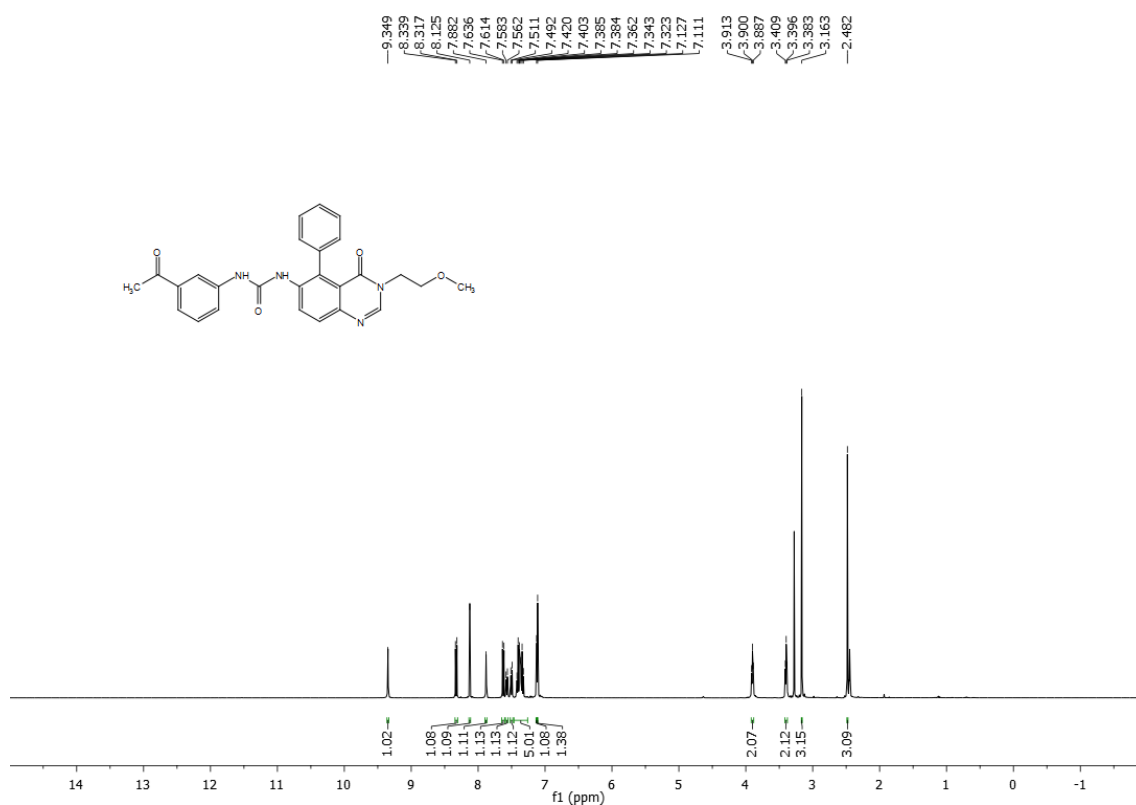
^1H NMR of compound **12** (300 MHz, d_6 -DMSO):



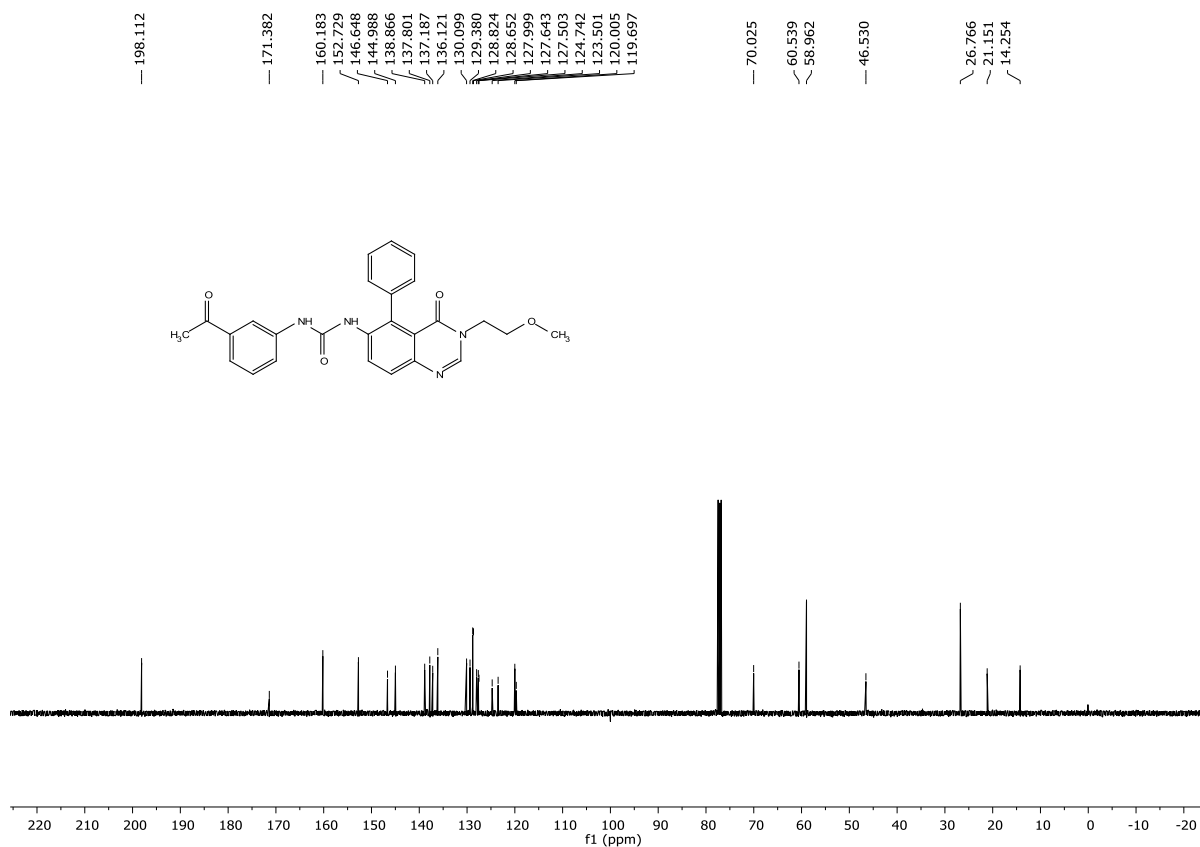
^{13}C NMR of compound **12** (100 MHz, CDCl_3):



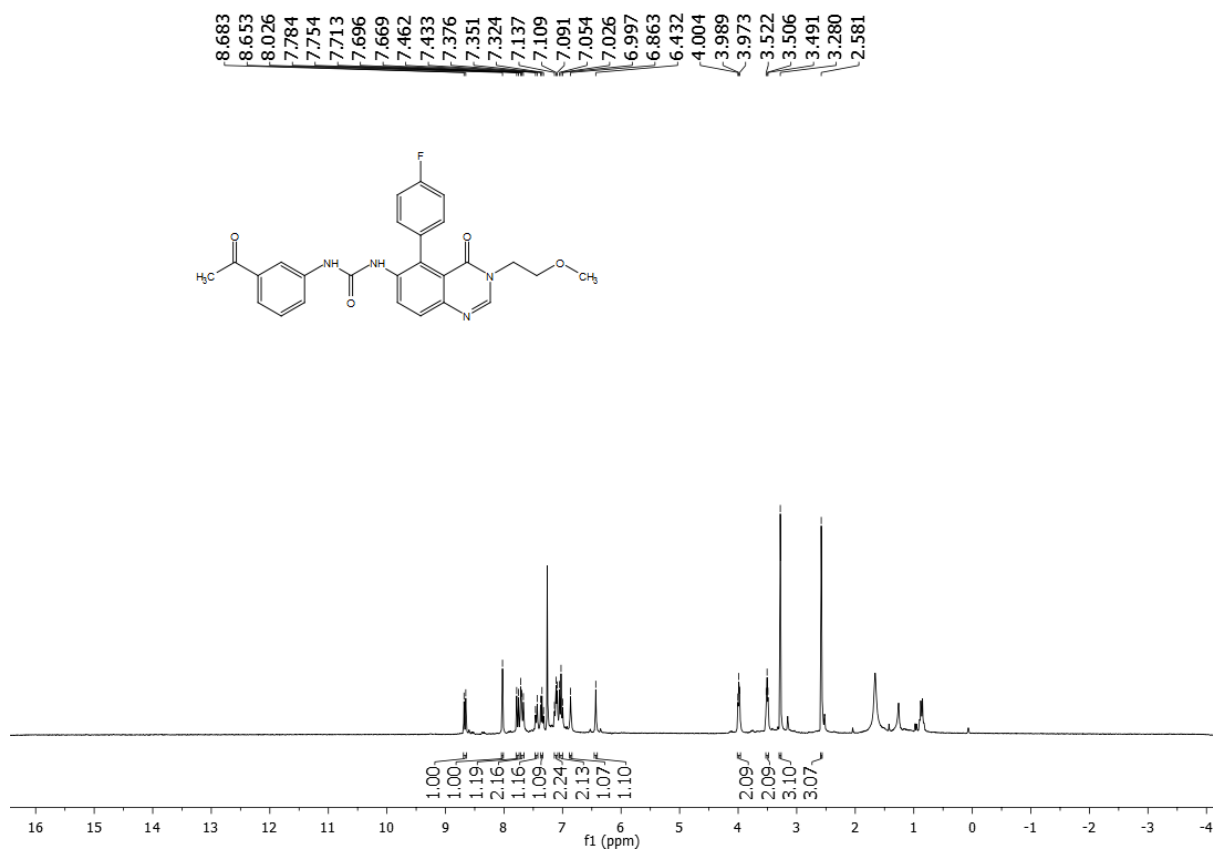
^1H NMR of compound **13** (400 MHz, d_6 -DMSO):



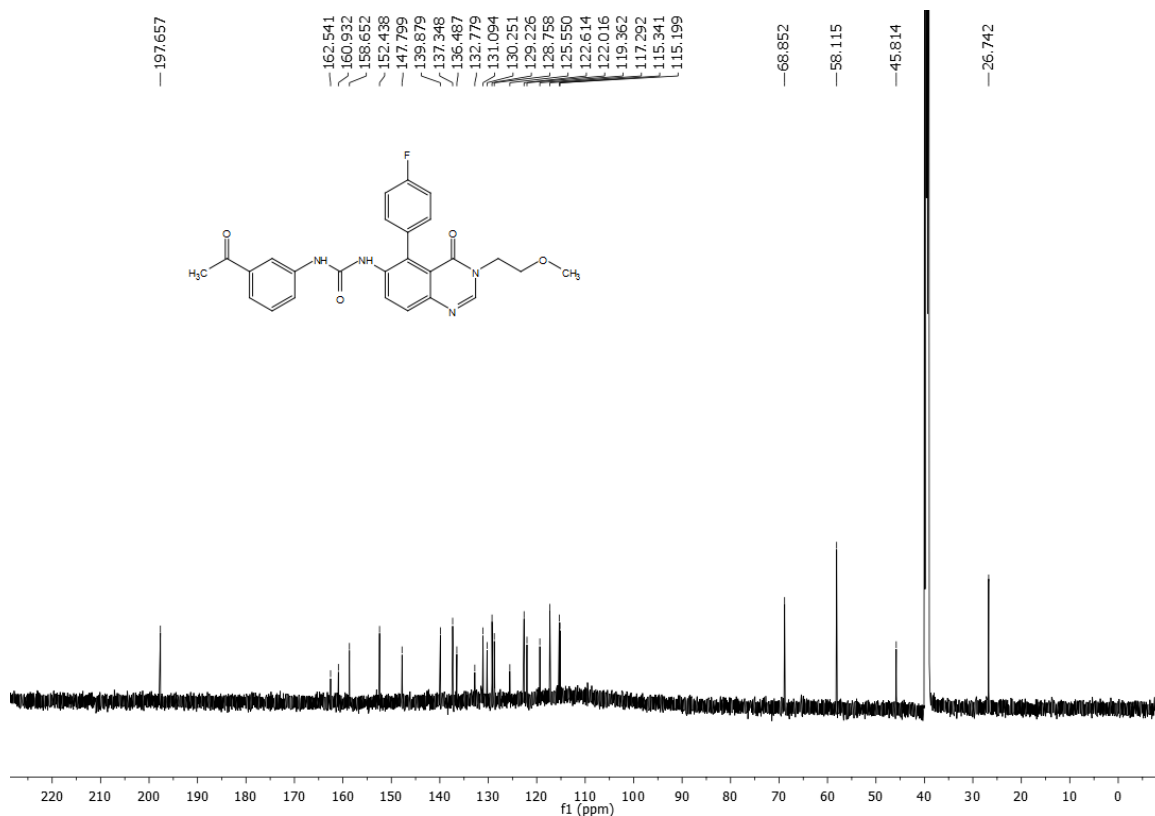
^{13}C NMR of compound **13** (100 MHz, d_6 -DMSO):



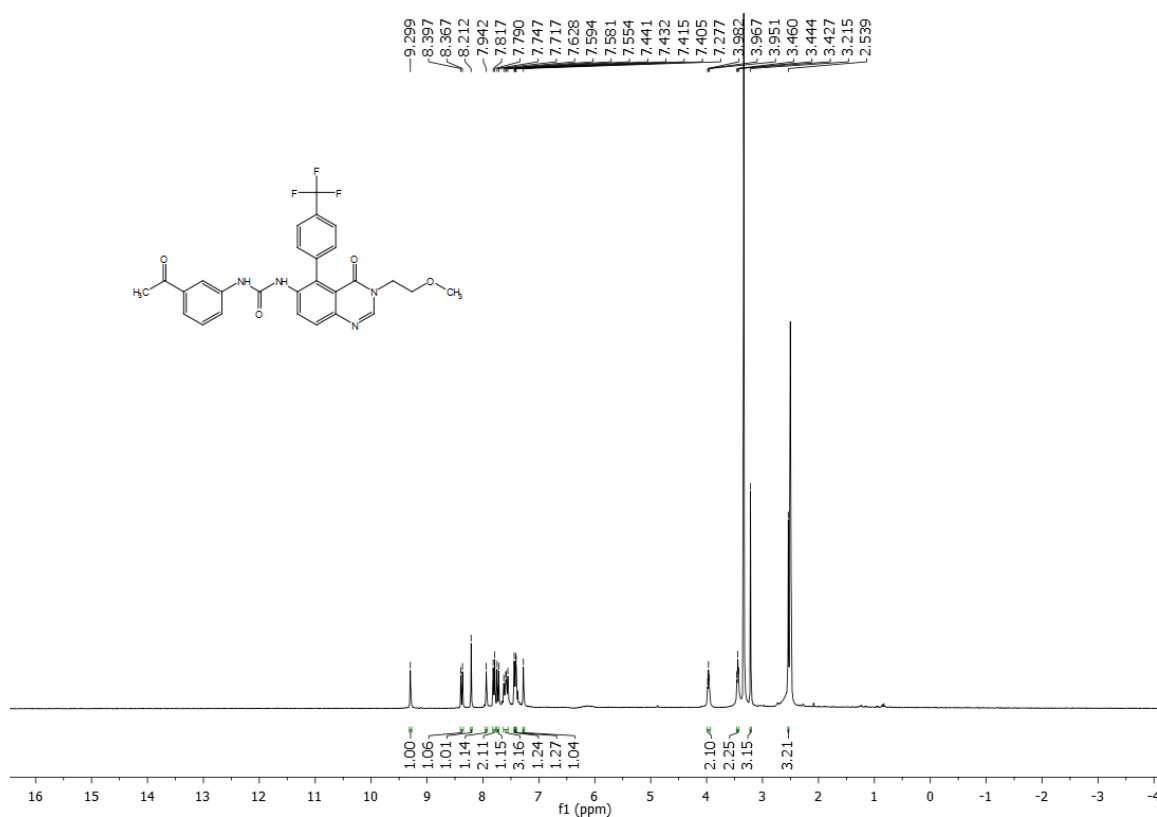
^1H NMR of compound **14** (600 MHz, CDCl_3):



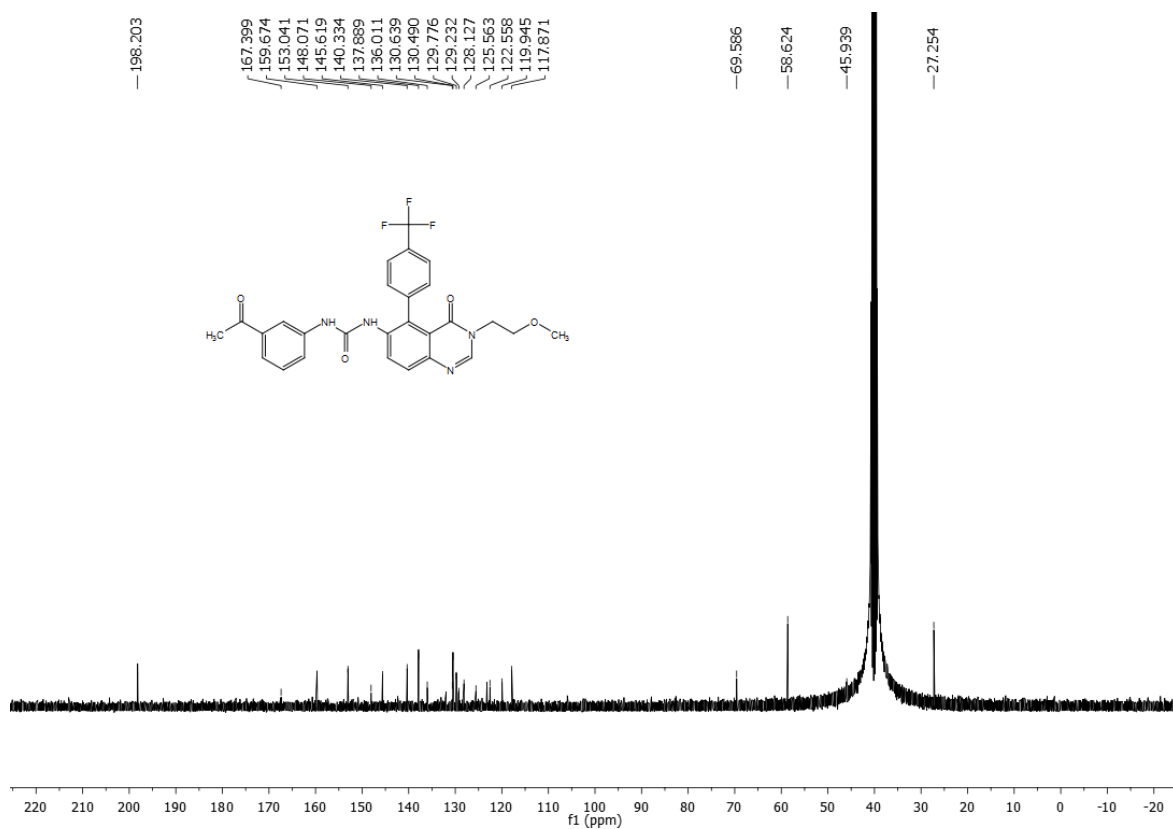
^{13}C NMR of compound **14** (150 MHz, d_6 -DMSO):

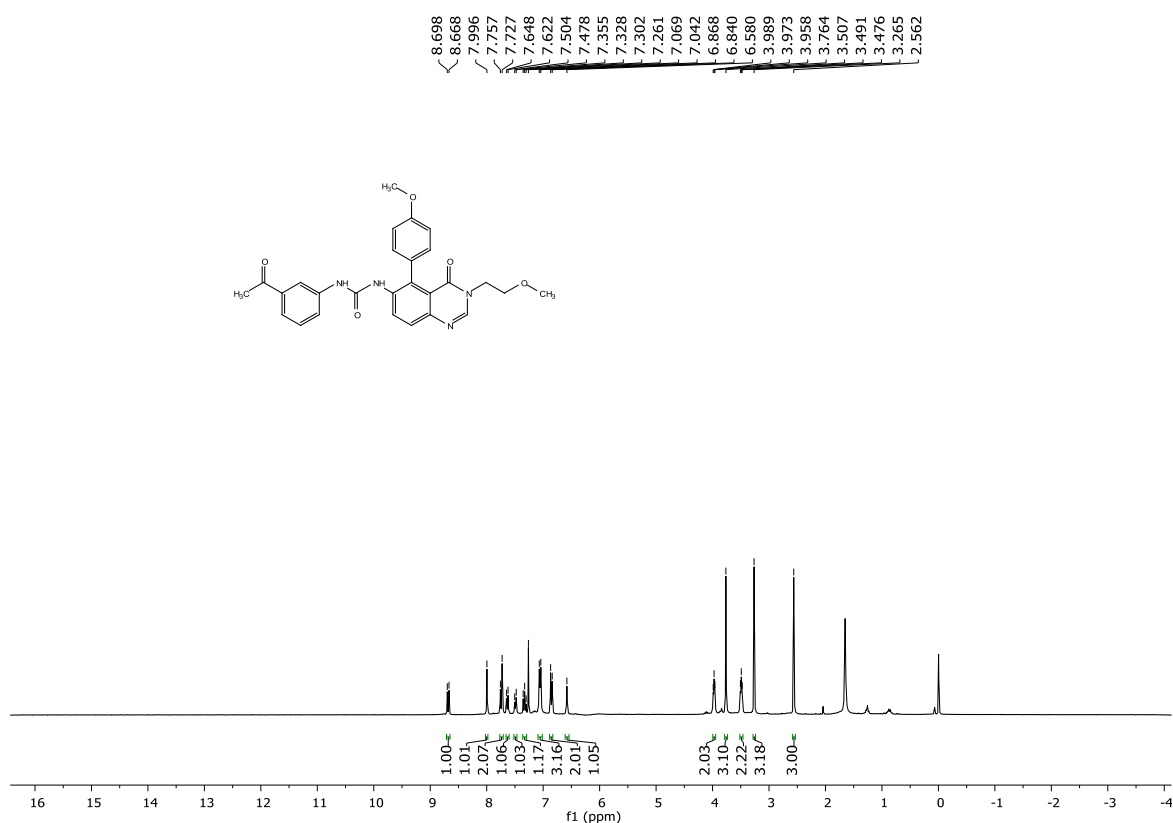
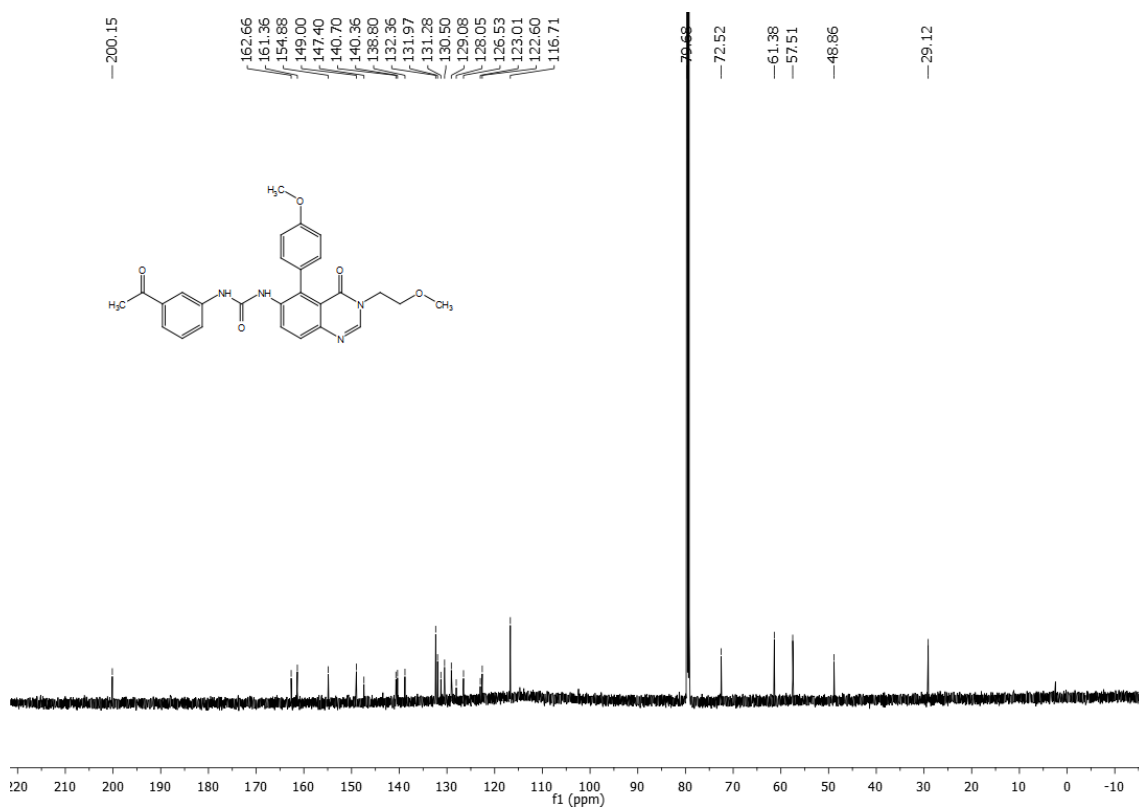


^1H NMR of compound **15** (300 MHz, d_6 -DMSO):

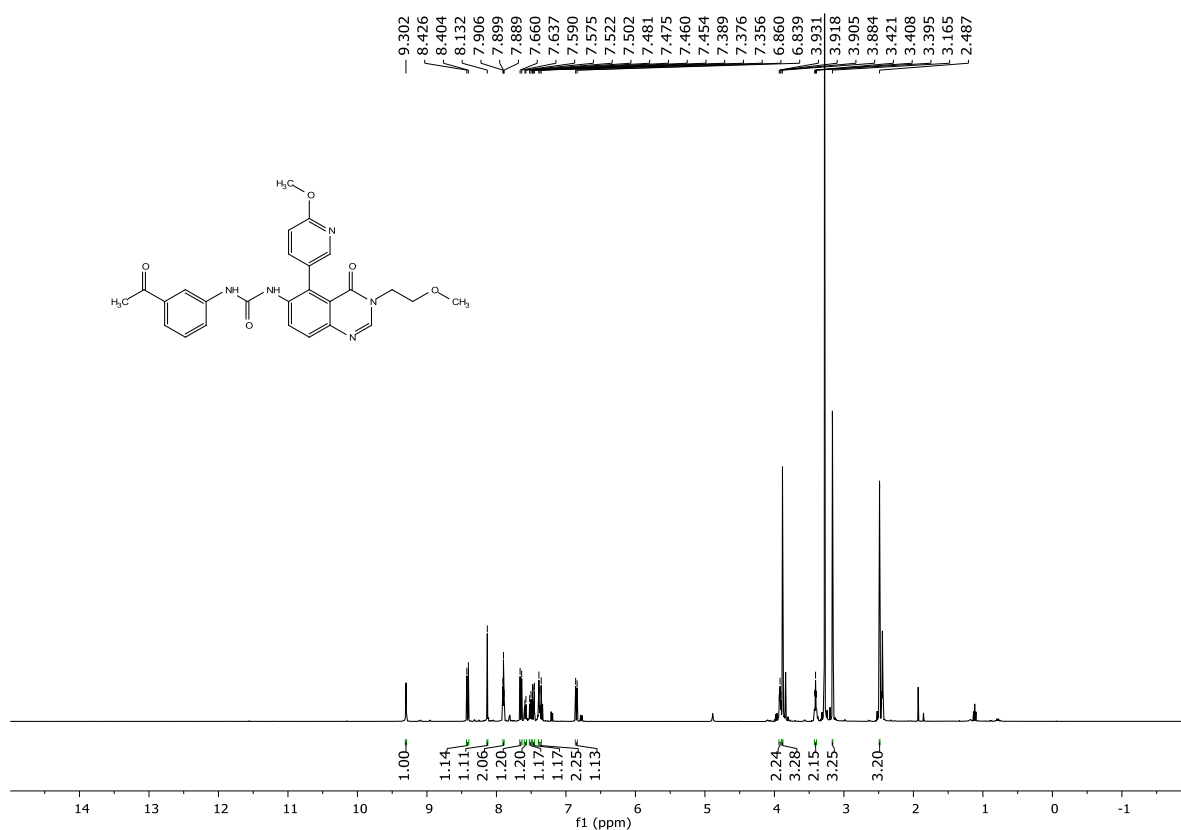


^{13}C NMR of compound **15** (100 MHz, d_6 -DMSO):

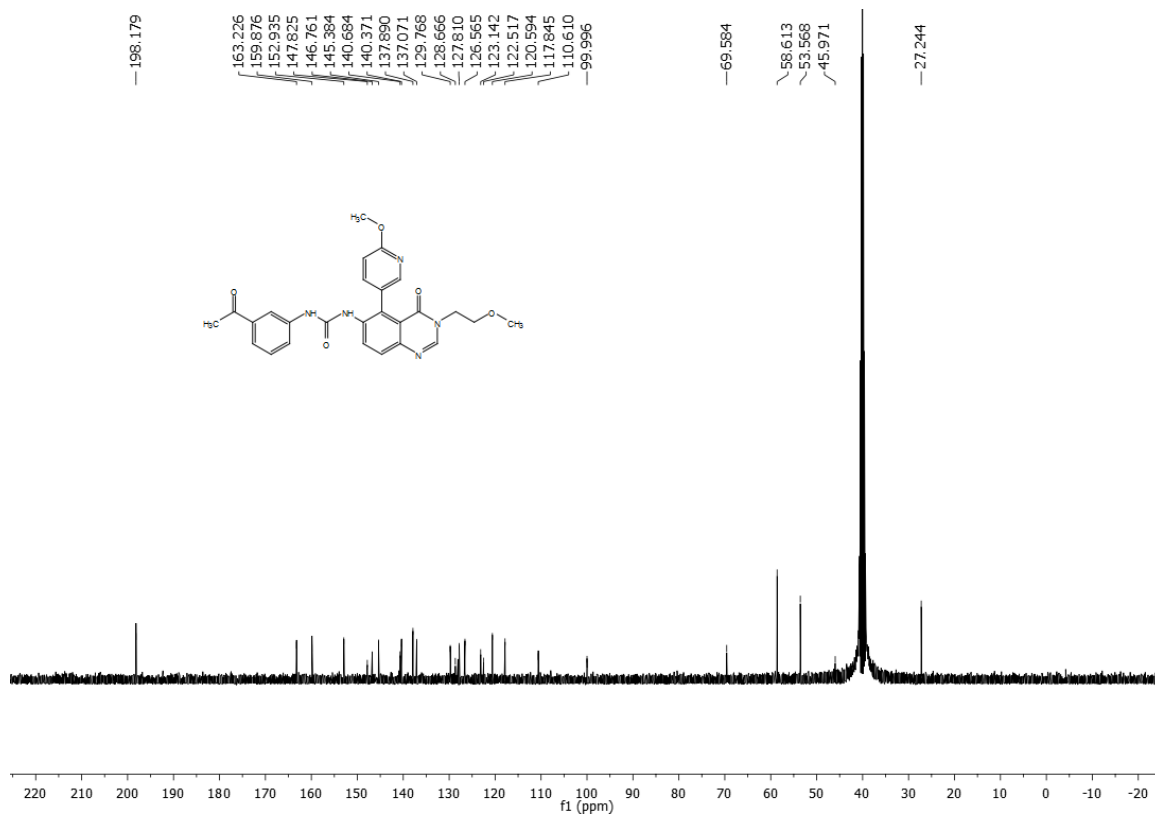


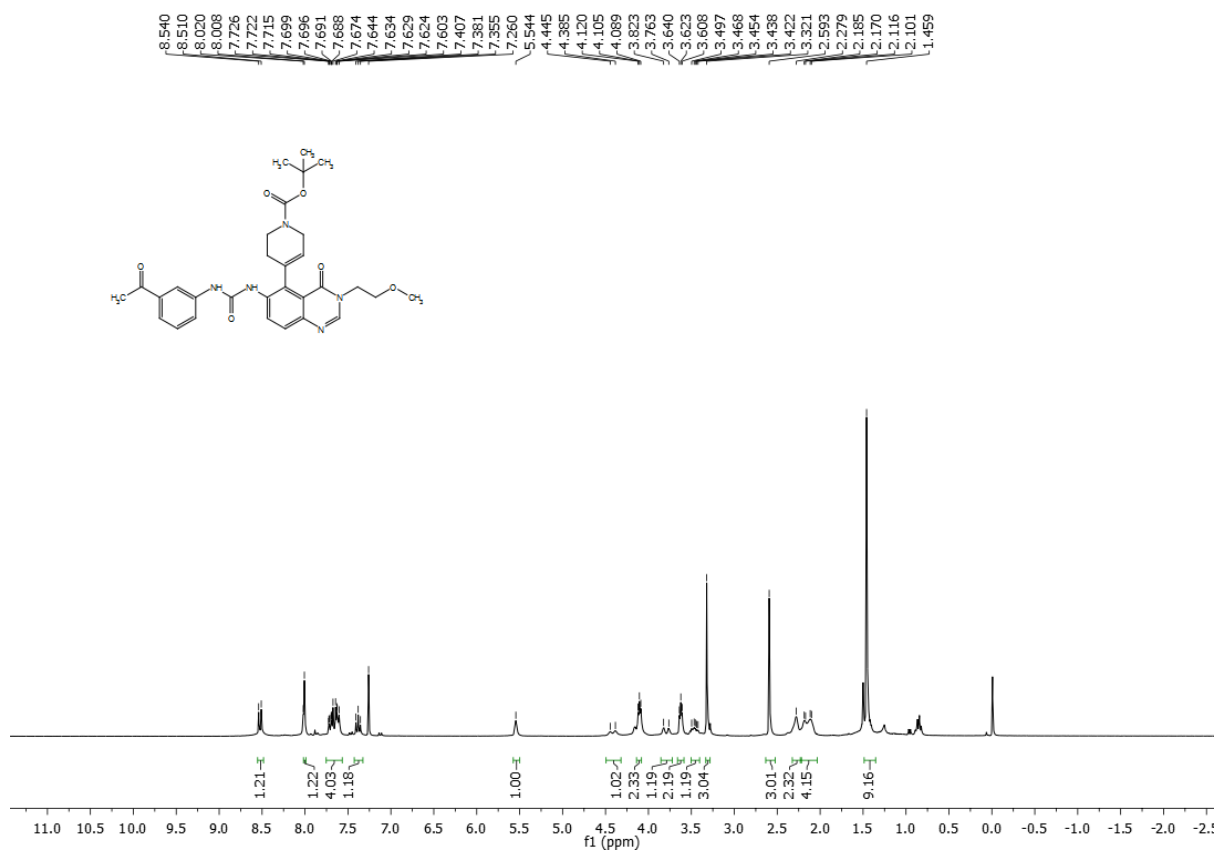
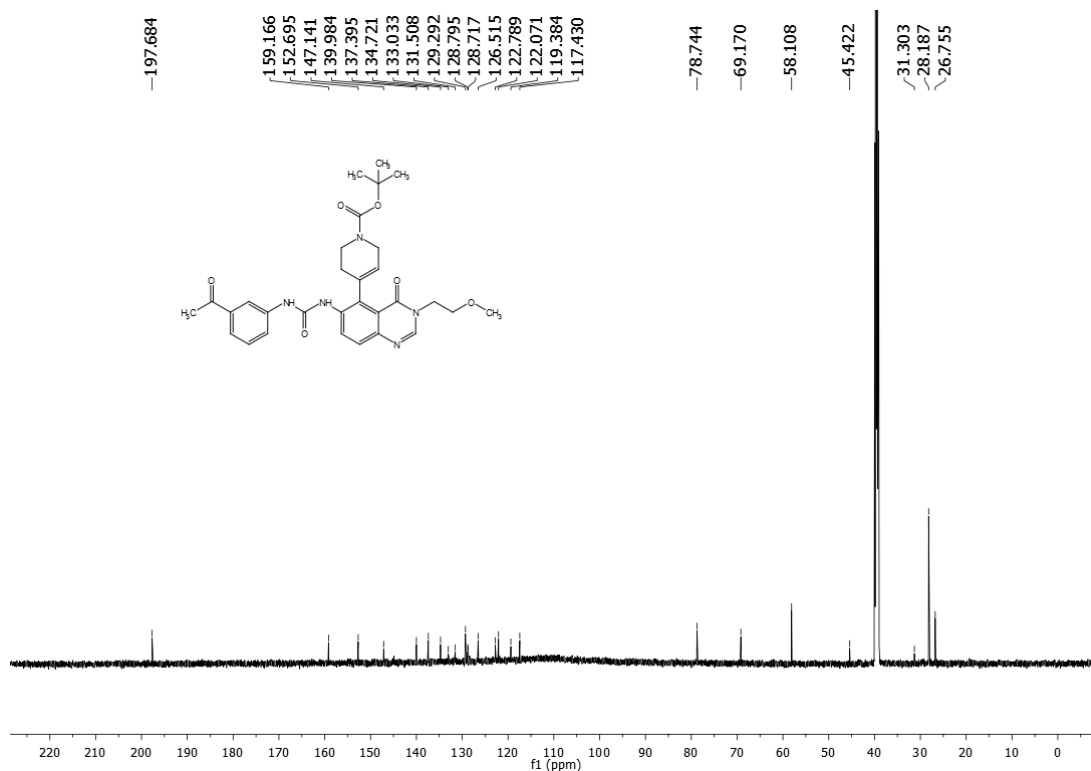
¹H NMR of compound **16** (300 MHz, CDCl₃):¹³C NMR of compound **16** (150 MHz, CDCl₃):

^1H NMR of compound **17** (400 MHz, d_6 -DMSO):

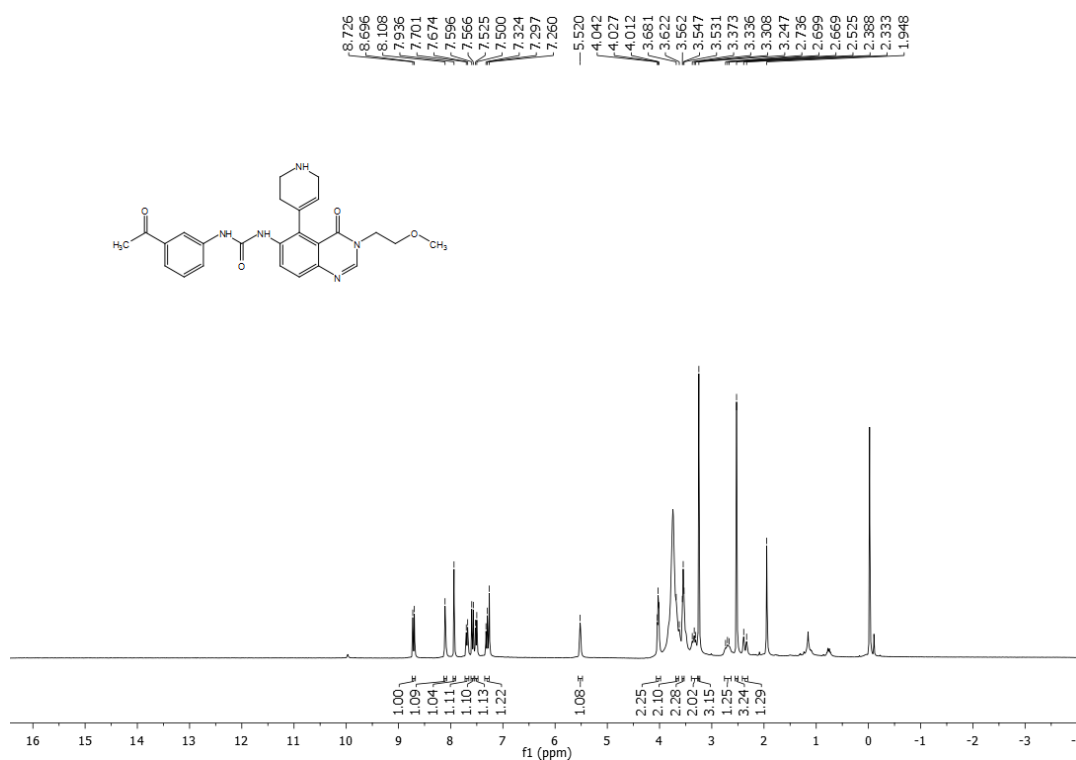


^{13}C NMR of compound **17** (100 MHz, d_6 -DMSO):

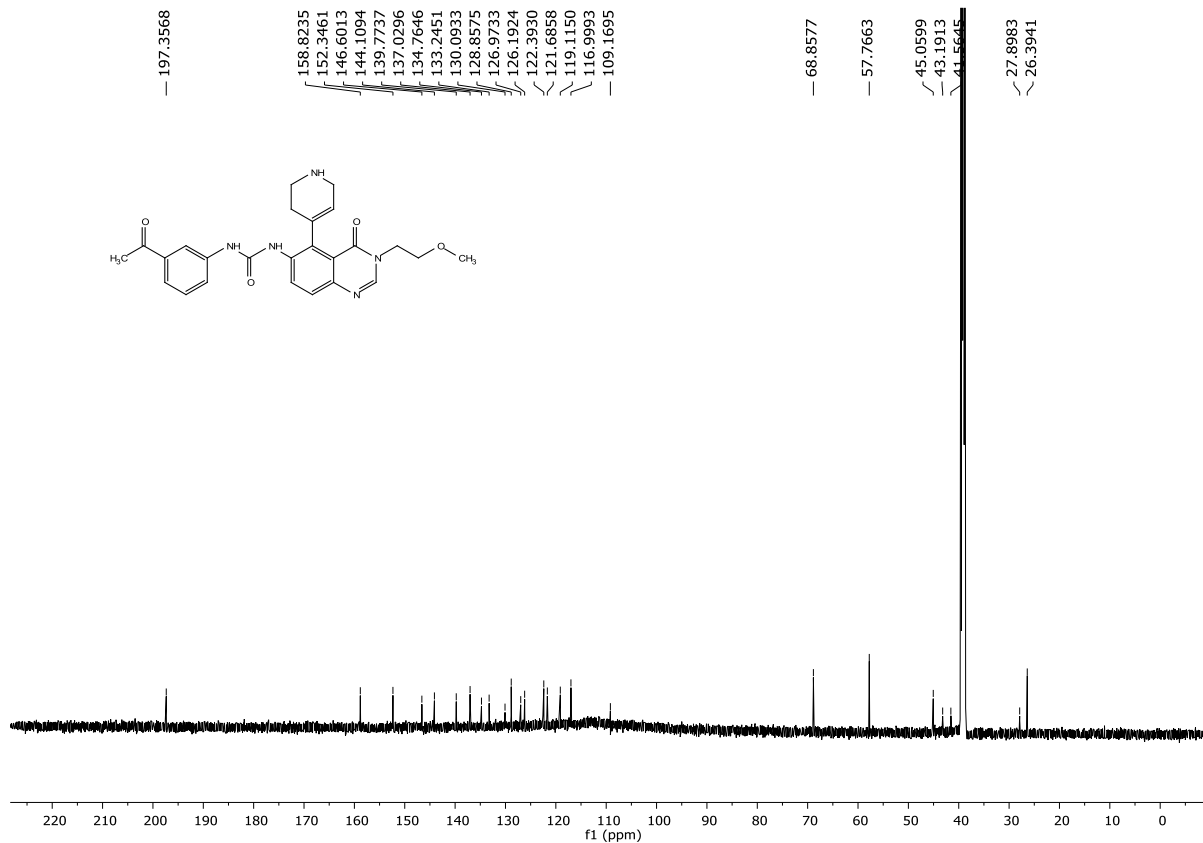


¹H NMR of compound **18** (300 MHz, CDCl₃):¹³C NMR of compound **18** (150 MHz, d₆-DMSO):

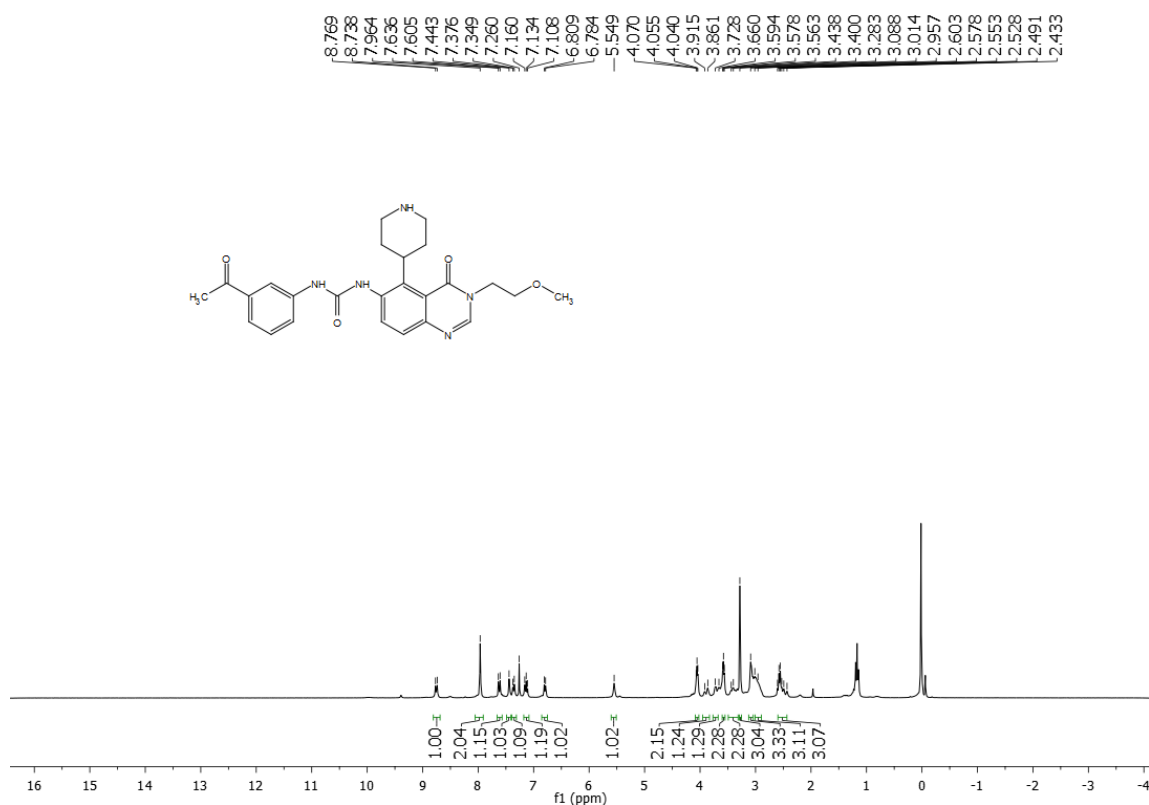
^1H NMR of compound **19** (300 MHz, CDCl_3):



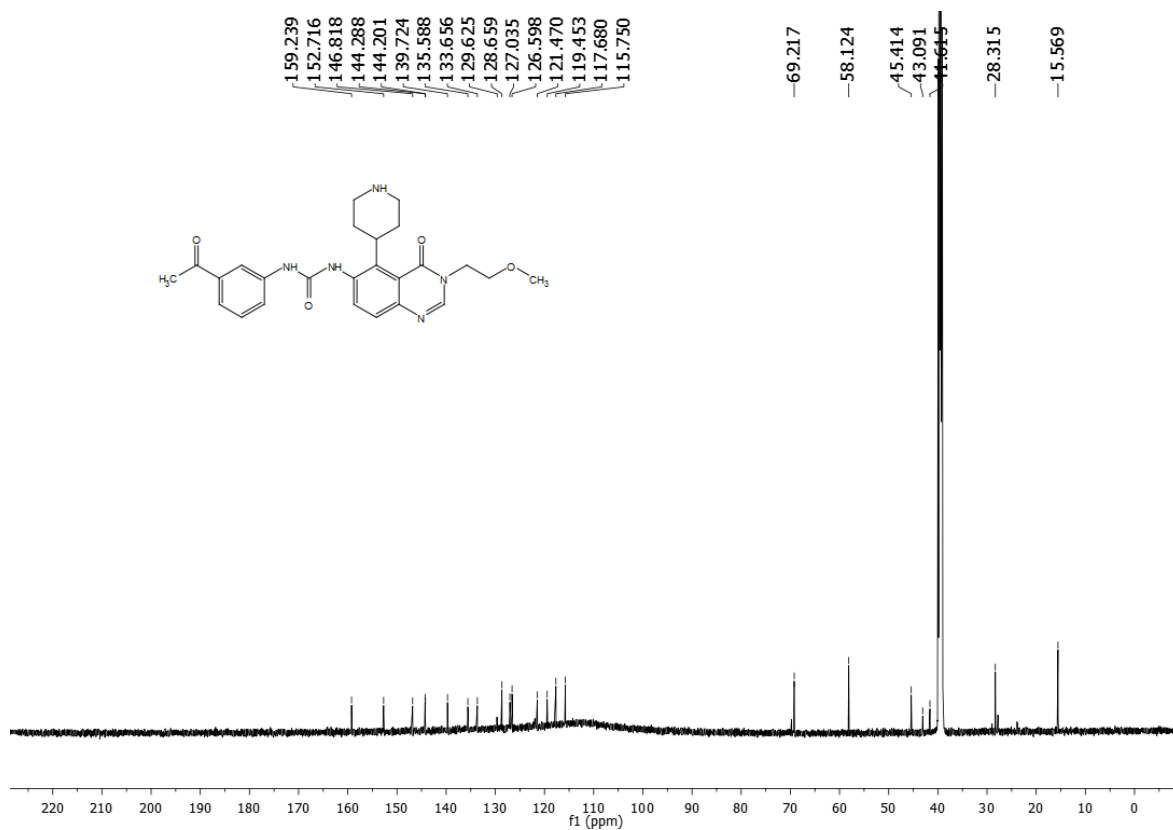
^{13}C NMR of compound **19** (150 MHz, d_6 -DMSO):

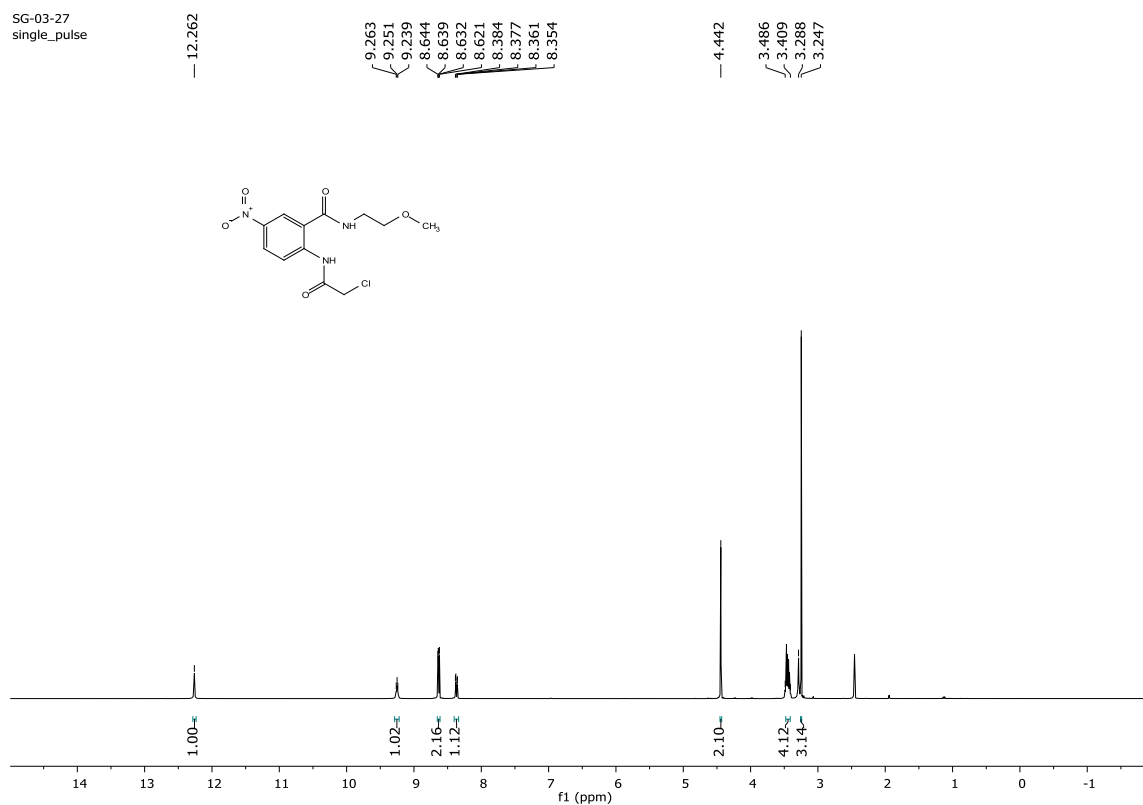
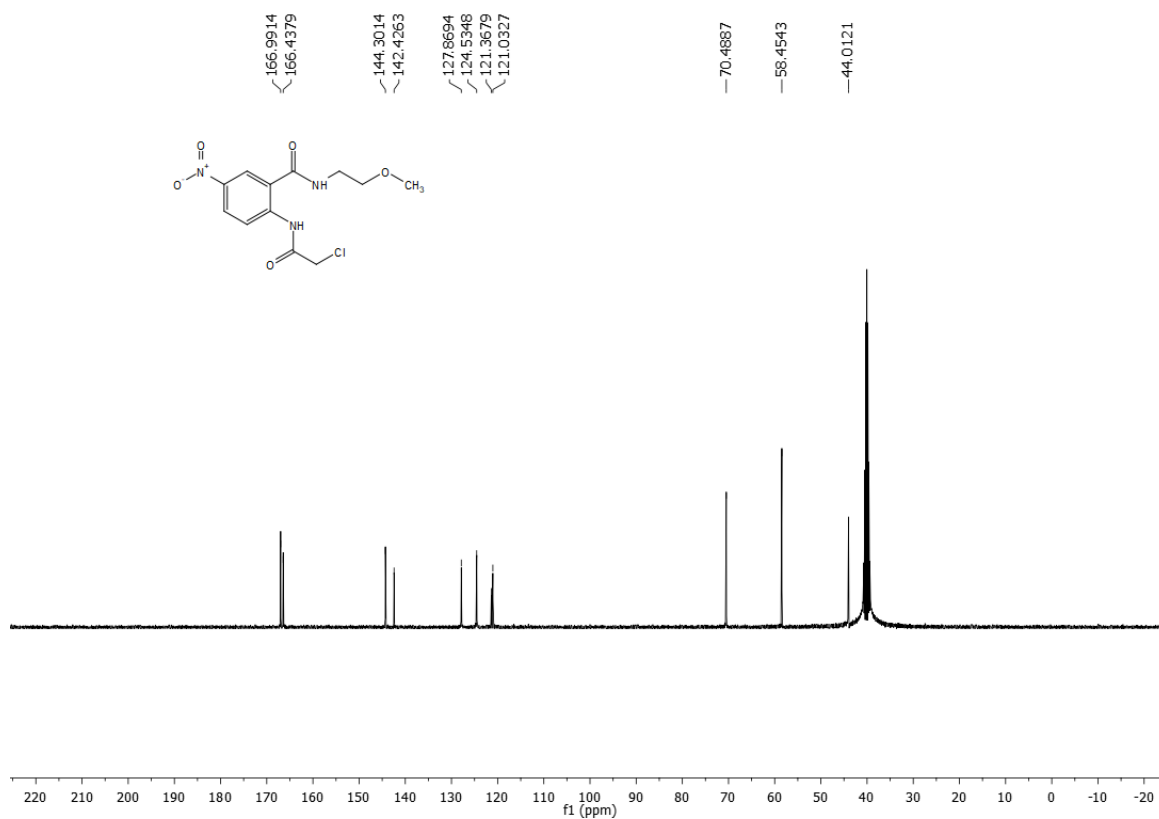


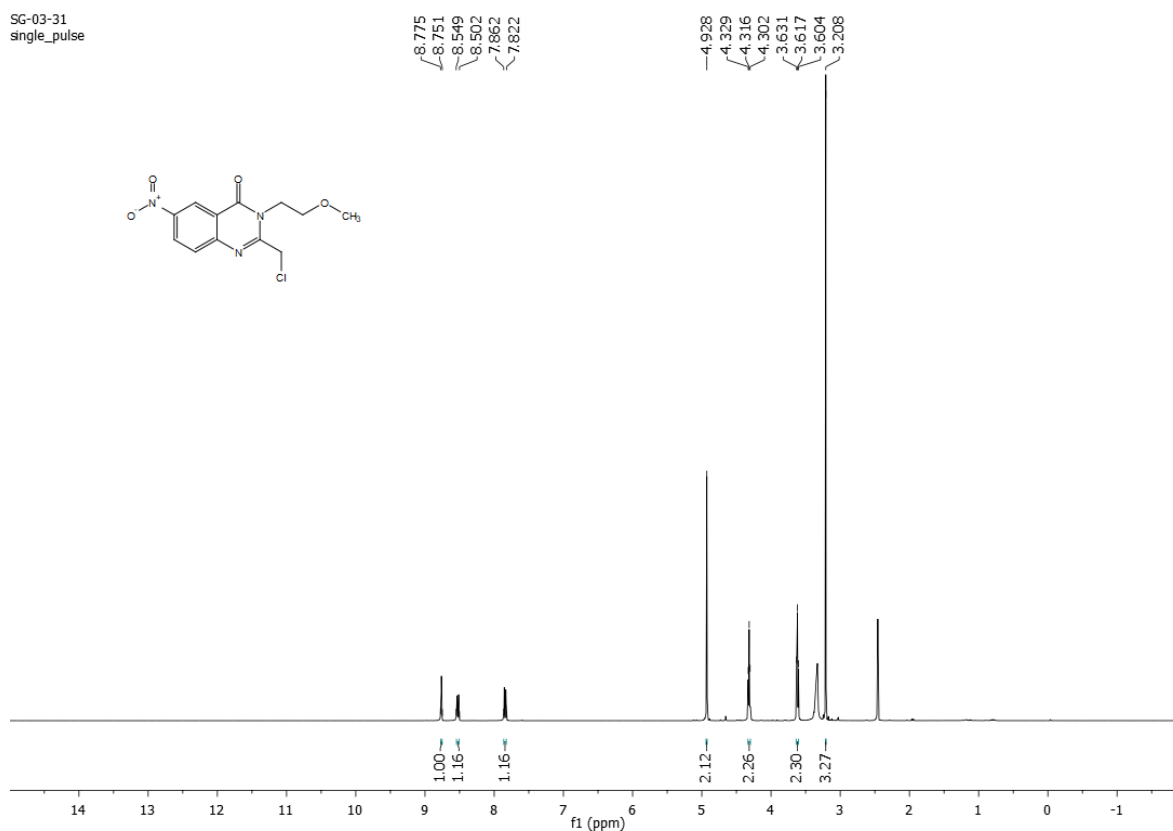
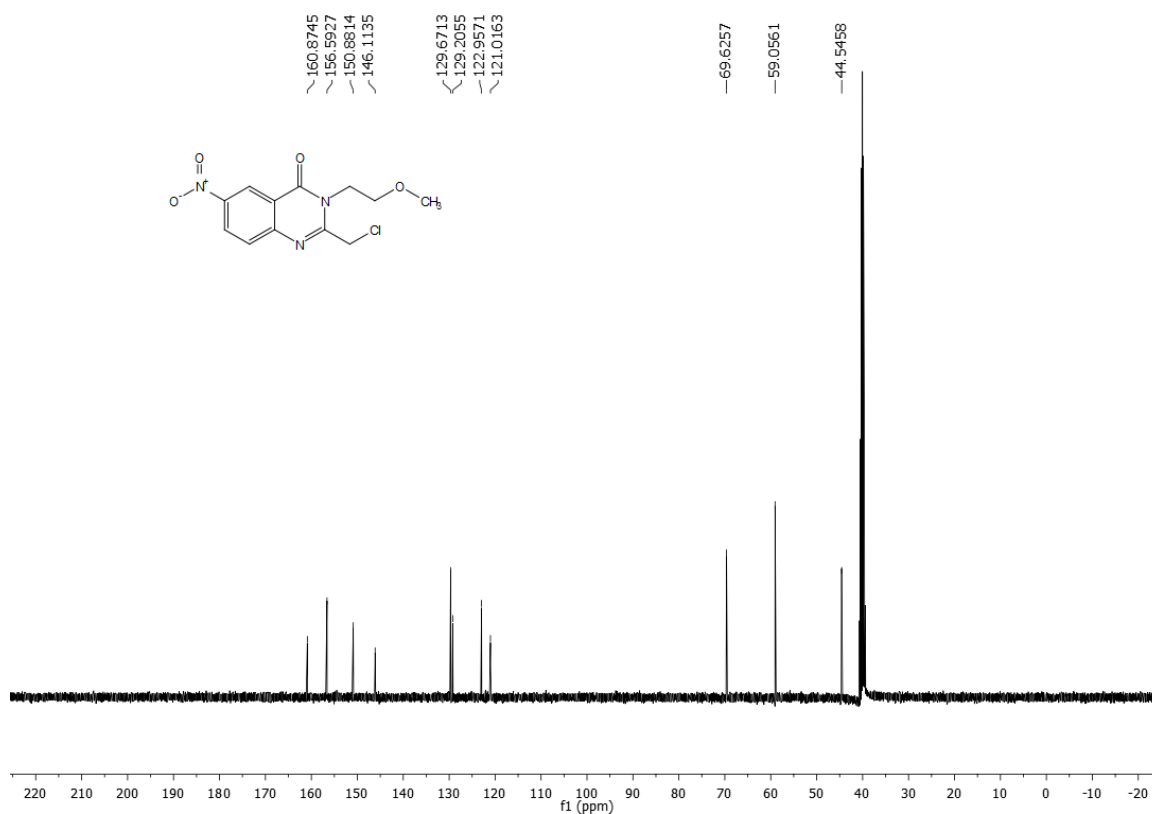
^1H NMR of compound **20** (400 MHz, d_6 -DMSO):

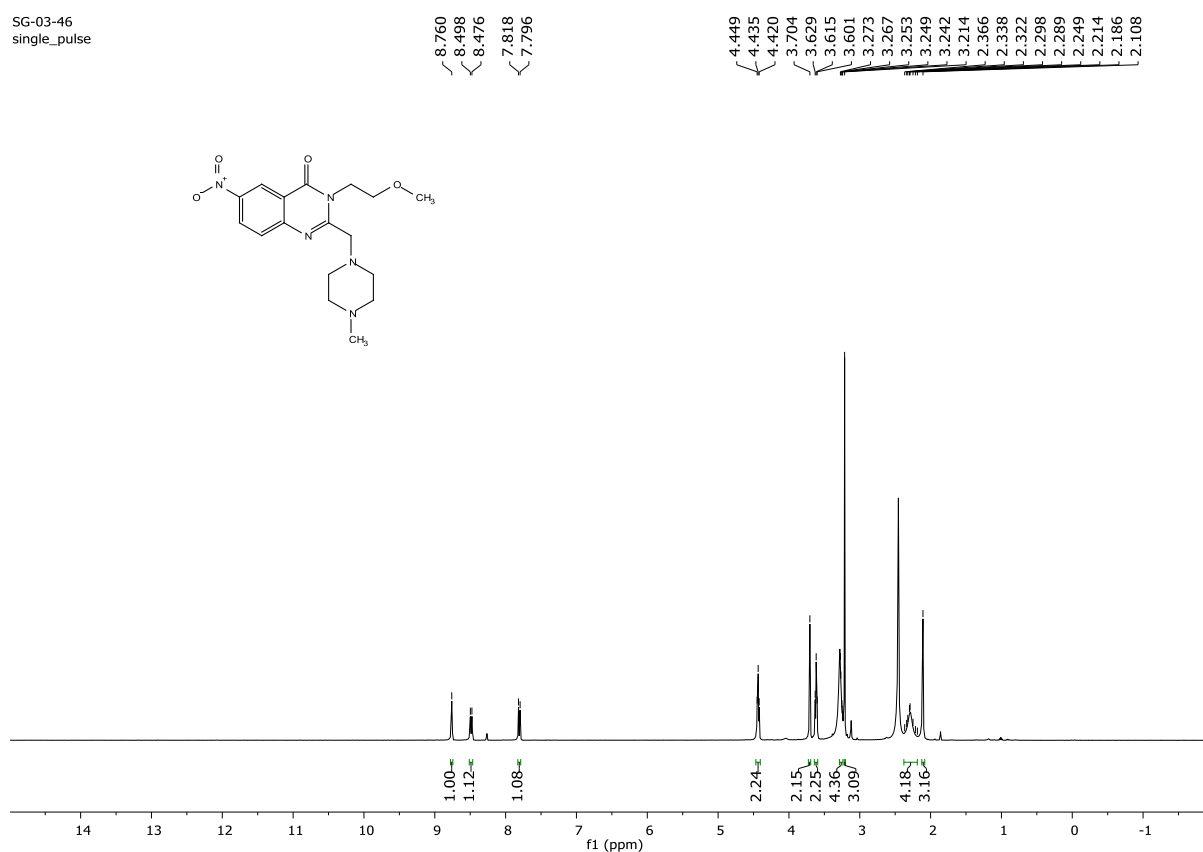
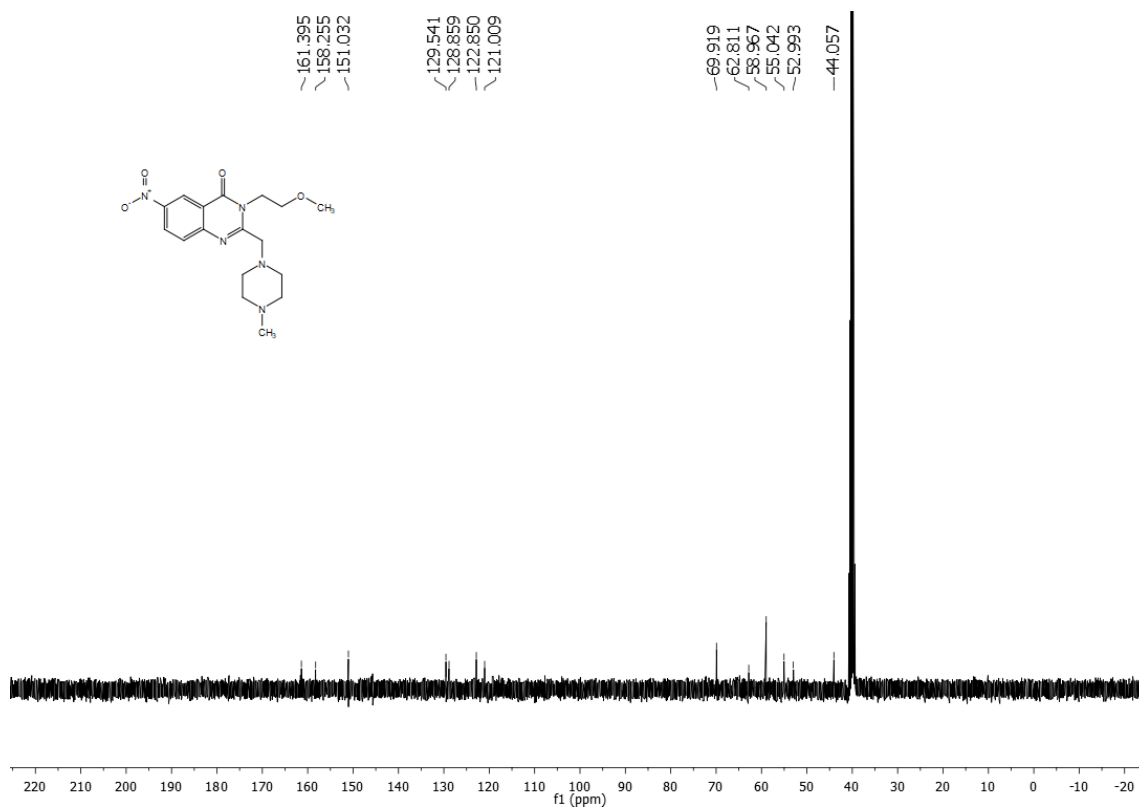


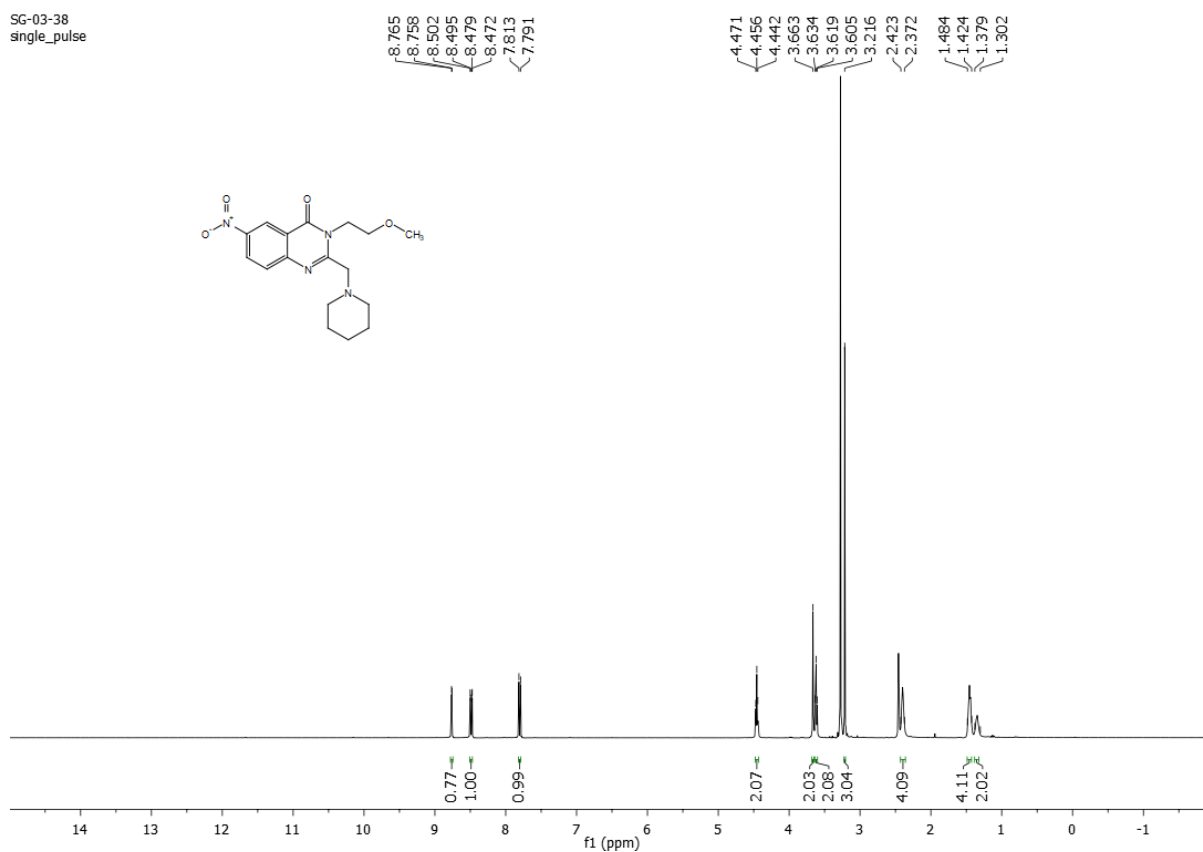
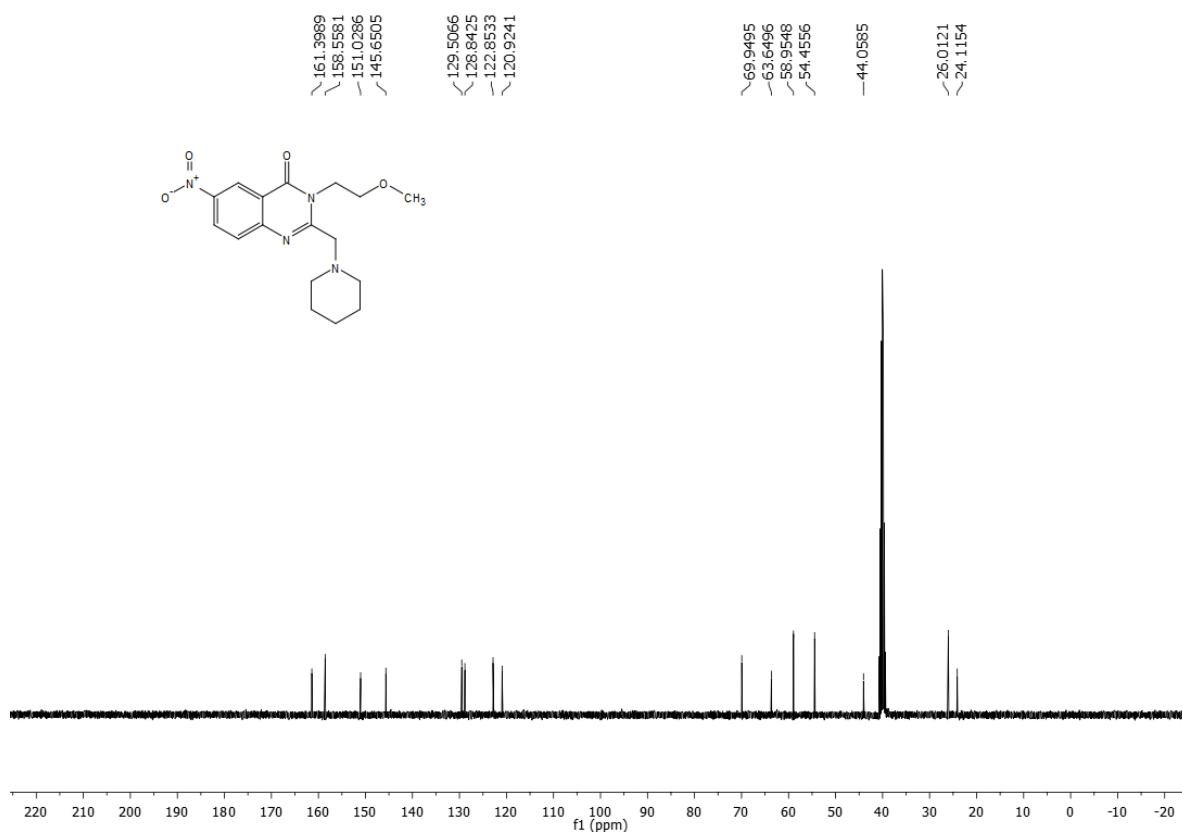
^{13}C NMR of compound **20** (100 MHz, d_6 -DMSO):

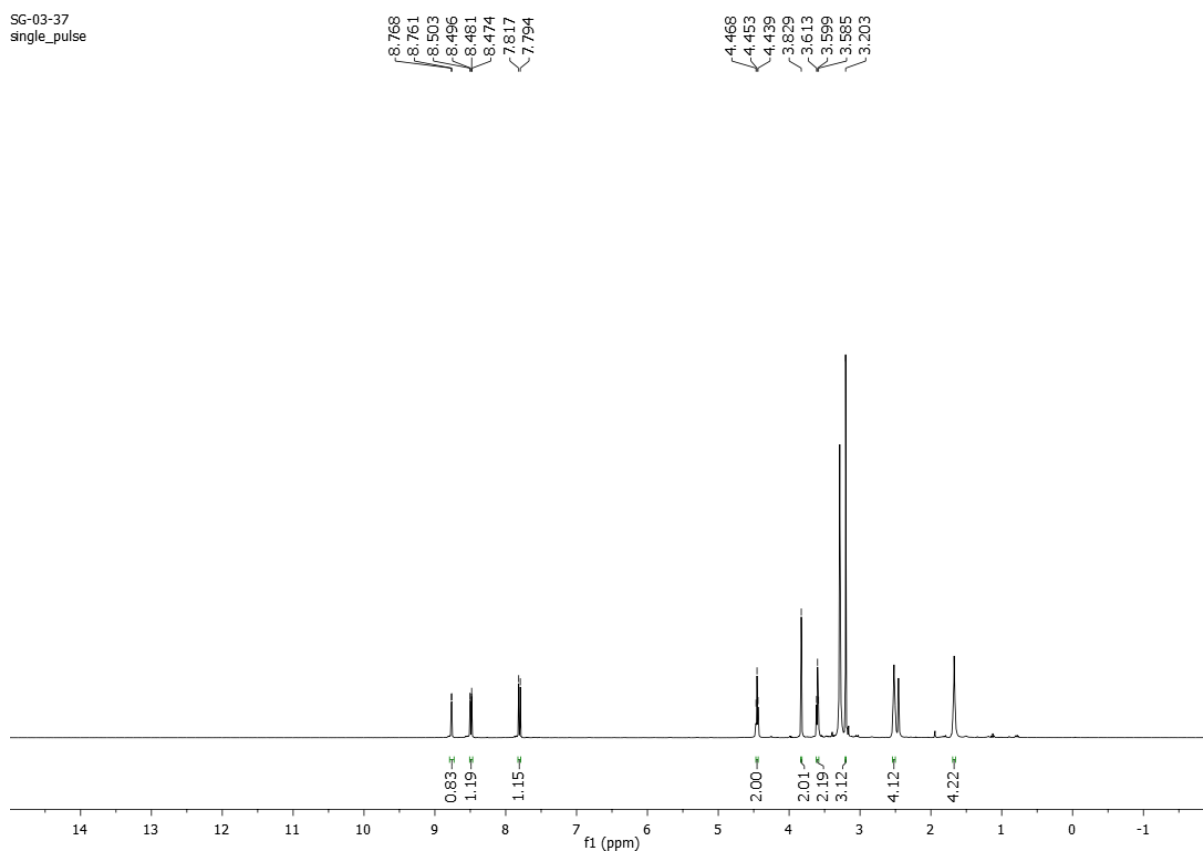
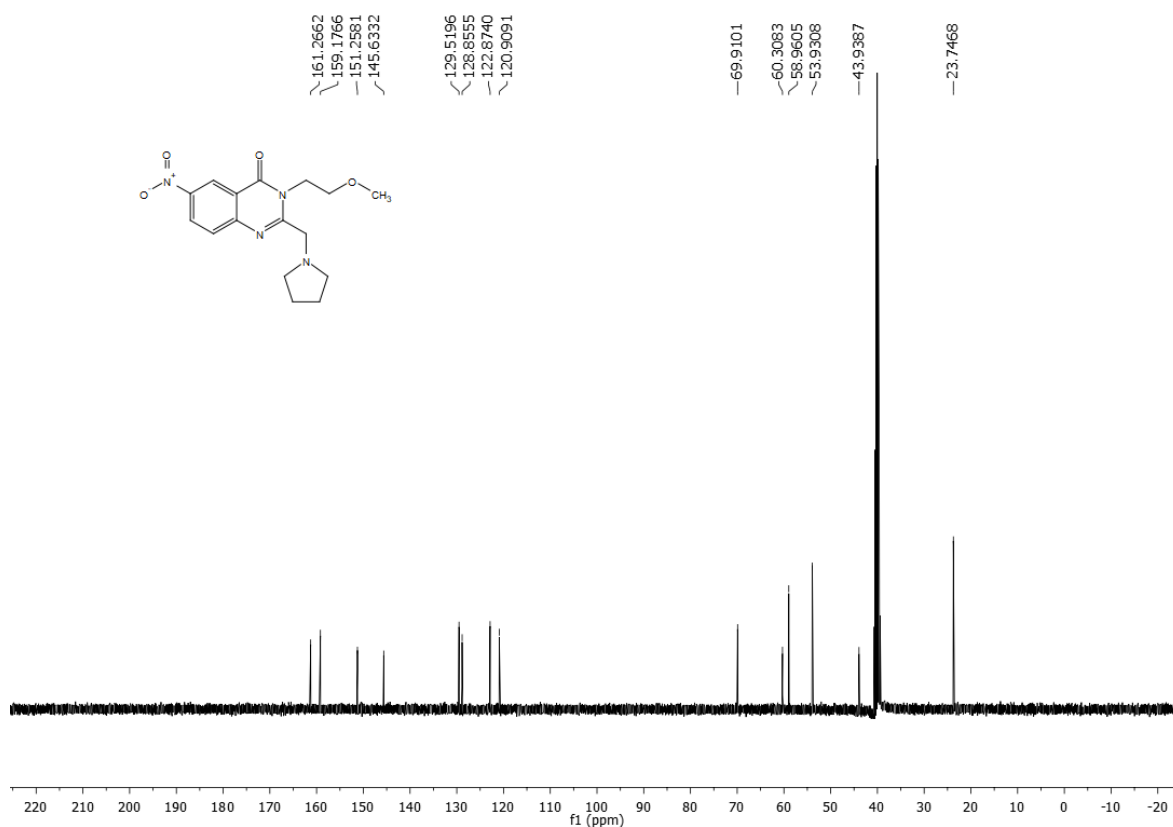


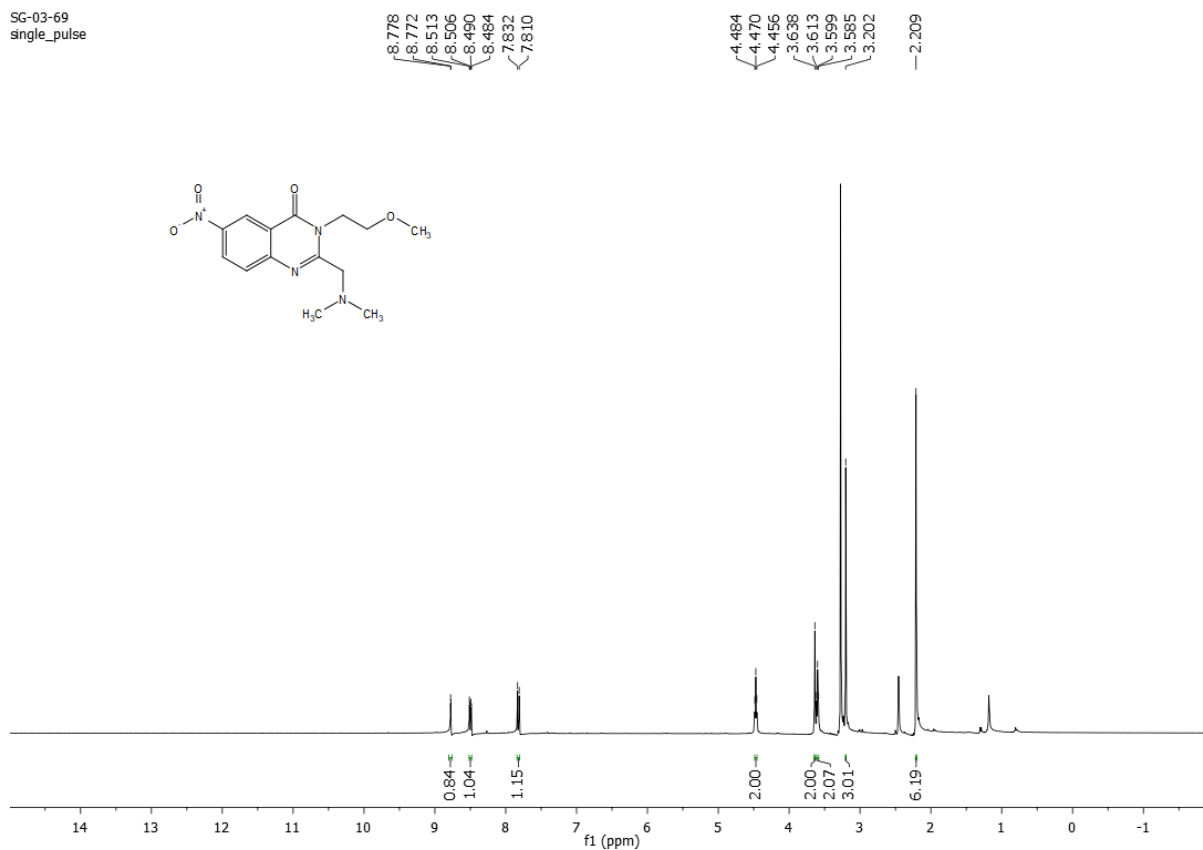
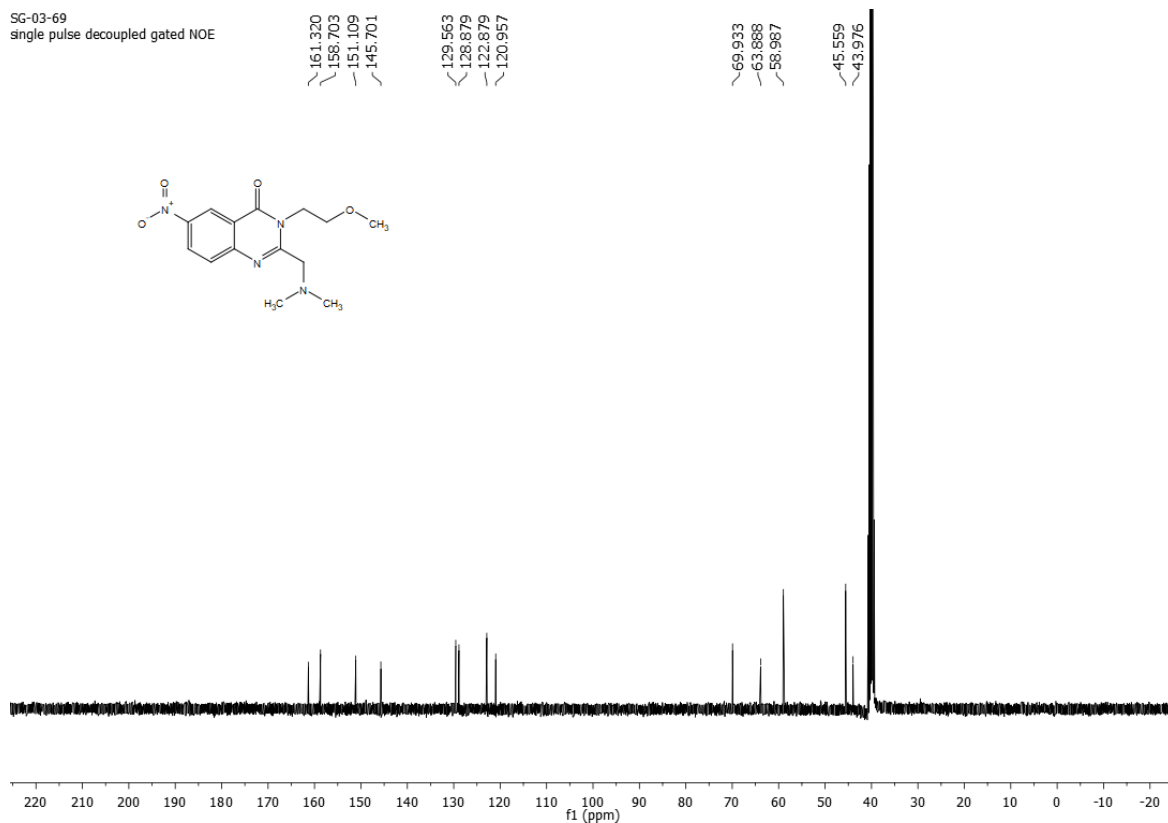
¹H NMR of compound 21 (400 MHz, d₆-DMSO):SG-03-27
single_pulse**¹³C NMR of compound 21 (100 MHz, d₆-DMSO):**

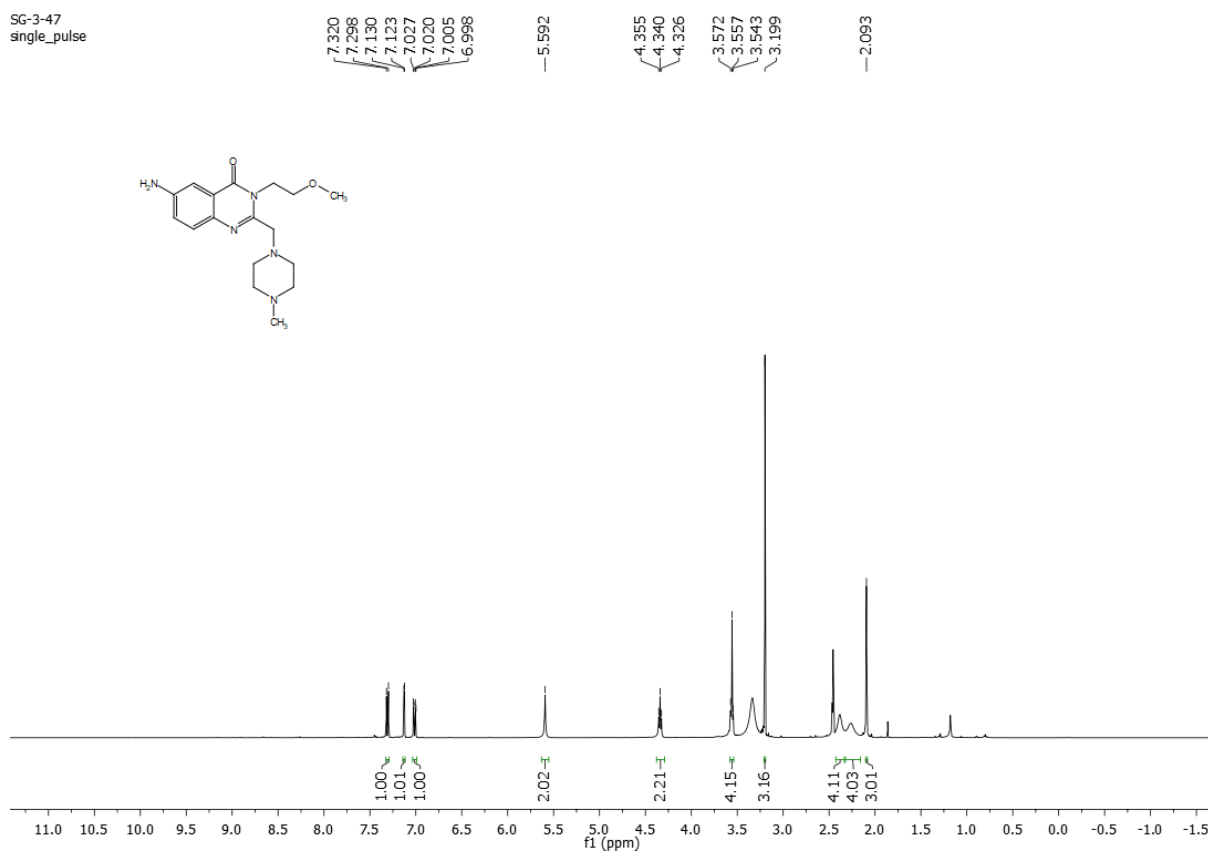
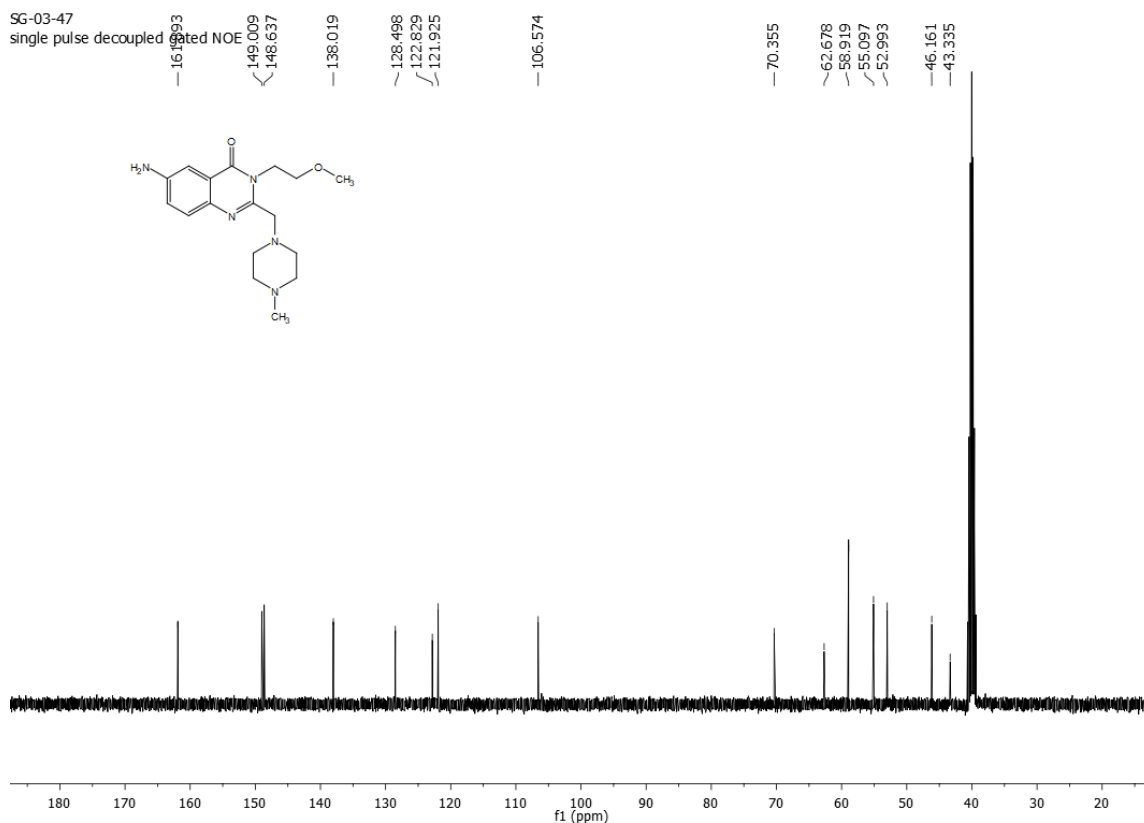
¹H NMR of compound **22** (400 MHz, *d*₆-DMSO):SG-03-31
single_pulse¹³C NMR of compound **22** (100 MHz, *d*₆-DMSO):

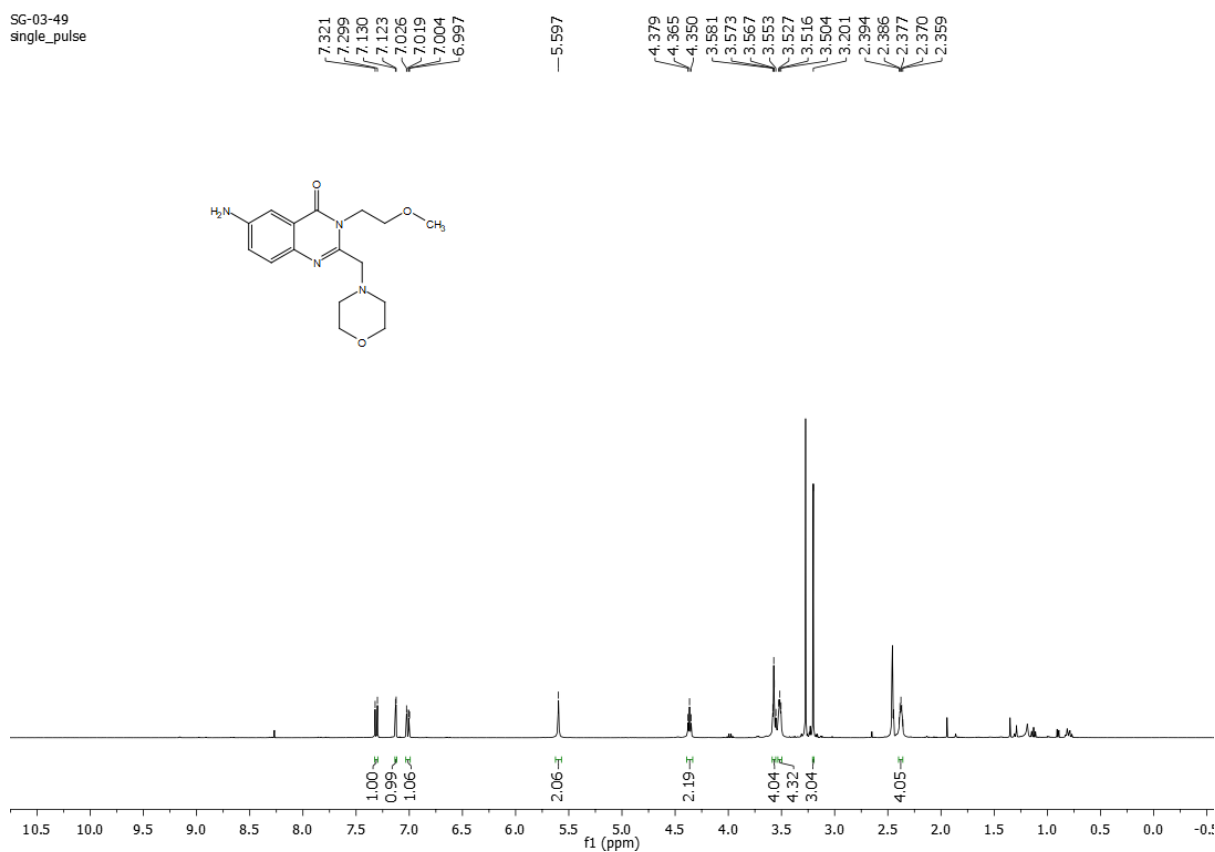
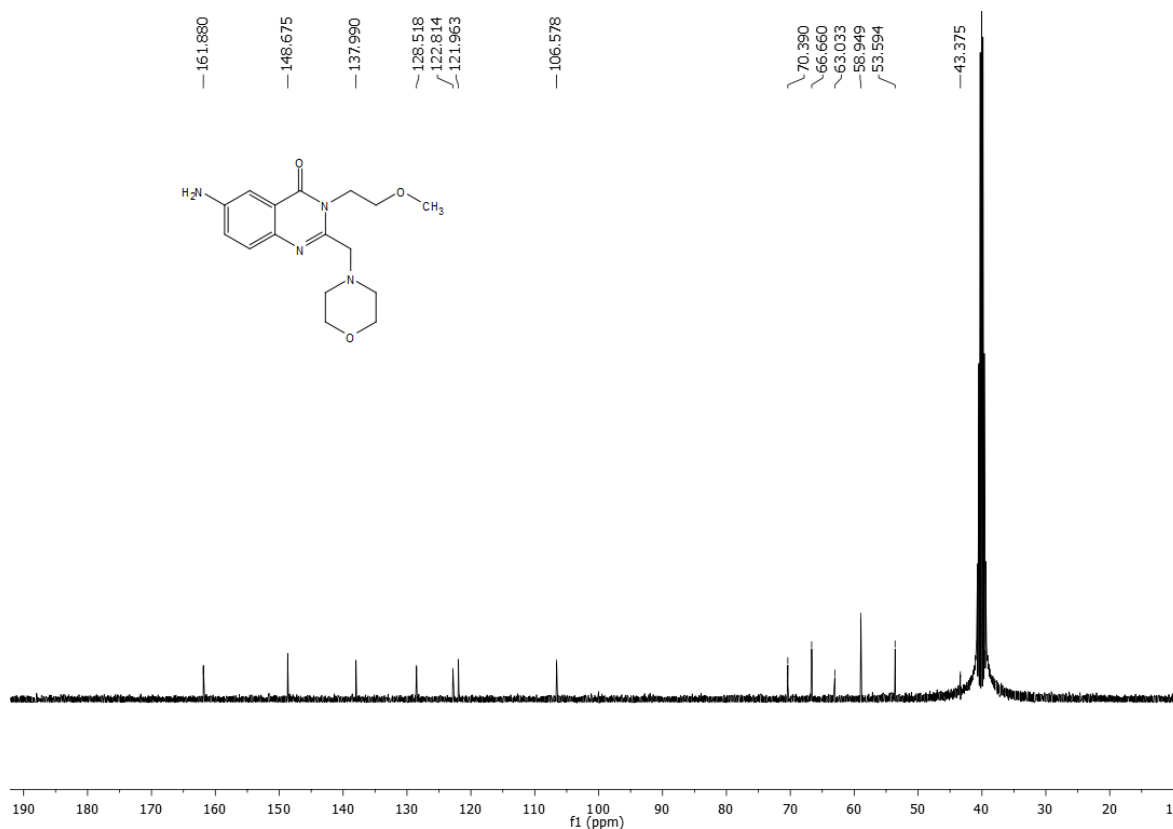
¹H NMR of compound 23 (400 MHz, *d*₆-DMSO):SG-03-46
single_pulse**¹³C NMR of compound 23 (100 MHz, *d*₆-DMSO):**

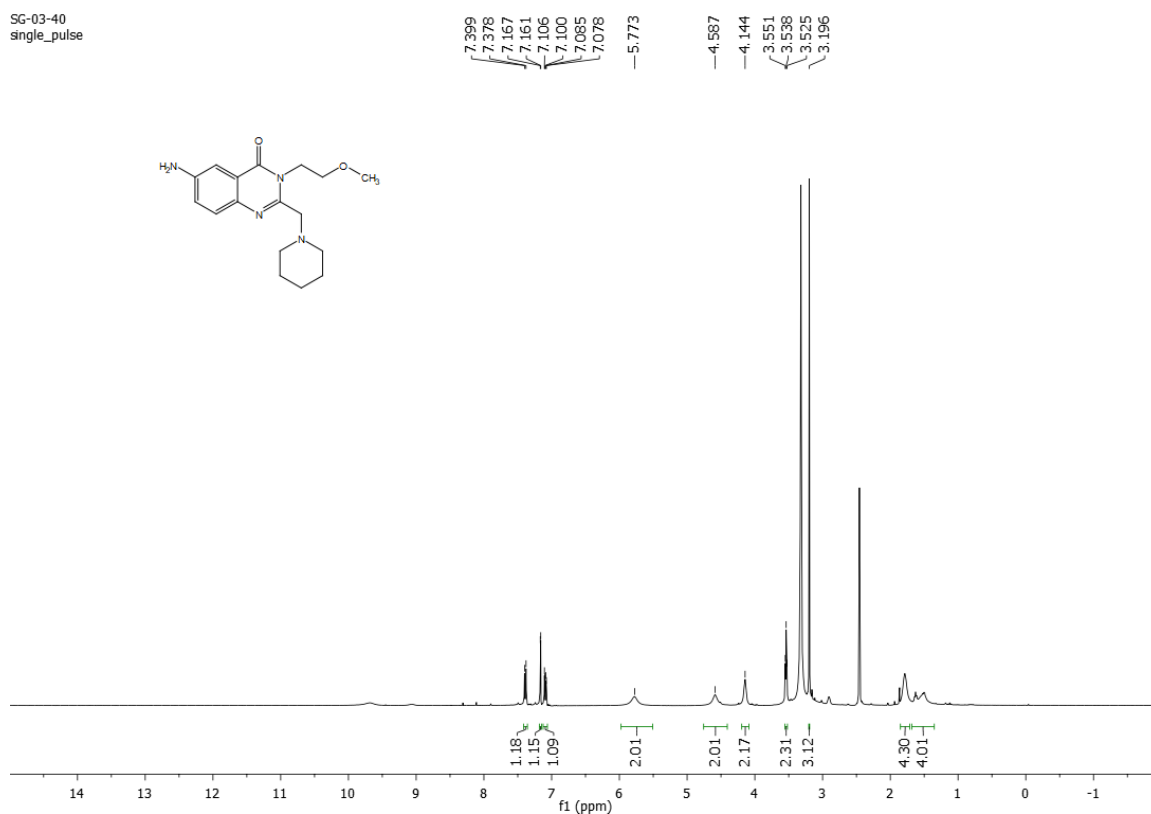
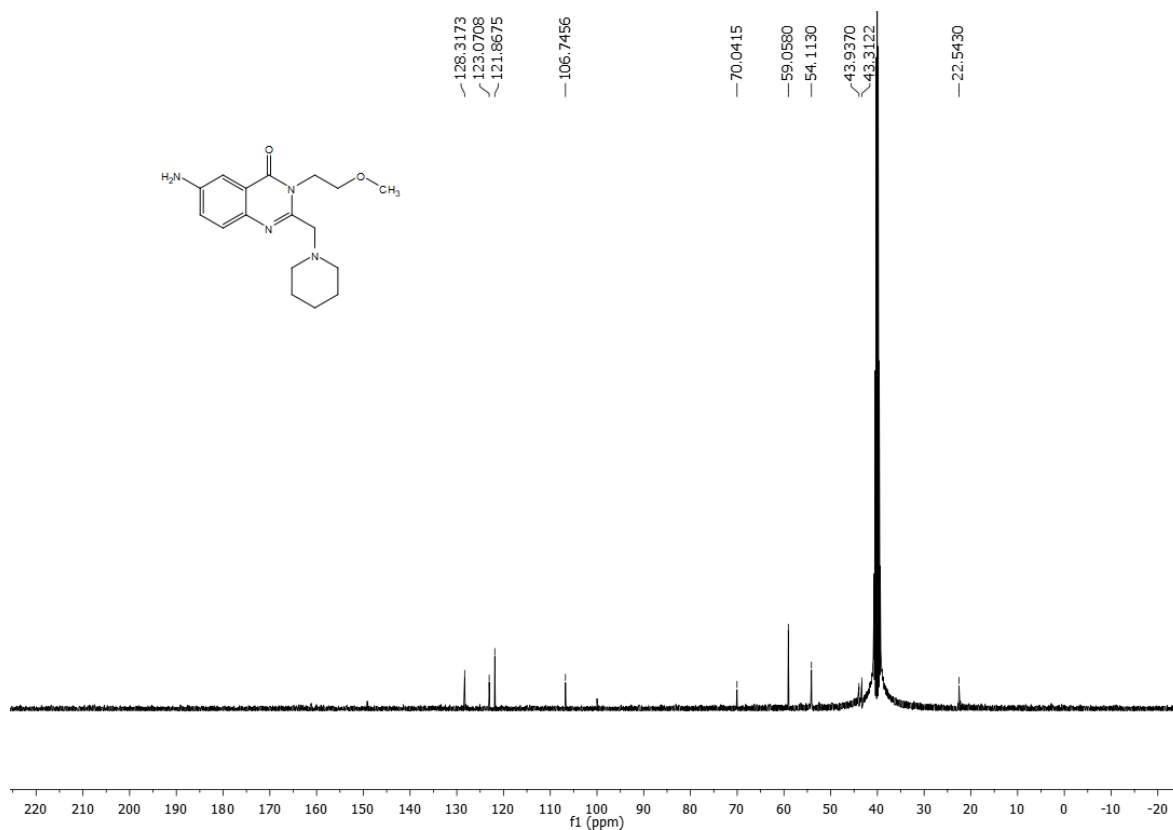
¹H NMR of compound **25** (400 MHz, *d*₆-DMSO):SG-03-38
single_pulse¹³C NMR of compound **25** (100 MHz, *d*₆-DMSO):

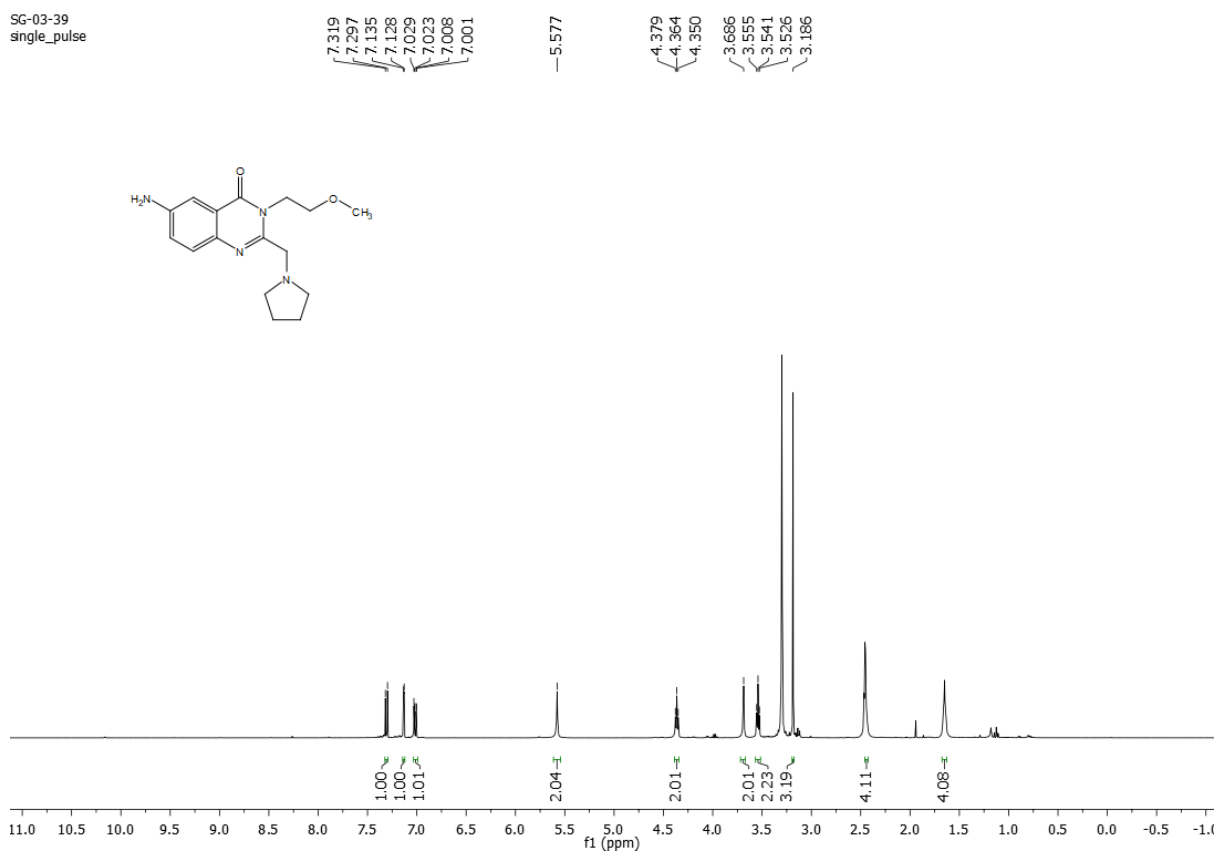
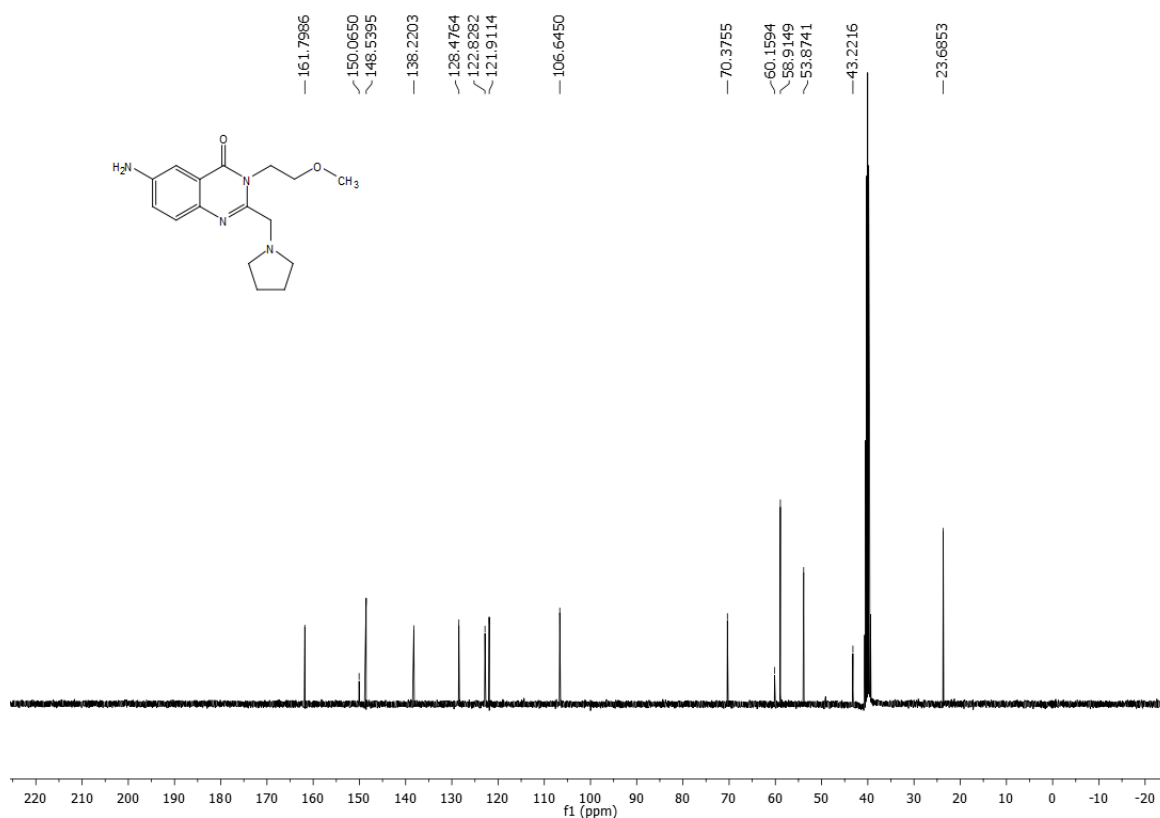
¹H NMR of compound **26** (400 MHz, *d*₆-DMSO):SG-03-37
single_pulse¹³C NMR of compound **26** (100 MHz, *d*₆-DMSO):

¹H NMR of compound 27 (400 MHz, *d*₆-DMSO):SG-03-69
single_pulse**¹³C NMR of compound 27 (100 MHz, *d*₆-DMSO):**SG-03-69
single pulse decoupled gated NOE

¹H NMR of compound **28** (400 MHz, *d*₆-DMSO):SG-3-47
single_pulse¹³C NMR of compound **28** (100 MHz, *d*₆-DMSO):SG-03-47
single pulse decoupled

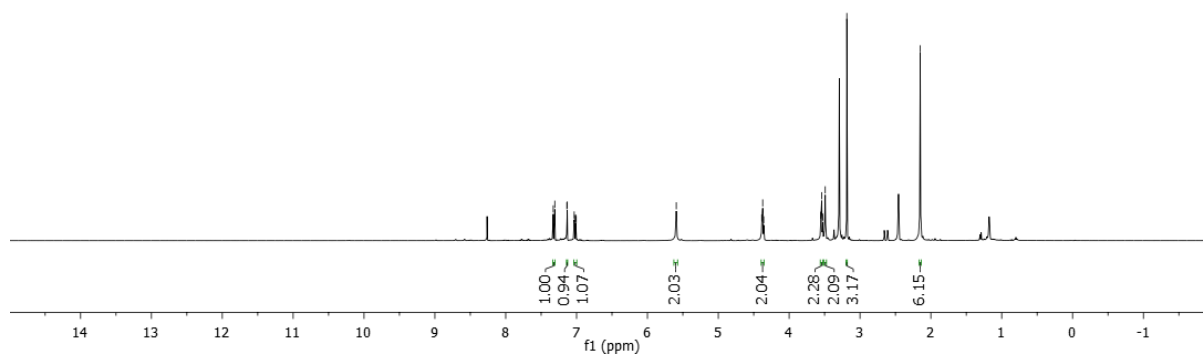
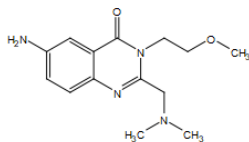
¹H NMR of compound **29** (400 MHz, *d*₆-DMSO):SG-03-49
single_pulse¹³C NMR of compound **29** (100 MHz, *d*₆-DMSO):

¹H NMR of compound 30 (400 MHz, *d*₆-DMSO):SG-03-40
single_pulse**¹³C NMR of compound 30 (100 MHz, *d*₆-DMSO):**

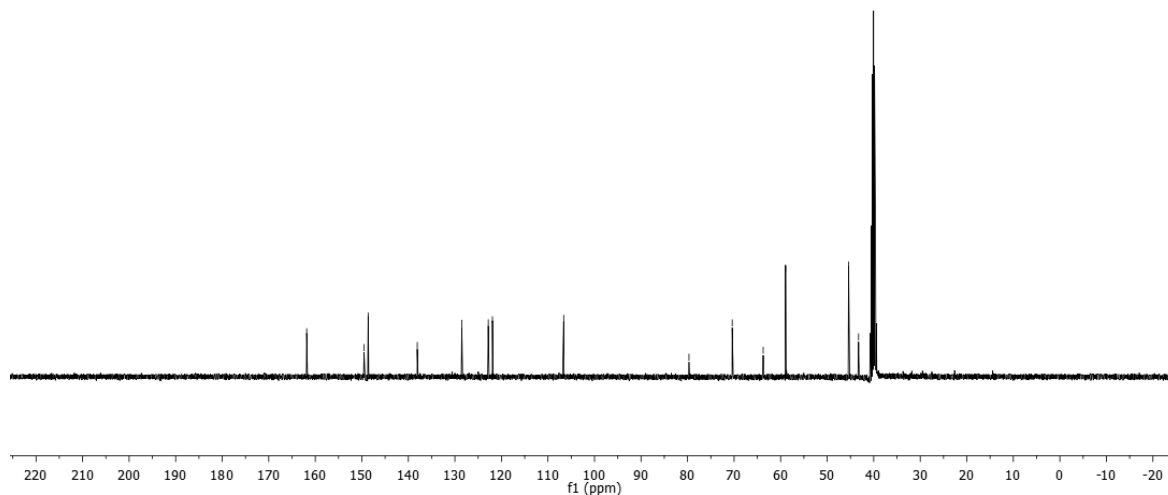
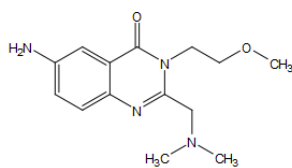
¹H NMR of compound 31 (400 MHz, *d*₆-DMSO):SG-03-39
single_pulse**¹³C NMR of compound 31 (100 MHz, *d*₆-DMSO):**

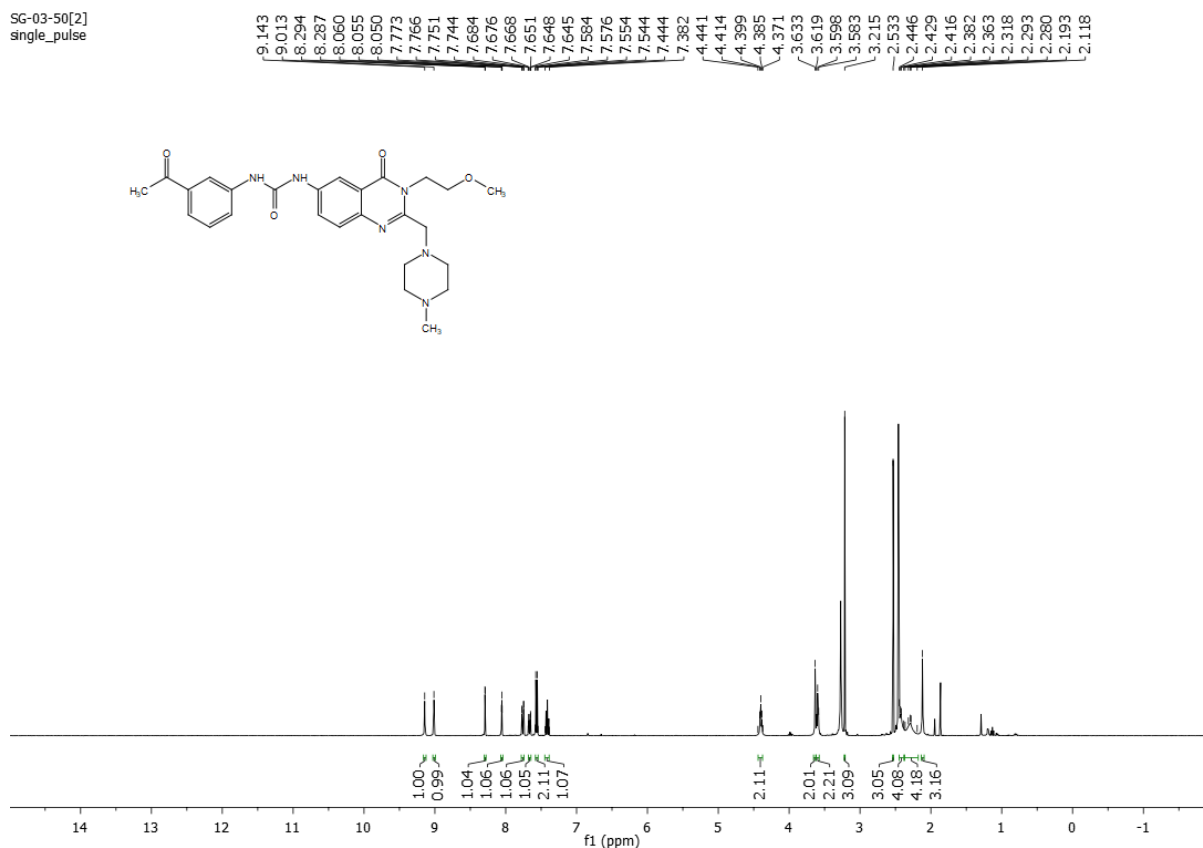
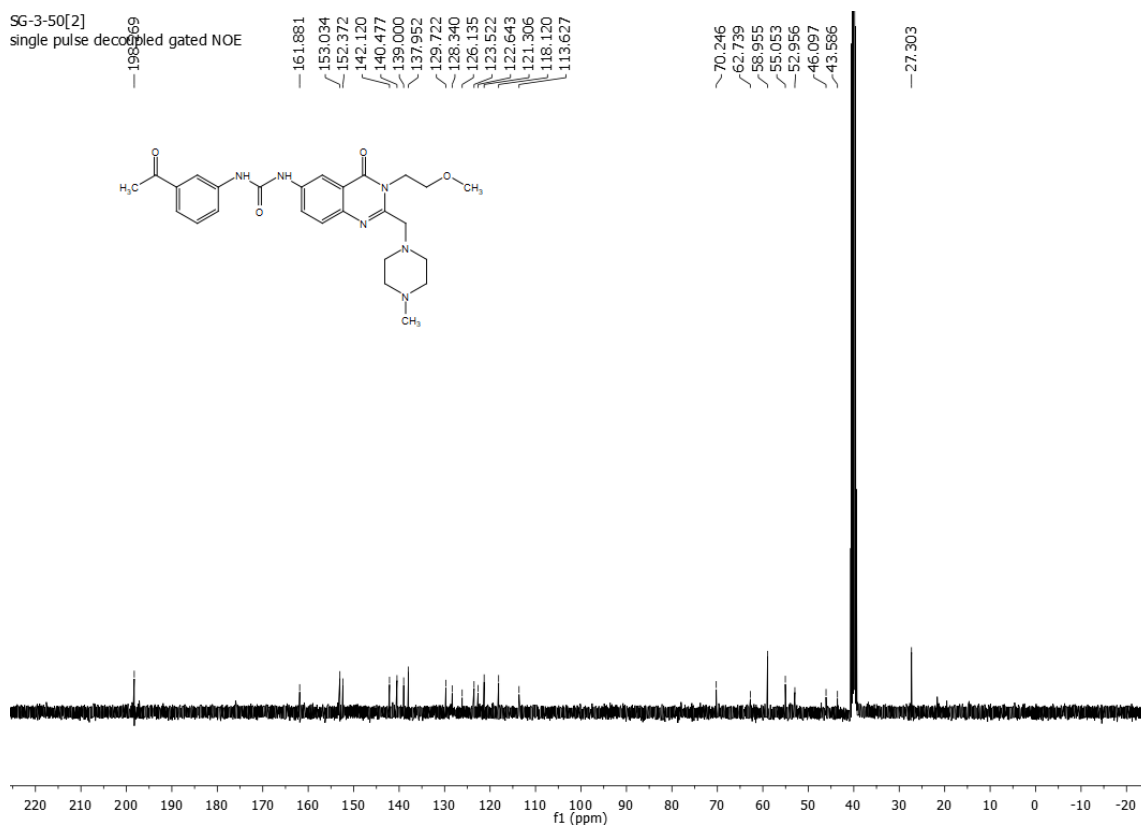
¹H NMR of compound 32 (400 MHz, *d*₆-DMSO):SG-3-70
single_pulse

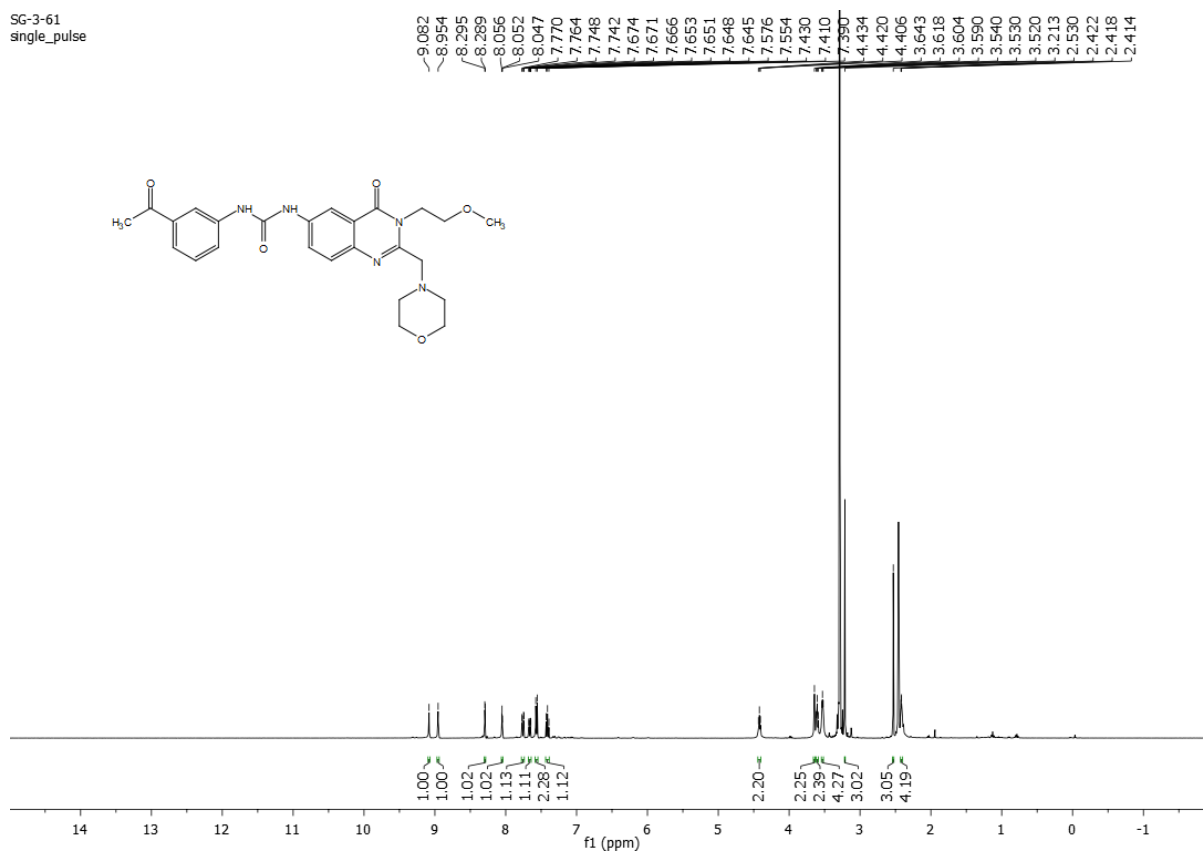
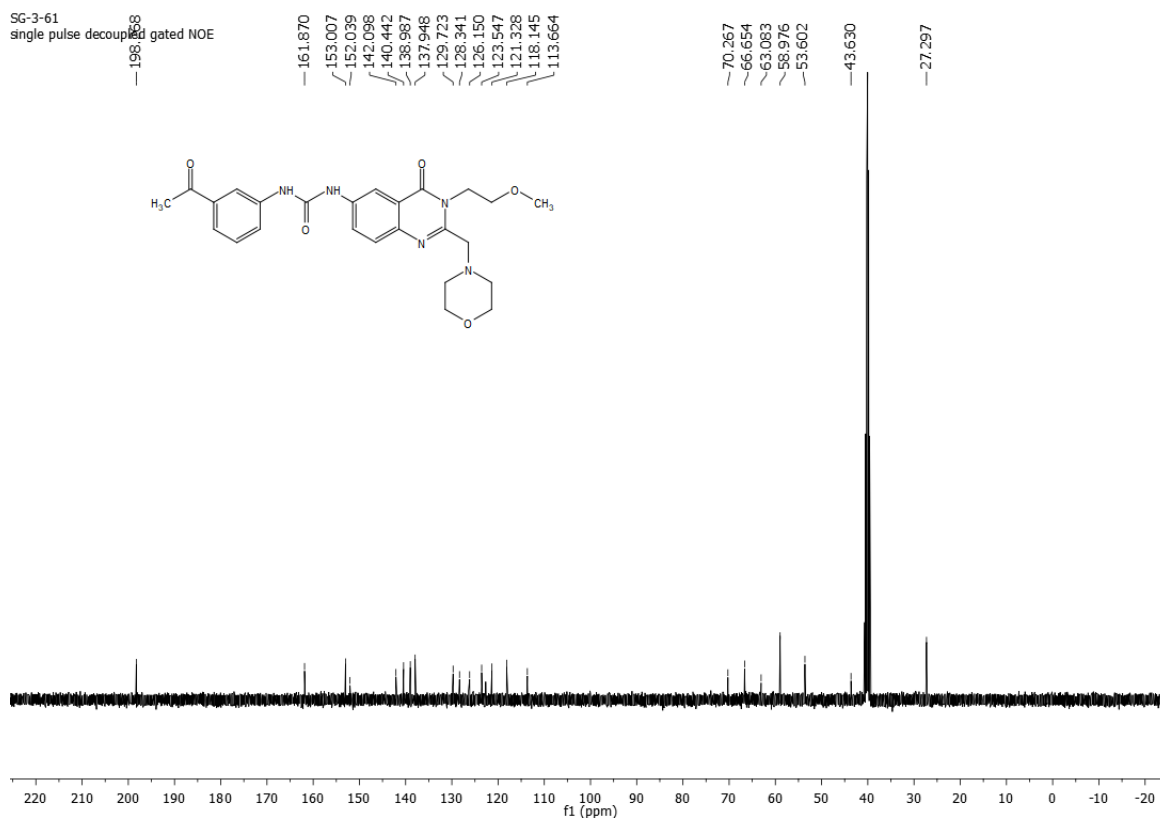
7.329 7.308 7.138 7.131 7.033 7.027 7.012 7.005 — 5.593 — 4.387 4.373 4.359 3.554 3.540 3.526 3.491 3.186 — 2.150

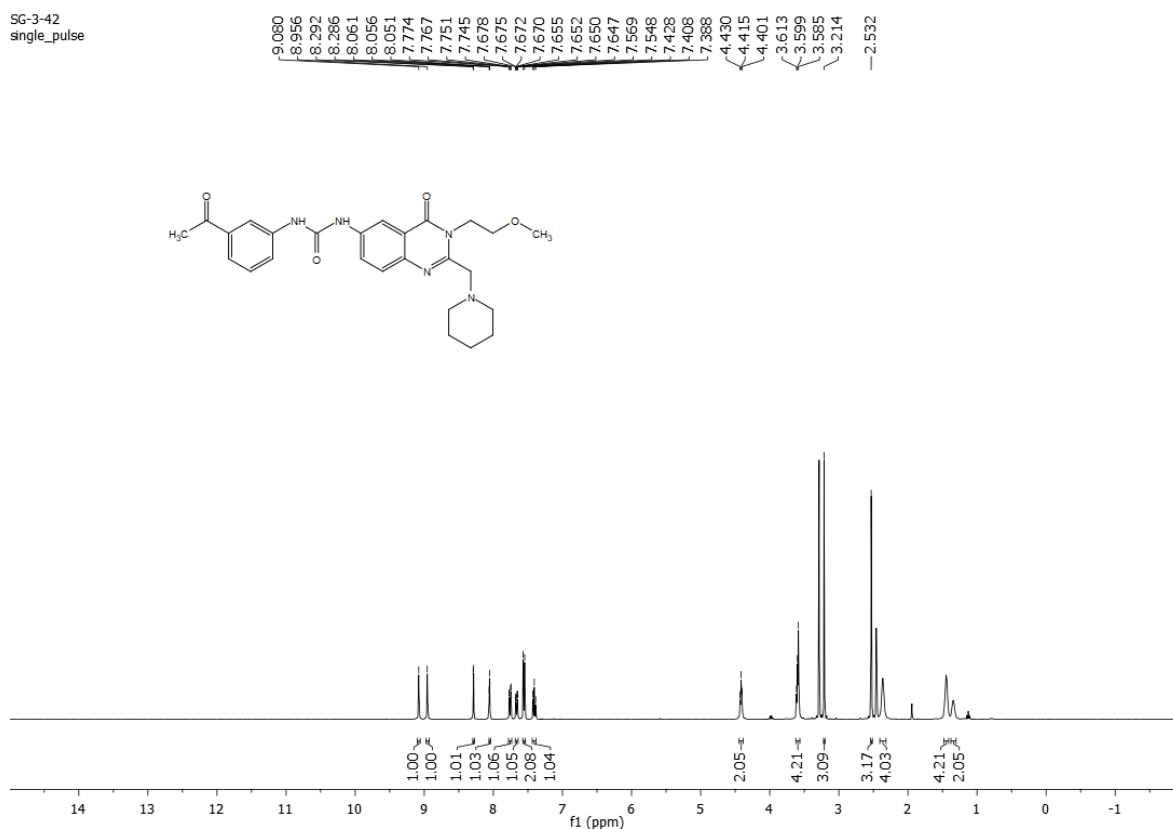
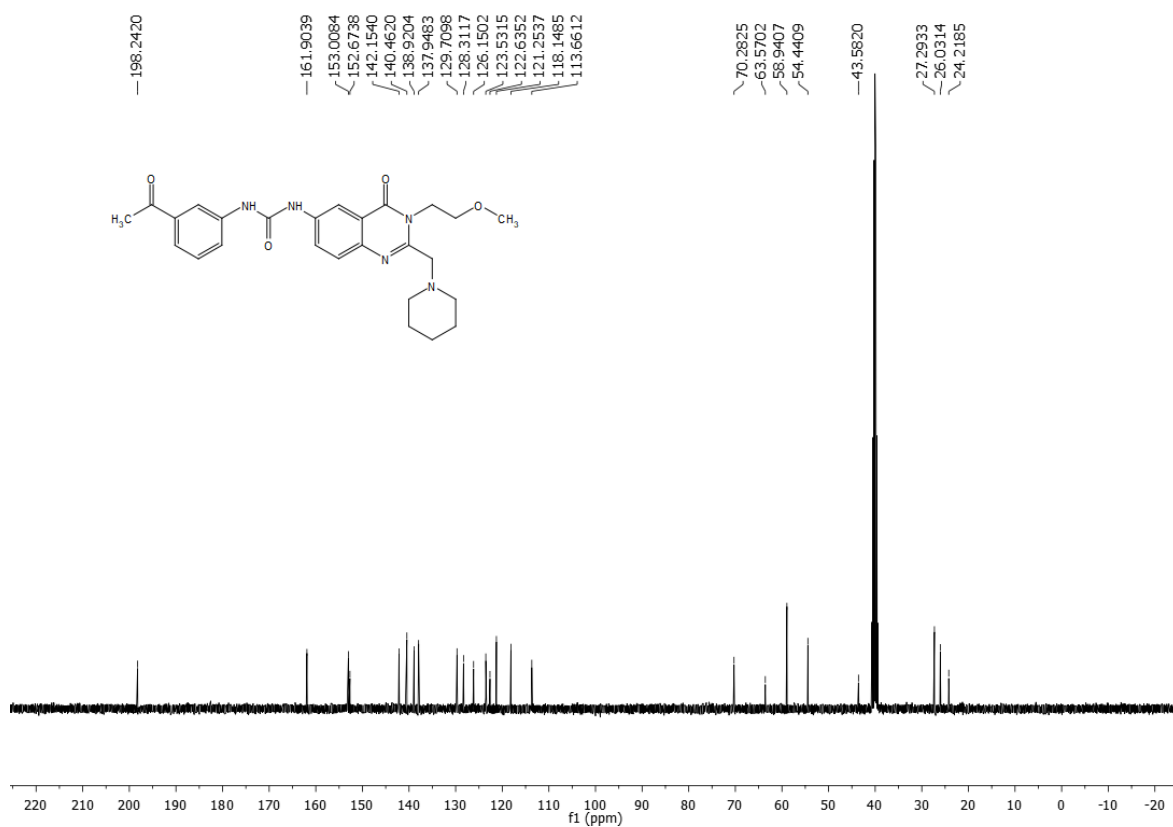
**¹³C NMR of compound 32 (100 MHz, *d*₆-DMSO):**SG-3-70
single pulse decoupled gated NOE

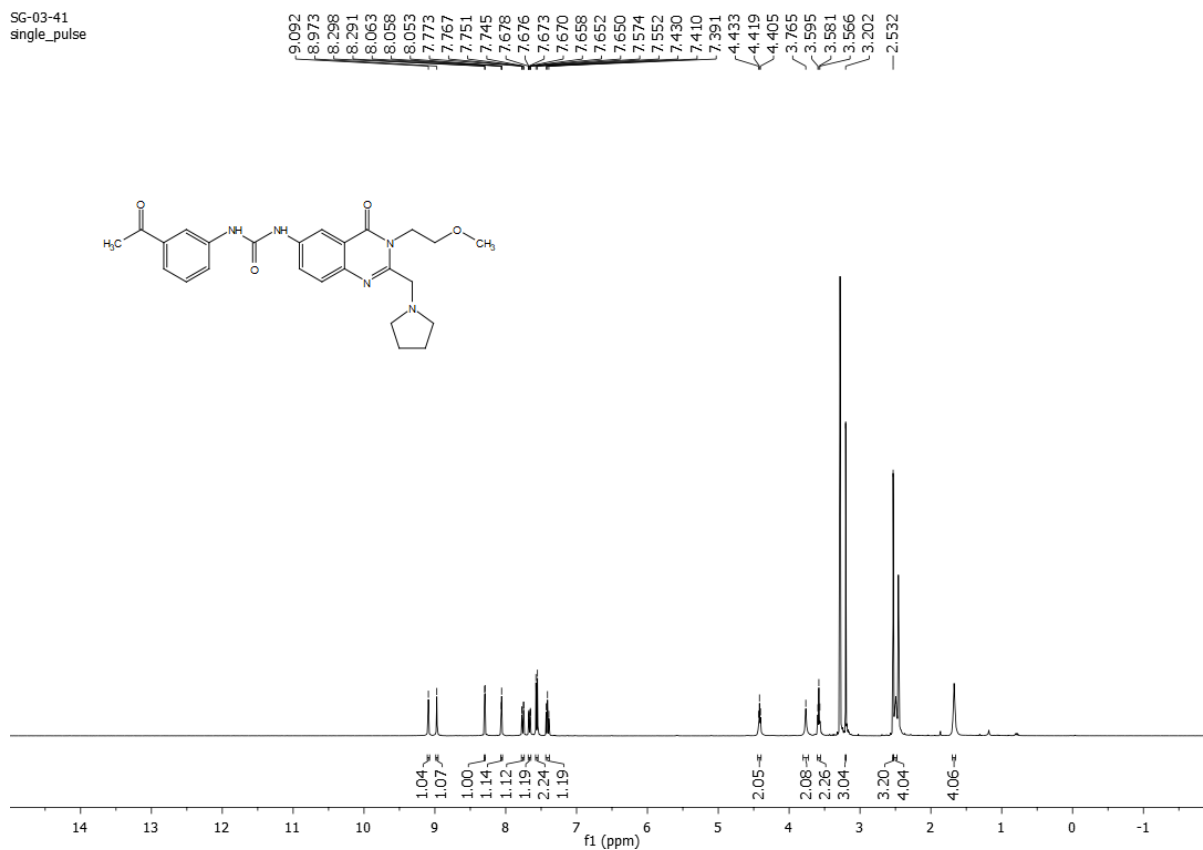
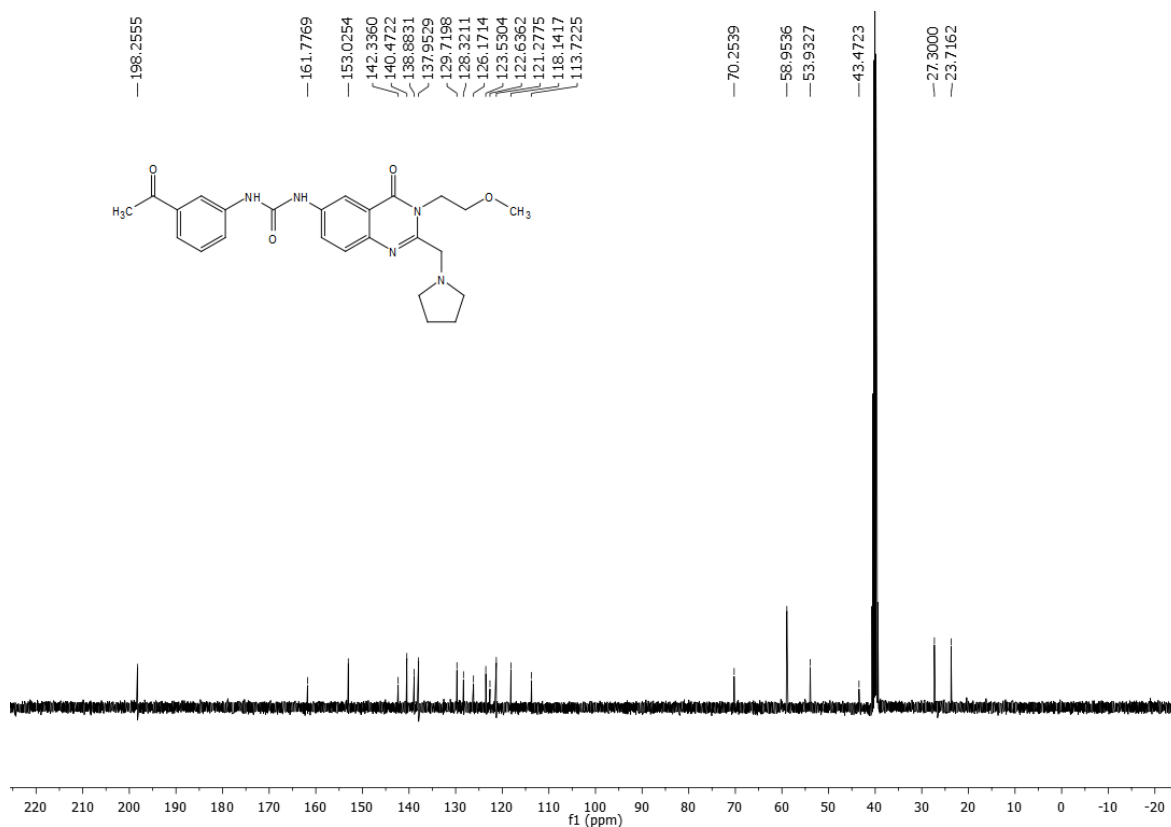
— 161.835 149.522 148.632 — 138.084 128.518 122.825 121.925 — 106.620 — 79.696 70.407 63.749 58.943 45.400 43.252

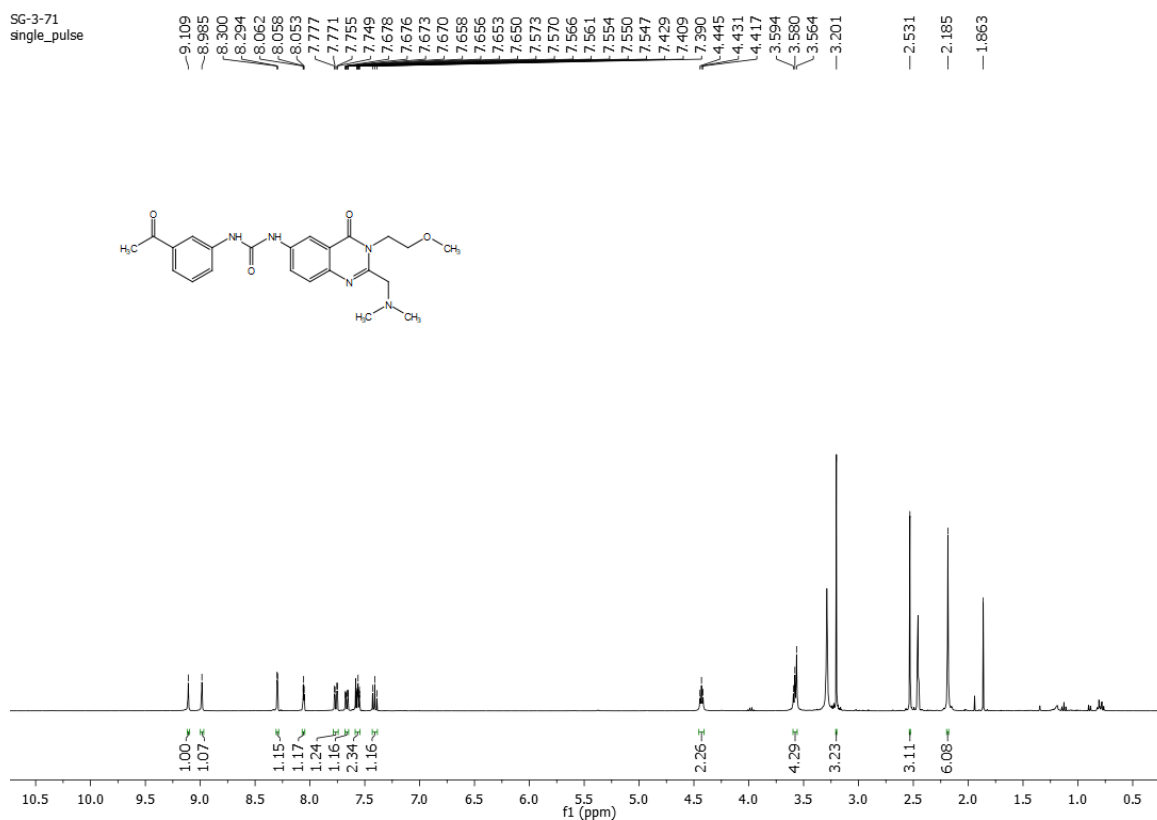
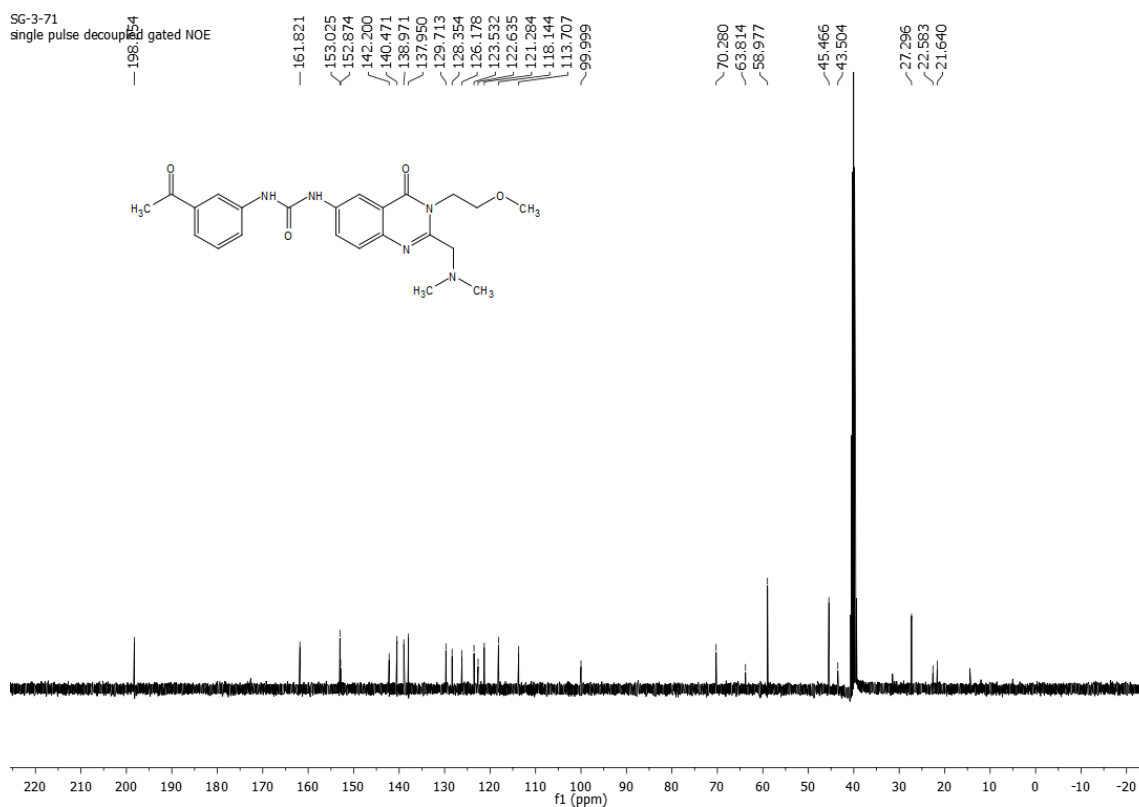


¹H NMR of compound 33 (400 MHz, *d*₆-DMSO):SG-03-50[2]
single_pulse**¹³C NMR of compound 33 (100 MHz, *d*₆-DMSO):**SG-3-50[2]
single_pulse decoupled gated NOE

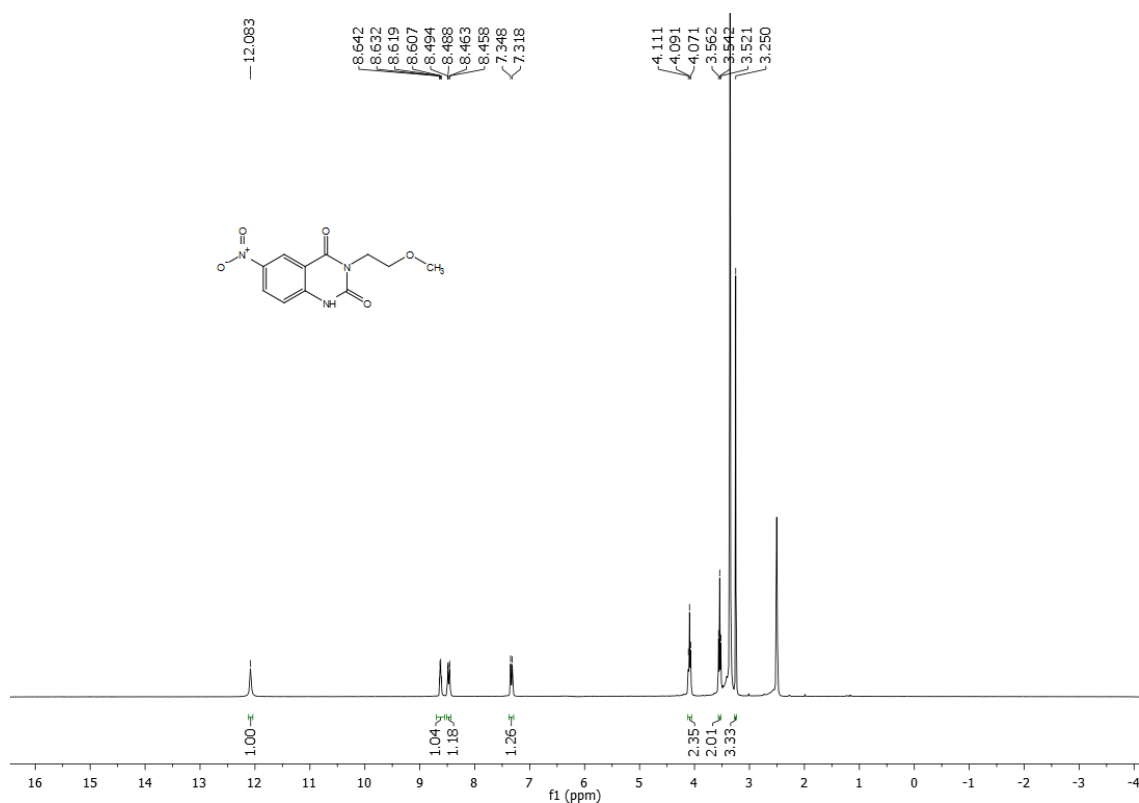
¹H NMR of compound **34** (400 MHz, *d*₆-DMSO):¹³C NMR of compound **34** (100 MHz, *d*₆-DMSO):

¹H NMR of compound 35 (400 MHz, *d*₆-DMSO):SG-3-42
single_pulse**¹³C NMR of compound 35 (100 MHz, *d*₆-DMSO):**

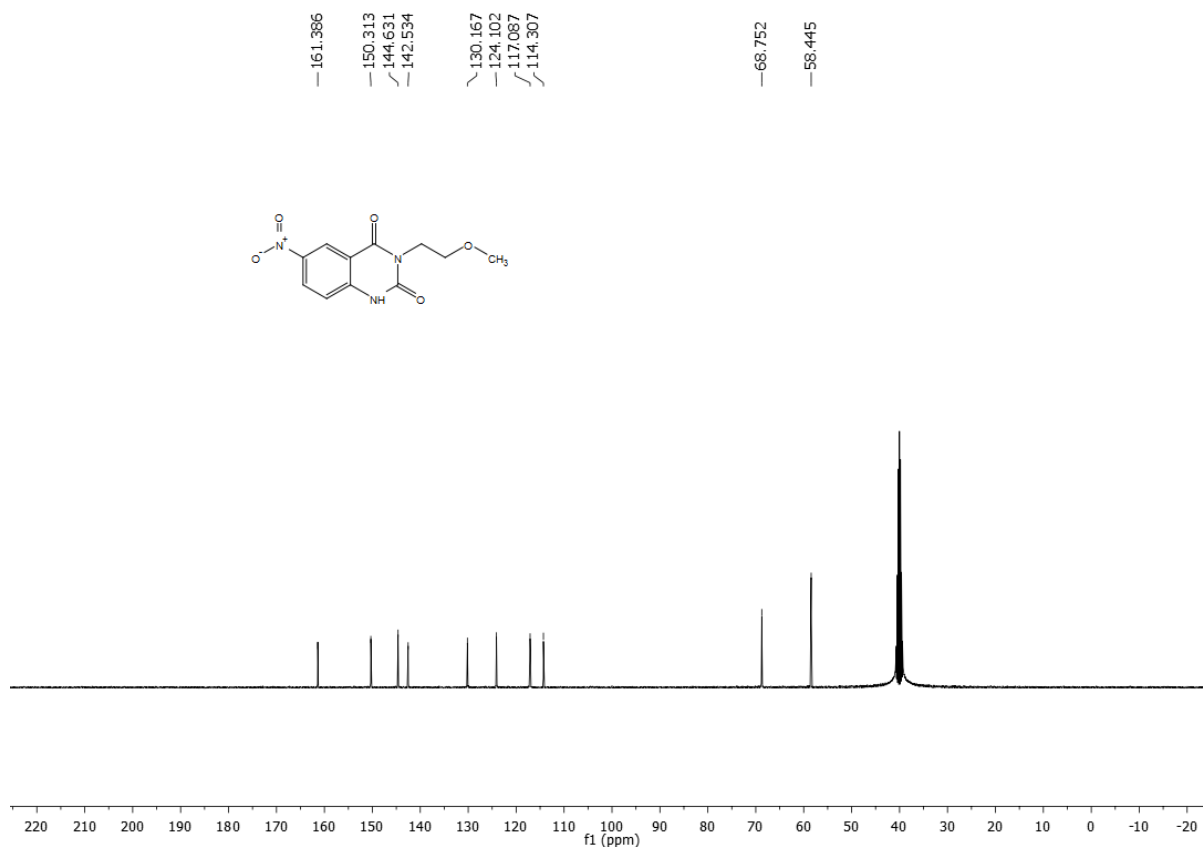
¹H NMR of compound **36** (400 MHz, *d*₆-DMSO):SG-03-41
single_pulse¹³C NMR of compound **36** (100 MHz, *d*₆-DMSO):

¹H NMR of compound 37 (400 MHz, *d*₆-DMSO):**¹³C NMR of compound 37 (100 MHz, *d*₆-DMSO):**

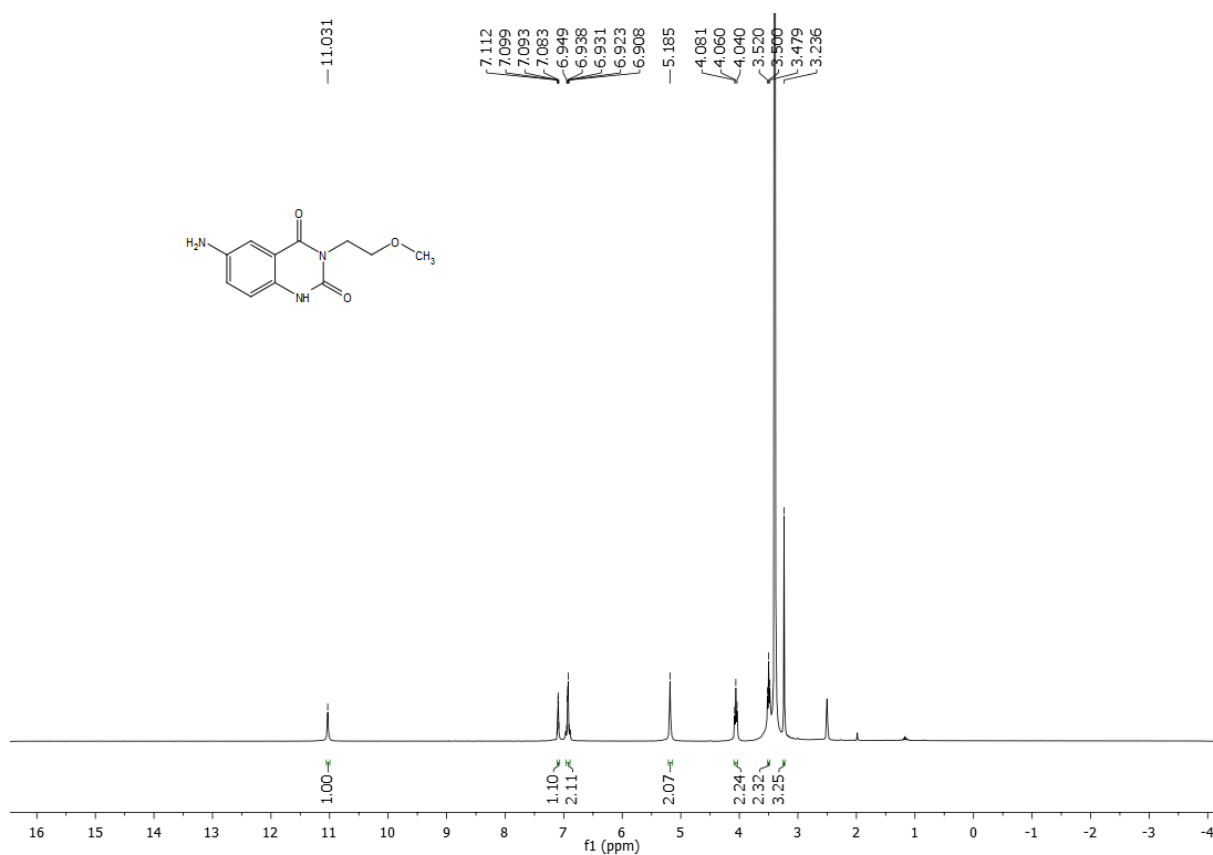
^1H NMR of compound **38** (400 MHz, d_6 -DMSO):



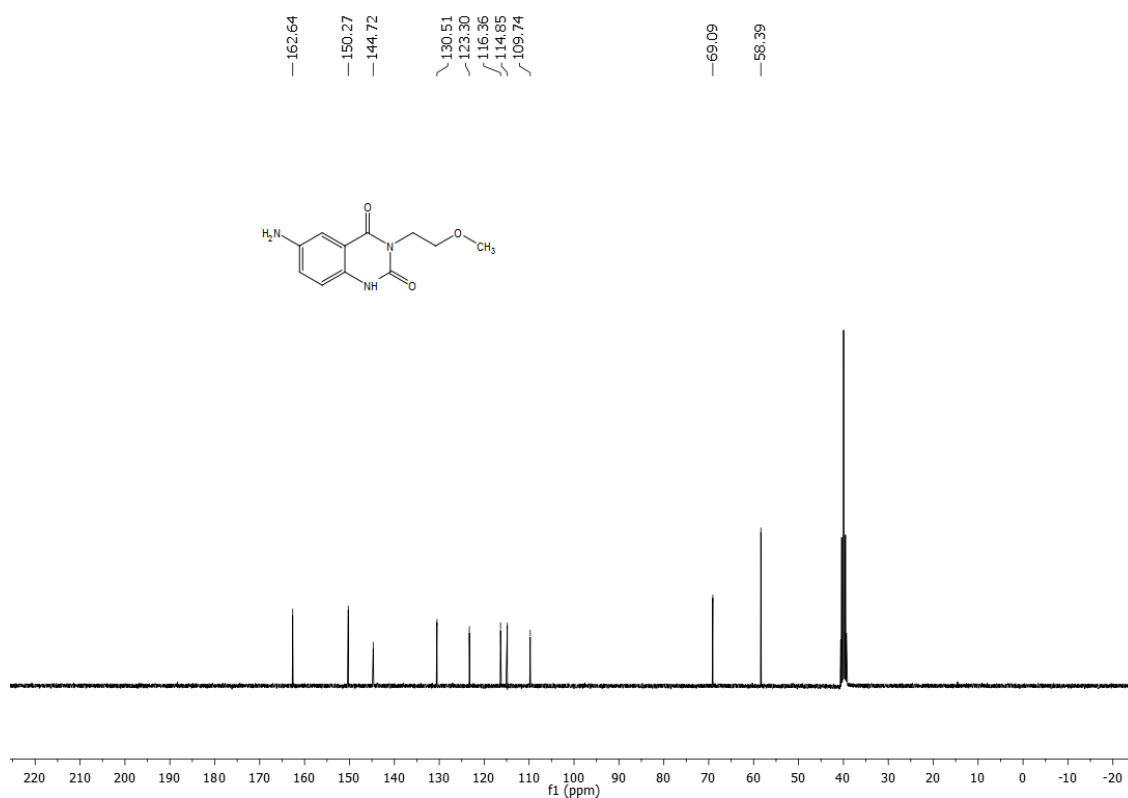
^{13}C NMR of compound **38** (100 MHz, d_6 -DMSO):



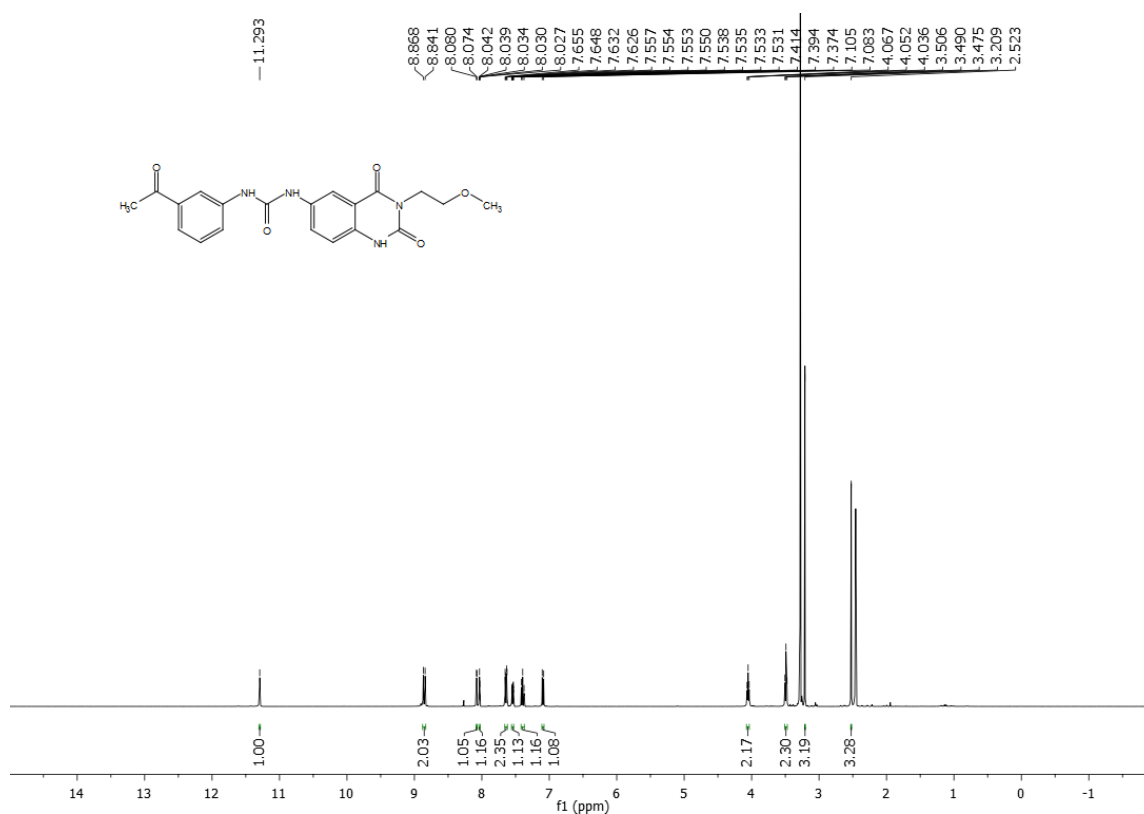
^1H NMR of compound **39** (600 MHz, d_6 -DMSO):



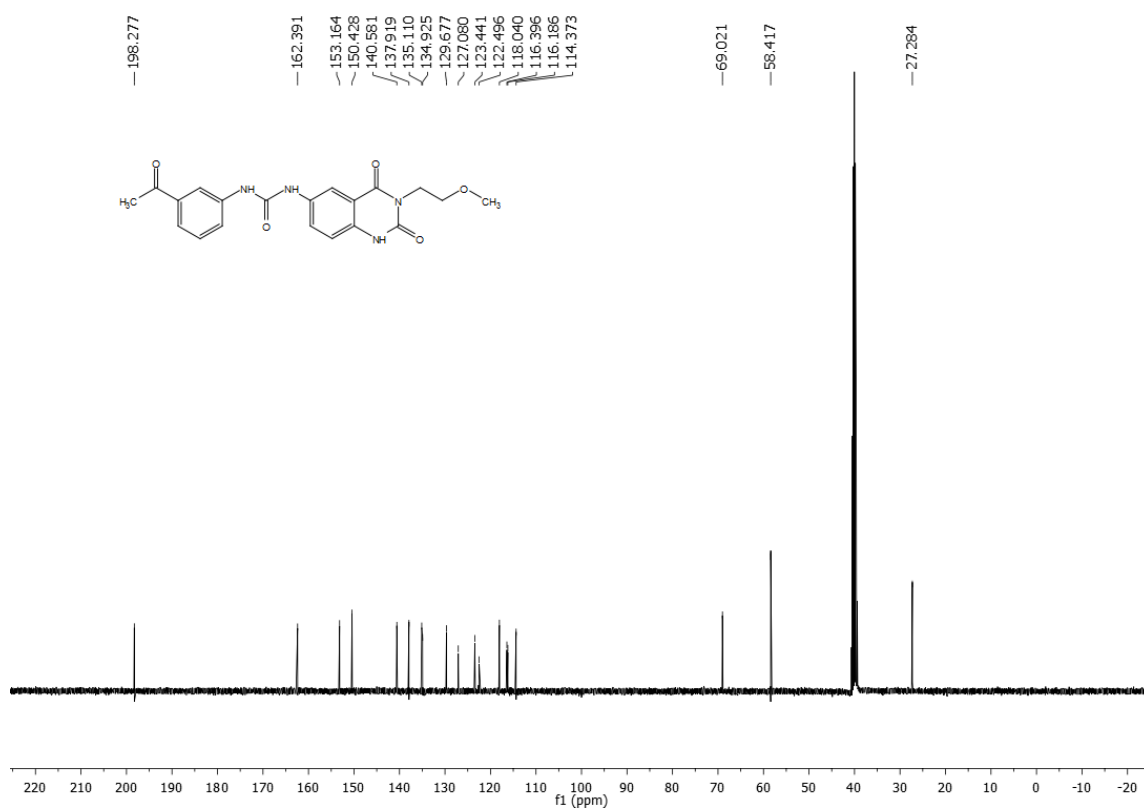
^{13}C NMR of compound **39** (100 MHz, d_6 -DMSO):



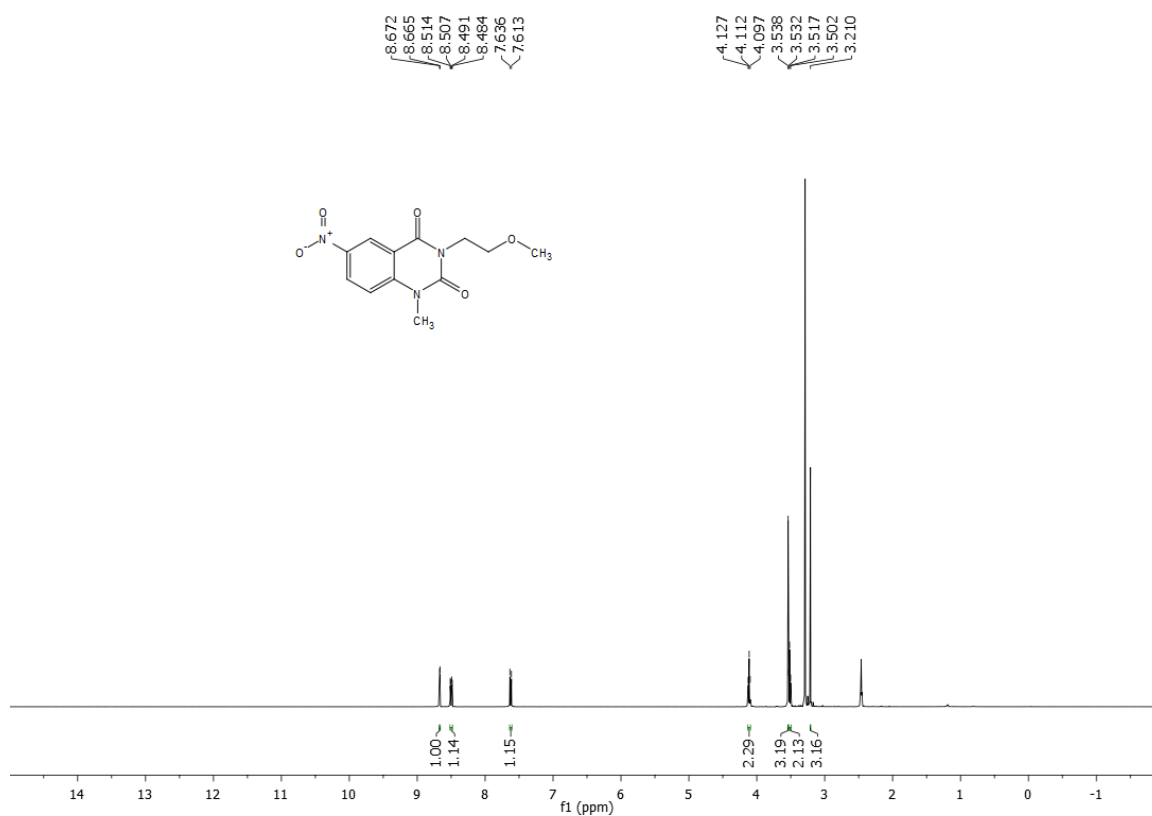
^1H NMR of compound **40** (400 MHz, d_6 -DMSO):



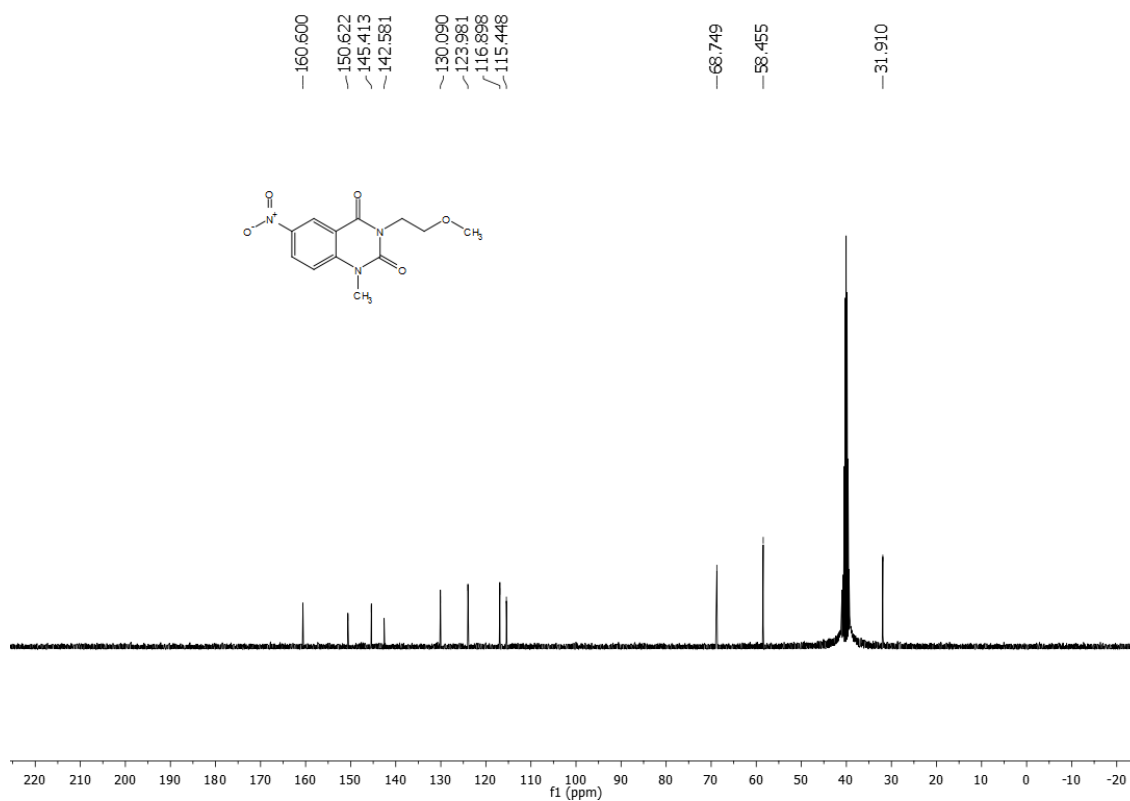
^{13}C NMR of compound **40** (100 MHz, d_6 -DMSO):



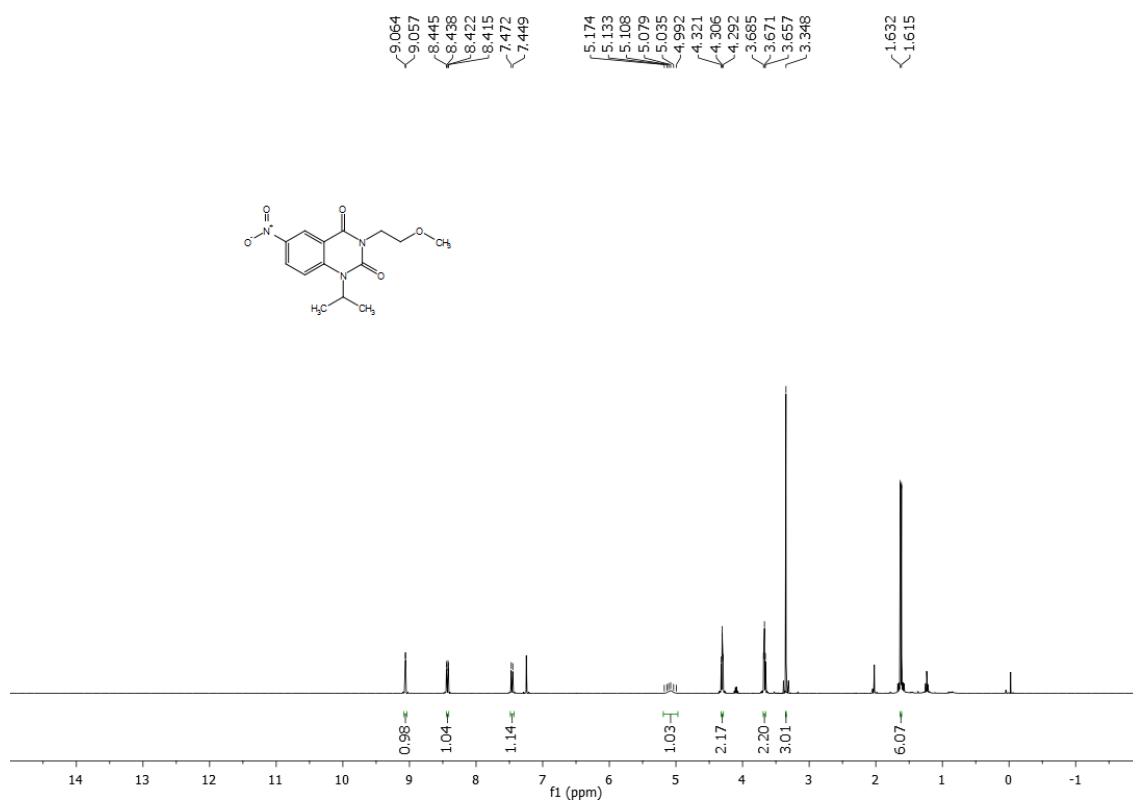
^1H NMR of compound **41** (400 MHz, d_6 -DMSO):



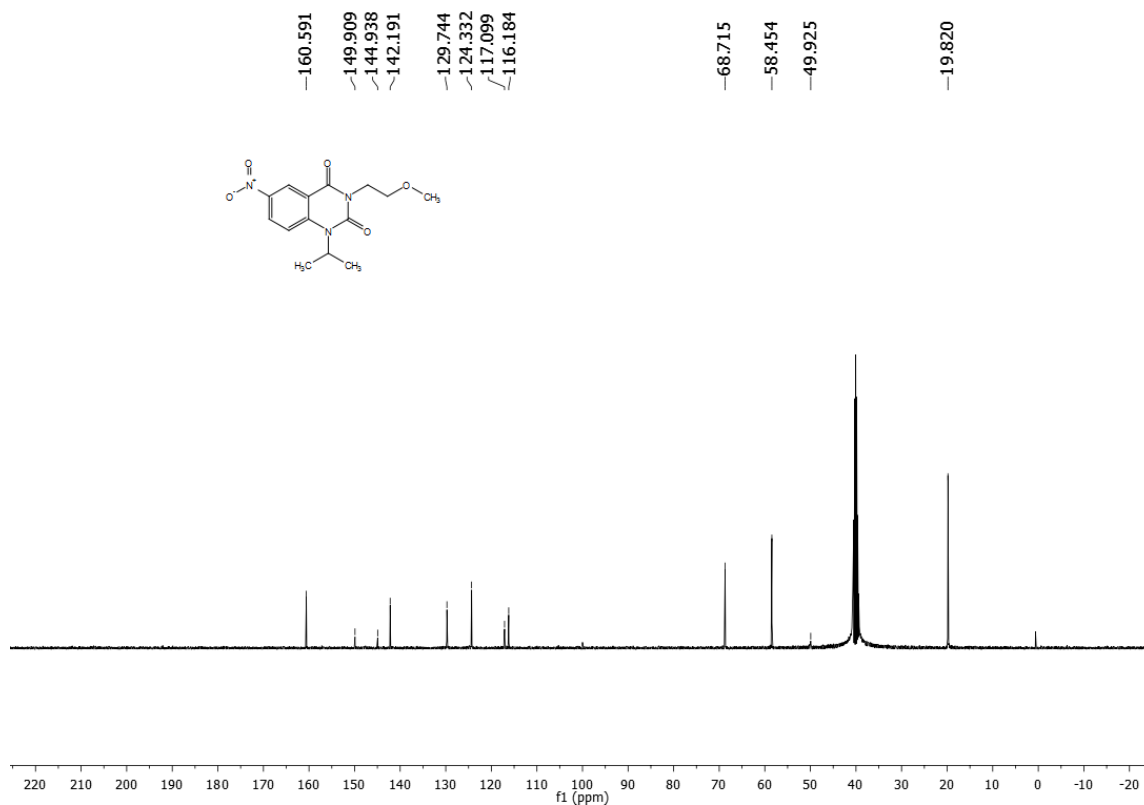
^{13}C NMR of compound **41** (100 MHz, d_6 -DMSO):

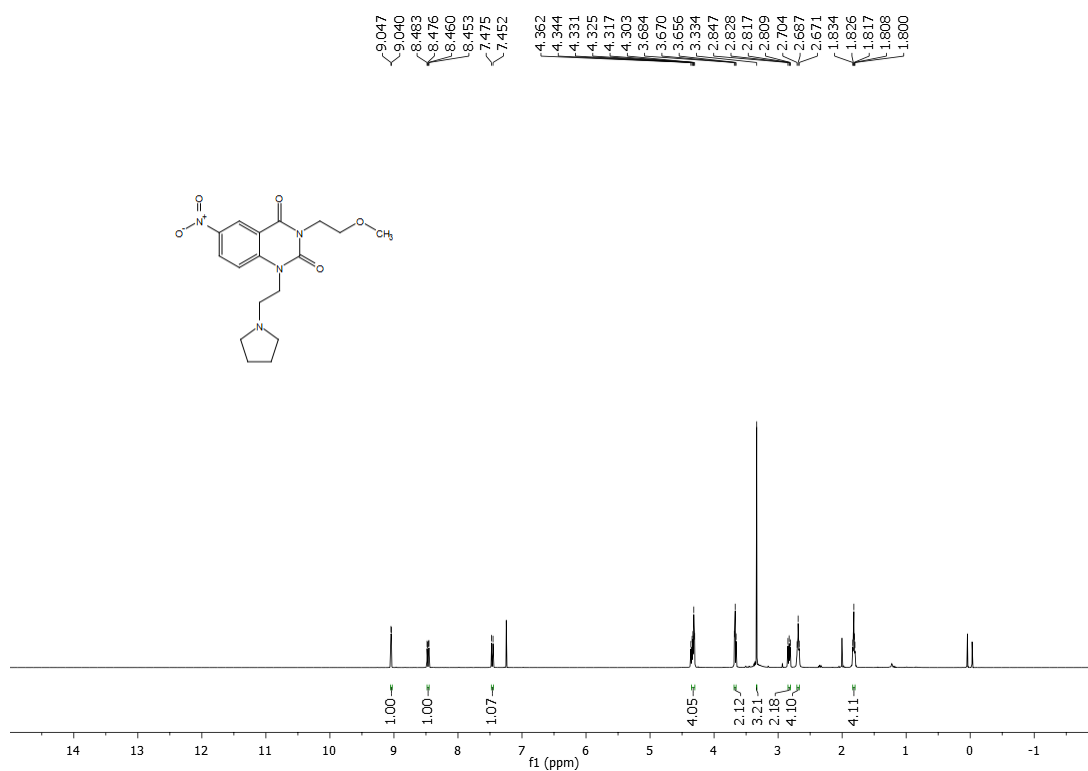
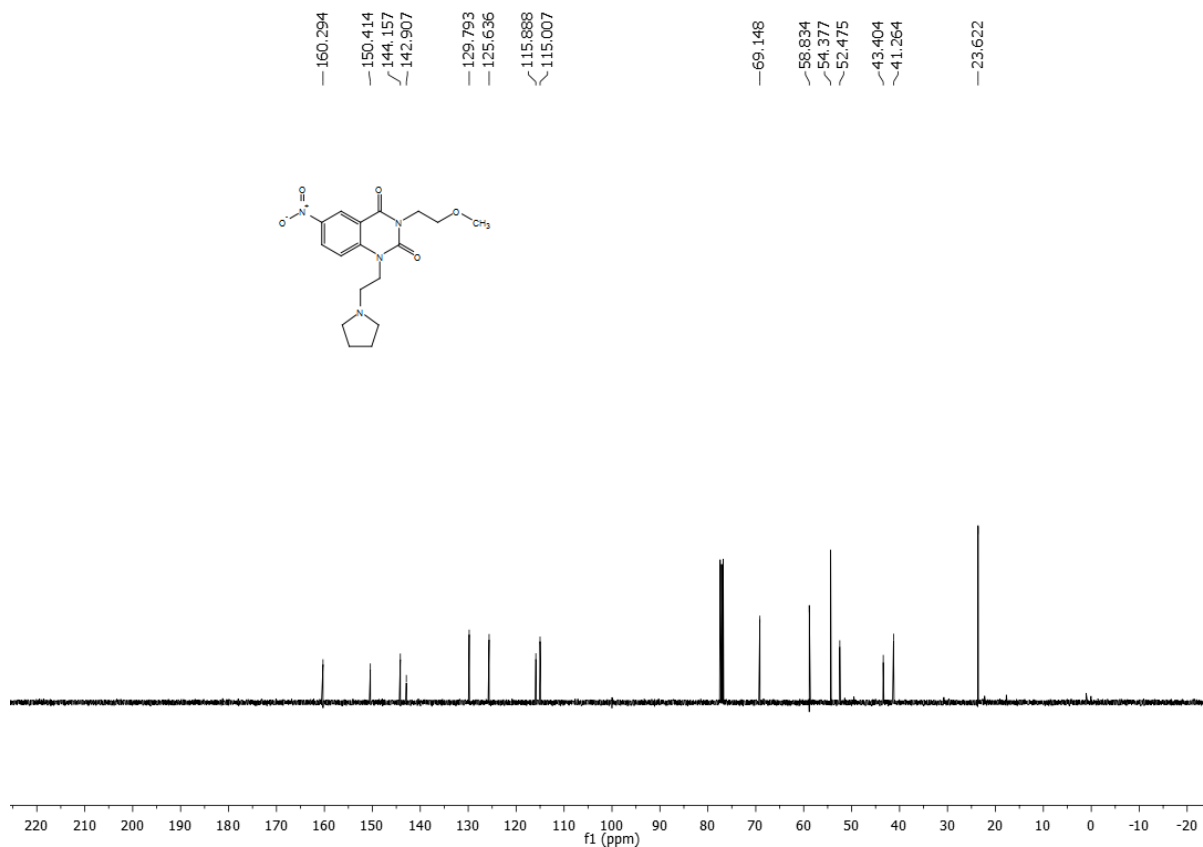


^1H NMR of compound **42** (400 MHz, CDCl_3):

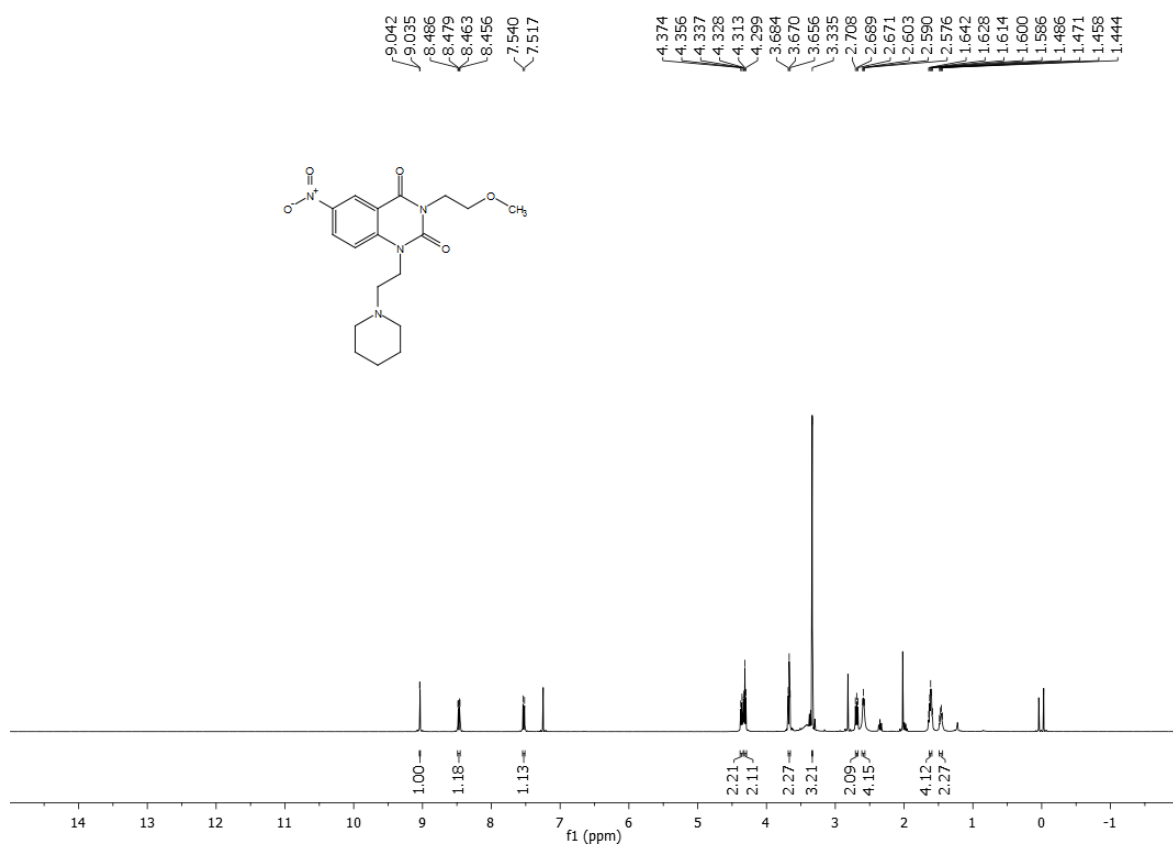


^{13}C NMR of compound **42** (100 MHz, d_6 -DMSO):

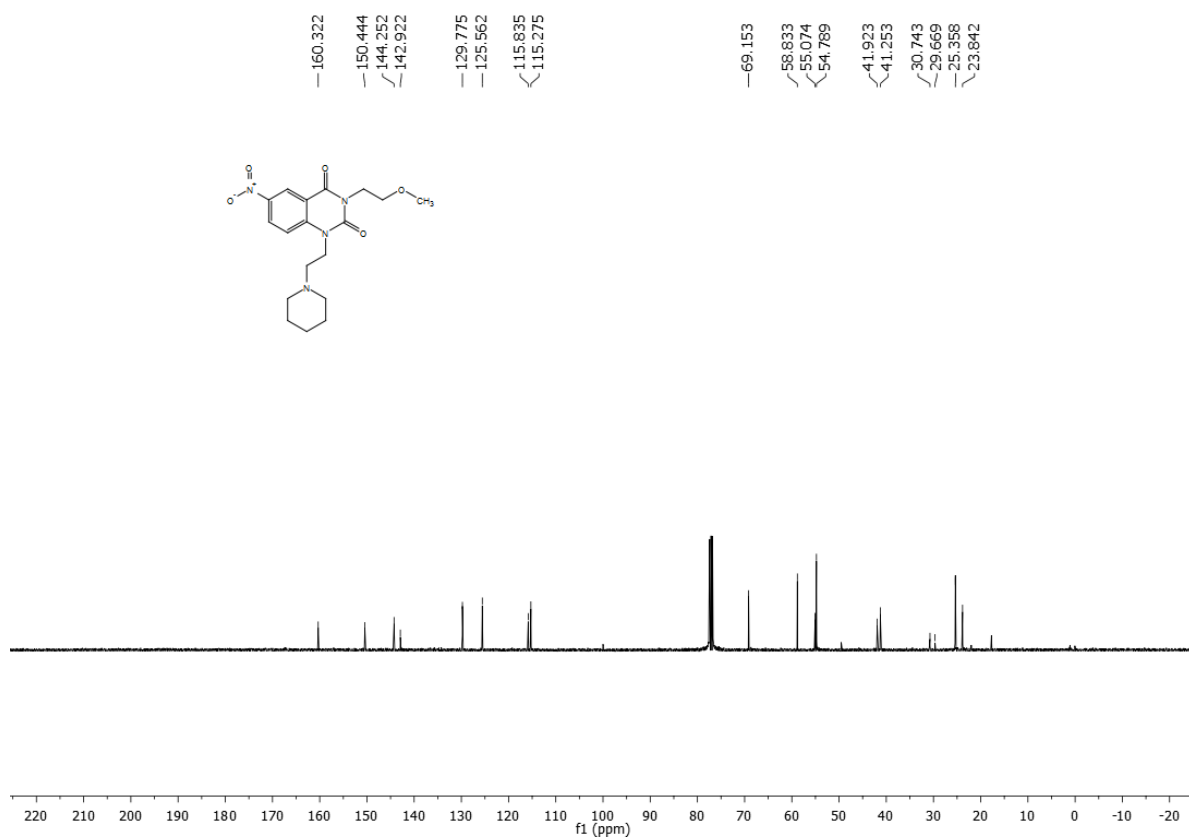


¹H NMR of compound **43** (400 MHz, CDCl₃):¹³C NMR of compound **43** (100 MHz, CDCl₃):

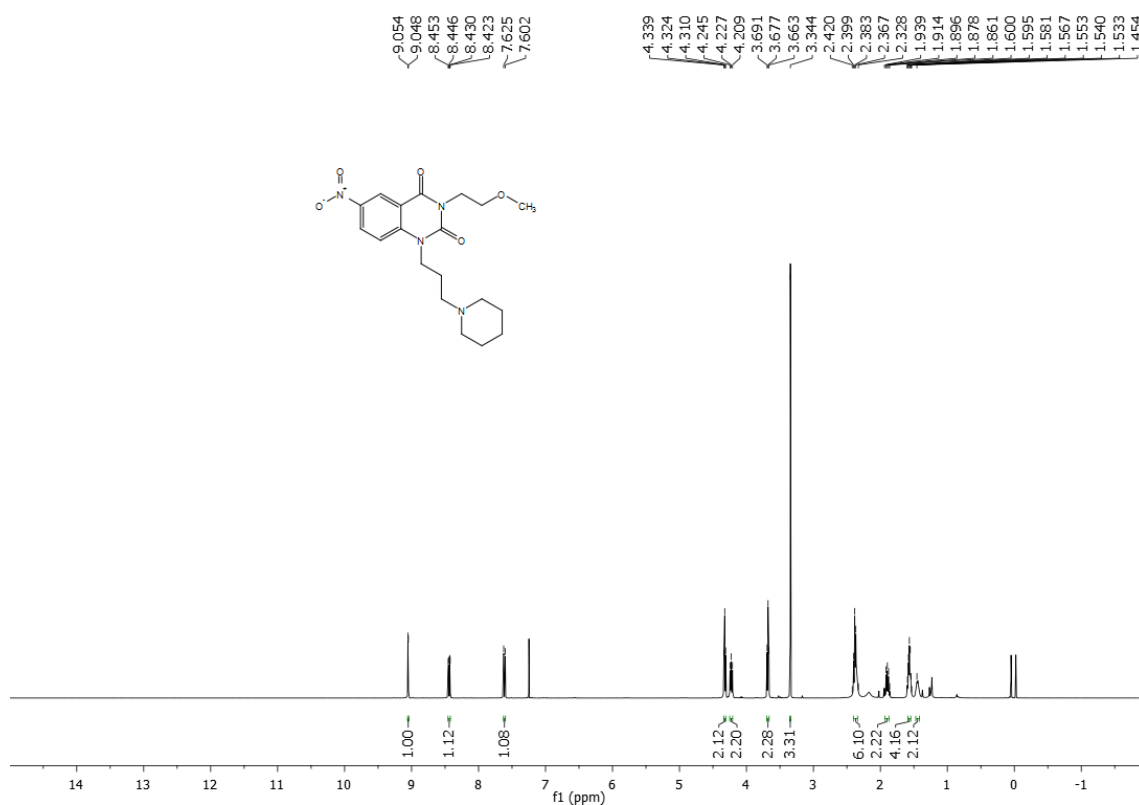
^1H NMR of compound **44** (400 MHz, CDCl_3):



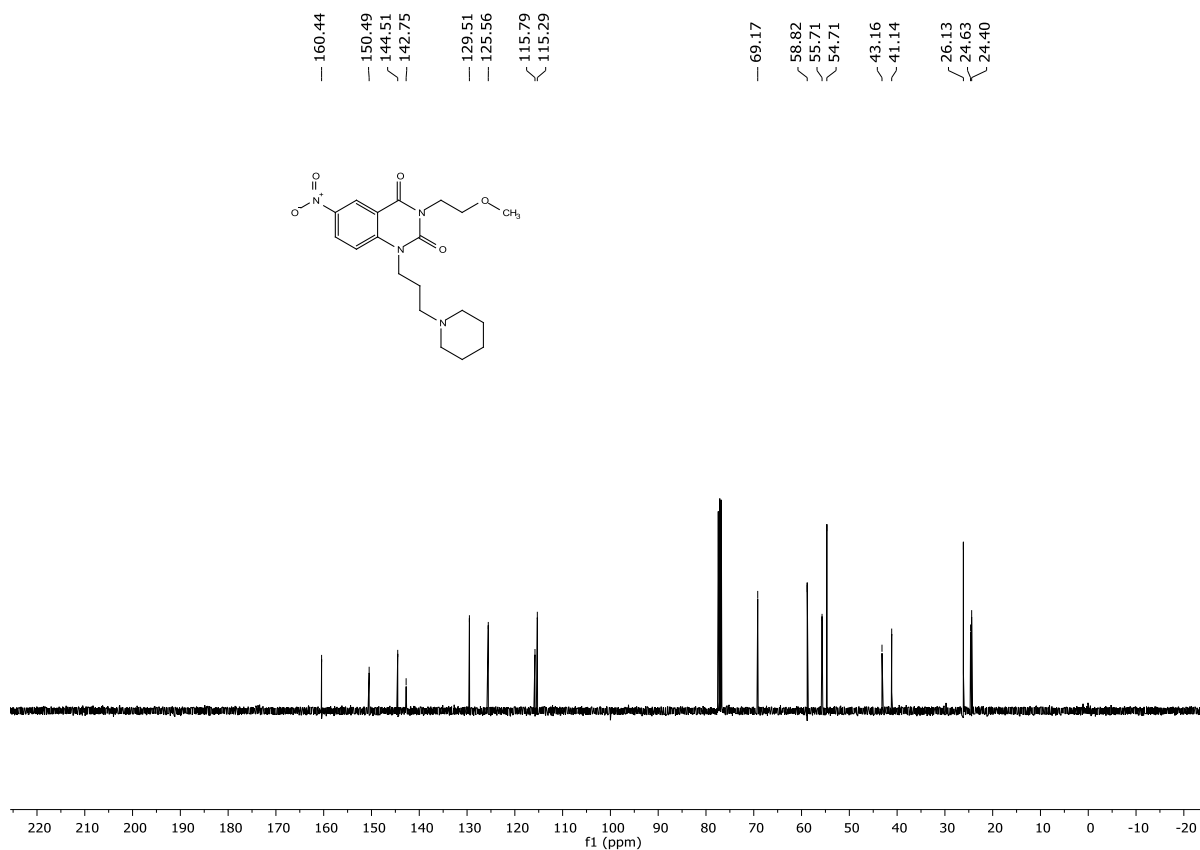
^{13}C NMR of compound **44** (100 MHz, CDCl_3):



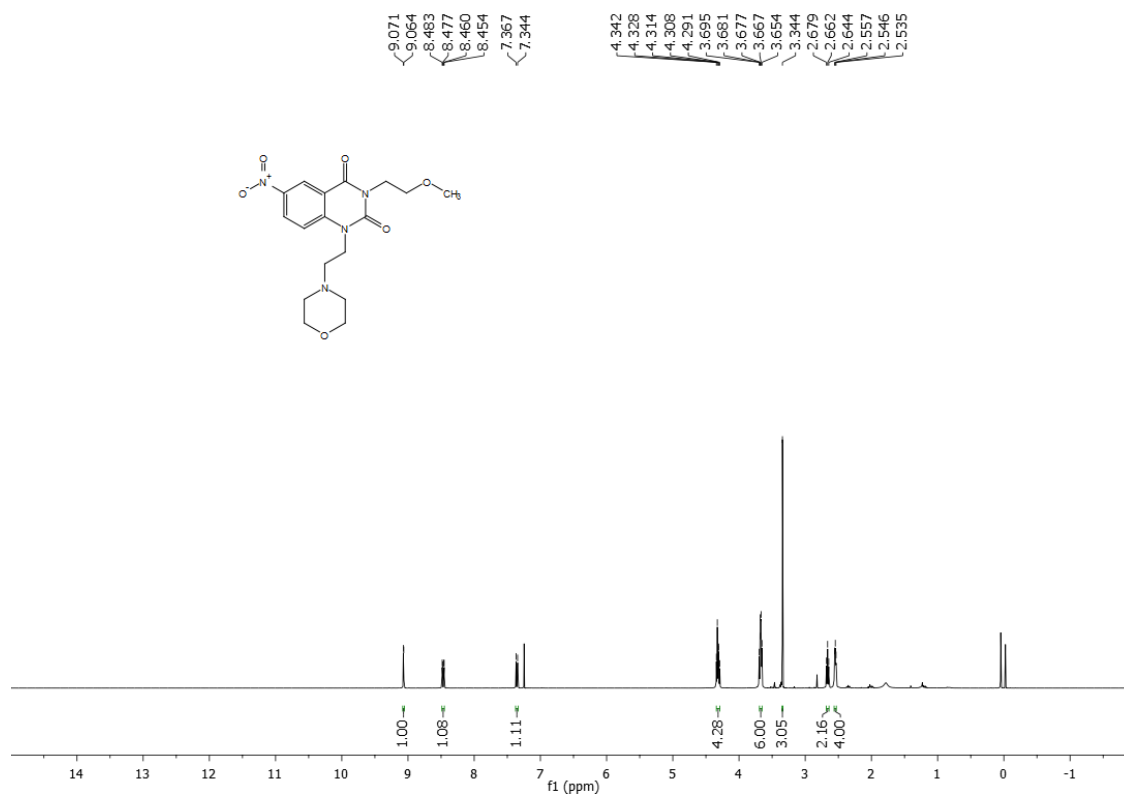
^1H NMR of compound **45** (400 MHz, CDCl_3):



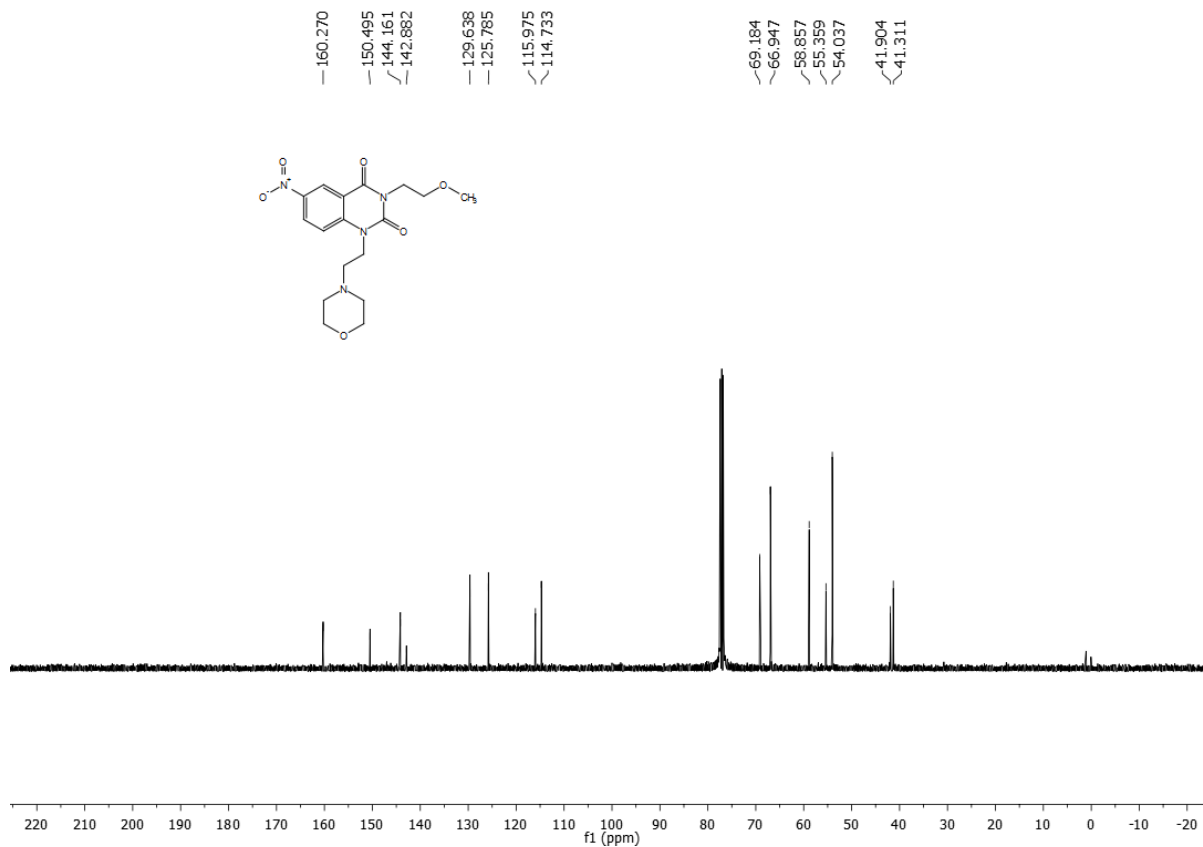
^{13}C NMR of compound **45** (100 MHz, CDCl_3):



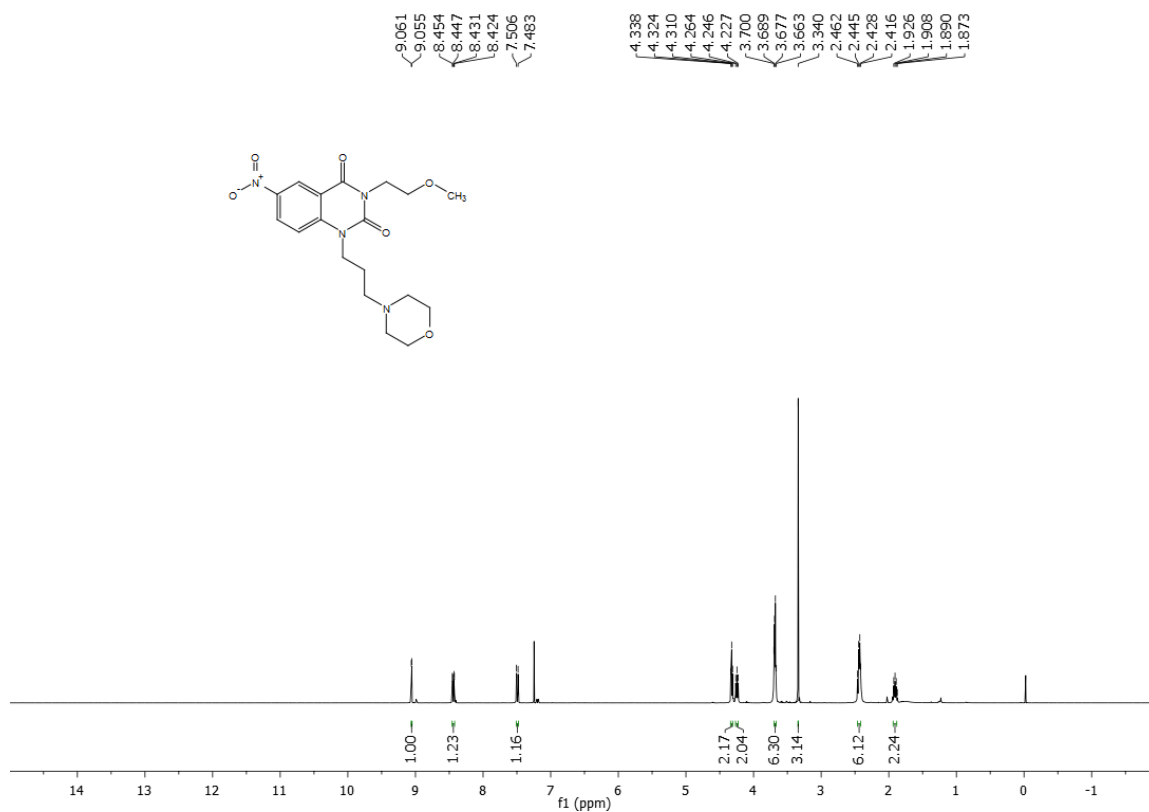
^1H NMR of compound **46** (400 MHz, CDCl_3):



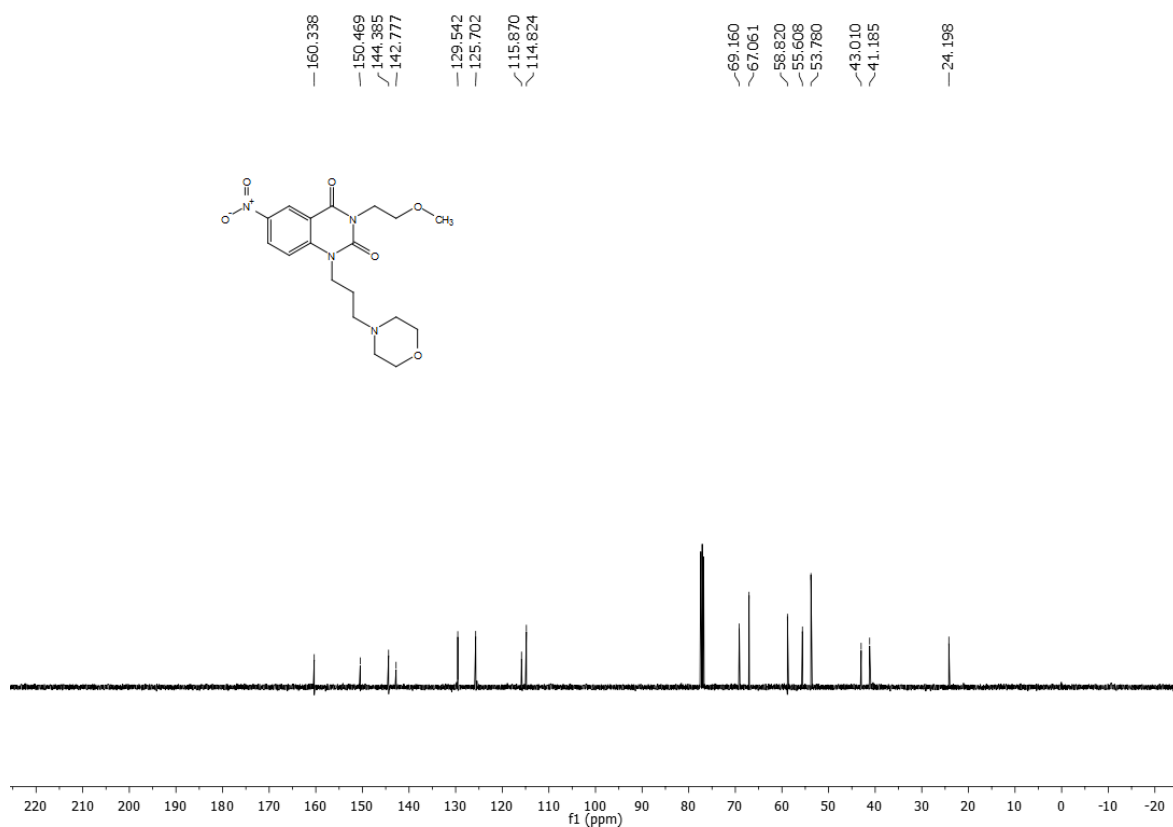
^{13}C NMR of compound **46** (100 MHz, CDCl_3):



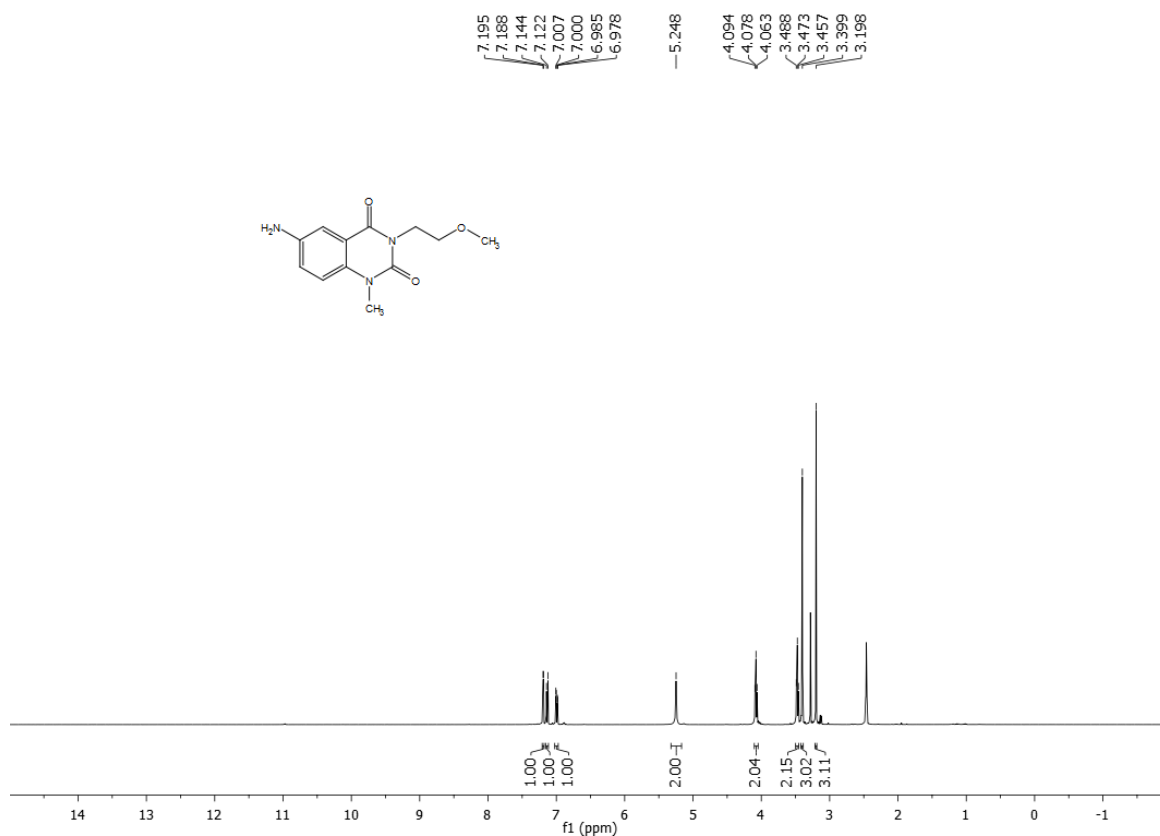
^1H NMR of compound **47** (400 MHz, CDCl_3):



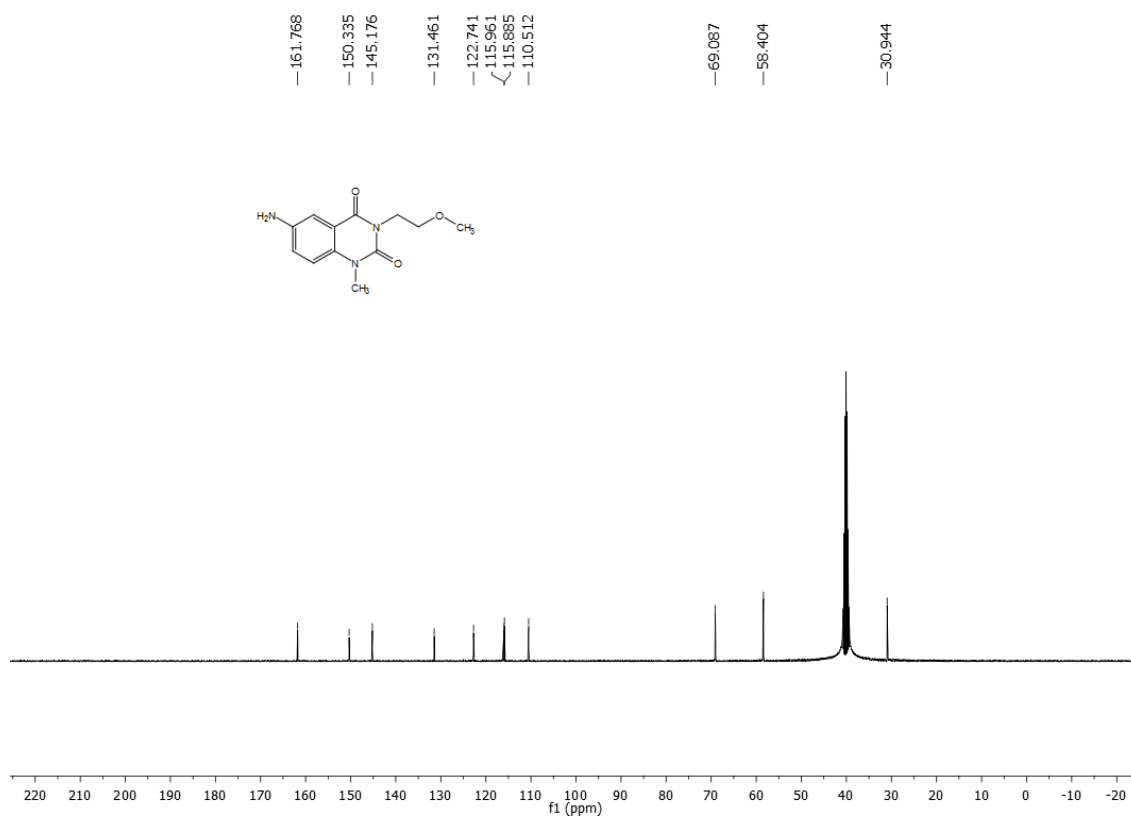
^{13}C NMR of compound **47** (100 MHz, CDCl_3):



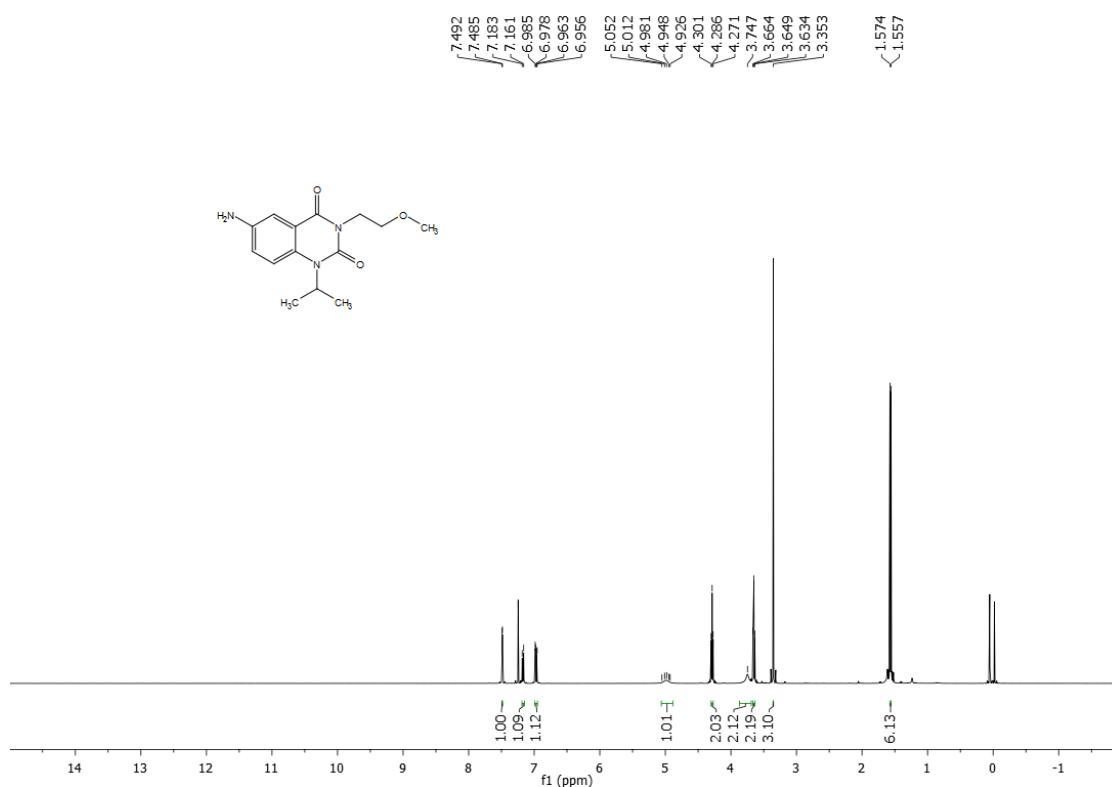
^1H NMR of compound **48** (400 MHz, d_6 -DMSO):



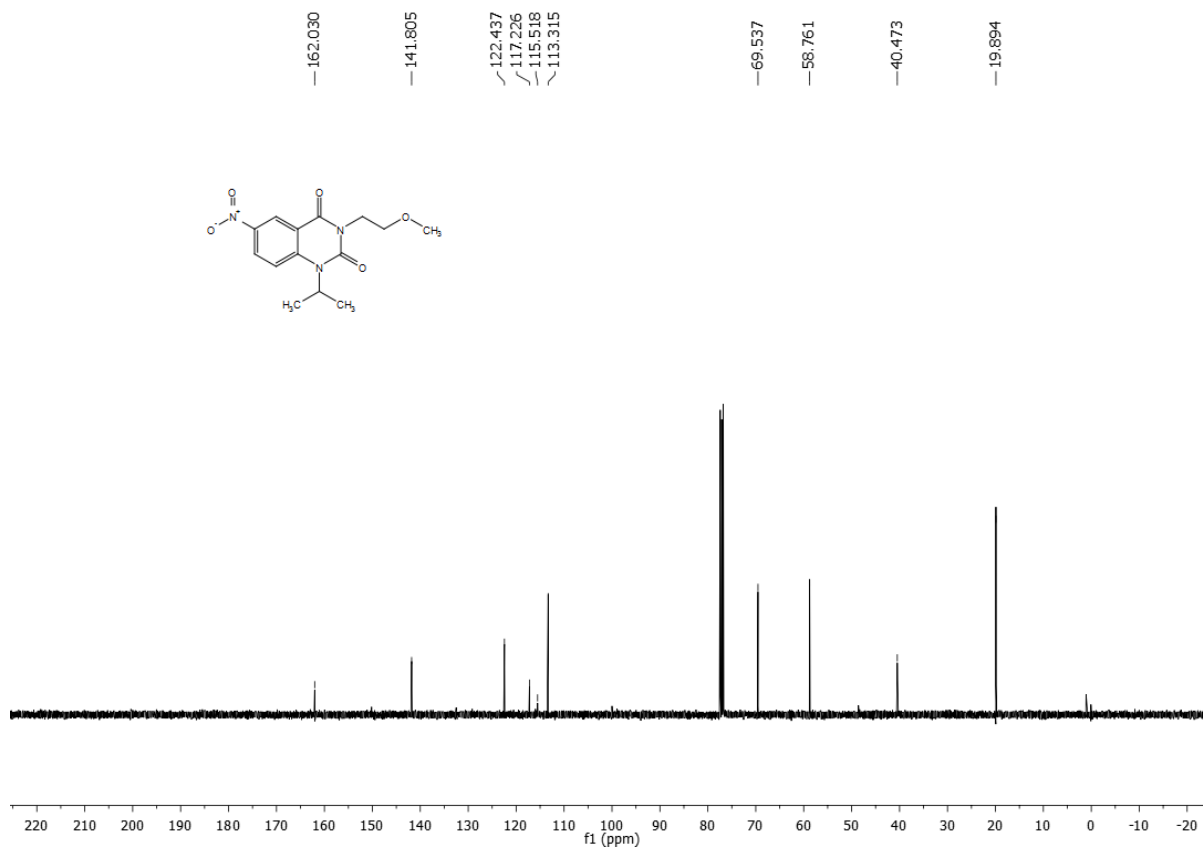
^{13}C NMR of compound **48** (100 MHz, d_6 -DMSO):



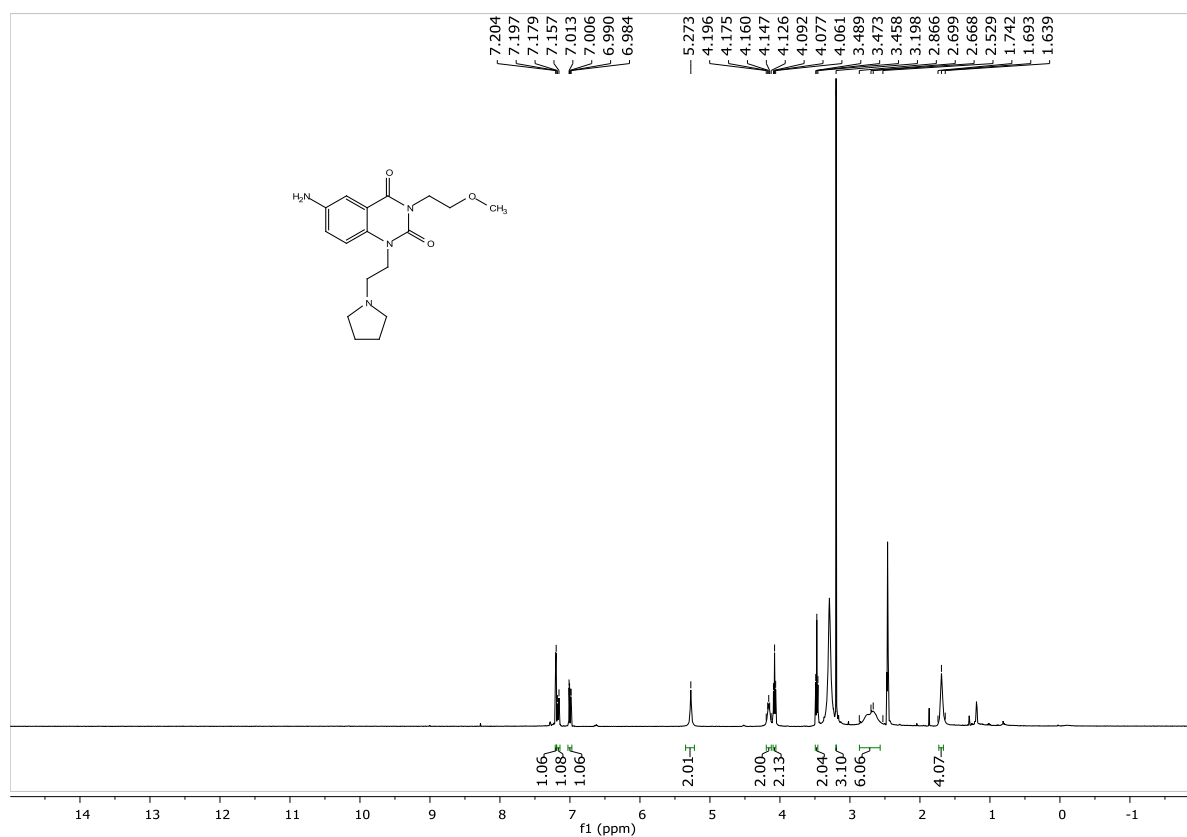
^1H NMR of compound **49** (400 MHz, CDCl_3):



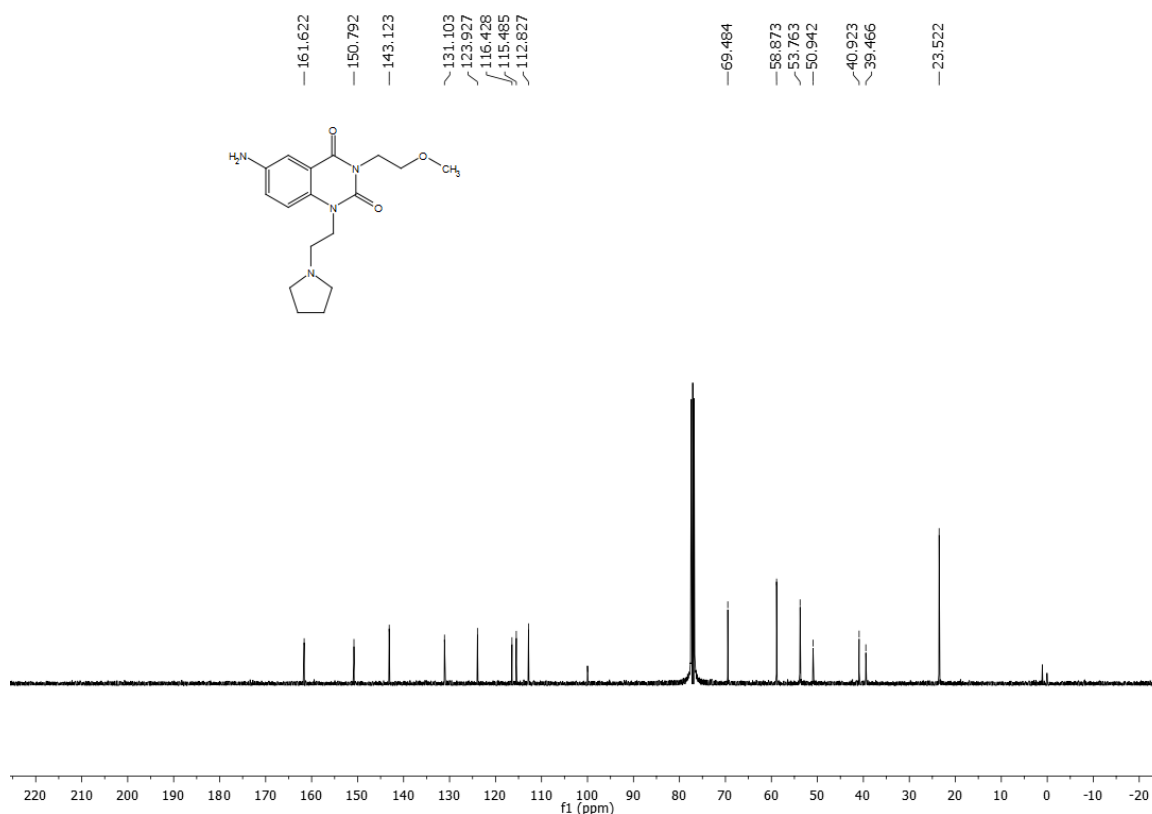
^{13}C NMR of compound **49** (100 MHz, CDCl_3):



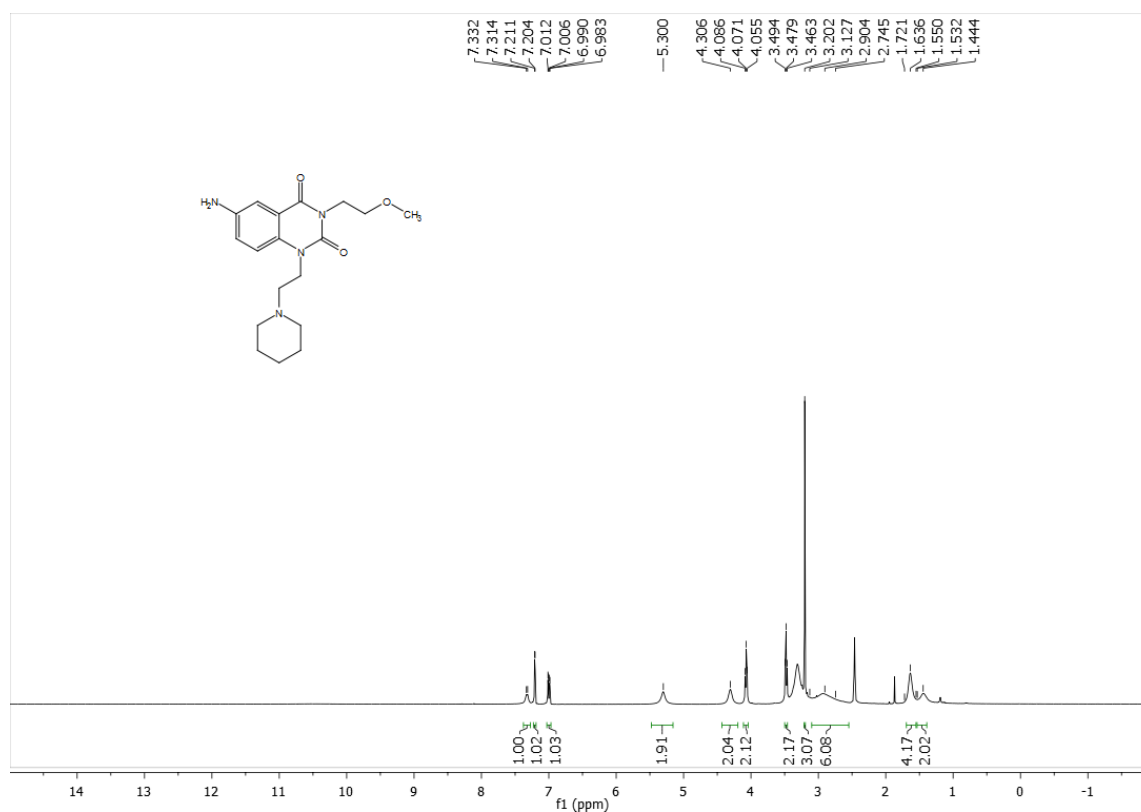
^1H NMR of compound **50** (400 MHz, d_6 -DMSO):



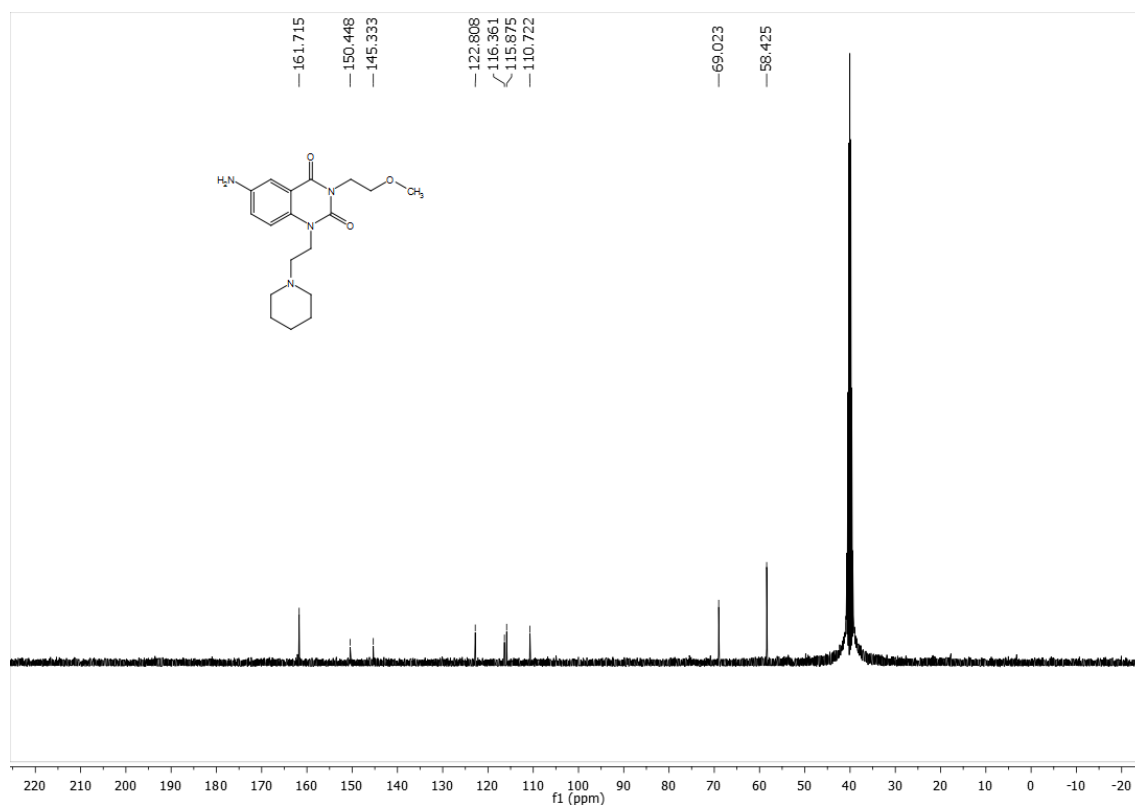
^{13}C NMR of compound **50** (100 MHz, d_6 -DMSO):



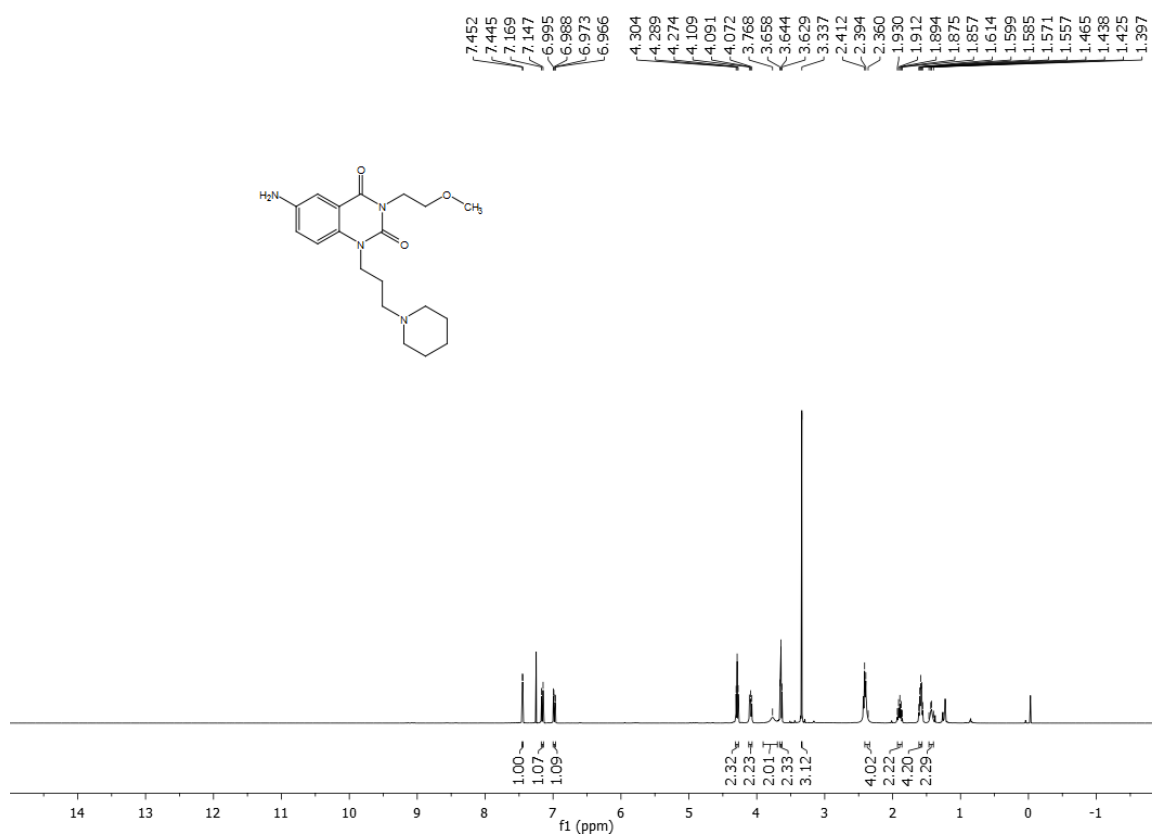
^1H NMR of compound **51** (400 MHz, d_6 -DMSO):



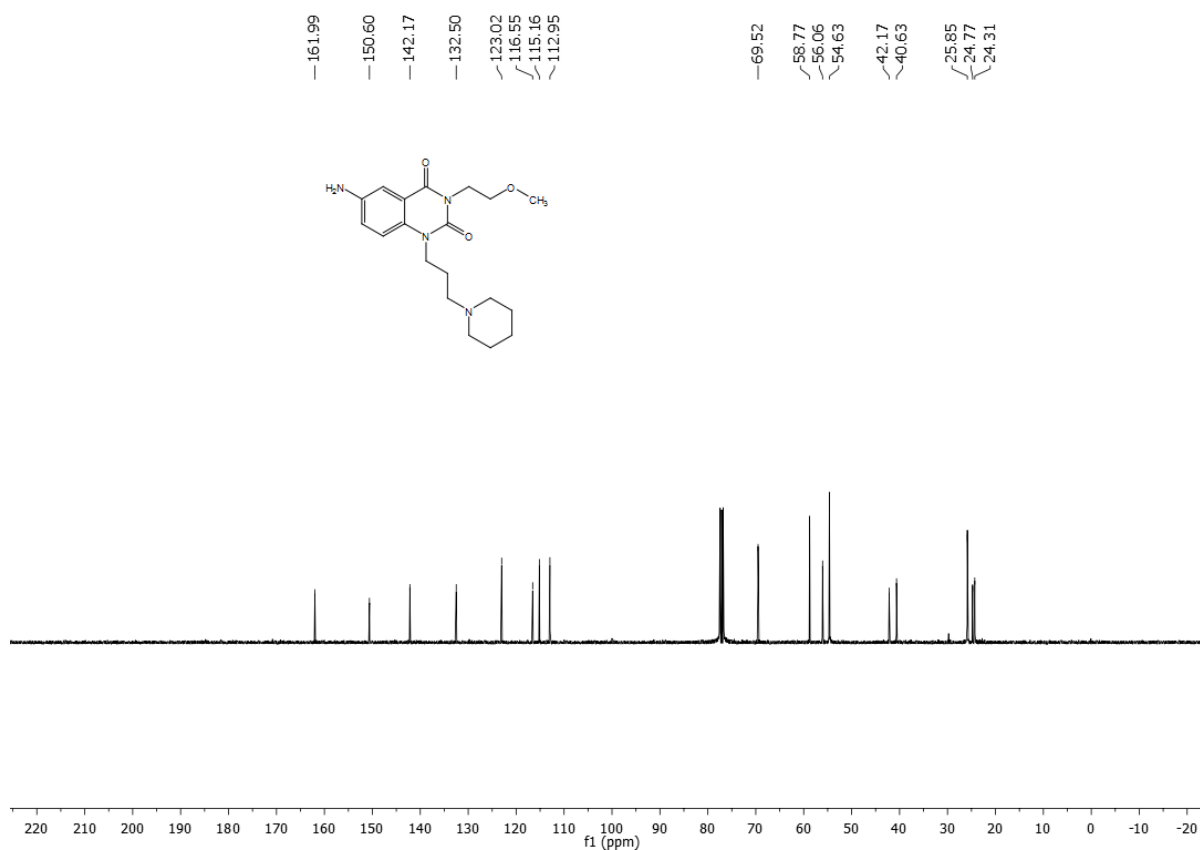
^{13}C NMR of compound **51** (100 MHz, d_6 -DMSO):



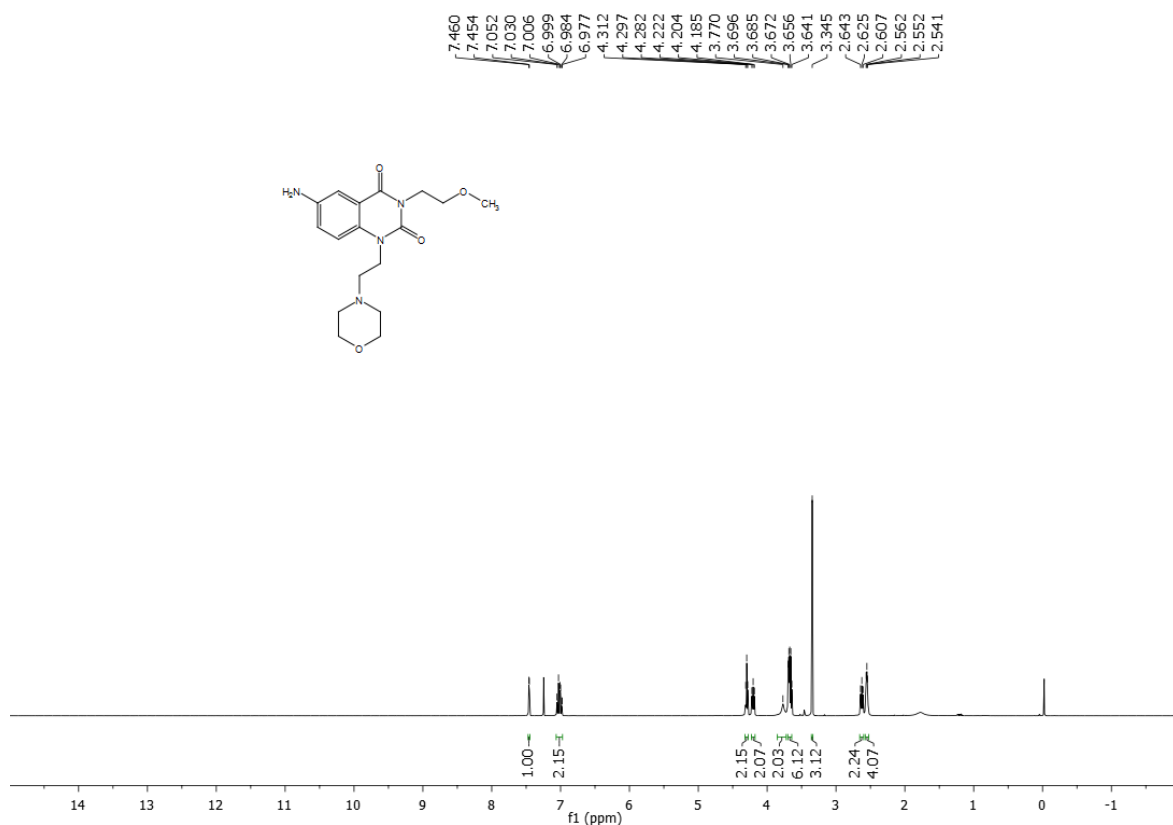
^1H NMR of compound **52** (400 MHz, CDCl_3):



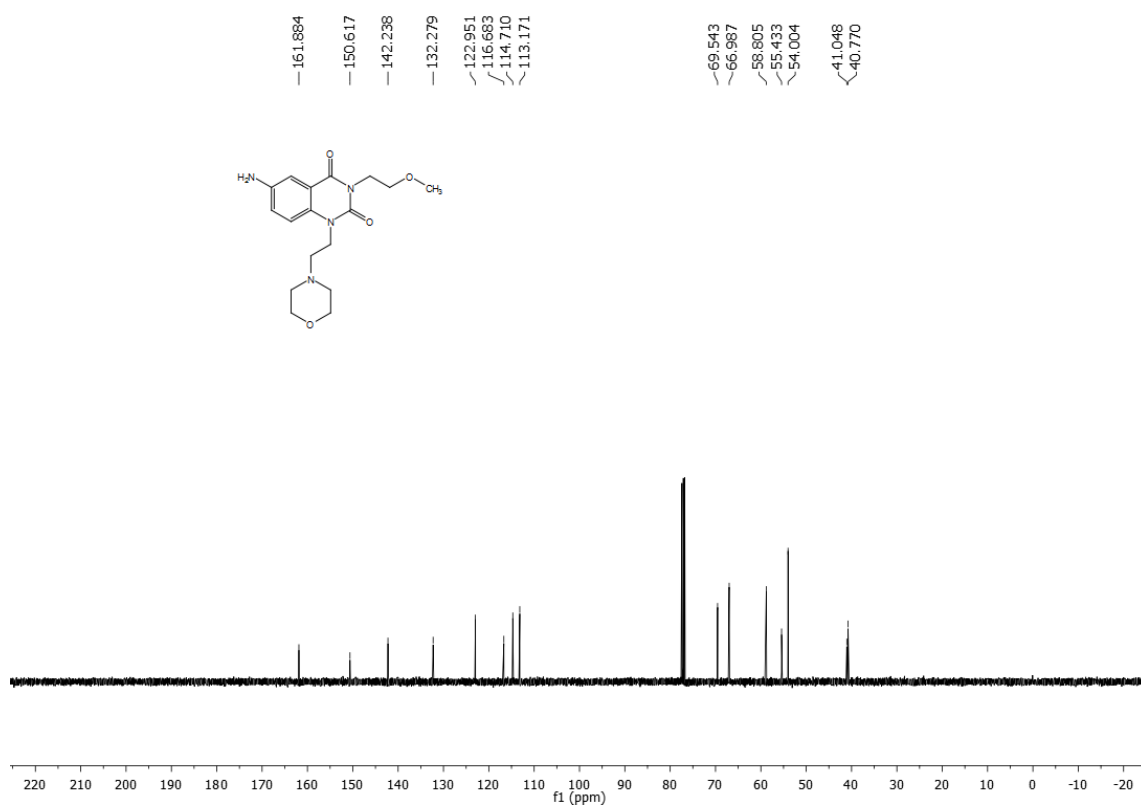
^{13}C NMR of compound **52** (100 MHz, CDCl_3):



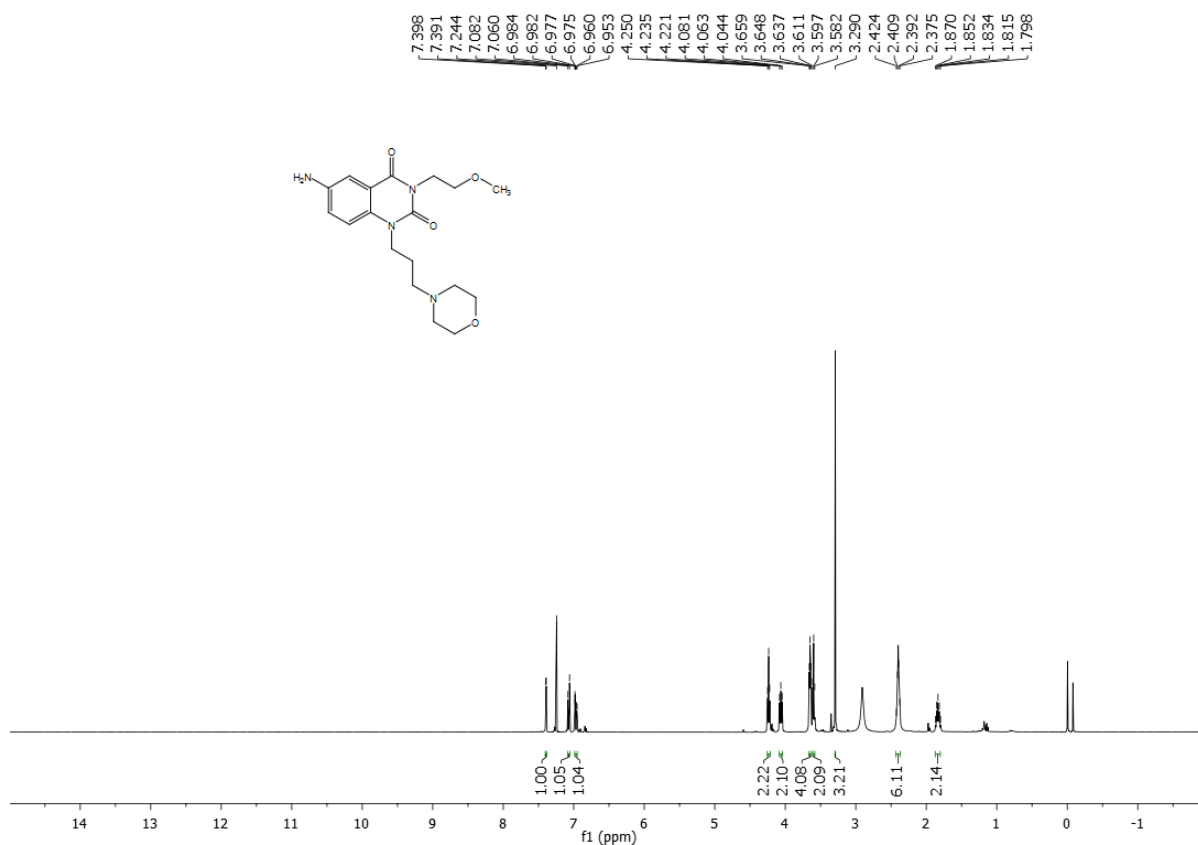
^1H NMR of compound **53** (400 MHz, CDCl_3):



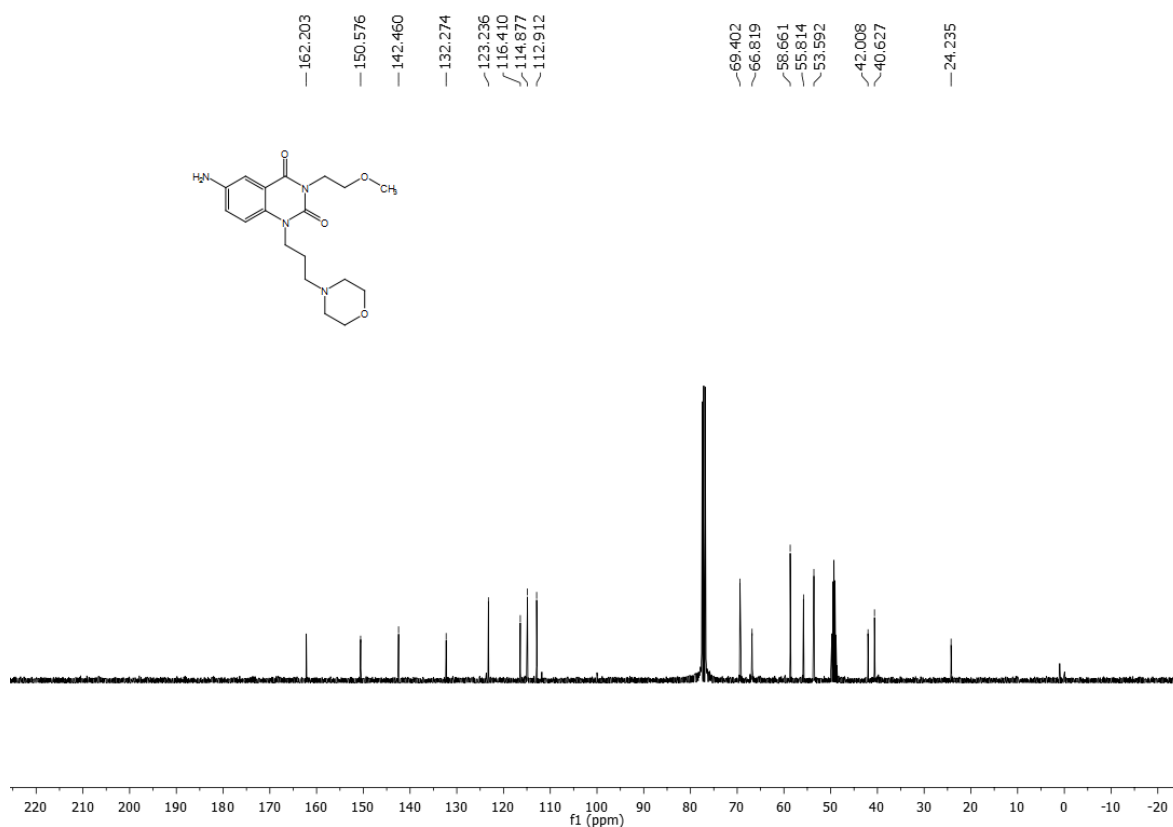
^{13}C NMR of compound **53** (100 MHz, CDCl_3):

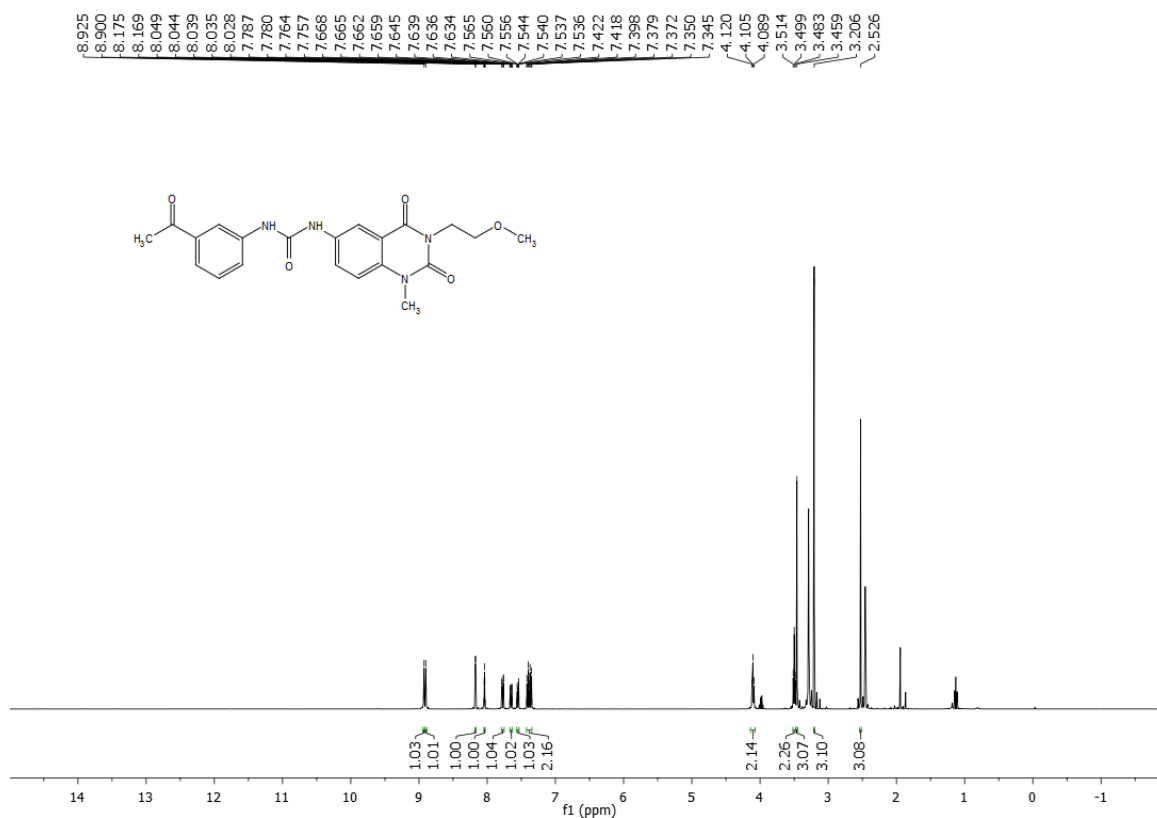
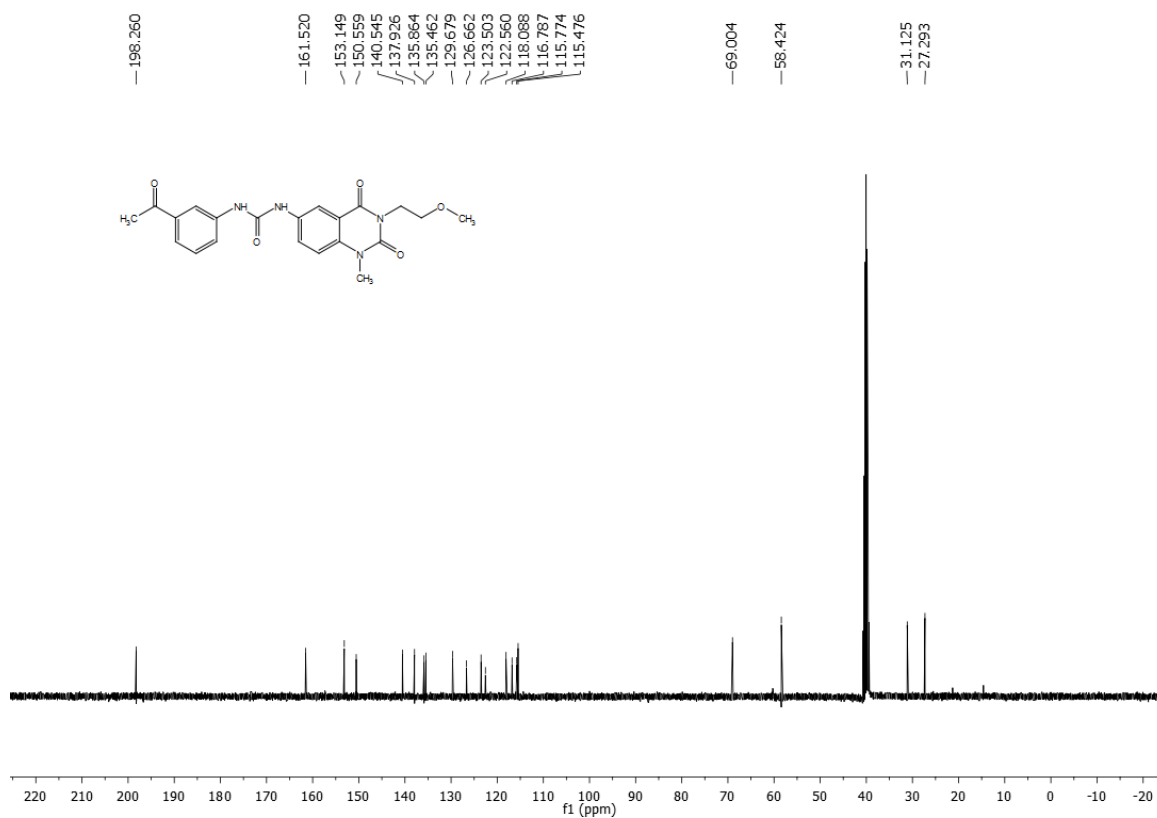


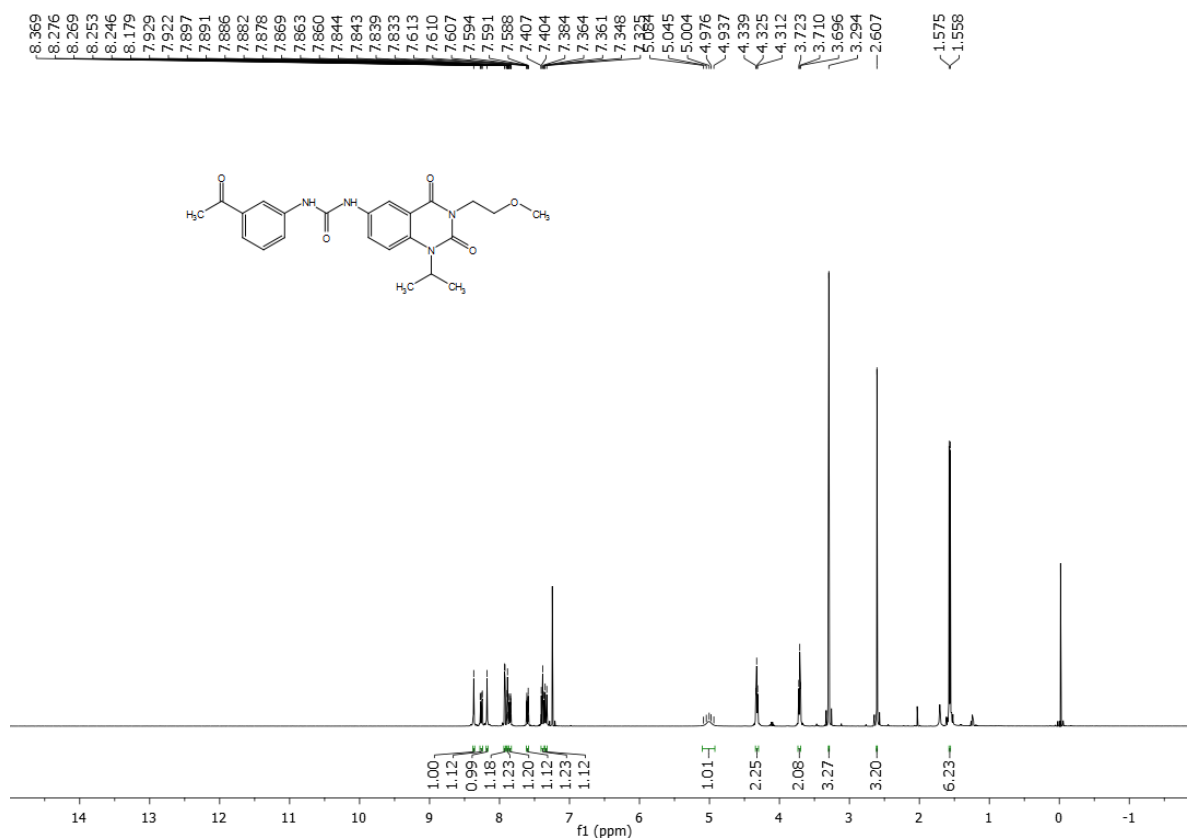
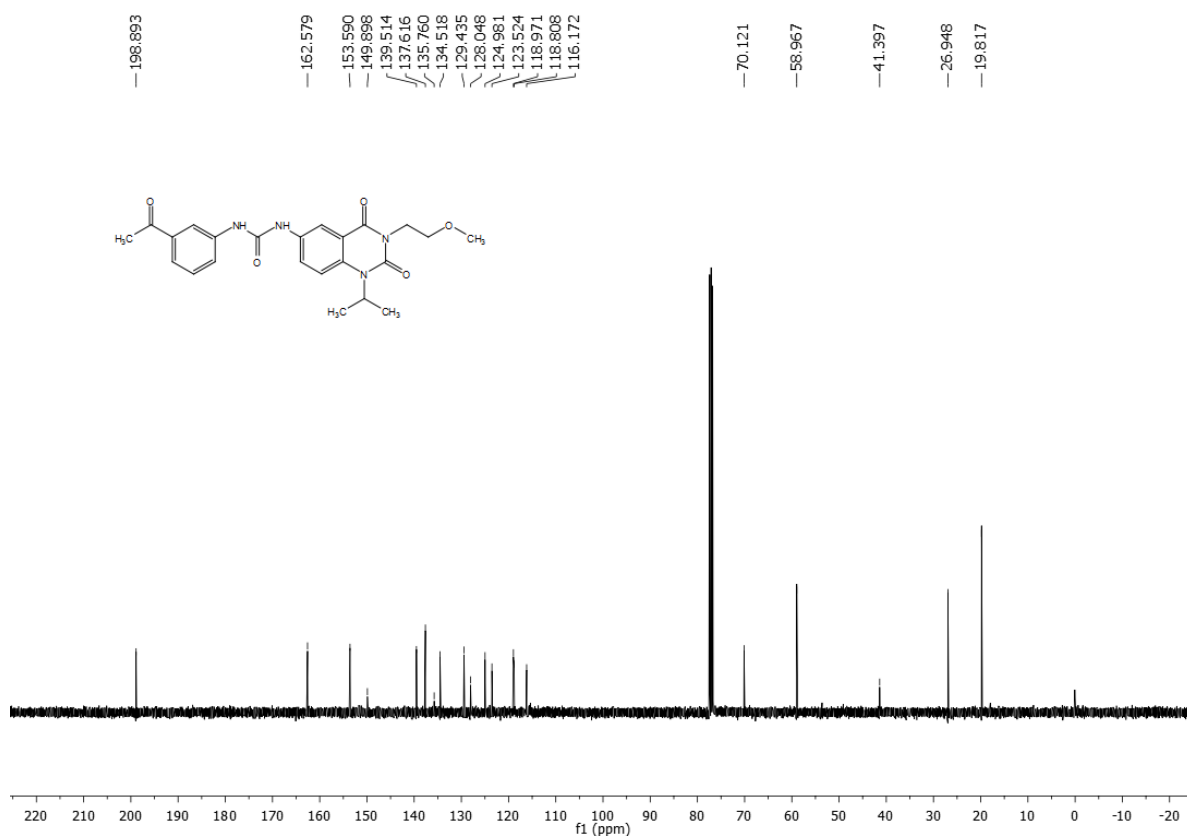
^1H NMR of compound **54** (400 MHz, CDCl_3):



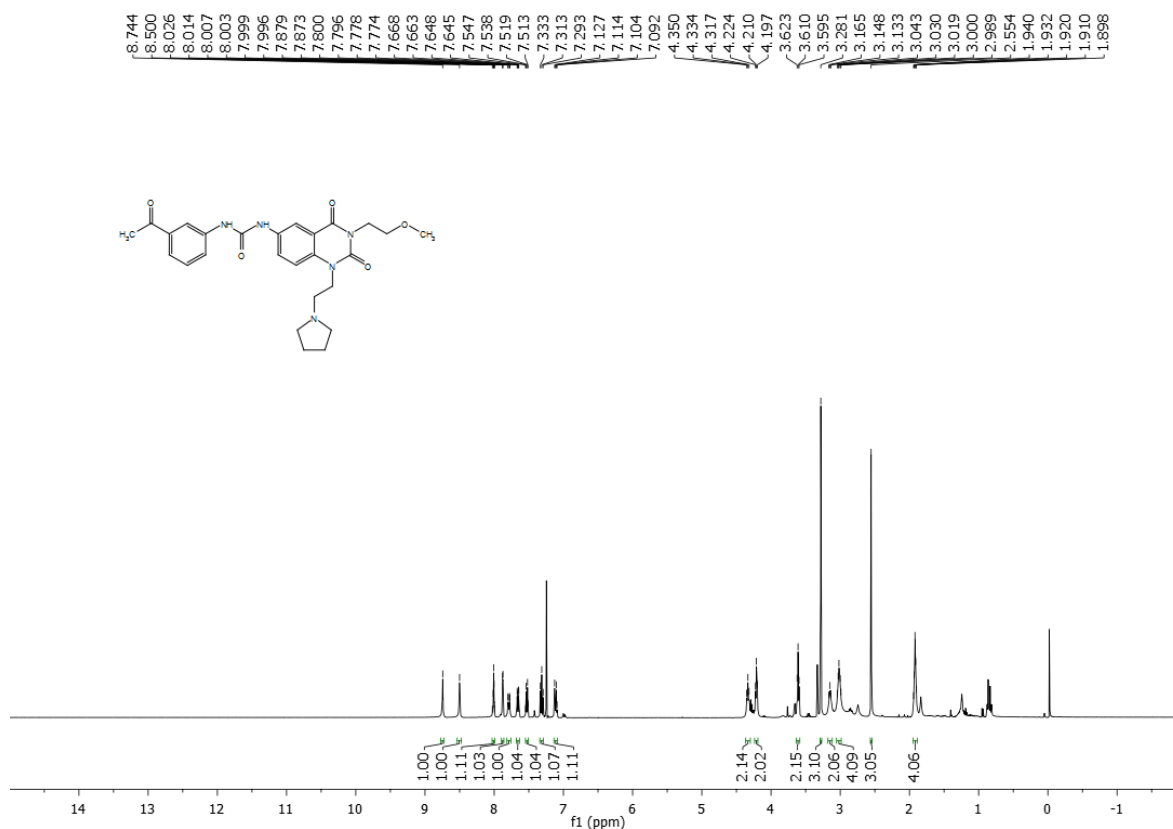
^{13}C NMR of compound **54** (100 MHz, CDCl_3):



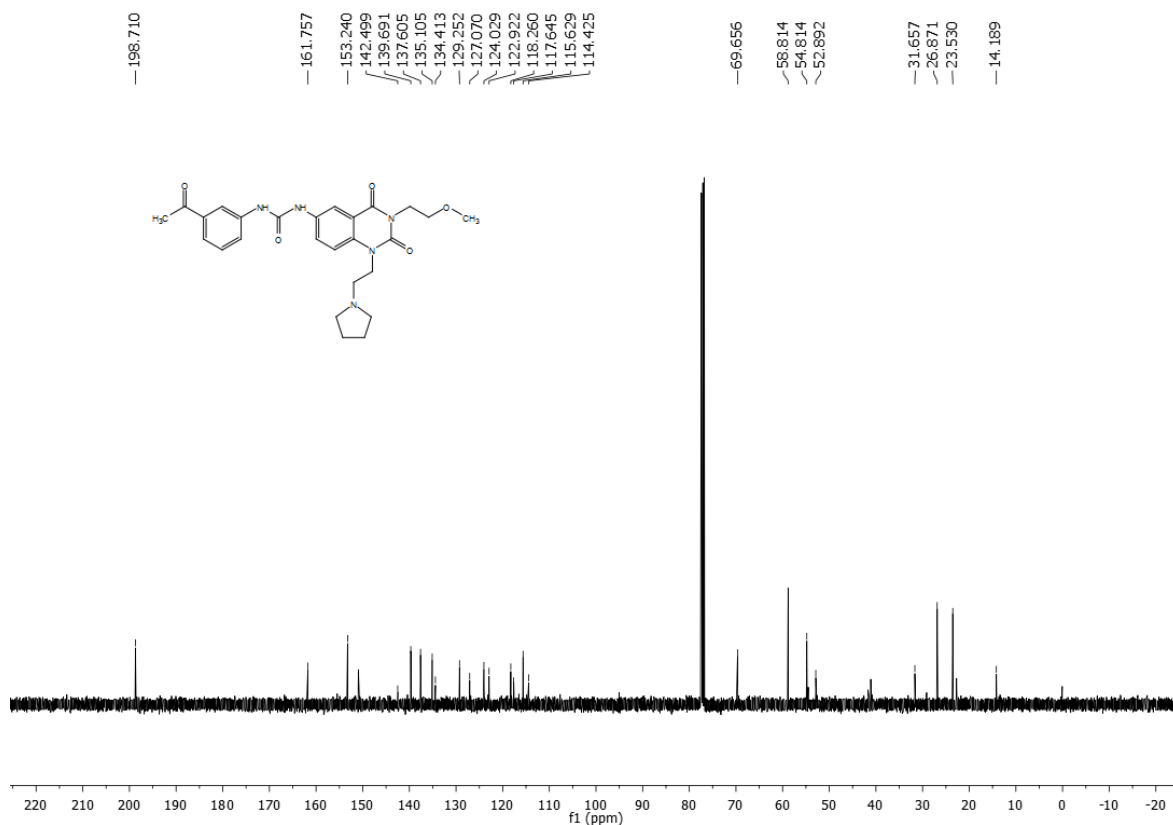
¹H NMR of compound **55** (400 MHz, *d*₆-DMSO):¹³C NMR of compound **55** (100 MHz, *d*₆-DMSO):

¹H NMR of compound **56** (400 MHz, CDCl₃):¹³C NMR of compound **56** (100 MHz, CDCl₃):

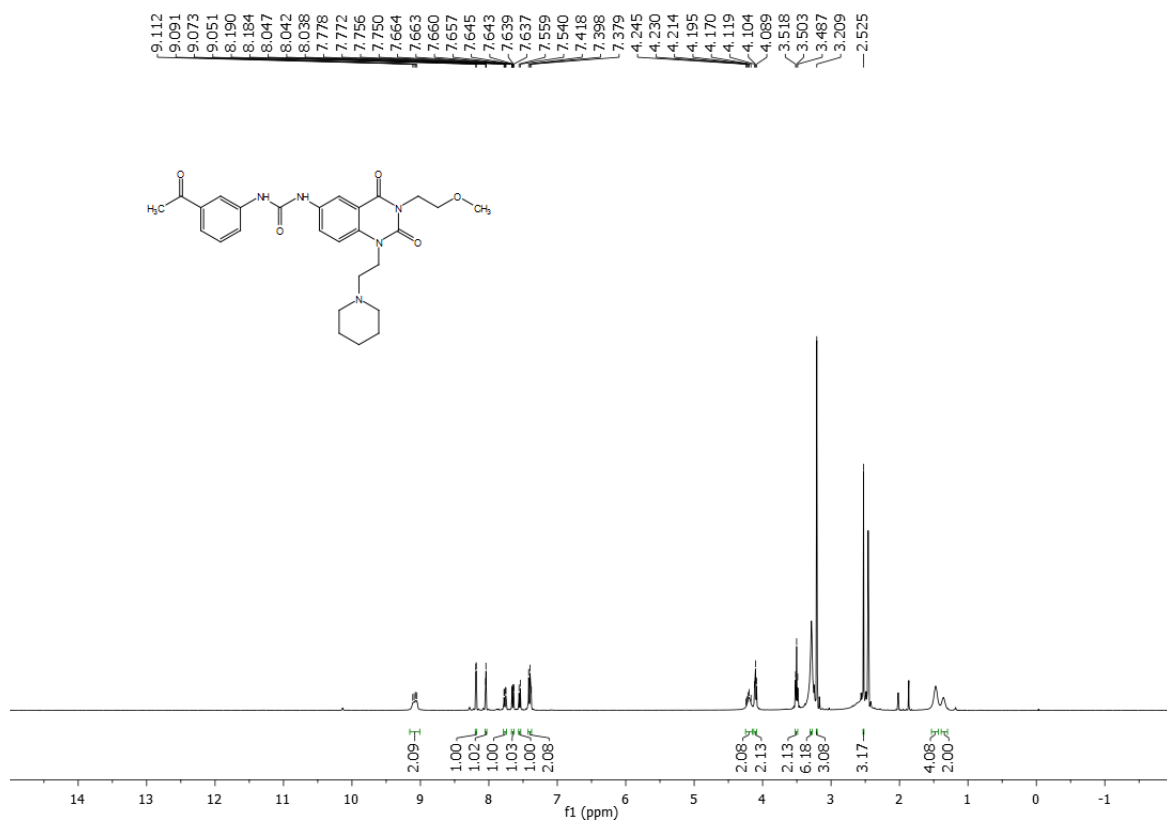
^1H NMR of compound **57** (400 MHz, d_6 -DMSO):



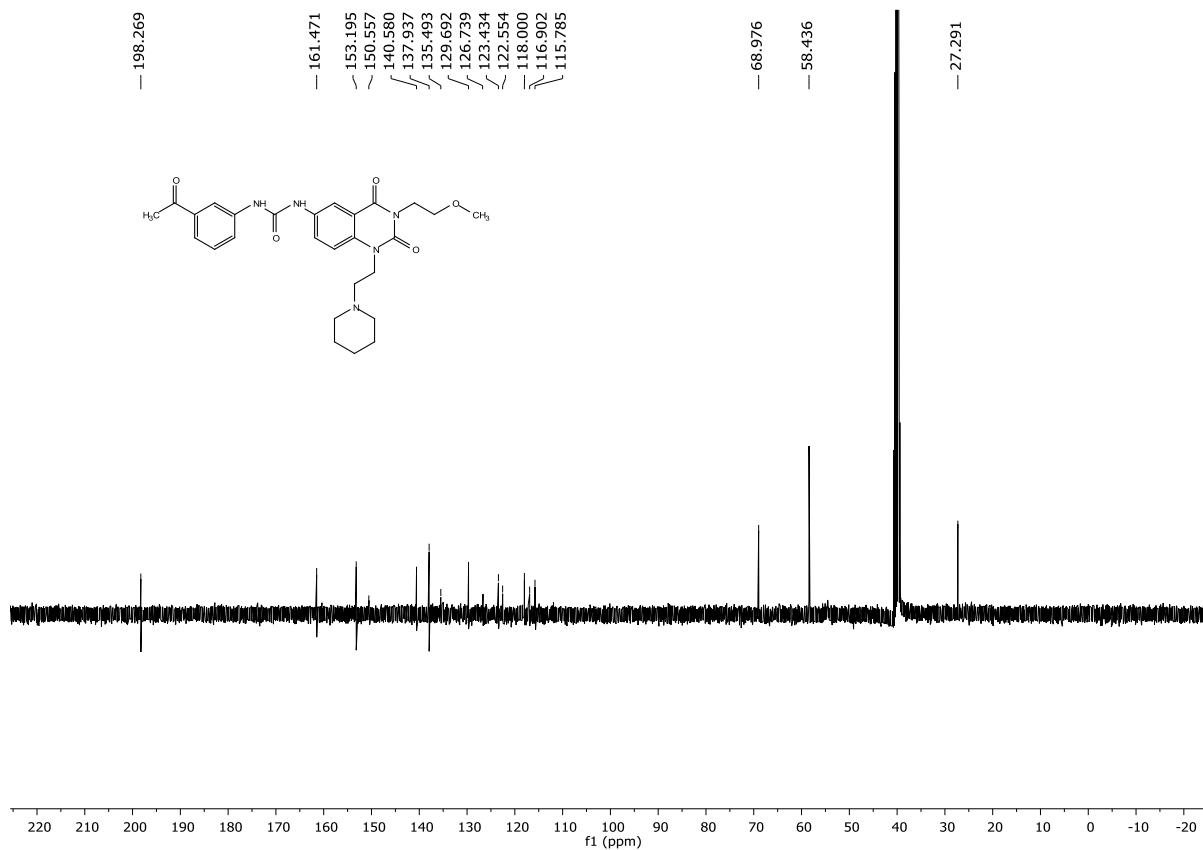
^{13}C NMR of compound **57** (100 MHz, CDCl_3):



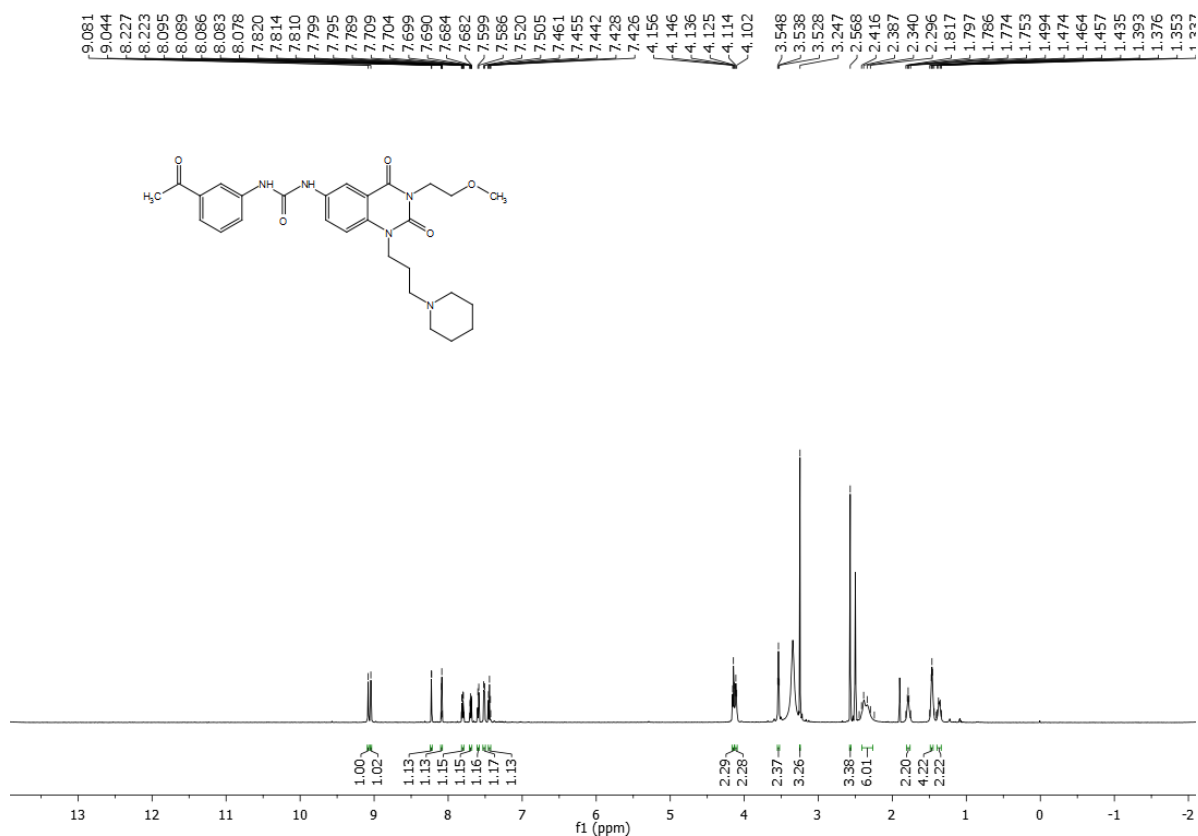
^1H NMR of compound **58** (400 MHz, d_6 -DMSO):



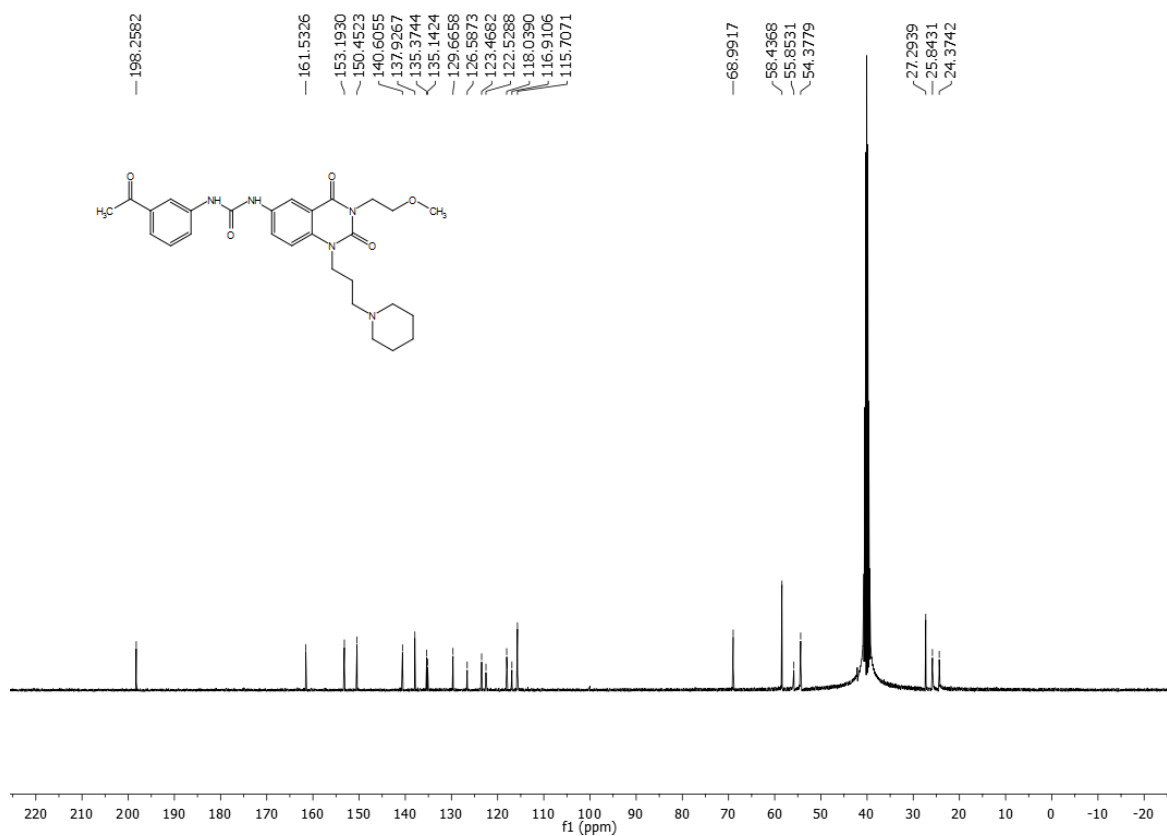
^{13}C NMR of compound **58** (100 MHz, d_6 -DMSO):



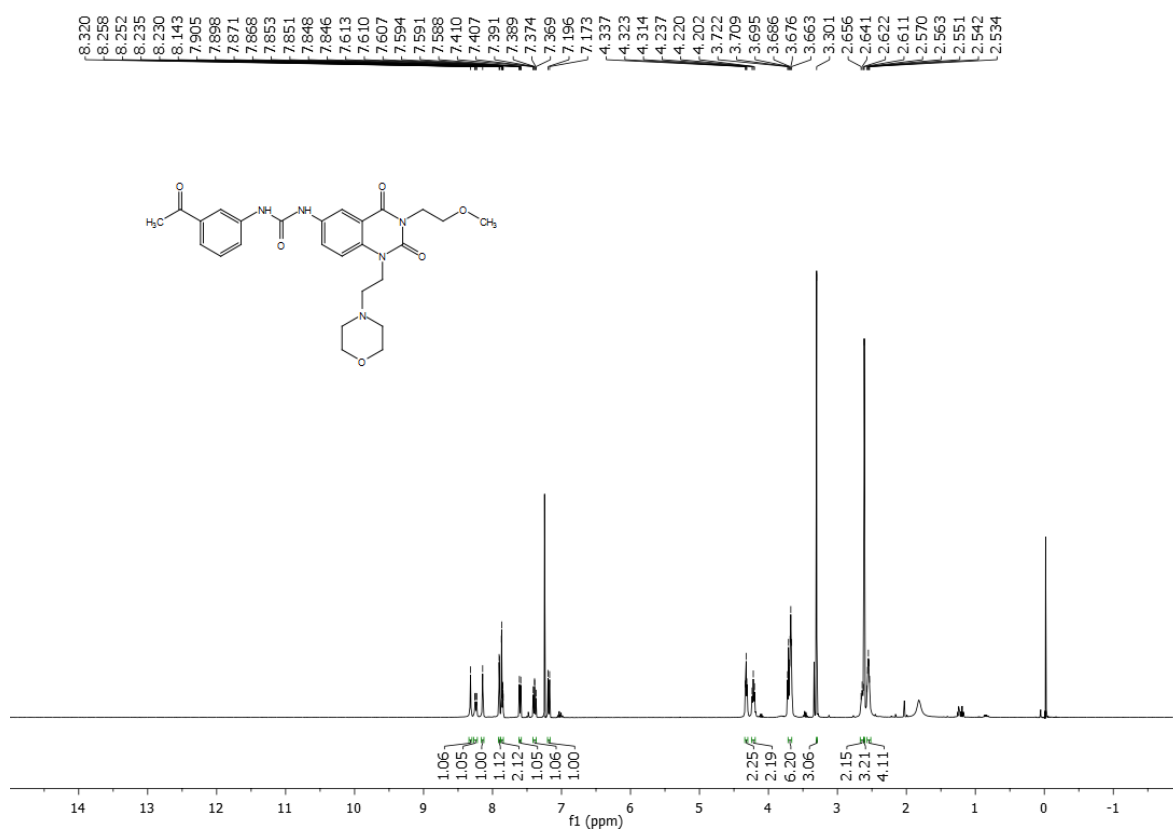
^1H NMR of compound **59** (400 MHz, d_6 -DMSO):



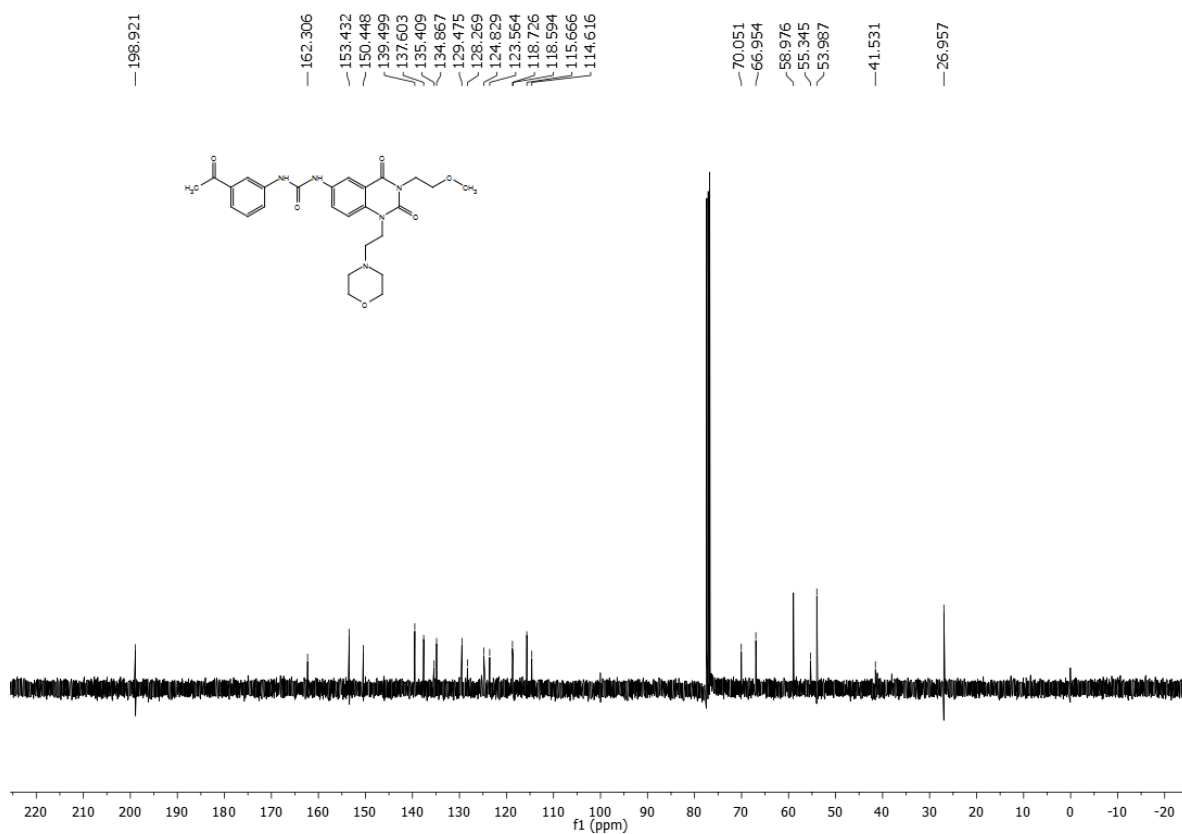
^{13}C NMR of compound **59** (100 MHz, d_6 -DMSO):



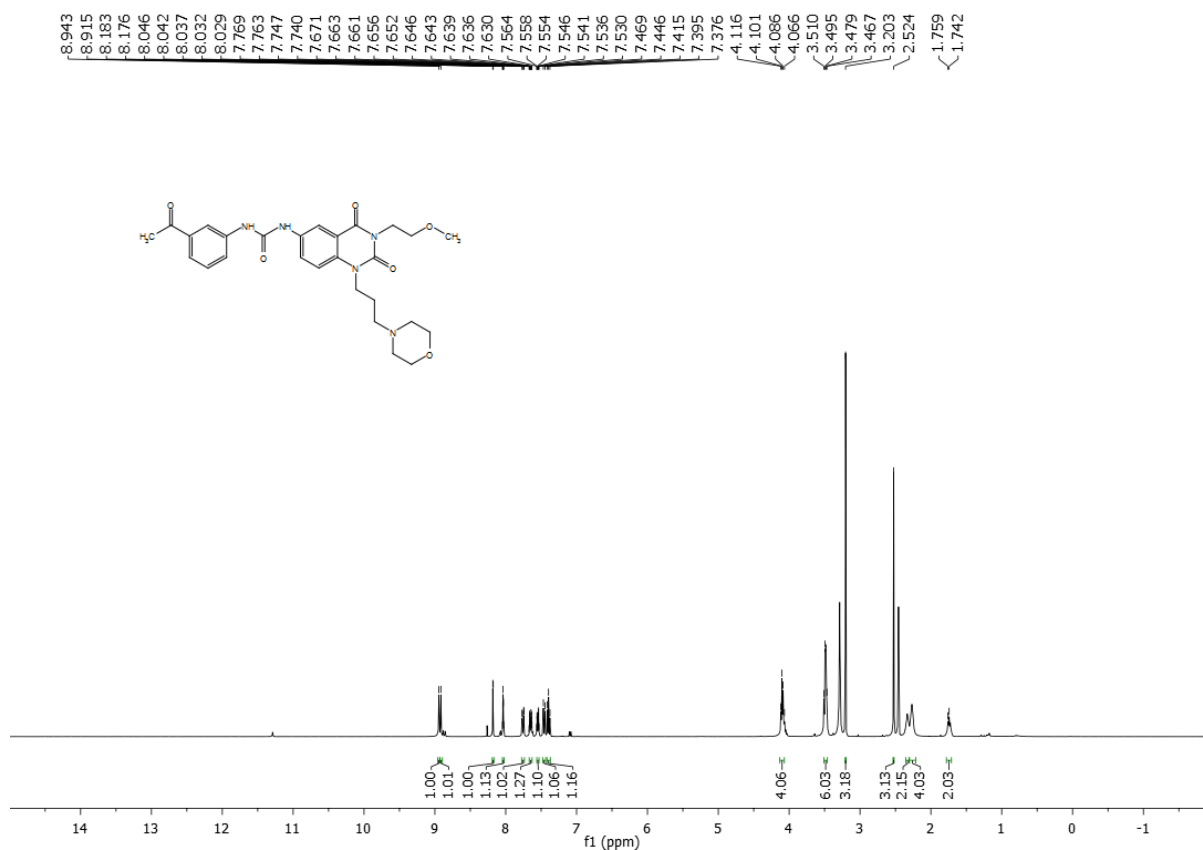
^1H NMR of compound **60** (400 MHz, d_6 -DMSO):



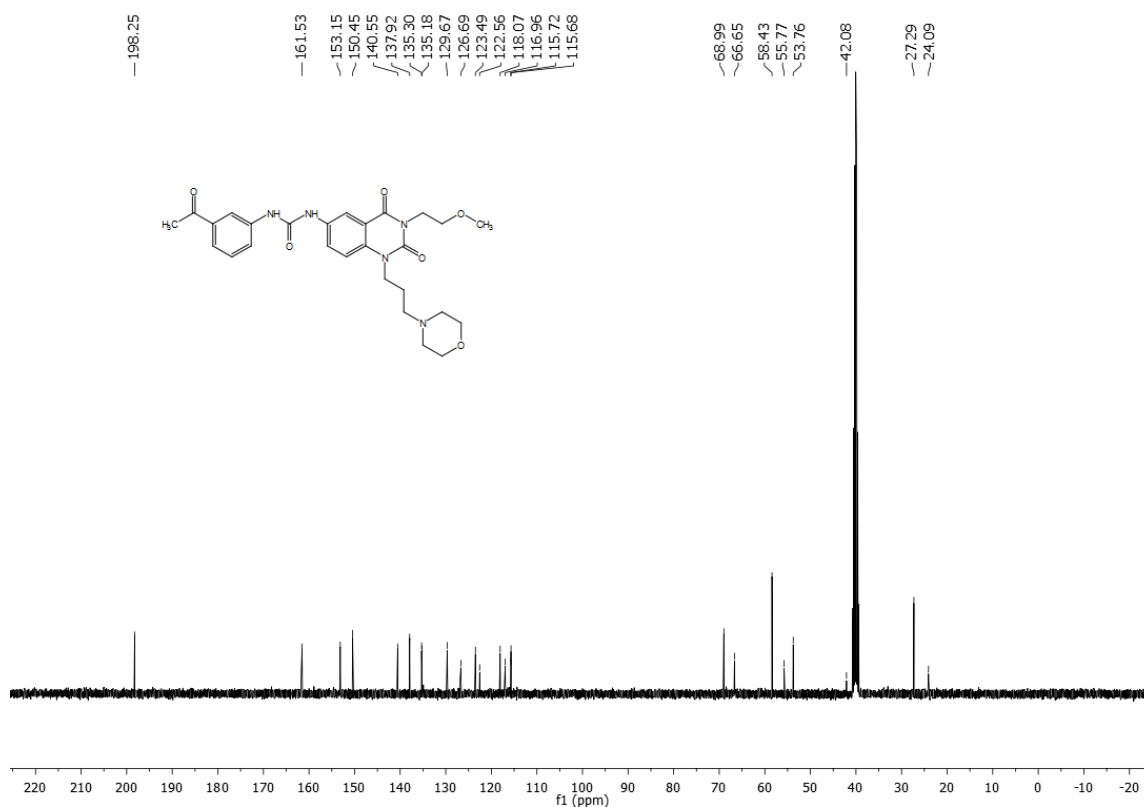
^{13}C NMR of compound **60** (100 MHz, d_6 -DMSO):



^1H NMR of compound **61** (400 MHz, d_6 -DMSO):



^{13}C NMR of compound **61** (100 MHz, d_6 -DMSO):



CHAPTER TWO

Design and synthesis of small molecule modulators of PPAR γ in ameliorating Non-Alcoholic Fatty Liver Disease (NAFLD)

CHAPTER TWO

Design and synthesis of small molecule modulators of PPAR γ in ameliorating Non-Alcoholic Fatty Liver Disease (NAFLD)

2.1 Introduction

Metabolic syndrome has become a major global health challenge, closely associated with obesity, insulin resistance, type 2 diabetes, and cardiovascular diseases, which are leading causes of illness and death worldwide.^{80,81} Currently, over a quarter of the global adult population is affected, and its prevalence is increasing among both adults and children, largely due to lifestyle factors such as high-calorie diets and low levels of physical activity. By definition, metabolic syndrome represents a disorder stemming from an imbalance in energy utilization and storage. Key features include abdominal obesity, hypertension, dyslipidemia (characterized by high triglycerides, low levels of high-density lipoprotein (HDL), and elevated low-density lipoprotein (LDL) cholesterol), insulin resistance with high fasting blood glucose, glucose intolerance, and pro-thrombotic and pro-inflammatory states. Individuals with this condition face a significantly increased risk to develop cardiovascular diseases and type 2 diabetes.⁸²⁻⁸⁴

Recent studies have also highlighted the role of obesity linked to metabolic syndrome in causing chronic low-grade inflammation, which predisposes individuals to additional health issues such as non-alcoholic fatty liver disease, sleep disorders, gallstones, polycystic ovary syndrome, asthma, and even certain cancers.^{85,86} Managing metabolic syndrome typically begins with lifestyle modifications aimed at restoring energy balance through reduced calorie intake and increased physical activity.⁸⁷ When lifestyle changes prove insufficient, pharmaceutical treatments are used to target specific aspects of the syndrome, such as weight management, insulin resistance, hypertension, dyslipidemia, hyperglycemia, and the associated pro-thrombotic and pro-inflammatory conditions.

In the treatment of type 2 diabetes, early strategies focused on lifestyle adjustments along with the use of insulin and its analogs.⁸⁸ Over time, several oral antidiabetic drugs have been developed, including sulfonylureas (to enhance insulin secretion), biguanides such as metformin (to improve insulin sensitivity), alpha-glucosidase inhibitors (to slow

carbohydrate digestion), meglitinides (to boost insulin secretion), and dipeptidyl peptidase-4 (DPP-4) inhibitors (to increase insulin production).^{89,90} Thiazolidinediones, which target the nuclear receptor PPAR γ , have been particularly significant for their ability to regulate insulin sensitivity, glucose metabolism, fatty acid storage, and inflammation.^{91,92}

Ongoing research continues to explore additional therapeutic approaches, focusing on pathways such as the nuclear factor-kappa B (NF- κ B) signaling, mitogen-activated protein kinase (MAPK) pathways, and fatty acid-binding proteins, among others involved in lipid metabolism. Among these, **PPAR γ** remains a highly promising target due to its capacity to simultaneously modulate multiple underlying mechanisms of metabolic syndrome, offering potential for more comprehensive and effective treatments.^{93,94}

2.1.1 PPAR γ and the metabolic regulation

Peroxisome proliferator-activated receptors (PPARs) are part of the nuclear receptor superfamily of ligand-activated transcription factors. To date, three PPAR subtypes have been identified, each encoded by separate genes: PPAR α , PPAR β/δ , and PPAR γ .^{95,96} These receptors regulate the expression of genes involved in processes such as adipogenesis, lipid metabolism, inflammation, and metabolic homeostasis. Activated by dietary fatty acids and their metabolites, PPARs function as lipid sensors that can significantly alter metabolic pathways.^{97,98} The transcription mechanism is consistent across all PPAR subtypes: upon ligand binding, PPARs form heterodimers with retinoid X receptors (RXRs), another class of nuclear receptors. These heterodimers then bind to specific DNA sequences called peroxisome proliferator response elements (PPREs) in target gene promoters, recruiting transcriptional cofactors to initiate gene expression.

The PPAR subtypes differ in tissue distribution and metabolic roles. PPAR α , primarily found in the liver, heart, kidney, and muscles, regulates lipid and lipoprotein metabolism.⁹⁹ PPAR β/δ is widely expressed but is present at low levels in the liver and plays a role in lipid metabolism and energy balance in adipose tissue, skeletal muscle, and the heart.¹⁰⁰ PPAR γ , which exists in two isoforms (PPAR γ 1 and PPAR γ 2), is key in adipocyte differentiation and glucose metabolism.¹⁰¹ While PPAR γ 1 is expressed in multiple tissues, including adipose tissue, large intestine, and hematopoietic cells, PPAR γ 2 is mostly restricted to white and brown adipose tissues. Endogenous ligands for

PPAR γ include fatty acids and prostanoids, which generally act as weaker agonists compared to synthetic thiazolidinedione compounds. While it remains uncertain if PPAR γ has specific endogenous ligands or functions as a broad lipid sensor, it is recognized as a master regulator of adipogenesis, glucose homeostasis, and inflammation. PPAR γ activation promotes the differentiation of preadipocytes into adipocytes and regulates genes essential for lipid storage and insulin sensitivity.¹⁰² In addition to metabolic roles, PPAR γ impacts immune function by modulating gene expression in macrophages and dendritic cells, influencing inflammation, immunity, and atherosclerosis.^{103,104} Its involvement in cell proliferation and apoptosis extends its significance to cancer biology, with PPAR γ expressed in tumors such as those of the lung, breast, colon, and prostate. PPAR γ activity is also regulated by post-translational modifications like phosphorylation. For example, phosphorylation at Ser273 by cyclin-dependent kinase 5 (Cdk5) has been linked to obesity. Some PPAR γ ligands, including certain thiazolidinediones like rosiglitazone, inhibit this phosphorylation, potentially enhancing anti-diabetic effects without causing the side effects associated with classical agonists. This mechanism has been proposed as a promising strategy for developing advanced anti-diabetic drugs.

The clinical use of PPAR γ agonists, specifically thiazolidinediones, began in the late 1990s for managing type 2 diabetes by improving insulin sensitivity. Troglitazone, the first approved drug of this class, was withdrawn due to severe hepatotoxicity despite its efficacy.¹⁰⁵ Rosiglitazone and pioglitazone remain in use, although concerns about cardiovascular and other side effects limit their application.¹⁰⁶ Rosiglitazone, for instance, has been associated with an increased risk of myocardial infarction and heart failure, whereas pioglitazone shows a comparatively safer profile but carries risks such as weight gain, fluid retention, and possibly bladder cancer.

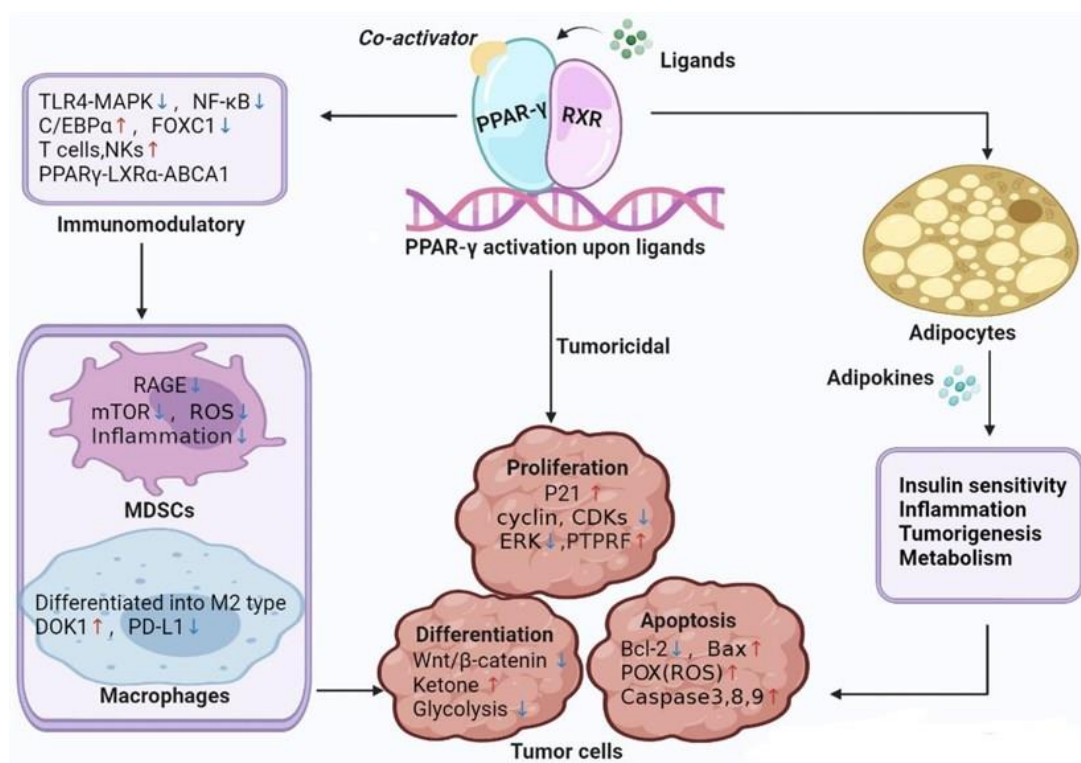


Figure 1. Regulatory effect of PPAR gamma upon ligand activation¹⁰⁷

2.1.2 Pharmacological Potential of PPAR

Numerous diseases have been linked to dysfunctions in PPAR γ activity. A detailed discussion of these conditions is provided in the following section.

2.1.2.1 Anti-Cancer effect

PPAR γ (Peroxisome Proliferator-Activated Receptor Gamma) plays a significant role in cancer treatment by targeting several pathways involved in tumor development and progression. It induces differentiation of cancer cells, shifting them from an undifferentiated, proliferative state to a more mature and less aggressive phenotype. PPAR γ also inhibits cell proliferation by downregulating key cell cycle regulators such as cyclins and oncogenes, while promoting apoptosis through activation of pro-apoptotic pathways, including the modulation of the Bcl-2 family of proteins and caspases.¹⁰⁸

Furthermore, PPAR γ exerts anti-angiogenic effects by suppressing the expression of pro-angiogenic factors like VEGF, which are crucial for tumor vascularization. It also inhibits metastasis by regulating cell adhesion molecules (e.g., E-cadherin) and reducing the activity of matrix metalloproteinases (MMPs) involved in extracellular matrix degradation. Additionally, PPAR γ 's anti-inflammatory properties reduce the production

of inflammatory cytokines (e.g., TNF- α , IL-6), which are often linked to tumor growth and progression.¹⁰⁹

Studies on synthetic PPAR γ agonists, such as thiazolidinediones (e.g., rosiglitazone, pioglitazone), and natural ligands, such as polyunsaturated fatty acids, highlight their potential in cancer therapy. These agonists are often explored in combination with chemotherapy or targeted therapies to enhance anticancer efficacy and combat drug resistance. However, the role of PPAR γ in cancer can be context-dependent, with both pro- and anti-tumorigenic effects reported in different cancer types, emphasizing the importance of personalized therapeutic approaches.

2.1.2.2 Neurodegenerative Disorder

PPAR γ , a ligand-activated nuclear receptor, plays a significant role in mitigating neurodegenerative diseases such as Alzheimer's and Parkinson's by modulating inflammation, oxidative stress, and cellular metabolism.¹¹⁰ Activation of PPAR γ reduces neuroinflammation by inhibiting pro-inflammatory cytokines and microglial activation, which are key drivers of neuronal damage. It also helps to counteract oxidative stress by enhancing mitochondrial function and promoting antioxidant gene expression, critical for neuronal health. Despite these promising preclinical findings, clinical trials have faced challenges, as many PPAR γ agonists fail to effectively cross the blood-brain barrier (BBB), limiting their potential therapeutic benefits. For example, while early trials with rosiglitazone showed some promise in Alzheimer's patients, larger Phase II and III studies failed to demonstrate significant cognitive improvements, and the development of rosiglitazone for Alzheimer's treatment was discontinued.¹¹¹ Similarly, pioglitazone did not prevent cognitive decline or improve neuropsychiatric symptoms in Alzheimer's or Parkinson's patients. However, some ongoing trials are exploring more targeted approaches, such as gemfibrozil, a PPAR α agonist, which may offer therapeutic benefits for Alzheimer's disease by modulating biomarkers. Additionally, novel BBB-penetrant compounds like leriglitazone show potential for improving outcomes in central nervous system disorders. Natural compounds like flavonoids, curcumin, and genistein, which indirectly activate PPAR γ , also offer promising therapeutic avenues by modulating neuroinflammation and oxidative stress. These insights suggest that PPAR γ remains a potential therapeutic target for neurodegenerative conditions, but further research is required to optimize drug delivery and improve clinical efficacy.¹¹²

2.1.2.3 Diabetes

PPAR γ plays a central role in the pathophysiology and treatment of Type 2 Diabetes Mellitus (T2DM) by regulating key metabolic processes such as insulin sensitivity, glucose homeostasis, and lipid metabolism. As a nuclear receptor, PPAR γ activation increases the expression of genes involved in glucose uptake, particularly in adipose tissue and skeletal muscle, through enhancing the translocation of glucose transporter (GLUT4).¹¹³ This improves insulin sensitivity and helps to reduce insulin resistance, which is a hallmark of T2DM. Additionally, PPAR γ regulates adipogenesis, facilitating the differentiation of pre-adipocytes into mature adipocytes, thereby ensuring proper lipid storage and preventing ectopic fat accumulation in tissues like the liver and muscle, which can worsen insulin resistance. PPAR γ also exerts anti-inflammatory effects, inhibiting the production of pro-inflammatory cytokines (such as TNF- α and IL-6) and reducing the activation of macrophages in adipose tissue. This reduction in systemic inflammation helps to counteract one of the primary contributors to insulin resistance. The therapeutic potential of PPAR γ in diabetes is largely realized through the use of thiazolidinediones (TZDs) like rosiglitazone and pioglitazone, which act as PPAR γ agonists to improve glycemic control by enhancing insulin sensitivity. However, their use is limited by side effects such as weight gain, fluid retention, and potential cardiovascular risks, which has spurred research into more selective PPAR γ modulators (SPPARMs) that aim to retain the beneficial effects while minimizing adverse reactions.^{114,115} Additionally, novel strategies, such as dual agonists targeting both PPAR γ and PPAR α or PPAR δ , are being explored to further enhance metabolic regulation and provide broader therapeutic benefits for T2DM.

2.1.2.4 Obesity and Adipocyte differentiation

Adipogenesis is the process by which pre-adipocyte precursor cells differentiate into mature adipocytes capable of storing lipids and secreting hormones and cytokines. This process is regulated by several genes involved in lipid metabolism, such as aP2, PPCK, acyl-CoA synthase, and LPL, which are all controlled by PPAR γ .¹¹⁶ Additionally, PPAR γ influences the expression of proteins like CD36 and FATP-1, which are crucial for lipid uptake in adipocytes.¹¹⁷ These genes contain peroxisome proliferator response elements (PPREs) in their regulatory regions. The primary function of PPAR γ is to inhibit cell proliferation, promoting the differentiation into fully mature adipocytes. While PPAR γ

plays a central role in this process, other PPAR isoforms, such as PPAR α and PPAR β , are also involved in signaling pathways that support adipocyte differentiation. PPAR γ further affects lipase activity, contributing to fat reduction in the liver. Dysregulation of PPAR γ activity can lead to elevated plasma cholesterol levels and obesity.

2.1.2.5 Non-Alcoholic Fatty Liver Disease (NAFLD)

Non-alcoholic fatty liver disease (NAFLD) encompasses a range of conditions, from simple hepatosteatosis to more severe stages such as non-alcoholic steatohepatitis (NASH), fibrosis, and cirrhosis. Currently, there are no FDA-approved treatments for NAFLD, and management mainly focuses on lifestyle changes. Peroxisome proliferator-activated receptors (PPARs), key regulators of lipid metabolism and inflammation, are promising targets for therapeutic interventions. In particular, PPAR α agonists like fenofibrate and gemfibrozil have shown improvements in liver function, lipid profiles, and insulin sensitivity, but they have limited effects on histological outcomes and are associated with side effects, including kidney dysfunction.¹¹⁸ The use of selective PPAR α modulators, such as pemafibrate, is being explored to enhance clinical efficacy while minimizing adverse effects.¹¹⁹ Pioglitazone, a PPAR γ agonist, remains the only pharmacological therapy recognized for NASH, demonstrating improvements in hepatic lipid deposition and inflammation despite limited effects on fibrosis. Other PPAR agonists, like troglitazone and rosiglitazone, have shown only temporary benefits, and their use has been hindered by safety concerns. However, recent studies on dual- and pan-PPAR agonists, such as elafibranor, saroglitazar, and lobeglitazone, show promise in reducing liver fat, inflammation, and fibrosis in NAFLD and NASH.¹²⁰ These emerging therapies, especially dual and pan-PPAR agonists, may offer better efficacy and safety profiles, and ongoing trials will further assess their potential to address the unmet clinical needs in NAFLD treatment

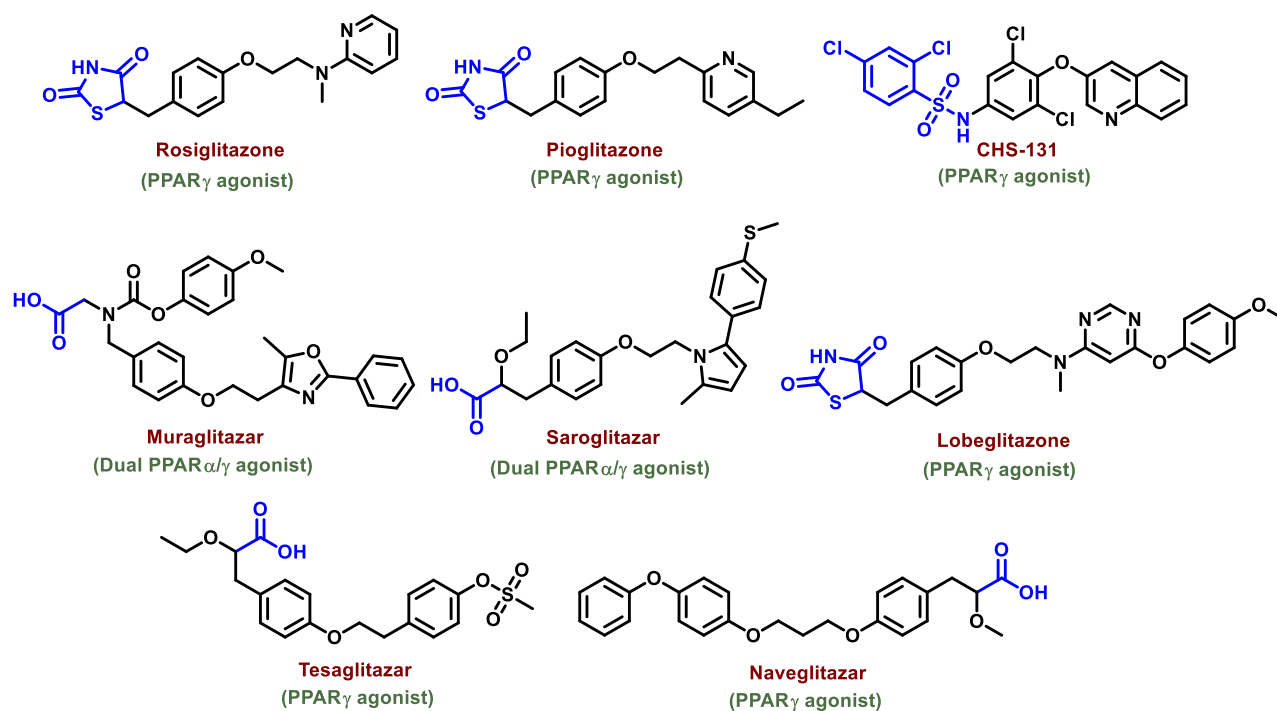


Figure 2. Examples of synthetic and natural PPAR γ and PPAR α/γ dual agonists

2.2 OBJECTIVE

PPAR γ is a pivotal therapeutic target in non-alcoholic fatty liver disease (NAFLD) due to its multifaceted roles in lipid metabolism, glucose homeostasis, and inflammation. By regulating genes involved in adipogenesis, PPAR γ promotes the storage of lipids in adipose tissue rather than in ectopic sites like the liver, effectively reducing hepatic lipid accumulation.¹²¹ This redistribution helps prevent lipotoxicity and subsequent liver damage, a hallmark of NAFLD. Moreover, PPAR γ enhances insulin sensitivity by increasing glucose uptake in peripheral tissues and suppressing hepatic gluconeogenesis, thereby addressing one of the central drivers of NAFLD progression—insulin resistance. Beyond its metabolic effects, PPAR γ exerts potent anti-inflammatory actions by inhibiting the nuclear factor-kappa B (NF- κ B) pathway, which is a key mediator of inflammation.¹²² This leads to a reduction in pro-inflammatory cytokines, such as TNF- α and IL-6, that contribute to the progression from simple steatosis to non-alcoholic steatohepatitis (NASH). Additionally, PPAR γ modulates hepatic stellate cell (HSC) activity, a critical process in fibrosis development. By deactivating HSCs and reducing extracellular matrix deposition, PPAR γ helps prevent the progression of NAFLD to advanced stages like cirrhosis.¹²³

PPAR γ controls ROS production by enhancing antioxidant defense mechanisms, improving mitochondrial function, and reducing oxidative stress, thereby protecting hepatocytes from toxicity.^{124,125} It upregulates antioxidant enzymes like superoxide dismutase and glutathione peroxidase, neutralizing ROS and preventing cellular damage. By improving mitochondrial fatty acid oxidation and inhibiting pro-inflammatory pathways such as NF- κ B, PPAR γ mitigates ROS-induced inflammation and apoptosis. These actions safeguard hepatocytes against oxidative stress and necrosis, which are pivotal in liver diseases like NAFLD.¹²⁶

Therapeutically, PPAR γ agonists reduce ROS levels and hepatocellular toxicity, making them valuable in managing oxidative stress-driven liver damage. Thus our primary objective was to develop novel small molecules that can activate PPAR γ to protect liver from ROS mediated hepatocellular dysfunction.

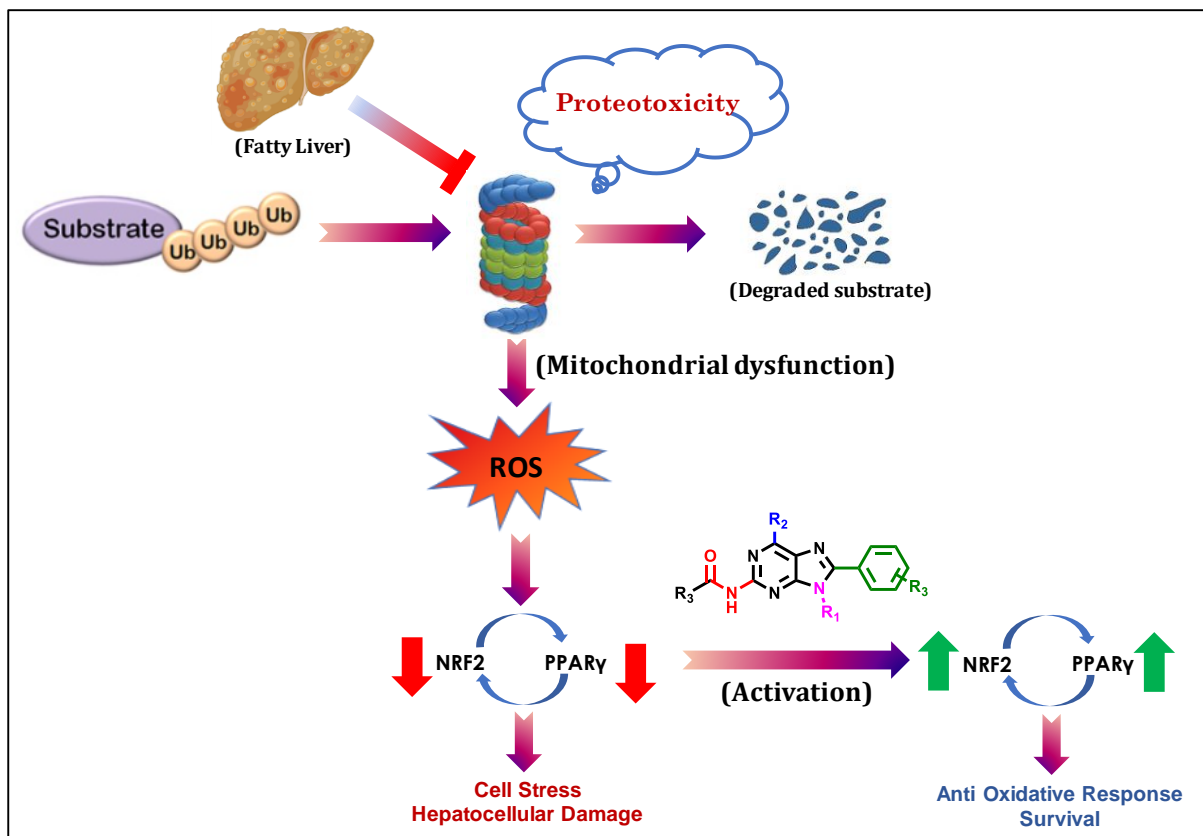


Figure 3. Harmful reactive oxygen species (ROS) generates through proteotoxicity occurred by mitochondrial dysfunction. As a result, downregulation of PPAR γ -NRF2 pathway occurs which can be elevated by small molecule PPAR γ agonist to reduce hepatocellular stress.

2.3 METHODOLOGY

2.3.1 Rational Design

Non-alcoholic steatohepatitis (NASH), the most severe form of non-alcoholic fatty liver disease (NAFLD), is a leading cause of chronic liver failure, driven primarily by oxidative stress and excessive production of reactive oxygen species (ROS). Peroxisome proliferator-activated receptors (PPARs) have emerged as critical regulators of liver metabolism, with PPAR γ demonstrating significant potential in alleviating cellular stress and reducing ROS levels. Therapeutically, PPAR γ agonists, including thiazolidinediones (TZDs) such as pioglitazone (ActosTM; Takeda Pharmaceuticals) and rosiglitazone (AvandiaTM; GlaxoSmithKline) have shown promise in improving liver histology, insulin sensitivity and metabolic parameters in NAFLD and NASH patients. These drugs also reduce hepatic steatosis and attenuate inflammation and fibrosis. However, while TZDs improve lipid profiles and adipokine regulation, their clinical utility is limited by adverse effects such as weight gain, fluid retention, cardiovascular risks, and, in some cases, hepatotoxicity and adipogenesis. Reports of edema, cardiomegaly, anemia, and hemodilution further compound these safety concerns.

We aim to rationally design and synthesize non-TZD-based pharmacophores that potently activate PPAR γ while minimizing adverse effects. A literature review revealed that the TZD group in known PPAR γ agonists, such as rosiglitazone and pioglitazone, as well as the carboxylic functionality in the dual PPAR α/γ agonist saroglitazar, serve as polar heads critical for substrate binding. These polar heads form a hydrogen-bonding network with the active site of the PPAR γ protein, which is essential for their activity.

Knowing the fact that purine scaffold is crucial in drug discovery due to its biological relevance, structural versatility, and its widespread use in developing therapeutics targeting enzymes, receptors, and nucleic acids, we started molecular library synthesis with purine core and investigated its PPAR γ agonism property. To retain the important pharmacological feature, we incorporated an amide linkage into purine-based derivatives, designed to mimic the polar head region and maintain the necessary interactions with the PPAR γ binding site (Figure 4).

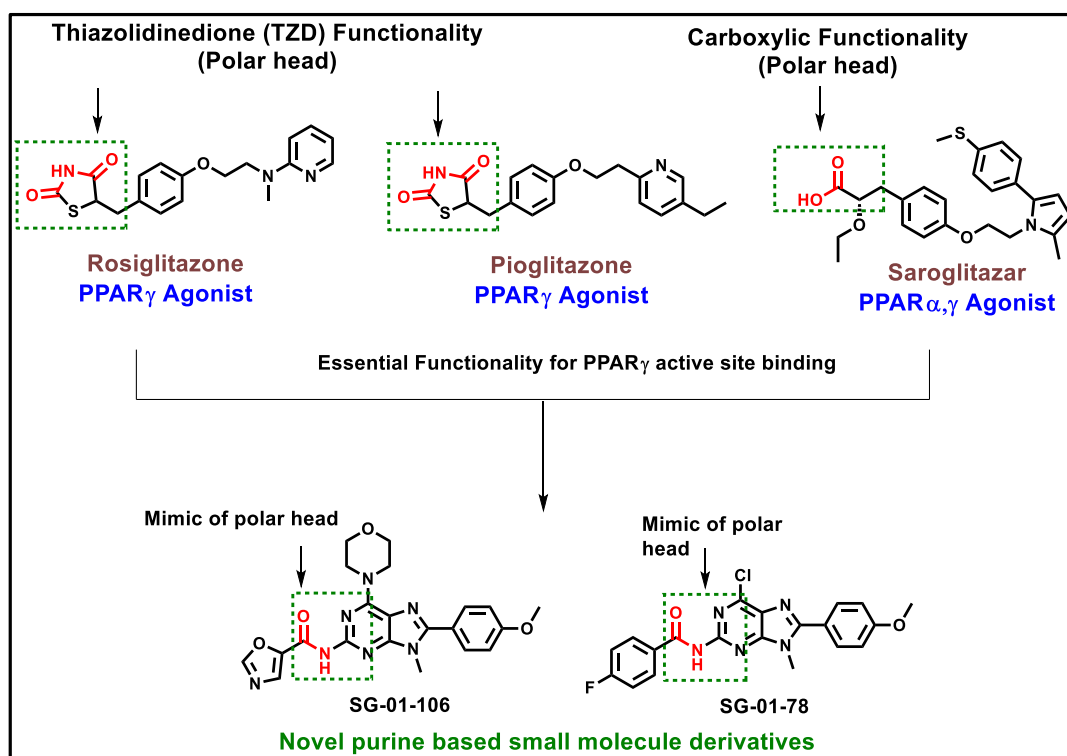


Figure 4. Rational design of non-TZD based pharmacophore as PPAR γ agonist

The co-crystal structure of PPAR γ in complex with known activator Rosiglitazone (PDB: 2PRG) reveals that Rosiglitazone is surrounded by Met 364, His 449, Tyr 473, His 323, Ser 289 at the binding site of PPAR γ and forming H-Bonds (green dashed) for stabilization. We hypothesized that our rationally designed purine-based pharmacophores could bind with the active site of PPAR γ protein, making similar kind of necessary interactions with the adjacent amino acids to act as a potent PPAR γ agonist.

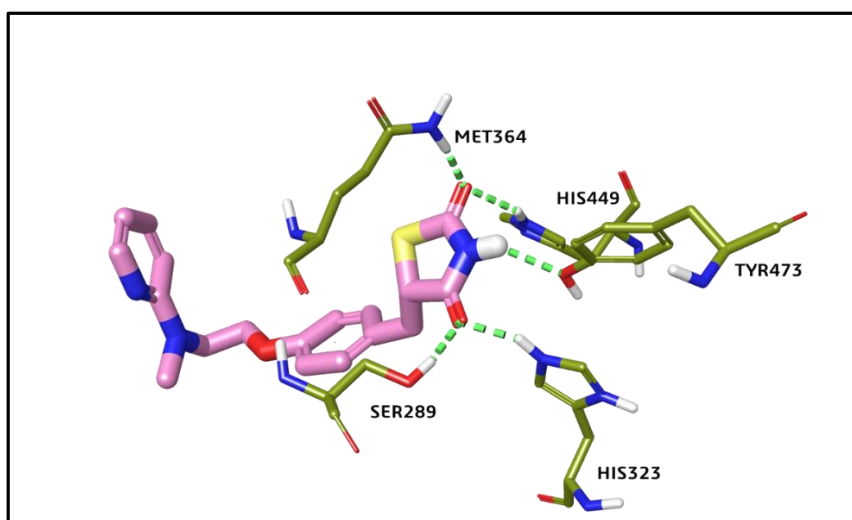
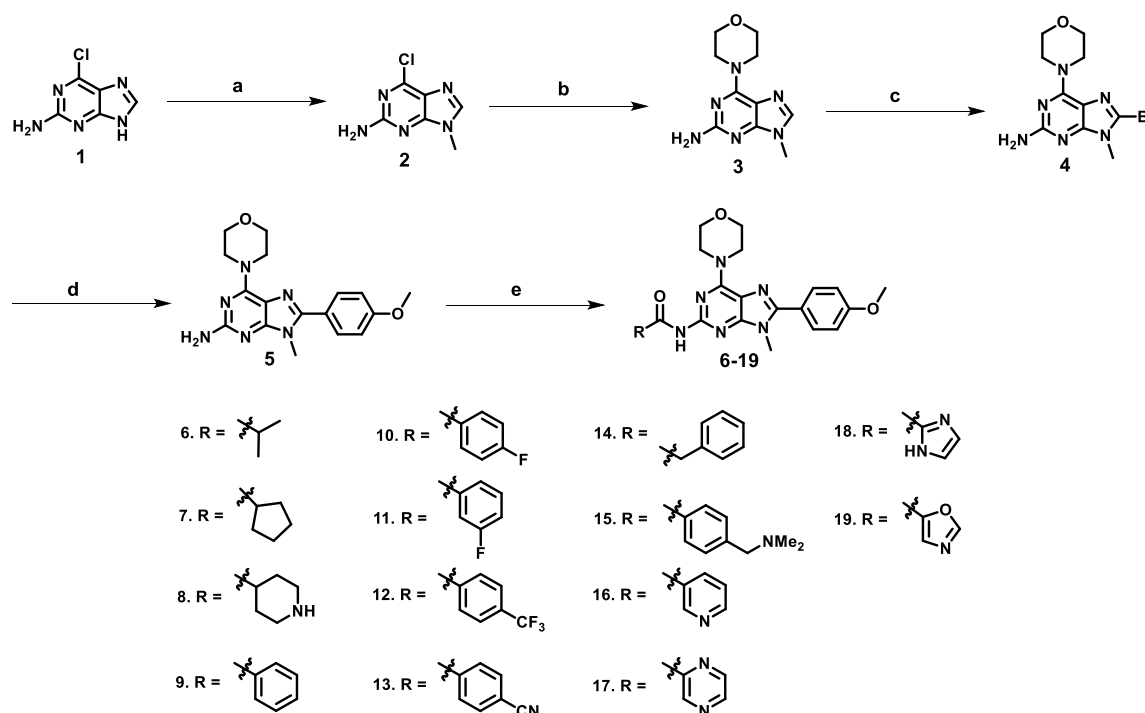


Figure 5. Co-crystal structure of PPAR γ with bound Rosiglitazone

2.3.2 Chemistry

Scheme 1 describes synthetic procedures, strategies and methods for the synthesis of purine analogues with modifications at the LHS position. Reaction strategies were started by methylation reaction of commercially available 2-Amino-6-chloropurine (**1**) by methyl iodide (CH_3I) (1.2 eqv) using K_2CO_3 (2 eqv) as base in dry DMF as a solvent at room temperature (25-30 °C) for 12-16 hours to afford **compound 2**. Reaction progress was monitored by checking TLC. Next, the C6 chloro (-Cl) group was substituted by morpholine group using K_2CO_3 (2 eqv) as base in dry ACN as a solvent at room temperature (25-30 °C) for 12-16 hours to afford **compound 3**. Bromination reaction of **compound 3** was carried out by using Bromine (1.2 eqv) in 2:1 mixture of 1,4-dioxane and 0.5 (M) NaOAc at room temperature (25-30 °C) for 6 hours to afford **compound 4**. Then, C-C cross-coupling reaction (Suzuki–Miyaura coupling) was carried out between the bromo derivative (**4**) and 4-methoxyphenylboronic acid (1.2 eqv) in presence of

Scheme 1^a:

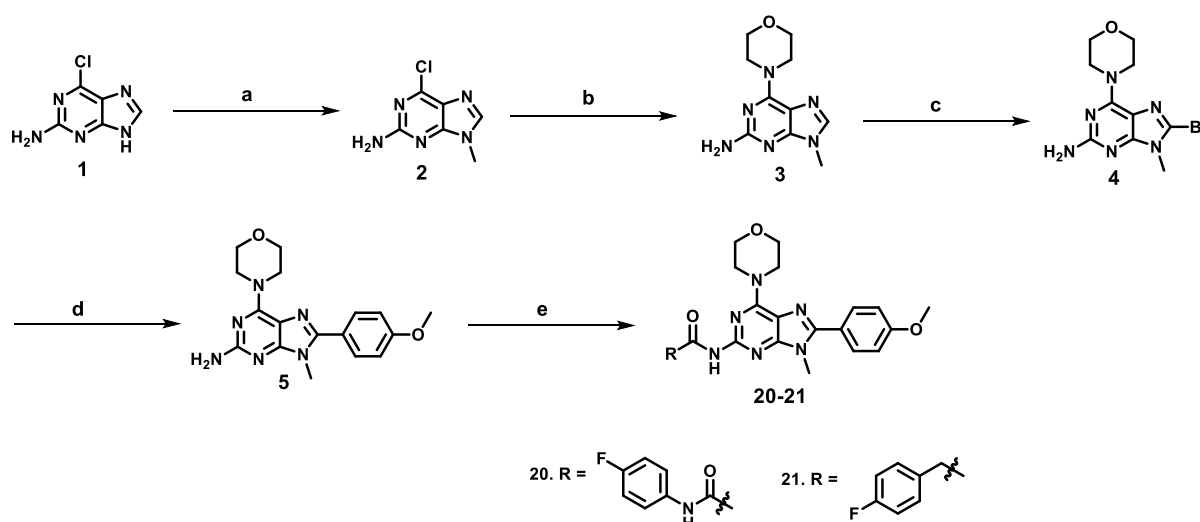


^aReagents and conditions: (a) K_2CO_3 (2 eqv), dry DMF, CH_3I (1.2 eqv), room temperature (25-30 °C), 12-16 h, (yield 75%); (b) K_2CO_3 (2 eqv), ACN, Morpholine (1.2 eqv), 90 °C, pressure tube, 2 h, (yield 80%); (c) Bromine (1.2 eqv), 1,4-dioxane, 0.5 (M) NaOAc, room temperature (25-30 °C), 6 h, (yield 72%); (d) 4-methoxyphenylboronic acid (1.2 eqv), $\text{Pd}(\text{PPh}_3)_4$ (0.1 eqv), dioxane/ H_2O (9:1), K_2CO_3 (2 eqv), 100-110 °C, 12-18 h, (yield 78%); (e) various aliphatic and aromatic acid chlorides (1.5 eqv), dry DCM, TEA (2 eqv), room temperature (25-30 °C), 12-16 h, (yield 50-60%)

$\text{Pd(PPh}_3)_4$ (0.1 eqv) as catalyst in dioxane/ H_2O (9:1 solvent ratio v/v) at 120 °C for 12–18 hours to get **compound 5**. In the next step the amide linkage was introduced by reacting **compound 5** with different commercially available aliphatic and aromatic acid chlorides (1.5 eqv) in dry DCM at room temperature (25–30 °C) for 2–3 hours to obtain compounds **6–19**.

In **scheme 2**, we introduced benzyl and urea linkages in place of amide linkage. **Compound 5** was reacted with 4-Fluorophenyl isocyanate in dry DCM using TEA as base at room temperature (25–30 °C) for 2–3 hours to obtain **compound 20**. Similarly, **compound 5** was reacted with 4-Fluorobenzyl bromide in dry DMF using NaH as base at room temperature (25–30 °C) for 2–3 hours to obtain **compound 21**.

Scheme 2^a:

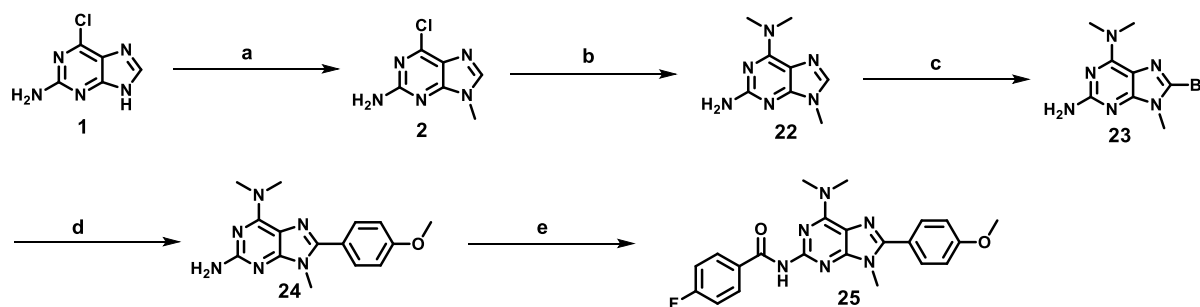


^aReagents and conditions: (a) K_2CO_3 (2 eqv), dry DMF, CH_3I (1.2 eqv), room temperature (25–30 °C), 12–16 h, (yield 75%); (b) K_2CO_3 (2 eqv), ACN, Morpholine (1.2 eqv), room temperature (25–30 °C), 12–16 h, (yield 80%); (c) Bromine (1.2 eqv), 1,4-dioxane, 0.5 (M) NaOAc, room temperature (25–30 °C), 6 h, (yield 72%); (d) 4-methoxyphenylboronic acid (1.2 eqv), $\text{Pd(PPh}_3)_4$ (0.1 eqv), dioxane/ H_2O (9:1), K_2CO_3 (2 eqv), 120 °C, 12–18 h, (yield 78%); (e) 4-Fluorophenyl isocyanate (1.2 eqv), dry DCM, TEA (2 eqv), room temperature (25–30 °C), 2 h, (yield 52%) for **compound 20**; 4-Fluorobenzyl bromide (1.2 eqv), NaH (1.2 eqv), Dry DMF, room temperature (25–30 °C), 2 h, (yield 56%) for **compound 21**.

In **scheme 3**, the C6 chloro (-Cl) group of **compound 2** was substituted by Dimethylamine group (1.2 eqv) using K_2CO_3 (2 eqv) as base in dry ACN as a solvent at room temperature (25–30 °C) for 12–16 hours to afford **compound 22**. Bromination reaction of **compound 22** was carried out by using Bromine (1.2 eqv) in 2:1 mixture of 1,4-dioxane and 0.5 (M) NaOAc at room temperature (25–30 °C) for 6 hours to afford **compound 23**. Then, C–C cross-coupling reaction (Suzuki–Miyaura coupling) was

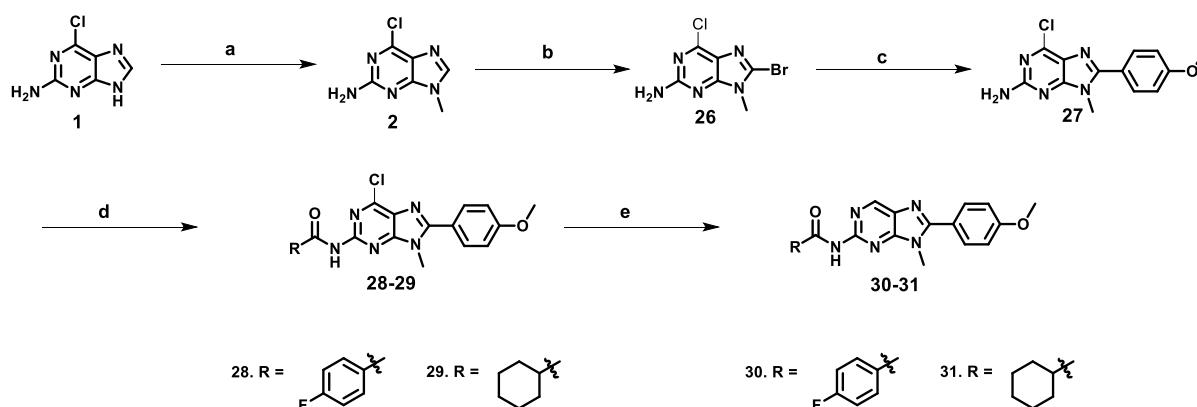
carried out between the bromo derivative (**23**) and 4-methoxyphenylboronic acid (1.2 eqv) in presence of $\text{Pd}(\text{PPh}_3)_4$ (0.1 eqv) as catalyst in dioxane/ H_2O (9:1 solvent ratio v/v) at 120 °C for 12–18 hours to get **compound 24**. In the next step, **Compound 24** was reacted with 4-fluorobenzoyl chloride (1.5 eqv) in dry DCM using TEA as base at room temperature (25–30 °C) for 2–3 hours to obtain **compound 25**.

Scheme 3^a:



^aReagents and conditions: (a) K_2CO_3 (2 eqv), dry DMF, CH_3I (1.2 eqv), room temperature (25–30 °C), 12–16 h, (yield 75%); (b) K_2CO_3 (2 eqv), ACN, Dimethylamine (1.2 eqv), room temperature (25–30 °C), 12–16 h, (yield 80%); (c) Bromine (1.2 eqv), 1,4-dioxane, 0.5 (M) NaOAc, room temperature (25–30 °C), 6 h, (yield 72%); (d) 4-methoxyphenylboronic acid (1.2 eqv), $\text{Pd}(\text{PPh}_3)_4$ (0.1 eqv), dioxane/ H_2O (9:1), K_2CO_3 (2 eqv), 120 °C, 12–18 h, (yield 78%); (e) 4-fluorobenzoyl chloride (1.5 eqv), dry DCM, TEA (2 eqv), room temperature (25–30 °C), 12–16 h, (yield 50–60%)

In **scheme 4**, **compound 2** was directly brominated by using Bromine (1.2 eqv) in 2:1 mixture of 1,4-dioxane and 0.5 (M) NaOAc at room temperature (25–30 °C) for 6 hours to afford **compound 26**. Suzuki coupling reaction between **compound 26** and 4-methoxyphenylboronic acid (1.2 eqv) was performed in presence of $\text{Pd}(\text{PPh}_3)_4$ (0.1 eqv) as catalyst in dioxane/ H_2O (9:1 solvent ratio v/v) at 120 °C for 12–18 hours to get **compound 27**. Next, **compound 27** was reacted with 4-fluorobenzoyl chloride (1.5 eqv) and Cyclohexanecarbonyl chloride (1.5 eqv) to yield compounds **28** and **29** respectively. Dechlorination reaction of **28** and **29** was performed by using H_2 / Pd-C in MeOH at room temperature (25–30 °C) for 3–4 hours to get compounds **30** and **31**.

Scheme 4^a:

^aReagents and conditions: (a) K_2CO_3 (2 eqv), dry DMF, CH_3I (1.2 eqv), room temperature (25–30 °C), 12–16 h, (yield 75%); (b) Bromine (1.2 eqv), 1,4-dioxane, 0.5 (M) NaOAc, room temperature (25–30 °C), 6 h, (yield 72%); (c) 4-methoxyphenylboronic acid (1.2 eqv), $Pd(PPh_3)_4$ (0.1 eqv), dioxane/ H_2O (9:1), K_2CO_3 (2 eqv), 120 °C, 12–18 h, (yield 78%); (d) various aliphatic and aromatic acid chlorides (1.5 eqv), dry DCM, TEA (2 eqv), room temperature (25–30 °C), 12–16 h, (yield 50–60%) (e) H_2 / Pd-C, MeOH, room temperature (25–30 °C), 4 h, (yield 52%).

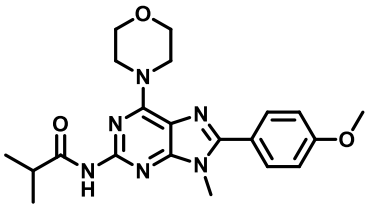
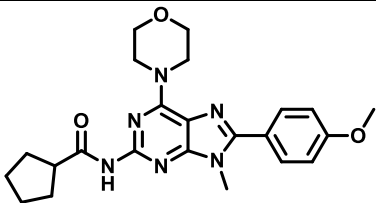
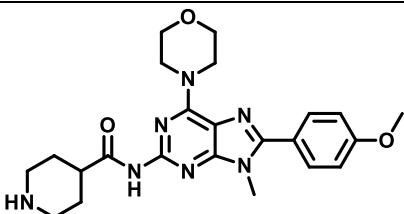
2.4 RESULTS AND DISCUSSION

In this study, we focused on optimizing purine-based derivatives to develop highly potent PPAR γ agonists through structure-activity relationship (SAR) studies and molecular docking analysis. PPAR γ interacts reciprocally with NRF2, a key regulator of the cellular antioxidant response, which governs the expression of critical antioxidant and detoxification enzymes such as superoxide dismutase (SOD) and NAD(P)H dehydrogenase [quinone] 1 (NQO1). To identify potential lead compounds, we evaluated their ability to enhance NRF2 expression under conditions of proteotoxic stress induced by the proteasomal inhibitor MG132 at concentrations of 10 μ M and 20 μ M. MG132, a broad-spectrum proteasome inhibitor, was used to induce proteotoxicity in the HepG2 hepatocellular carcinoma cell line. Both PPAR γ and NRF2, known for their antioxidant roles, are autoactivated in response to such stress, working to mitigate ROS levels and protect cells. Notably, PPAR γ acts as a transcription factor that modulates antioxidant responses via NRF2 activation, creating a bidirectional regulatory mechanism. Compounds that enhance NRF2 expression through PPAR γ -mediated antioxidant pathways in the presence of MG132 may help counteract proteotoxicity and reduce ROS-induced cellular damage. To validate the activity of the compounds, we performed immunoblotting (Western blot) to assess NRF2 expression levels, followed by densitometric analysis to confirm the profiles of the tested compounds. This approach allowed us to identify promising candidates with potential therapeutic effects against oxidative stress-related hepatocellular damage.

2.4.1 SAR development

First batch of derivatives were prepared where aliphatic substitutions were coupled with **compound 5** via amide linkage. At first a small isopropyl group was attached to prepare **compound 6** and checked for its ability to enhance NRF2 expression. **Compound 6** could not express NRF2 enhancement in western blot analysis data. Next, cyclopentyl and piperidine moieties were incorporated in place of isopropyl group in **compound 7** and **8** and checked their agonistic potential. But both of them did not show any significant NRF2 enhancement.

Table 1. Activity chart based on western blot analysis

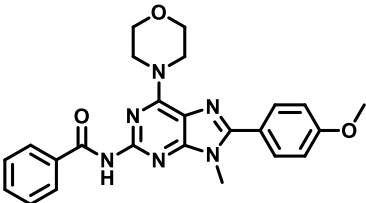
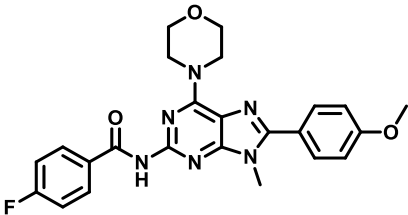
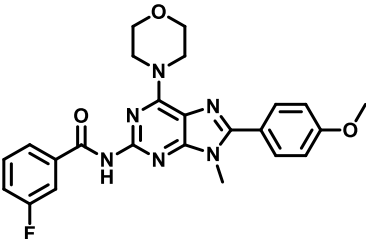
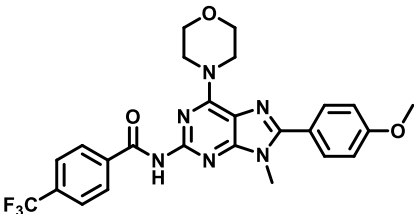
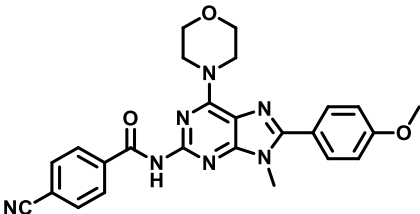
Compound	Structure	NRF2 expression ^a
6		—
7		—
8		—

^aActivity profile: '—', not active; '+', moderately active; '++', best active. NRF2 expression was checked through western blot analysis in presence of MG132. Compound concentration was 10 μ M.

Next batch of compounds were prepared by introducing aromatic substituents in **compound 5** through amide connectivity. **Compound 9** with unsubstituted phenyl ring showed moderate activity in enhancing NRF2 expression. Then a small Fluoro (-F) group was introduced at the C4 position of the phenyl ring of **Compound 9** to synthesise **compound 10**. It showed remarkable enhancement of NRF2 expression.

To determine the positional importance of the fluoro (-F) group, we shifted its position from C4 to C3 position of the phenyl ring to synthesise **compound 11**. Western blot analysis showed moderate activation of NRF2 upon using **compound 11**. Next, to find out the effect of bulkier substitutions **compound 12** with trifluoromethyl (-CF₃) and **compound 13** with cyano (-CN) groups were synthesised and checked their agonistic potential. Both of them did not show any significant NRF2 enhancement.

Table 2. Activity chart based on western blot analysis

Compound	Structure	NRF2 expression ^a
9		+
10		++
11		+
12		—
13		—

^aActivity profile: '—', not active; '+', moderately active; '++', best active. NRF2 expression was checked through western blot analysis in presence of MG132. Compound concentration was 10 μ M.

To ascertain the chemical space at LHS position of **compound 9** a methylene spacer was introduced and **compound 14** was synthesised. It showed moderate NRF2 activation. **Compound 15** was prepared with CH₂-NMe₂ group which did not show any activity. Thus a larger group at LHS is not well tolerated.

Table 3. Activity chart based on western blot analysis

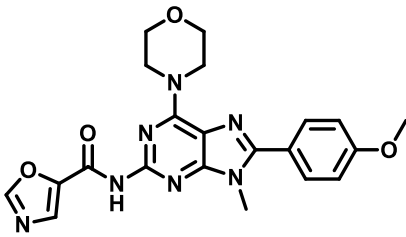
Compound	Structure	NRF2 expression ^a
14		+
15		—

^aActivity profile: '—', not active; '+', moderately active; '++', best active. NRF2 expression was checked through western blot analysis in presence of MG132. Compound concentration was 10 μ M.

Next, we focused on introducing some aromatic heterocyclic groups in place of phenyl ring. Thus, **compound 16** with pyridine, **compound 17** with pyrazine, **compound 18** with imidazole and **compound 19** with oxazole ring were synthesised. Among them only **compound 19** showed moderate NRF2 expression.

Table 4. Activity chart based on western blot analysis

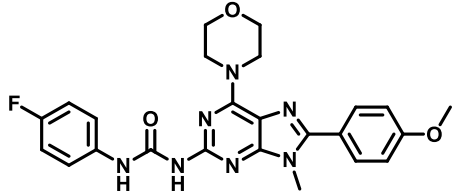
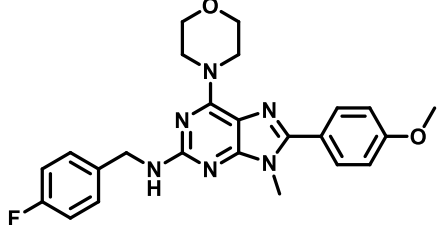
Compound	Structure	NRF2 expression ^a
16		—
17		—
18		—

Compound	Structure	NRF2 expression ^a
19		+

^aActivity profile: '-', not active; '+', moderately active; '++', best active. NRF2 expression was checked through western blot analysis in presence of MG132. Compound concentration was 10 μ M.

Since only **compound 10** has shown prominent NRF2 activity so far, we next synthesized two derivatives, **compound 20** and **compound 21**, incorporating urea and benzyl linkages, respectively, in place of the amide linkage in **compound 10**. Unfortunately, none of the synthesized derivatives altered NRF2 levels compared to the control group. This result highlights the importance of the amide linkage over other possible coupling strategies in maintaining or enhancing NRF2 activity.

Table 5. Activity chart based on western blot analysis

Compound	Structure	NRF2 expression ^a
20		—
21		—

^aActivity profile: '-', not active; '+', moderately active; '++', best active. NRF2 expression was checked through western blot analysis in presence of MG132. Compound concentration was 10 μ M.

In the next stage of optimization, we focused our attention on the C6 position of the purine core, keeping other essential features constant. At first a small functional group – NMe₂ was introduced in place of morpholine ring in **compound 25**. It did not show any enhancement in NRF2 expression. Next, a small chloro (-Cl) group was attached at C6 position in **compound 28** and checked its agonistic potential. To our delight, **compound 28** showed very prominent NRF2 band intensity with respect to control. The in vitro

ADME profile of **compound 28** demonstrated moderate aqueous solubility of 3.52 µg/mL at pH 7.4 (Table 7) with better plasma stability in human (85.93% remaining after 2 hours) (Table 8) and liver microsomal stability (human CL_{int}: 23.44 µL/min/mg protein, half-life: 73.93 min) which imparts suitable druglike properties in the compound. To investigate further the importance of aromatic 4-fluorophenyl group at LHS in **compound 28** we substituted it with an aliphatic cyclohexyl group and synthesised **compound 29** which failed to activate NRF2 expression. Later the deschloro derivative (**30**) of **compound 28** was prepared which also showed outstanding NRF2 expression. **Compound 30** demonstrated moderate aqueous solubility (4.17 µg/mL at pH 7.4, Table 7) alongside enhanced stability in human plasma, with 96.58% remaining intact after 2 hours (Table 8). **Table 6.** Activity chart based on western blot analysis

Table 6. Activity chart based on western blot analysis

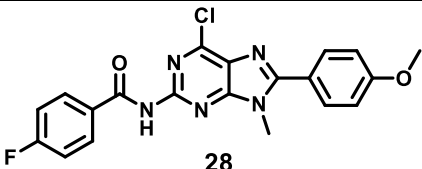
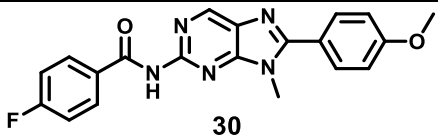
Compound	Structure	NRF2 expression ^a
25		—
28		++
29		—
30		++
31		—

^aActivity profile: '—', not active; '+', moderately active; '++', best active. NRF2 expression was checked through western blot analysis in presence of MG132. Compound concentration was 10 µM.

It also exhibited favorable liver microsomal stability, characterized by a low intrinsic clearance rate (CL_{int}: 8.05 μ L/min/mg protein) and an extended half-life of 236.23 minutes. These properties establish **compound 30** as a promising lead candidate for further development.

But the deschloro derivative (**31**) of **compound 29** was found inactive which suggests that the aromatic 4-fluorophenyl group at LHS plays a key role in imposing agonistic property.

Table 7. *in-vitro* ADME studies for synthesized compounds (Log D and Aq. Solubility)

Compound	PSA ^a (Å ²)	LogD	Aq. solubility pH : 7.4 (μ g / mL)
 28	78.65	3.39	3.52
 30	78.65	2.82	4.17
Ketoconazole ^b	—	3.54	—
Metoprolol ^c	—	-0.28	—
Propanolol ^d	—	0.84	—
Albendazole ^e	—	—	2.2

^aPolar surface area.

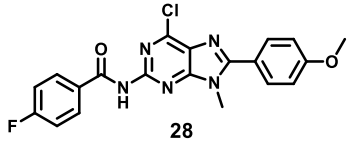
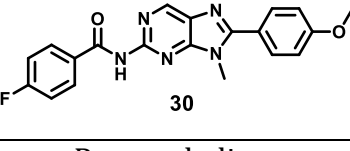
^bKetoconazole was taken as standard for logD determination.

^cMetoprolol was taken as standard for logD determination.

^dPropanolol was taken as standard for logD determination.

^eAlbendazole was taken as standard for the aqueous solubility test.

Table 8. *in-vitro* ADME studies for synthesized compounds (Plasma stability and metabolic stability)

Compound	Human Plasma Stability ^f	Human Metabolic Stability	
		CL int protein (μL/min/mg)	Half-life (min)
 28	85.93	23.44	73.93
 30	96.58	8.05	236.2
Propantheline ^g	0.0	—	—
Verapamil ^h	—	248.5	2.8

^fMean% remaining after 2 h^gPropantheline was taken as standard for human and mice plasma stability experiments.^hVerapamil was taken as standard for metabolic stability experiments in both humans and mice

2.4.2 Biological Discussion

2.4.2.1 Confocal Microscopy Studies

MG132, also known as carbobenzoxy-L-leucyl-L-leucyl-L-leucinal, is a potent, reversible, and cell-permeable proteasome inhibitor commonly used to induce cellular stress responses, such as the unfolded protein response (UPR) and oxidative stress. These properties make it a valuable tool for investigating pathways involved in managing proteotoxicity. To evaluate the ability of the synthesized active compounds (**28**, **30**, and **19**) to mitigate MG132-induced reactive oxygen species (ROS) production, a CellROX assay was performed. Treatment of HepG2 cells with MG132 induces significant cellular stress, resulting in elevated ROS levels that can compromise cell viability. In the assay, blue dots represent the nuclei of HepG2 cells, while red dots indicate ROS accumulation caused by MG132-induced stress (Figure 5). Following MG132 treatment, a marked increase in ROS generation (red dots) was observed. However, cells treated with rosiglitazone, a known PPAR γ activator, showed a clear reduction in ROS accumulation, demonstrating its ability to counteract oxidative stress. Similarly, when MG132-challenged HepG2 cells were treated with the synthesized active compounds (**28**, **30**, and

19), a significant reduction in ROS production was observed, as evidenced by fewer red dots. These findings from confocal microscopy experiments demonstrate the potential of our synthesized PPAR γ activators to effectively reduce ROS accumulation and alleviate oxidative stress in HepG2 cells.

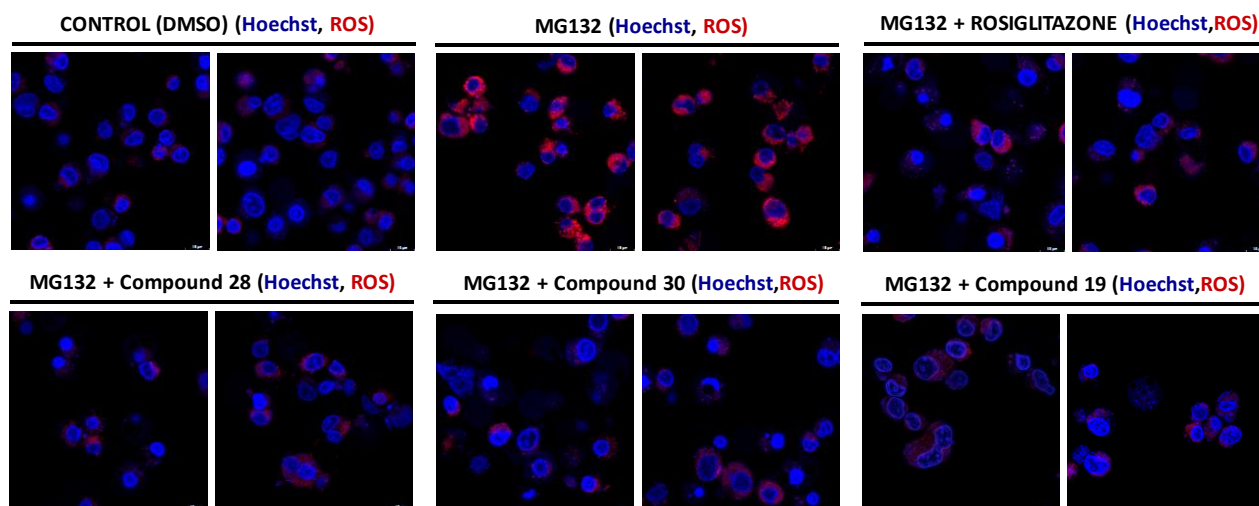


Figure 6. Images of HepG2 cells for ROS (Reactive Oxygen Species) detection upon treatment with DMSO in Control well, MG132, MG132 with Rosiglitazone and MG132 along with **Compounds 28, 30 and 19** treatment using confocal microscopy.

2.4.2.2 qPCR Studies for gene expression

PPAR γ helps control cellular stress by activating NRF2, a master regulator of the antioxidant response. NRF2 enhances the expression of various antioxidant and detoxification enzymes, such as superoxide dismutase (SOD) and NAD(P)H dehydrogenase [quinone] 1 (NQO1), which work to neutralize reactive oxygen species (ROS) and protect cells from oxidative damage. Through this regulatory interplay, PPAR γ plays a crucial role in maintaining cellular redox balance and reducing stress-induced damage. To evaluate the selectivity of our synthesized derivatives in pan PPAR family a qPCR study was conducted to find out the gene expression PPAR α , PPAR δ and PPAR γ and its downstream target genes in HepG2 cells after treatment with DMSO in Control well, MG132, MG132 with Rosiglitazone and MG132 along with active compounds. It was observed that expression of PPAR γ and its downstream genes such as NRF2, NQO1 and SOD1 was elevated prominently than PPAR α and PPAR δ and their downstream genes which suggests the selectivity of our synthesized derivatives (**Compound 10, 19, 28, 30**) towards PPAR γ (Figure 6).

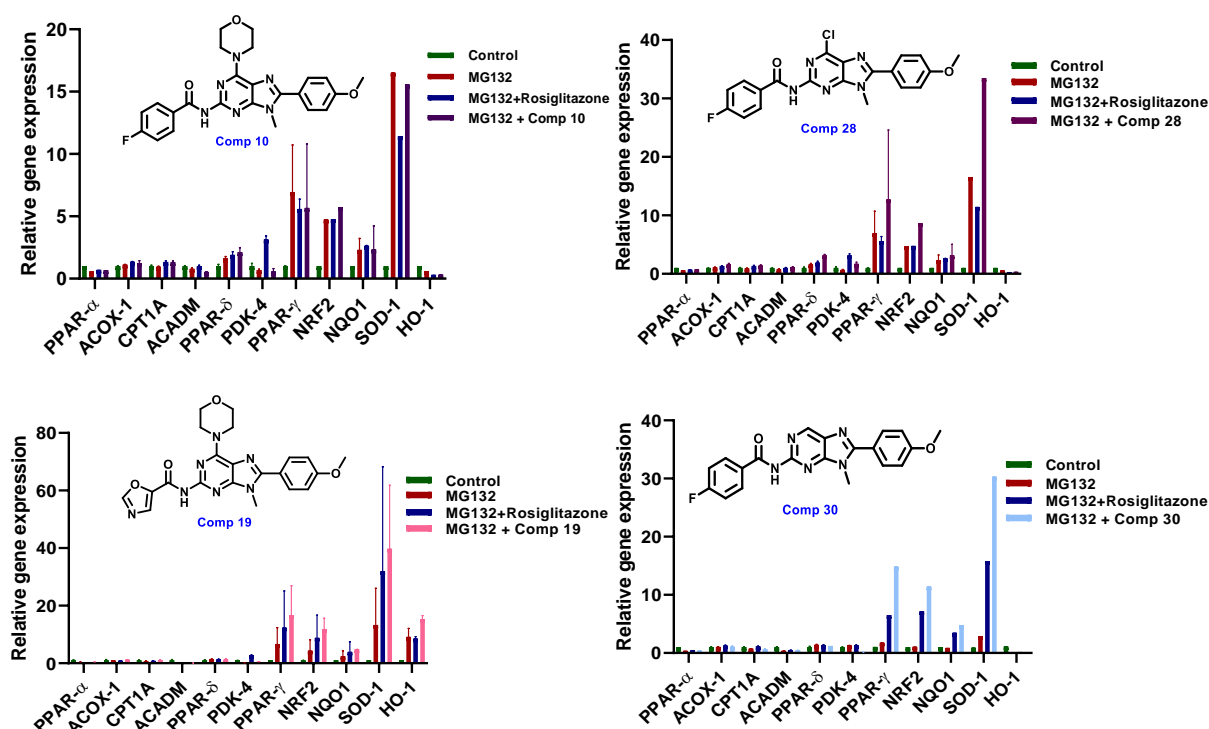


Figure 7. qPCR analysis data of PPAR α , PPAR δ and PPAR γ and its downstream target genes in HepG2 cells after treatment with DMSO in Control well, MG132, MG132 with Rosiglitazone and MG132 along with active compounds (10, 19, 28, 30).

2.4.2.3 Cellular thermal shift assay

The Cellular Thermal Shift Assay (CETSA) is a biophysical method used to study protein stability and ligand binding in live cells, lysates, or tissues. It works on the principle that ligand binding alters a protein's thermal stability, which can be measured by heating samples to different temperatures and analysing the soluble fraction of proteins post-heating. CETSA has gained importance in drug discovery for confirming drug-target engagement under physiological conditions, thereby ensuring the compound binds specifically to its intended target. Beyond drug validation, it provides insights into protein dynamics, signalling pathways, and cellular stress responses. This method is particularly useful for identifying resistance mechanisms, optimizing lead compounds, and understanding protein interactions in complex cellular environments. CETSA's ability to monitor protein behaviour in its native setting makes it a powerful tool in both basic and translational research, enabling the development of more effective and targeted therapies.

To determine the binding affinity of our synthesised PPAR γ agonists with PPAR γ protein cellular thermal shift assay (CETSA) was performed. Upon compound treatment in HepG2 cell lysate the critical melting point temperature of PPAR γ protein increased in comparison with vehicle control. This experiment suggests that due to protein (PPAR γ)-ligand (compound) binding thermal stability is increased.

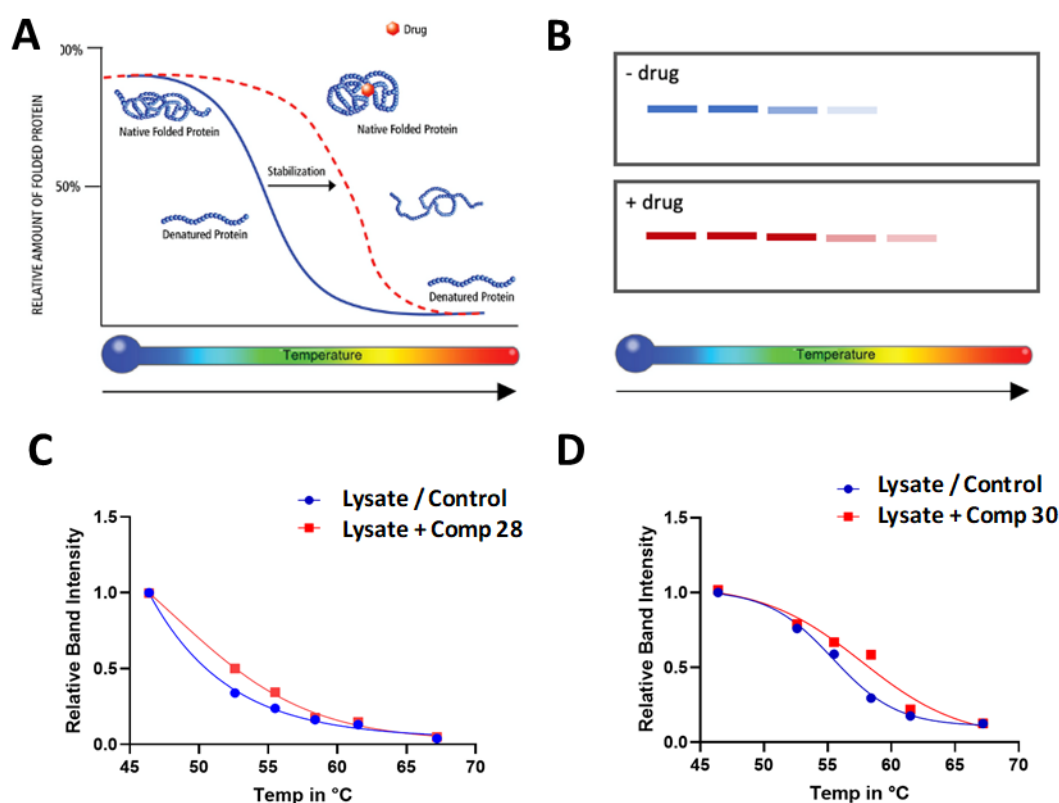


Figure 8. Overview of CETSA experiment. **(A)** Native folded proteins (blue solid line) denature at lower temperatures than native folded proteins associated with drug (red dotted line). **(B)** The results of the CETSA assay are visualized by identifying the presence of native folded protein after heat treatment. Bands indicate that native folded protein is present at the temperature tested. **(C)** and **(D)** Graphical representation of CETSA of Compounds **28** and **30** in HepG2 cells at various temperature points between 45°C to 70°C.

2.4.2.4 Half maximal effective concentration (EC₅₀) determination

A dose-response study was performed using the PPAR γ Transcription Factor Assay Kit to evaluate the half-maximal effective concentration (EC₅₀) of synthesized compounds. **Compound 28** exhibited an EC₅₀ value of 886.3 nM, while **Compound 30** demonstrated superior potency with an EC₅₀ of 214.6 nM. Notably, **Compound 30** outperformed the known PPAR γ agonist rosiglitazone, which has an EC₅₀ value of 257.3 nM. These results highlight **Compound 30** as a promising candidate for further development as a PPAR γ agonist with enhanced activity.

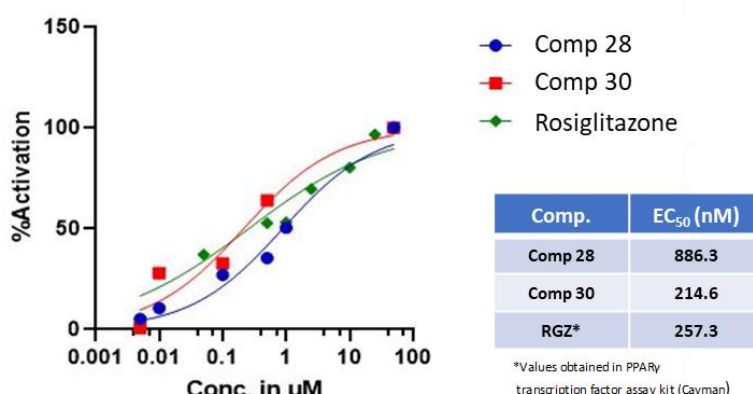


Figure 9. Graphical representation of EC₅₀ (Half maximal effective concentration) of Compounds **28** (886.3 nM) and **30** (214.6 nM) in HepG2 cells at various doses.

All the biological studies and their graphical representation were conducted by Sujay Krishna Maity from Dr. Partha Chakrabarti's lab, CSIR - IICB.

2.4.3 Molecular Docking

The lead compound demonstrated a strong ability to activate PPAR γ -NRF2 pathway to control ROS production and thereby can reduce ROS-mediated hepatotoxicity. To further understand its mechanism, molecular docking studies were conducted to evaluate its potential interaction with the binding site of PPAR γ protein. We selected the a X-ray crystallographic structure of PPAR γ (PDB: 2PRG), co-crystallized with Rosiglitazone. **Compound 30** was chosen as a representative and was subjected to dock against the receptor protein, in the same binding site, that of rosiglitazone. The protein and ligand were separately prepared at pH 7.4 before proceeding for docking. CDOCKER module of Biovia Discovery Studio was employed for the task, using CHARMM forcefield. The pose-clustering radius was set to 0.1 Å, starting with 10 random conformations followed by

heating-cooling dynamics for pose generation. The suitable and plausible binding pose for **compound 30** was identified, where the fluorophenyl part of the ligand occupied a hydrophobic cavity of PPAR γ , interacting with Gln286, via a fluorine-mediated H-bond (Figure 8A). The solvent exposed methoxy part also is showing H-bond interaction with Glu343. The overall pharmacophore is stabilised by these two hydrogen bonds, from both ends of the molecule. An additional amide- π interaction with Cys285 holds further strengthens the binding.

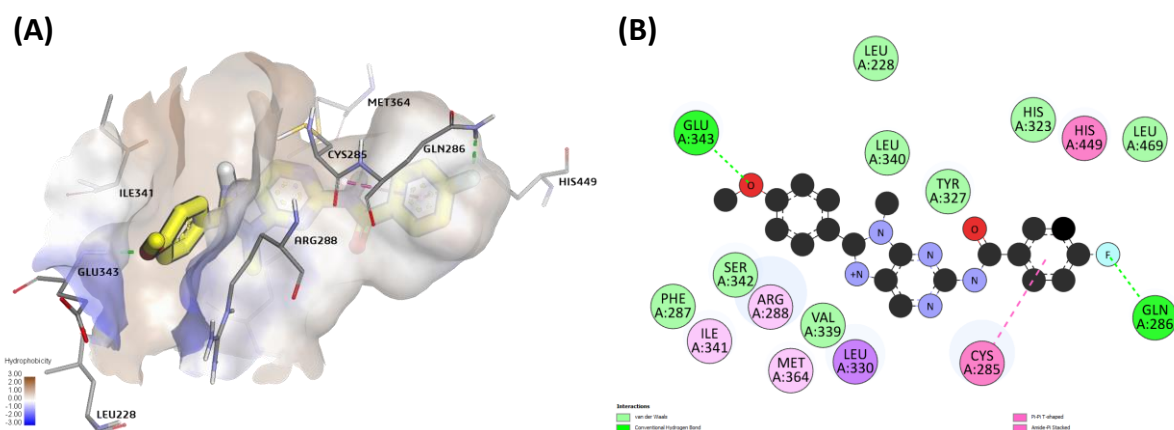


Figure 10. Molecular docking of the lead compound (**compound 30**) in the active site of PPAR γ protein. **A.** Binding interaction of **compound 30** with PPAR γ . The surface view of the receptor protein is represented in brown, **compound 30** in light yellow and interacting residues in thin grey sticks. **B.** The 2-dimensional representation of the interaction. The green and magenta dotted lines represent hydrogen bonds and amide- π interactions respectively.

2.5 CONCLUSION AND OUTCOME

Non-alcoholic steatohepatitis (NASH), the most severe manifestation of non-alcoholic fatty liver disease (NAFLD), is a key driver of chronic liver failure, predominantly caused by oxidative stress and elevated reactive oxygen species (ROS) levels. PPAR γ (peroxisome proliferator-activated receptor gamma) plays a crucial role in controlling ROS levels by regulating the expression of antioxidant enzymes and modulating oxidative stress pathways. In diseased condition, due to the mitochondrial dysfunction excess ROS accumulation takes place in hepatocytes which in turn downregulate the PPAR γ -NRF2 pathway and as a result, cell stress and hepatocellular damage occurs. Thiazolidinediones (TZDs) have shown significant potential as PPAR γ activators; however, their clinical application is restricted by severe adverse effects. Our study underscores the synthesis and systematic development of a novel purine-based chemotype designed to bind effectively to the active site of the PPAR γ protein, activating the PPAR γ -NRF2 pathway and mitigating ROS-induced hepatocellular dysfunction. Our synthesised **compounds 19, 28 and 30** significantly reduced ROS production as observed in CellRox kit assay (Figure 5). These compounds are selective towards PPAR γ as they elevated only the expression of PPAR γ and its downstream genes such as NRF2, NQO1 and SOD1 (Figure 6). The binding affinity of **compound 28 and 30** with PPAR γ protein was established by cellular thermal shift assay (CETSA) experiment. The critical melting point temperature of PPAR γ protein increased upon compound binding (Figure 7). In PPAR γ Transcription Factor Kit assay revealed the half-maximal effective concentration (EC₅₀) of **compound 30** as 214.6 nM which better than that of marketed known PPAR γ activator rosiglitazone (EC₅₀ = 257.3 nM) (Figure 7). Hence, as a nutshell, we have successfully synthesised purine scaffold based small molecule PPAR γ activators which have potential to ameliorate ROS induce hepatocellular proteotoxicity.

2.6 EXPERIMENTAL SECTION

General methods

All starting materials, reagents, and solvents were purchased from commercial suppliers and used without further purification. Dry solvents were either commercially purchased or dried using a standard protocol. Reactions that had a sensitivity toward moisture or oxygen were carried out under a dry nitrogen or argon atmosphere. All the TLC experiments were performed on silica gel plates (Merck silica gel 60, F254). The spots were visualized under UV light ($\lambda = 254$ and 365 nm) or by using the appropriate stain. Compounds were purified using a Teledyne ISCO CombiFlash Rf system using a 230–400 mesh size silica gel. ^1H NMR was recorded at 300 MHz (Bruker-DPX), 400 MHz (JEOL), and 600 MHz (Bruker AVANCE) frequencies, and ^{13}C NMR spectra were recorded at 75 MHz (Bruker-DPX), 100 MHz (JEOL), and 150 MHz (Bruker AVANCE) frequencies in CDCl_3 or CD_3OD or d_6 -DMSO using tetramethylsilane as the internal standard. The following abbreviations were used to explain multiplicities: s = singlet, d = doublet, t = triplet, q = quartet, m = multiplet, brs. = broad singlet. The coupling constant, J, was reported in the Hertz unit (Hz). High-resolution mass spectroscopy, HRMS (m/z), was carried out using ESI (Q-ToF Micro mass spectrometer), and ESI (LTQ Orbitrap XL mass spectrometer). The purity of all the compounds was determined to be >95%, analyzed using an Agilent Infinity Prep. HPLC system using a BioSuite Phenyl reverse-phase column (75×7.5 mm, $10 \mu\text{m}$ particle size, 1000 \AA pore size). Mobile phase A was composed of 0.1% TFA in water and mobile phase B of 10% water in acetonitrile for 4–6 min and a flow rate of 1 mL/min with detection at 254 nm wavelengths.

General Procedure A: Amide formation reaction

Compound **5** (1 mmol) was taken in dry DCM (2 mL) and TEA (2 mmol) was added and reaction mixture was allowed to stir at room temperature for 15 mins keeping nitrogen atmosphere. Then suitable aromatic or aliphatic acid chloride (1.5 mmol) was added drop wise in the reaction mixture at ice cold condition and stirred for another 30 mins at room temperature. Reaction was monitored by checking TLC. After completion, workup was done with water and ethyl acetate and then organic layer was evaporated. Column chromatography was performed to get the pure product.

Synthesis of 6-chloro-9-methyl-9H-purin-2-amine (2): 2-amino-6-chloropurine **1** (5gm, 29.48 mmol) was taken in dry DMF (30mL) and K₂CO₃ (8.13gm, 58.96 mmol) was added. Then the reaction mixture was stirred in room temperature for 30 mins keeping nitrogen atmosphere. Next, MeI (1.83 mL, 29.48 mmole) was added dropwise at 0 °C temperature and the reaction mixture was allowed to stir at room temperature for 12-16 hours. After completion of the reaction solvent was evaporated in reduced pressure and the product was purified by column chromatography (Silica gel, mesh size 100-200) eluting (5% MeOH/ CHCl₃) to obtain compound **2** (3.7gm, 70%) as off white solid. ¹H NMR (400 MHz, d₆-DMSO) δ in ppm 8.04 (s, 1H), 7.66 (s, 2H), 3.64 (s, 3H). ¹³C NMR (100 MHz, d₆-DMSO) δ in ppm 157.22, 153.42, 151.47, 142.54, 118.20, 30.10. HRMS (ESI) *m/z* (M + H)⁺ calculated for C₆H₆ClN₅ 184.0390; found, 184.0395. Melting point: 168 °C.

Synthesis of 9-methyl-6-morpholino-9H-purin-2-amine (3): Compound **2** (2gm, 10.92 mmol), K₂CO₃ (3.01gm, 21.85 mmol) and morpholine (8.82mL, 100.9mmol) were taken in a pressure tube and stirred at 90 °C temperature for 2hrs. After completion of the reaction solvent was evaporated in reduced pressure and the product was purified by column chromatography (Silica gel, mesh size 100-200) eluting (3% MeOH/ CHCl₃) to obtain compound **3** (1.58gm, 80%) as off white solid. ¹H NMR (300 MHz, d₆-DMSO) δ in ppm 7.71 (s, 1H), 5.92 (s, 2H), 4.14-4.04 (m, 4H), 3.70-3.62 (m, 4H), 3.54 (s, 3H). HRMS (ESI) *m/z* (M + H)⁺ calculated for C₁₀H₁₄N₆O 235.1307; found, 235.1310. Melting point: 150 °C.

Synthesis of 8-bromo-9-methyl-6-morpholino-9H-purin-2-amine (4): Compound **3** (1gm, 4.27 mmol) was dissolved in a (9:1) mixture of Dioxane and 0.5(M) NaOAc solution (10 mL). Then liq. Bromine (0.4 mL, 6.4 mmol) was added dropwise in reaction mixture and stirred at room temperature for 6 hours. After completion of the reaction mixture was washed with satd solution of Na₂S₂O₃ and extracted with EtOAc. The product was then purified by column chromatography (Silica gel, mesh size 100-200) eluting (50% EtOAc-Hexane) to obtain **4** (0.959g, 72%) as pale yellow amorphous solid. ¹H NMR (300 MHz, d₆-DMSO) δ in ppm 6.07 (s, 2H), 4.06-3.92 (m, 4H), 3.70-3.63 (m, 4H), 3.49 (s, 3H). HRMS (ESI) *m/z* (M + H)⁺ calculated for C₁₀H₁₃BrN₆O 313.0412; found, 313.0411. Melting point: 144 °C.

Synthesis of 8-(4-methoxyphenyl)-9-methyl-6-morpholino-9H-purin-2-amine (5): Compound **4** (1gm, 3.20 mmole), 4-methoxyphenylboronic acid (0.729gm, 4.8 mmol),

K₂CO₃ (1.1gm, 8 mmol) were dissolved in (9:1) mixture of Dioxane and water (15mL) and purged with Ar gas for 30 min. Then catalyst Pd(PPh₃)₄ (0.369 gm, 0.32 mmole) was added and the reaction mixture and stirred at 100°C-110 °C for overnight. Reaction was monitored by checking TLC. After completion, workup was done with water and ethyl acetate and then organic layer was evaporated. The product was then purified by column chromatography (Silica gel, mesh size 100-200) eluting (50% EtOAc-Hexane) to obtain **5** (0.872 g, 80%) as off white solid. ¹H NMR (300 MHz, d₆-DMSO) δ in ppm 7.68-7.65 (m, 2H), 7.04-7.00 (m, 2H), 5.90 (s, 2H), 4.15-4.05 (m, 4H), 3.78 (s, 3H), 3.67-3.62 (m, 4H), 3.59 (s, 3H). ¹³C NMR (100 MHz, d₆-DMSO) δ in ppm 160.43, 159.82, 155.55, 153.89, 146.33, 130.45, 123.12, 114.58, 113.86, 66.81, 55.83, 30.58. HRMS (ESI) *m/z* (M + H)⁺ calculated for C₁₇H₂₀N₆O₂ 341.1726; found, 341.1724 Melting point: 170 °C.

Synthesis of N-(8-(4-methoxyphenyl)-9-methyl-6-morpholino-9H-purin-2-yl) isobutyramide (6):

The following compound was made by general procedure **A** using **5** (0.050 gm, 0.14 mmol), isobutyryl chloride (0.016 gm, 0.22 mmol), TEA (0.039mL, 0.28 mmol) in dry DCM (2 mL) to obtain compound **7** (0.041 g, 65%) as off white solid. ¹H NMR (300 MHz, CDCl₃) δ in ppm 7.77 (s, 1H), 7.70-7.64 (m, 2H), 7.04-6.98 (m, 2H), 4.38-4.23 (m, 4H), 3.87 (s, 3H), 3.84-3.81 (m, 4H), 3.16 (s, 3H), 3.18-2.94 (m, 1H), 1.27 (d, *J* = 6.9 Hz, 6H). ¹³C NMR (100 MHz, CDCl₃) δ in ppm 160.90, 154.04, 153.57, 151.81, 148.99, 130.37, 122.37, 116.91, 114.35, 67.16, 55.52, 30.78, 19.48. HRMS (ESI) *m/z* (M + H)⁺ calculated for C₂₁H₂₆N₆O₃ 411.2145; found, 411.2140. Melting point: 174 °C.

Synthesis of N-(8-(4-methoxyphenyl)-9-methyl-6-morpholino-9H-purin-2-yl) cyclopentanecarboxamide (7): The following compound was made by general procedure **A** using **5** (0.050 gm, 0.14 mmol), cyclopentanecarbonyl chloride (0.025 gm, 0.22 mmol), TEA (0.039mL, 0.28 mmol) in dry DCM (2 mL) to obtain compound **7** (0.041 g, 65%) as off white solid. ¹H NMR (300 MHz, CDCl₃) δ in ppm 7.74 (s, 1H), 7.70-7.66 (m, 2H), 7.04-7.00 (m, 2H), 4.40-4.21 (m, 4H), 3.87 (s, 3H), 3.84-3.81 (m, 4H), 3.78 (s, 3H), 2.04-1.93 (m, 5H), 1.83-1.73 (m, 2H), 1.65-1.58 (m, 2H). ¹³C NMR (100 MHz, CDCl₃) δ in ppm 160.90, 154.05, 153.57, 151.86, 148.96, 130.36, 122.39, 116.89, 114.34, 67.16, 55.52, 30.77, 30.39, 26.15. HRMS (ESI) *m/z* (M + H)⁺ calculated for C₂₃H₂₉N₆O₃ 437.2301; found, 437.2309. Melting point: 148 °C.

Synthesis of *N*-(8-(4-methoxyphenyl)-9-methyl-6-morpholino-9H-purin-2-yl) piperidine-4-carboxamide (8):

The following compound was made by general procedure **A** using **5** (0.050 gm, 0.14 mmol), piperidine-4-carboxyl chloride (0.030mL, 0.22 mmol), TEA (0.039mL, 0.28 mmol) in dry DCM (2mL) to obtain compound **8** (0.051 g, 67%) as off white solid. ¹H NMR (300 MHz, CDCl₃) δ in ppm 8.18 (s, 1H), 7.69-7.65 (m, 2H), 7.05-7.00 (m, 2H), 4.37-4.15 (m, 4H), 3.88 (s, 3H), 3.83-3.77 (m, 4H), 3.76 (s, 3H), 3.57-3.47 (m, 2H), 3.16-3.02 (m, 2H), 2.29-2.11 (m, 5H). ¹³C NMR (100 MHz, d₆-DMSO) δ in ppm 160.87, 154.09, 153.23, 152.17, 148.97, 130.79, 122.46, 116.49, 114.70, 66.77, 55.90, 43.09, 31.03, 25.58. HRMS (ESI) *m/z* (M + H)⁺ calculated for C₂₃H₃₀N₇O₃ 452.2410; found, 452.2417. Melting point: 150 °C.

Synthesis of *N*-(8-(4-methoxyphenyl)-9-methyl-6-morpholino-9H-purin-2-yl) benzamide (9):

The following compound was made by general procedure **A** using **5** (0.050gm, 0.14 mmol), benzoyl chloride (0.025mL, 0.22 mmol), TEA (0.039mL, 0.28 mmol) in dry DCM (2mL) to obtain compound **9** (0.042 g, 65%) as off white solid. ¹H NMR (400 MHz, d₆-DMSO) δ in ppm 10.43 (s, 1H), 7.88-7.85 (m, 2H), 7.78-7.74 (m, 2H), 7.54-7.50 (m, 1H), 7.47-7.42 (m, 2H), 7.09-7.05 (m, 2H), 4.37-3.96 (m, 4H), 3.80 (s, 3H), 3.73 (s, 3H), 3.67-3.63 (m, 4H). ¹³C NMR (100 MHz, d₆-DMSO) δ in ppm 66.35, 160.89, 154.21, 153.14, 152.47, 149.18, 135.66, 131.98, 130.83, 128.73, 128.46, 122.49, 116.88, 114.69, 66.78, 55.90, 31.06, 26.09. HRMS (ESI) *m/z* (M + H)⁺ calculated for C₂₄H₂₅N₆O₃ 445.1988; found, 445.1985. Melting point: 156 °C.

Synthesis of 4-fluoro-*N*-(8-(4-methoxyphenyl)-9-methyl-6-morpholino-9H-purin-2-yl)benzamide (10): The following compound was made by general procedure **A** using **5** (0.050 gm, 0.14 mmol), 4-Fluorobenzoyl chloride (0.026mL, 0.22 mmol), TEA (0.039mL, 0.28 mmol) in dry DCM (2mL) to obtain compound **10** (0.051 g, 76%) as off white solid. ¹H NMR (400 MHz, d₆-DMSO) δ in ppm 10.48 (s, 1H), 7.96-7.93 (m, 2H), 7.78-7.74 (m, 2H), 7.29-7.25 (m, 2H), 7.09-7.05 (m, 2H), 4.27-4.03 (m, 4H), 3.80 (s, 3H), 3.73 (m, 3H), 3.68-3.64 (m, 4H). ¹³C NMR (100 MHz, d₆-DMSO) δ in ppm 165.59, 161.05, 153.41, 151.49, 149.58, 131.51, 131.44, 131.34, 130.93, 122.05, 116.54, 115.90, 115.68, 114.74, 66.66, 55.93, 31.28. HRMS (ESI) *m/z* (M + H)⁺ calculated for C₂₄H₂₅FN₆O₃ 463.1894; found, 463.1888. Melting point: 170 °C.

Synthesis of 3-fluoro-*N*-(8-(4-methoxyphenyl)-9-methyl-6-morpholino-9H-purin-2-yl)benzamide (11): The following compound was made by general procedure **A** using **5**

(0.050 gm, 0.14 mmol), 3-Fluorobenzoyl chloride (0.026 mL, 0.22 mmol), TEA (0.039 mL, 0.28 mmol) in dry DCM (2mL) to obtain compound **11** (0.051 g, 76%) as off white solid. ^1H NMR (300 MHz, d_6 -DMSO) δ in ppm 10.26 (s, 1H), 7.84-7.68 (m, 4H), 7.58-7.50 (m, 1H), 7.45-7.39 (m, 1H), 7.14-7.08 (m, 2H), 4.33-4.08 (m, 4H), 3.84 (s, 1H), 3.77 (s, 1H), 3.74-3.66 (m, 4H). ^{13}C NMR (100 MHz, d_6 -DMSO) δ in ppm 163.59, 161.16, 160.91, 154.16, 153.13, 152.21, 149.26, 138.00, 130.92, 130.84, 124.66, 122.46, 118.99, 116.94, 115.36, 114.69, 66.75, 55.87, 31.07. HRMS (ESI) m/z ($M + H$) $^+$ calculated for $\text{C}_{24}\text{H}_{25}\text{FN}_6\text{O}_3$ 463.1894; found, 463.1898. Melting point: 172 °C.

Synthesis of *N*-(8-(4-methoxyphenyl)-9-methyl-6-morpholino-9H-purin-2-yl)-4-(trifluoromethyl)benzamide (12): The following compound was made by general procedure **A** using **5** (0.050 gm, 0.14 mmol), 4-(trifluoromethyl)benzoyl chloride (0.032mL, 0.22 mmol), TEA (0.039mL, 0.28mmol) in dry DCM (2mL) to obtain compound **12** (0.049 g, 66%) as off white solid. ^1H NMR (300 MHz, d_6 -DMSO) δ in ppm 10.78 (s, 1H), 8.05-8.00 (m, 2H), 7.87-7.83 (m, 2H), 7.81-7.77 (m, 2H), 7.13-7.08 (m, 2H), 4.23-4.03 (m, 4H), 3.84 (s, 3H), 3.76 (s, 3H), 3.69-3.63 (m, 4H). ^{13}C NMR (100 MHz, d_6 -DMSO) δ in ppm 165.88, 160.92, 154.14, 153.02, 152.21, 149.25, 139.92, 130.84, 129.27, 125.70, 125.66, 122.43, 116.89, 114.70, 66.72, 55.89, 31.05. HRMS (ESI) m/z ($M + H$) $^+$ calculated for $\text{C}_{24}\text{H}_{24}\text{FN}_6\text{O}_3$ 513.1862; found, 513.1868. Melting point: 148 °C.

Synthesis of 4-cyano-*N*-(8-(4-methoxyphenyl)-9-methyl-6-morpholino-9H-purin-2-yl)benzamide (13): The following compound was made by general procedure **A** using **5** (0.050 gm, 0.14 mmol), 4-cyanobenzoyl chloride (0.032gm, 0.22 mmol), TEA (0.039mL, 0.28mmol) in dry DCM (2mL) to obtain compound **13** (0.039 g, 58%) as off white solid. ^1H NMR (300 MHz, CDCl_3) δ in ppm 10.79 (s, 1H), 8.00-7.94 (m, 4H), 7.82-7.76 (m, 2H), 7.13-7.08 (m, 2H), 4.27-4.04 (m, 4H), 3.84 (s, 3H), 3.75 (m, 3H), 3.71-3.64 (m, 4H). ^{13}C NMR (100 MHz, d_6 -DMSO) δ in ppm 160.92, 154.11, 153.01, 152.12, 149.28, 132.78, 130.85, 129.20, 122.42, 118.89, 116.90, 114.70, 114.02, 113.92, 66.75, 55.90, 31.05. HRMS (ESI) m/z ($M + H$) $^+$ calculated for $\text{C}_{25}\text{H}_{44}\text{N}_7\text{O}_3$ 470.1941; found, 470.1948. Melting point: 194 °C.

Synthesis of *N*-(8-(4-methoxyphenyl)-9-methyl-6-morpholino-9H-purin-2-yl)-2-phenylacetamide (14): The following compound was made by general procedure **A** using **5** (0.050 gm, 0.14 mmol), phenyl acetylchloride (0.024gm, 0.22mmol), TEA (0.039mL, 0.28mmol) in dry DCM (2mL) to obtain compound **14** (0.030 g, 48%) as off

white solid. ^1H NMR (300 MHz, CDCl_3) δ in ppm 7.83 (s, 1H), 7.71-7.63 (m, 2H), 7.36-7.25 (m, 5H), 7.05-6.98 (m, 2H), 4.37-4.27 (m, 4H), 4.21-4.07 (m, 2H), 3.87 (s, 3H), 3.81-3.76 (m, 4H), 3.76 (s, 3H). ^{13}C NMR (100 MHz, CDCl_3) δ in ppm 160.93, 153.92, 153.51, 151.63, 149.06, 134.91, 131.61, 130.38, 129.64, 128.81, 127.15, 122.30, 116.96, 114.36, 67.13, 55.53, 30.82. HRMS (ESI) m/z ($\text{M} + \text{H}$) $^+$ calculated for $\text{C}_{25}\text{H}_{27}\text{N}_6\text{O}_3$ 459.2145; found, 459.2149. Melting point: 156 °C.

Synthesis of 4-((dimethylamino)methyl)-N-(8-(4-methoxyphenyl)-9-methyl-6-morpholino-9H-purin-2-yl)benzamide (15): The following compound was made by general procedure A using **5** (0.050 gm, 0.14 mmol), 4-((dimethylamino)methyl)benzoyl chloride (0.039gm, 0.22 mmol), TEA (0.039 mL, 0.28mmol) in dry DCM (2mL) to obtain compound **15** (0.033 g, 45%) as off white solid. ^1H NMR (400 MHz, CDCl_3) δ in ppm 8.46 (s, 1H), 8.00-7.97 (m, 2H), 7.81-7.76 (m, 2H), 7.69-7.66 (m, 2H), 7.03-6.99 (m, 2H), 4.64-4.27 (m, 4H), 4.21 (s, 3H), 3.86 (s, 3H), 3.82 (s, 2H), 3.82-3.80 (m, 4H), 2.77 (s, 6H). ^{13}C NMR (100 MHz, CDCl_3) δ in ppm 164.31, 160.97, 149.34, 131.50, 130.42, 128.51, 122.28, 117.38, 114.37, 109.06, 67.16, 60.97, 55.53, 42.59, 30.92. HRMS (ESI) m/z ($\text{M} + \text{H}$) $^+$ calculated for $\text{C}_{27}\text{H}_{32}\text{N}_7\text{O}_3$ 502.2567; found, 502.2569. Melting point: 146 °C.

Synthesis of N-(8-(4-methoxyphenyl)-9-methyl-6-morpholino-9H-purin-2-yl)nicotinamide (16): The following compound was made by general procedure C using **5** (0.050 gm, 0.14 mmol), nicotinic acid (0.027gm, 0.22 mmol), TEA (0.039mL, 0.28mmol) in dry DCM (2mL) to obtain compound **16** (0.038 g, 58%) as off white solid. ^1H NMR (300 MHz, d_6 -DMSO- d_6) δ in ppm 10.77 (s, 1H), 9.00 (s, 1H), 8.75-8.69 (m, 1H), 8.23-8.19 (m, 1H), 7.81-7.78 (m, 2H), 7.54-7.50 (m, 1H), 7.12-7.09 (m, 2H), 4.31-4.06 (m, 4H), 3.84 (s, 3H), 3.76 (s, 3H), 3.72-3.65 (m, 4H). ^{13}C NMR (100 MHz, d_6 -DMSO) δ in ppm 160.91, 154.13, 153.08, 152.39, 152.21, 149.43, 149.25, 136.13, 130.84, 122.44, 116.90, 114.69, 66.76, 55.90, 31.06. HRMS (ESI) m/z ($\text{M} + \text{H}$) $^+$ calculated for $\text{C}_{23}\text{H}_{24}\text{N}_7\text{O}_3$ 446.1941; found, 446.1946. Melting point: 178 °C.

Synthesis of N-(8-(4-methoxyphenyl)-9-methyl-6-morpholino-9H-purin-2-yl)pyrazine-2-carboxamide (17): The following compound was made by general procedure A using **5** (0.050 gm, 0.14 mmol), Pyrazinecarboxylic acid (0.027gm, 0.22 mmol), TEA (0.039mL, 0.28mmol) in dry DCM (2mL) to obtain compound **17** (0.038 g, 58%) as off white solid. ^1H NMR (300 MHz, CDCl_3) δ in ppm 10.10 (s, 1H), 9.55 (d, J = 6.0Hz, 1H), 8.81 (d, J = 3.6Hz, 1H), 8.64-8.61 (m, 1H), 7.73-7.68 (m, 2H), 7.06-7.00 (m, 2H), 4.46-

4.31 (m, 4H), 3.88 (s, 3H), 3.86 (s, 3H), 3.86-3.82 (m, 4H). ^{13}C NMR (100 MHz, CDCl_3) δ in ppm 160.95, 160.24, 154.08, 153.58, 151.25, 149.35, 147.69, 145.05, 144.63, 142.49, 130.42, 122.36, 117.48, 114.36, 67.21, 55.53, 30.92. HRMS (ESI) m/z ($\text{M} + \text{H}$) $^+$ calculated for $\text{C}_{22}\text{H}_{23}\text{N}_8\text{O}_3$ 447.1893; found, 447.1888. Melting point: 182 °C.

Synthesis of *N*-(8-(4-methoxyphenyl)-9-methyl-6-morpholino-9H-purin-2-yl)-1H-imidazole-2-carboxamide (18): The following compound was made by general procedure A using **5** (0.050 gm, 0.14 mmol), 1H-Imidazole-2-carbonyl chloride (0.021gm, 0.22 mmol), TEA (0.039mL, 0.28 mmol) in dry DCM (2mL) to obtain compound **18** (0.041 g, 62%) as off white solid. ^1H NMR (300 MHz, CDCl_3) δ in ppm 10.78 (s, 1H), 9.50 (s, 1H), 7.73-7.67 (m, 2H), 7.25-7.20 (m, 2H), 7.05-7.00 (m, 2H), 4.43-4.25 (m, 4H), 3.85 (s, 3H), 3.84-3.78 (m, 7H). ^{13}C NMR (100 MHz, CDCl_3) δ in ppm 160.92, 155.94, 153.85, 153.82, 153.48, 151.16, 149.53, 146.68, 130.44, 122.13, 120.09, 117.30, 114.31, 67.11, 55.47, 30.80. HRMS (ESI) m/z ($\text{M} + \text{H}$) $^+$ calculated for $\text{C}_{21}\text{H}_{23}\text{N}_8\text{O}_3$ 435.1893; found, 435.1882. Melting point: 178 °C.

Synthesis of *N*-(8-(4-methoxyphenyl)-9-methyl-6-morpholino-9H-purin-2-yl)oxazole-5-carboxamide (19):

The following compound was made by general procedure A using **5** (0.050 gm, 0.14 mmol), 5-Oxazolecarboxylic acid (0.024gm, 0.22 mmol), TEA (0.039mL, 0.28mmol) in dry DCM (2mL) to obtain compound **19** (0.033 g, 52%) as off white solid. ^1H NMR (300 MHz, CDCl_3) δ in ppm 8.47 (s, 1H), 7.98 (s, 1H), 7.88 (s, 1H), 7.72-7.67 (m, 2H), 7.05-7.00 (m, 2H), 4.43-4.26 (m, 4H), 3.87 (s, 3H), 3.86-3.83 (m, 4H), 3.82 (s, 3H). ^{13}C NMR (100 MHz, CDCl_3) δ in ppm 160.99, 153.91, 153.74, 153.47, 151.55, 150.88, 149.41, 145.71, 131.72, 130.42, 122.25, 117.50, 114.37, 67.17, 55.53, 30.90. HRMS (ESI) m/z ($\text{M} + \text{H}$) $^+$ calculated for $\text{C}_{21}\text{H}_{22}\text{N}_7\text{O}_4$ 436.1733; found, 436.1728. Melting point: 188 °C.

Synthesis of 1-(4-fluorophenyl)-3-(8-(4-methoxyphenyl)-9-methyl-6-morpholino-9H-purin-2-yl)urea (20): Compound **5** (0.050 gm, 0.14 mmol) was dissolved in dry DCM (2mL) and TEA (0.039mL, 0.28mmol) was added. After 15 mins 4-Fluorophenyl isocyanate (0.032 gm, 0.22 mmol), was added in cooling and the reaction mixture was allowed to stir for 1hr at room temperature. Reaction was monitored by checking TLC. After completion of the reaction, the reaction mixture was worked up by using EtOAc and water. Pure compound was isolated after purification in flash chromatography using 80% Pet ether in EtOAc (V/V) to afford **20** as off-white solid (yield 52%). ^1H NMR (300 MHz,

CDCl₃) δ in ppm 11.51 (s, 1H), 7.71-7.65 (m, 2H), 7.15 (s, 1H), 7.07-7.01 (m, 4H), 4.39-4.27 (m, 4H), 3.89 (s, 3H), 3.87-3.84 (m, 4H), 3.83 (s, 3H). ¹³C NMR (100 MHz, *d*₆-DMSO) δ in ppm 13C NMR (101 MHz, DMSO-D₆) δ 164.88, 163.59, 161.16, 160.91, 154.16, 153.13, 152.20, 149.26, 130.84, 124.66, 122.45, 116.94, 115.13, 114.69, 66.78, 55.90, 31.07. HRMS (ESI) *m/z* (M + H)⁺ calculated for C₂₄H₂₅FN₇O₃ 478.2003; found, 478.2008. Melting point: 170 °C.

Synthesis of *N*-(4-fluorobenzyl)-8-(4-methoxyphenyl)-9-methyl-6-morpholino-9H-purin-2-amine (21): Compound **5** (0.050 gm, 0.14 mmol) was dissolved in dry DMF (2mL) and NaH (0.006 gm, 0.28 mmol) was added. After 15 mins 4-Fluorobenzyl bromide (0.041 gm, 0.22 mmol), was added in cooling and the reaction mixture was allowed to stir for 1hr at room temperature. Reaction was monitored by checking TLC. After completion of the reaction, the reaction mixture was worked up by using EtOAc and chilled water. Pure compound was isolated after purification in flash chromatography using 50% Pet ether in EtOAc (V/V) to afford **21** as off-white solid (yield 56%). ¹H NMR (300 MHz, CDCl₃) δ in ppm 7.68-7.61 (m, 2H), 7.38-7.31 (m, 2H), 7.04-6.94 (m, 4H), 5.09-5.01 (m, 1H), 4.61 (d, *J*= 6.0Hz, 2H), 4.33-4.18 (m, 4H), 3.86 (s, 3H), 3.81-3.75 (m, 4H), 3.70 (s, 3H). ¹³C NMR (100 MHz, *d*₆-DMSO) δ in ppm 160.92, 154.14, 153.02, 152.20, 149.25, 130.84, 129.27, 125.70, 122.42, 116.89, 114.69, 66.73, 55.89, 31.05. HRMS (ESI) *m/z* (M + H)⁺ calculated for C₂₄H₂₆FN₆O₂ 449.2101; found, 449.2106. Melting point: 172 °C.

Synthesis of *N*6,*N*6,9-trimethyl-9H-purine-2,6-diamine (22): Compound **2** (2gm, 10.92 mmol), K₂CO₃ (3.01gm, 21.85 mmol) and dimethylamine (25mL, 100.9mmol) were taken in a pressure tube and stirred at 90°C temperature for 2hrs. After completion of the reaction solvent was evaporated in reduced pressure and the product was purified by column chromatography (Silica gel, mesh size 100-200) eluting (3% MeOH/ CHCl₃) to obtain compound **22** (1.47gm, 80%) as off white solid.

Synthesis of 8-bromo-*N*6,*N*6,9-trimethyl-9H-purine-2,6-diamine (23): Compound **22** (1gm, 5.20 mmol) was dissolved in a (9:1) mixture of Dioxane and 0.5 (M) NaOAc solution (10mL). Then liq. Bromine (0.36mL, 7.80 mmol) was added dropwise in reaction mixture and stirred at room temperature for overnight. After completion of the reaction mixture was washed with satd. solution of Na₂S₂O₃ and extracted with EtOAc. The product was then purified by column chromatography (Silica gel, mesh size 100-200) eluting (50% EtOAc-Hexane) to obtain compound **23** (1.01g, 72%) as pale yellow amorphous solid.

Synthesis of 8-(4-methoxyphenyl)-N6,N6,9-trimethyl-9H-purine-2,6-diamine (24):

Compound **23** (1gm, 3.70 mmole), 4-methoxyphenylboronic acid (0.710 gm, 4.4 mmol), K_2CO_3 (1.02 gm, 7.40 mmol) were dissolved in (9:1) mixture of Dioxane and water (15mL) and purged with Ar gas for 30 min. Then catalyst $Pd(PPh_3)_4$ (0.427 gm, 0.37 mmole) was added and the reaction mixture and stirred at 100°C-110 °C for overnight. Reaction was monitored by checking TLC. After completion, workup was done with water and ethyl acetate and then organic layer was evaporated. The product was then purified by column chromatography (Silica gel, mesh size 100-200) eluting (70% EtOAc-Hexane) to obtain **24** (0.872 g, 78%) as off white solid.

Synthesis of N-(6-(dimethylamino)-8-(4-methoxyphenyl)-9-methyl-9H-purin-2-yl)-4-fluorobenzamide (25):

The following compound was made by general procedure **A** using **24** (0.10 gm, 0.33 mmol), 4-fluorobenzoyl chloride (0.068 gm, 0.49 mmol), TEA (0.04 mL, 0.49 mmol) in dry DCM (2mL) to obtain compound **25** (0.081 g, 58%) as off white solid. 1H NMR (300 MHz, $CDCl_3$) δ in ppm 8.30 (s, 1H), 7.97-7.90 (m, 2H), 7.73-7.67 (m, 2H), 7.73-7.67 (m, 2H), 7.19-7.11 (m, 2H), 7.06-7.00 (m, 2H), 3.87 (s, 3H), 3.82 (s, 3H), 3.53 (br.s, 6H). ^{13}C NMR (100 MHz, d_6 -DMSO) δ in ppm 165.22, 160.79, 154.35, 153.77, 152.30, 148.76, 131.28, 131.19, 130.74, 122.70, 117.14, 115.75, 115.53, 114.68, 55.89, 31.04. HRMS (ESI) m/z ($M + H$)⁺ calculated for $C_{22}H_{22}N_6O_2$ 421.1788; found, 421.1792. Melting point: 190 °C.

Synthesis of 8-bromo-6-chloro-9-methyl-9H-purin-2-amine (26):

Compound **2** (1gm, 5.46 mmol) was dissolved in a (9:1) mixture of Dioxane and 0.5 (M) NaOAc solution (10 mL). Then liq. Bromine (0.41mL, 8.19 mmol) was added dropwise in reaction mixture and stirred at room temperature for overnight. After completion of the reaction mixture was washed with satd solution of $Na_2S_2O_3$ and extracted with EtOAc. The product was then purified by column chromatography (Silica gel, mesh size 100-200) eluting (50% EtOAc-Hexane) to obtain compound **26** (0.926g, 65%) as pale yellow amorphous solid. 1H NMR (300 MHz, d_6 -DMSO) δ in ppm 6.98 (s, 2H), 3.27 (s, 3H). ^{13}C NMR (100 MHz, d_6 -DMSO) δ in ppm 164.99, 160.27, 153.09, 135.26, 128.67, 35.61. HRMS (ESI) m/z ($M + H$)⁺ calculated for $C_6H_5BrClN_5$ 261.9495; found, 261.9499. Melting point: 168 °C.

Synthesis of 6-chloro-8-(4-methoxyphenyl)-9-methyl-9H-purin-2-amine (27):

Compound **26** (1gm, 3.83 mmole), 4-methoxyphenylboronic acid (0.729 gm, 5.74 mmol), K_2CO_3 (1.05 gm, 7.66 mmol) were dissolved in (9:1) mixture of Dioxane and water (15

mL) and purged with Ar gas for 30 min. Then catalyst Pd(PPh₃)₄ (0.429 gm, 0.38 mmole) was added and the reaction mixture and stirred at 100°C-110°C for overnight. Reaction was monitored by checking TLC. After completion, workup was done with water and ethyl acetate and then organic layer was evaporated. The product was then purified by column chromatography (Silica gel, mesh size 100-200) eluting (50% EtOAc-Hexane) to obtain **27** (0.872 g, 74%) as off white solid. ¹H NMR (300 MHz, CDCl₃) δ in ppm 7.76-7.70 (m, 2H), 7.06-7.00 (m, 2H), 5.08 (s, 2H), 3.88 (s, 3H), 3.77 (s, 3H). ¹³C NMR (100 MHz, CDCl₃) δ in ppm 161.51, 155.76, 153.73, 135.33, 131.97, 130.71, 128.64, 114.41, 113.23, 55.46, 30.81. HRMS (ESI) *m/z* (M + H)⁺ calculated for C₆H₆BrClN₅ 290.0809; found, 290.0812. Melting point: 140 °C.

Synthesis of *N*-(6-chloro-8-(4-methoxyphenyl)-9-methyl-9H-purin-2-yl)-4-fluorobenzamide (28):

The following compound was made by general procedure **A** using **27** (0.10 gm, 0.34 mmol), 4-fluorobenzoic acid (0.070gm, 0.50 mmol), TEA (0.039 mL, 0.28 mmol) in dry DCM (2mL) to obtain compound **28** (0.070 g, 54%) as off white solid. ¹H NMR (300 MHz, CDCl₃) δ in ppm 8.71 (s, 1H), 8.01-8.96 (m, 2H), 7.84-7.78 (m, 2H), 7.23-7.15 (m, 2H), 7.09-7.04 (m, 2H), 3.96 (s, 3H), 3.90 (s, 3H). ¹³C NMR (100 MHz, CDCl₃) δ in ppm 164.18, 163.81, 161.88, 156.11, 155.04, 151.40, 149.41, 131.00, 130.19, 128.51, 120.82, 116.18, 115.96, 114.53, 55.58, 31.63. HRMS (ESI) *m/z* (M + H)⁺ calculated for C₂₀H₁₆ClFN₅O₂ 412.0977; found, 412.0985. Melting point: 170 °C.

Synthesis of *N*-(6-chloro-8-(4-methoxyphenyl)-9-methyl-9H-purin-2-yl)cyclohexanecarboxamide (29):

The following compound was made by general procedure **A** using **27** (0.10 gm, 0.34 mmol), cyclohexane carbonyl chloride (0.1 mL, 0.50 mmol), TEA (0.039 mL, 0.28 mmol) in dry DCM (2mL) to obtain compound **29** (0.060 g, 48 %) as off white solid. HRMS (ESI) *m/z* (M + H)⁺ calculated for C₂₀H₂₃ClN₅O₂ 400.1540; found, 400.1548. Melting point: 166 °C.

Synthesis of 4-fluoro-*N*-(8-(4-methoxyphenyl)-9-methyl-9H-purin-2-yl)benzamide (30): Compound **29** (0.05 gm, 0.12 mmol) was dissolved in MeOH (2mL) and pinch of 10 % wet Pd/C was added. Reaction mixture was degassed by passing nitrogen and H₂ gas was passed for 2 hours to get fully reduced compound. Reaction was thoroughly monitored by checking TLC. Upon completion of the reaction, Pd/C was filtered through celite bed and MeOH was evaporated in vacuum to obtain compound **30** (0.036 g, 80 %)

as light brown solid. ^1H NMR (300 MHz, CDCl_3) δ in ppm 8.90 (s, 1H), 8.75 (s, 1H), 8.00-7.96 (m, 2H), 7.80-7.76 (m, 2H), 7.19-7.14 (m, 2H), 7.07-7.03 (m, 2H), 3.93 (s, 3H), 3.88 (s, 3H). ^{13}C NMR (100 MHz, CDCl_3) δ in ppm 166.56, 164.04, 161.74, 156.00, 154.72, 152.33, 147.72, 130.79, 130.09, 121.30, 116.11, 115.89, 114.55, 100.00, 55.57, 30.97. HRMS (ESI) m/z ($\text{M} + \text{H}$) $^+$ calculated for $\text{C}_{20}\text{H}_{17}\text{FN}_5\text{O}_2$ 378.1366; found, 378.1372. Melting point: 154 °C.

Synthesis of N-(8-(4-methoxyphenyl)-9-methyl-9H-purin-2-yl)cyclohexane carboxamide (31):

Compound **30** (0.05 gm, 0.13 mmol) was dissolved in MeOH (2mL) and pinch of 10 % wet Pd/C was added. Reaction mixture was degassed by passing nitrogen and H_2 gas was passed for 2 hours to get fully reduced compound. Reaction was thoroughly monitored by checking TLC. Upon completion of the reaction, Pd/C was filtered through celite bed and MeOH was evaporated in vacuum to obtain compound **31** (0.030 g, 81 %) as light brown solid. ^1H NMR (300 MHz, CDCl_3) δ in ppm 8.89 (s, 1H), 8.33 (s, 1H), 8.79-8.76 (m, 2H), 7.07-7.05 (m, 2H), 3.91 (s, 3H), 3.88 (s, 3H), 2.85-2.67 (m, 1H), 2.08-1.98 (m, 2H), 1.91-1.81 (m, 2H), 1.75-1.65 (m, 2H), 1.36-1.28 (m, 4H). HRMS (ESI) m/z ($\text{M} + \text{H}$) $^+$ calculated for $\text{C}_{20}\text{H}_{24}\text{N}_5\text{O}_2$ 366.1930; found, 366.1934. Melting point: 168 °C.

2.7 REFERENCES

- (80) Roberts, C. K.; Hevener, A. L.; Barnard, R. J. Metabolic Syndrome and Insulin Resistance: Underlying Causes and Modification by Exercise Training. *Compr. Physiol.* **2013**, 3 (1), 1–58. <https://doi.org/10.1002/cphy.c110062>.
- (81) Grundy, S. M. Obesity, Metabolic Syndrome, and Cardiovascular Disease. *J. Clin. Endocrinol. Metab.* **2004**, 89 (6), 2595–2600. <https://doi.org/10.1210/jc.2004-0372>.
- (82) Mohamed, S. M.; Shalaby, M. A.; El-Shiekh, R. A.; El-Banna, H. A.; Emam, S. R.; Bakr, A. F. Metabolic Syndrome: Risk Factors, Diagnosis, Pathogenesis, and Management with Natural Approaches. *Food Chem. Adv.* **2023**, 3, 100335. <https://doi.org/https://doi.org/10.1016/j.focha.2023.100335>.
- (83) Deprince, A.; Haas, J. T.; Staels, B. Dysregulated Lipid Metabolism Links NAFLD to Cardiovascular Disease. *Mol. Metab.* **2020**, 42, 101092. <https://doi.org/https://doi.org/10.1016/j.molmet.2020.101092>.
- (84) Bazmandegan, G.; Abbasifard, M.; Nadimi, A. E.; Alinejad, H.; Kamiab, Z. Cardiovascular Risk Factors in Diabetic Patients with and without Metabolic Syndrome: A Study Based on the Rafsanjan Cohort Study. *Sci. Rep.* **2023**, 13 (1), 559. <https://doi.org/10.1038/s41598-022-27208-5>.
- (85) Ion, R.-M.; Sibianu, M.; Hutanu, A.; Beresescu, F. G.; Sala, D. T.; Flavius, M.; Rosca, A.; Constantin, C.; Scurtu, A.; Moriczi, R.; Muresan, M. G.; Gabriel, P.; Niculescu, R.; Neagoe, R. M. A Comprehensive Summary of the Current Understanding of the Relationship between Severe Obesity, Metabolic Syndrome, and Inflammatory Status. *J. Clin. Med.* **2023**, 12 (11). <https://doi.org/10.3390/jcm12113818>.
- (86) Qureshi, K.; Abrams, G. A. Metabolic Liver Disease of Obesity and Role of Adipose Tissue in the Pathogenesis of Nonalcoholic Fatty Liver Disease. *World journal of gastroenterology*. United States July 2007, pp 3540–3553. <https://doi.org/10.3748/wjg.v13.i26.3540>.
- (87) Dalle Grave, R.; Calugi, S.; Centis, E.; Marzocchi, R.; El Ghoch, M.; Marchesini, G. Lifestyle Modification in the Management of the Metabolic Syndrome: Achievements and Challenges. *Diabetes. Metab. Syndr. Obes.* **2010**, 3, 373–385. <https://doi.org/10.2147/DMSOTT.S13860>.
- (88) Nyenwe, E. A.; Jerkins, T. W.; Umpierrez, G. E.; Kitabchi, A. E. Management of Type 2 Diabetes: Evolving Strategies for the Treatment of Patients with Type 2 Diabetes. *Metabolism.* **2011**, 60 (1), 1–23. <https://doi.org/10.1016/j.metabol.2010.09.010>.
- (89) Dahlén, A. D.; Dashi, G.; Maslov, I.; Attwood, M. M.; Jonsson, J.; Trukhan, V.; Schiöth, H. B. Trends in Antidiabetic Drug Discovery: FDA Approved Drugs, New Drugs in Clinical Trials and Global Sales. *Front. Pharmacol.* **2022**, 12. <https://doi.org/10.3389/fphar.2021.807548>.
- (90) Bailey, C. J. Antidiabetic Drugs Other than Insulin BT - Encyclopedia of Molecular

- Pharmacology; Offermanns, S., Rosenthal, W., Eds.; Springer Berlin Heidelberg: Berlin, Heidelberg, 2008; pp 116–125. https://doi.org/10.1007/978-3-540-38918-7_109.
- (91) Quinn, C. E.; Hamilton, P. K.; Lockhart, C. J.; McVeigh, G. E. Thiazolidinediones: Effects on Insulin Resistance and the Cardiovascular System. *Br. J. Pharmacol.* **2008**, *153* (4), 636–645. <https://doi.org/10.1038/sj.bjp.0707452>.
- (92) Basak, S.; Murmu, A.; Matore, B. W.; Roy, P. P.; Singh, J. Thiazolidinedione an Auspicious Scaffold as PPAR- γ Agonist: Its Possible Mechanism to Manoeuvre against Insulin Resistant Diabetes Mellitus. *Eur. J. Med. Chem. Reports* **2024**, *11*, 100160. <https://doi.org/https://doi.org/10.1016/j.ejmcr.2024.100160>.
- (93) Ahmadian, M.; Suh, J. M.; Hah, N.; Liddle, C.; Atkins, A. R.; Downes, M.; Evans, R. M. PPAR γ Signaling and Metabolism: The Good, the Bad and the Future. *Nat. Med.* **2013**, *19* (5), 557–566. <https://doi.org/10.1038/nm.3159>.
- (94) Fiévet, C.; Fruchart, J.-C.; Staels, B. PPAR α and PPAR γ Dual Agonists for the Treatment of Type 2 Diabetes and the Metabolic Syndrome. *Curr. Opin. Pharmacol.* **2006**, *6* (6), 606–614. <https://doi.org/10.1016/j.coph.2006.06.009>.
- (95) Christofides, A.; Konstantinidou, E.; Jani, C.; Boussiotis, V. A. The Role of Peroxisome Proliferator-Activated Receptors (PPAR) in Immune Responses. *Metabolism*. **2021**, *114*, 154338. <https://doi.org/10.1016/j.metabol.2020.154338>.
- (96) Guan, Y.; Breyer, M. D. Peroxisome Proliferator-Activated Receptors (PPARs): Novel Therapeutic Targets in Renal Disease. *Kidney Int.* **2001**, *60* (1), 14–30. <https://doi.org/https://doi.org/10.1046/j.1523-1755.2001.00766.x>.
- (97) Li, Y.; Pan, Y.; Zhao, X.; Wu, S.; Li, F.; Wang, Y.; Liu, B.; Zhang, Y.; Gao, X.; Wang, Y.; Zhou, H. Peroxisome Proliferator-Activated Receptors: A Key Link between Lipid Metabolism and Cancer Progression. *Clin. Nutr.* **2024**, *43* (2), 332–345. <https://doi.org/https://doi.org/10.1016/j.clnu.2023.12.005>.
- (98) Grygiel-Górniak, B. Peroxisome Proliferator-Activated Receptors and Their Ligands: Nutritional and Clinical Implications--a Review. *Nutr. J.* **2014**, *13*, 17. <https://doi.org/10.1186/1475-2891-13-17>.
- (99) Lin, Y.; Wang, Y.; Li, P.-F. PPAR α : An Emerging Target of Metabolic Syndrome, Neurodegenerative and Cardiovascular Diseases. *Front. Endocrinol. (Lausanne)*. **2022**, *13*, 1074911. <https://doi.org/10.3389/fendo.2022.1074911>.
- (100) Palomer, X.; Barroso, E.; Pizarro-Delgado, J.; Peña, L.; Botteri, G.; Zarei, M.; Aguilar, D.; Montori-Grau, M.; Vázquez-Carrera, M. PPAR β/δ : A Key Therapeutic Target in Metabolic Disorders. *Int. J. Mol. Sci.* **2018**, *19* (3). <https://doi.org/10.3390/ijms19030913>.
- (101) Mu, F.; Jing, Y.; Ning, B.; Huang, J.; Cui, T.; Guo, Y.; You, X.; Yan, X.; Li, H.; Wang, N. Peroxisome Proliferator-Activated Receptor γ Isoforms Differentially Regulate Preadipocyte Proliferation, Apoptosis, and Differentiation in Chickens. *Poult. Sci.* **2020**, *99* (12), 6410–6421.

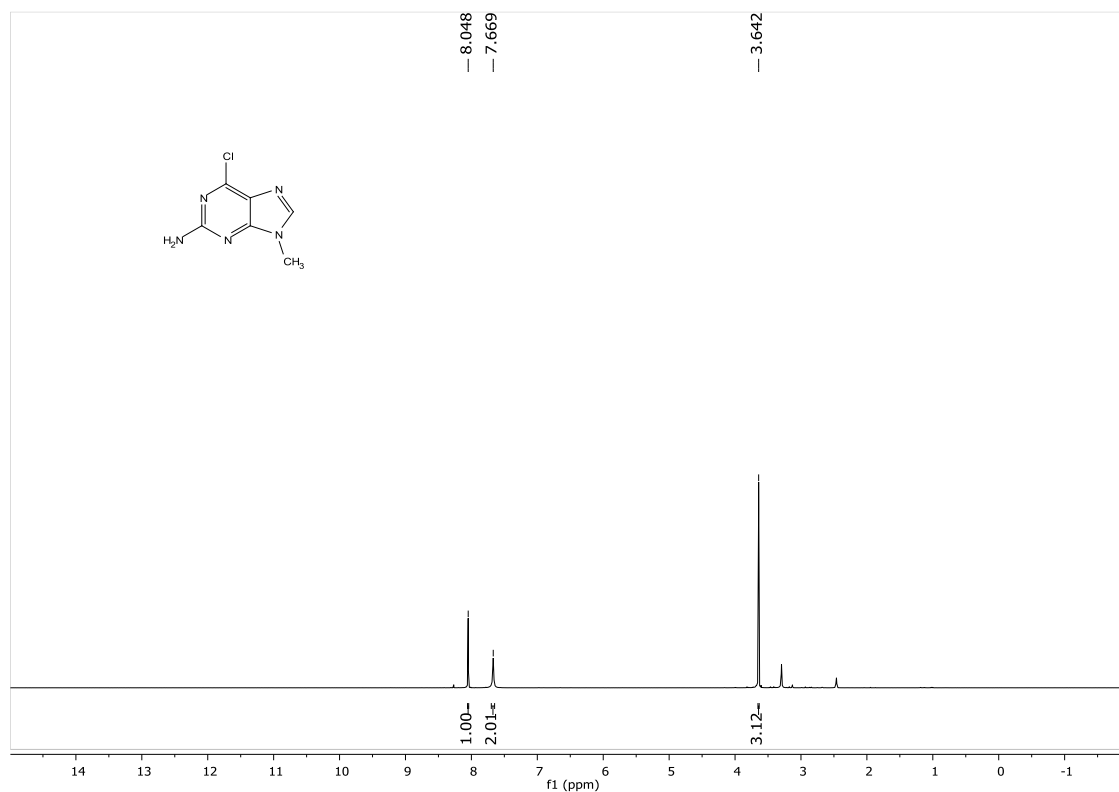
- <https://doi.org/https://doi.org/10.1016/j.psj.2020.09.086>.
- (102) Ma, X.; Wang, D.; Zhao, W.; Xu, L. Deciphering the Roles of PPAR γ in Adipocytes via Dynamic Change of Transcription Complex. *Front. Endocrinol. (Lausanne)*. **2018**, 9, 473. <https://doi.org/10.3389/fendo.2018.00473>.
- (103) Yu, L.; Gao, Y.; Aaron, N.; Qiang, L. A Glimpse of the Connection between PPAR γ and Macrophage. *Front. Pharmacol.* **2023**, 14, 1254317. <https://doi.org/10.3389/fphar.2023.1254317>.
- (104) Zheng, Y.; Shao, M.; Zheng, Y.; Sun, W.; Qin, S.; Sun, Z.; Zhu, L.; Guan, Y.; Wang, Q.; Wang, Y.; Li, L. PPARs in Atherosclerosis: The Spatial and Temporal Features from Mechanism to Druggable Targets. *J. Adv. Res.* **2024**. <https://doi.org/https://doi.org/10.1016/j.jare.2024.03.020>.
- (105) Wang, L.; Waltenberger, B.; Pferschy-Wenzig, E.-M.; Blunder, M.; Liu, X.; Malainer, C.; Blazevic, T.; Schwaiger, S.; Rollinger, J. M.; Heiss, E. H.; Schuster, D.; Kopp, B.; Bauer, R.; Stuppner, H.; Dirsch, V. M.; Atanasov, A. G. Natural Product Agonists of Peroxisome Proliferator-Activated Receptor Gamma (PPAR γ): A Review. *Biochem. Pharmacol.* **2014**, 92 (1), 73–89. <https://doi.org/10.1016/j.bcp.2014.07.018>.
- (106) Papoushek, C. The “Glitazones”: Rosiglitazone and Pioglitazone. *J. Obstet. Gynaecol. Canada JOGC = J. d’obstetrique Gynecol. du Canada JOGC* **2003**, 25 (10), 853–857. [https://doi.org/10.1016/s1701-2163\(16\)30676-4](https://doi.org/10.1016/s1701-2163(16)30676-4).
- (107) Chi, T.; Wang, M.; Wang, X.; Yang, K.; Xie, F.; Liao, Z.; Wei, P. PPAR- γ Modulators as Current and Potential Cancer Treatments. *Front. Oncol.* **2021**, 11, 737776. <https://doi.org/10.3389/fonc.2021.737776>.
- (108) Cheng, S.; Qian, K.; Wang, Y.; Wang, G.; Liu, X.; Xiao, Y.; Wang, X. PPAR γ Inhibition Regulates the Cell Cycle, Proliferation and Motility of Bladder Cancer Cells. *J. Cell. Mol. Med.* **2019**, 23 (5), 3724–3736. <https://doi.org/10.1111/jcmm.14280>.
- (109) Yang, X. Y.; Wang, L. H.; Farrar, W. L. A Role for PPAR γ in the Regulation of Cytokines in Immune Cells and Cancer. *PPAR Res.* **2008**, 2008, 961753. <https://doi.org/10.1155/2008/961753>.
- (110) Titus, C.; Hoque, M. T.; Bendayan, R. PPAR Agonists for the Treatment of Neuroinflammatory Diseases. *Trends Pharmacol. Sci.* **2024**, 45 (1), 9–23. <https://doi.org/https://doi.org/10.1016/j.tips.2023.11.004>.
- (111) Prashantha Kumar, B. R.; Kumar, A. P.; Jose, J. A.; Prabitha, P.; Yuvaraj, S.; Chipurupalli, S.; Jeyarani, V.; Manisha, C.; Banerjee, S.; Jeyabalan, J. B.; Mohankumar, S. K.; Dhanabal, S. P.; Justin, A. Minutes of PPAR- γ Agonism and Neuroprotection. *Neurochem. Int.* **2020**, 140, 104814. <https://doi.org/https://doi.org/10.1016/j.neuint.2020.104814>.
- (112) Pizcueta, P.; Vergara, C.; Emanuele, M.; Vilalta, A.; Rodríguez-Pascau, L.; Martinell, M. Development of PPAR γ Agonists for the Treatment of Neuroinflammatory and Neurodegenerative Diseases: Leriglitazone as a Promising Candidate. *Int. J. Mol.*

- Sci.* **2023**, *24* (4). <https://doi.org/10.3390/ijms24043201>.
- (113) Dalen, K. T.; Ulven, S. M.; Bamberg, K.; Gustafsson, J.-Å.; Nebb, H. I. Expression of the Insulin-Responsive Glucose Transporter GLUT4 in Adipocytes Is Dependent on Liver X Receptor A*. *J. Biol. Chem.* **2003**, *278* (48), 48283–48291. <https://doi.org/https://doi.org/10.1074/jbc.M302287200>.
- (114) Chiarelli, F.; Di Marzio, D. Peroxisome Proliferator-Activated Receptor-Gamma Agonists and Diabetes: Current Evidence and Future Perspectives. *Vasc. Health Risk Manag.* **2008**, *4* (2), 297–304. <https://doi.org/10.2147/vhrm.s993>.
- (115) Frkic, R. L.; Richter, K.; Bruning, J. B. The Therapeutic Potential of Inhibiting PPAR γ Phosphorylation to Treat Type 2 Diabetes. *J. Biol. Chem.* **2021**, *297* (3), 101030. <https://doi.org/https://doi.org/10.1016/j.jbc.2021.101030>.
- (116) Bou, M.; Montfort, J.; Le Cam, A.; Ralli  re, C.; Lebre  t, V.; Gabillard, J.-C.; Weil, C.; Guti  rrez, J.; Rescan, P.-Y.; Capilla, E.; Navarro, I. Gene Expression Profile during Proliferation and Differentiation of Rainbow Trout Adipocyte Precursor Cells. *BMC Genomics* **2017**, *18* (1), 347. <https://doi.org/10.1186/s12864-017-3728-0>.
- (117) Mar  chal, L.; Laviolette, M.; Rodrigue-Way, A.; Sow, B.; Brochu, M.; Caron, V.; Tremblay, A. The CD36-PPAR γ Pathway in Metabolic Disorders. *Int. J. Mol. Sci.* **2018**, *19* (5). <https://doi.org/10.3390/ijms19051529>.
- (118) Lange, N. F.; Graf, V.; Caussy, C.; Dufour, J.-F. PPAR-Targeted Therapies in the Treatment of Non-Alcoholic Fatty Liver Disease in Diabetic Patients. *Int. J. Mol. Sci.* **2022**, *23* (8). <https://doi.org/10.3390/ijms23084305>.
- (119) Yamashita, S.; Masuda, D.; Matsuzawa, Y. Pemafibrate, a New Selective PPAR α Modulator: Drug Concept and Its Clinical Applications for Dyslipidemia and Metabolic Diseases. *Curr. Atheroscler. Rep.* **2020**, *22* (1), 5. <https://doi.org/10.1007/s11883-020-0823-5>.
- (120) Jain, M. R.; Giri, S. R.; Bhoi, B.; Trivedi, C.; Rath, A.; Rathod, R.; Ranvir, R.; Kadam, S.; Patel, H.; Swain, P.; Roy, S. S.; Das, N.; Karmakar, E.; Wahli, W.; Patel, P. R. Dual PPAR α/γ Agonist Saroglitazar Improves Liver Histopathology and Biochemistry in Experimental NASH Models. *Liver Int. Off. J. Int. Assoc. Study Liver* **2018**, *38* (6), 1084–1094. <https://doi.org/10.1111/liv.13634>.
- (121) Chen, H.; Tan, H.; Wan, J.; Zeng, Y.; Wang, J.; Wang, H.; Lu, X. PPAR- γ Signaling in Nonalcoholic Fatty Liver Disease: Pathogenesis and Therapeutic Targets. *Pharmacol. Ther.* **2023**, *245*, 108391. <https://doi.org/https://doi.org/10.1016/j.pharmthera.2023.108391>.
- (122) Meng, Q.-Q.; Feng, Z.-C.; Zhang, X.-L.; Hu, L.-Q.; Wang, M.; Zhang, H.-F.; Li, S.-M. PPAR- γ Activation Exerts an Anti-Inflammatory Effect by Suppressing the NLRP3 Inflammasome in Spinal Cord-Derived Neurons. *Mediators Inflamm.* **2019**, *2019*, 6386729. <https://doi.org/10.1155/2019/6386729>.
- (123) Hazra, S.; Miyahara, T.; Rippe, R. A.; Tsukamoto, H. PPAR Gamma and Hepatic Stellate Cells. *Comp. Hepatol.* **2004**, *3* Suppl 1 (Suppl 1), S7.

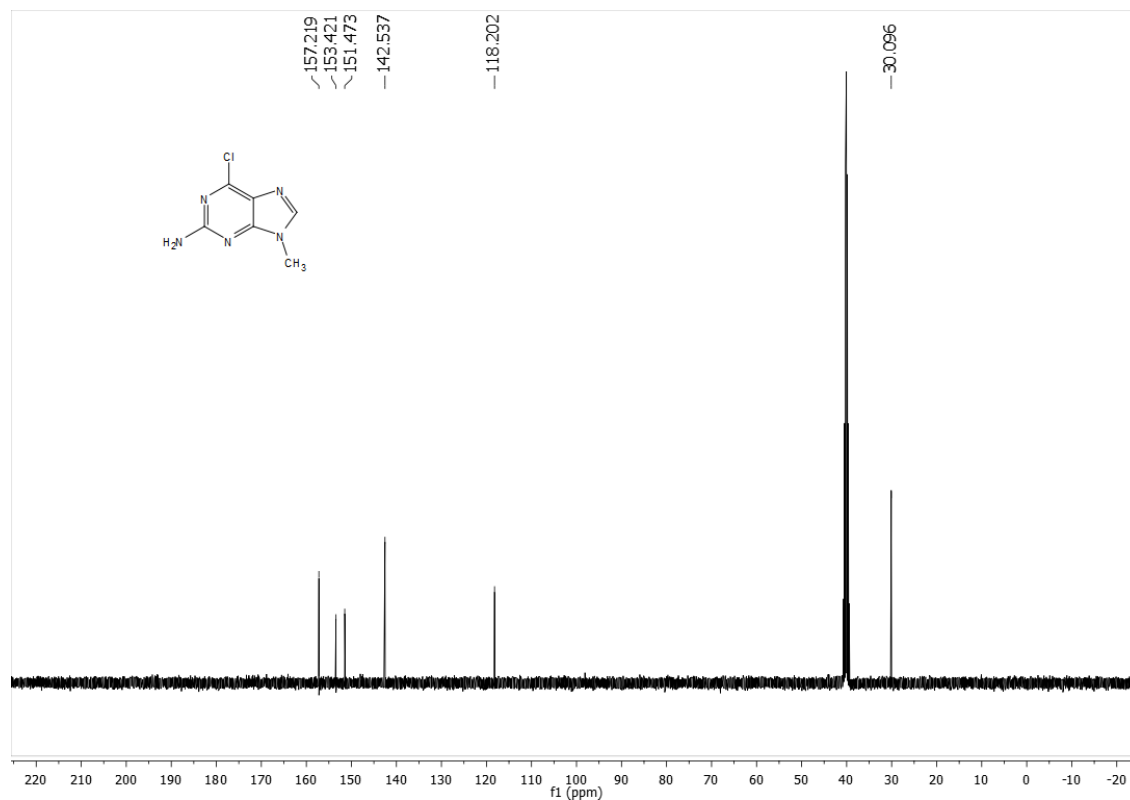
- <https://doi.org/10.1186/1476-5926-2-S1-S7>.
- (124) Corona, J. C.; Duchon, M. R. PPAR γ as a Therapeutic Target to Rescue Mitochondrial Function in Neurological Disease. *Free Radic. Biol. Med.* **2016**, *100*, 153–163. <https://doi.org/https://doi.org/10.1016/j.freeradbiomed.2016.06.023>.
- (125) Park, J.-S.; Rustamov, N.; Roh, Y.-S. The Roles of NFR2-Regulated Oxidative Stress and Mitochondrial Quality Control in Chronic Liver Diseases. *Antioxidants*. 2023. <https://doi.org/10.3390/antiox12111928>.
- (126) Kim, T.; Yang, Q. Peroxisome-Proliferator-Activated Receptors Regulate Redox Signaling in the Cardiovascular System. *World J. Cardiol.* **2013**, *5* (6), 164–174. <https://doi.org/10.4330/wjc.v5.i6.164>.

2.8 ANNEXURE

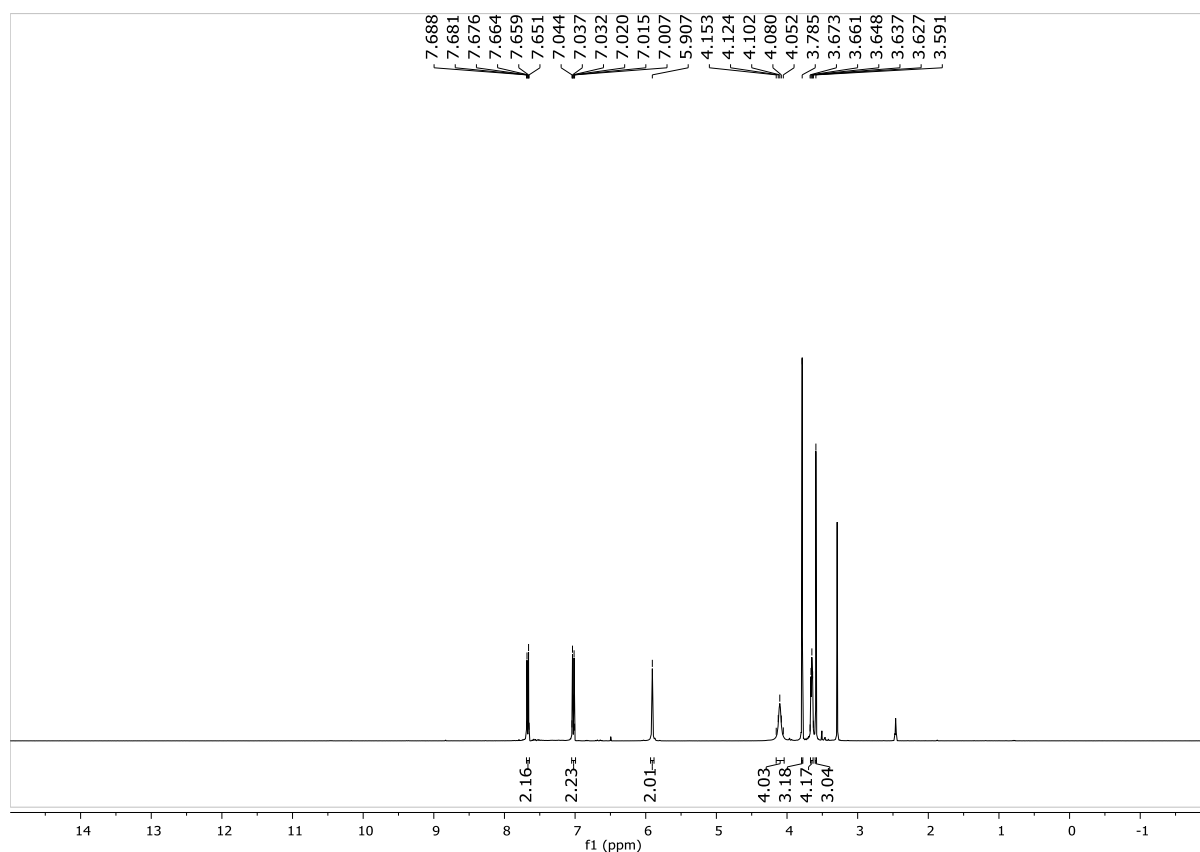
^1H NMR of compound **2** (400 MHz, d_6 -DMSO):



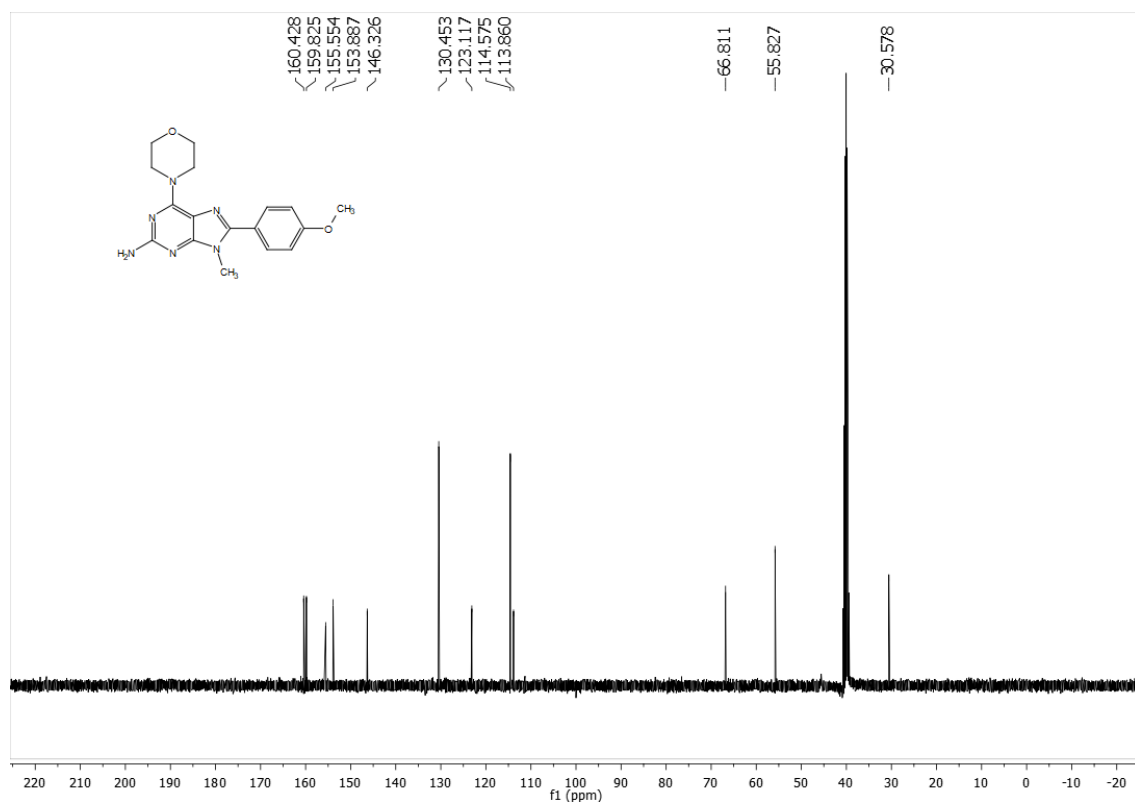
^{13}C NMR of compound **2** (100 MHz, d_6 -DMSO):



^1H NMR of compound **5** (400 MHz, d_6 -DMSO):

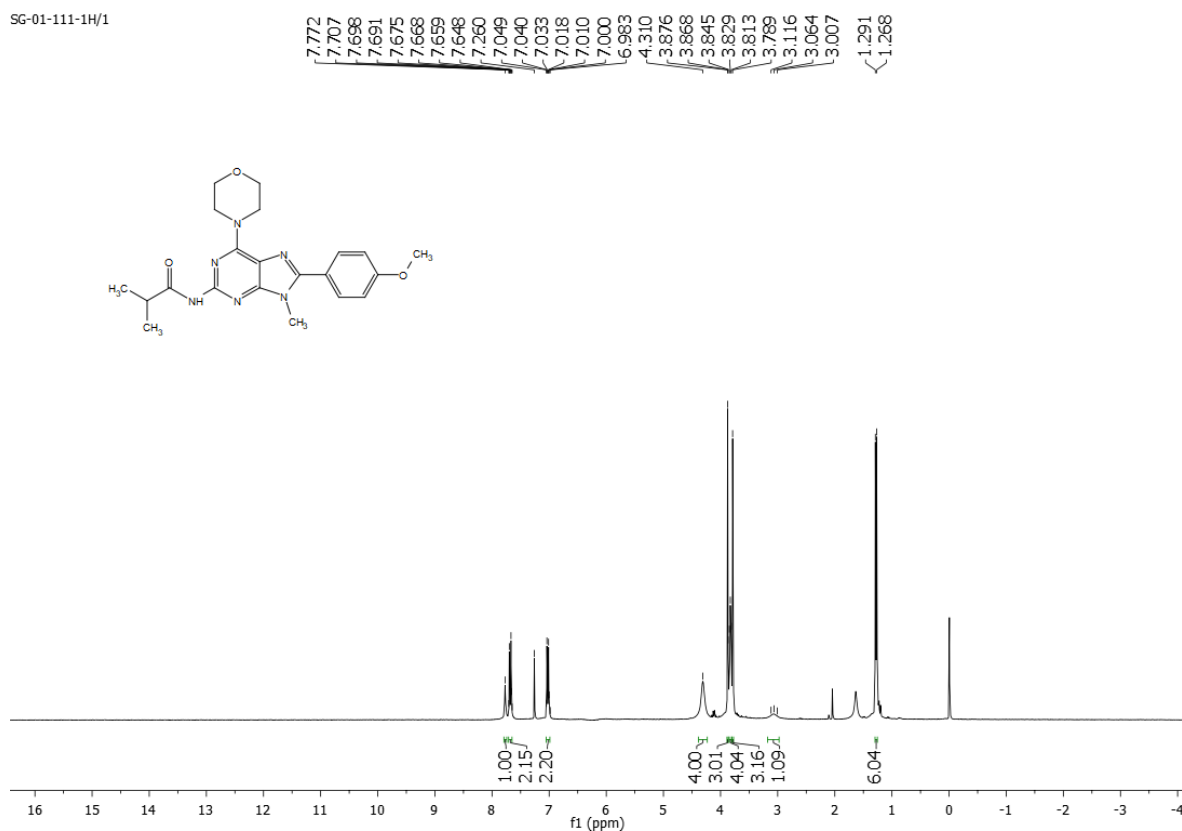
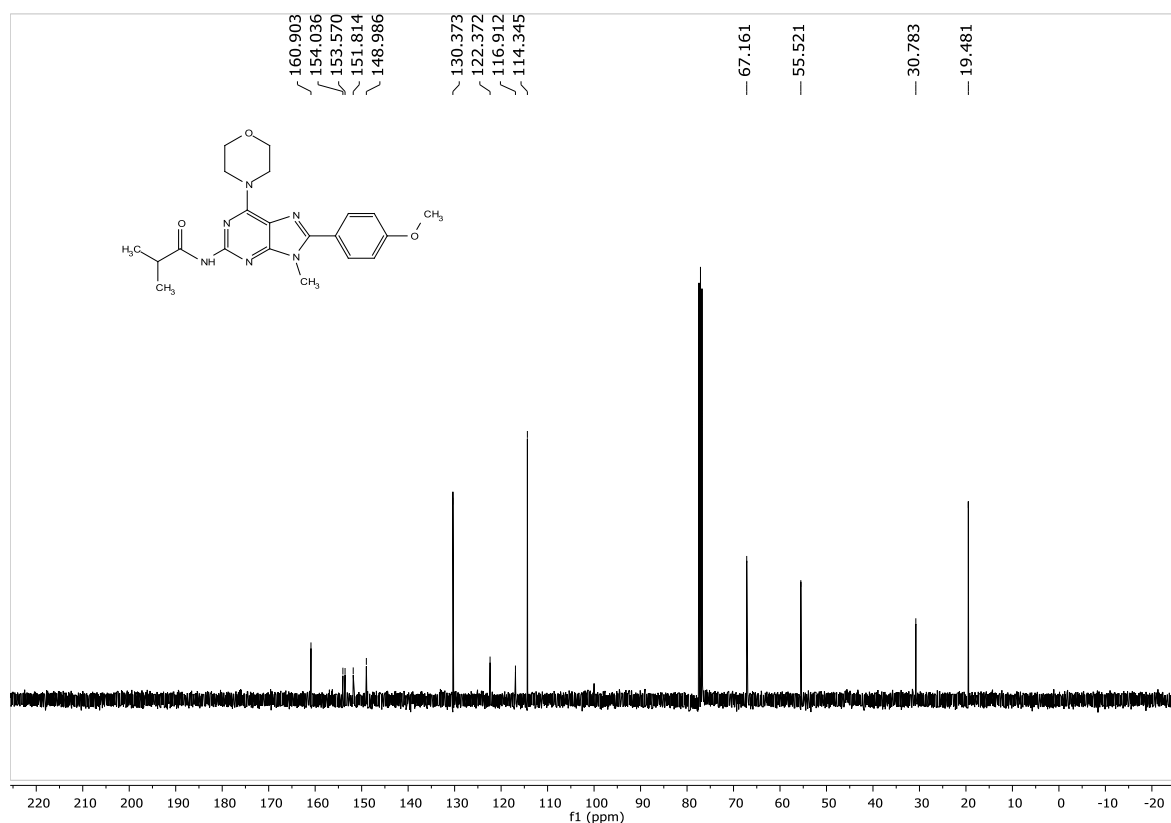


^{13}C NMR of compound **5** (100 MHz, d_6 -DMSO):



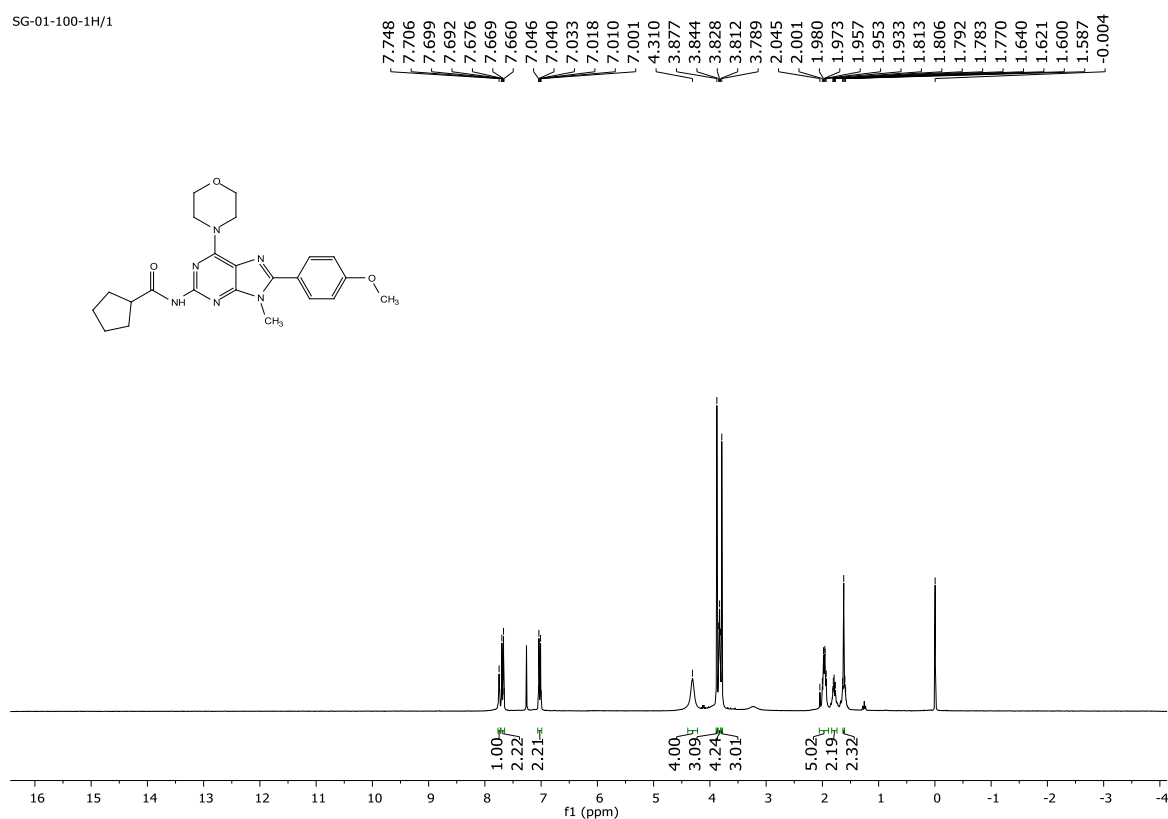
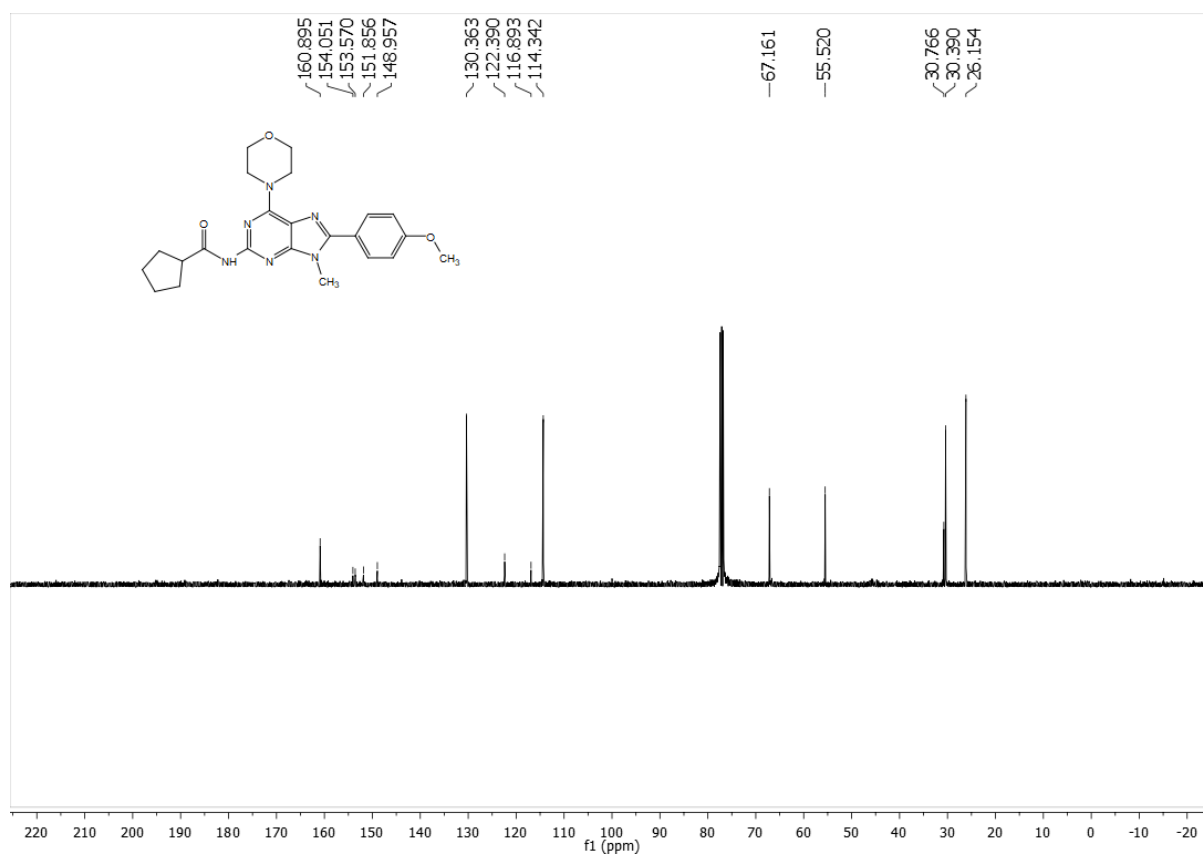
¹H NMR of compound **6** (300 MHz, CDCl₃):

SG-01-111-1H/1

¹³C NMR of compound **6** (100 MHz, CDCl₃):

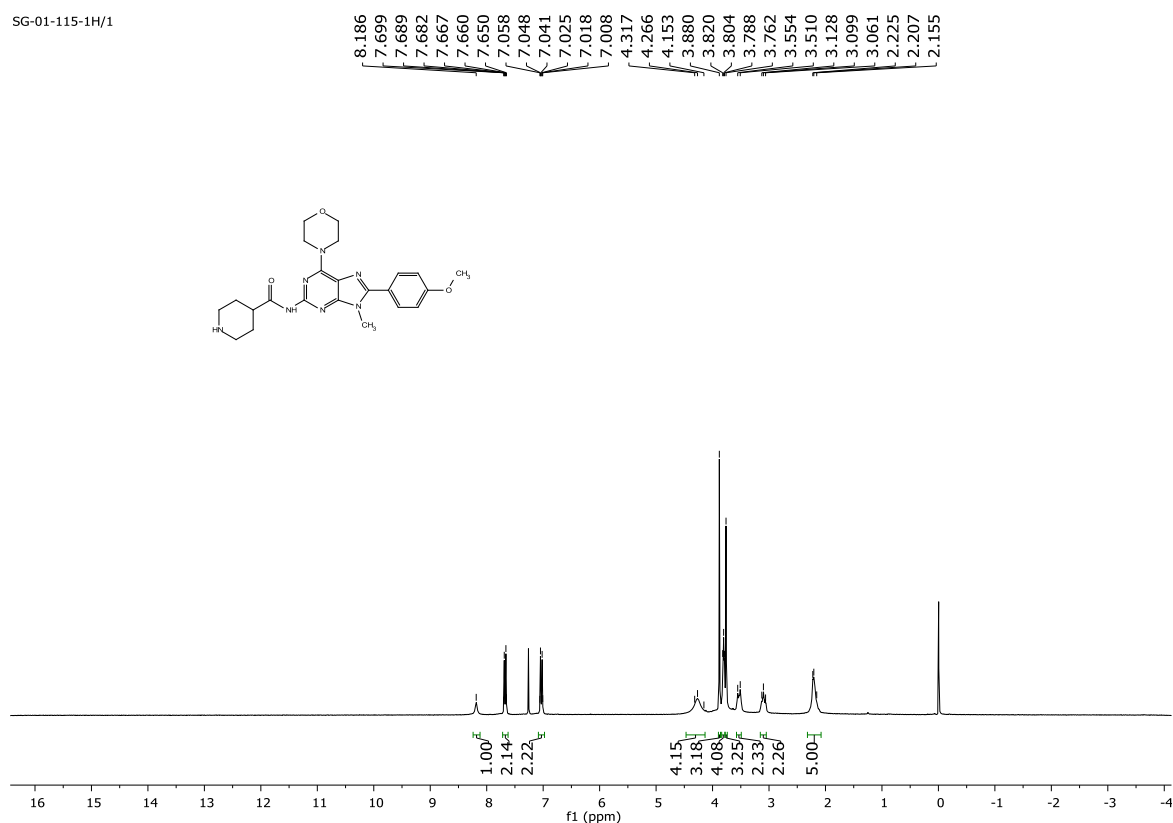
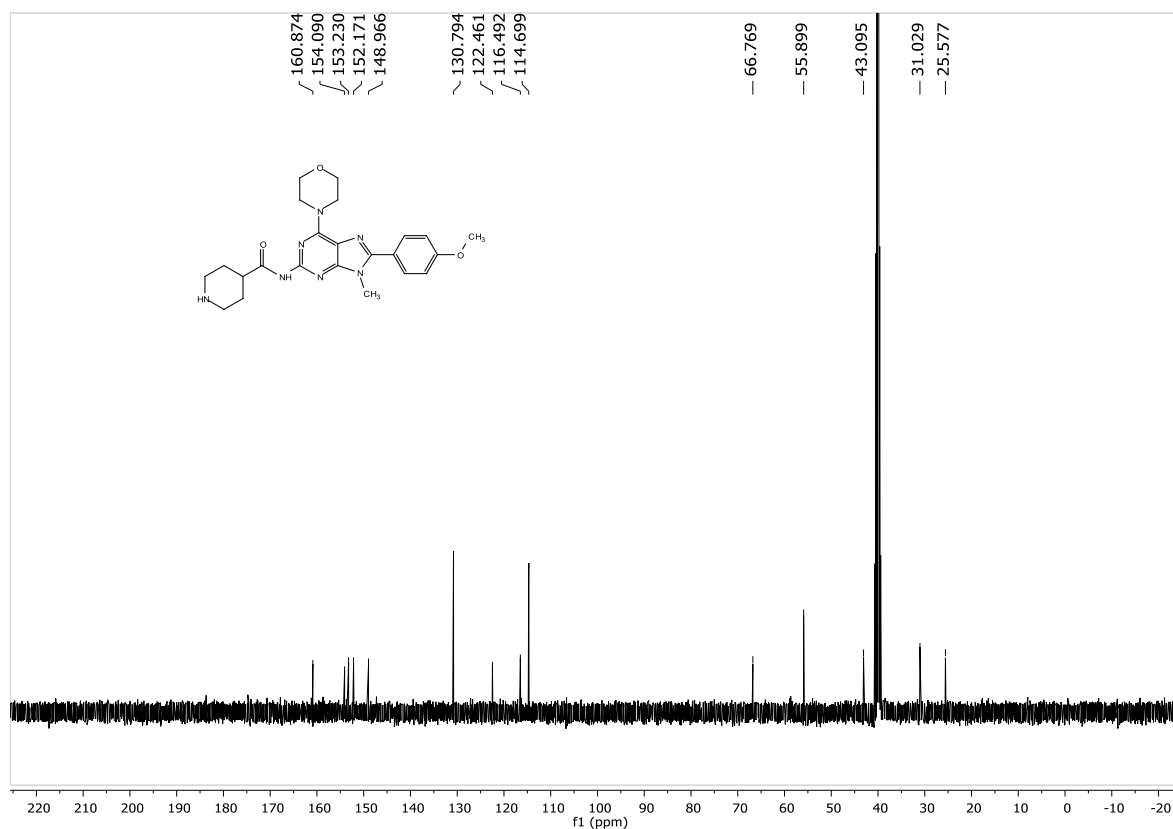
¹H NMR of compound 7 (400 MHz, CDCl₃):

SG-01-100-1H/1

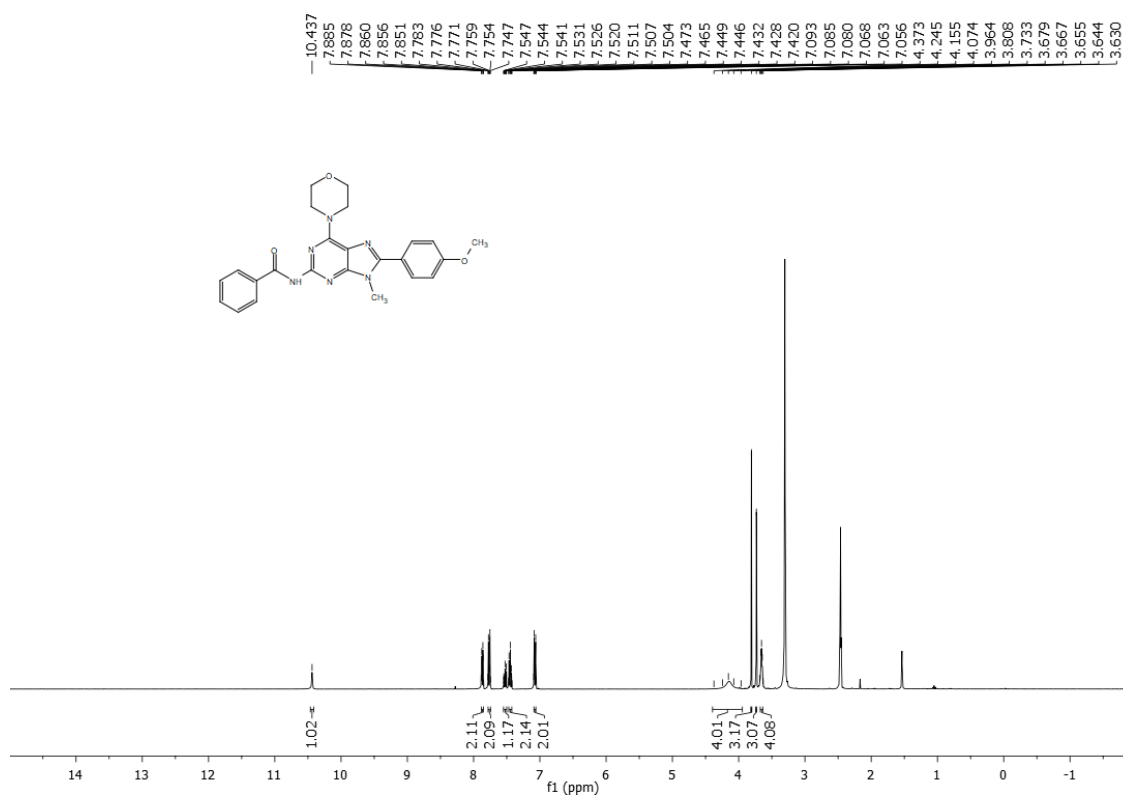
¹³C NMR of compound 7 (100 MHz, CDCl₃):

¹H NMR of compound **8** (400 MHz, CDCl₃):

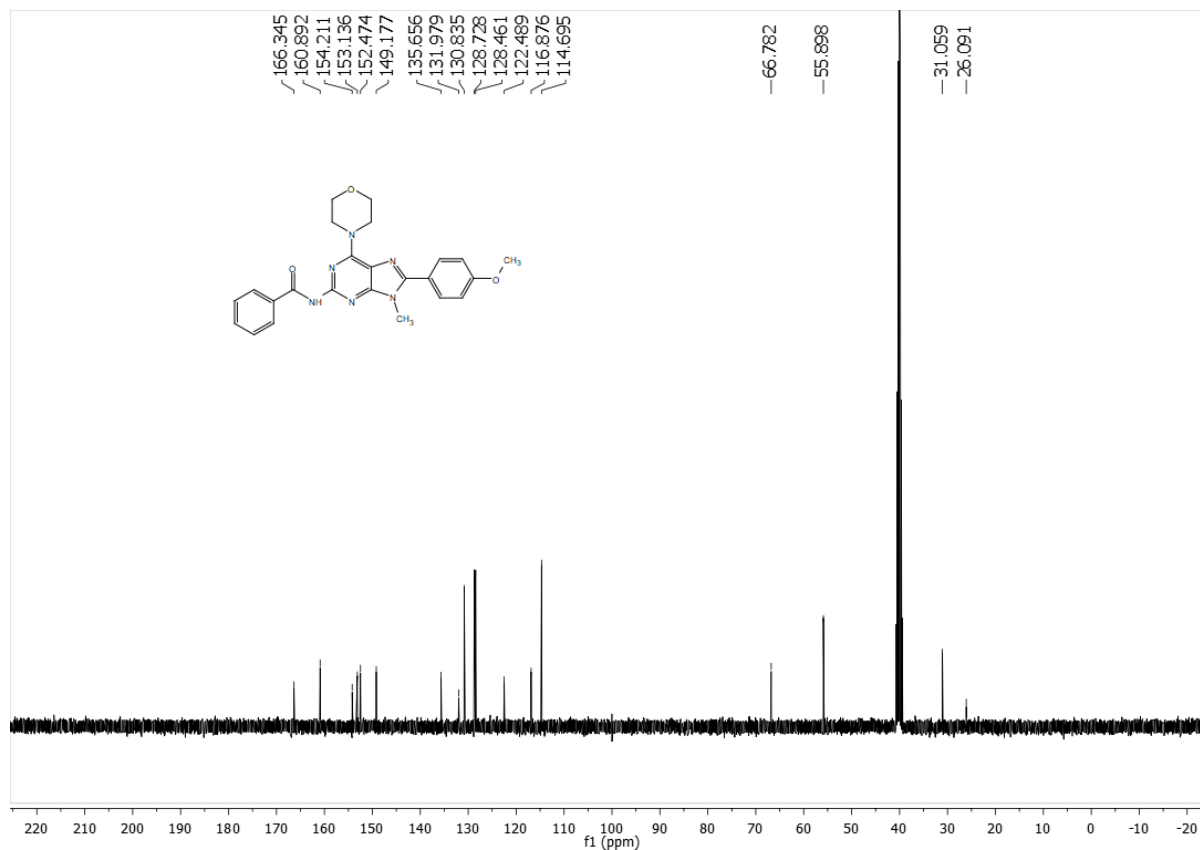
SG-01-115-1H/1

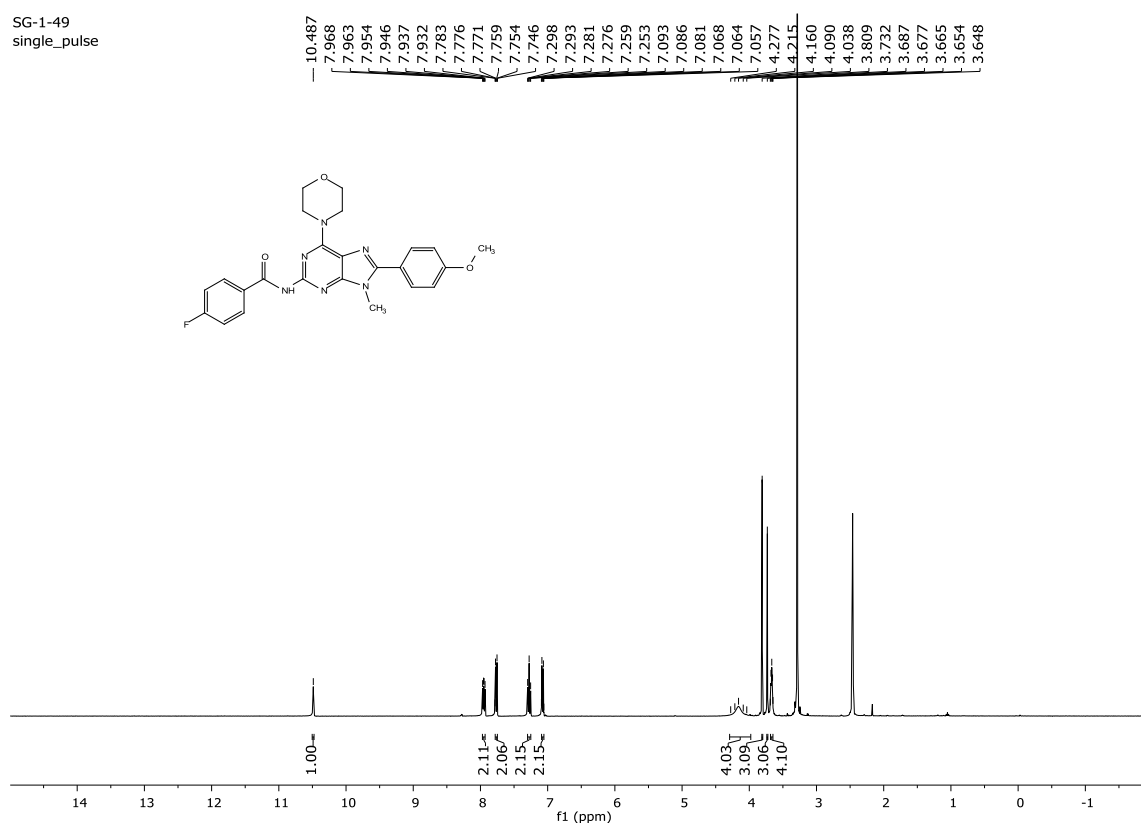
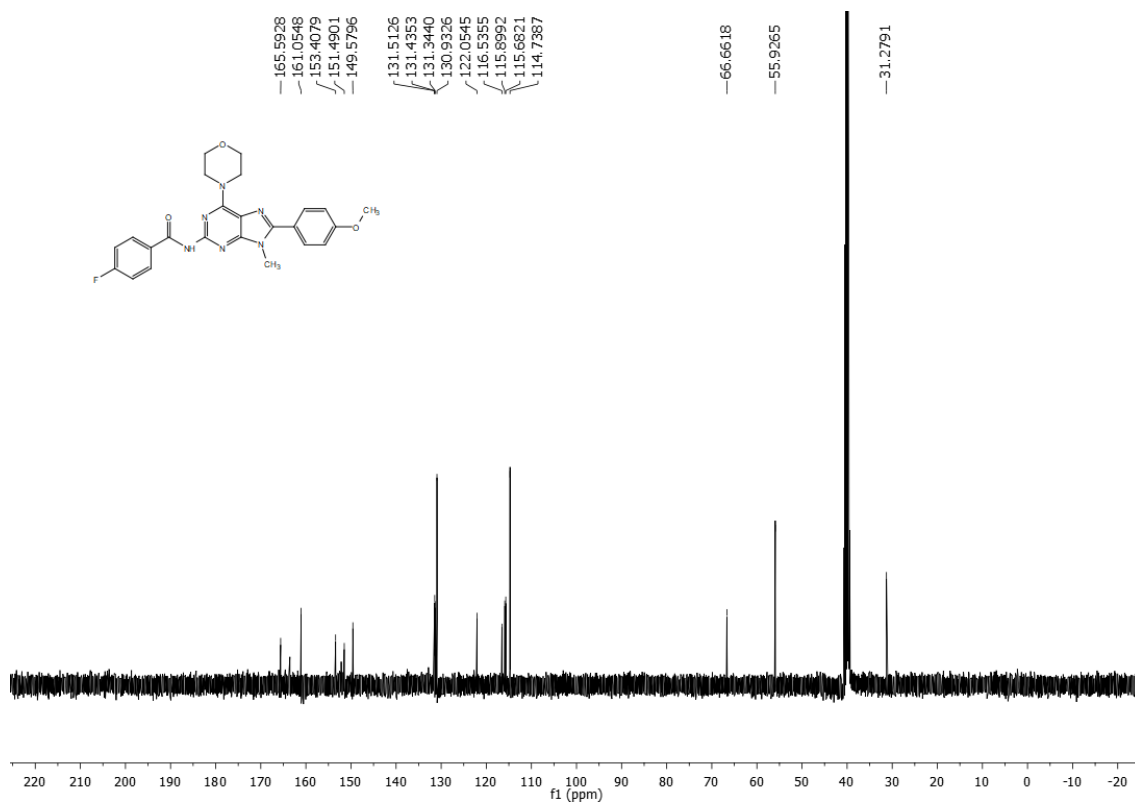
¹³C NMR of compound **8** (100 MHz, d₆-DMSO):

^1H NMR of compound **9** (400 MHz, d_6 -DMSO):



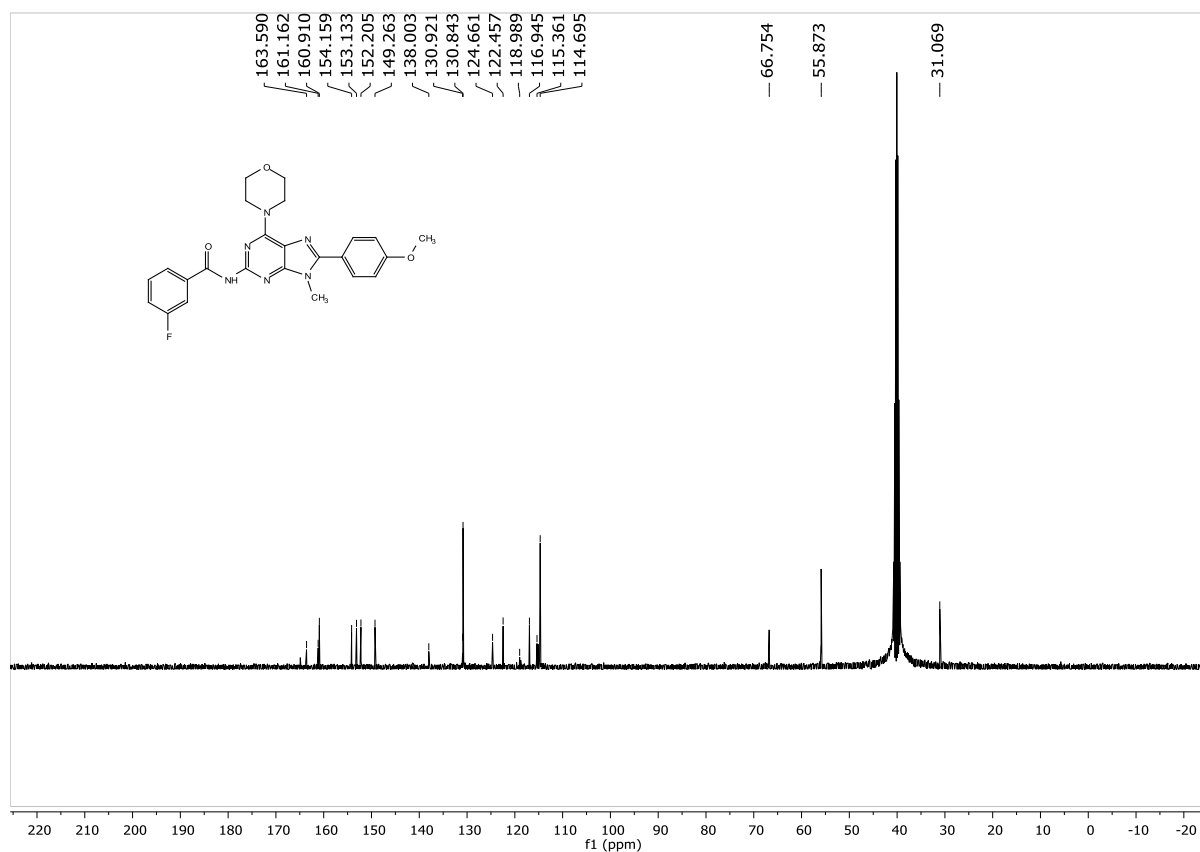
^{13}C NMR of compound **9** (100 MHz, d_6 -DMSO):

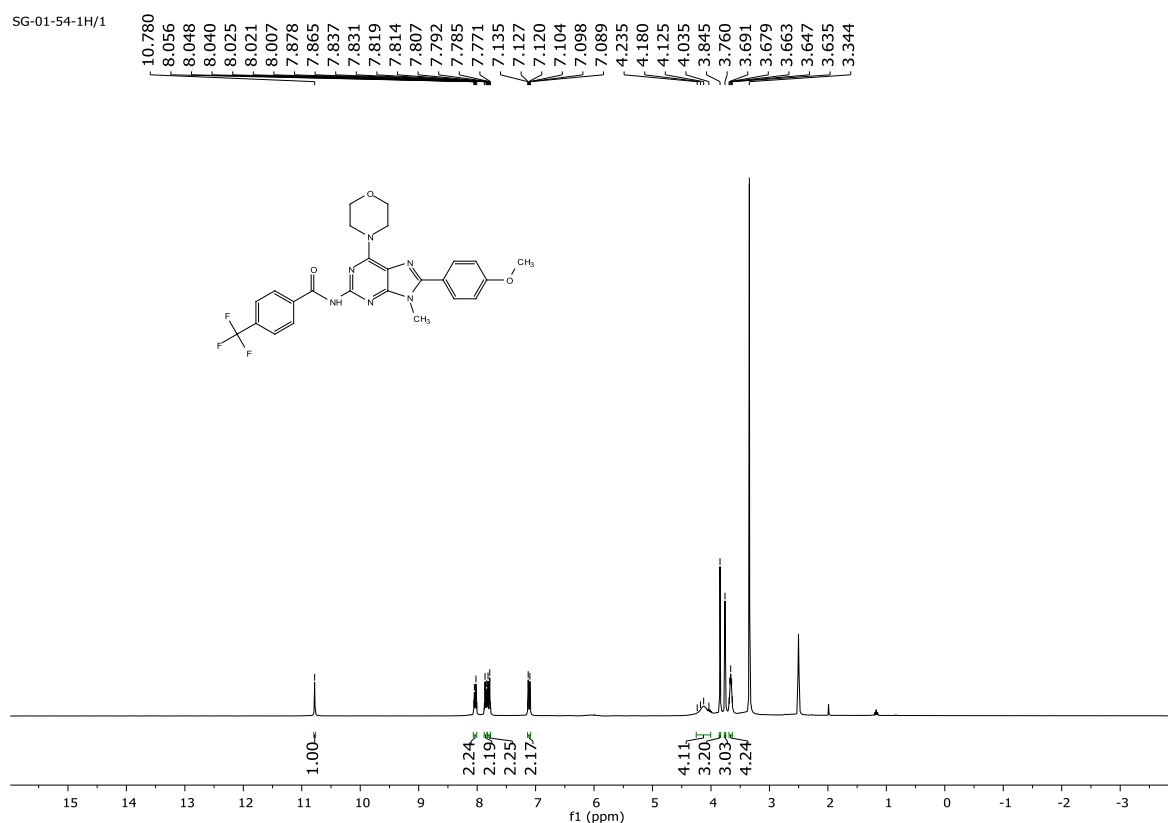
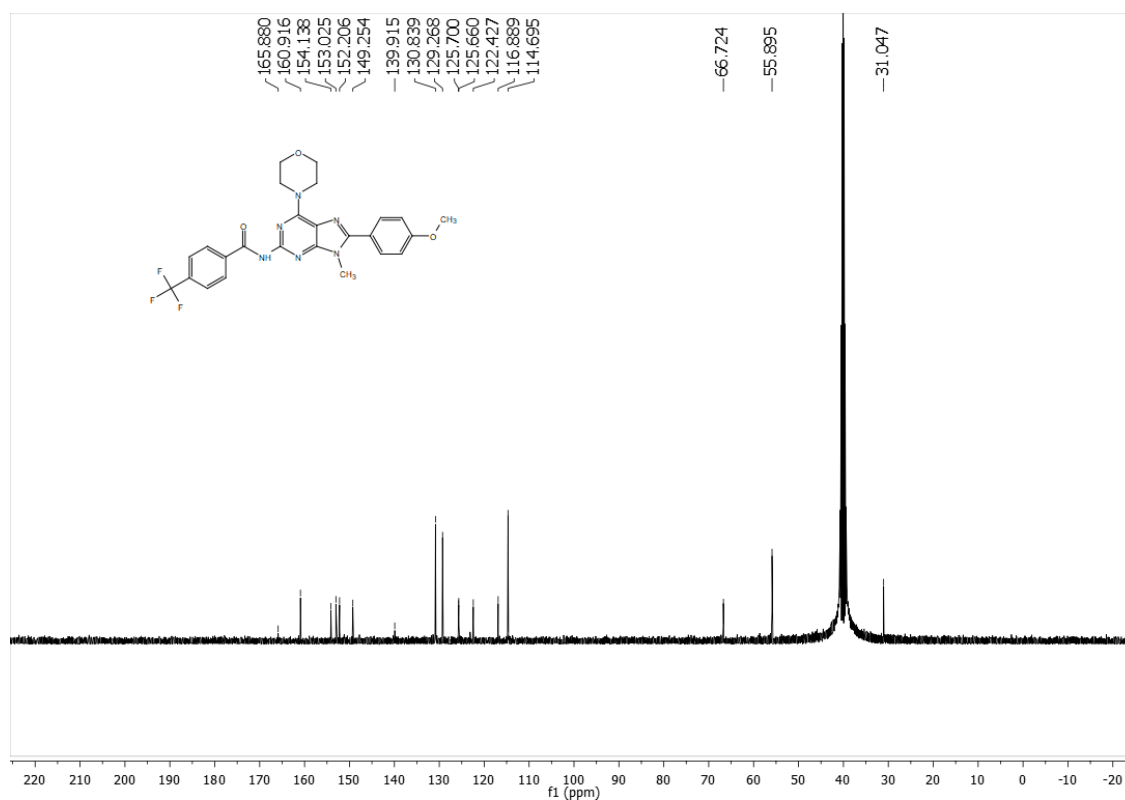


¹H NMR of compound 10 (400 MHz, d₆-DMSO):SG-1-49
single_pulse**¹³C NMR of compound 10 (100 MHz, d₆-DMSO):**

¹H NMR of compound **11** (400 MHz, *d*₆-DMSO):

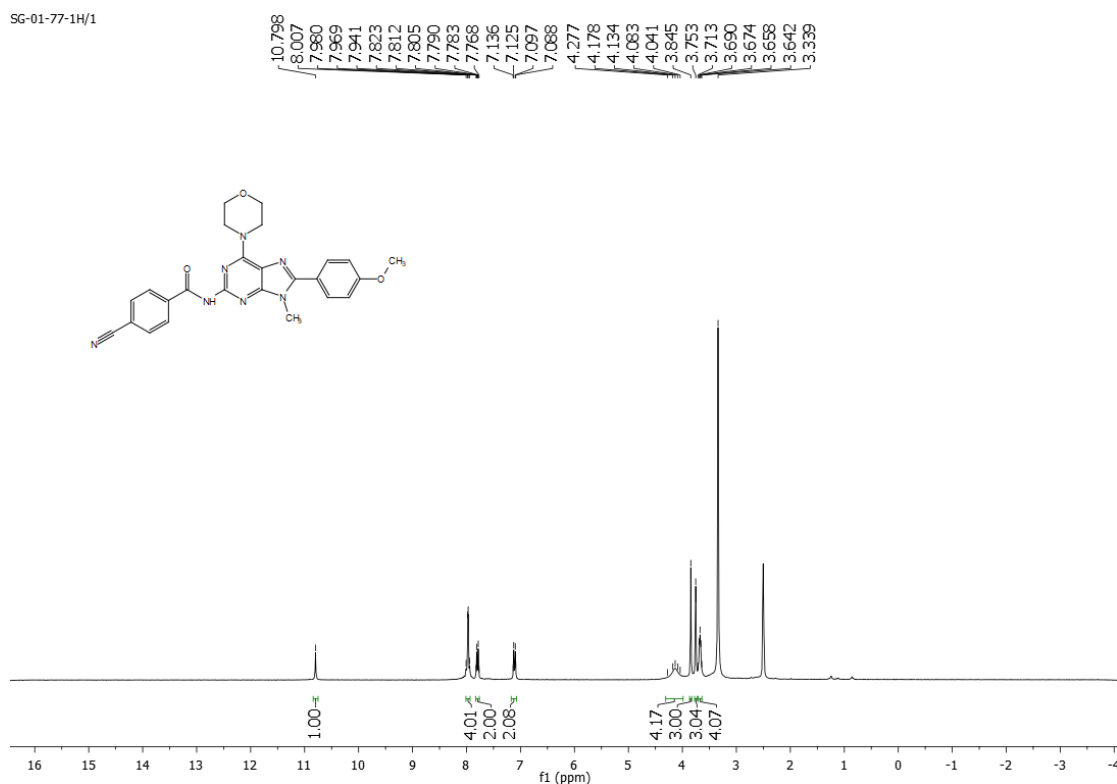
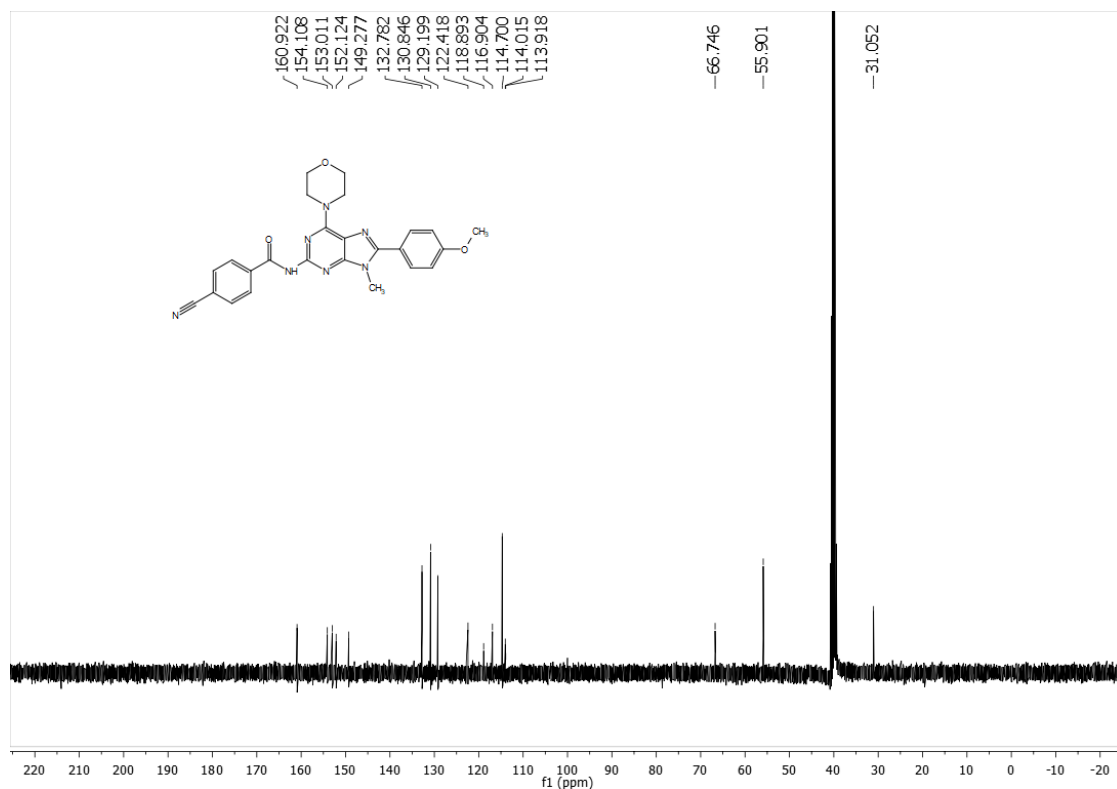
SG-01-68-1H/1

¹³C NMR of compound **11** (100 MHz, *d*₆-DMSO):

¹H NMR of compound 12 (400 MHz, d₆-DMSO):**¹³C NMR of compound 12 (100 MHz, d₆-DMSO):**

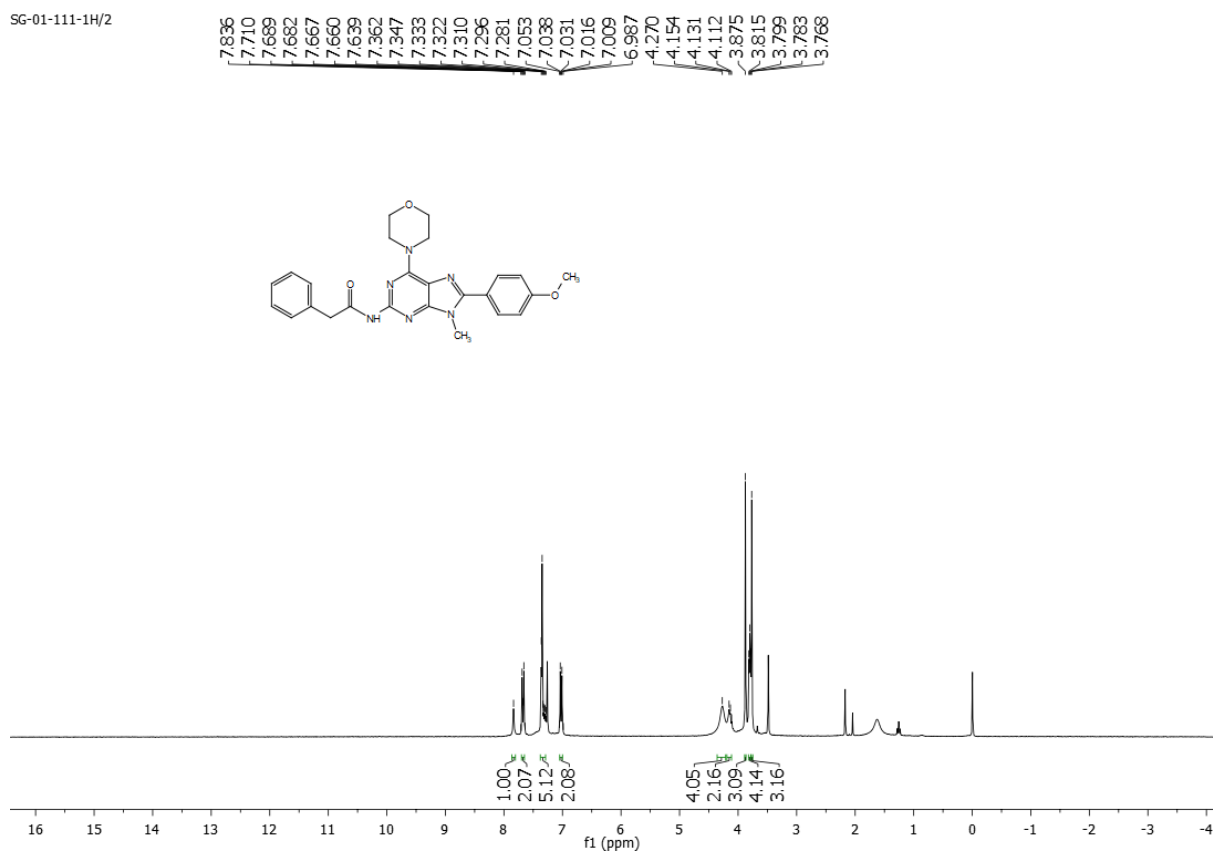
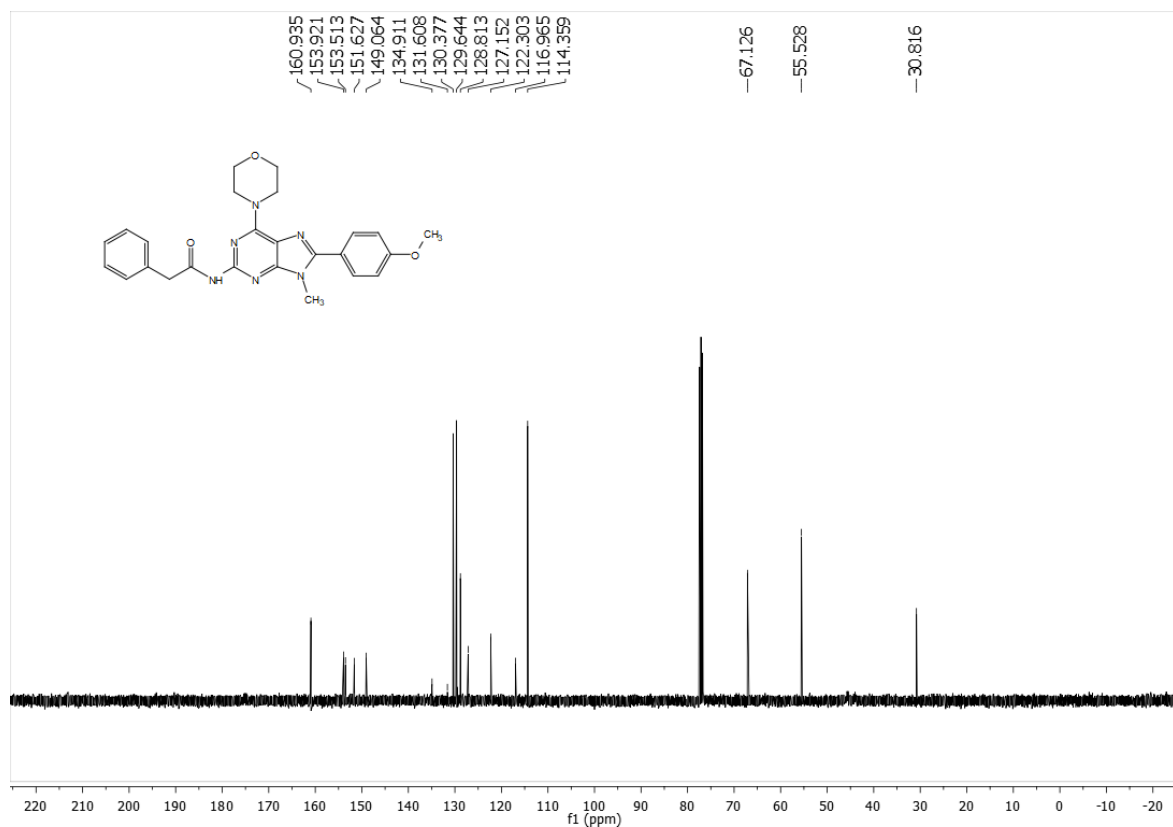
¹H NMR of compound **13** (400 MHz, *d*₆-DMSO):

SG-01-77-1H/1

¹³C NMR of compound **13** (100 MHz, *d*₆-DMSO):

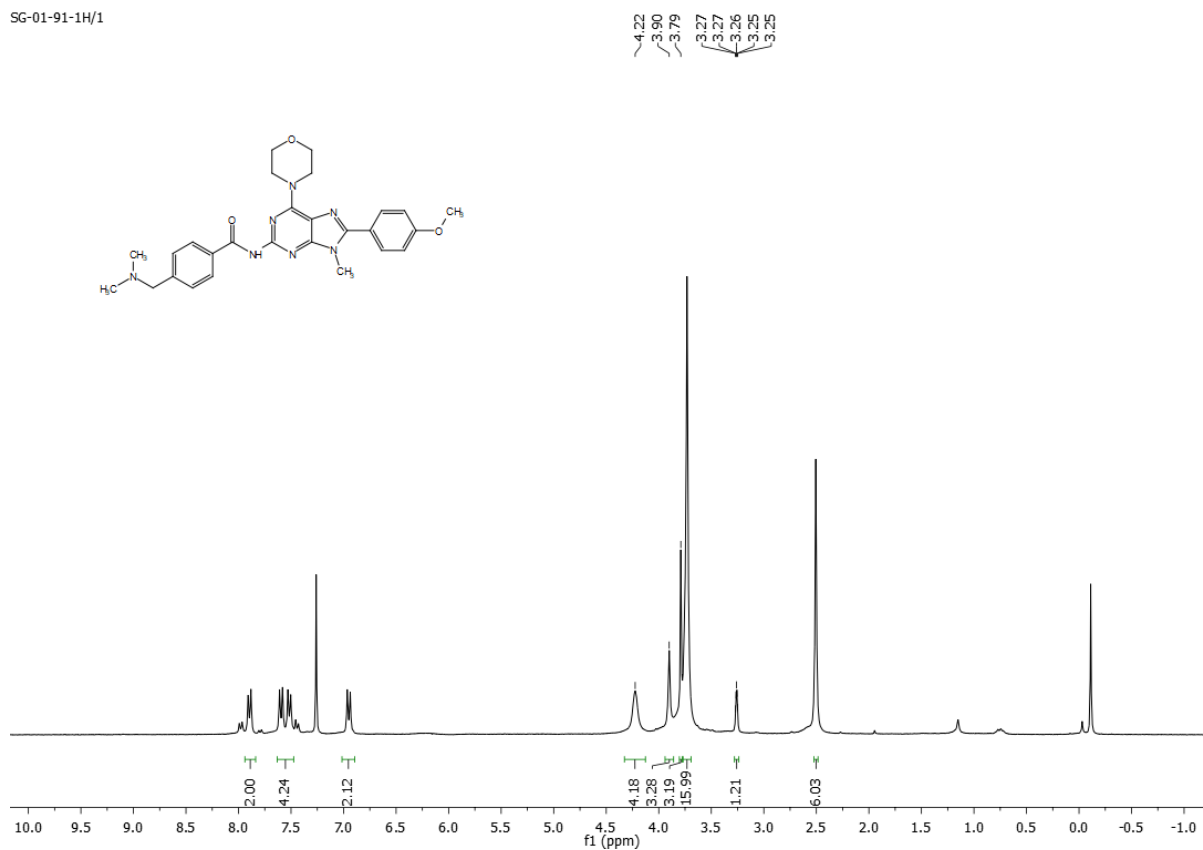
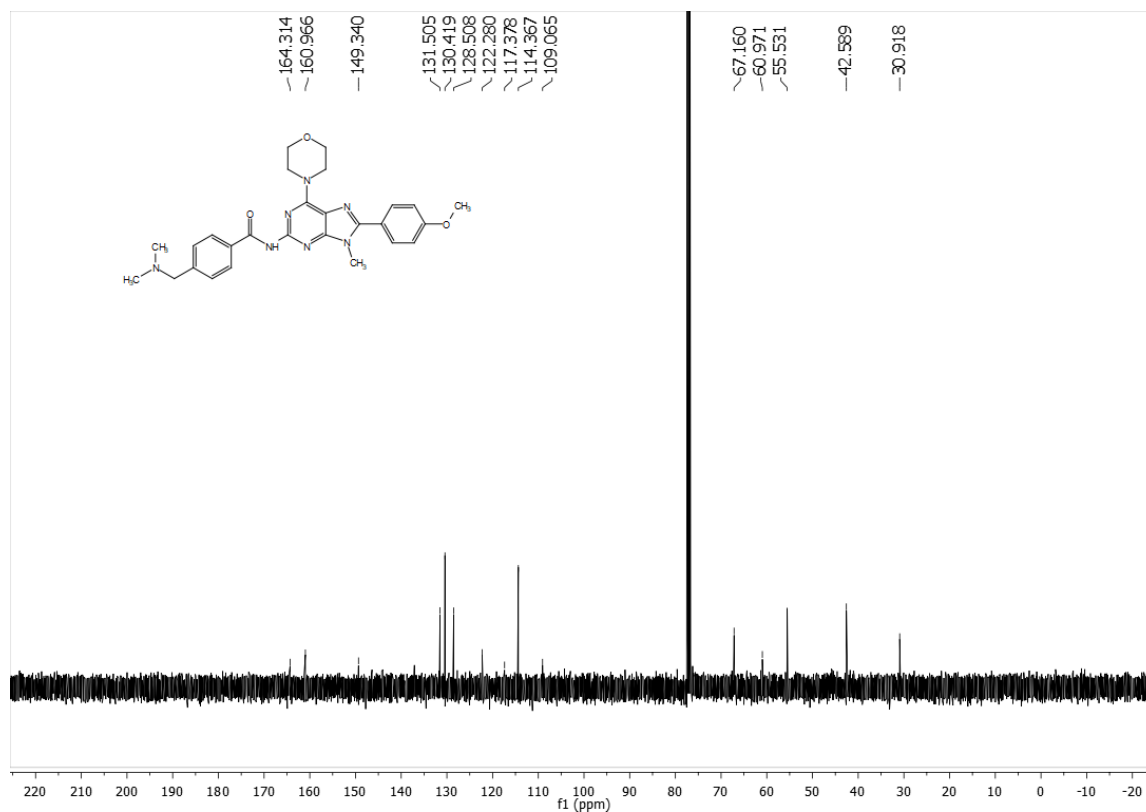
¹H NMR of compound **14** (400 MHz, CDCl₃):

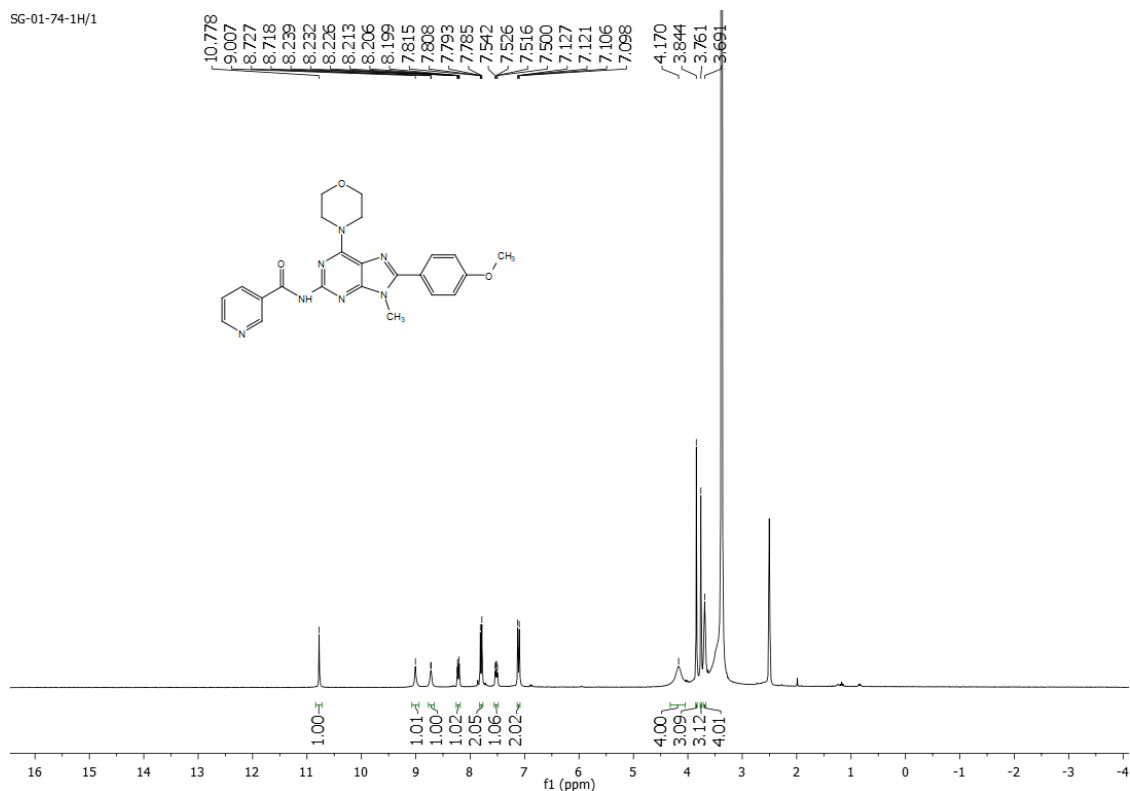
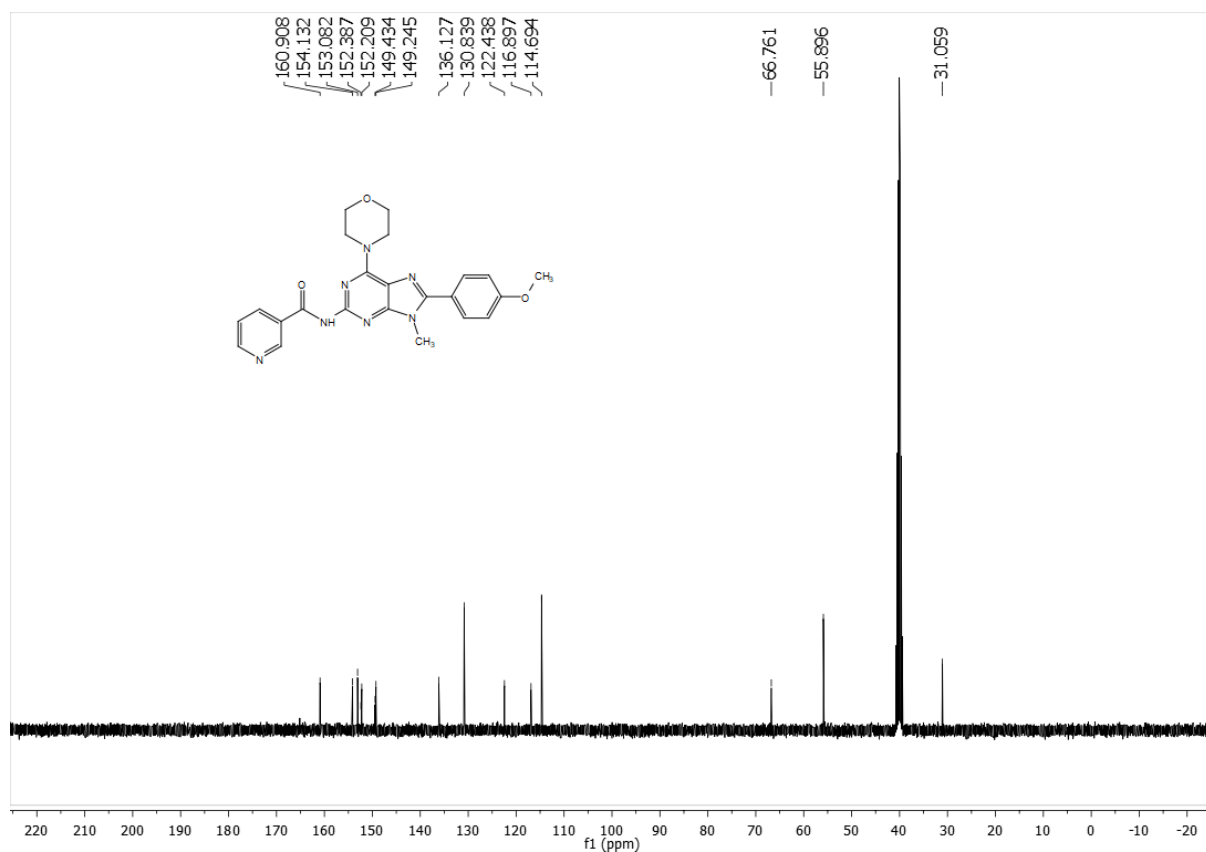
SG-01-111-1H/2

¹³C NMR of compound **14** (100 MHz, CDCl₃):

¹H NMR of compound **15** (400 MHz, CDCl₃):

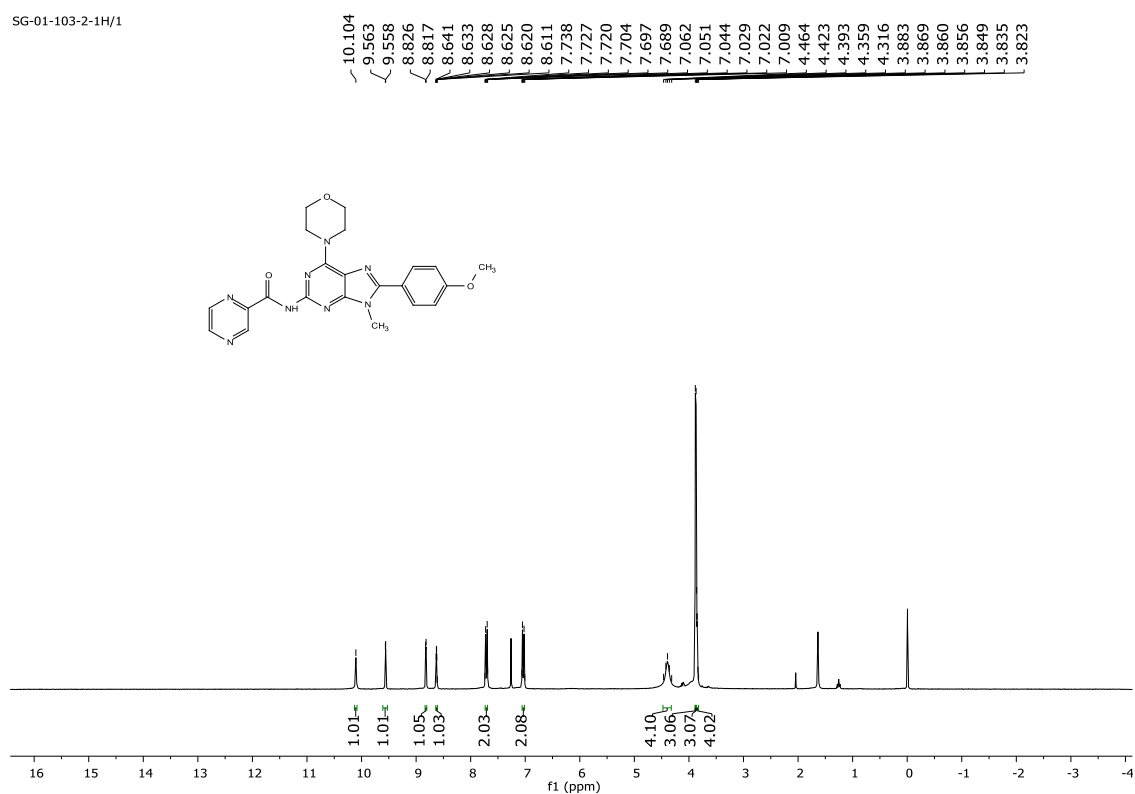
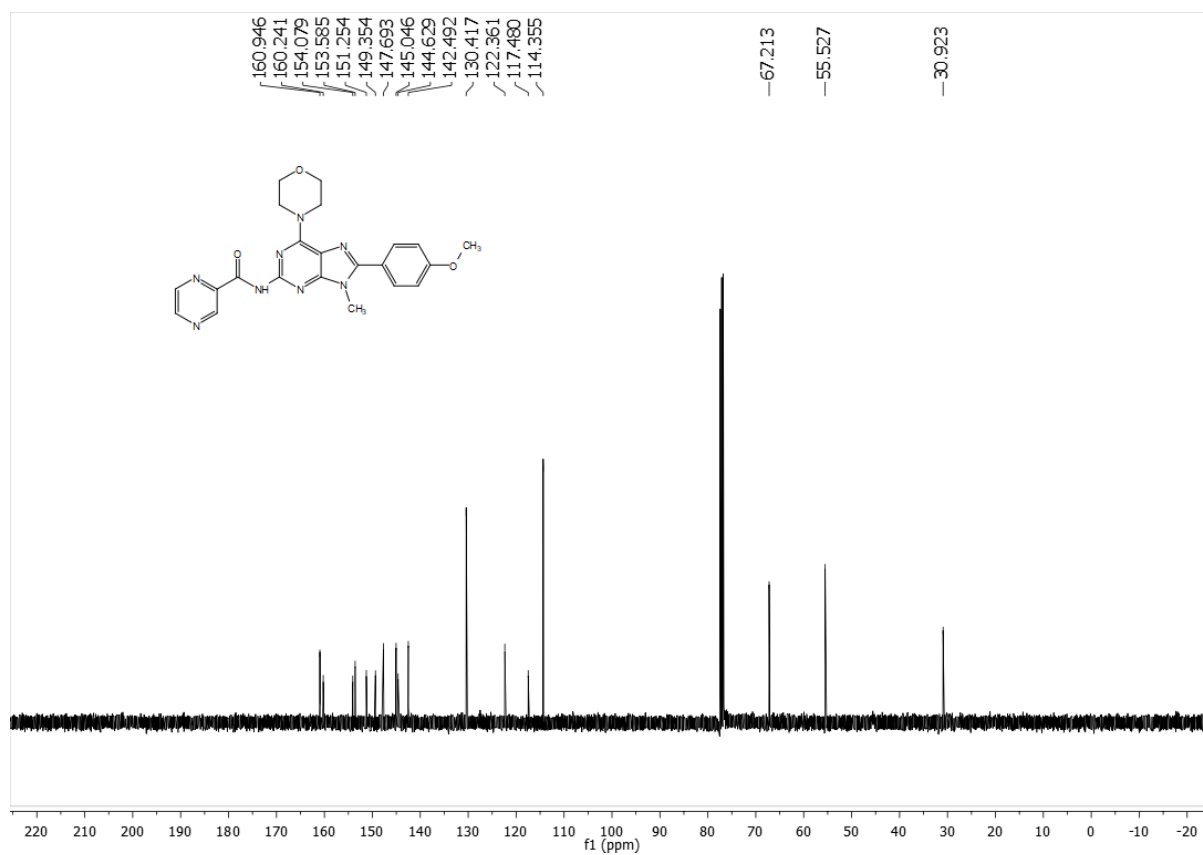
SG-01-91-1H/1

¹³C NMR of compound **15** (100 MHz, CDCl₃):

¹H NMR of compound **16** (400 MHz, *d*₆-DMSO):¹³C NMR of compound **16** (100 MHz, *d*₆-DMSO):

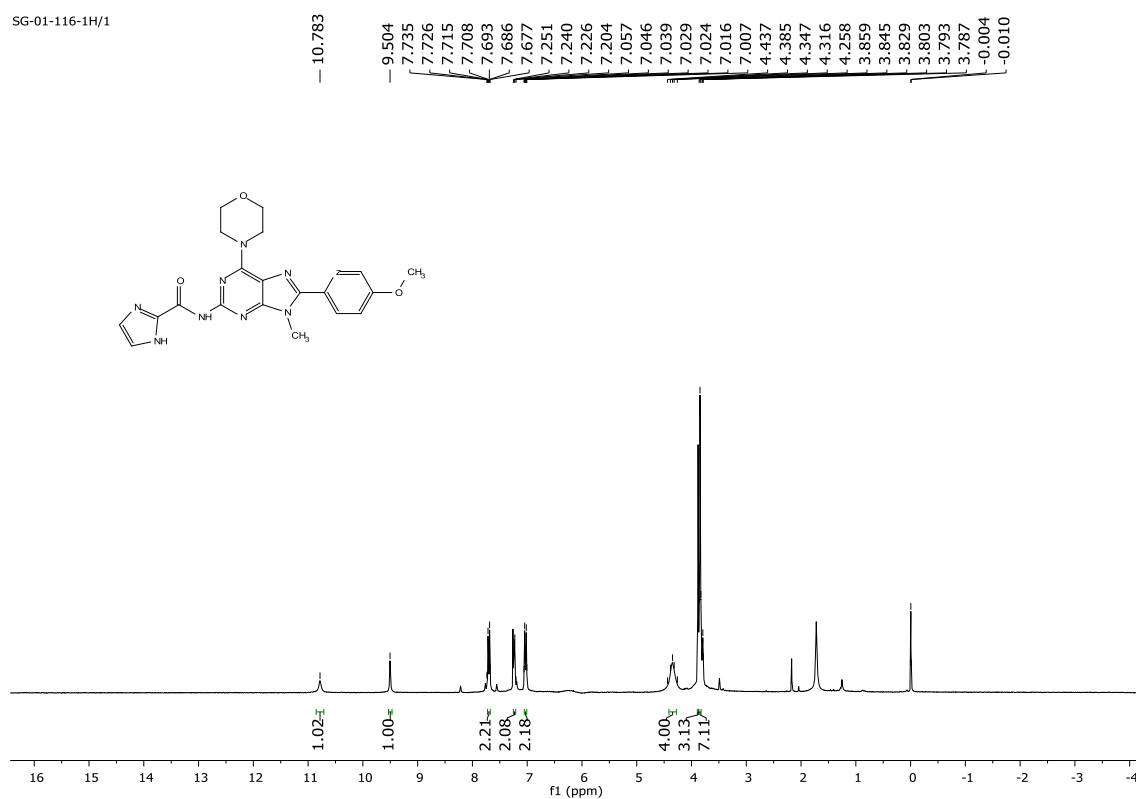
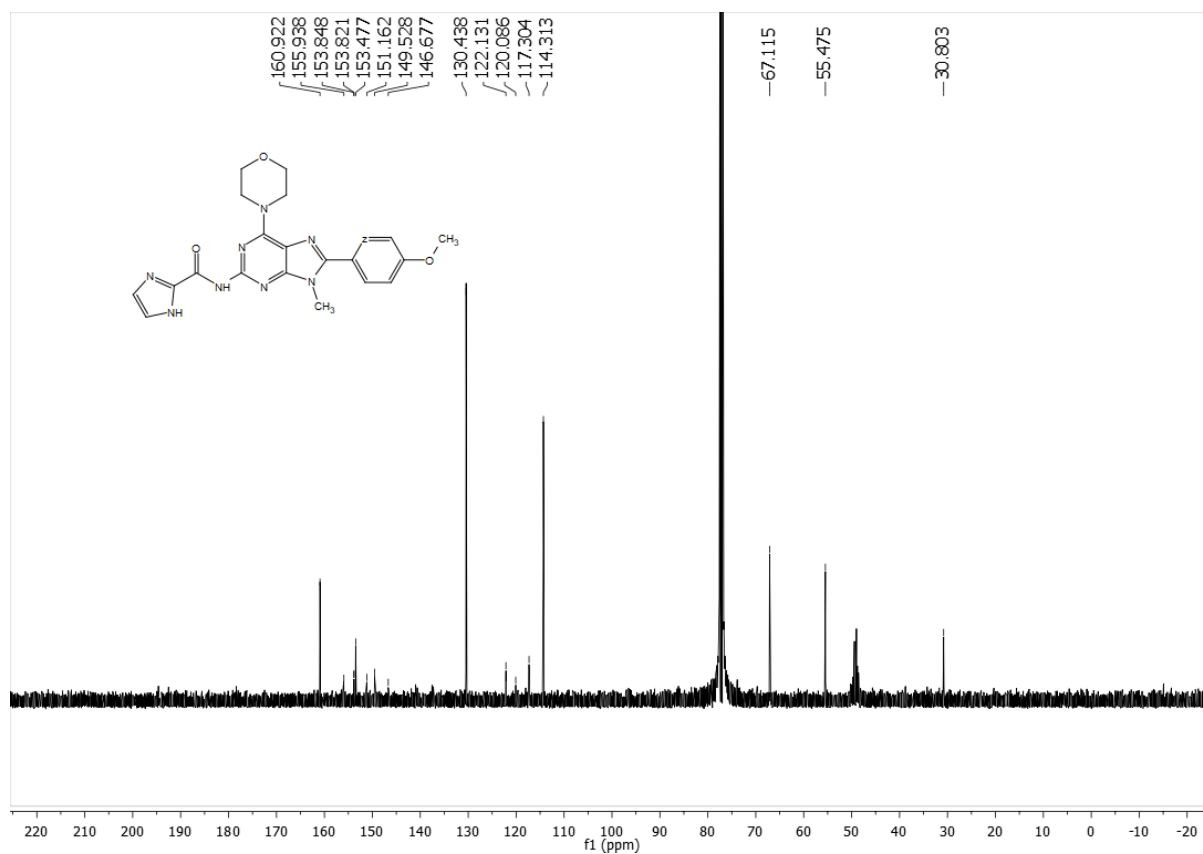
¹H NMR of compound **17** (400 MHz, CDCl₃):

SG-01-103-2-1H/1

¹³C NMR of compound **17** (100 MHz, CDCl₃):

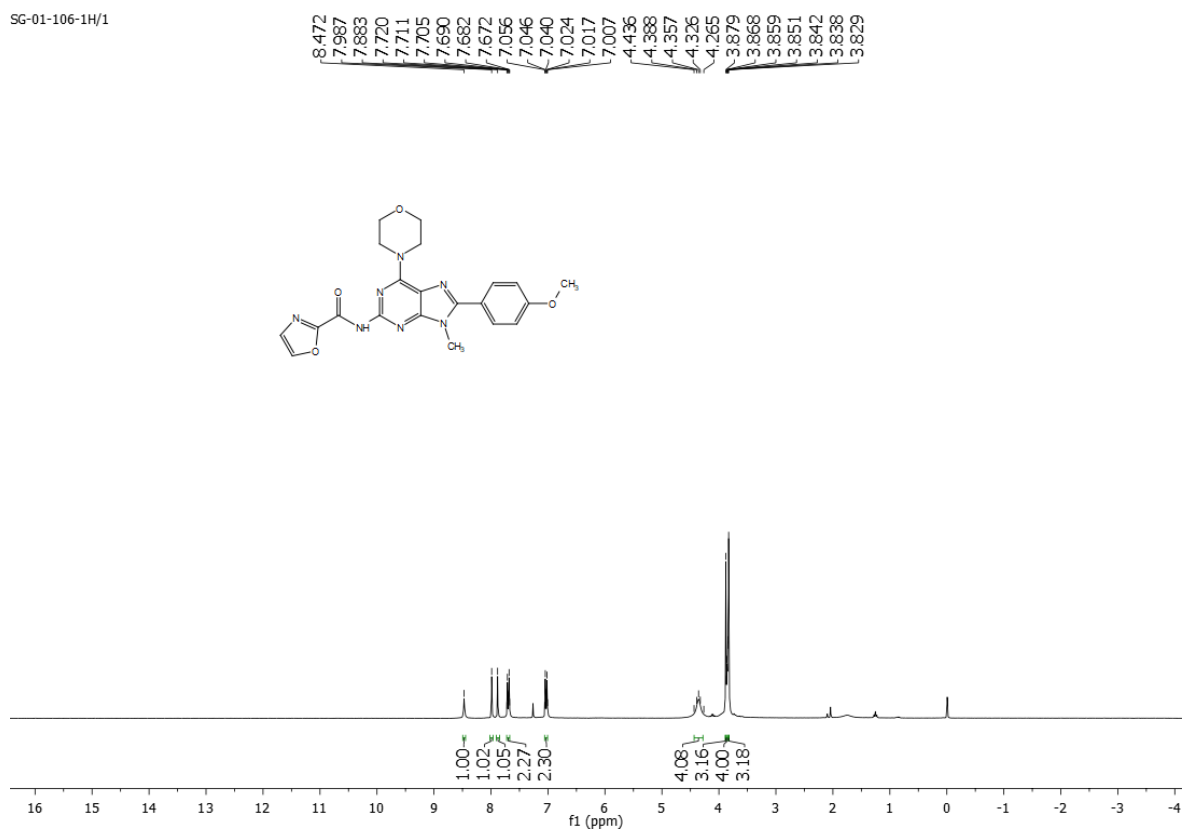
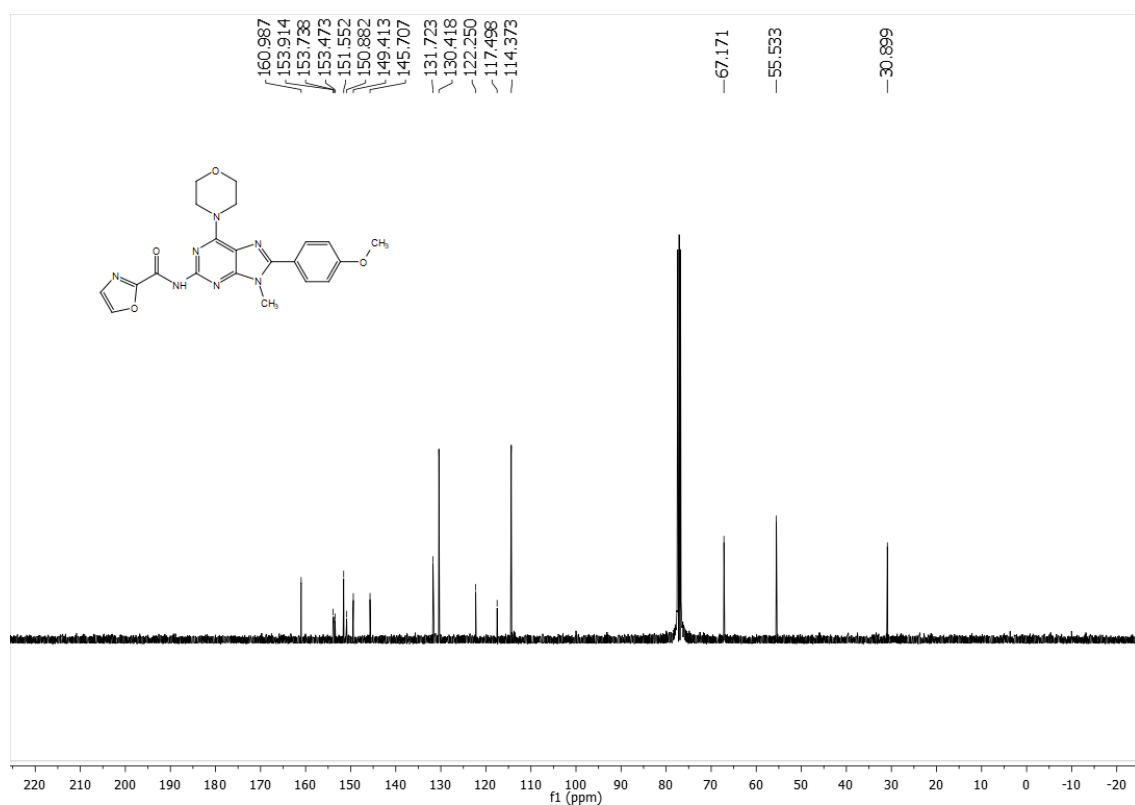
^1H NMR of compound **18** (400 MHz, CDCl_3):

SG-01-116-1H/1

 ^{13}C NMR of compound **18** (100 MHz, CDCl_3):

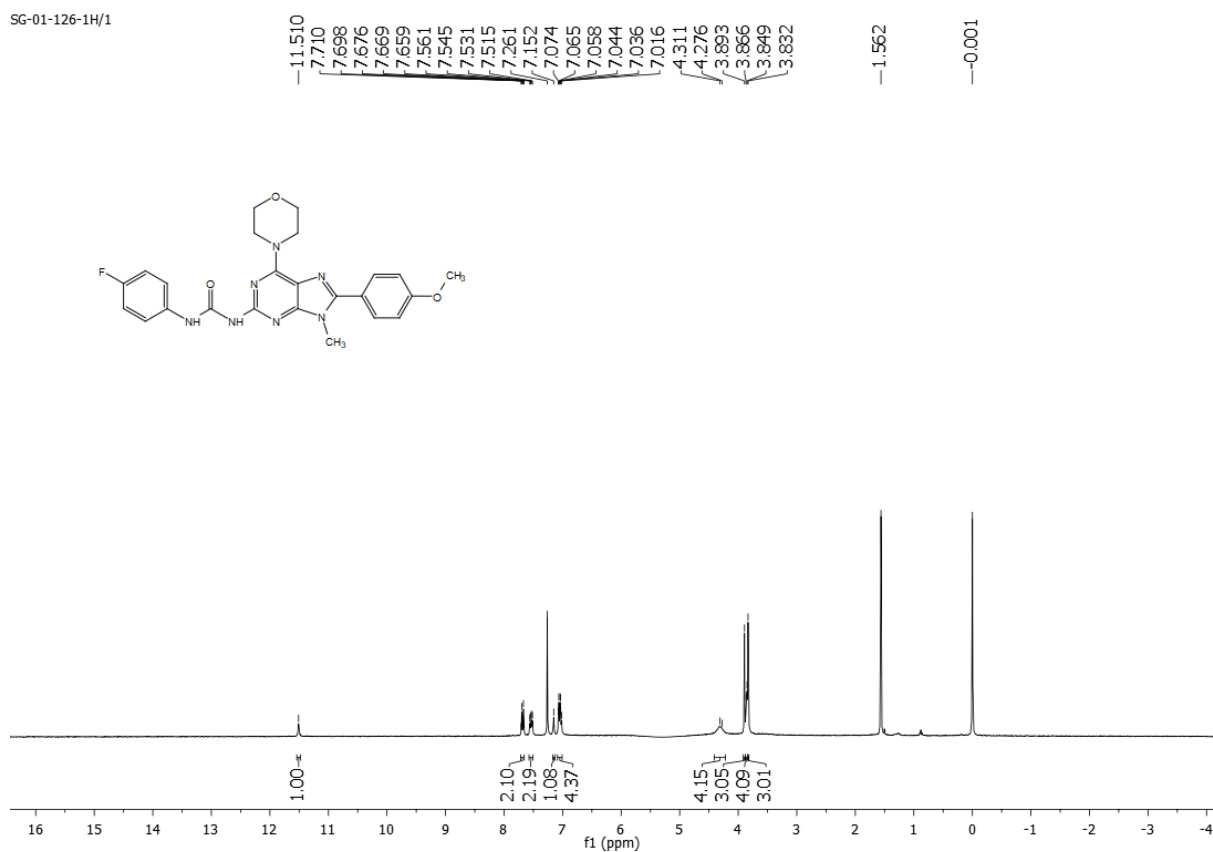
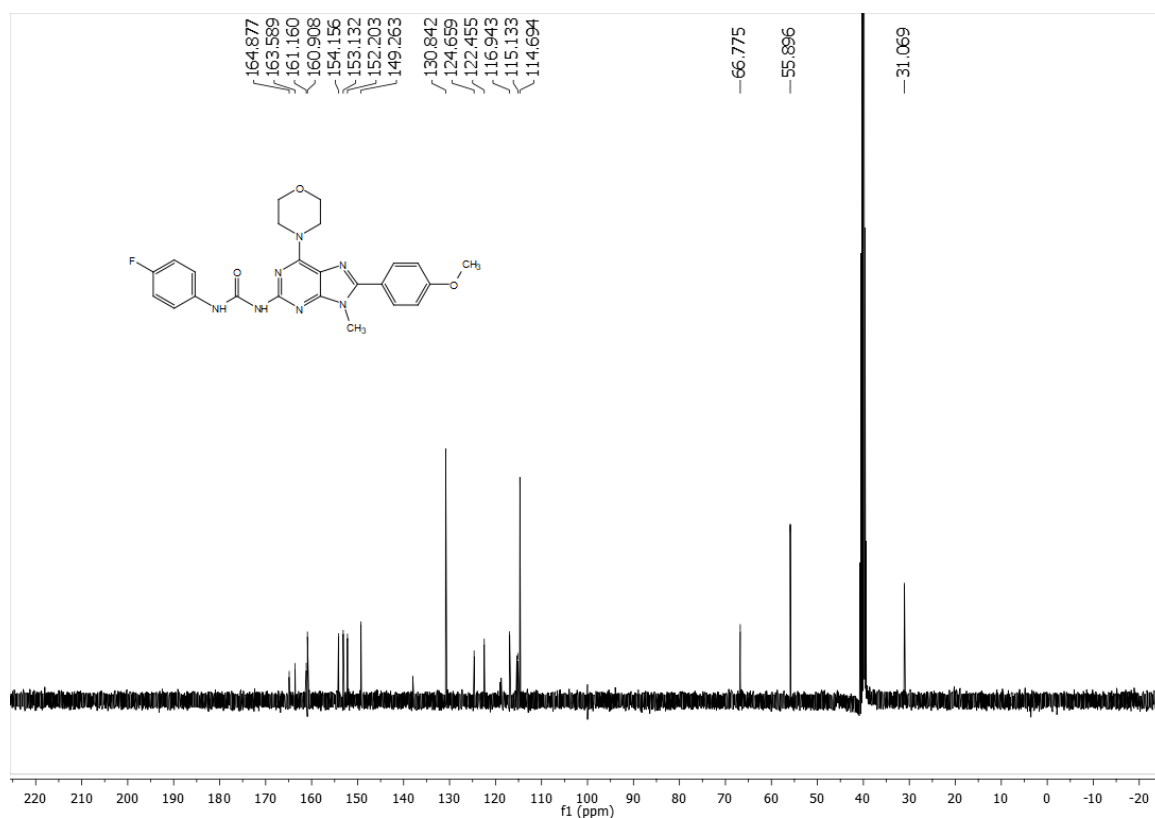
¹H NMR of compound **19** (400 MHz, CDCl₃):

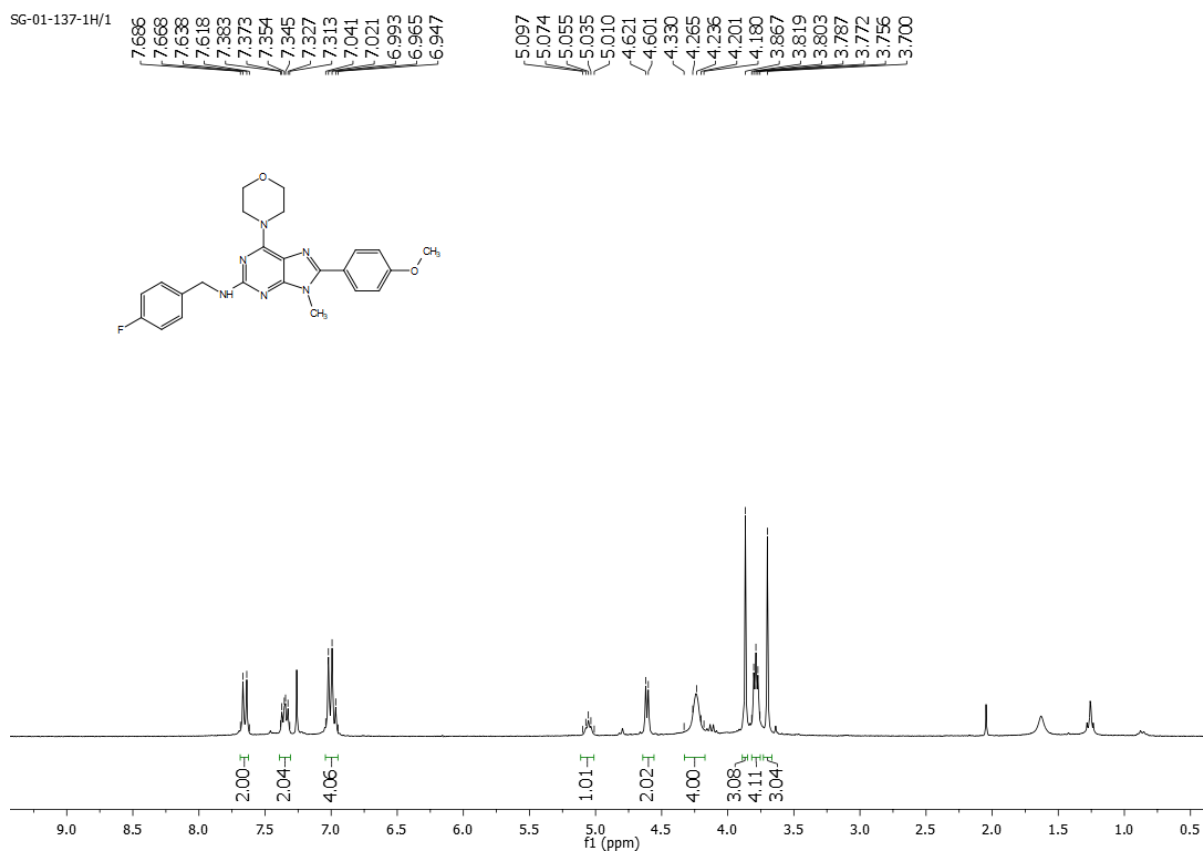
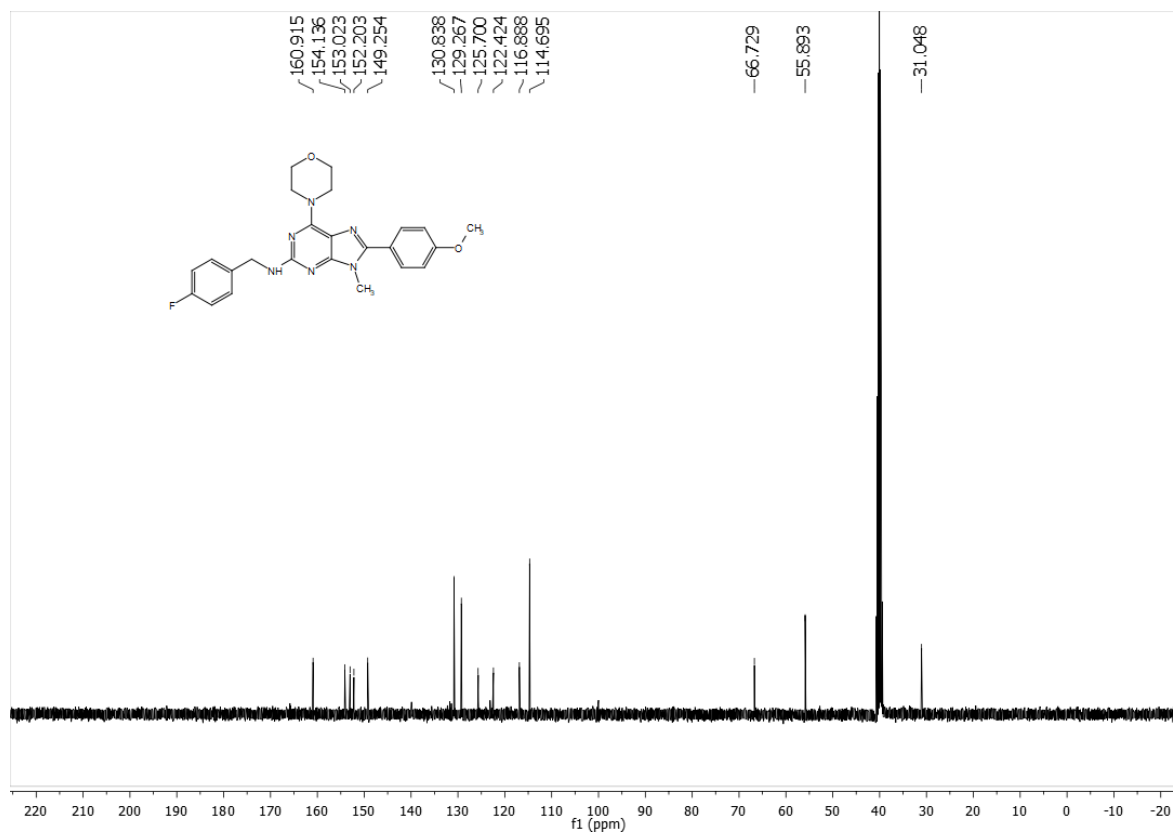
SG-01-106-1H/1

¹³C NMR of compound **19** (100 MHz, CDCl₃):

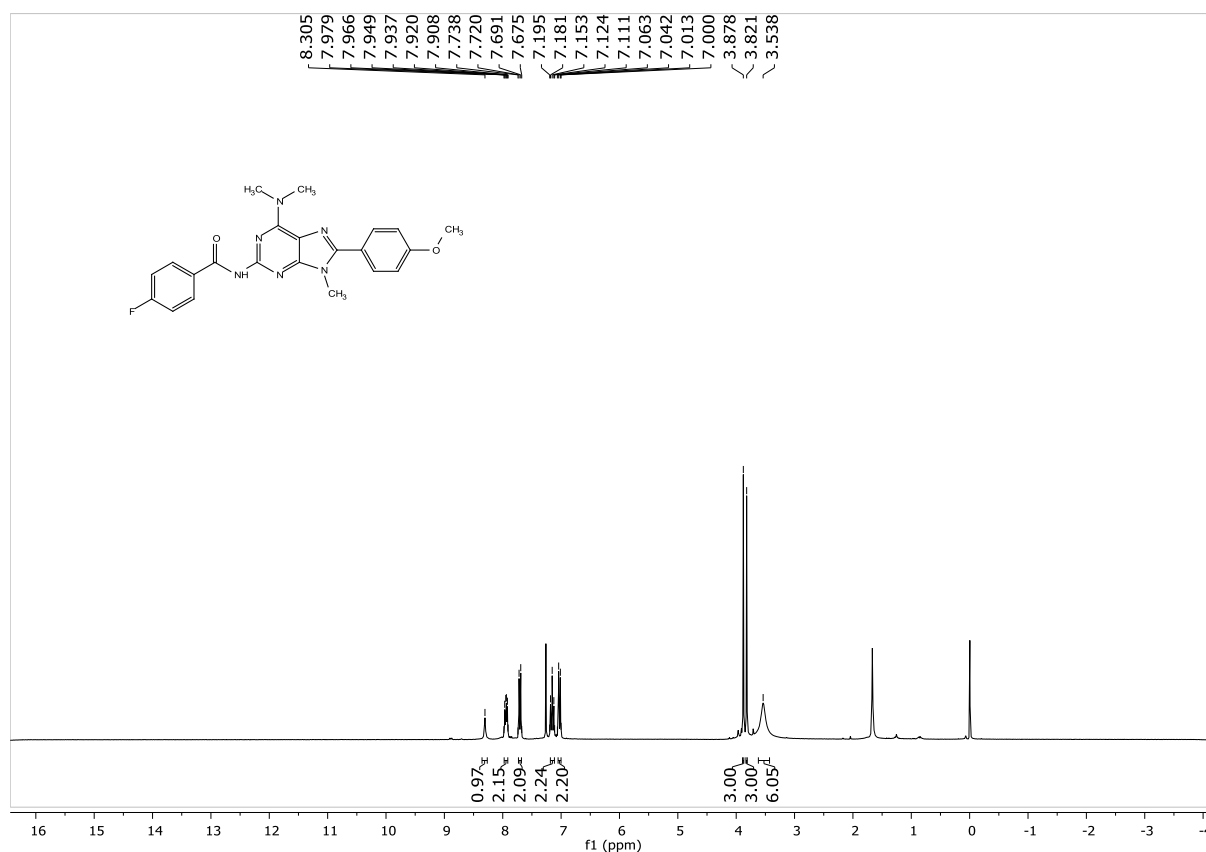
¹H NMR of compound **20** (400 MHz, CDCl₃):

SG-01-126-1H/1

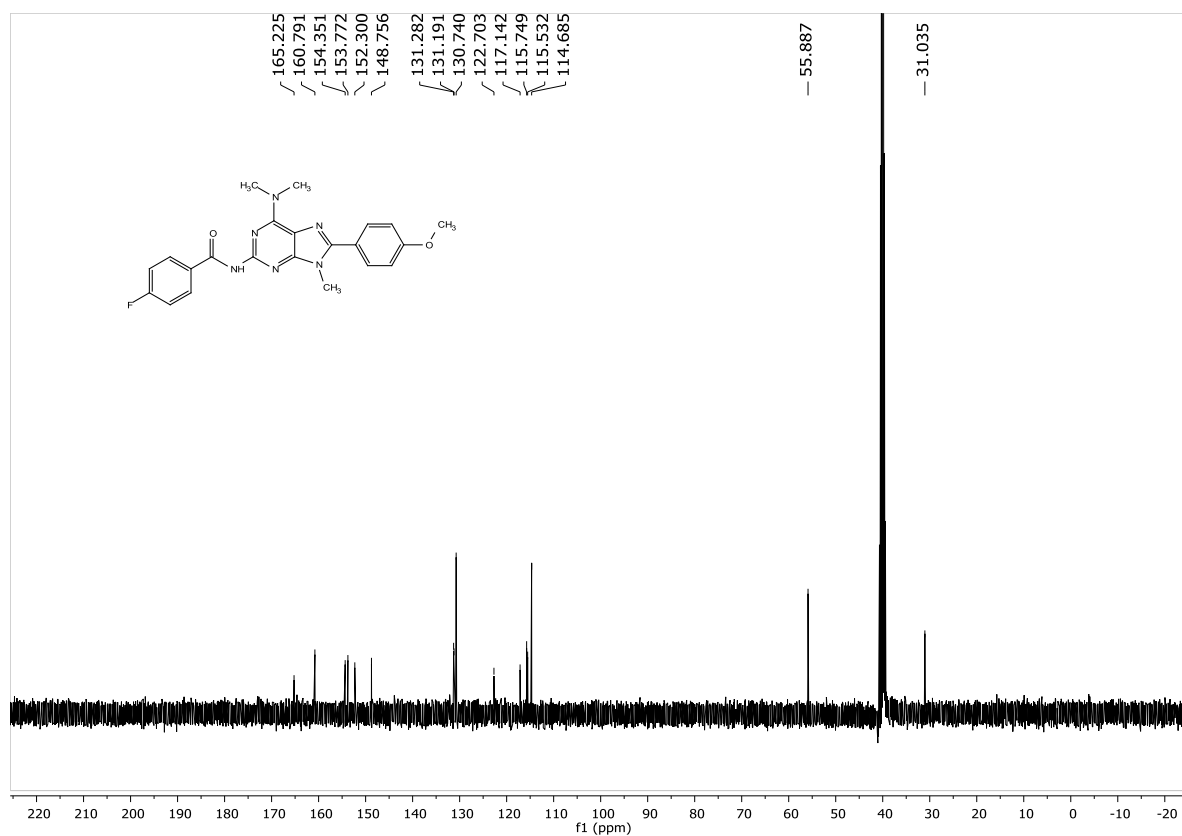
¹³C NMR of compound **20** (100 MHz, d₆-DMSO):

¹H NMR of compound **21** (400 MHz, CDCl₃):¹³C NMR of compound **21** (100 MHz, d₆-DMSO):

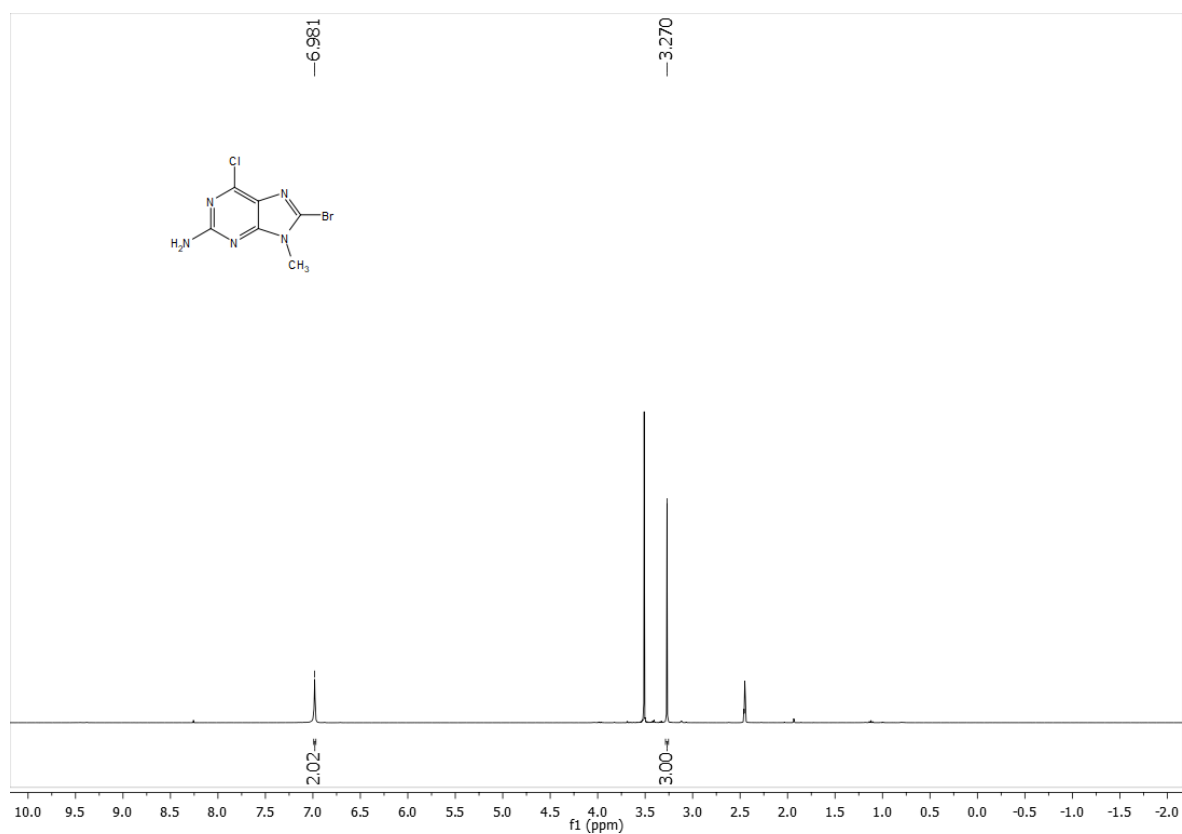
^1H NMR of compound **25** (400 MHz, d_6 -DMSO):



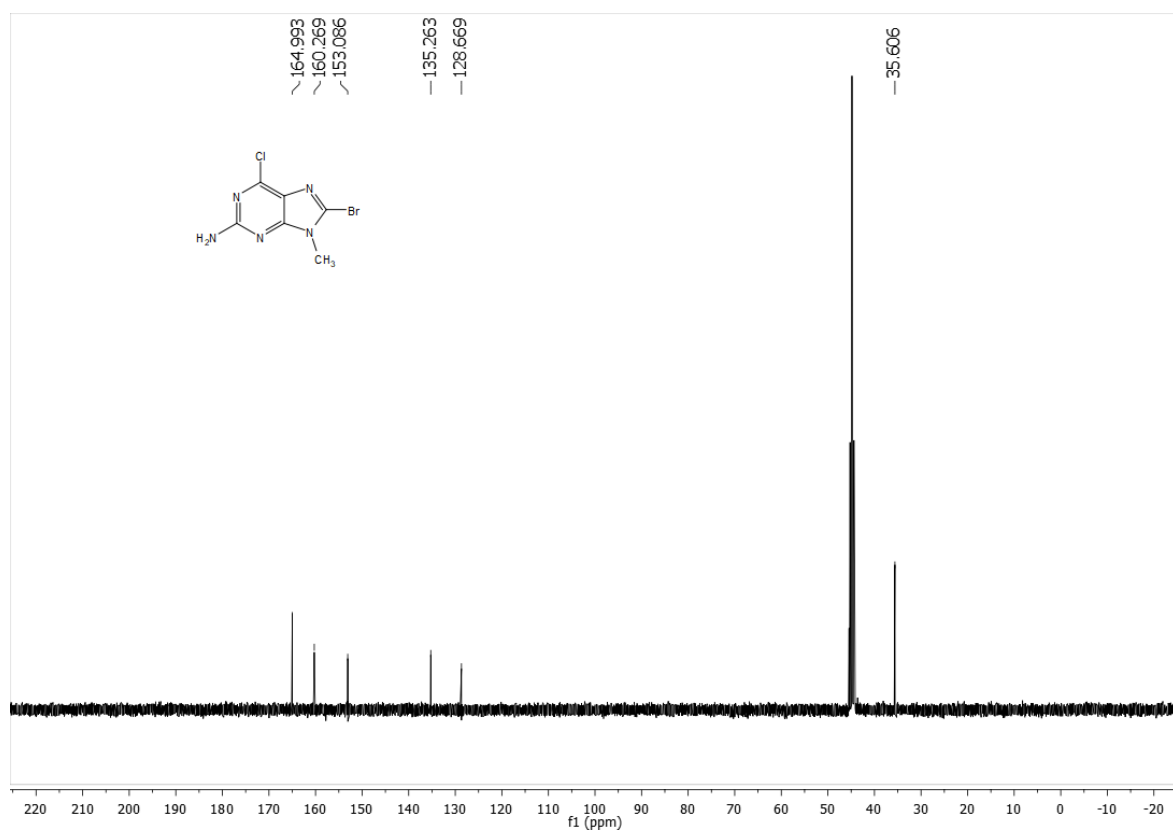
^{13}C NMR of compound **25** (100 MHz, d_6 -DMSO):



^1H NMR of compound **26** (400 MHz, d_6 -DMSO):

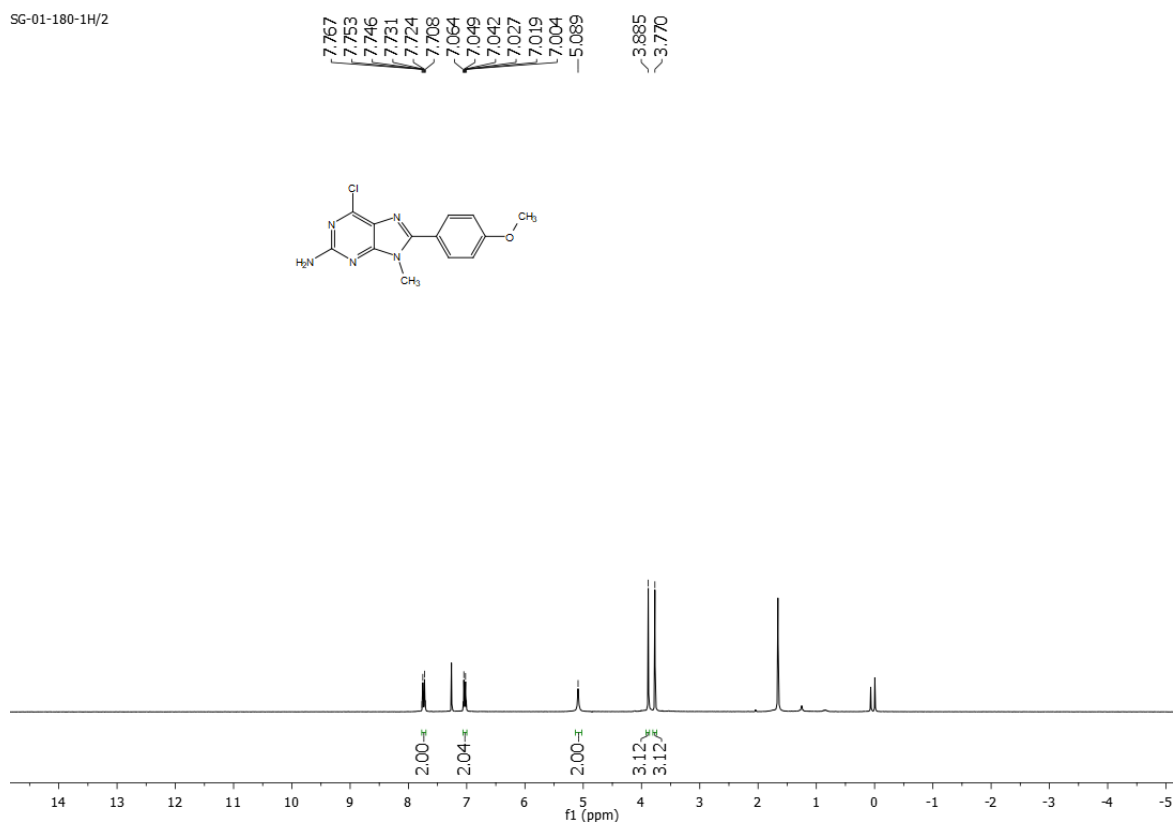
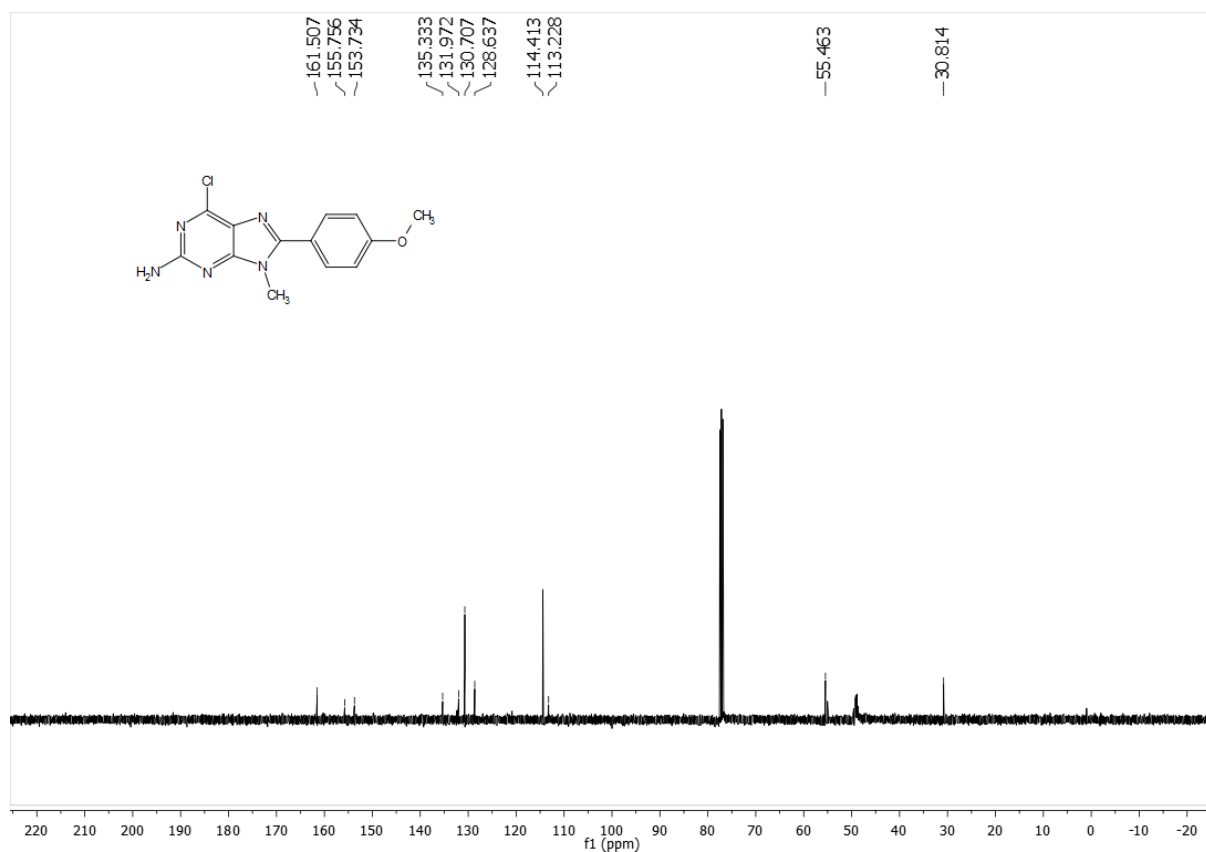


^{13}C NMR of compound **26** (100 MHz, d_6 -DMSO):



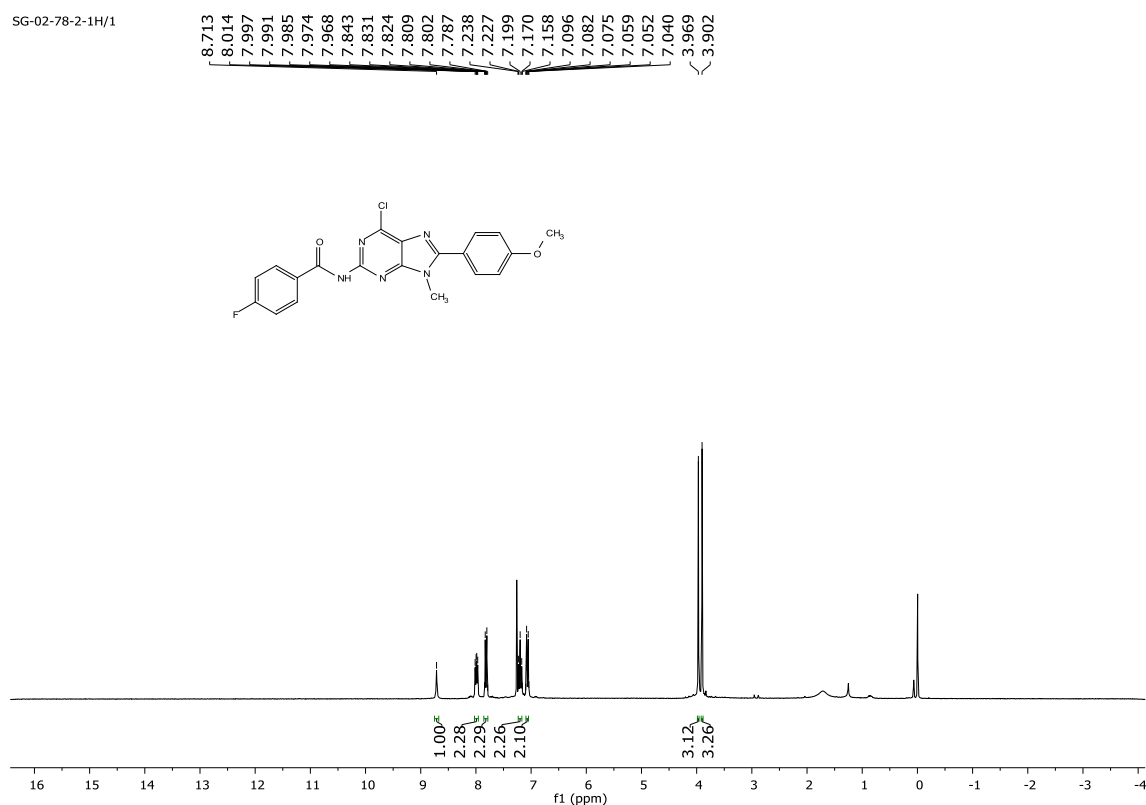
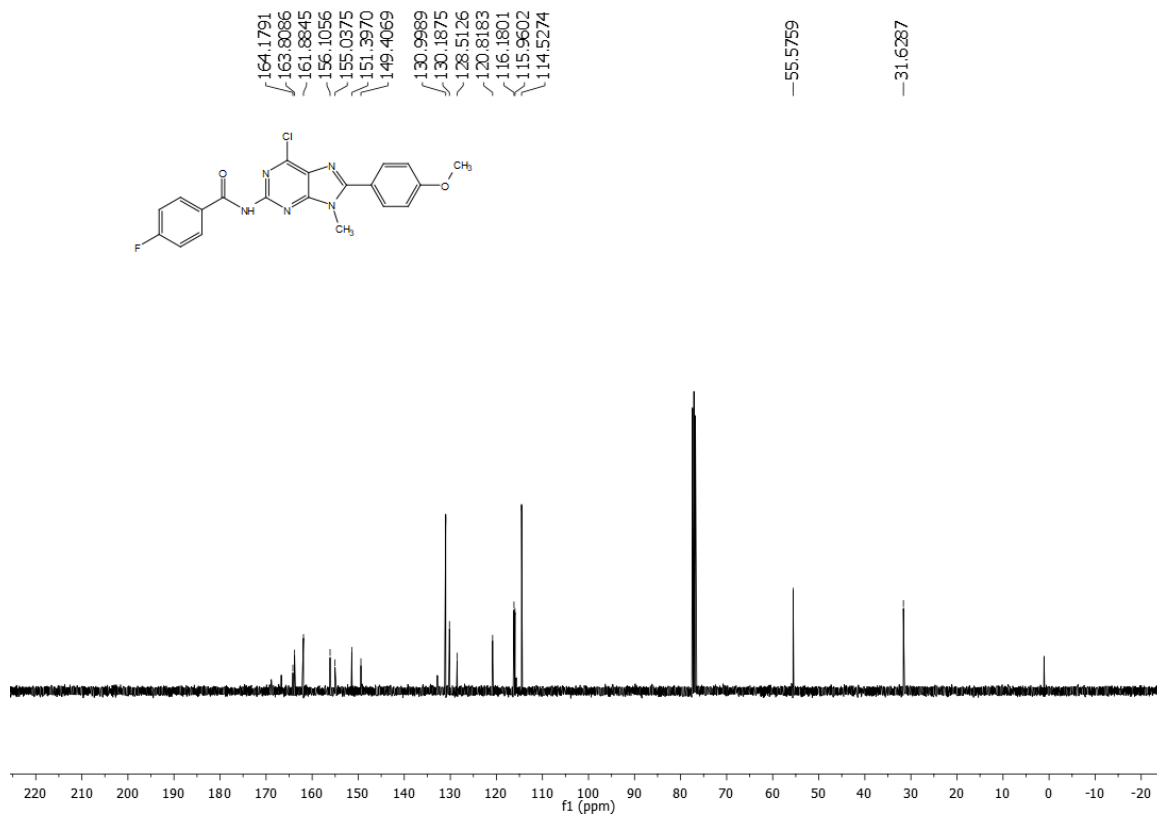
¹H NMR of compound **27** (400 MHz, CDCl₃):

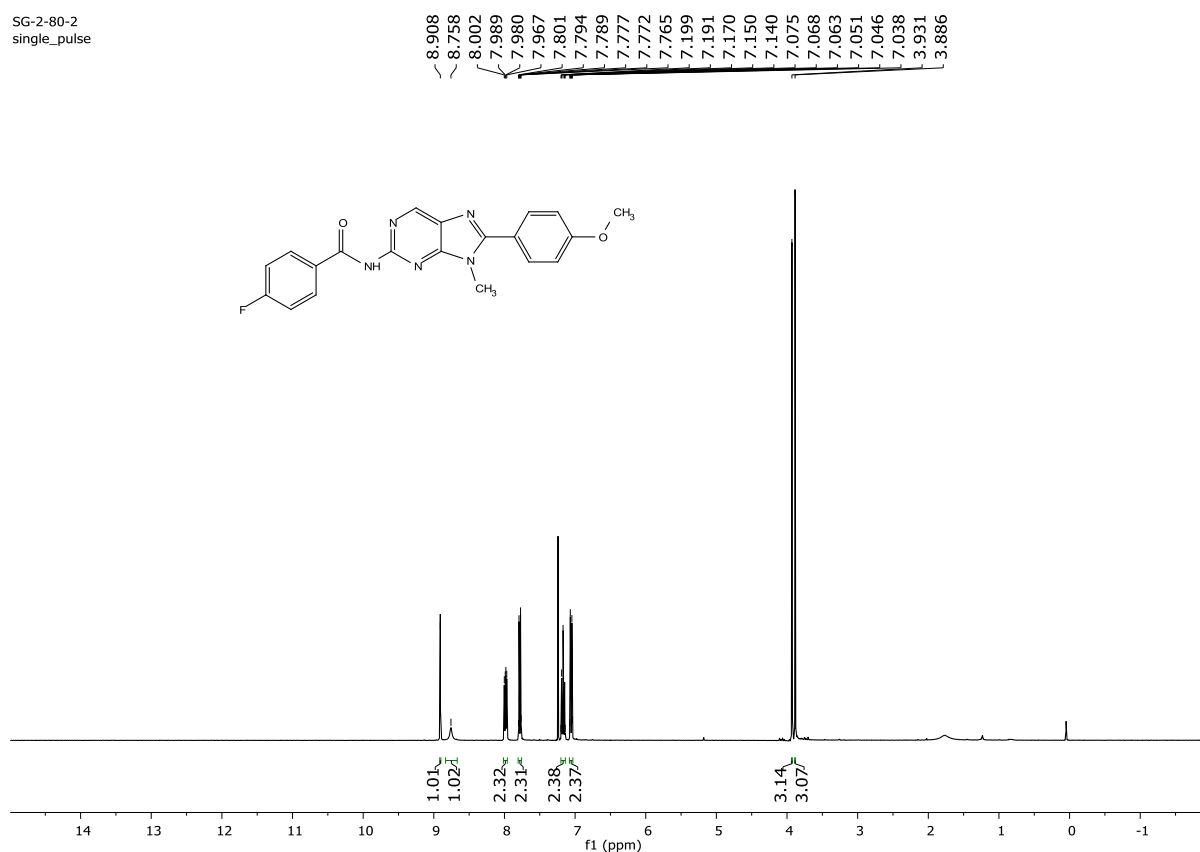
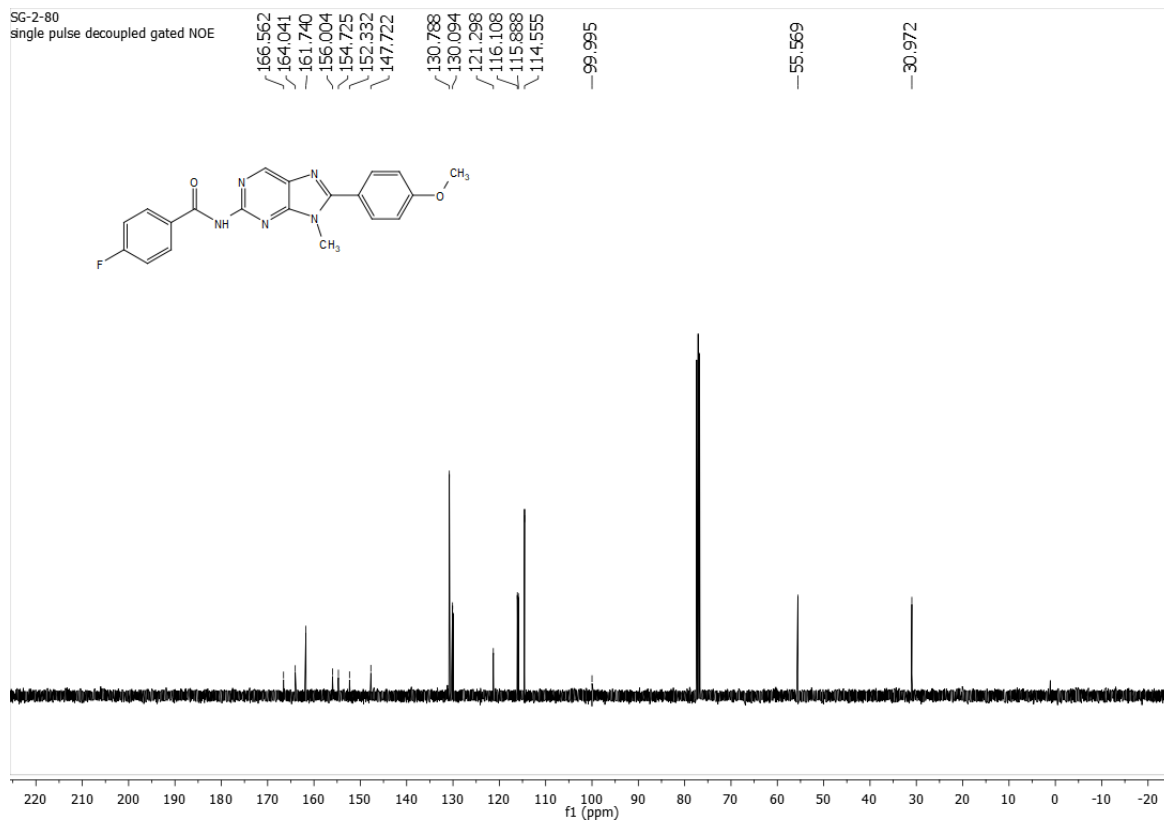
SG-01-180-1H/2

¹³C NMR of compound **27** (100 MHz, CDCl₃):

¹H NMR of compound **28** (400 MHz, CDCl₃):

SG-02-78-2-1H/1

¹³C NMR of compound **28** (100 MHz, CDCl₃):

¹H NMR of compound **30** (400 MHz, CDCl₃):SG-2-80-2
single_pulse¹³C NMR of compound **30** (100 MHz, CDCl₃):SG-2-80
single pulse decoupled gated NOE

CHAPTER THREE

Mechanistic insights into Piezo1 agonist Yaddle1 as a novel adjuvant for T cell activation

CHAPTER THREE

Mechanistic insights into Piezo1 agonist Yaddle1 as a novel adjuvant for T cell activation

3.1 Brief idea about Ion-Channels

Ion channels are specialized membrane proteins that facilitate the movement of ions, such as sodium (Na^+), potassium (K^+), calcium (Ca^{2+}), and chloride (Cl^-), across cell membranes.¹²⁷ They are essential for numerous physiological processes, including the generation of electrical signals in nerves and muscles, maintenance of cellular homeostasis, and sensory perception.^{128,129} Ion channels enable selective and rapid ion flow by opening and closing in response to various stimuli, such as changes in membrane voltage, ligand binding, mechanical forces, and temperature shifts. The structure of ion channels generally includes a pore domain that allows ions to pass, a selectivity filter to ensure specificity for certain ions, and a gating mechanism that responds to external or internal signals. Based on their gating mechanisms, ion channels are broadly classified as voltage-gated, ligand-gated, mechanosensitive, and temperature-gated channels.^{130,131} Each type plays a crucial role in cellular signaling, as they allow cells to respond dynamically to their environment. Because of their central role in maintaining physiological balance, disruptions in ion channel function, known as channelopathies, are associated with various diseases, including epilepsy, cardiac arrhythmias, cystic fibrosis, and chronic pain syndromes. Due to their accessibility on the cell membrane and specificity, ion channels are significant targets for therapeutic drugs, with ongoing research aiming to develop modulators for various channel types to treat these conditions.^{132,133}

3.2 Structure and Mechanism of Ion Channels

Ion channels are typically composed of multiple subunits that form a pore through which ions move. Their structure includes several distinct domains. This central domain forms the ion-conducting pathway and typically contains a selectivity filter that determines which ions can pass. Ion channels open and close in response to various stimuli. Gating mechanisms include:

- **Voltage-Gated:** Respond to changes in membrane potential.

- **Ligand-Gated:** Activated by binding specific molecules (e.g., neurotransmitters).
- **Temperature-Gated:** Sensitive to temperature changes.
- **Mechanosensitive:** Respond to mechanical forces such as stretch or pressure.

Channels can rapidly switch between open, closed, and inactivated states to precisely control ion flow in response to physiological needs.

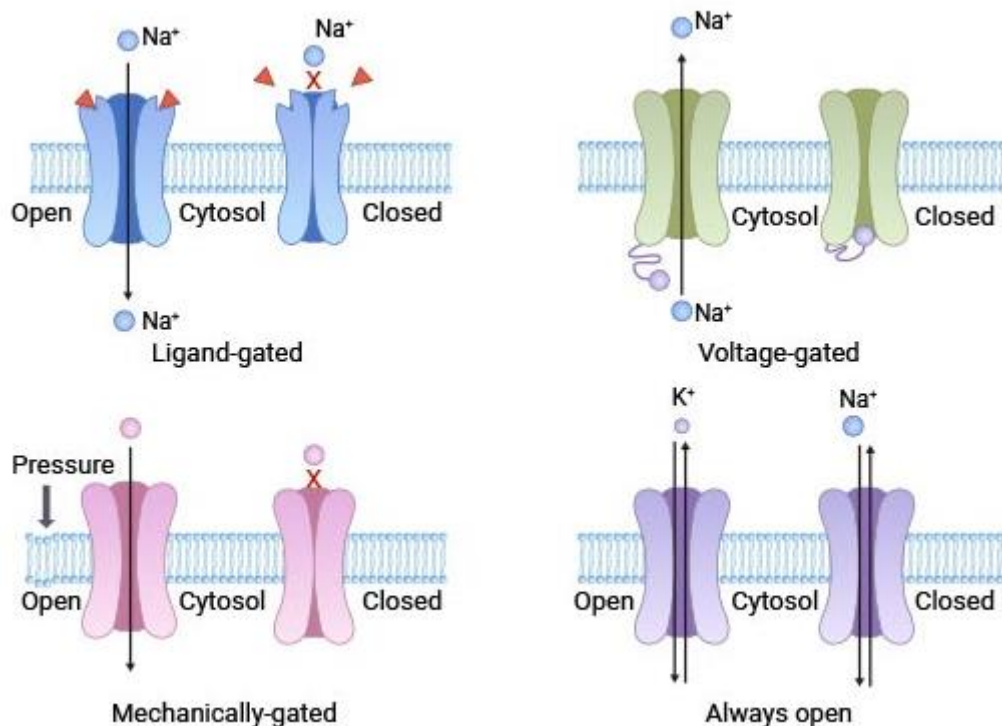


Figure 1. Ion channels of different gating types ¹³⁴

3.3 Types of Ion Channels

Ion channels are classified based on the stimuli that open or close them, the ions they selectively allow to pass, and their structural properties. Broadly, ion channels are categorized into **voltage-gated**, **ligand-gated**, **mechanosensitive**, and **temperature-gated channels**. Each type plays distinct physiological roles and is specialized for particular functions across different cell types and tissues.

3.3.1 Voltage-Gated Ion Channels

Voltage-gated ion channels (VGICs) open or close in response to changes in the membrane potential. These channels are crucial for generating and propagating electrical

signals, particularly in excitable cells like neurons and muscle cells. VGICs include various types, such as voltage-gated sodium (Nav), potassium (Kv), and calcium (Cav).^{135,136}

3.3.1.1 Voltage-Gated Sodium Channels (Nav)

This is essential for initiating and propagating action potentials in neurons and muscle cells. Nav opens in response to membrane depolarization, allowing an influx of Na^+ , which further depolarizes the cell and triggers the action potential. Nav channels are fundamental in nervous system communication and muscle contraction. Their rapid activation and inactivation are key for the "all-or-nothing" nature of action potentials. Mutations in Nav channels can lead to diseases like epilepsy and certain pain disorders.^{137,138}

3.3.1.2 Voltage-Gated Potassium Channels (Kv)

Kv channels restore the resting membrane potential after depolarization. They open as the membrane potential becomes positive during an action potential, allowing K^+ to exit the cell, repolarizing and stabilizing the membrane. Kv channels are essential for resetting the membrane potential after each action potential, ensuring proper timing and frequency of neuronal firing. Dysfunction in Kv channels is associated with conditions like epilepsy, cardiac arrhythmias, and ataxia.¹³⁹

3.3.1.3 Voltage-Gated Calcium Channels (Cav)

Cav channels control the influx of Ca^{2+} , a critical second messenger involved in various intracellular processes. They open in response to membrane depolarization, allowing Ca^{2+} entry, which triggers intracellular events such as neurotransmitter release, muscle contraction, and gene expression. Cav channels are pivotal in cardiac and smooth muscle contraction, synaptic transmission, and other Ca^{2+} -dependent processes. Abnormalities in Cav channels are implicated in disorders like cardiac arrhythmias, migraine, and neurodegenerative diseases.^{140,141}

3.3.2. Ligand-Gated Ion Channels

Ligand-gated ion channels (LGICs) open in response to the binding of specific extracellular molecules, typically neurotransmitters. These channels are vital in synaptic

transmission and cellular communication, allowing rapid ion flow in response to chemical signals.

3.3.2.1 Nicotinic Acetylcholine Receptors (nAChRs)

Mediate fast excitatory synaptic transmission, particularly at neuromuscular junctions. Open upon binding acetylcholine (ACh), allowing Na^+ and K^+ ions to flow, leading to depolarization of the postsynaptic cell. nAChRs are essential in muscle contraction and autonomic nervous system responses. Deficiencies or mutations can lead to myasthenia gravis, a condition characterized by muscle weakness.¹⁴²

3.3.2.2 GABA Receptors

Mediate inhibitory synaptic transmission in the brain. Open upon binding gamma-aminobutyric acid (GABA), allowing Cl^- ions to enter the cell, which hyperpolarizes and inhibits neuronal firing. GABA receptors are critical for maintaining inhibitory control within neural circuits, thus balancing excitation and preventing overactivity. Malfunctioning GABA receptors are associated with epilepsy, anxiety, and sleep disorders.¹⁴³

3.3.3. Temperature-Gated Ion Channels

Temperature-gated ion channels, primarily from the transient receptor potential (TRP) family, respond to changes in temperature and various chemical stimuli. These channels are essential for thermosensation and pain perception.

3.3.3.1 TRPV1 (Transient Receptor Potential Vanilloid 1)

Activated by heat, acidic conditions, and capsaicin (the compound in chili peppers that causes a burning sensation). Opens at temperatures above 43°C , allowing Ca^{2+} and Na^+ to enter, which depolarizes sensory neurons. TRPV1 contributes to pain perception and the detection of noxious heat. Overactivity is associated with chronic pain conditions, and TRPV1 antagonists are being explored for pain management.¹⁴⁴

3.3.3.2 TRPM8 (Transient Receptor Potential Melastatin 8)

Activated by cold temperatures and menthol. Opens at temperatures below 25°C , allowing cations to flow and resulting in a cooling sensation. TRPM8 is involved in detecting environmental cold and mediates responses to cooling agents like menthol.

Abnormal function may contribute to altered pain sensitivity and is linked to conditions involving neuropathic pain.¹⁴⁵

Ion channels are fundamental to cellular communication and function, with each type serving specific physiological roles and responses to external and internal stimuli. Their dysfunction is linked to numerous channelopathies, making them vital therapeutic targets in neurodegenerative, cardiovascular, pain, and respiratory diseases. This diversity in ion channel types highlights their importance in physiology and provides opportunities for pharmacological interventions tailored to treat ion channel-related disorders.

3.3.4. Mechanosensitive Ion Channels

Mechanosensitive ion channels (MSCs) respond to mechanical forces such as pressure, stretch, and changes in membrane tension. These channels play crucial roles in sensory perception and cellular mechanotransduction.¹⁴⁶

3.3.4.1 Piezo Channels (Piezo1 and Piezo2)

Detect mechanical forces, such as touch and pressure. Respond to membrane deformation by opening a pore that allows cations, particularly Ca^{2+} to enter the cell. Piezo channels are critical for mechanosensory processes, including touch perception, blood flow regulation, and cell volume control. Mutations in Piezo1 are associated with hereditary xerocytosis, a condition affecting red blood cell morphology.¹⁴⁷

3.3.4.2 TREK-1 and TRAAK Channels

Respond to mechanical stretch and contribute to cell volume regulation and mechanotransduction. These potassium channels open in response to changes in membrane tension, helping cells respond to mechanical stimuli. Involved in neural adaptation to mechanical stress, pressure sensation, and thermosensation. Mutations are associated with altered pain sensitivity and can contribute to mood disorders.¹⁴⁸

3.4 Mechanosensitive ion channels: Piezo Channels

Mechanotransduction is a key biological process that enables cells—whether eukaryotic or prokaryotic—to translate mechanical forces into electrochemical signals. This process is essential for a range of physiological functions, such as touch, pain perception, balance,

bone health, and blood pressure regulation. Mechanotransduction relies primarily on mechanosensitive ion channels, or mechanotransducers, which initiate responses like membrane depolarization in excitable cells or calcium signaling in non-excitable cells.¹⁴⁹ These initial responses then trigger complex downstream signaling cascades, leading to specific cellular and physiological outcomes. The detailed mechanisms by which mechanosensitive ion channels operate in living systems were largely unknown until 2010, when Ardem Patapoutian and his team discovered Piezo proteins, a type of mechanosensitive ion channel.¹⁵⁰ This discovery marked a significant breakthrough in understanding how cells detect and respond to mechanical forces, earning Patapoutian the 2021 Nobel Prize in Physiology or Medicine. Piezo proteins have since shed light on the critical role of mechanotransduction in health and disease, deepening our knowledge of the molecular basis of mechanosensitivity and its impact on cellular function.

Piezo proteins, which include Piezo1 and Piezo2, are evolutionarily conserved ion channel proteins known for their significant role in mechanotransduction across various systems in the body. Over the past decade, research has shown that Piezo1 is expressed in multiple tissues, such as lymphatic vessels, the cardiovascular system, immune cells, and bone. Its functions include regulating lymphatic and vascular development, blood pressure, cell migration, immune responses, and maintaining homeostasis in erythrocytes, bones, and epithelial tissues.¹⁵¹ Piezo1 also serves as a mechanoreceptor, responding to traction forces to influence the differentiation of neural and mesenchymal stem cells.¹⁵² In contrast, Piezo2 is primarily found in sensory neurons, where it plays a key role in detecting tactile pain, gentle touch, airway stretch, proprioception and regulating heart rate.¹⁵³ Given these crucial physiological roles, mutations in piezo proteins—either gain-of-function or loss-of-function—are linked to several disorders. For example, Piezo1 dysfunction is associated with dehydrated hereditary stomatocytosis, lymphatic dysplasia, and osteoporosis, while mutations in Piezo2 can lead to conditions such as distal arthrogryposis, Marden-Walker syndrome, scoliosis, respiratory defects, impaired proprioception, and bladder control issues. These findings highlight the therapeutic potential of piezo proteins, suggesting they could serve as novel targets for treating various conditions related to mechanosensation and mechanotransduction.^{154,155}

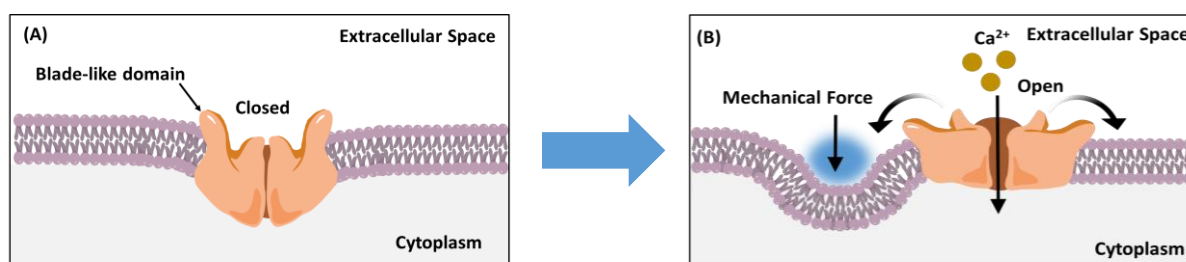


Figure 2. Piezo1 channel is situated at cell membrane. (A) In absence of any mechanical stimulation Piezo1 channel remain closed. (B) When any mechanical force is experienced by cell membrane Piezo1 channel gets open up and Ca^{2+} ion influx occurs.

3.4.1 Structural Determination of Piezo1

Piezo1 possesses a distinctive three-blade, propeller-shaped structure, which sets it apart from other mechanically activated (MA) ion channels. This homotrimeric channel has large subunits (with 2521 amino acids in humans and 2547 in mice), organized into critical regions necessary for its mechanosensitive function: the central ion-conducting pore and the three propeller-like blades. (Figure 2) ^{156–158}

3.4.1.1 Pore Module and Gating Mechanism

The pore module of Piezo1 comprises the last two transmembrane helices, known as the outer helix (OH) and inner helix (IH), along with the C-terminal extracellular domain (CED) and the intracellular C-terminal domain (CTD). The CED, acting as the cap of the ion-conducting pathway, is located between the OH and IH helices, with the cap sealed at the top. Ions enter via fenestration sites just above the membrane, where the hydrophobic residues of the IH helices form a constriction, or "neck," in the middle of the membrane. The pore includes two transmembrane gates regulated potentially by membrane lipids.

3.4.1.2 Ion Pathways

After ions pass through the pore, they enter the cytosol through two main pathways: either through a 10 Å constriction site or through three side portals gated by lateral plugs.

3.4.1.3 Propeller Blade Structure

Each blade in the Piezo1 structure has a 36-transmembrane helical organization, split into nine transmembrane helical units (THUs). The final THU9 is linked to the OH through an anchor domain, which plays a crucial role in mechanotransduction. Intracellularly, three 90 Å-long beams, connecting THU7 and THU8, help transmit mechanical force from

the flexible N-terminal region (THU1-3) of the blades to the central pore, further contributing to Piezo1's mechanosensitivity.

3.4.1.4 Membrane Dome Mechanism

Piezo1's curved blade deforms the membrane, creating a dome structure. Channel opening leads to membrane flattening, which in turn expands the dome into a planar conformation, generating the free energy needed for Piezo1 gating. This membrane dome hypothesis aligns with the force-from-lipids (FFL) model, where mechanosensitivity is modulated by membrane curvature and tension. Additionally, Piezo1's connection to the cytoskeleton through the cadherin- β -catenin-vinculin complex and interactions with E-cadherin support the force-from-filament (FFF) model, allowing the channel to integrate long-range mechanical signals from the cytoskeleton.

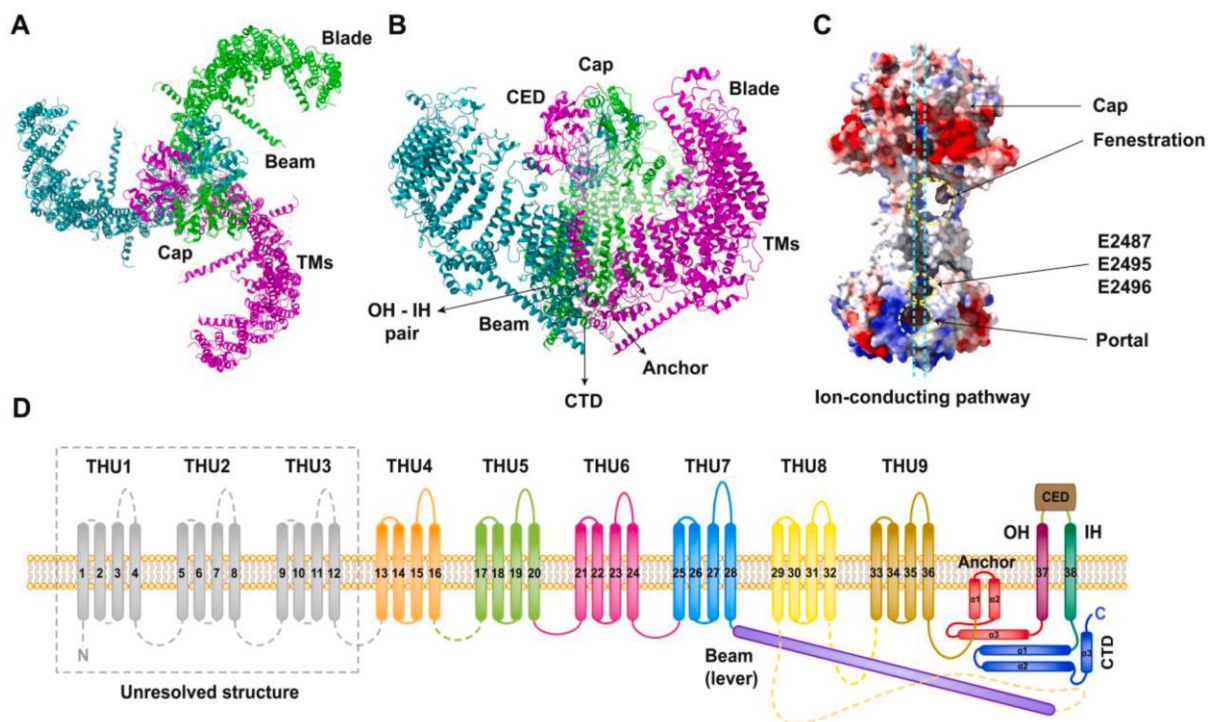


Figure 3. Structural and topological model of mouse Piezo1 (mPiezo1) protein (PDB code 6B3R). (A) Extracellular view of Piezo1, showing the three-bladed, propeller-like structure. (B) Side view of Piezo1, with major domains labeled to reveal the transmembrane helices (TMs), anchor, beam, C-terminal domain (CTD), C-terminal extracellular domain (CED), and the outer helix – inner helix (OH – IH) pair. The CED trimerizes to form the extracellular cap of the ion-conducting pathway. (C) The pore module represented as a surface electrostatic potential map. The ion-conducting pathway is marked with azure dashed lines. The two fenestration sites and the intracellular side portals are indicated with yellow-dashed circles. (D) The 38-TM topological model of Piezo1, showing the featured domains as demonstrated in (B). The dashed lines indicate unresolved structure.¹⁵⁹

3.4.2 Biological Function of Piezo1 Channel

Piezo1 channel proteins are broadly expressed across various cell types, including osteoblasts, immune cells, and cancer cells, where they play critical roles in mechanotransduction. Through sensing and responding to mechanical forces, Piezo1 is involved in numerous cellular processes under both normal and disease states.

3.4.2.1 Role of Piezo1 in Bone

Bone homeostasis depends on a balance between resorption by osteoclasts and new bone formation by osteoblasts, both processes influenced by mechanical forces. According to Wolff's law, bone adapts to mechanical stress, increasing in strength with exercise and weakening with reduced stimulation, such as prolonged bed rest or spaceflight. Piezo1, a mechanosensitive ion channel highly expressed in osteoblasts, is essential in this adaptive remodeling. Piezo1 deficiency leads to impaired osteogenesis, increased bone resorption, and spontaneous fractures. Conversely, activating Piezo1 in adult mice increases markers of bone formation and boosts bone mass. Piezo1 also mediates osteoblast-osteoclast signaling and promotes angiogenesis, crucial for fracture repair. Piezo1 levels are lower in osteoporosis patients, suggesting its potential as a therapeutic target to counteract osteoporosis and bone loss due to reduced mechanical loading.^{160,161}

3.4.2.2 Role of Piezo1 Channel in the Cardiovascular System

Piezo1, a crucial mechanosensitive ion channel, is widely expressed in endothelial cells of vascular and lymphatic vessels, where it plays a vital role in vascular health. Activated by blood flow shear stress and pressure-induced membrane stretch, Piezo1 is essential for vascular remodeling, valve morphogenesis, and blood pressure regulation. Its absence disrupts vascular development and can be embryonically lethal. Piezo1-mediated calcium influx drives endothelial cell alignment, migration, and angiogenesis, partly through matrix metalloproteinases (MMP2 and MT1-MMP) activation. Additionally, Piezo1 modulates endothelial inflammation via integrin signaling and regulates blood pressure alongside Piezo2 by functioning as a baroreceptor. Mutations in Piezo1 are linked to conditions such as hereditary stomatocytosis and generalized lymphatic dysplasia (GLD), with animal models confirming Piezo1's importance in lymphatic valve formation. Piezo1's roles suggest it as a potential therapeutic target for vascular disorders, including atherosclerosis, hypertension, DHS, and GLD.^{162,163}

3.4.2.3 Role of Piezo1 Channel in Innate Immunity

Innate immune cells are known to respond to mechanical forces, but recent studies have clarified Piezo1's specific role in these responses. Solis et al. found that Piezo1 activation in macrophages and monocytes, triggered by cyclical hydrostatic pressure, induces transcription of AP-1 and Edn1, which stabilize HIF1 α , promoting inflammation. Mice with Piezo1 knockout in myeloid cells showed reduced lung inflammation in models of bacterial infection and pulmonary fibrosis, indicating Piezo1's role in disease pathology. Additionally, Geng et al. demonstrated that TLR4 enhances macrophage bactericidal activity via Piezo1, with LPS stimulation activating Piezo1-dependent calcium influx that supports phagocytosis. Piezo1 is also involved in T cell development, proliferation, and polarization of TH1 and TH17 cells, while restricting Treg cells in autoimmune neuroinflammation models. Thus, Piezo1 is integral to immune responses and is a potential therapeutic target for treating bacterial infections, pulmonary fibrosis, and autoimmune diseases.^{164,165}

3.4.2.4 Role of Piezo1 Channel in Human Cancer

Piezo1 is overexpressed in multiple cancers, including oral, gliomas, bladder, breast, colorectal, and gastric cancers, where it promotes cell proliferation, migration, and invasion, as shown in The Cancer Genome Atlas (TCGA). Silencing Piezo1 reduces these malignant behaviors and increases apoptosis. Mechanistically, Piezo1-mediated Ca²⁺ influx activates tumor-related pathways like ERK1/2, Akt/mTOR, and YAP, and promotes HIF-1 α overexpression, which supports angiogenesis and epithelial-to-mesenchymal transition (EMT). Piezo1 also interacts with TFF1 to enhance cancer cell migration and invasion. High Piezo1 expression correlates with poor survival in cancer patients, highlighting its potential as a diagnostic and prognostic biomarker. In non-small-cell lung cancer (NSCLC), however, Piezo1 is downregulated, with lower levels aiding tumor growth and reducing patient survival.^{166,167}

3.4.3 Development of Piezo1 Channel Modulators

The Piezo1 ion channel has garnered attention for its critical role in a range of physiological and pathological processes, positioning it as a potential biomarker for early disease diagnosis.¹⁶⁸ Modulating Piezo1 activity through specific agents offers a promising therapeutic strategy for several conditions, including osteoporosis,

dehydrated hereditary stomatocytosis (DHS), generalized lymphatic dysplasia (GLD), autoimmune encephalomyelitis, and various cancers. While the discovery of Piezo1 is relatively recent and aspects such as its ligand-binding crystal structure and detailed physiological mechanisms are still being elucidated, substantial progress has been made in developing Piezo1 modulators. Recent research has focused on various compounds that can effectively influence Piezo1 activity, paving the way for potential therapeutic applications.¹⁶⁹

3.4.3.1 Non-specific and Competitive inhibitors of Piezo1

Piezo1 inhibitors come in two categories: non-specific and competitive. Non-specific inhibitors like *Ruthenium Red (RR)* and *GsMTx4*, as well as *Amyloid β* peptides and fatty acids such as *margaric acid (MA)*, inhibit Piezo1 alongside other channels by altering membrane mechanics or blocking the pore. RR specifically inhibits inward Piezo1 currents, while GsMTx4, derived from tarantula venom, inhibits by modulating channel gating.^{170,171} Competitive inhibitors like *Dooku1*, a Yoda1 derivative, selectively bind Piezo1 to reduce Ca^{2+} influx, with applications in treating cardiac hypertrophy, thrombosis, and neuroinflammation.¹⁷² *Tubeimoside I*, a saponin from Chinese medicine, selectively inhibits Piezo1-mediated responses in endothelial cells, with potential anti-tumor effects.¹⁷³ *Salvianolic Acid B (SalB)* from *Salvia miltiorrhiza* offers cardiovascular benefits, reducing atherosclerosis and promoting endothelial cell differentiation.¹⁷⁴ *Jatrorrhizine (Jat)*, an alkaloid, effectively inhibits Piezo1 to reduce vascular inflammation by blocking endothelial-mesenchymal transition (EndMT).¹⁷⁵ Lastly, *Escin*, a triterpenoid from horse chestnut, suppresses Piezo1-induced inflammatory responses, showing promise in vascular protection and chronic venous insufficiency treatment.¹⁷⁶ Together, these inhibitors highlight Piezo1 as a target for diverse conditions, including cardiovascular, neurological, and inflammatory diseases.

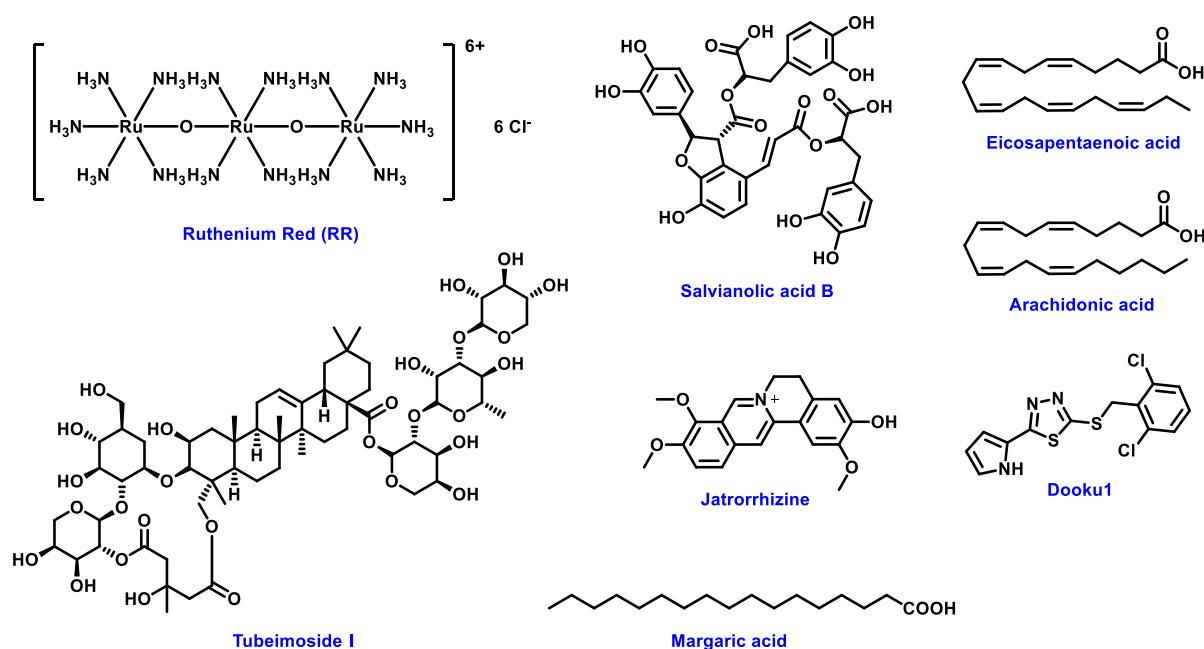


Figure 4. Structures of non-specific and competitive inhibitors of Piezo1

3.4.3.2 Piezo1 Channel Specific Agonists

Yoda1 is the first synthetic agonist for the Piezo1 channel, discovered by Syeda and colleagues through high-throughput screening of around 3.25 million of compounds using a cell-based fluorescence assay.¹⁷⁷ It activates both human and mouse Piezo1 with moderate potency, having EC₅₀ values of 17.1 μM and 26.6 μM, respectively. Yoda1 directly binds to Piezo1, as shown in studies involving reconstituted protein assays and molecular docking. Key structural elements, such as the 2,6-dichlorobenzyl and thioether groups, are critical for its agonistic activity, and altering these components significantly reduces efficacy. Molecular simulations identified an allosteric binding pocket specific to Piezo1, explaining Yoda1's selectivity. Yoda1 acts as a “molecular wedge” to lower the threshold for Piezo1 channel activation. It binds within a hydrophobic pocket around 40 Å from the central ion-conducting pore, specifically situated between Piezo repeats A and B on each subunit.^{178,158} Structural modifications have yielded several Yoda1 analogues, such as Dooku1, which acts as a Piezo1 antagonist.¹⁷² Recent patents present new analogues with enhanced activity and potential therapeutic applications, like treating osteoporosis, though Yoda1's poor solubility limits its clinical prospects. Additionally, two new Piezo1 agonists, Jedi1 and Jedi2, were identified, which activate Piezo1 through a different mechanism than Yoda1, suggesting multiple allosteric sites.¹⁷⁹ Parsonage et al. altered the pyrazine group in Yoda1 to develop KC159 and its potassium salt KC289,

achieving improved activation efficiency on Piezo1. These compounds showed EC₅₀ values of 0.28 μ M and 0.15 μ M, respectively, indicating higher potency than Yoda1, which has an EC₅₀ of 0.60 μ M.¹⁸⁰ These findings expand the potential for Piezo1-targeted therapies, though further studies are needed to explore their binding affinities and pathways.

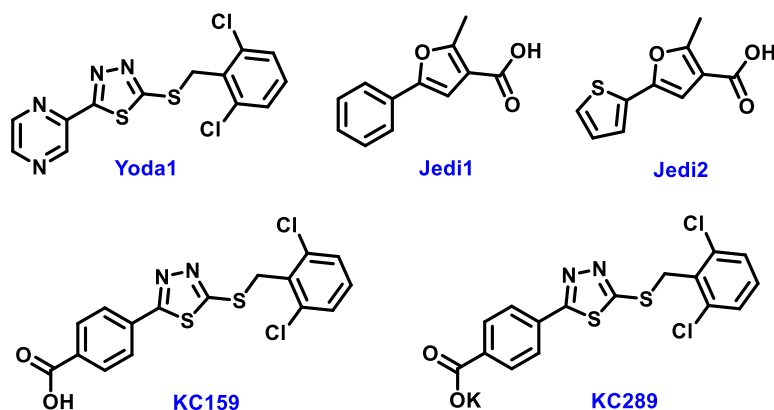


Figure 5. Known selective Piezo1 agonists.

3.5 OBJECTIVE

The mammalian immune system is divided into two branches; innate immune system and adaptive immune system. The innate immune system, consisting of cells like neutrophils, macrophages, NK cells, and dendritic cells, recognizes pathogens and initiates an inflammatory response, which then activates the adaptive immune system. Adaptive immunity includes T and B cells, which proliferate and differentiate to address specific threats. After eliminating pathogens, most adaptive cells die, but memory cells remain to respond quickly to future infections. T cells play a vital role in adaptive immunity, activated via T cell receptors (TCRs) when interacting with antigen-presenting cells (APCs). APCs present antigens bound to MHC molecules, stabilizing TCR and APC binding and initiating intracellular signaling through CD3. CD8 cytotoxic T cells and CD4 helper T cells bind MHC class I and class II molecules, respectively, facilitating TCR and APC interaction. This recognition triggers actin-driven membrane reorganization, leading to the immunological synapse formation, crucial for an effective immune response.^{181–184}

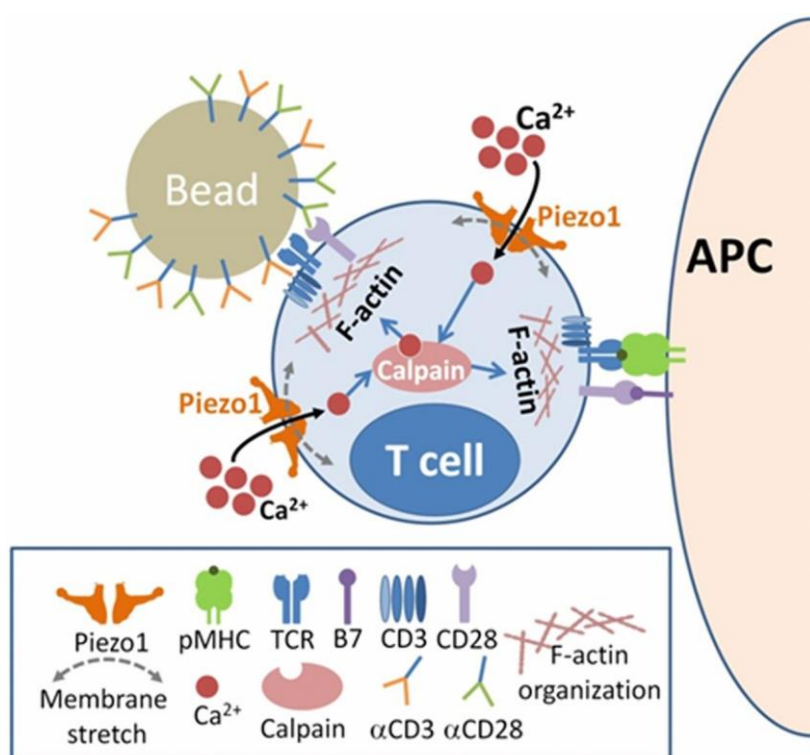


Figure 6. Proposed model for the role of Piezo1 in human T cell activation. Membrane stretch during immune synapse formation triggers Piezo1 activation and Ca²⁺ influx, which, in turn, activate calpain. Calpain activation helps in the organization of the cortical actin scaffold, thereby optimizing human T cell activation.¹⁸⁵

Although structurally similar, Piezo1 and Piezo2 proteins have distinct physiological roles due to their varied expression across different organs. Dr. Dipyaman Ganguly and his group first identified that Piezo1, but not Piezo2, is present in T cells, which are essential for adaptive immunity.^{185,186} The precise role of Piezo1 in immune regulation remains unclear, though it shows significant expression in human T cells. Their study investigated Piezo1's function as a specialized mechanosensor in T-cell activation and identified it as a unique mechanotransducer involved in T-cell regulation (TCR), proposing a mechanistic pathway (Figure 6). Piezo1 can be activated by mechanical force or chemical agonists, such as Yoda1, which was used in this study to explore Piezo1-driven T-cell activation pathways. Piezo1 acts as a cation channel, mediating extracellular calcium influx upon activation. In T cells, TCR cross-linking with bead-immobilized anti-CD3/anti-CD28 antibodies also triggers rapid calcium influx, but this response is significantly reduced in CD4⁺ and CD8⁺ T cells lacking Piezo1.¹⁸⁷

The increase in cytosolic Ca²⁺ concentrations activates a range of calcium-dependent signaling pathways, impacting many cellular functions.¹⁸⁸ Because Piezo proteins play a pivotal role in regulating Ca²⁺ influx in response to mechanical stimuli, they have emerged as significant targets for pharmaceutical research, especially in therapeutic areas affected by disrupted cellular signaling. Their modulation holds promise for developing treatments for conditions such as hypertension, chronic pain, osteoporosis, and immune disorders, where altered mechanotransduction may contribute to disease pathology. Consequently, Piezo channel modulators represent a potential tool for both physiological studies and therapeutic intervention in diseases influenced by abnormal calcium signaling. To study Piezo channels without mechanical force, researchers are exploring chemical compounds that can activate them directly.

Interestingly, among a vast library of 3.25 million of compounds, Yoda1 emerged as the sole identified agonist of Piezo1.¹⁷⁷ Our research aims to clarify the specific structural features of Yoda1 that enable Piezo1 activation, providing insights that could drive the development of next-generation Piezo1 activators with therapeutic potential. Piezo1 agonists hold promise for expanding T cells in anticancer immunotherapy and advancing vaccine adjuvants that enhance T-cell activation. Piezo1's crucial role in modulating immune responses highlights its potential in developing new immunomodulators.

3.6 METHODOLOGY

3.6.1 Rational Design

To determine the key structural requirements for effective Piezo1 modulation, we designed and synthesized a focused library of small molecules based on the molecular structure of Yoda1. By dissecting Yoda1's structure into distinct zones—namely, the 2,6-dichlorobenzyl group (zone A), the sulfur-ether linkage (zone B), the thiadiazole ring (zone C), and the pyrazine ring (zone D)—we systematically explored each zone's role in activating Piezo1 (Figure 7). For this purpose, one structural region was modified at a time, while the others were held constant, allowing us to assess each region's contribution to Piezo1 gating and activity modulation. This approach provided insights into how each part of Yoda1 contributes to its binding affinity, potency, and activation mechanism. Such detailed mapping is instrumental for developing next-generation Piezo1 modulators, which could lead to more refined tools for studying Piezo1 functions and potential therapeutic agents targeting conditions influenced by Piezo1 activity. The activation of Piezo1 is characterized by an influx of cations, particularly calcium ions (Ca^{2+}), which is critical for various cellular signaling pathways. Therefore, measuring intracellular calcium levels serves as an effective method to assess the activation of Piezo1 by candidate compounds.

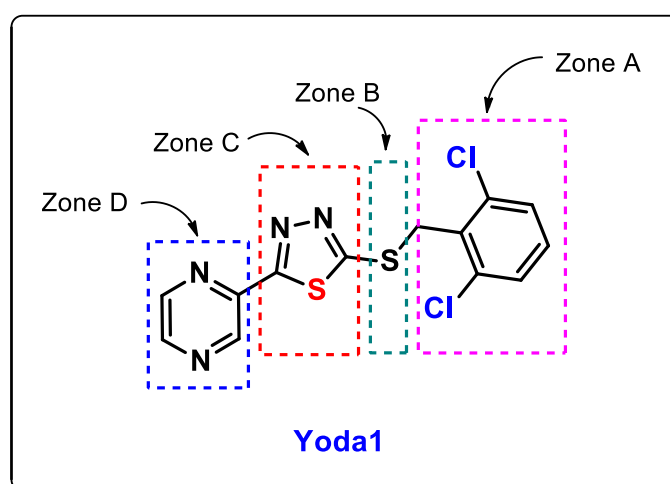


Figure 7. The structure of selective Piezo1 agonist Yoda1 is subdivided into four parts: 2,6-dichlorobenzyl moiety (zone A), S-ethereal connection (zone B), thiadiazole ring (zone C), and pyrazine ring (zone D).

The initial screening assays aimed at identifying Piezo1 agonists utilized a HEK293A cell line genetically modified to express Piezo1-mCherry. These assays were conducted at

concentrations of 15 and 25 μM , with Yoda1 employed as a positive control for comparison (Figure 8A–C). The screening process focused on identifying compounds that triggered a calcium response in cells expressing Piezo1 while exhibiting no response in those lacking the channel. This selectivity was crucial for identifying potential agonists for further evaluation (Figure 8B, C).

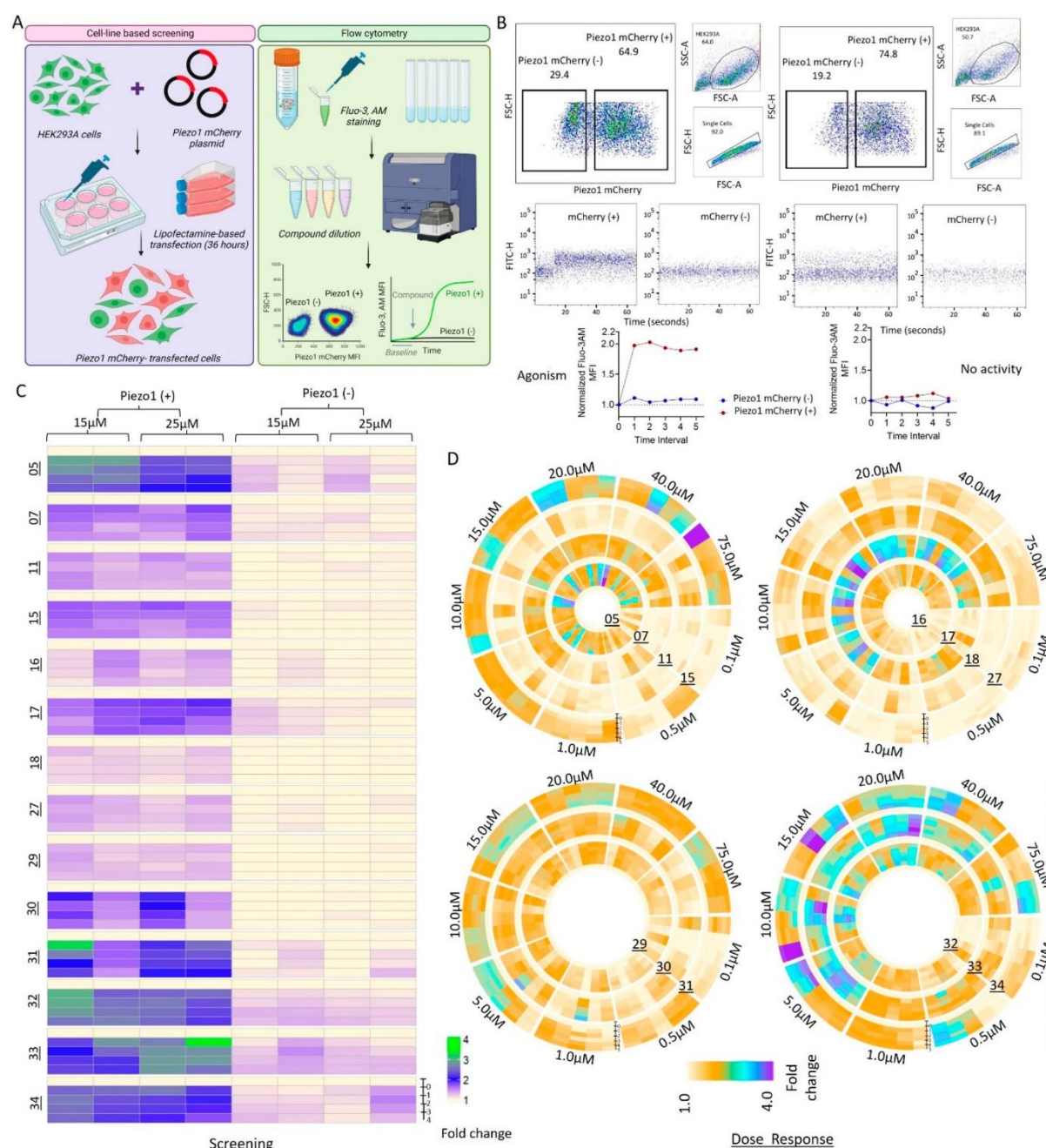


Figure 8. Screening and dose-response assays for potential Piezo1 agonists. **(A)** Experimental workflow. The HEK293A cell line was transfected with a Piezo1 mCherry-expressing plasmid. Compound screening and dose-response assays were performed by flow cytometric detection of the calcium response in Piezo1-expressing HEK293A cells. **(B)** Flow cytometry gating principle and analysis for measuring the activated Piezo1-induced calcium response (see Experimental Section). **(C)** Heat map showing the results of Piezo1 agonist screening at doses of 15 and 25 μM . Each small block represents the time-dependent calcium

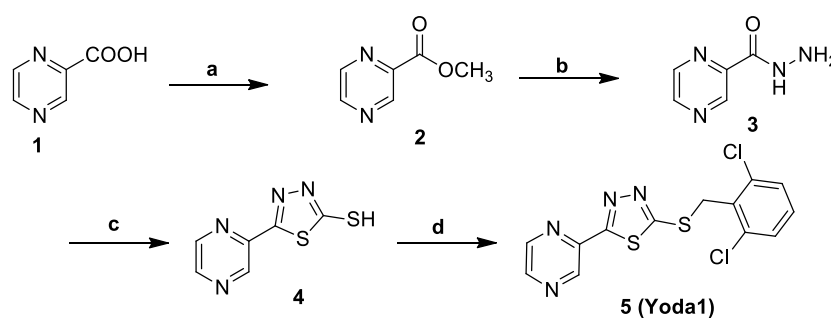
response for each compound at the doses specified at T_0 or the baseline followed by T_1 – T_4 . T_0 depicts the baseline calcium signal before the addition of the compound, and T_1 – T_4 represent calcium response data binned into regular time intervals of 30 s after the addition of the compound. Each horizontal block represents the response for the compound number tested. The left portion of the heat map depicts the calcium response from Piezo1 mCherry-expressing or Piezo1 (+) cells, while the right portion of the heat map depicts the minimal response from cells that lack expression of Piezo1 mCherry or Piezo1 (–) cells. The scale bar (bottom right) denotes the magnitude of the calcium response quantified by its fold change. Each compound was tested in duplicate for each dose. **(D)** Circos heat maps of the time-dependent dose response of each compound performed at 0.1, 0.5, 1.0, 5.0, 10, 15, 20, 40, and 75 μM . Each concentric block represents the response to the specified compound. Each small block represents the individual response of each experimental replicate. Each sector of a concentric block is the specified dose. Each row is a time interval, baseline (T_0), and T_1 – T_5 . T_0 depicts the baseline calcium signal before any compound addition, and T_1 – T_5 represents the calcium response data binned into regular time intervals of 10 s after the addition of the compound (see Biological Assay for a detailed description of the analysis). The scale bar denotes the magnitude of the calcium response quantified by its fold change (fold change = 1, baseline response). The dose response was performed in replicates of five for each dose tested per compound.

Recognizing that Piezo1 is prominently expressed in primary human T cells and plays an essential role in TCR-mediated activation and chemokine-induced migration, we implemented a flow cytometry-based assay to thoroughly assess the agonistic potential of various compounds. We measured calcium influx in response to a range of concentrations, spanning from 0.1 to 75 μM , to determine how effectively these compounds could activate Piezo1. From the dose-response experiment, we calculated key pharmacological parameters, including the half-maximal effective concentration (MEC_{50}) and maximum efficacy (E_{max}), through detailed dose-response curves (Figure 7 D). Moreover, we focused on the compounds' ability to induce calcium influx in primary human CD4^+ T-lymphocytes (Figure 13). Each compound's effect on calcium levels was quantified by calculating the fold change in calcium influx compared to baseline measurements. Compounds achieving an average calcium response of 1.2-fold or greater were flagged as “+” and are categorized as such in Tables 1 and 2. This comprehensive approach allows us to not only screen for effective agonists but also to gain insights into their mechanisms of action within T-cell activation pathways.

3.6.2 Chemistry

Yoda1 is a well-characterized chemical agonist known for its ability to activate Piezo1 without requiring mechanical force or other cellular interactions. To confirm the reliability of our assay system, we synthesized Yoda1 to serve as a positive control. The synthesis process, outlined in Scheme 1, commenced with the commercially available pyrazine carboxylic acid (**1**). This compound was transformed into its methyl ester (**2**) by refluxing with methanol and concentrated sulfuric acid for 12 to 16 hours. Next, the methyl ester (**2**) was treated with hydrazine monohydrate (4eqv.) in ethanol at reflux for three hours, yielding pyrazinehydrazide (**3**). The formation of the thiadiazole ring (**4**) involved a two-step reaction. Initially, **compound 3** was reacted with potassium hydroxide (2 eqv.) and carbon disulfide (1.5 eqv.) in ethanol at room temperature for two hours. The precipitate formed was filtered and treated with concentrated sulfuric acid at 0°C, then stirred for 30 minutes at room temperature. The reaction was quenched using crushed ice, leading to precipitation, which was then filtered to obtain the pure product, **compound 4**, as a white solid. The final step involved benzylation of **compound 4** by reacting it with 2,6-dichlorobenzyl bromide in dry acetone, using potassium carbonate as the base at room temperature for 2-3 hrs, resulting in the formation of Yoda1 (**compound 5**).

Scheme 1: ^a

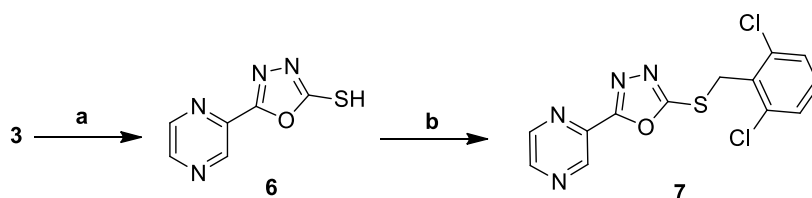


^a**Reagents and conditions:** **(a)** MeOH, Conc. H₂SO₄, reflux, 12-16 hrs, 87%; **(b)** Hydrazine monohydrate, Ethanol, reflux, 3 hrs, 67%; **(c) i)** CS₂, KOH, Ethanol, rt, 2 hrs; **ii)** Conc. H₂SO₄, 0 °C - rt, 30 min, 55%; **(d)** 2,6-dichlorobenzylbromide, K₂CO₃, dry acetone, rt, 2-3 hrs, 82%.

Syeda et al. noted that Yoda1 exhibits poor solubility at higher concentrations (greater than 20 µM), which we also encountered in our experimental work. We hypothesized that this solubility issue might be linked to the sulfur atom present in the central thiadiazole core of the Yoda1 molecule. To address this, we initiated a series of developmental studies

aimed at substituting the sulfur atom in the central thiadiazole ring of Yoda1 (**5**) with other heteroatoms such as oxygen and nitrogen, thereby creating oxadiazole and triazole derivatives in zone C, while maintaining the other structural components unchanged. The synthetic pathway for **compound 7** is illustrated in Scheme 2. Initially, the intermediate pyrazine hydrazide (**3**) was dissolved in ethanol and reacted with potassium hydroxide (2 eqv.) and carbon disulfide (1.5 eqv.) under reflux conditions for 12 to 16 hours to yield **compound 6**. Subsequently, benzylation of **compound 6** was carried out by reacting it with 2,6-dichlorobenzyl bromide (1.2 eqv.) in dry acetonitrile (ACN) as the solvent, using potassium carbonate (1.2 eqv.) as the base under reflux for 2-3 hours to produce compound 7.

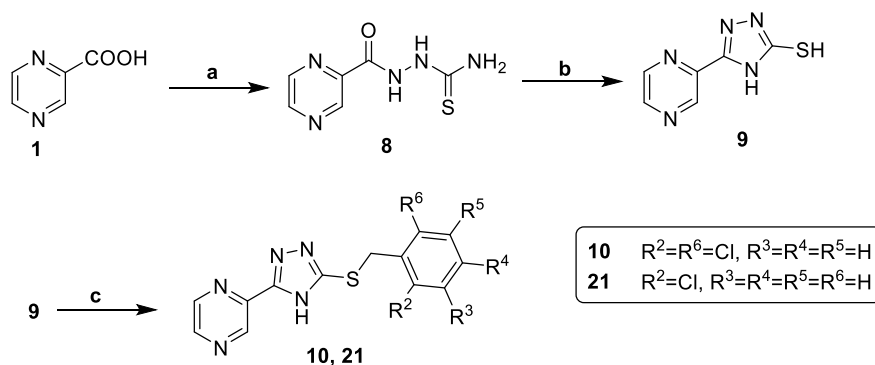
Scheme 2: ^a



Reagents and conditions: (a) CS₂, KOH, Ethanol, reflux, 12-16 hrs, 55%; (b) Different types substituted benzyl bromides or, Different types substituted benzyl methanesulphonate, Dry acetonitrile, reflux, 3 hrs, 85%

Our next objective was to incorporate a triazole ring into zone C (Figure 2B). To achieve this, we utilized the synthetic route outlined in Scheme 3. Initially, we conducted an amide coupling reaction between pyrazine carboxylic acid (**1**) and hydrazine carbothioamide (1.2 eqv.) to obtain **compound 8**. This reaction took place in dry dimethylformamide (DMF), utilizing HATU (1.2 eqv.) as the coupling agent and DIPEA (2 eqv.) as the base at room temperature for 4-5 hrs. Subsequently, the triazole intermediate (**9**) was synthesized through a cyclization reaction with 5% sodium hydroxide under reflux conditions for 3 hours. Following this, the benzylation of **compound 9** was carried out by reacting it with various benzyl bromides (1.2 eqv.) in dry acetonitrile (ACN) as the solvent, with potassium carbonate (1.2 eqv.) serving as the base, also under reflux for 2-3 hrs. This synthetic strategy successfully yielded **compounds 10** and **21**.

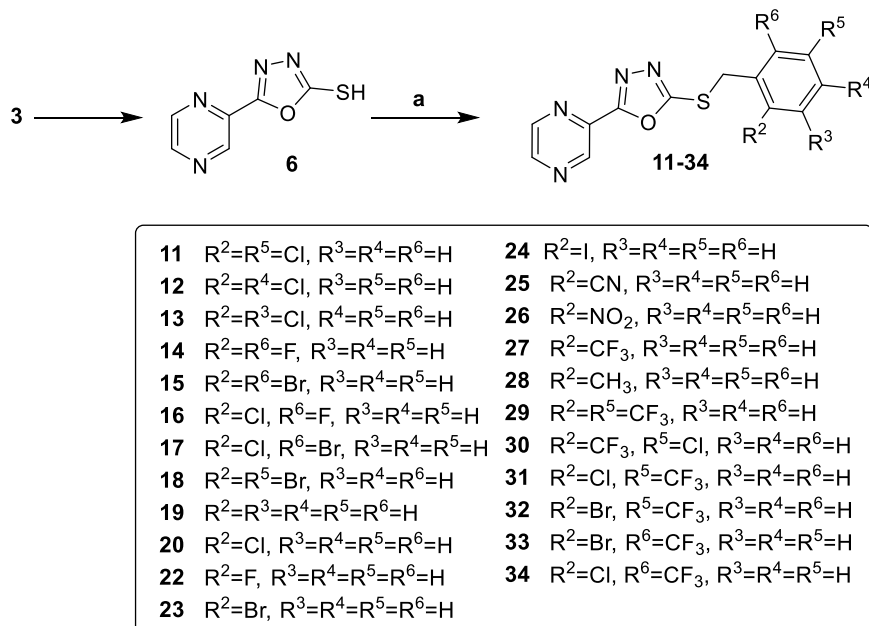
Scheme 3: ^a



Reagents and conditions: (a) hydrazinecarbothioamide, DMF, DIPEA, HATU, rt, 4-5 hrs, 70%; (b) 5% NaOH, reflux, 3 hrs, 67%; (c) Different types substituted benzyl bromides, Dry acetonitrile, reflux, 2-3 hrs, 70-80%.

Scheme 4 details the synthetic pathway for the creation of oxadiazole derivatives **11-34**. In this process, the intermediate **compound 6** was reacted with a variety of substituted benzyl bromides (1.1 eqv.) in dry acetonitrile (ACN) under reflux conditions for 2-3 hrs. This reaction facilitated the formation of the desired oxadiazole derivatives, expanding the library of compounds for further evaluation.

Scheme 4: ^a

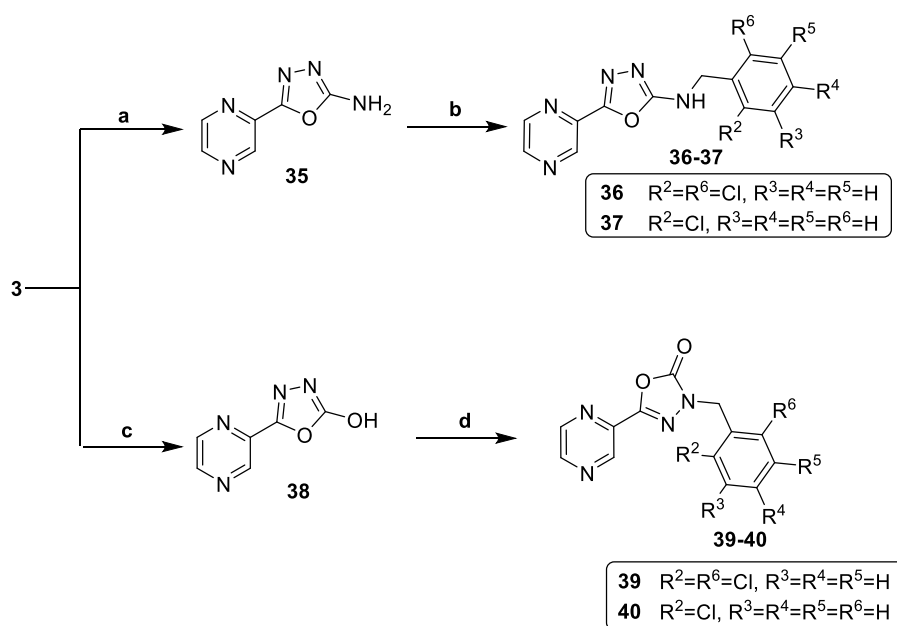


Reagents and conditions: (a) Different types of substituted benzyl bromides, Dry acetonitrile, reflux, 2-3 hrs, 70-90%

Next, we focused on substituting the ethereal sulfur linkage in zone B with alternative heteroatoms such as nitrogen and oxygen (Figure 7). Scheme 5 outlines the synthetic approach for producing N-benzyl analogs, starting with the common intermediate **3**.

When **compound 3** was treated with cyanogen bromide (1.2 equivalents) in ethanol, it yielded the intermediate oxadiazole-2-amine (**35**). Subsequent substitution reactions with 2,6-dichlorobenzyl bromide (1.2 eqv.) and 2-chlorobenzyl bromide (1.2 eqv.) in dry DMF produced derivatives **36** and **37**, respectively. Additionally, using CDI (1.2 eqv.) facilitated cyclization of intermediate **3**, resulting in **compound 38**. This compound further reacted with sodium hydroxide in a 1:1 mixture of THF and water to generate benzyl-substituted derivatives **39** and **40** using both 2,6-dichlorobenzyl bromide and 2-chlorobenzyl bromide.

Scheme 5: ^a

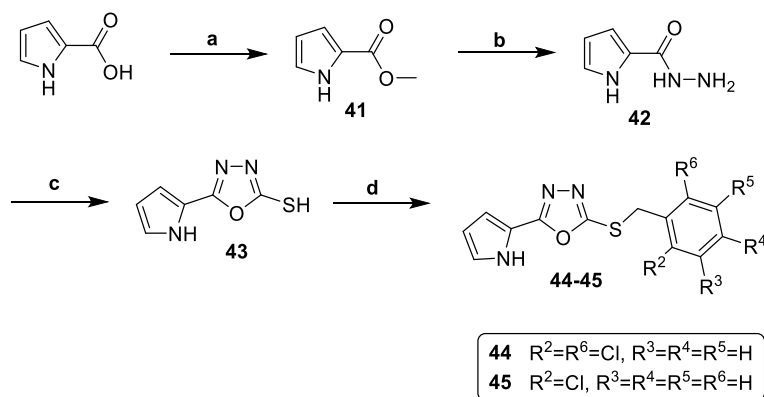


^aReagents and conditions: **(a)** Cyanogen bromide, Ethanol, reflux, 2 hrs, 62%; **(b)** Different types substituted benzyl bromides, NaH, Dry DMF, rt, 2 hrs, 60-70%; **(c)** CDI, dry THF, rt, 3 hrs, 55%; **(d)** NaOH, THF: H₂O- 1:1, rt, 3 hrs, 70-80%.

Next, we aimed to modify zone D by substituting the pyrazine moiety with a pyrrole ring. Scheme 6 details the synthetic procedures for producing pyrrole-containing derivatives **44** and **45**. The synthesis commenced with commercially available pyrrole-2-carboxylic acid, from which the methyl ester (**41**) was generated using methanol and concentrated sulfuric acid under reflux conditions for 12-16 hrs. Following this, **compound 41** was treated with hydrazine monohydrate (4 eqv.) in ethanol at reflux for 3 hrs to yield pyrrole-2-carbohydrazide (**42**). This compound was then dissolved in ethanol and reacted with potassium hydroxide (2 eqv.) and carbon disulfide (1.5 eqv.) under reflux for an additional 12-16 hrs, producing compound **43**. Finally, derivatives **44** and **45** were

synthesized through substitution reactions with 2,6-dichlorobenzyl bromide (1.2 eqv.) and 2-chlorobenzyl bromide (1.2 eqv.) in dry DMF, using potassium hydroxide (1.2 eqv.) as a base at 80°C for 2 hours.

Scheme 6: ^a

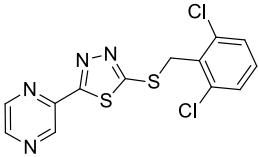
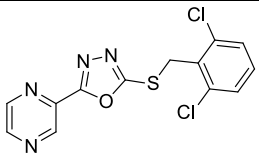
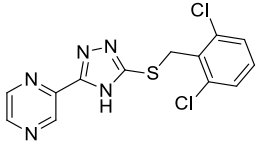
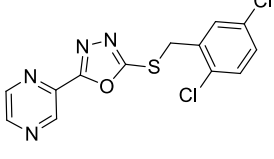


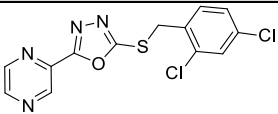
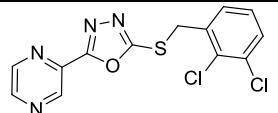
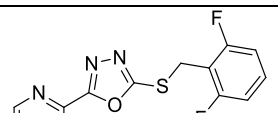
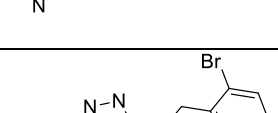
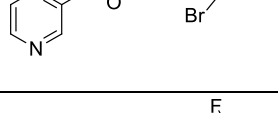
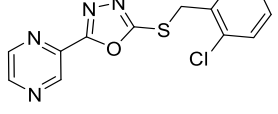
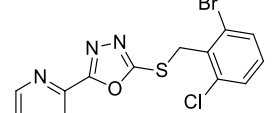
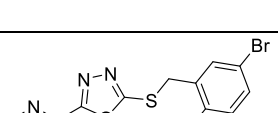
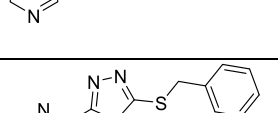
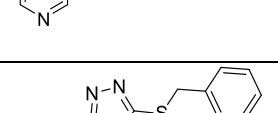
Reagents and conditions: (a) MeOH, Conc. H_2SO_4 , reflux, 12-16 hrs, 85%; (b) Hydrazine monohydrate, Ethanol, reflux, 3 hrs, 75%; (c) CS_2 , KOH, Ethanol, reflux, 12-16 hrs, 60%; (d) Different types substituted benzyl bromides, DMF, 80°C, 2hrs, 80-85%

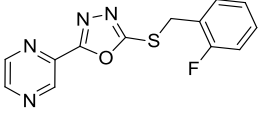
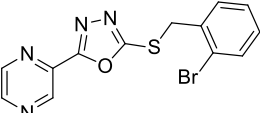
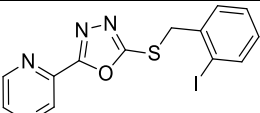
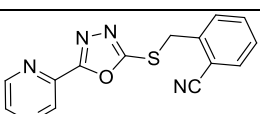
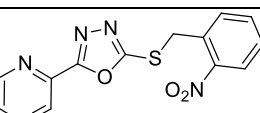
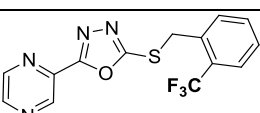
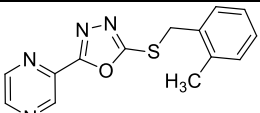
3.7 RESULTS AND DISCUSSION

In a dose-response analysis, Yoda1 demonstrated a dose-dependent increase in calcium influx, achieving a half-maximal effective concentration (MEC_{50}) of approximately 0.50 μM and a maximum efficacy (E_{max}) value of 2.4-fold (Table 1). Smith et al. identified Yoda1's binding site within Piezo1's mechanosensory domain, located between the distal extracellular blades and the proximal intracellular beams, which influences ion channel conductivity. Yoda1 functions as a "molecular wedge," binding between repeats A and B of Piezo1 and decoupling these repeats to promote activation. Computational docking studies in Biovia Discovery Studio¹⁸⁹ (Libdock module)¹⁹⁰⁻¹⁹² using the Piezo1 structure (PDB: 6B3R after a 2.4 μs MD simulation) further revealed that Yoda1 interacts with specific residues: Arg2098, Cys2087, and Phe2090 in Repeat A, and Tyr1692, Met1719, Val1714, and Phe1715 in Repeat B. These residues align closely with those in human Piezo1, exhibiting 82.5% structural similarity.

Table 1. Dose dependency of hPiezo1 agonists: 1st stage modification

Comp. ^a	Structure	Doses for showing agonistic activity in Piezo1 protein (μM) ^b							MEC_{50} (μM) ^c	E_{max} (Fold Change) ^c
		0.1	0.5	1	5	10	15	20		
5 (Yoda1)		—	+	+	+	+	+	+	0.50 ± 0.45	2.4
7		—	—	+	+	+	+	+	1.34 ± 0.85	2.07
10		NP	NP	NP	NP	NP	—	—	NP	NP
11		—	—	—	—	+	+	+	0.57 ± 1.01	1.25

Comp. ^a	Structure	Doses for showing agonistic activity in Piezo1 protein (μ M) ^b							MEC ₅₀ (μ M) ^c	E _{max} (Fold Change) ^c
		0.1	0.5	1	5	10	15	20		
12		NP	NP	NP	NP	NP	—	—	NP	NP
13		NP	NP	NP	NP	NP	—	—	NP	NP
14		NP	NP	NP	NP	NP	—	—	NP	NP
15		—	+	+	+	+	+	+	2.10 ± 1.71	2.5
16		—	—	—	+	+	+	+	1.09 ± 1.01	1.55
17		—	+	+	+	+	+	+	1.04 ± 0.73	2.9
18		—	—	—	—	+	+	+	9.90 ± 6.16	1.9
19		NP	NP	NP	NP	NP	—	—	NP	NP
20		NP	NP	NP	NP	NP	—	—	NP	NP
21		NP	NP	NP	NP	NP	—	—	NP	NP

Comp. ^a	Structure	Doses for showing agonistic activity in Piezo1 protein (μM) ^b							MEC ₅₀ (μM) ^c	E _{max} (Fold Change) ^c
		0.1	0.5	1	5	10	15	20		
22		NP	NP	NP	NP	NP	—	—	NP	NP
23		NP	NP	NP	NP	NP	—	—	NP	NP
24		NP	NP	NP	NP	NP	—	—	NP	NP
25		NP	NP	NP	NP	NP	—	—	NP	NP
26		NP	NP	NP	NP	NP	—	—	NP	NP
27		—	—	—	—	+	+	+	2.06 ± 0.21	1.35
28		NP	NP	NP	NP	NP	—	—	NP	NP

^aAll compounds depicted in the table were synthesized. ^bAgonistic activity of all compounds was tested in Piezo1 protein overexpressed HEK293A cell in different concentrations (Data indicated for 0.1 μM to 20 μM). ^cThe MEC₅₀ and E_{max} values are calculated via reporter assay with HEK293A cells transfected with mCherry-Piezo1 (MEC₅₀ ± standard error, n = 5). Here ‘+’ denotes an average Ca²⁺ influx response of ≥ 1.2-fold with respect to baseline measurement (1-fold) upon compound addition. ‘-’ denotes an average Ca²⁺ influx response of < 1.2-fold with respect to baseline measurement. NP: Not Performed.

* Responses have been marked for doses from 0.1 μM to 20 μM , since compounds with agonistic response at these doses have also showed agonism at 40 μM and 75 μM , which have been omitted from the current table to avoid complexity.

Then, we replaced the thiadiazole core of Yoda1 with oxadiazole and synthesized **compound 7** (Scheme 2) and tested its agonistic effect at concentrations of 15 μM and 25 μM . With activity observed at 15 μM , we performed a dose-response analysis, noting calcium influx activation in mCherry-Piezo1-overexpressing HEK293T cells starting from

1 μM (Table 1). The derivative achieved an MEC_{50} of 1.34 μM and an E_{max} of 2.07-fold, failed to surpass Yoda1's efficacy. These findings align closely with the results of Evans et al.¹⁷² To validate the activity of **compound 7**, a molecular docking analysis was performed which revealed that its C2 and C6 chloro groups on the phenyl ring form two halogen bonds with key amino acids, namely Cys2087 and Phe1715 in Piezo repeats A and B, with bond lengths and angles of 3.2 Å and 159°, respectively (Figure 9C). This interaction enables **compound 7** to act as a wedge, similar to Yoda1. Additionally, Met1719, Tyr1692, and Arg2098 engage the molecule through $\text{S}\cdots\pi$, $\pi\cdots\pi$, and $\text{cation}\cdots\pi$ interactions, reinforcing its binding. The binding pocket features both hydrophobic and hydrophilic regions, with the polar pyrazine ring oriented toward the hydrophilic area and the halogenated benzyl ring positioned within the deeper hydrophobic groove (Figure 9D).

Next, we modified the central core in Zone C (Figure 7) by synthesizing the triazole derivative **10**, which retained the 2,6-dichloro benzyl component (Scheme 3), anticipating it would exhibit similar activity in Ca^{2+} ion influx assays. However, **compound 10** did not activate Ca^{2+} influx, even at a concentration of 25 μM (Table 1). This result was unexpected, particularly given that the sulfur-to-oxygen substitution preserved Yoda1's agonistic potential, whereas replacing sulfur with nitrogen completely abolished this activity. This finding suggests that the central heteroatom plays a critical role in the mechanism of Piezo1 activation, where certain atom types within the core structure may contribute to the compound's agonistic properties, likely through specific interactions or electronic effects that nitrogen cannot replicate. This discovery highlights the importance of core structure heteroatoms in designing effective Piezo1 modulators.

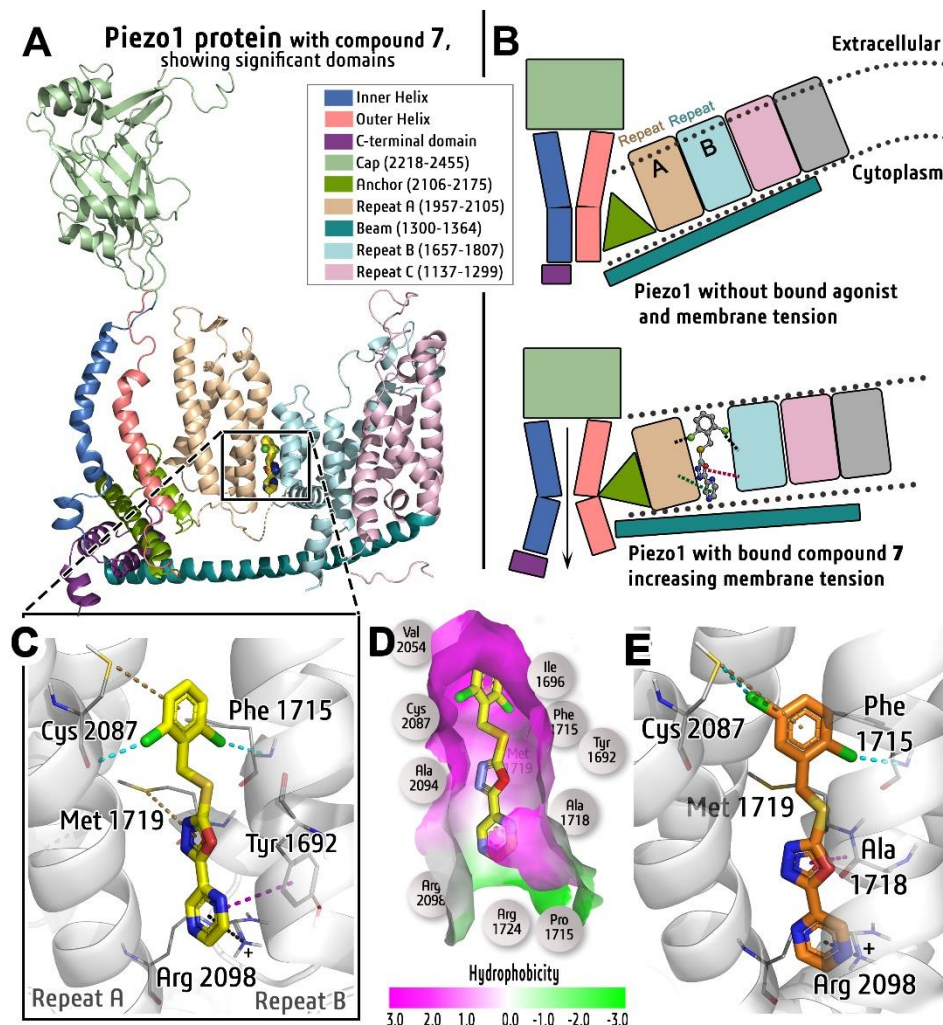


Figure 9. (A) Compound 7 bound to Piezo1 protein, indicating its different repeat regions (B) Compound 7 as a wedge between Repeat-A and B, facilitating channel opening. Docked pose of 7 (C) and 11 (E) (yellow and orange respectively) onto Piezo1 (white); The hydrogen, halogen bonds, S $\cdots\pi$, $\pi\cdots\pi$ and cation $\cdots\pi$ interactions represented as green, cyan, yellow, magenta and black dashed lines respectively. (D) The binding pocket of 7 shows distinct hydrophobic and hydrophilic parts.

Upon observing the active agonists, **compounds 5** and **7**, both featuring two chlorine atoms at the C2 and C6 positions of the phenyl ring (Zone A), we turned our focus to exploring the spatial significance of these chloro groups. To investigate, we retained one chlorine at the ortho (C2) position while varying the other around the phenyl ring to create three positional isomers: **compound 11** with a 2,5-dichloro substitution, **compound 12** with 2,4-dichloro, and **compound 13** with 2,3-dichloro (Scheme 4). Testing their agonistic effects at 15 μM and 25 μM , only **compound 11** (2,5-dichloro) demonstrated Ca^{2+} ion influx, with an MEC_{50} of 0.57 μM , comparable to Yoda1's 0.50 μM . However, its E_{max} was lower at 1.25-fold, approximately half of Yoda1's (2.40-fold) and **compound 7**'s (2.07-fold), indicating limited activity compared to Yoda1 or **compound**

7. This finding highlighted the necessity of specific chloro placements for Piezo1 activation, as the alternative 2,4 and 2,3 positions in **compounds 12** and **13** showed no agonistic activity. Molecular docking analysis suggested that the shift of one chlorine from C6 to C5 in **compound 11** altered interactions, forming a weaker halogen bond (distance: 2.9 Å; angle: 148°) with the sulfur atom, rather than the carbonyl oxygen of Cys2087 as seen in Yoda1 and **compound 7** (Figure 9E). The C2 chlorine appeared critical, acting as an anchor by forming a stable halogen bond with Phe1715 (repeat B), while the secondary chlorine bonded with Cys2087 in repeat A. This pattern appears vital for effective Piezo1 modulation.

In **compounds 12** and **13**, despite retaining a chlorine atom at the C2 position, relocating the second chlorine to the C4 or C3 position completely abolished agonistic activity. This can be attributed to the disruption in forming a crucial halogen bond with Cys2087 in Repeat A, a key interaction required for Piezo1 activation. Based on this, we hypothesized that if the 2,6-dichloro configuration in Yoda1 (**compound 5**) and **compound 7** enabled essential halogen bonding with repeats A and B of Piezo1, then replacing the dichloro with difluoro or dibromo might yield similar agonistic effects. To test this hypothesis, we synthesized **compound 14** with a 2,6-difluoro substitution and **compound 15** with a 2,6-dibromo substitution on the phenyl ring in Zone A. Interestingly, while **compound 14** with difluoro groups showed no Ca^{2+} influx at 25 μM , **compound 15** with dibromo groups triggered Ca^{2+} influx at both 15 μM and 25 μM in initial screenings. Further dose-response analysis of **compound 15** revealed an MEC_{50} of 2.10 μM , higher than that of **compound 7**. This result highlights the potential for specific halogen substitutions at the 2,6-positions to maintain agonistic activity, although the efficacy may vary depending on the halogen type, with bromine demonstrating better compatibility than fluorine for Piezo1 activation.

We propose that the inability of fluorine atoms in **compound 14** to form the necessary halogen bonds with Piezo1 residues is due to their small atomic size and lack of a sigma-hole, which is required for halogen bonding. Unlike chlorine or bromine atoms, fluorine does not exhibit a sigma-hole due to its high electronegativity and compact size, limiting its capacity for halogen bonding. In contrast, bromine atoms in **compound 15** possess a larger atomic radius and weaker electronegativity, which leads to a more prominent sigma-hole. This characteristic facilitates the formation of essential halogen bonds with

the Piezo1 binding site residues, thereby enabling **compound 15** to activate Piezo1 and induce Ca^{2+} ion influx. Based on our structure-activity relationship (SAR) findings, we conclude that both the type of halogen atom and its spatial positioning on the phenyl ring are critical for effective Piezo1 activation. This highlights the role of specific halogen-substitution patterns in promoting the required molecular interactions for Piezo1 agonism and subsequent Ca^{2+} signaling.

The study progressed by introducing mixed halogen substitutions in Zone A. Specifically, one chloro group in **compound 7** was replaced with either a fluoro group (**compound 16**) or a bromo group (**compound 17**). Both compounds successfully induced Ca^{2+} influx during the initial screening at 15 μM and 25 μM concentrations. After further dose-response assays, **compounds 16** and **17** demonstrated MEC_{50} values of 1.09 μM and 1.04 μM , respectively, which are similar. However, the E_{max} values differed significantly: **compound 16** showed an E_{max} of 1.55-fold, while **compound 17** reached an E_{max} of 2.90-fold (Table 1). This variance highlights that MEC_{50} alone does not capture the full extent of their activity. The chloro and bromo groups in **compounds 16** and **17** likely form similar halogen bonds as seen in previously active analogs. Although fluorine generally does not engage in halogen bonding due to its high electronegativity and small size, the presence of an electron-withdrawing chloro group at the C2 position may induce a slight sigma-hole in the fluorine atom. This effect could enable weak halogen or halogen-mediated hydrogen bonding interactions, an interaction likely absent in difluoro-substituted **compound 14**, which showed no activity. Thus, these findings suggest that both the nature and positioning of halogens are crucial for effective Piezo1 activation in HEK293T cells overexpressing Piezo1. **Compound 11**, with a 2,5-dichloro substitution, exhibited a distinctive profile: it achieved a low E_{max} value but displayed a favorable MEC_{50} , suggesting a potential functional relevance of the C2 and C5 positions. To explore this further, the dichloro groups in **compound 11** were replaced with dibromo groups, resulting in **compound 18**. **Compound 18** demonstrated a significantly higher MEC_{50} value of 9.90 μM compared to **compound 11**, indicating reduced potency. However, its E_{max} of 1.9-fold was comparable to that of the oxadiazole-derivative **7**.

To further validate the importance of the dual-halogen interaction in Zone A, **compound 19** was synthesized without any halogen groups on the benzyl ring. As anticipated, the lack of halogens led to a complete loss of Piezo1 activation potential, even at a high

concentration of 25 μM , highlighting the critical role of halogen presence for effective Piezo1 binding. Following this, we tested if a single halogen at the C2 position of the phenyl ring could provide sufficient activity. **Compound 20**, with just one chloro group at C2, was synthesized but displayed no activity, indicating that a single C2 halogen alone is insufficient to promote Piezo1 agonism. To probe further, we generated a mono-chloro derivative of **compound 10**, designated as **compound 21**, which similarly lacked agonistic activity at concentrations up to 25 μM . This inactivity was consistent when we introduced single fluoro, bromo, and iodo substitutions at C2 (**compounds 22, 23, and 24**, respectively); none of these compounds showed Piezo1 activation at the highest tested dose (25 μM). These findings reinforce the hypothesis that two halogen atoms in specific positions are crucial for binding efficacy. The binding model (Figure 9B) suggests that the dual halogen interactions with Repeat A and B within the Piezo1 structure are essential for stabilizing the agonistic conformation, supporting our hypothesis on the spatial requirements of halogen substitutions for effective Piezo1 activation.

The exploration of bioisosteric replacements in Zone A of Yoda1 has provided valuable insights into the structural requirements for Piezo1 agonism. Given the lack of conclusive structural data on Piezo1-ligand interactions, a systematic approach to modifying Yoda1's structure has allowed for the identification of essential interactions through structure-activity relationships (SAR). Computational analysis suggested that mono-halogenated derivatives (**20-24**) lack the geometrical rigidity seen in di-halo-substituted compounds (e.g., **7, 14-18**), potentially explaining their inability to activate Piezo1. This rigidity likely helps maintain the precise spatial arrangement necessary for effective binding at Piezo1's mechanosensory domains. In seeking alternatives to di-halo substituents, attention was turned toward bioisosteric replacements of the chloro group at the C2 position of the phenyl ring in **compound 20**. Testing cyano (**25**), nitro (**26**), trifluoromethyl (**27**), and methyl (**28**) substitutions at concentrations of 15 μM and 25 μM revealed that only the trifluoromethyl derivative (**compound 27**) showed agonistic activity. Remarkably, **compound 27** exhibited a dose-dependent response with an MEC_{50} of 2.06 μM , although with a lower maximum efficacy compared to di-halo compounds. The trifluoromethyl group's agonistic activity highlights a new structural cue that can activate Piezo1. Unlike other mono-substituted compounds, which failed to show activity, the trifluoromethyl group appears to contribute unique electronic or steric properties that enable activation without a direct halogen atom. This finding is particularly

interesting as it opens new avenues for designing mono-substituted Piezo1 agonists with potentially distinct interaction profiles, broadening the scope of potential Piezo1-targeted modulators.

The molecular docking analysis of **compound 27**, featuring a trifluoromethyl ($-\text{CF}_3$) group, has unveiled intriguing interaction dynamics at the binding site of Piezo1. Instead of forming halogen bonds like its chlorinated counterparts (Yoda1 and **compound 7**), the $-\text{CF}_3$ group engages in unique interactions such as tetrel interactions ($\text{F}_3\text{C}\cdots\text{O}=\text{C}$) and orthogonal multipolar interactions ($\text{CF}_3\cdots\text{C}=\text{O}$). This structural exploration revealed that **compound 27** is surrounded by key residues—Arg2098, Tyr1962, Phe1715, Cys2087, Met1719, and Phe2090—which contribute to a robust interaction network. The hydrophobic characteristics of the $-\text{CF}_3$ group allow it to engage effectively with nearby hydrophobic residues (Ile1696, Val1714, Phe1715, and Met1719). Notably, it forms tetrel interactions with Pro1711 and multipolar interactions with Val1714. Additionally, the $-\text{CF}_3$ group's branching structure facilitates a CF_3 -mediated hydrogen bond with Phe1715, which helps to compensate for the lack of halogen bonding typically observed in other agonists. An additional hydrogen bond is formed through the nitrogen of the pyrazinyl moiety, which hooks into Repeat A via Arg2098. These findings suggest that the trifluoromethyl group provides a novel mechanism for interaction that is distinct from traditional halogen bonding, illustrating the complexity and potential of alternative functional groups in modulating Piezo1 activity. This opens exciting pathways for future research into piezoelectric activators.

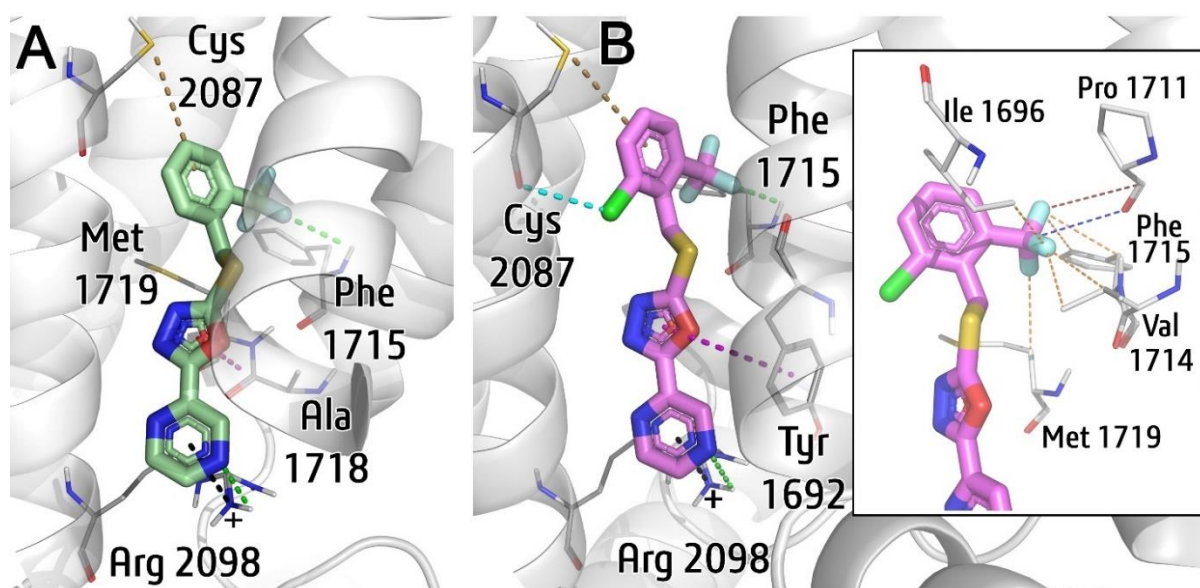
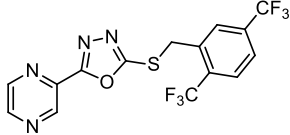
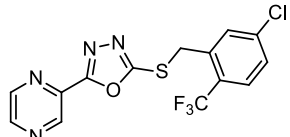
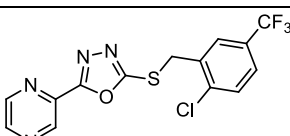
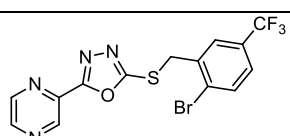
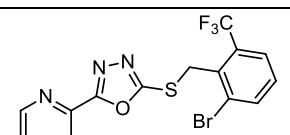
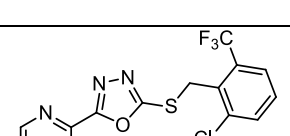
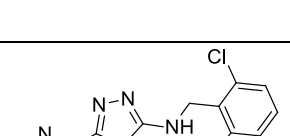
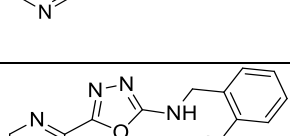


Figure 10. Docked pose of **27** (A) and **34** (B) (green and magenta tubes, respectively) against Piezo1 (white). The hydrogen, halogen bonds, $S \cdots \pi$, $\pi \cdots \pi$, and cation $\cdots\pi$ interactions represented as green, cyan, yellow, magenta, and black dashed lines respectively. (B: inset) Tetrel, multipolar, and hydrophobic interactions shown in blue, brown, and orange thin dashed lines. Figures generated in Schrödinger PyMOL.

The synthesis of **compound 28**, a methyl-substituted derivative lacking any fluorine atoms, served as a negative control to further confirm the significance of the trifluoromethyl group in Piezo1 activation. As anticipated, **compound 28** failed to activate Piezo1 even at a concentration of 25 μM . This outcome highlights the essential role of tetrel bonding—where the trifluoromethyl group can engage in interactions that are crucial for agonistic activity—reinforcing the idea that structural features, such as the presence and arrangement of halogens, significantly influence the efficacy of compounds in modulating Piezo1.

The development of **compound 29** with a 2,5-di-trifluoromethyl substitution represents a significant advancement in our SAR studies. The observed MEC_{50} value of 1.00 μM for this compound indicates a notable enhancement in potency compared to the mono-trifluoromethyl derivative (**compound 27**) with an MEC_{50} of 2.06 μM . This increase in potency suggests that the presence of an additional trifluoromethyl group contributes synergistically to the activation of the Piezo1 protein, underscoring the importance of substituent position and identity in modulating biological activity.

Table 2. Dose dependency of hPiezo1 agonists: 2nd stage modification

Comp. ^a	Structure	Doses for showing agonistic activity in Piezo1 protein (μM) ^b							MEC ₅₀ (μM) ^c	E _{max} (μM) ^c
		0.1	0.5	1	5	10	15	20		
29		—	—	+	+	+	+	+	1.00 ± 1.37	1.68
30		—	+	+	+	+	+	+	0.55 ± 0.97	1.7
31		—	+	+	+	+	+	+	0.88 ± 0.51	2.3
32		—	+	+	+	+	+	+	0.60 ± 0.10	2.3
33		+	+	+	+	+	+	+	0.46 ± 0.40	2.7
34 (Yaddle1)		+	+	+	+	+	+	+	0.40 ± 0.48	2.6
36		—	—	—	—	—	—	—	NP	NP
37		—	—	—	—	—	—	—	NP	NP

Comp. ^a	Structure	Doses for showing agonistic activity in Piezo1 protein (μM) ^b							MEC ₅₀ (μM) ^c	E _{max} (μM) ^c
		0.1	0.5	1	5	10	15	20		
39		—	—	—	—	—	—	—	NP	NP
40		—	—	—	—	—	—	—	NP	NP
44		—	—	—	—	—	—	—	NP	NP
45		—	—	—	—	—	—	—	NP	NP

^aAll compounds depicted in the table were synthesized. ^bAgonistic activity of all compounds was tested in Piezo1 protein overexpressed HEK293A cell in different concentrations (Data indicated for 0.1 μM to 20 μM). ^cThe MEC₅₀ and E_{max} values are calculated via reporter assay with HEK293A cells transfected with mCherry-Piezo1 (MEC₅₀ \pm standard error, n = 5). Here '+' denotes an average Ca²⁺ influx response of ≥ 1.2 -fold with respect to baseline measurement (1-fold) upon compound addition. '-' denotes an average Ca²⁺ influx response of < 1.2 -fold with respect to baseline measurement. NP: Not Performed.

* Responses have been marked for doses from 0.1 μM to 20 μM , since compounds with agonistic response at these doses have also showed agonism at 40 μM and 75 μM , which have been omitted from the current table to avoid complexity.

We next developed **compound 30** by substituting one of the -Cl groups in **compound 11** with a -CF₃ group at the C2 position of the benzyl ring, and then created **compound 31** by reversing the positions of these groups. Both compounds exhibited activity in the initial screening at 15 μM , with dose-response assays revealing MEC₅₀ values of 0.55 μM for **compound 30** and 0.88 μM for **compound 31**. Building on these findings, we synthesized **compound 32**, which combined the bromine from **compound 18** at the C2 position and the trifluoromethyl group from **compound 31** at the C5 position. This compound also activated the Piezo1 channel, achieving a MEC₅₀ value of 0.60 μM , comparable to that of **compound 11** (0.57 μM). This progression emphasizes the

importance of specific substitutions and spatial arrangements in enhancing the agonistic potency towards the Piezo1 protein.

We synthesized **compound 33**, featuring a 2-bromo-6-trifluoromethyl substitution, and **compound 34**, which has a 2-chloro-6-trifluoromethyl substitution. The MEC₅₀ value of **compound 33** was determined to be 0.46 μ M, closely matching that of the established Piezo1 agonist Yoda1 (0.50 μ M). Our structure-activity relationship (SAR) studies indicate that the trifluoromethyl (-CF₃) group is crucial for enhancing agonistic activity, regardless of whether it is placed at the C2 or C5 position of the phenyl ring in Zone A. **Compound 34** exhibited an even lower MEC₅₀ value of 0.40 μ M, demonstrating comparable potency to Yoda1 and a significant improvement over **compound 7**, which had an MEC₅₀ of 1.34 μ M. Molecular docking analysis for **compound 34** revealed a halogen bond between the C6 chloro group and the carbonyl oxygen of Cys2087, alongside a strong hydrogen bond between the -CF₃ group and Phe1715. Additionally, potential tetrel, multipolar, and hydrophobic interactions at the Piezo1 active site were identified, contributing to its efficacy. The presence of multiple interaction types—including halogen, hydrogen, and tetrel bonding—suggests that **compound 34** adopts a stable conformation essential for effective binding to the Piezo1 protein.

To further investigate the σ -holes associated with the halogen substituents at C2 and C6, we conducted single-point density functional theory (DFT) calculations on the optimized molecular geometries. In **compound 7**, positive potentials were observed on both chlorine atoms, supporting our hypothesis about the existence of σ -holes that facilitate halogen-bond interactions. Conversely, mono-chloro **compound 20** lacked positive charge accumulation on the chlorine surface, which aligned with its inactivity in initial screenings. DFT analysis of **compound 27** indicated robust tetrel interactions stemming from its trifluoro-substituted carbon. Furthermore, the DFT evaluation of **compound 10** revealed an even distribution of positive charge across the molecule, indicating an absence of σ -holes at the C-Cl axes and correlating with its lack of activity against Piezo1. Based on these findings, we proposed that "Yaddle1" (**compound 34**) featuring chloro and CF₃ groups at the C6 and C2 positions, respectively, would likely show strong agonistic activity. DFT calculations supported this hypothesis, showing that the carbon bonded to trifluoromethyl (-CF₃) continues to act as a tetrel center, while the chlorine at

C6 accumulates a positive charge on its outer surface. This creates a distinct " σ -hole" along the C–Cl axis, enhancing its potential for interactions (Figure 11D).

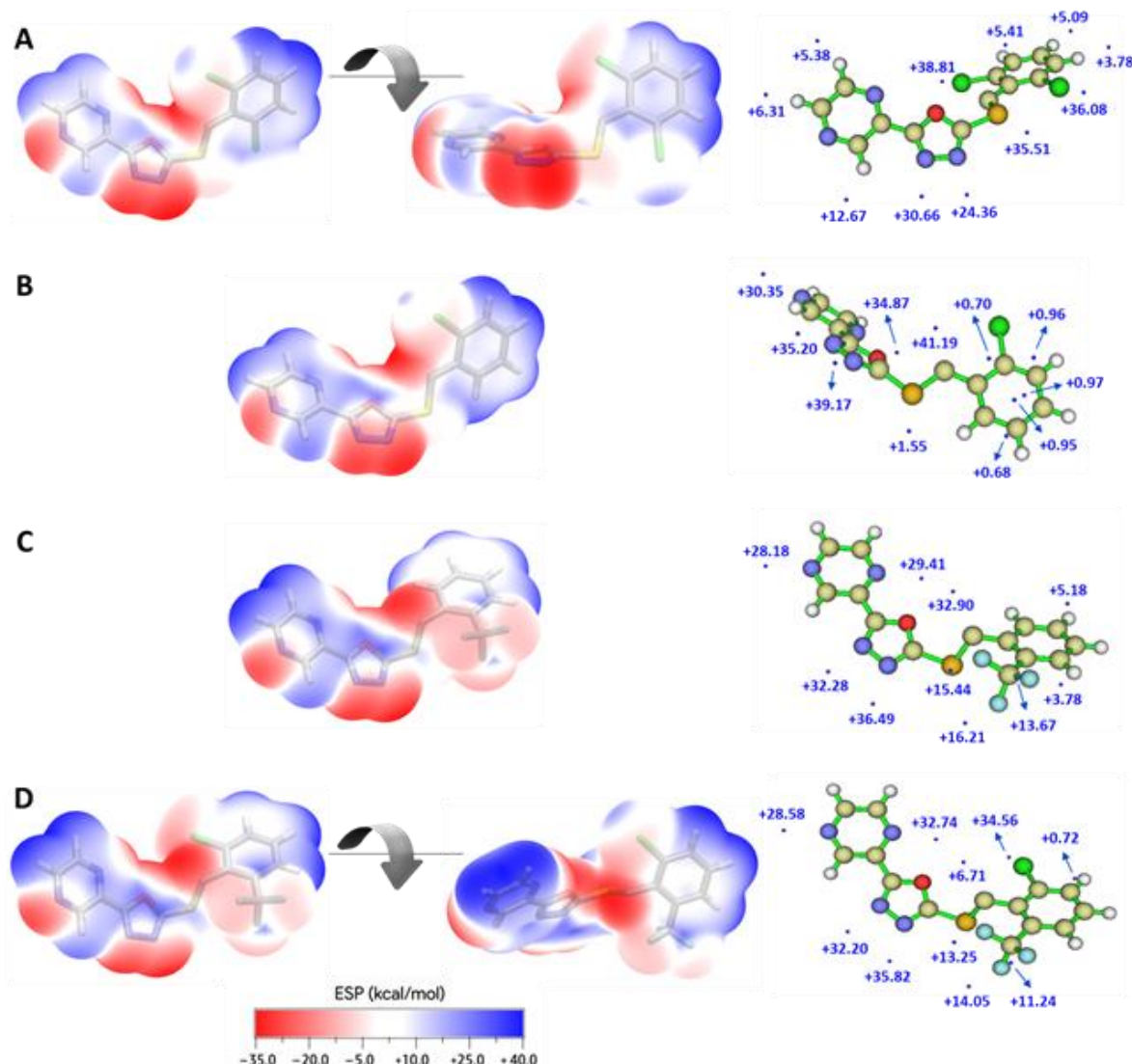


Figure 11. Molecular electrostatic potential (Hartrees) at 0.001 e/bohr³ isodensity surface for (A) 7, (B) 20, (C) 27 and (D) 34. ESP-mapped (kcal/mol) molecular surfaces of the above compounds were calculated with Gaussian 09 at the B3LYP/6-31+g(d,p) level of theory.^{193,194} Wave function analyses were furnished by the Multiwfn 3.2.1 program,^{195,196} and all isosurface maps were rendered using VMD 1.9.4¹⁹⁷ based on the outputs of Multiwfn. Surface regions with negative ESP values are omitted for clarity.

Having gained a clearer view of the positional significance of substituents in Zone A of Yoda1, we explored modifying the sulfur linkage in Zone B by replacing it with nitrogen or oxygen. This led to the synthesis of **compounds 36** and **37** with a nitrogen linker (Scheme 5). However, these changes resulted in a complete loss of agonistic activity, underscoring the essential role of the sulfur bridge. Since the only difference between **compound 7** and **compound 36** is this linker, it appears that the sulfur atom is necessary

for Piezo1 activation, and replacing it with nitrogen disrupts this activity. Similarly, replacing sulfur with oxygen produced unexpected compounds featuring a 3,4-oxadiazole-(3H)-2-one structure due to the stability of the keto form over the amidol form in tautomeric equilibrium. In **compound 39**, a 2,6-dichlorobenzyl group was attached to the oxadiazole nitrogen instead of oxygen at the 2-position, confirmed by X-ray crystallography. Its 2-chloro derivative (**compound 40**) was also synthesized, but neither compound could activate Piezo1 at 15 μM or 25 μM concentrations. Furthermore, studies by David Beech's group highlighted the role of the pyrazine moiety in Zone D of Yoda1, leading to the development of the antagonist Dooku1 (**compound 44**), which selectively inhibits Yoda1-induced Piezo1 activation.¹⁷² We synthesized Dooku1 and its monochloro derivative (**compound 45**) to assess their efficacy. However, neither compound triggered Ca^{2+} influx through the Piezo1 channel at concentrations up to 25 μM .

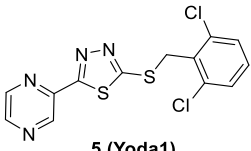
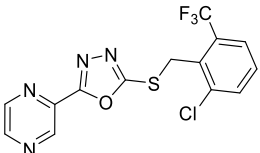
These SAR results reveal that the unique configuration, specific geometric arrangement, and distinct positioning of chemical subunits enable these agonists to interact with Piezo1's Repeat A and Repeat B regions in a specific configuration.

[Note: Some of the compounds was initially synthesized by my lab senior Dr. Barnali Paul. I have to resynthesis those for purification as well as biological assays validation. DFT Study was assisted by Dr. Himadri Sekhar Sarkar and Molecular docking was assisted by Uddipta Ghosh Dastidar.]

3.7.1 Solubility

Previous studies have indicated that Yoda1 encounters solubility limitations at concentrations above 20 μM . To explore this further, we measured the kinetic solubility of Yoda1 (**compound 5**) alongside our lead compound, Yaddle1 (**compound 34**). Results revealed that Yaddle1 exhibits a kinetic solubility of $26.72 \mu\text{M} \pm 1.8 \mu\text{M}$ at pH 7.4, a substantial improvement over Yoda1's solubility of $1.22 \pm 0.11 \mu\text{M}$ at the same pH level (Table 3). This enhanced solubility likely arises from the oxygen in the 1,3,4-oxadiazole ring in Yaddle1, as oxygen's higher electronegativity provides improved solubility compared to the sulfur in Yoda1's 1,3,4-thiadiazole ring.^{198,199} Additionally, the trifluoromethyl ($-\text{CF}_3$) group in Yaddle1 contributes favorable physicochemical properties and binding affinity for effective Piezo1 activation.

Table 3: Kinetic solubility of synthesized compounds

Compound	Kinetic Solubility Study in PBS, pH 7.4 (μM)
 5 (Yoda1)	1.22 ± 0.11
 34 (Yaddle1)	26.72 ± 1.8
Diethylstilbesterol ^a	14.36 ± 0.23
Diclofenac Sodium ^b	205.29 ± 1.68

^aDiethylstilbesterol was taken as a negative standard for the kinetic solubility test.

^bDiclofenac Sodium was taken as a positive standard for the kinetic solubility test.

The test was validated against a dose response curve with linearity of $R^2 = 0.999$

3.7.2 Validation of Potential Piezo1 Agonists in Primary Human CD4⁺ T cells

Piezo1, a mechanosensitive ion channel, is predominantly expressed in T cells, where Ca^{2+} influx mediated by Piezo1 activation plays a crucial role in T cell activation and, consequently, in enhancing the immune response. Initial assays in HEK293A cells identified several potential Piezo1 agonists, which were subsequently validated in primary human T-lymphocytes at 15 μM and 25 μM concentrations. Using Fluo-3, AM dye for calcium imaging, the kinetics of Ca^{2+} influx was monitored over time intervals (T1 to T4) after agonist addition. Six compounds (**7**, **15**, **17**, **27**, **29**, and **34**) demonstrated at least a two-fold increase in Piezo1 activation relative to baseline, highlighting them as effective agonists (Figure 13). Notably, **compound 34** (Yaddle1), which had shown the highest potency in vitro (MEC_{50} : 0.40 μM), also exhibited superior activity in CD4⁺ T cells compared to the mono-CF₃-substituted **compound 27**.

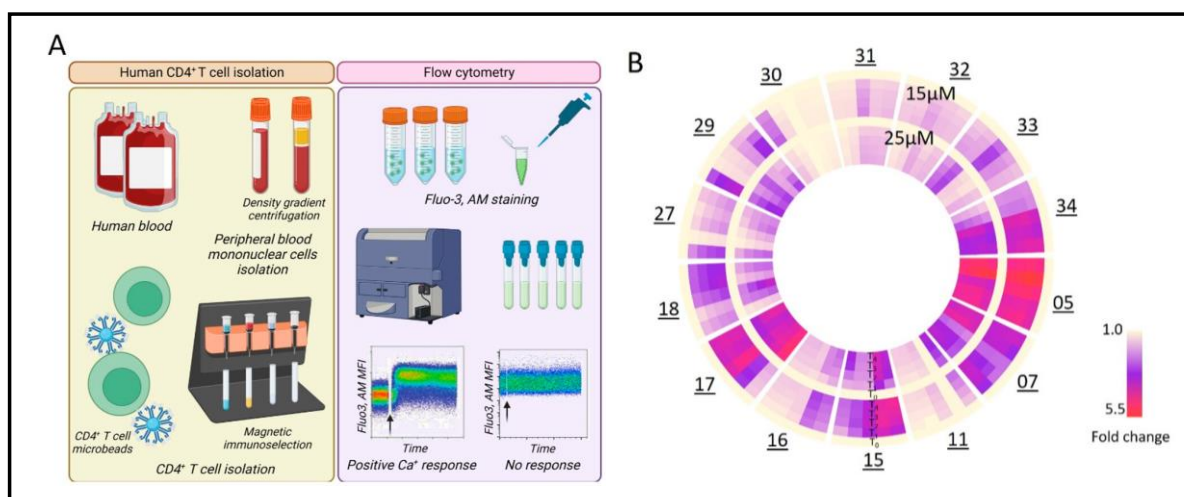


Figure 12. Primary human CD4⁺ T cell validation of potential Piezo1 agonists. **A.** Experimental workflow of isolation of CD4⁺ T cells from human peripheral blood. Peripheral blood mononuclear cells (PBMCs) are isolated from the blood through sucrose-based density centrifugation. CD4⁺ T cells were isolated through magnetic immunoselection using microbeads coupled with CD4-specific antibodies. **B.** Circos heatmap of validation of Piezo1 agonists in primary human CD4⁺ T lymphocytes at 15 μ M and 25 μ M.

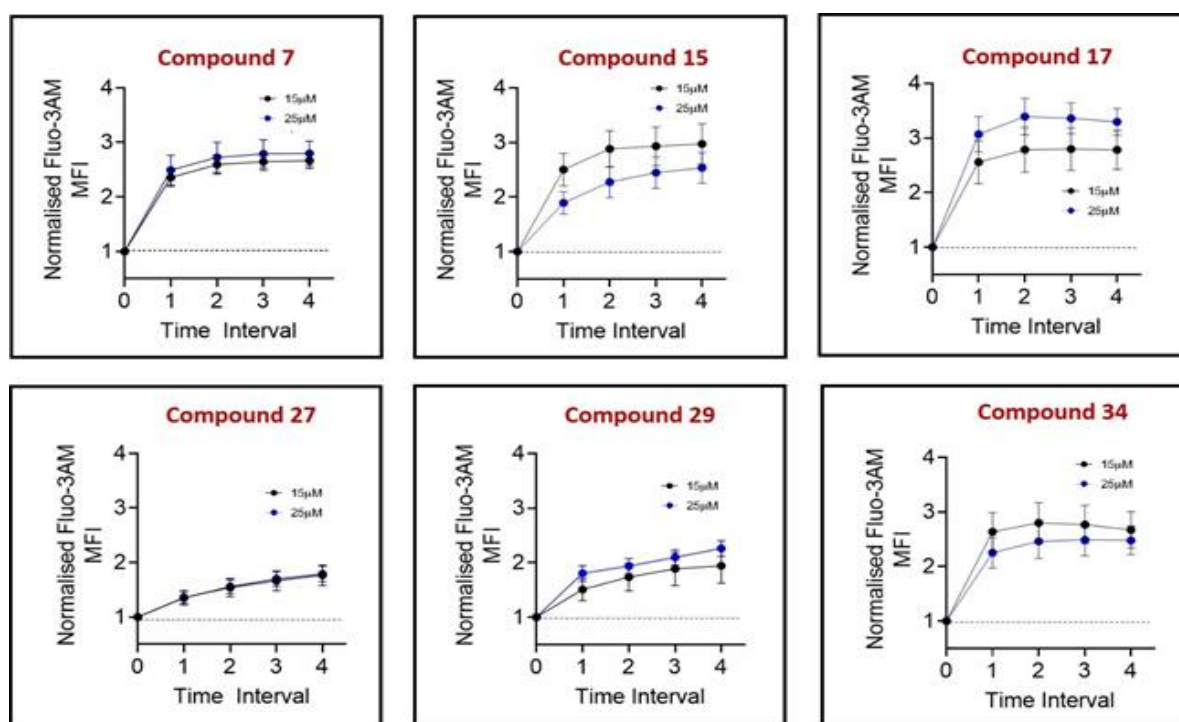


Figure 13. Piezo1 agonistic activity as determined by CD4⁺ T cell primary assay. Representative plots of some active compounds from reporter assay of mCherry-Piezo1 protein overexpressed in HEK293 cell are tested in CD4⁺ T cell in 15 μ M (black) and 25 μ M (blue) concentrations over a specific period of time. The normalized MFI response of each compound is plotted against the time interval. (n=5, Mean \pm SEM shown in graph).

3.7.3 Cytotoxicity Assay

To evaluate potential toxicity, an MTT assay was conducted on primary human peripheral blood mononuclear cells (PBMCs) with compounds Yoda1 (**5**), **27**, and **34** at doses ranging from 0.1 to 20 μ M at 6 and 24 h after the addition of the compound. Results indicated no significant reduction in cell viability at the tested concentrations, reinforcing that these compounds, including lead **compound 34**, exhibit low toxicity (Figure 14).

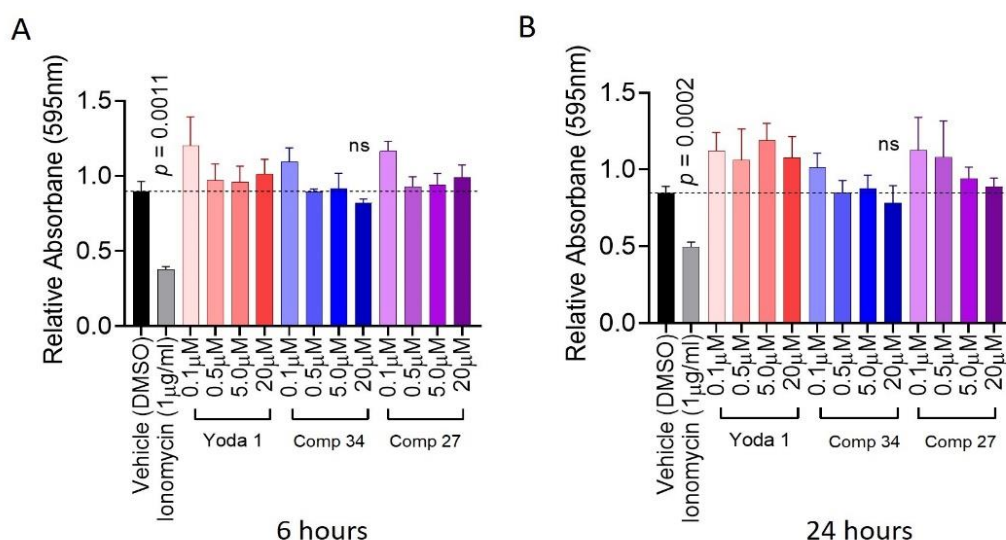


Figure 14. Toxicities of the following compounds: **Yoda1**, **Comp 34** (lead) and **Comp 27** were evaluated through MTT assay at **A**. 6 hours and **B**. 24 hours post treatment. Toxicities were measured at 0.1 μ M, 0.5 μ M, 5.0 μ M and 20.0 μ M for each compound tested. Relative absorbance was measured by calculating the ratio of absorbance at 595nm between treated and untreated conditions. The vehicle (DMSO) was used at a concentration of 1% by volume (highest concentration used in our dose response assays) as a negative control. Ionomycin, a potent calcium ionophore, was used as a positive control of toxicity.

Piezo1's role in T cell activation—specifically through its influence on immunological synapse formation and T cell receptor (TCR) signalling—further underscores its potential as a target for immunomodulation. T cells, through their interactions with antigen-presenting cells (APCs), utilize mechanical forces in TCR-peptide-MHC binding, facilitated by Piezo1's mechanosensitive function. This pathway suggests that Piezo1 agonists, validated in T cells, could support immune responses by strengthening T cell activation through the stabilization of the immunological synapse.

All the biological studies and their graphical representation were conducted by Dr. Chinky Shiu Chen Liu and Suravi Mukherjee from Dr. Dipyaman Ganguly's lab, CSIR - IICB.

3.8 CONCLUSION AND OUTCOME

This work systematically explores the structure-activity relationship (SAR) of Piezo1 protein agonist Yoda1 by modifying chemical subunits in zones A, B, C, and D, leading to the identification of Yaddle1 (**34**) as a superior alternative with improved potency and solubility. In zone C, replacing the sulfur atom in the thiadiazole core of Yoda1 with oxygen (oxadiazole) improved kinetic stability and solubility while maintaining Piezo1 activation capability. In contrast, triazolyl derivatives failed to activate the protein, underscoring the importance of the heterocyclic core. In zone A, halogen substitutions on the benzyl ring were evaluated. Compounds with 2,6-dihalo substitutions (e.g. **5**, **15**, **16**, **17**) demonstrated higher activity than those with 2,5-dihalo substitutions (e.g. **11**, **18**). Molecular docking revealed stronger halogen bonding interactions for C2, C6 substitutions compared to C2, C5. The trifluoromethyl (-CF₃) group emerged as a novel Piezo1-activating moiety, forming diverse non-covalent interactions such as hydrogen, tetrel, and multipolar bonds. Mono -CF₃ derivative **27** activated Piezo1, whereas mono-chloro derivative **20** did not, highlighting the functional significance of -CF₃. Combining -CF₃ and halogens enhanced potency, with the 5-chloro-2-CF₃ derivative (**30**) showing an MEC₅₀ of 0.55 μM. The most potent agonist, Yaddle1 (**34**), featuring -Cl at C2 and -CF₃ at C6, achieved an MEC₅₀ of 0.40 μM, supported by molecular docking insights. In zone B, replacing the sulfur linkage with nitrogen significantly reduced Piezo1 activation, confirming the critical role of sulfur in maintaining bioactivity.

Yaddle1 demonstrated 10-fold improved solubility over Yoda1 (26.72 μM vs. 1.22 μM at pH 7.4) and effectively triggered Ca²⁺ influx in human CD4⁺ T cells. This makes Yaddle1 a promising candidate for vaccine adjuvant development, offering enhanced solubility, potency, and the ability to target optimal T-cell activation for next-generation immunological applications.

3.9 EXPERIMENTAL SECTION

General methods

All starting materials, reagents, and solvents were purchased from commercial suppliers and used without further purification. Dry solvents were either commercially purchased or dried using a standard protocol. Reactions that had a sensitivity toward moisture or oxygen were carried out under a dry nitrogen or argon atmosphere. All the TLC experiments were performed on silica gel plates (Merck silica gel 60, F254). The spots were visualized under UV light ($\lambda = 254$ and 365 nm) or by using the appropriate stain. Compounds were purified using a Teledyne ISCO Combi Flash R_f system using a 230–400 mesh size silica gel. ¹H NMR was recorded at 300 MHz (Bruker-DPX), 400 MHz (JEOL), and 600 MHz (Bruker AVANCE) frequencies, and ¹³C NMR spectra were recorded at 75 MHz (Bruker-DPX), 100 MHz (JEOL), and 150 MHz (Bruker AVANCE) frequencies in CDCl₃ or CD₃OD or *d*₆-DMSO using tetramethylsilane as the internal standard. The following abbreviations were used to explain multiplicities: s = singlet, d = doublet, t = triplet, q = quartet, m = multiplet, brs. = broad singlet. The coupling constant, *J*, was reported in the Hertz unit (Hz). High-resolution mass spectroscopy, HRMS (*m/z*), was carried out using ESI (Q-ToF Micro mass spectrometer), and ESI (LTQ Orbitrap XL mass spectrometer). The purity of all the compounds was determined to be >95% and analyzed using an Agilent Infinity Prep. HPLC system using a BioSuite Phenyl reverse-phase column (75 × 7.5 mm, 10 μm particle size, 1000 Å pore size). Mobile phase A was composed of 0.1% TFA in water and mobile phase B of 10% water in acetonitrile for 4–6 min and a flow rate of 1 mL/min with detection at 254 nm wavelengths.

Synthesis of methyl pyrazine-2-carboxylate (2): Pyrazine-2-carboxylic acid **1** (2 g, 16.12 mmol) was taken in 15 mL MeOH and 1 mL conc. H₂SO₄ was added to it. The reaction mixture was heated to reflux for 12–16 hrs. Progress of the reaction was monitored through TLC, and after completion of the reaction, MeOH was evaporated and the crude mixture was then washed with water and extracted with EtOAc. The organic layer was dried over Na₂SO₄ and evaporated in a rotary evaporator to obtain the crude, which was then purified in a flash column using 230–400 mesh size silica gel and 10% EtOAc in Pet ether as eluent to obtain the compound **2** as brown gummy material (yield: 87%). ¹H NMR (400 MHz, *d*₆-DMSO) δ in ppm 9.16 (d, *J* = 1.2 Hz, 1H), 8.85 (d, *J* = 2.4 Hz, 1H), 8.78–8.77 (m, 1H), 3.88 (s, 3H); ¹³C NMR (100 MHz, *d*₆-DMSO) δ in ppm 164.63, 148.67,

146.06, 145.34, 143.48, 53.25; HRMS (ESI) m/z (M + H)⁺ calculated for C₆H₆N₂O₂ 138.0429; found: 138.0466. Melting Point: 172 °C.

Synthesis of pyrazine-2-carbohydrazide (3): Compound **2** (1.5 g, 10.86 mmol) was dissolved in 15 mL ethanol. 1 mL (43.44 mmol) of 85% hydrazine monohydrate was added and the reaction mixture was refluxed for 3 hrs. Progress of the reaction was monitored through TLC, and after completion of the reaction the crude mixture was then washed with water and extracted with EtOAc. The organic layer was dried over Na₂SO₄ and evaporated in a rotary evaporator to obtain the crude, which was then purified in a flash column using 230-400 mesh size silica gel and 80% EtOAc/Pet ether as eluent to obtain the compound **3** as an off-white solid (yield: 67%). ¹H NMR (400 MHz, *d*₆-DMSO) δ in ppm 10.08 (s, 1H), 9.08 (d, *J* = 1.6 Hz, 1H), 8.78 (d, *J* = 2.4 Hz, 1H), 8.66-8.63 (m, 1H), 4.60 (s, 2H); ¹³C NMR (100 MHz, *d*₆-DMSO) δ in ppm 162.02, 147.77, 145.41, 143.99, 143.74; HRMS (ESI) m/z (M + H)⁺ calculated for C₅H₆N₄O 138.0542; found: 138.0503. Melting Point: 198 °C.

Synthesis of 5-(pyrazin-2-yl)-1,3,4-thiadiazole-2-thiol (4): Compound **3** (500 mg, 3.62 mmol) was dissolved in ethanol (10 mL) followed by the addition of KOH (406 mg, 7.24 mmol) and carbon disulfide (0.3 mL, 5.43 mmol). The reaction mixture was stirred at room temperature for 2 hrs. After completion of the reaction, a precipitate was formed, which was filtered and washed with ethanol. This precipitate was directly treated with conc. H₂SO₄ (3 mL) at 0 °C and the reaction mixture was allowed to come at room temperature and stirred for 30 min. The reaction was quenched with crushed ice and precipitation occurred. Filtrations of the reaction mixture provided the pure product **4** as off-white solid (yield: 55%). ¹H NMR (400 MHz, *d*₆-DMSO) δ in ppm 9.24 (d, *J* = 1.2 Hz, 1H), 8.81 (d, *J* = 2.4 Hz, 1H), 8.76-8.74 (m, 2H). ¹³C NMR (100 MHz, *d*₆-DMSO) δ in ppm 189.53, 159.57, 147.04, 145.19, 143.30, 141.67; HRMS (ESI) m/z (M + H)⁺ calculated for C₆H₄N₄S₂ 195.9877; found: 195.9869. Melting Point: 176 °C.

Synthesis of 2-((2,6-dichlorobenzyl)thio)-5-(pyrazin-2-yl)-1,3,4-thiadiazole (5): Compound **4** (200 mg, 1.02 mmol) was dissolved in dry acetone (10 mL) followed by the addition of K₂CO₃ (169 mg, 1.22 mmol) and 2,6-dichlorobenzylbromide (354 mg, 1.22 mmol). The reaction mixture was stirred at room temperature for 3 hrs. After completion of the reaction, solid K₂CO₃ was filtered out and residue was washed with acetone. Then the filtrate was concentrated and a solid was formed which was purified by column

chromatography using 30% EtOAc/Pet ether as eluent and recrystallized from ethanol to afford compound **5** as a white solid (yield: 82%). ^1H NMR (400 MHz, CDCl_3) δ in ppm 9.54 (d, J = 0.8 Hz, 1H), 8.65 (d, J = 2.4 Hz, 1H), 8.59-8.58 (m, 1H), 7.34 (d, J = 7.6 Hz, 1H), 7.22-7.17 (m, 1H), 5.00 (s, 2H); ^{13}C NMR (100 MHz, CDCl_3) δ in ppm 168.00, 167.72, 145.71, 144.73, 144.16, 142.33, 136.27, 131.58, 129.82, 128.52, 34.44; HRMS (ESI) m/z ($M + \text{H}$) $^+$ calculated for $\text{C}_{13}\text{H}_8\text{Cl}_2\text{N}_4\text{S}_2$ 353.9567; found: 353.9551. Melting Point: 180 °C. HPLC Purity: 98.84%.

Synthesis of 5-(pyrazin-2-yl)-1,3,4-oxadiazole-2-thiol (6): Compound **3** (500 mg, 3.62 mmol) was dissolved in EtOH (10 mL) followed by the addition of KOH (406 mg, 7.24 mmol) and carbon disulfide (0.3 mL, 5.43 mmol). The reaction mixture was refluxed for 12-16 hrs. Progress of the reaction was monitored through TLC, and after completion of the reaction, EtOH was removed at reduced pressure. The crude mixture was then washed with water and extracted with EtOAc. Evaporation of the organic solvent afforded compound **6** as a pale yellow solid (yield: 55%). ^1H NMR (400 MHz, d_6 -DMSO) δ in ppm 9.20 (d, J = 1.6 Hz, 1H), 8.85 (d, J = 2.4 Hz, 1H), 8.84-8.82 (m, 1H); ^{13}C NMR (100 MHz, d_6 -DMSO) δ in ppm 178.60, 158.68, 147.42, 145.47, 143.62, 138.79. HRMS (ESI) m/z ($M + \text{H}$) $^+$ calculated for $\text{C}_6\text{H}_4\text{N}_4\text{OS}$ 181.0106; found: 181.0185. Melting Point: 186 °C.

Synthesis of 2-((2,6-dichlorobenzyl)thio)-5-(pyrazin-2-yl)-1,3,4-oxadiazole (7): Compound **6** (50 mg, 0.27 mmol) was dissolved in dry ACN (4 mL) and 2,6-dichlorobenzylbromide (94 mg, 0.32 mmol) was added into the reaction mixture. The reaction mixture was refluxed for 3 hrs. Progress of the reaction was monitored through TLC, and after completion of the reaction the crude mixture was then washed with water and extracted with EtOAc. Evaporation of the organic solvent afforded compound **7** as an off-white solid (yield: 85%). ^1H NMR (300 MHz, CDCl_3) δ in ppm 9.45 (d, J = 1.6 Hz, 1H), 8.75-8.73 (m, 2H), 7.36 (d, J = 10.4 Hz, 2H), 7.26-7.19 (m, 1H), 4.93 (s, 2H); ^{13}C NMR (75 MHz, CDCl_3) δ in ppm 165.91, 163.37, 146.48, 144.63, 143.96, 139.36, 136.23, 131.09, 130.12, 128.61, 33.18; HRMS (ESI) m/z ($M + \text{Na}$) $^+$ calculated for $\text{C}_{13}\text{H}_8\text{Cl}_2\text{N}_4\text{OS}$ 360.9694, found: 360.9684. Melting Point: >220 °C. HPLC Purity: 98.27%.

Synthesis of 2-(pyrazine-2-carbonyl)hydrazinecarbothioamide (8): HATU (3.67 g, 9.67 mmol) was added to a stirring solution of Pyrazine-2-carboxylic acid **1** (1 g, 8.06 mmol) in dry DMF (10 mL) and the reaction mixture was allowed to stir at room temperature for 30 min. Hydrazinecarbothioamide (0.6 mL, 9.67 mmol) was added

dropwise to the reaction mixture followed by the dropwise addition of DIPEA (2.8 mL, 16.12 mmol) and the contents of the reaction mixture were stirred for another 1.5 h at room temperature (25-30 °C). The reaction was monitored through TLC, and after completion of the reaction the crude mixture was then washed with water and extracted with EtOAc. Pure compound **8** was isolated as an off-white solid (yield: 70%) by column chromatography separation (Eluent: 30% EtOAc in pet ether). ¹H NMR (400 MHz, *d*₆-DMSO) δ in ppm 8.56 (s, 1H), 7.48 (s, 1H), 7.12 (s, 1H), 4.23 (s, 2H); ¹³C NMR (75 MHz, CDCl₃) δ in ppm 162.01, 147.76, 145.41, 143.98, 143.73; HRMS (ESI) *m/z* (M + H)⁺ calculated for C₆H₇N₅OS 198.0450; found: 198.0441. Melting Point: 156 °C.

Synthesis of 5-(pyrazin-2-yl)-4H-1,2,4-triazole-3-thiol (9): Compound **8** (500 mg, 2.53 mmol) was taken in 5mL 5% NaOH solution and the reaction mixture was stirred for 3 hrs. at reflux condition. The reaction was monitored through TLC. After completion of the reaction, the reaction mixture was then neutralized with 1 (N) HCl solution and extracted with EtOAc. The organic layer was dried over Na₂SO₄ and evaporated in a rotary evaporator to obtain the crude, which was then purified in a flash column using 230-400 mesh size silica gel with 70% EtOAc in Pet ether as eluent to obtain the compound **9** as off-white solid (yield: 67%). ¹H NMR (400 MHz, *d*₆-DMSO) δ in ppm 9.14 (d, *J* = 0.8Hz, 1H), 8.72-8.70 (m, 2H); ¹³C NMR (100 MHz, *d*₆-DMSO) δ in ppm 168.50, 146.26, 144.89, 142.85, 141.32; HRMS (ESI) *m/z* (M + H)⁺ calculated for C₆H₅N₅S 180.0344; found: 180.0335. Melting Point: 191 °C.

Synthesis of 2-(5-((2,6-dichlorobenzyl)thio)-4H-1,2,4-triazol-3-yl)pyrazine (10): Compound **9** (100 mg, 0.55 mmol) was dissolved in dry ACN (4 mL) and 2,6-dichlorobenzylbromide (191 mg, 0.66 mmol) was added into the reaction mixture. The reaction mixture was refluxed for 3 hrs. Progress of the reaction was monitored through TLC, and after completion of the reaction the crude mixture was then washed with water and extracted with EtOAc. The organic layer was dried over Na₂SO₄ and evaporated in a rotary evaporator to obtain the crude, which was then purified in a flash column using 230-400 mesh size silica gel with 30% EtOAc in Pet ether as eluent to obtain the compound **10** as off-white solid (yield: 70%). ¹H NMR (400 MHz, CDCl₃) δ in 9.41 (d, *J* = 1.6Hz, 1H), 8.68-8.65 (m, 1H), 8.64-8.62 (m, 1H), 7.29 (d, *J* = 8.0Hz, 2H), 7.13 (t, *J* = 8.8Hz, 1H), 4.75 (s, 2H); ¹³C NMR (100 MHz, CDCl₃) δ in ppm 144.93, 144.33, 142.96, 135.91,

132.87, 129.37, 128.39, 33.56. HRMS (ESI) m/z ($M + H$)⁺ calculated for $C_{13}H_9Cl_2N_5S$ 338.0034; found: 338.0028; Melting Point: 198 °C; HPLC Purity: 98.65%.

Synthesis of 2-((2,5-dichlorobenzyl)thio)-5-(pyrazin-2-yl)-1,3,4-oxadiazole (11):

Compound **6** (50 mg, 0.27 mmol) was dissolved in dry ACN (4 mL) and 2,5-dichlorobenzylbromide (66 mg, 0.27 mmol) was added into the reaction mixture. The reaction mixture was refluxed for 3 hrs. Progress of the reaction was monitored through TLC, and after completion of the reaction the crude mixture was then washed with water and extracted with EtOAc. The organic layer was dried over Na_2SO_4 and evaporated in a rotary evaporator to obtain the crude, which was then purified in a flash column using 230-400 mesh size silica gel with 20% EtOAc in Pet ether as eluent to obtain the compound **11** as off-white solid (yield: 72%). 1H NMR (300 MHz, $CDCl_3$) δ in ppm 9.42 (d, J = 1.5 Hz, 1H), 8.74-8.71 (m, 2H), 7.68 (d, J = 2.4 Hz, 1H), 7.34 (d, J = 5.7 Hz, 1H), 7.24 (dd, J = 8.4 Hz, 2.4 Hz, 1H), 4.62 (s, 2H); ^{13}C NMR (75 MHz, $CDCl_3$) δ in ppm 165.90, 163.23, 146.38, 144.51, 143.81, 139.16, 134.98, 132.76, 132.58, 131.25, 130.76, 129.69, 34.08. HRMS (ESI) m/z ($M + Na$)⁺ calculated for $C_{13}H_8Cl_2N_4OS$ 360.9694; found: 360.9681; Melting Point: 210 °C; HPLC Purity: 99.02%.

Synthesis of 2-((2,4-dichlorobenzyl)thio)-5-(pyrazin-2-yl)-1,3,4-oxadiazole (12):

Compound **6** (50 mg, 0.27 mmol) was dissolved in dry ACN (4 mL) and 2,4-dichlorobenzylbromide (66 mg, 0.27 mmol) was added into the reaction mixture. The reaction mixture was refluxed for 3 hrs. Progress of the reaction was monitored through TLC, and after completion of the reaction the crude mixture was then washed with water and extracted with EtOAc. The organic layer was dried over Na_2SO_4 and evaporated in a rotary evaporator to obtain the crude, which was then purified in a flash column using 230-400 mesh size silica gel with 20% EtOAc in Pet ether as eluent to obtain the compound **12** as off-white solid (yield: 78%). 1H NMR (300 MHz, $CDCl_3$) δ in ppm 9.41 (d, J = 1.5 Hz, 1H), 8.74-8.71 (m, 2H), 7.62 (d, J = 8.1 Hz, 1H), 7.43 (d, J = 2.1 Hz, 1H), 7.22 (dd, J = 8.4 Hz, 2.1 Hz, 1H), 4.62 (s, 2H); ^{13}C NMR (75 MHz, $CDCl_3$) δ in ppm 166.0, 163.2, 146.4, 144.5, 143.8, 139.1, 135.0, 134.9, 132.3, 131.9, 129.6, 127.3, 33.9; HRMS (ESI) m/z ($M + Na$)⁺ calculated for $C_{13}H_8Cl_2N_4OS$ 360.9694; found: 360.9681; Melting Point: 208 °C; HPLC Purity: 99.75%.

Synthesis of 2-((2,3-dichlorobenzyl)thio)-5-(pyrazin-2-yl)-1,3,4-oxadiazole (13):

Compound **6** (50 mg, 0.27 mmol) was dissolved in dry ACN (4 mL) and 2,3-

dichlorobenzylbromide (66 mg, 0.27 mmol) was added into the reaction mixture. The reaction mixture was refluxed for 3 hrs. Progress of the reaction was monitored through TLC, and after completion of the reaction the crude mixture was then washed with water and extracted with EtOAc. The organic layer was dried over Na₂SO₄ and evaporated in a rotary evaporator to obtain the crude, which was then purified in a flash column using 230-400 mesh size silica gel with 20% EtOAc in Pet ether as eluent to obtain the compound **13** as off-white solid (yield: 80%). ¹H NMR (300 MHz, CDCl₃) δ in ppm 9.41 (d, *J* = 1.5 Hz, 1H), 8.76-8.71 (m, 2H), 7.60 (dd, *J* = 7.5 Hz, 1.5 Hz, 1H), 7.43 (dd, *J* = 8.1 Hz, 1.8 Hz, 1H), 7.18 (t, *J* = 7.8 Hz, 1H), 4.70 (s, 2H); ¹³C NMR (75 MHz, CDCl₃) δ in ppm 166.2, 163.2, 146.4, 144.6, 143.8, 139.2, 135.6, 133.6, 132.7, 130.4, 129.7, 127.4, 35.2; HRMS (ESI) *m/z* (M + Na)⁺ calculated for C₁₃H₈Cl₂N₄OS 360.9694; found: 360.9681; Melting Point: 202 °C; HPLC Purity: 98.96%.

Synthesis of 2-((2,6-difluorobenzyl)thio)-5-(pyrazin-2-yl)-1,3,4-oxadiazole (14):

Compound **6** (50 mg, 0.27 mmol) was dissolved in dry ACN (4 mL) and 2,6-difluorobenzylbromide (56 mg, 0.27 mmol) was added into the reaction mixture. The reaction mixture was refluxed for 3 hrs. Progress of the reaction was monitored through TLC, and after completion of the reaction the crude mixture was then washed with water and extracted with EtOAc. The organic layer was dried over Na₂SO₄ and evaporated in a rotary evaporator to obtain the crude, which was then purified in a flash column using 230-400 mesh size silica gel with 20% EtOAc in Pet ether as eluent to obtain the compound **14** as off-white solid (yield: 80%). ¹H NMR (400 MHz, CDCl₃) δ in ppm 9.37 (d, *J* = 0.8 Hz, 1H), 8.70-8.67 (m, 2H), 7.28-7.21 (m, 1H), 6.91-6.84 (m, 2H), 4.60 (s, 2H); ¹³C NMR (100 MHz, CDCl₃) δ in ppm 165.72, 163.42, 162.70, 160.20, 160.13, 146.53, 144.67, 144.01, 139.40, 130.41, 111.80, 111.55, 24.39. HRMS (ESI) *m/z* (M + H)⁺ calculated for C₁₃H₈F₂N₄OS 307.0465; found: 307.0457; Melting Point: >220 °C; HPLC Purity: 98.92%.

Synthesis of 2-((2,6-dibromobenzyl)thio)-5-(pyrazin-2-yl)-1,3,4-oxadiazole (15):

Compound **6** (50 mg, 0.27 mmol) was dissolved in dry ACN (4 mL) and 2,6-dibromobenzylbromide (87 mg, 0.27 mmol) was added into the reaction mixture. The reaction mixture was refluxed for 3 hrs. Progress of the reaction was monitored through TLC, and after completion of the reaction the crude mixture was then washed with water and extracted with EtOAc. The organic layer was dried over Na₂SO₄ and evaporated in a rotary evaporator to obtain the crude, which was then purified in a flash column using

230-400 mesh size silica gel with 20% EtOAc in Pet ether as eluent to obtain the compound **15** as off-white solid (yield: 74%). ¹H NMR (400 MHz, CDCl₃) δ in ppm 9.42 (s, 1H), 8.72 (s, 1H), 7.55 (d, *J* = 8.0Hz, 2H), 7.04 (t, *J* = 8.0Hz, 1H), 4.80 (s, 2H); ¹³C NMR (100 MHz, CDCl₃) δ 165.90, 163.45, 146.55, 144.70, 144.07, 139.48, 134.00, 132.76, 130.98, 126.07, 39.21. HRMS (ESI) *m/z* (M + H)⁺ calculated for C₁₃H₈Br₂N₄OS 426.8864; found: 426.8857; Melting Point: >220 °C; HPLC Purity: 98.63%.

Synthesis of 2-((2-chloro-6-fluorobenzyl)thio)-5-(pyrazin-2-yl)-1,3,4-oxadiazole (16): Compound **6** (50 mg, 0.27 mmol) was dissolved in dry ACN (4 mL) and 2-chloro-6-fluorobenzylbromide (60 mg, 0.27 mmol) was added into the reaction mixture. The reaction mixture was refluxed for 3 hrs. Progress of the reaction was monitored through TLC, and after completion of the reaction the crude mixture was then washed with water and extracted with EtOAc. The organic layer was dried over Na₂SO₄ and evaporated in a rotary evaporator to obtain the crude, which was then purified in a flash column using 230-400 mesh size silica gel with 20% EtOAc in Pet ether as eluent to obtain the compound **16** as off-white solid (yield: 73%). ¹H NMR (400 MHz, *d*₆-DMSO) δ in ppm 9.28 (d, *J* = 1.2Hz, 1H), 8.83 (d, *J* = 2.4Hz, 1H), 8.82-8.81 (m, 1H), 7.42-7.38 (m, 1H), 7.37-7.34 (m, 1H), 7.26-7.21 (m, 1H), 4.65 (s, 2H); ¹³C NMR (151 MHz, *d*₆-DMSO) δ in ppm 164.32, 162.05, 160.40, 147.61, 145.59, 143.95, 139.12, 135.02, 131.62, 126.34, 122.32, 115.43, 28.76; HRMS (ESI) *m/z* (M + H)⁺ calculated for C₁₃H₈ClFN₄OS 323.0170; found: 323.0162; Melting Point: 196 °C; HPLC Purity: 98.80%.

Synthesis of 2-((2-bromo-6-chlorobenzyl)thio)-5-(pyrazin-2-yl)-1,3,4-oxadiazole (17): Compound **6** (50 mg, 0.27 mmol) was dissolved in dry ACN (4 mL) and 2-bromo-6-chlorobenzylbromide (76 mg, 0.27 mmol) was added into the reaction mixture. The reaction mixture was refluxed for 3 hrs. Progress of the reaction was monitored through TLC, and after completion of the reaction the crude mixture was then washed with water and extracted with EtOAc. The organic layer was dried over Na₂SO₄ and evaporated in a rotary evaporator to obtain the crude, which was then purified in a flash column using 230-400 mesh size silica gel with 20% EtOAc in Pet ether as eluent to obtain the compound **17** as off-white solid (yield: 85%). ¹H NMR (400 MHz, CDCl₃) δ in ppm 9.42 (d, *J* = 1.2Hz, 1H), 8.74-8.70 (m, 2H), 7.52 (d, *J* = 8.0Hz, 1H), 7.38 (d, *J* = 8.0Hz, 1H), 7.15-7.13 (m, 1H), 4.94 (s, 2H); ¹³C NMR (100 MHz, CDCl₃) δ in ppm 165.95, 163.46, 146.55, 144.69, 144.07, 139.48, 136.14, 132.65, 132.07, 130.59, 129.37, 126.32, 36.23; HRMS (ESI) *m/z*

(M + H)⁺ calculated for C₁₃H₈ClBrN₄OS 382.9369; found: 382.9387; Melting Point: 198 °C; HPLC Purity: 98.00%.

Synthesis of 2-((2,5-bis(trifluoromethyl)benzyl)thio)-5-(pyrazin-2-yl)-1,3,4-oxadiazole (18): Compound **6** (50 mg, 0.27 mmol) was dissolved in dry ACN (4 mL) and 2,5-bis(trifluoromethyl)benzylbromide (83 mg, 0.27 mmol) was added into the reaction mixture. The reaction mixture was refluxed for 3 hrs. Progress of the reaction was monitored through TLC, and after completion of the reaction the crude mixture was then washed with water and extracted with EtOAc. The organic layer was dried over Na₂SO₄ and evaporated in a rotary evaporator to obtain the crude, which was then purified in a flash column using 230-400 mesh size silica gel with 20% EtOAc in Pet ether as eluent to obtain the compound **18** as off-white solid (yield: 72%). ¹H NMR (400 MHz, CDCl₃) δ in ppm 9.42 (s, 1H), 8.72 (d, *J* = 6.8 Hz, 1H), 8.11 (s, 1H), 7.83 (d, *J* = 8.4 Hz, 1H), 7.69 (d, *J* = 8.4 Hz, 1H), 4.80 (s, 2H); ¹³C NMR (100 MHz, CDCl₃) δ in ppm 165.81, 163.59, 146.63, 144.67, 144.05, 139.30, 135.73, 129.09, 129.05, 127.45, 127.39, 125.59, 125.55, 122.15, 32.93; HRMS (ESI) *m/z* (M + H)⁺ calculated for C₁₃H₈Br₂N₄OS 426.8864; found: 426.8846; Melting Point: 188 °C; HPLC Purity: 98.33%.

Synthesis of 2-(benzylthio)-5-(pyrazin-2-yl)-1,3,4-oxadiazole (19): Compound **6** (50 mg, 0.27 mmol) was dissolved in dry ACN (4 mL) and benzylbromide (46 mg, 0.27 mmol) was added into the reaction mixture. The reaction mixture was refluxed for 3 hrs. Progress of the reaction was monitored through TLC, and after completion of the reaction the crude mixture was then washed with water and extracted with EtOAc. The organic layer was dried over Na₂SO₄ and evaporated in a rotary evaporator to obtain the crude, which was then purified in a flash column using 230-400 mesh size silica gel with 10% EtOAc in Pet ether as eluent to obtain the compound **19** as off-white solid (yield: 80%). ¹H NMR (400 MHz, *d*₆-DMSO) δ in ppm 9.42 (d, *J* = 1.6 Hz, 1H), 8.73-8.71 (m, 2H), 7.48-7.45 (m, 2H), 7.37-7.30 (m, 3H), 4.58 (s, 2H); ¹³C NMR (100 MHz, CDCl₃) δ in ppm 166.5, 163.2, 146.4, 144.6, 144.0, 139.5, 135.2, 129.3, 128.9, 128.3, 36.9; HRMS (ESI) *m/z* (M + Na)⁺ calculated for C₁₃H₁₀N₄OS 293.0473; found: 293.0473; Melting Point: 166 °C; HPLC Purity: 99.09%.

Synthesis of 2-((2-chlorobenzyl)thio)-5-(pyrazin-2-yl)-1,3,4-oxadiazole (20): Compound **6** (50 mg, 0.27 mmol) was dissolved in dry ACN (4 mL) and 2-chlorobenzylbromide (55 mg, 0.27 mmol) was added into the reaction mixture. The

reaction mixture was refluxed for 3 hrs. Progress of the reaction was monitored through TLC, and after completion of the reaction the crude mixture was then washed with water and extracted with EtOAc. The organic layer was dried over Na₂SO₄ and evaporated in a rotary evaporator to obtain the crude, which was then purified in a flash column using 230-400 mesh size silica gel with 10% EtOAc in Pet ether as eluent to obtain the compound **20** as an off-white solid (yield: 82%). ¹H NMR (600 MHz, CDCl₃) δ in ppm 9.41 (d, *J* = 1.2 Hz, 1H), 8.73-8.72 (m, 2H), 7.65 (dd, *J* = 7.8 Hz, 2.4 Hz, 1H), 7.41 (dd, *J* = 7.8 Hz, 1.2 Hz, 1H), 7.27-7.14 (m, 2H), 4.68 (s, 2H); ¹³C NMR (150 MHz, CDCl₃) δ in ppm 166.5, 163.2, 146.4, 144.6, 143.9, 139.4, 134.5, 133.3, 131.6, 129.9, 129.8, 127.1, 34.7; HRMS (ESI) *m/z* (M + Na)⁺ calculated for C₁₃H₉ClN₄OS 327.0083; found: 327.0082; Melting Point: 170 °C; HPLC Purity: 99.25%.

2-((2-chlorobenzyl)thio)-4H-1,2,4-triazol-3-yl)pyrazine (21): Compound **9** (50 mg, 0.28 mmol) was dissolved in dry ACN (4 mL) and 2,6-dichlorobenzylbromide (67 mg, 0.28 mmol) was added into the reaction mixture. The reaction mixture was refluxed for 3 hrs. Progress of the reaction was monitored through TLC, and after completion of the reaction the crude mixture was then washed with water and extracted with EtOAc. The organic layer was dried over Na₂SO₄ and evaporated in a rotary evaporator to obtain the crude, which was then purified in a flash column using 230-400 mesh size silica gel with 70% EtOAc in Pet ether as eluent to obtain the compound **21** as off-white solid (yield: 70%). ¹H NMR (400 MHz, CDCl₃) δ in ppm 9.28 (s, 1H), 8.54 (d, *J* = 10.4 Hz, 2H), 7.34 (d, *J* = 5.6 Hz, 1H), 7.27 (d, *J* = 7.6 Hz, 1H), 7.12-7.04 (m, 2H), 4.47 (s, 2H); ¹³C NMR (100 MHz, CDCl₃) δ in ppm 144.99, 144.30, 143.07, 134.85, 134.24, 130.99, 129.70, 129.11, 126.94, 100.01, 95.17, 34.90; HRMS (ESI) *m/z* (M + H)⁺ calculated for C₁₃H₁₀ClN₅S 304.0424; found 304.0414. Melting Point: 162 °C.

Synthesis of 2-((2-fluorobenzyl)thio)-5-(pyrazin-2-yl)-1,3,4-oxadiazole (22): Compound **6** (50 mg, 0.27 mmol) was dissolved in dry ACN (4 mL) and 2-fluorobenzylbromide (51 mg, 0.27 mmol) was added into the reaction mixture. The reaction mixture was refluxed for 3 hrs. Progress of the reaction was monitored through TLC, and after completion of the reaction the crude mixture was then washed with water and extracted with EtOAc. The organic layer was dried over Na₂SO₄ and evaporated in a rotary evaporator to obtain the crude, which was then purified in a flash column using 230-400 mesh size silica gel with 10% EtOAc in Pet ether as eluent to obtain the compound

22 as off-white solid (yield: 75%). ^1H NMR (600 MHz, d_6 -DMSO) δ in ppm 9.41 (d, J = 1.2 Hz, 1H), 8.73-8.71 (m, 2H), 7.56 (t, J = 7.8 Hz, 1H), 7.32-7.28 (m, 1H), 7.12-7.06 (m, 2H), 4.60 (s, 2H); ^{13}C NMR (150 MHz, CDCl_3) δ in ppm 166.28, 163.21, 161.85, 160.20, 146.43, 144.59, 143.92, 139.33, 131.46, 130.26, 124.36, 122.70, 115.64, 30.15; HRMS (ESI) m/z ($\text{M} + \text{Na}$) $^+$ calculated for $\text{C}_{13}\text{H}_9\text{FN}_4\text{OS}$ 311.0379; found: 311.0367; Melting Point: 178 °C; HPLC Purity: 99.44%.

Synthesis of 2-((2-bromobenzyl)thio)-5-(pyrazin-2-yl)-1,3,4-oxadiazole (23):

Compound **6** (50 mg, 0.27 mmol) was dissolved in dry ACN (4 mL) and 2-bromobenzylbromide (67 mg, 0.27 mmol) was added into the reaction mixture. The reaction mixture was refluxed for 3 hrs. Progress of the reaction was monitored through TLC, and after completion of the reaction the crude mixture was then washed with water and extracted with EtOAc. The organic layer was dried over Na_2SO_4 and evaporated in a rotary evaporator to obtain the crude, which was then purified in a flash column using 230-400 mesh size silica gel with 10% EtOAc in Pet ether as eluent to obtain the compound **23** as an off-white solid (yield: 86%). ^1H NMR (300 MHz, CDCl_3) δ in ppm 9.43 (d, J = 1.2 Hz, 1H), 8.75-8.73 (m, 2H), 7.69 (dd, J = 7.5 Hz, 1.5 Hz, 1H), 7.62 (dd, J = 8.1 Hz, 1.5 Hz, 1H), 7.33-7.28 (m, 1H), 7.23-7.17 (m, 1H), 4.71 (s, 2H); ^{13}C NMR (75 MHz, CDCl_3) δ in ppm 166.4, 163.2, 146.4, 144.6, 143.9, 139.3, 135.0, 133.1, 131.6, 129.9, 127.7, 124.8, 37.3; HRMS (ESI) m/z ($\text{M} + \text{Na}$) $^+$ calculated for $\text{C}_{13}\text{H}_9\text{BrN}_4\text{OS}$ 370.9578; found: 370.9584; Melting Point: 182 °C; HPLC Purity: 99.78%.

Synthesis of 2-((2-iodobenzyl)thio)-5-(pyrazin-2-yl)-1,3,4-oxadiazole (24):

Compound **6** (50 mg, 0.27 mmol) was dissolved in dry ACN (4 mL) and 2-iodobenzylbromide (80 mg, 0.27 mmol) was added into the reaction mixture. The reaction mixture was refluxed for 3 hrs. Progress of the reaction was monitored through TLC, and after completion of the reaction the crude mixture was then washed with water and extracted with EtOAc. The organic layer was dried over Na_2SO_4 and evaporated in a rotary evaporator to obtain the crude, which was then purified in a flash column using 230-400 mesh size silica gel with 10% EtOAc in Pet ether as eluent to obtain the compound **24** as an off-white solid (yield: 70%). ^1H NMR (400 MHz, CDCl_3) δ in ppm 9.39 (s, 1H), 8.71-8.68 (m, 2H), 7.85 (dd, J = 8 Hz, 0.8 Hz, 1H), 7.65 (dd, J = 7.6 Hz, 1.6 Hz, 1H), 7.31-7.27 (m, 1H), 6.99-6.95 (m, 1H), 4.66 (s, 2H); ^{13}C NMR (100 MHz, CDCl_3) δ in ppm 166.32, 163.29, 146.46, 144.65, 143.98, 139.95, 139.46, 138.23, 131.06, 130.02, 128.73,

100.73, 42.16; HRMS (ESI) m/z (M + H)⁺ calculated for C₁₃H₉N₄OS 396.9620; found: 396.9611; Melting Point: 168 °C; HPLC Purity: 98.27%.

Synthesis of 2-(((5-(pyrazin-2-yl)-1,3,4-oxadiazol-2-yl)thio)methyl)benzonitrile (25): Compound **6** (50 mg, 0.27 mmol) was dissolved in dry ACN (4 mL) and 2-cyanobenzylbromide (53 mg, 0.27 mmol) was added into the reaction mixture. The reaction mixture was refluxed for 3 hrs. Progress of the reaction was monitored through TLC, and after completion of the reaction the crude mixture was then washed with water and extracted with EtOAc. The organic layer was dried over Na₂SO₄ and evaporated in rotary evaporator to obtain the crude, which was then purified in a flash column using 230-400 mesh size silica gel with 10% EtOAc in Pet ether as eluent to obtain the compound **25** as off-white solid (yield: 76%). ¹H NMR (400 MHz, CDCl₃) δ in ppm 9.37 (d, J = 1.2 Hz, 1H), 8.71-8.69 (m, 2H), 7.76 (d, J = 8.0 Hz, 1H), 7.66 (dd, J = 8.0 Hz, 1.2 Hz, 1H), 7.55 (dd, J = 7.6 Hz, 1.6 Hz, 1H), 7.39 (dd, J = 7.6 Hz, 1.2 Hz, 1H), 4.71 (s, 2H); ¹³C NMR (100 MHz, CDCl₃) δ in ppm 165.5, 163.5, 146.6, 144.7, 144.0, 139.5, 139.3, 133.3, 133.2, 130.9, 128.8, 117.1, 112.9, 34.6; HRMS (ESI) m/z (M + Na)⁺ calculated for C₁₄H₉N₅OS 318.0426; found: 318.0420; Melting Point: 198 °C; HPLC Purity: 99.55%.

Synthesis of 2-((2-nitrobenzyl)thio)-5-(pyrazin-2-yl)-1,3,4-oxadiazole (26): Compound **6** (50 mg, 0.27 mmol) was dissolved in dry ACN (4 mL) and 2-nitrobenzylbromide (58 mg, 0.27 mmol) was added into the reaction mixture. The reaction mixture was refluxed for 3 hrs. Progress of the reaction was monitored through TLC, and after completion of the reaction the crude mixture was then washed with water and extracted with EtOAc. The organic layer was dried over Na₂SO₄ and evaporated in a rotary evaporator to obtain the crude, which was then purified in a flash column using 230-400 mesh size silica gel with 10% EtOAc in Pet ether as eluent to obtain the compound **26** as an off-white solid (yield: 78%). ¹H NMR (600 MHz, CDCl₃) δ in ppm 9.40 (d, J = 1.2 Hz, 1H), 8.73 (d, J = 2.4 Hz, 1H), 8.72-8.671 (m, 1H), 8.16 (dd, J = 8.4 Hz, 1.2 Hz, 1H), 7.89 (dd, J = 7.8 Hz, 1.8 Hz, 1H), 7.64-7.61 (m, 1H), 7.52-7.49 (m, 1H), 4.91 (s, 2H); ¹³C NMR (100 MHz, CDCl₃) δ in ppm 166.52, 163.29, 146.46, 144.64, 143.97, 139.44, 134.53, 133.39, 131.64, 129.93, 129.86, 127.19, 34.73; HRMS (ESI) m/z (M + Na)⁺ calculated for C₁₃H₉N₅O₃S 338.0324; found: 338.0325; Melting Point: 210 °C; HPLC Purity: 99.65%.

Synthesis of 2-(pyrazin-2-yl)-5-((2-(trifluoromethyl)benzyl)thio)-1,3,4-oxadiazole (27): Compound **6** (50 mg, 0.27 mmol) was dissolved in dry ACN (4 mL) and 2-

trifluoromethylbenzylbromide (64 mg, 0.27 mmol) was added into the reaction mixture. The reaction mixture was refluxed for 3 hrs. Progress of the reaction was monitored through TLC, and after completion of the reaction the crude mixture was then washed with water and extracted with EtOAc. The organic layer was dried over Na₂SO₄ and evaporated in a rotary evaporator to obtain the crude, which was then purified in a flash column using 230-400 mesh size silica gel with 10% EtOAc in Pet ether as eluent to obtain the compound **27** as an off-white solid (yield: 82%). ¹H NMR (400 MHz, CDCl₃) δ in ppm 9.42 (d, *J* = 0.4 Hz, 1H), 8.74-8.72 (m, 2H), 7.80 (d, *J* = 7.6 Hz, 1H), 7.69 (d, *J* = 8.0 Hz, 1H), 7.56-7.51 (m, 1H), 7.66-7.41 (m, 1H), 4.78 (s, 1H); ¹³C NMR (100 MHz, CDCl₃) δ in ppm 163.38, 146.53, 144.67, 144.01, 139.41, 134.10, 132.50, 132.17, 129.04, 128.59, 125.61, 122.88, 33.38; HRMS (ESI) *m/z* (M + H)⁺ calculated for C₁₄H₉F₃N₄OS 339.0527; found: 339.0532; Melting Point: 204 °C; HPLC Purity: 98.42%.

Synthesis of 2-((2-methylbenzyl)thio)-5-(pyrazin-2-yl)-1,3,4-oxadiazole (28):

Compound **6** (50 mg, 0.27 mmol) was dissolved in dry ACN (4 mL) and 2-methylbenzylbromide (50 mg, 0.27 mmol) was added into the reaction mixture. The reaction mixture was refluxed for 3 hrs. Progress of the reaction was monitored through TLC, and after completion of the reaction the crude mixture was then washed with water and extracted with EtOAc. The organic layer was dried over Na₂SO₄ and evaporated in a rotary evaporator to obtain the crude, which was then purified in a flash column using 230-400 mesh size silica gel with 10% EtOAc in Pet ether as eluent to obtain the compound **28** as an off-white solid (yield: 86%). ¹H NMR (300 MHz, CDCl₃) δ in ppm 9.42 (d, *J* = 1.2 Hz, 1H), 8.74-8.70 (m, 2H), 7.43 (d, *J* = 7.2 Hz, 1H), 7.24-7.17 (m, 3H), 4.61 (s, 2H), 2.45 (s, 3H); ¹³C NMR (150 MHz, CDCl₃) δ in ppm 166.58, 163.04, 146.41, 144.58, 143.95, 139.39, 137.22, 132.58, 130.83, 130.40, 128.74, 126.48, 35.20, 19.26; HRMS (ESI) *m/z* (M + Na)⁺ calculated for C₁₄H₁₂N₄OS 307.0630; found: 307.0630; Melting Point: 192 °C; HPLC Purity: 98.64%.

Synthesis of 2-((2,5-bis(trifluoromethyl)benzyl)thio)-5-(pyrazin-2-yl)-1,3,4-oxadiazole (29):

Compound **6** (50 mg, 0.27 mmol) was dissolved in dry ACN (4 mL) and 2,5-bis(trifluoromethyl)benzylbromide (83 mg, 0.27 mmol) was added into the reaction mixture. The reaction mixture was refluxed for 3 hrs. Progress of the reaction was monitored through TLC, and after completion of the reaction the crude mixture was then washed with water and extracted with EtOAc. The organic layer was dried over Na₂SO₄

and evaporated in a rotary evaporator to obtain the crude, which was then purified in a flash column using 230-400 mesh size silica gel with 20% EtOAc in Pet ether as eluent to obtain the compound **29** as an off-white solid (yield: 72%). ¹H NMR (400 MHz, CDCl₃) δ in ppm 9.42 (s, 1H), 8.72 (d, *J* = 6.8 Hz, 1H), 8.11 (s, 1H), 7.83 (d, *J* = 8.4 Hz, 1H), 7.69 (d, *J* = 8.4 Hz, 1H), 4.80 (s, 2H); ¹³C NMR (100 MHz, CDCl₃) δ in ppm 165.81, 163.59, 146.63, 144.67, 144.05, 139.30, 135.73, 129.09, 129.05, 127.45, 127.39, 125.59, 125.55, 122.15, 32.93; HRMS (ESI) *m/z* (M + H)⁺ calculated for C₁₅H₈F₆N₄OS 407.0401; found: 407.0398; Melting Point: 206 °C; HPLC Purity: 99.12%.

Synthesis of 2-((5-chloro-2-(trifluoromethyl)benzyl)thio)-5-(pyrazin-2-yl)-1,3,4-oxadiazole (30): Compound **6** (50 mg, 0.27 mmol) was dissolved in dry ACN (4 mL) and 2-(bromomethyl)-4-chloro-1-(trifluoromethyl)benzene (73 mg, 0.27 mmol) was added into the reaction mixture. The reaction mixture was refluxed for 3 hrs. Progress of the reaction was monitored through TLC, and after completion of the reaction the crude mixture was then washed with water and extracted with EtOAc. The organic layer was dried over Na₂SO₄ and evaporated in a rotary evaporator to obtain the crude, which was then purified in a flash column using 230-400 mesh size silica gel with 20% EtOAc in Pet ether as eluent to obtain the compound **30** as an off-white solid (yield: 75%). ¹H NMR (400 MHz, CDCl₃) δ in ppm 9.29 (d, *J* = 1.6 Hz, 1H), 8.84 (d, *J* = 2.4 Hz, 1H), 8.83-8.82 (m, 1H), 7.90 (d, *J* = 2.0 Hz, 1H), 7.77 (d, *J* = 8.4 Hz, 1H), 7.62-7.59 (m, 1H), 4.71 (s, 1H); ¹³C NMR (100 MHz, *d*₆-DMSO) δ in ppm 164.75, 163.97, 147.61, 145.60, 144.00, 139.22, 138.15, 137.32, 132.50, 129.36, 129.12, 33.22; HRMS (ESI) *m/z* (M + H)⁺ calculated for C₁₄H₈ClF₃N₄OS 373.0138; found: 373.0126; Melting Point: 196 °C; HPLC Purity: 96.28%.

Synthesis of 2-((2-chloro-5-(trifluoromethyl)benzyl)thio)-5-(pyrazin-2-yl)-1,3,4-oxadiazole (31): Compound **6** (50 mg, 0.27 mmol) was dissolved in dry ACN (4 mL) and 2-(bromomethyl)-1-chloro-4-(trifluoromethyl)benzene (73 mg, 0.27 mmol) was added into the reaction mixture. The reaction mixture was refluxed for 3 hrs. Progress of the reaction was monitored through TLC, and after completion of the reaction the crude mixture was then washed with water and extracted with EtOAc. The organic layer was dried over Na₂SO₄ and evaporated in a rotary evaporator to obtain the crude, which was then purified in a flash column using 230-400 mesh size silica gel with 20% EtOAc in Pet ether as eluent to obtain the compound **31** as an off-white solid (yield: 74%). ¹H NMR (400 MHz, *d*₆-DMSO) δ in ppm 9.28 (d, *J* = 1.6 Hz, 1H), 8.83 (d, *J* = 2.4 Hz, 1H), 8.81-8.80 (m,

1H), 8.03 (d, J = 2.4Hz, 1H), 7.73 (d, J = 8.4Hz, 1H), 7.69 (m, 1H), 4.72 (s, 1H); ^{13}C NMR (100 MHz, d_6 -DMSO) δ in ppm 164.82, 163.91, 147.59, 145.56, 143.97, 139.19, 138.37, 136.00, 131.33, 129.10, 128.61, 128.29, 127.24, 34.45; HRMS (ESI) m/z ($M + H$)⁺ calculated for $\text{C}_{14}\text{H}_8\text{ClF}_3\text{N}_4\text{OS}$ 373.0138; found: 373.0127; Melting Point: 196 °C; HPLC Purity: 97.53%.

Synthesis of 2-((2-bromo-5-(trifluoromethyl)benzyl)thio)-5-(pyrazin-2-yl)-1,3,4-oxadiazole (32): Compound **6** (50 mg, 0.27 mmol) was dissolved in dry ACN (4 mL) and 1-bromo-2-(bromomethyl)-4-(trifluoromethyl)benzene (85 mg, 0.27 mmol) was added into the reaction mixture. The reaction mixture was refluxed for 3 hrs. Progress of the reaction was monitored through TLC, and after completion of the reaction the crude mixture was then washed with water and extracted with EtOAc. The organic layer was dried over Na_2SO_4 and evaporated in a rotary evaporator to obtain the crude, which was then purified in a flash column using 230-400 mesh size silica gel with 20% EtOAc in Pet ether as eluent to obtain the compound **32** as an off-white solid (yield: 86%). ^1H NMR (400 MHz, d_6 -DMSO) δ in ppm 9.28 (d, J = 1.2Hz, 1H), 8.83 (d, J = 2.4Hz, 1H), 8.81-8.80 (m, 1H), 8.02 (d, J = 2.0Hz, 1H), 7.89 (d, J = 8.0Hz, 1H), 7.59 (dd, J = 8.4Hz, 2.0Hz, 1H), 4.71 (s, 1H); ^{13}C NMR (100 MHz, d_6 -DMSO) δ in ppm 164.78, 163.91, 147.58, 145.56, 143.98, 139.20, 137.63, 134.67, 129.30, 128.93, 127.23, 125.55, 122.84, 37.05; HRMS (ESI) m/z ($M + H$)⁺ calculated for $\text{C}_{14}\text{H}_8\text{BrF}_3\text{N}_4\text{OS}$ 416.9646; 416.9640; Melting Point: 212 °C; HPLC Purity: 98.77%.

Synthesis of 2-((2-bromo-6-(trifluoromethyl)benzyl)thio)-5-(pyrazin-2-yl)-1,3,4-oxadiazole (33): Compound **6** (50 mg, 0.27 mmol) was dissolved in dry ACN (4 mL) and 1-bromo-2-(bromomethyl)-3-(trifluoromethyl)benzene (85 mg, 0.27 mmol) was added into the reaction mixture. The reaction mixture was refluxed for 3 hrs. Progress of the reaction was monitored through TLC, and after completion of the reaction the crude mixture was then washed with water and extracted with EtOAc. The organic layer was dried over Na_2SO_4 and evaporated in a rotary evaporator to obtain the crude, which was then purified in a flash column using 230-400 mesh size silica gel with 20% EtOAc in Pet ether as eluent to obtain the compound **33** as an off-white solid (yield: 89%). ^1H NMR (400 MHz, d_6 -DMSO) δ in ppm 9.31 (d, J = 1.6Hz, 1H), 8.85 (d, J = 2.8Hz, 1H), 8.83-8.82 (m, 1H), 8.05 (d, J = 7.6Hz, 1H), 7.81 (d, J = 8.0Hz, 1H), 7.54-7.50 (m, 1H), 4.81 (s, 1H); ^{13}C NMR (100 MHz, d_6 -DMSO) δ in ppm 164.47, 164.04, 147.66, 145.62, 144.07, 139.20, 138.49, 132.96, 131.47, 130.30, 128.25, 126.88, 126.82, 35.06; HRMS (ESI) m/z ($M + H$)⁺

calculated for C₁₄H₈BrF₃N₄OS 416.9633; found 416.9629; Melting Point: 206 °C; HPLC Purity: 97.47%.

Synthesis of 2-((2-chloro-6-(trifluoromethyl)benzyl)thio)-5-(pyrazin-2-yl)-1,3,4-oxadiazole (34): Compound **6** (50 mg, 0.27 mmol) was dissolved in dry ACN (4 mL) and 2-(bromomethyl)-1-chloro-3-(trifluoromethyl)benzene (73 mg, 0.27 mmol) was added into the reaction mixture. The reaction mixture was refluxed for 3 hrs. Progress of the reaction was monitored through TLC, and after completion of the reaction the crude mixture was then washed with water and extracted with EtOAc. The organic layer was dried over Na₂SO₄ and evaporated in a rotary evaporator to obtain the crude, which was then purified in a flash column using 230-400 mesh size silica gel with 20% EtOAc in Pet ether as eluent to obtain the compound **34** as an off-white solid (yield: 90%). ¹H NMR (400 MHz, *d*₆-DMSO) δ in ppm 9.31 (d, *J* = 1.2 Hz, 1H), 8.85 (d, *J* = 2.4 Hz, 1H), 8.83-8.82 (m, 1H), 7.89 (d, *J* = 8.0 Hz, 1H), 7.79 (d, *J* = 7.6 Hz, 1H), 7.63-7.59 (m, 1H), 4.80 (s, 1H); ¹³C NMR (100 MHz, *d*₆-DMSO) δ in ppm 164.45, 164.07, 147.68, 145.63, 144.06, 139.18, 137.16, 135.06, 131.54, 131.35, 130.24, 129.94, 126.24, 32.21; HRMS (ESI) *m/z* (M + H)⁺ calculated for C₁₄H₈ClF₃N₄OS 373.0138; found: 373.0127; Melting Point: 208 °C; HPLC Purity: 97.63%.

Synthesis of 5-(pyrazin-2-yl)-1,3,4-oxadiazol-2-amine (35): Compound **3** (500 mg, 3.62 mmol) was dissolved in MeOH (10 mL) and cyanogen bromide (384 mg, 3.62 mmol) was added and the mixture was refluxed for 1 hr. The resulting mixture was cooled and neutralized with a saturated NaHCO₃ solution. A solid was precipitated out and it was filtered and washed, dried, and recrystallized from ethanol to provide compound **35** as a yellow solid (yield: 62%). ¹H NMR (300 MHz, *d*₆-DMSO) δ in ppm 9.17 (d, *J* = 1.5 Hz, 1H), 8.74-8.72 (m, 2H), 7.58 (s, 2H); ¹³C NMR (75 MHz, *d*₆-DMSO) δ in ppm 165.37, 156.03, 145.80, 145.11, 142.74, 140.22; HRMS (ESI) *m/z* (M + H)⁺ calculated for C₆H₅N₅O 164.0572; found 164.0578. Melting Point: 166 °C;

Synthesis of N-(2,6-dichlorobenzyl)-5-(pyrazin-2-yl)-1,3,4-oxadiazol-2-amine (36): Compound **35** (50 mg, 0.30 mmol) was dissolved in dry DMF (5 mL). NaH (7.2 mg, 0.30 mmol) was added to the reaction mixture keeping N₂-atmosphere at 0°C and stirred for 30 min at room temperature. 2,6-dichlorobenzylbromide (71 mg, 0.30 mmol) was then added at 0°C and the reaction mixture was stirred at room temperature for 3 hrs. Progress of the reaction was monitored through TLC and after completion of the reaction the crude

mixture was then washed with satd. NH_4Cl solution and extracted with EtOAc. The organic layer was dried over Na_2SO_4 and evaporated in a rotary evaporator to obtain the crude, which was then purified in a flash column using 230-400 mesh size silica gel with 20% EtOAc in Pet ether as eluent to obtain the compound **36** as off-white solid (yield: 76%). ^1H NMR (600 MHz, CDCl_3) δ in ppm 9.02 (d, $J = 1.2$ Hz, 1H), 8.61-8.60 (m, 2H), 7.38 (d, $J = 7.8$ Hz, 2H), 7.28-7.24 (m, 1H), 5.25 (s, 2H); ^{13}C NMR (150 MHz, CDCl_3) δ in ppm 149.64, 145.52, 144.27, 142.91, 139.33, 136.89, 130.38, 128.58, 45.75; HRMS (ESI) m/z ($M + H$) $^+$ calculated for $\text{C}_{13}\text{H}_9\text{Cl}_2\text{N}_5\text{O}$ 322.0262; found: 322.0262; Melting Point: 192 $^\circ\text{C}$.

Synthesis of *N*-(2-chlorobenzyl)-5-(pyrazin-2-yl)-1,3,4-oxadiazol-2-amine (37):

Compound **35** (50 mg, 0.30 mmol) was dissolved in dry DMF (5 mL). NaH (7.2 mg, 0.30 mmol) was added to the reaction mixture keeping N_2 -atmosphere at 0°C and stirred for 30 min at room temperature. 2-chlorobenzylbromide (61 mg, 0.30 mmol) was then added at 0°C and the reaction mixture was stirred at room temperature for 3 hrs. Progress of the reaction was monitored through TLC and after completion of the reaction the crude mixture was then washed with satd. NH_4Cl solution and extracted with EtOAc. The organic layer was dried over Na_2SO_4 and evaporated in a rotary evaporator to obtain the crude, which was then purified in a flash column using 230-400 mesh size silica gel with 20% EtOAc in Pet ether as eluent to obtain the compound **37** as off-white solid (yield: 80%). ^1H NMR (400 MHz, CDCl_3) δ in ppm 9.07 (s, 1H), 8.63 (s, 2H), 7.40-7.34 (m, 2H), 7.27-7.24 (m, 2H), 5.12 (s, 2H); ^{13}C NMR (100 MHz, CDCl_3) δ in ppm 155.83, 149.94, 145.83, 144.52, 142.88, 139.33, 133.45, 132.71, 129.88, 129.55, 129.53, 127.19, 48.23; HRMS (ESI) m/z ($M + H$) $^+$ calculated for $\text{C}_{13}\text{H}_{10}\text{ClN}_5\text{O}$ 288.0652; found: 288.0654; Melting Point: 208 $^\circ\text{C}$; HPLC Purity: 95.66%.

Synthesis of 5-(pyrazin-2-yl)-1,3,4-oxadiazol-2-ol (38):

Compound **3** (500 mg, 3.62 mmol) was dissolved in dry THF (10 mL) and CDI (587 mg, 3.62 mmol) was added to the reaction mixture and the mixture was stirred at room temperature for 4 hrs. Progress of the reaction was monitored through TLC, and after completion of the reaction THF was removed under reduced pressure. The crude mixture was washed with water and extracted with EtOAc. The organic layer was dried over Na_2SO_4 and evaporated in a rotary evaporator to obtain the crude, which was then purified in a flash column using 230-400 mesh size silica gel with 5% MeOH in CHCl_3 as eluent to obtain the compound **38** as an off-white solid (yield: 55%). ^1H NMR (400 MHz, d_6 -DMSO) δ in ppm 10.08 (s, 1H), 9.08 (d,

$J = 1.6\text{ Hz}$, 1H), 8.79 (d, $J = 2.4\text{ Hz}$), 8.65-8.64 (m, 1H); ^{13}C NMR (100 MHz, d_6 -DMSO) δ in ppm 162.02, 147.77, 145.41, 143.99, 143.74; HRMS (ESI) m/z (M)⁺ calculated for $\text{C}_6\text{H}_4\text{N}_4\text{O}_2$ 164.0334; found: 164.0331; Melting Point: 176 °C.

Synthesis of 3-(2,6-dichlorobenzyl)-5-(pyrazin-2-yl)-1,3,4-oxadiazol-2(3H)-one (39):

Compound **38** (50 mg, 0.30 mmol) was dissolved in a 1:1 mixture of THF (3.0 mL) and H_2O (3.0 mL). Then NaOH (15 mg, 0.36 mmol) was added into the reaction mixture and allowed to stir at room temperature. After 30 min of stirring 2,6-dichlorobenzylbromide reagent (72 mg, 0.30 mmol) was added and stirred at room temperature for 3 hrs. Progress of the reaction was monitored through TLC, and after completion of the reaction, THF was removed under reduced pressure. The crude mixture was washed with water and extracted with EtOAc. The organic layer was dried over Na_2SO_4 and evaporated in a rotary evaporator to obtain the crude, which was then purified in a flash column using 230-400 mesh size silica gel with 40% EtOAc in Pet ether as eluent to obtain the compound **39** as off-white solid (yield: 70%). ^1H NMR (600 MHz, CDCl_3) δ in ppm 9.08 (s, 1H), 8.68 (s, 2H), 7.39 (d, $J = 8.4\text{ Hz}$, 2H), 7.28 (d, $J = 7.8\text{ Hz}$, 1H), 5.34 (s, 2H); ^{13}C NMR (150 MHz, CDCl_3) δ in ppm 152.3, 150.7, 146.3, 144.6, 143.0, 139.2, 136.9, 130.7, 129.4, 128.7, 45.2; HRMS (ESI) m/z ($M + \text{Na}$)⁺ calculated for $\text{C}_{13}\text{H}_8\text{Cl}_2\text{N}_4\text{O}_2$ 344.9922; found: 344.9924; Melting Point: 206 °C; HPLC Purity: 98.99%.

Synthesis of 3-(2-chlorobenzyl)-5-(pyrazin-2-yl)-1,3,4-oxadiazol-2(3H)-one (40):

Compound **38** (50 mg, 0.30 mmol) was dissolved in a 1:1 mixture of THF (3.0 mL) and H_2O (3.0 mL). Then NaOH (15 mg, 0.36 mmol) was added into the reaction mixture and allowed to stir at room temperature. After 30 min of stirring 2-chlorobenzylbromide reagent (61 mg, 0.30 mmol) was added and stirred at room temperature for 3 hrs. Progress of the reaction was monitored through TLC, and after completion of the reaction, THF was removed under reduced pressure. The crude mixture was washed with water and extracted with EtOAc. The organic layer was dried over Na_2SO_4 and evaporated in a rotary evaporator to obtain the crude, which was then purified in a flash column using 230-400 mesh size silica gel with 40% EtOAc in Pet ether as eluent to obtain the compound **40** as off-white solid (yield: 75%). ^1H NMR (600 MHz, CDCl_3) δ in ppm 9.12 (d, $J = 1.2\text{ Hz}$, 1H), 8.71-8.70 (m, 2H), 7.43 (dd, $J = 6.6\text{ Hz}$, 1.8 Hz, 1H), 7.40 (dd, $J = 6.6\text{ Hz}$, 2.4 Hz, 1H), 7.32-7.29 (m, 2H), 5.17 (s, 2H); ^{13}C NMR (150 MHz, CDCl_3) δ in ppm 152.7, 150.8, 146.5, 144.8, 142.9, 139.1, 133.7, 131.8, 130.3, 130.0, 129.9, 127.3, 47.8; HRMS (ESI) m/z

(M + Na)⁺ calculated for C₁₃H₉ClN₄O₂ 311.0312; found: 311.0299; Melting Point: 214 °C; HPLC Purity: 96.58%.

Synthesis of methyl 1H-pyrrole-2-carboxylate (41): Pyrrole-2-carboxylic acid (2 g, 18.01 mmol) was taken in 15 mL MeOH and 1 mL conc. H₂SO₄ was added to it. The reaction mixture was heated to reflux for 12-16 hrs. Progress of the reaction was monitored through TLC, and after completion of the reaction MeOH was evaporated and the crude mixture was then washed with water and extracted with EtOAc. The organic layer was dried over Na₂SO₄ and evaporated in a rotary evaporator to obtain the crude, which was then purified in a flash column using 230-400 mesh size silica gel and 30% EtOAc/Pet ether as solvent system to obtain the compound **41** as brown gummy material (yield: 85%). ¹H NMR (400 MHz, *d*₆-DMSO) δ in ppm 11.83 (s, 1H), 6.97-6.95 (m, 1H), 6.75-6.73 (m, 1H), 6.13-6.11 (m, 1H), 3.70 (s, 1H); ¹³C NMR (100 MHz, *d*₆-DMSO) δ in ppm 161.35, 124.59, 122.26, 115.58, 110.07, 51.50; HRMS (ESI) *m/z* (M + H)⁺ calculated for C₆H₇NO₂ 125.0477; found: 125.0489. ¹H NMR (400 MHz, *d*₆-DMSO) δ in ppm 11.83 (s, 1H), 6.97-6.95 (m, 1H), 6.75-6.73 (m, 1H), 6.13-6.11 (m, 1H), 3.70 (s, 1H); ¹³C NMR (100 MHz, *d*₆-DMSO) δ in ppm 161.35, 124.59, 122.26, 115.58, 110.07, 51.50. HRMS (ESI) *m/z* (M + H)⁺ calculated for C₁₃H₉ClN₄O₂ 126.0555; found: 126.0562; Melting Point: 152 °C.

Synthesis of 1H-pyrrole-2-carbohydrazide (42): Compound **41** (1.5 g, 12 mmol) was dissolved in 15 mL ethanol. 1 mL of 85% hydrazine monohydrate was added and the reaction mixture was refluxed for 3 hrs. Progress of the reaction was monitored through TLC, and after completion of the reaction the crude mixture was then washed with water and extracted with EtOAc. The organic layer was dried over Na₂SO₄ and evaporated in a rotary evaporator to obtain the crude, which was then purified in a flash column using 230-400 mesh size silica gel and EtOAc/Pet ether as solvent system to obtain the compound **42** as an off-white solid (yield: 75%). ¹H NMR (400 MHz, *d*₆-DMSO) δ in ppm 11.37 (s, 1H), 9.17 (s, 1H), 6.79-6.76 (m, 1H), 6.70-6.66 (m, 1H), 6.01-5.98 (m, 1H), 4.23 (s, 2H); ¹³C NMR (100 MHz, *d*₆-DMSO) δ in ppm 182.37, 159.56, 145.04, 142.55, 140.73. HRMS (ESI) *m/z* (M + H)⁺ calculated for C₁₃H₉ClN₄O₂ 126.0667; found: 126.0668. Melting Point: 164 °C.

Synthesis of 5-(1H-pyrrol-2-yl)-1,3,4-oxadiazole-2-thiol (43): Compound **42** (500 mg, 3.0 mmol) was dissolved in EtOH (10 mL) followed by the addition of KOH (336 mg, 6.0 mmol) and carbon disulfide (0.3 mL, 4.5 mmol). The reaction mixture was refluxed for

12-16 hrs. Progress of the reaction was monitored through TLC, and after completion of the reaction, EtOH was removed at reduced pressure. The crude mixture was then washed with water and extracted with EtOAc. Evaporation of the organic solvent afforded compound **43** as pale yellow solid (yield: 60%). ^1H NMR (400 MHz, d_6 -DMSO) δ in ppm 14.44 (s, 1H), 12.12 (s, 1H), 7.06-7.03 (m, 1H), 6.77-6.74 (m, 1H), 6.23-6.20 (m, 1H); ^{13}C NMR (100 MHz, d_6 -DMSO) δ in ppm 176.72, 156.62, 124.68, 114.76, 113.06, 110.64; HRMS (ESI) m/z ($M + H$) $^+$ calculated for $\text{C}_6\text{H}_5\text{N}_3\text{OS}$ 168.0232; found: 168.0225. Melting Point: 182 °C.

Synthesis of 2-((2,6-dichlorobenzyl)thio)-5-(1H-pyrrol-2-yl)-1,3,4-oxadiazole (44):

Compound **43** (50 mg, 0.30 mmol) was dissolved in dry ACN (4 mL) and 2,6-dichlorobenzylbromide (71 mg, 0.30 mmol) was added into the reaction mixture. The reaction mixture was refluxed for 3 hrs. Progress of the reaction was monitored through TLC, and after completion of the reaction the crude mixture was then washed with water and extracted with EtOAc. The organic layer was dried over Na_2SO_4 and evaporated in a rotary evaporator to obtain the crude, which was then purified in a flash column using 230-400 mesh size silica gel with 20% EtOAc in Pet ether as eluent to obtain the compound **44** as an off-white solid (yield: 85%). ^1H NMR (400 MHz, CDCl_3) δ in ppm 9.94 (s, 1H), 7.32 (d, $J = 8.0\text{Hz}$, 2H), 7.19 (dd, $J = 8.8\text{Hz}$, 7.6Hz, 1H), 7.05-7.04 (m, 1H), 6.83-6.81 (m, 1H), 6.33-6.31 (m, 1H), 4.75 (s, 2H); ^{13}C NMR (100 MHz, CDCl_3) δ in ppm 161.50, 161.28, 136.07, 131.75, 129.96, 128.60, 123.63, 115.25, 113.29, 110.43, 33.41; HRMS (ESI) m/z ($M + H$) $^+$ calculated for $\text{C}_{13}\text{H}_9\text{Cl}_2\text{N}_3\text{OS}$ 325.9922; found: 325.9915; Melting Point: 196 °C; HPLC Purity: 97.88%.

Synthesis of 2-((2-chlorobenzyl)thio)-5-(1H-pyrrol-2-yl)-1,3,4-oxadiazole (45):

Compound **43** (50 mg, 0.30 mmol) was dissolved in dry ACN (4 mL) and 2-chlorobenzylbromide (61 mg, 0.30 mmol) was added into the reaction mixture. The reaction mixture was refluxed for 3 hrs. Progress of the reaction was monitored through TLC, and after completion of the reaction the crude mixture was then washed with water and extracted with EtOAc. The organic layer was dried over Na_2SO_4 and evaporated in a rotary evaporator to obtain the crude, which was then purified in a flash column using 230-400 mesh size silica gel with 20% EtOAc in Pet ether as eluent to obtain the compound **45** as off-white solid (yield: 80%). ^1H NMR (400 MHz, CDCl_3) δ in ppm 9.86 (s, 1H), 7.55 (dd, $J = 7.2\text{Hz}$, 2.4Hz, 1H), 7.38 (dd, $J = 8.0\text{Hz}$, 2.0Hz, 1H), 7.25-7.18 (m, 2H), 7.04-

7.02 (m, 1H), 6.82-6.80 (m, 1H), 6.32-6.30 (m, 1H), 4.57 (s, 2H); ^{13}C NMR (100 MHz, CDCl_3) δ in ppm 161.94, 161.12, 134.37, 133.58, 131.26, 129.88, 129.71, 127.16, 123.48, 115.21, 113.09, 110.38, 34.81; HRMS (ESI) m/z ($\text{M} + \text{H}$) $^+$ calculated for $\text{C}_{13}\text{H}_{10}\text{ClN}_3\text{OS}$ 292.0311; found: 292.0308; Melting Point: 192 °C; HPLC Purity: 97.43%.

3.10 REFERENCES

- (127) Ashcroft, F. M. From Molecule to Malady. *Nature* **2006**, *440* (7083), 440–447.
<https://doi.org/10.1038/nature04707>.
- (128) Waszkielewicz, A. M.; Gunia, A.; Szkaradek, N.; Słoczyńska, K.; Krupińska, S.; Marona, H. Ion Channels as Drug Targets in Central Nervous System Disorders. *Curr. Med. Chem.* **2013**, *20* (10), 1241–1285.
<https://doi.org/10.2174/0929867311320100005>.
- (129) Su, J.; Song, Y.; Zhu, Z.; Huang, X.; Fan, J.; Qiao, J.; Mao, F. Cell-Cell Communication: New Insights and Clinical Implications. *Signal Transduct. Target. Ther.* **2024**, *9* (1), 196. <https://doi.org/10.1038/s41392-024-01888-z>.
- (130) Oiki, S. Channel Function Reconstitution and Re-Animation: A Single-Channel Strategy in the Postcrystal Age. *J. Physiol.* **2015**, *593* (12), 2553–2573.
<https://doi.org/10.1113/JP270025>.
- (131) Kurachi, Y.; North, A. Ion Channels: Their Structure, Function and Control – an Overview. *The Journal of Physiology*. January 2004, pp 245–247.
<https://doi.org/10.1113/jphysiol.2003.057703>.
- (132) Conte Camerino, D.; Tricarico, D.; Desaphy, J.-F. Ion Channel Pharmacology. *Neurotherapeutics* **2007**, *4* (2), 184–198.
<https://doi.org/https://doi.org/10.1016/j.nurt.2007.01.013>.
- (133) Imbrici, P.; Liantonio, A.; Camerino, G. M.; De Bellis, M.; Camerino, C.; Mele, A.; Giustino, A.; Pierno, S.; De Luca, A.; Tricarico, D.; Desaphy, J.-F.; Conte, D. Therapeutic Approaches to Genetic Ion Channelopathies and Perspectives in Drug Discovery. *Front. Pharmacol.* **2016**, *7*.
<https://doi.org/10.3389/fphar.2016.00121>.
- (134) Cusabio. *Ion Channels: A Switch that Controls the Entry and Exit of Ions*.
<https://www.cusabio.com/Transmembrane/Ion-Channels-A-Switch-that-Controls-the-Entry-and-Exit-of-Ions.html>.
- (135) Catterall, W. A. Structure and Function of Voltage-Gated Ion Channels. *Trends Neurosci.* **1993**, *16* (12), 500–506.

- [https://doi.org/https://doi.org/10.1016/0166-2236\(93\)90193-P](https://doi.org/https://doi.org/10.1016/0166-2236(93)90193-P).
- (136) Catterall, W. A. Voltage-Gated Sodium Channels at 60: Structure, Function and Pathophysiology. *J. Physiol.* **2012**, 590 (11), 2577–2589.
<https://doi.org/https://doi.org/10.1113/jphysiol.2011.224204>.
- (137) Wang, J.; Ou, S.-W.; Wang, Y.-J. Distribution and Function of Voltage-Gated Sodium Channels in the Nervous System. *Channels (Austin)*. **2017**, 11 (6), 534–554.
<https://doi.org/10.1080/19336950.2017.1380758>.
- (138) de Lera Ruiz, M.; Kraus, R. L. Voltage-Gated Sodium Channels: Structure, Function, Pharmacology, and Clinical Indications. *J. Med. Chem.* **2015**, 58 (18), 7093–7118.
<https://doi.org/10.1021/jm501981g>.
- (139) Bryant, S. H. 30 - Ion Channels as Targets for Genetic Disease; SPERELAKIS, N. B. T.-C. P. S. B., Ed.; Academic Press, 1995; pp 413–427.
<https://doi.org/https://doi.org/10.1016/B978-0-12-656970-4.50036-1>.
- (140) Catterall, W. A. Voltage-Gated Calcium Channels. *Cold Spring Harb. Perspect. Biol.* **2011**, 3 (8), a003947. <https://doi.org/10.1101/cshperspect.a003947>.
- (141) Bourinet, E.; Zamponi, G. W. Block of Voltage-Gated Calcium Channels by Peptide Toxins. *Neuropharmacology* **2017**, 127, 109–115.
<https://doi.org/https://doi.org/10.1016/j.neuropharm.2016.10.016>.
- (142) Hogg, R. C.; Raggenbass, M.; Bertrand, D. Nicotinic Acetylcholine Receptors: From Structure to Brain Function. *Rev. Physiol. Biochem. Pharmacol.* **2003**, 147, 1–46.
<https://doi.org/10.1007/s10254-003-0005-1>.
- (143) Huang, Z. J.; Scheiffele, P. GABA and Neuroligin Signaling: Linking Synaptic Activity and Adhesion in Inhibitory Synapse Development. *Curr. Opin. Neurobiol.* **2008**, 18 (1), 77–83. <https://doi.org/10.1016/j.conb.2008.05.008>.
- (144) Tominaga, M.; Tominaga, T. Structure and Function of TRPV1. *Pflugers Arch.* **2005**, 451 (1), 143–150. <https://doi.org/10.1007/s00424-005-1457-8>.
- (145) Izquierdo, C.; Martín-Martínez, M.; Gómez-Monterrey, I.; González-Muñiz, R. TRPM8 Channels: Advances in Structural Studies and Pharmacological Modulation. *Int. J. Mol. Sci.* **2021**, 22 (16).

- <https://doi.org/10.3390/ijms22168502>.
- (146) Yang, C.; Zhang, X.; Guo, Y.; Meng, F.; Sachs, F.; Guo, J. Mechanical Dynamics in Live Cells and Fluorescence-Based Force/Tension Sensors. *Biochim. Biophys. Acta - Mol. Cell Res.* **2015**, *1853* (8), 1889–1904. <https://doi.org/https://doi.org/10.1016/j.bbamcr.2015.05.001>.
- (147) Wu, J.; Lewis, A. H.; Grandl, J. Touch, Tension, and Transduction - The Function and Regulation of Piezo Ion Channels. *Trends Biochem. Sci.* **2017**, *42* (1), 57–71. <https://doi.org/10.1016/j.tibs.2016.09.004>.
- (148) Noël, J.; Zimmermann, K.; Busserolles, J.; Deval, E.; Alloui, A.; Diochot, S.; Guy, N.; Borsotto, M.; Reeh, P.; Eschalier, A.; Lazdunski, M. The Mechano-Activated K⁺ Channels TRAAK and TREK-1 Control Both Warm and Cold Perception. *EMBO J.* **2009**, *28* (9), 1308–1318. <https://doi.org/10.1038/emboj.2009.57>.
- (149) Bakhshandeh, B.; Sorboni, S. G.; Ranjbar, N.; Deyhimfar, R.; Abtahi, M. S.; Izady, M.; Kazemi, N.; Noori, A.; Pennisi, C. P. Mechanotransduction in Tissue Engineering: Insights into the Interaction of Stem Cells with Biomechanical Cues. *Exp. Cell Res.* **2023**, *431* (2), 113766. <https://doi.org/https://doi.org/10.1016/j.yexcr.2023.113766>.
- (150) Coste, B.; Mathur, J.; Schmidt, M.; Earley, T. J.; Ranade, S.; Petrus, M. J.; Dubin, A. E.; Patapoutian, A. Piezo1 and Piezo2 Are Essential Components of Distinct Mechanically Activated Cation Channels. *Science (80-.).* **2010**, *330* (6000), 55–60. <https://doi.org/10.1126/science.1193270>.
- (151) Mulhall, E. M.; Gharpure, A.; Lee, R. M.; Dubin, A. E.; Aaron, J. S.; Marshall, K. L.; Spencer, K. R.; Reiche, M. A.; Henderson, S. C.; Chew, T.-L.; Patapoutian, A. Direct Observation of the Conformational States of PIEZO1. *Nature* **2023**, *620* (7976), 1117–1125. <https://doi.org/10.1038/s41586-023-06427-4>.
- (152) Liu, H.; Hu, J.; Zheng, Q.; Feng, X.; Zhan, F.; Wang, X.; Xu, G.; Hua, F. Piezo1 Channels as Force Sensors in Mechanical Force-Related Chronic Inflammation. *Front. Immunol.* **2022**, *13*. <https://doi.org/10.3389/fimmu.2022.816149>.
- (153) Ranade, S. S.; Woo, S.-H.; Dubin, A. E.; Moshourab, R. A.; Wetzel, C.; Petrus, M.; Mathur, J.; Bégay, V.; Coste, B.; Mainquist, J.; Wilson, A. J.; Francisco, A. G.; Reddy,

- K.; Qiu, Z.; Wood, J. N.; Lewin, G. R.; Patapoutian, A. Piezo2 Is the Major Transducer of Mechanical Forces for Touch Sensation in Mice. *Nature* **2014**, *516* (7529), 121–125. <https://doi.org/10.1038/nature13980>.
- (154) Lee, S.; Park, S.; Kim, H. Y.; Chae, J. H.; Ko, J. M. Extended Phenotypes of PIEZO1-Related Lymphatic Dysplasia Caused by Two Novel Compound Heterozygous Variants. *Eur. J. Med. Genet.* **2021**, *64* (10), 104295. <https://doi.org/https://doi.org/10.1016/j.ejmg.2021.104295>.
- (155) Alper, S. L. Chapter Four - Genetic Diseases of PIEZO1 and PIEZO2 Dysfunction. In *Piezo Channels*; Gottlieb, P. A. B. T.-C. T. in M., Ed.; Academic Press, 2017; Vol. 79, pp 97–134. <https://doi.org/https://doi.org/10.1016/bs.ctm.2017.01.001>.
- (156) Saotome, K.; Murthy, S. E.; Kefauver, J. M.; Whitwam, T.; Patapoutian, A.; Ward, A. B. Structure of the Mechanically Activated Ion Channel Piezo1. *Nature* **2018**, *554* (7693), 481–486. <https://doi.org/10.1038/nature25453>.
- (157) Nosyreva, E. D.; Thompson, D.; Syeda, R. Identification and Functional Characterization of the Piezo1 Channel Pore Domain. *J. Biol. Chem.* **2021**, *296*, 100225. <https://doi.org/https://doi.org/10.1074/jbc.RA120.015905>.
- (158) Botello-Smith, W. M.; Jiang, W.; Zhang, H.; Ozkan, A. D.; Lin, Y.-C.; Pham, C. N.; Lacroix, J. J.; Luo, Y. A Mechanism for the Activation of the Mechanosensitive Piezo1 Channel by the Small Molecule Yoda1. *Nat. Commun.* **2019**, *10* (1), 4503. <https://doi.org/10.1038/s41467-019-12501-1>.
- (159) Thien, N. D.; Hai-Nam, N.; Anh, D. T.; Baecker, D. Piezo1 and Its Inhibitors: Overview and Perspectives. *Eur. J. Med. Chem.* **2024**, *273*, 116502. <https://doi.org/https://doi.org/10.1016/j.ejmech.2024.116502>.
- (160) Du, Y.; Xu, B.; Li, Q.; Peng, C.; Yang, K. The Role of Mechanically Sensitive Ion Channel Piezo1 in Bone Remodeling. *Front. Bioeng. Biotechnol.* **2024**, *12*, 1342149. <https://doi.org/10.3389/fbioe.2024.1342149>.
- (161) Wang, L.; You, X.; Lotinun, S.; Zhang, L.; Wu, N.; Zou, W. Mechanical Sensing Protein PIEZO1 Regulates Bone Homeostasis via Osteoblast-Osteoclast Crosstalk. *Nat. Commun.* **2020**, *11* (1), 282. <https://doi.org/10.1038/s41467-019-14146-6>.
- (162) Yuan, W.; Zhang, X.; Fan, X. The Role of the Piezo1 Mechanosensitive Channel in

- Heart Failure. *Curr. Issues Mol. Biol.* **2023**, 45 (7), 5830–5848.
<https://doi.org/10.3390/cimb45070369>.
- (163) Coste, B.; Delmas, P. PIEZO Ion Channels in Cardiovascular Functions and Diseases. *Circ. Res.* **2024**, 134 (5), 572–591.
<https://doi.org/10.1161/CIRCRESAHA.123.322798>.
- (164) Xing, H.; Liu, H.; Chang, Z.; Zhang, J. Research Progress on the Immunological Functions of Piezo1 a Receptor Molecule That Responds to Mechanical Force. *Int. Immunopharmacol.* **2024**, 139, 112684.
<https://doi.org/https://doi.org/10.1016/j.intimp.2024.112684>.
- (165) Tang, Y.; Zhao, C.; Zhuang, Y.; Zhong, A.; Wang, M.; Zhang, W.; Zhu, L. Mechanosensitive Piezo1 Protein as a Novel Regulator in Macrophages and Macrophage-Mediated Inflammatory Diseases. *Front. Immunol.* **2023**, 14.
<https://doi.org/10.3389/fimmu.2023.1149336>.
- (166) Zhang, Y.; Zou, W.; Dou, W.; Luo, H.; Ouyang, X. Pleiotropic Physiological Functions of Piezo1 in Human Body and Its Effect on Malignant Behavior of Tumors. *Front. Physiol.* **2024**, 15. <https://doi.org/10.3389/fphys.2024.1377329>.
- (167) Yu, J.-L.; Liao, H.-Y. Piezo-Type Mechanosensitive Ion Channel Component 1 (Piezo1) in Human Cancer. *Biomed. Pharmacother.* **2021**, 140, 111692.
<https://doi.org/https://doi.org/10.1016/j.biopha.2021.111692>.
- (168) Braidotti, N.; Chen, S. N.; Long, C. S.; Cojoc, D.; Sbaizero, O. Piezo1 Channel as a Potential Target for Hindering Cardiac Fibrotic Remodeling. *International Journal of Molecular Sciences*. 2022. <https://doi.org/10.3390/ijms23158065>.
- (169) Fotiou, E.; Martin-Almedina, S.; Simpson, M. A.; Lin, S.; Gordon, K.; Brice, G.; Atton, G.; Jeffery, I.; Rees, D. C.; Mignot, C.; Vogt, J.; Homfray, T.; Snyder, M. P.; Rockson, S. G.; Jeffery, S.; Mortimer, P. S.; Mansour, S.; Ostergaard, P. Novel Mutations in PIEZO1 Cause an Autosomal Recessive Generalized Lymphatic Dysplasia with Non-Immune Hydrops Fetalis. *Nat. Commun.* **2015**, 6, 8085.
<https://doi.org/10.1038/ncomms9085>.
- (170) Tapia, R.; Velasco, I. Ruthenium Red as a Tool to Study Calcium Channels, Neuronal Death and the Function of Neural Pathways. *Neurochem. Int.* **1997**, 30

- (2), 137–147. [https://doi.org/10.1016/s0197-0186\(96\)00056-3](https://doi.org/10.1016/s0197-0186(96)00056-3).
- (171) Ostrow, K. L.; Mammoser, A.; Suchyna, T.; Sachs, F.; Oswald, R.; Kubo, S.; Chino, N.; Gottlieb, P. A. CDNA Sequence and in Vitro Folding of GsMTx4, a Specific Peptide Inhibitor of Mechanosensitive Channels. *Toxicon* **2003**, *42* (3), 263–274. [https://doi.org/10.1016/s0041-0101\(03\)00141-7](https://doi.org/10.1016/s0041-0101(03)00141-7).
- (172) Evans, E. L.; Cuthbertson, K.; Endesh, N.; Rode, B.; Blythe, N. M.; Hyman, A. J.; Hall, S. J.; Gaunt, H. J.; Ludlow, M. J.; Foster, R.; Beech, D. J. Yoda1 Analogue (Dooku1) Which Antagonizes Yoda1-Evoked Activation of Piezo1 and Aortic Relaxation. *Br. J. Pharmacol.* **2018**, *175* (10), 1744–1759. <https://doi.org/10.1111/bph.14188>.
- (173) Liu, S.; Pan, X.; Cheng, W.; Deng, B.; He, Y.; Zhang, L.; Ning, Y.; Li, J. Tubeimoside I Antagonizes Yoda1-Evoked Piezo1 Channel Activation. *Front. Pharmacol.* **2020**, *11*, 768. <https://doi.org/10.3389/fphar.2020.00768>.
- (174) Pan, X.; Wan, R.; Wang, Y.; Liu, S.; He, Y.; Deng, B.; Luo, S.; Chen, Y.; Wen, L.; Hong, T.; Xu, H.; Bian, Y.; Xia, M.; Li, J. Inhibition of Chemically and Mechanically Activated Piezo1 Channels as a Mechanism for Ameliorating Atherosclerosis with Salvianolic Acid B. *Br. J. Pharmacol.* **2022**, *179* (14), 3778–3814. <https://doi.org/10.1111/bph.15826>.
- (175) Hong, T.; Pan, X.; Xu, H.; Zheng, Z.; Wen, L.; Li, J.; Xia, M. Jatrorrhizine Inhibits Piezo1 Activation and Reduces Vascular Inflammation in Endothelial Cells. *Biomed. Pharmacother.* **2023**, *163*, 114755. <https://doi.org/https://doi.org/10.1016/j.biopha.2023.114755>.
- (176) Wang, Y.; Chu, T.; Pan, X.; Bian, Y.; Li, J. Escin Ameliorates Inflammation via Inhibiting Mechanical Stretch and Chemically Induced Piezo1 Activation in Vascular Endothelial Cells. *Eur. J. Pharmacol.* **2023**, *956*, 175951. <https://doi.org/10.1016/j.ejphar.2023.175951>.
- (177) Syeda, R.; Florendo, M. N.; Cox, C. D.; Kefauver, J. M.; Santos, J. S.; Martinac, B.; Patapoutian, A. Piezo1 Channels Are Inherently Mechanosensitive. *Cell Rep.* **2016**, *17* (7), 1739–1746. <https://doi.org/https://doi.org/10.1016/j.celrep.2016.10.033>.
- (178) Jiang, W.; Wijerathne, T. D.; Zhang, H.; Lin, Y.-C.; Jo, S.; Im, W.; Lacroix, J. J.; Luo, Y.

- L. Structural and Thermodynamic Framework for PIEZO1 Modulation by Small Molecules. *Proc. Natl. Acad. Sci.* **2023**, *120* (50), e2310933120.
<https://doi.org/10.1073/pnas.2310933120>.
- (179) Wang, Y.; Chi, S.; Guo, H.; Li, G.; Wang, L.; Zhao, Q.; Rao, Y.; Zu, L.; He, W.; Xiao, B. A Lever-like Transduction Pathway for Long-Distance Chemical- and Mechano-Gating of the Mechanosensitive Piezo1 Channel. *Nat. Commun.* **2018**, *9* (1), 1300.
<https://doi.org/10.1038/s41467-018-03570-9>.
- (180) Parsonage, G.; Cuthbertson, K.; Endesh, N.; Murciano, N.; Hyman, A. J.; Revill, C. H.; Povstyan, O. V; Chuntharpursat-Bon, E.; Debant, M.; Ludlow, M. J.; Futers, T. S.; Lichtenstein, L.; Kinsella, J. A.; Bartoli, F.; Rotordam, M. G.; Becker, N.; Brüggemann, A.; Foster, R.; Beech, D. J. Improved PIEZO1 Agonism through 4-Benzoic Acid Modification of Yoda1. *Br. J. Pharmacol.* **2023**, *180* (16), 2039–2063.
<https://doi.org/https://doi.org/10.1111/bph.15996>.
- (181) Capitani, N.; Baldari, C. T. The Immunological Synapse: An Emerging Target for Immune Evasion by Bacterial Pathogens. *Front. Immunol.* **2022**, *13*.
<https://doi.org/10.3389/fimmu.2022.943344>.
- (182) Shah, K.; Al-Haidari, A.; Sun, J.; Kazi, J. U. T Cell Receptor (TCR) Signaling in Health and Disease. *Signal Transduct. Target. Ther.* **2021**, *6* (1), 412.
<https://doi.org/10.1038/s41392-021-00823-w>.
- (183) Mariuzza, R. A.; Agnihotri, P.; Orban, J. The Structural Basis of T-Cell Receptor (TCR) Activation: An Enduring Enigma. *J. Biol. Chem.* **2020**, *295* (4), 914–925.
<https://doi.org/10.1074/jbc.REV119.009411>.
- (184) Gasteiger, G.; D’Osualdo, A.; Schubert, D. A.; Weber, A.; Bruscia, E. M.; Hartl, D. Cellular Innate Immunity: An Old Game with New Players. *J. Innate Immun.* **2017**, *9* (2), 111–125. <https://doi.org/10.1159/000453397>.
- (185) Liu, C. S. C.; Raychaudhuri, D.; Paul, B.; Chakrabarty, Y.; Ghosh, A. R.; Rahaman, O.; Talukdar, A.; Ganguly, D. Cutting Edge: Piezo1 Mechanosensors Optimize Human T Cell Activation. *J. Immunol.* **2018**, *200* (4), 1255–1260.
<https://doi.org/10.4049/jimmunol.1701118>.
- (186) Liu, C. S. C.; Mandal, T.; Biswas, P.; Hoque, M. A.; Bandopadhyay, P.; Sinha, B. P.;

- Sarif, J.; D'Rozario, R.; Sinha, D. K.; Sinha, B.; Ganguly, D. Piezo1 Mechanosensing Regulates Integrin-Dependent Chemotactic Migration in Human T Cells. *Elife* **2024**, 12. <https://doi.org/10.7554/eLife.91903>.
- (187) Garlie, N. K.; LeFever, A. V.; Siebenlist, R. E.; Levine, B. L.; June, C. H.; Lum, L. G. T Cells Coactivated with Immobilized Anti-CD3 and Anti-CD28 as Potential Immunotherapy for Cancer. *J. Immunother.* **1999**, 22 (4), 336–345. <https://doi.org/10.1097/00002371-199907000-00007>.
- (188) Bagur, R.; Hajnóczky, G. Intracellular Ca(2+) Sensing: Its Role in Calcium Homeostasis and Signaling. *Mol. Cell* **2017**, 66 (6), 780–788. <https://doi.org/10.1016/j.molcel.2017.05.028>.
- (189) Diller, D. J.; Merz, K. M. J. High Throughput Docking for Library Design and Library Prioritization. *Proteins* **2001**, 43 (2), 113–124. [https://doi.org/10.1002/1097-0134\(20010501\)43:2<113::aid-prot1023>3.0.co;2-t](https://doi.org/10.1002/1097-0134(20010501)43:2<113::aid-prot1023>3.0.co;2-t).
- (190) Diller, D. J.; Li, R. Kinases, Homology Models, and High Throughput Docking. *J. Med. Chem.* **2003**, 46 (22), 4638–4647. <https://doi.org/10.1021/jm020503a>.
- (191) Rao, S. N.; Head, M. S.; Kulkarni, A.; LaLonde, J. M. Validation Studies of the Site-Directed Docking Program LibDock. *J. Chem. Inf. Model.* **2007**, 47 (6), 2159–2171. <https://doi.org/10.1021/ci6004299>.
- (192) Lacroix, J. J.; Botello-Smith, W. M.; Luo, Y. Probing the Gating Mechanism of the Mechanosensitive Channel Piezo1 with the Small Molecule Yoda1. *Nat. Commun.* **2018**, 9 (1), 2029. <https://doi.org/10.1038/s41467-018-04405-3>.
- (193) Ferreira de Freitas, R.; Schapira, M. A Systematic Analysis of Atomic Protein–Ligand Interactions in the PDB. *Medchemcomm* **2017**, 8 (10), 1970–1981. <https://doi.org/10.1039/C7MD00381A>.
- (194) Burns, R. J.; Mati, I. K.; Muchowska, K. B.; Adam, C.; Cockroft, S. L. Quantifying Through-Space Substituent Effects. *Angew. Chemie Int. Ed.* **2020**, 59 (38), 16717–16724. <https://doi.org/https://doi.org/10.1002/anie.202006943>.
- (195) Yu, S.; Ward, J. S.; Truong, K.-N.; Rissanen, K. Carbonyl Hypoiodites as Extremely Strong Halogen Bond Donors. *Angew. Chemie Int. Ed.* **2021**, 60 (38), 20739–20743. <https://doi.org/https://doi.org/10.1002/anie.202108126>.

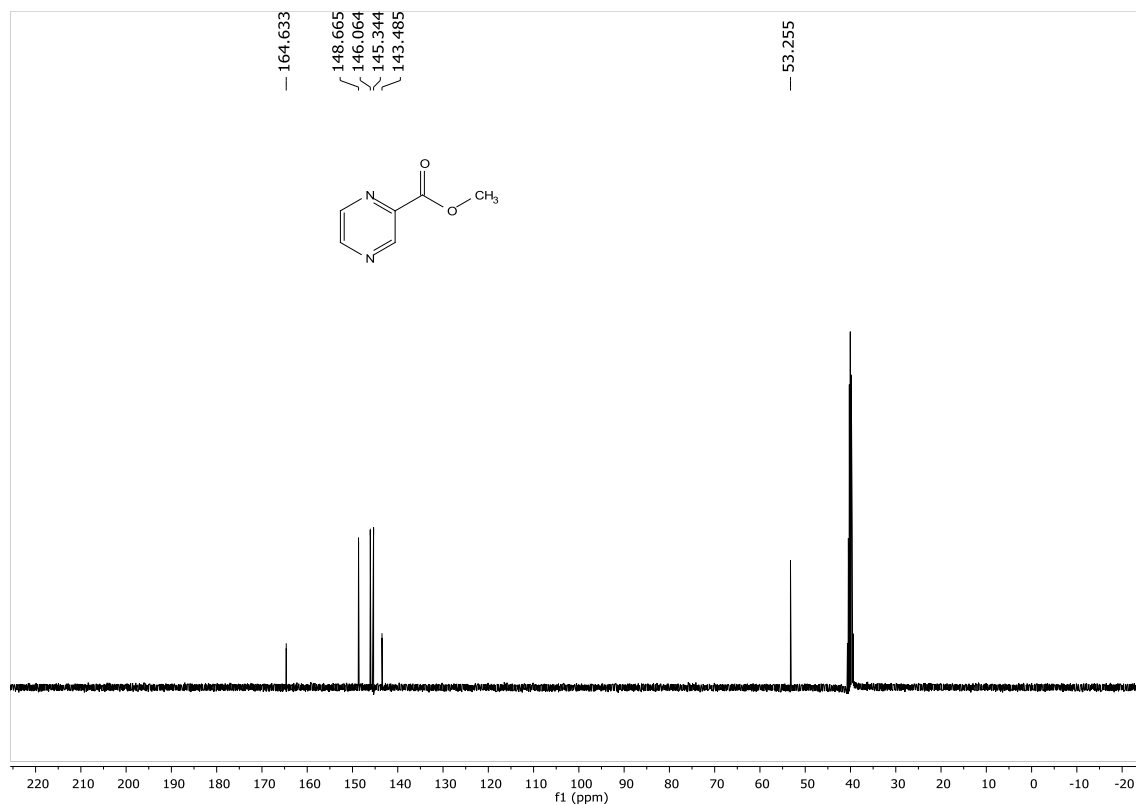
- (196) Lu, T.; Chen, F. Multiwfn: A Multifunctional Wavefunction Analyzer. *J. Comput. Chem.* **2012**, *33* (5), 580–592.
<https://doi.org/https://doi.org/10.1002/jcc.22885>.
- (197) Lu, T.; Manzetti, S. Wavefunction and Reactivity Study of Benzo[a]Pyrene Diol Epoxide and Its Enantiomeric Forms. *Struct. Chem.* **2014**, *25* (5), 1521–1533.
<https://doi.org/10.1007/s11224-014-0430-6>.
- (198) El-Masry, R. M.; Kadry, H. H.; Taher, A. T.; Abou-Seri, S. M. Comparative Study of the Synthetic Approaches and Biological Activities of the Bioisosteres of 1,3,4-Oxadiazoles and 1,3,4-Thiadiazoles over the Past Decade. *Molecules*. 2022.
<https://doi.org/10.3390/molecules27092709>.
- (199) Liu, F.; Yang, C.; Li, S.; Wu, X.; Xue, K.; Zhou, Y.; Liang, X.; Cheng, X.; Shi, Q.; Su, W. Design and Biological Features of Platinum (II) Complexes with 3-Hydroxy-3-(Trifluoromethyl)Cyclobutane-1,1-Dicarboxylate as a Leaving Ligand. *Eur. J. Med. Chem.* **2022**, *242*, 114673.
<https://doi.org/https://doi.org/10.1016/j.ejmech.2022.114673>.

3.11 ANNEXURE

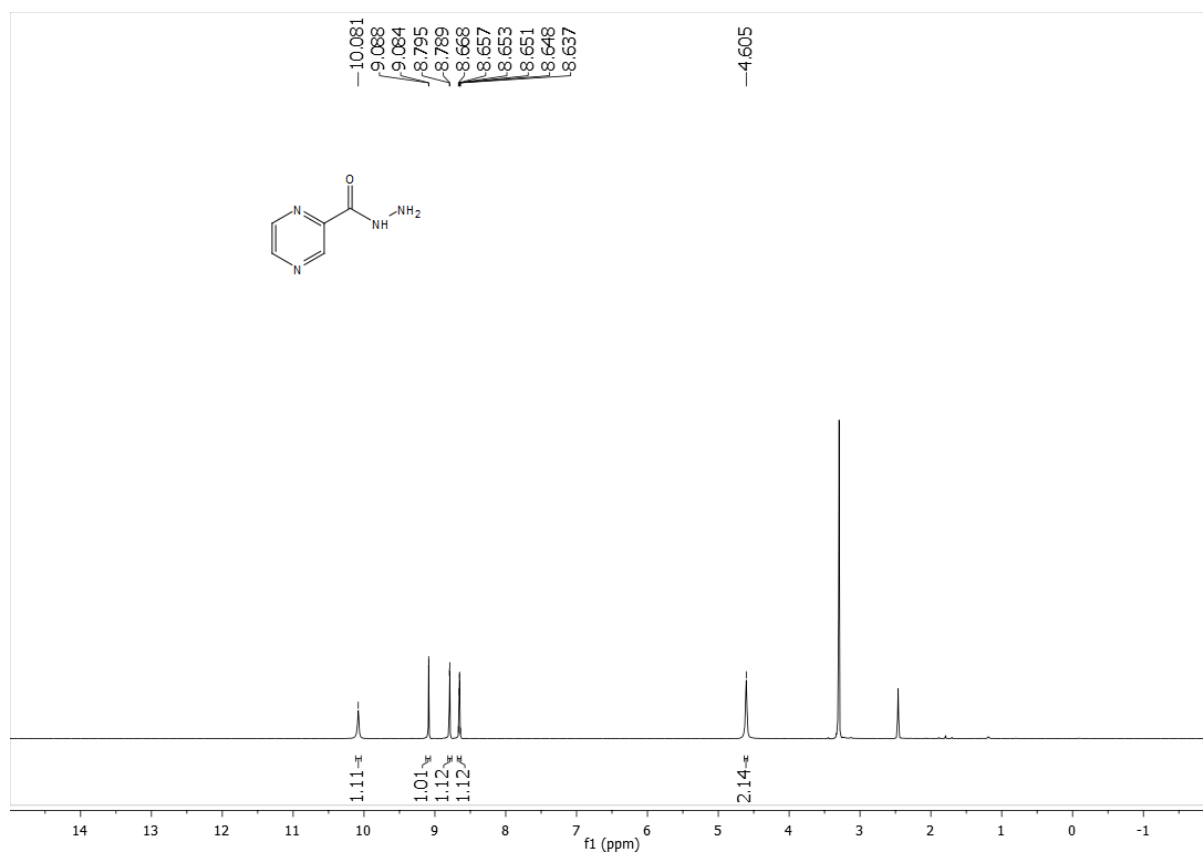
^1H NMR of compound **2** (400 MHz, d_6 -DMSO):



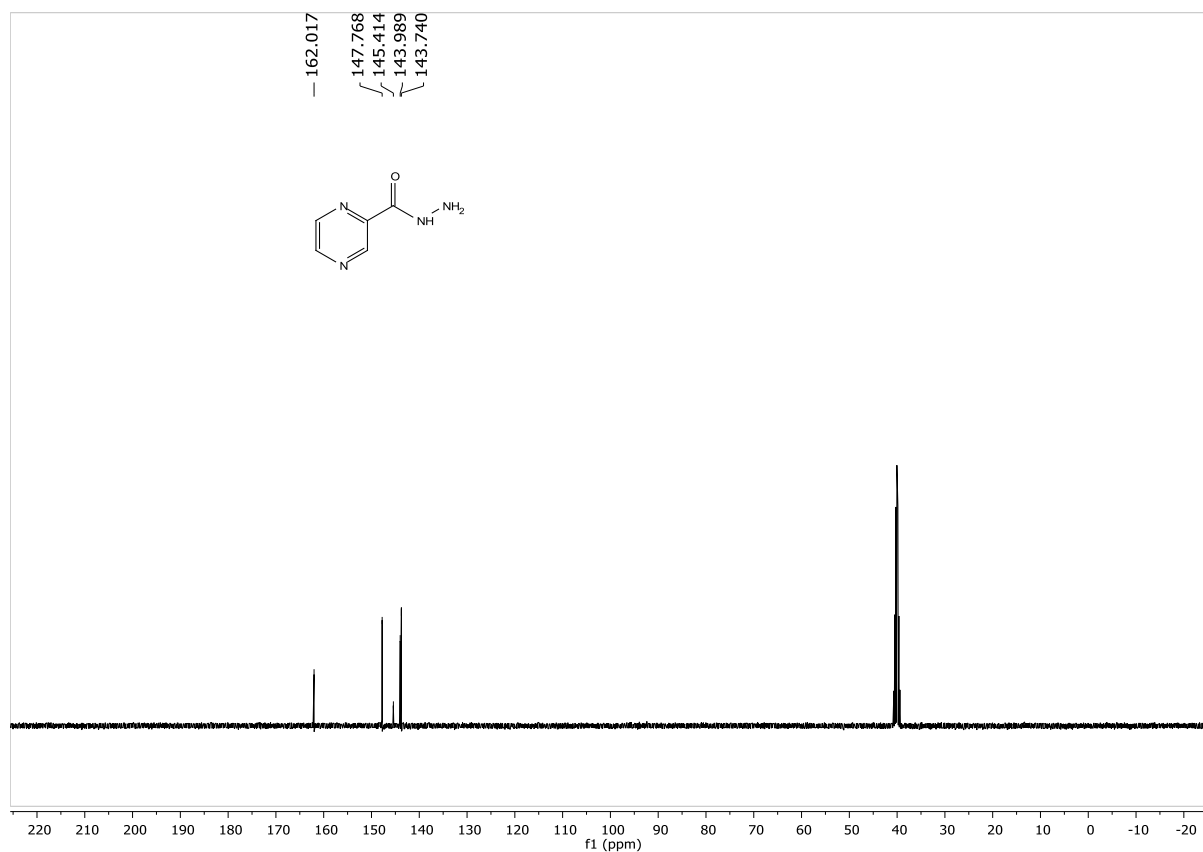
^{13}C NMR of compound **2** (100 MHz, d_6 -DMSO):



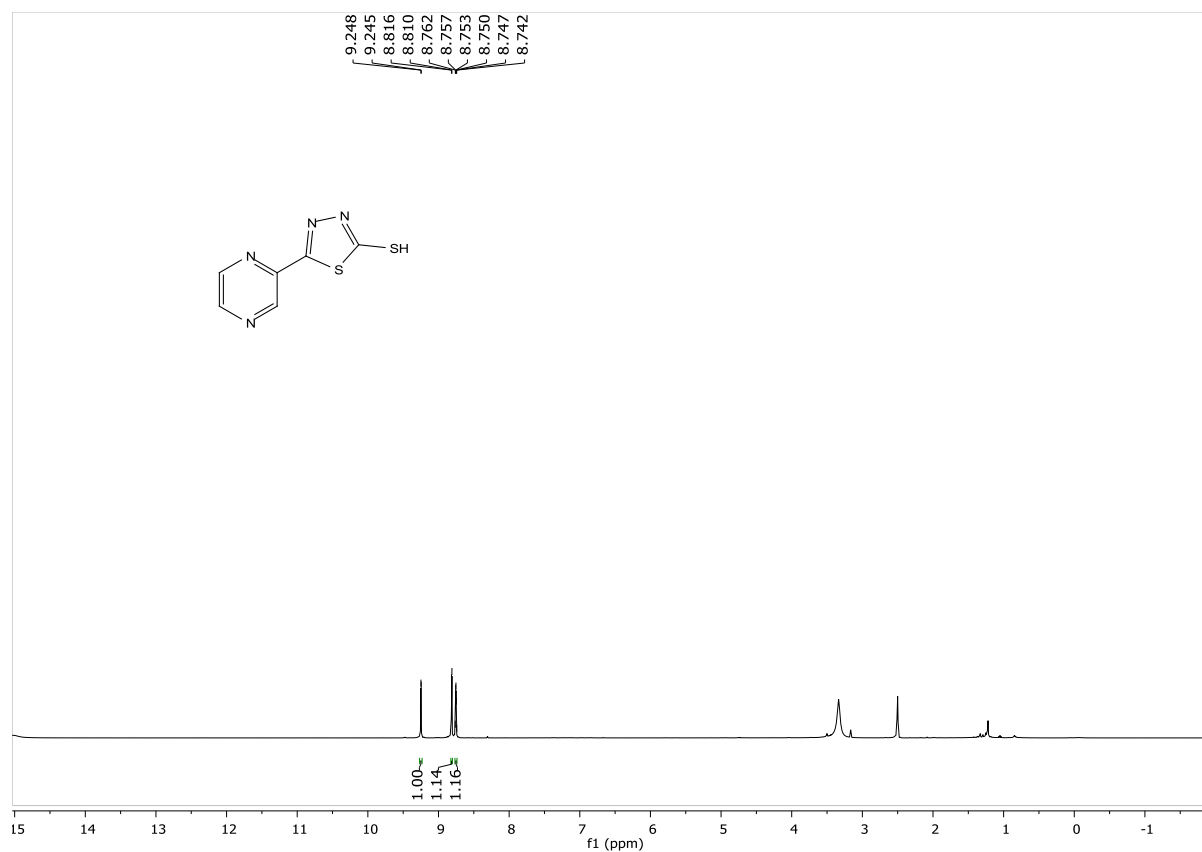
^1H NMR of compound **3** (400 MHz, d_6 -DMSO):



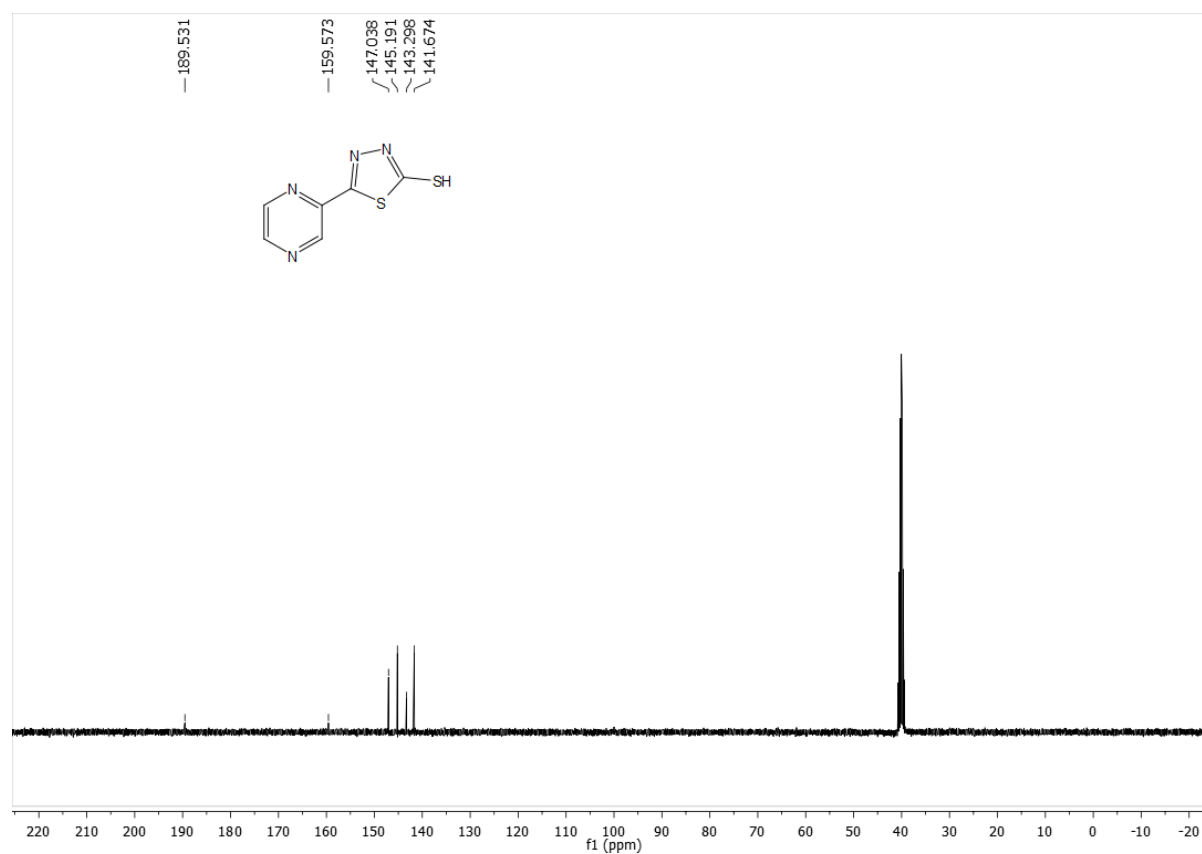
^{13}C NMR of compound **3** (100 MHz, d_6 -DMSO):



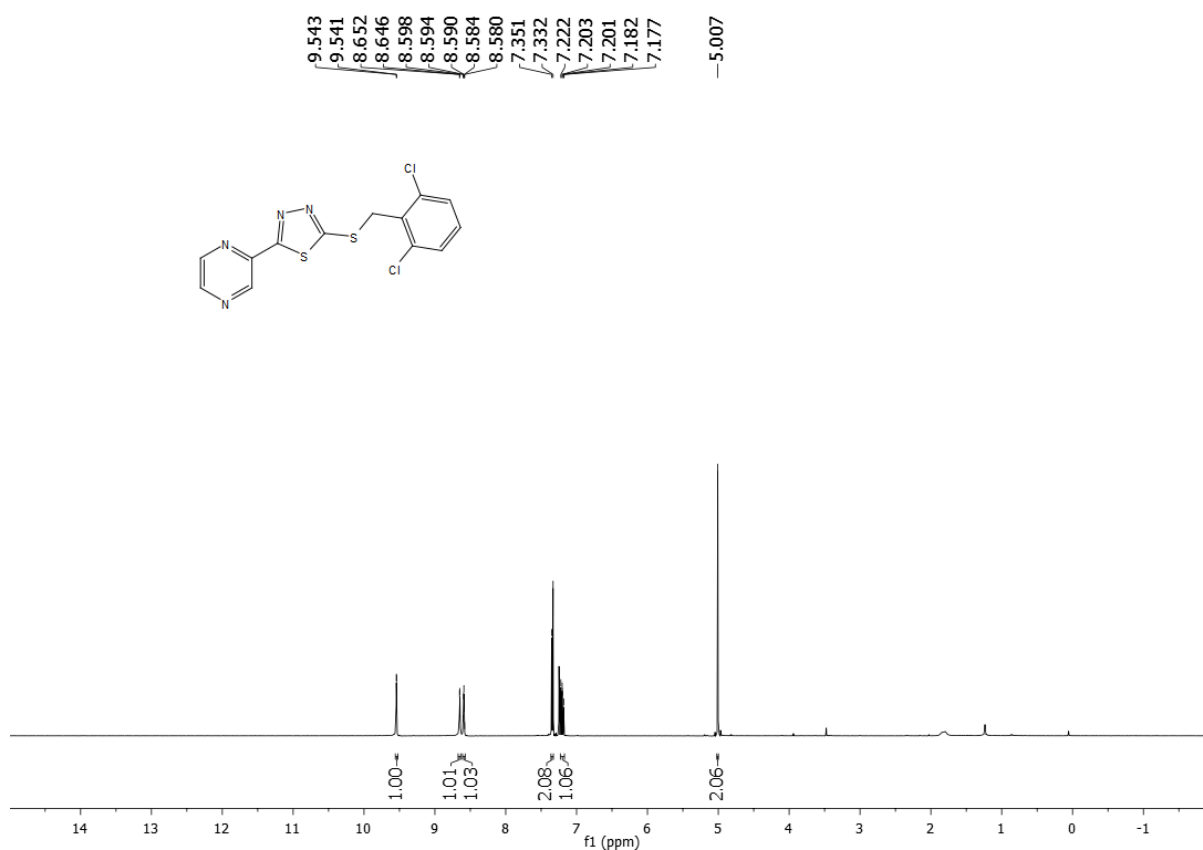
^1H NMR of compound **4** (400 MHz, d_6 -DMSO):



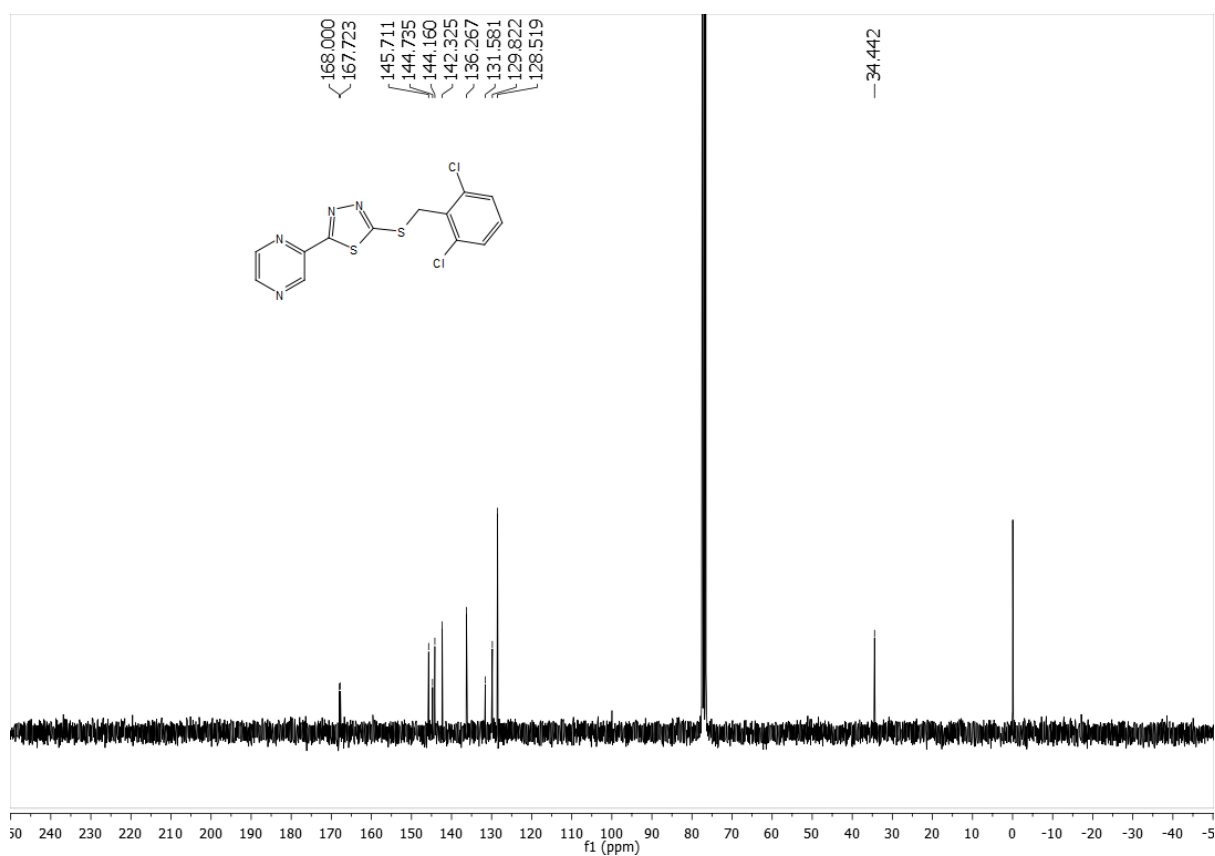
^{13}C NMR of compound **4** (100 MHz, d_6 -DMSO):



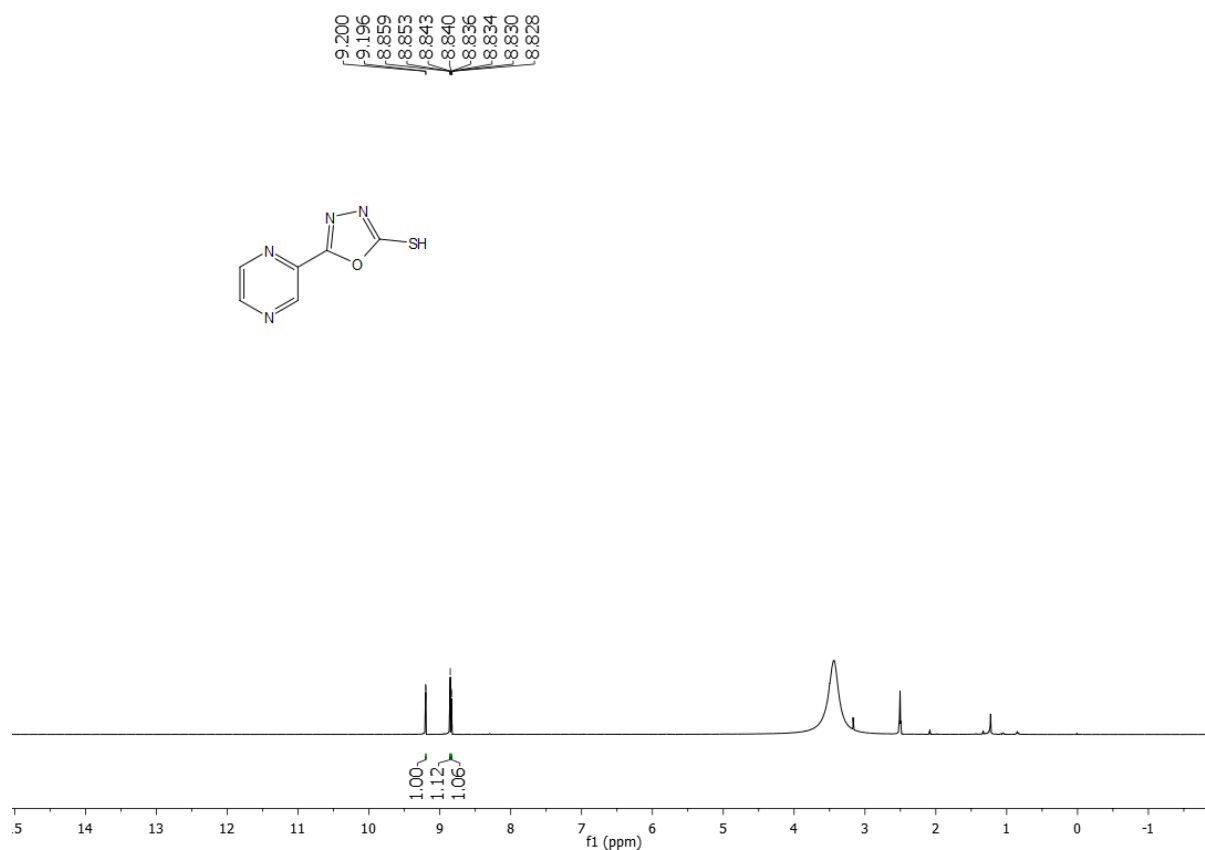
^1H NMR of compound **5** (400 MHz, CDCl_3):



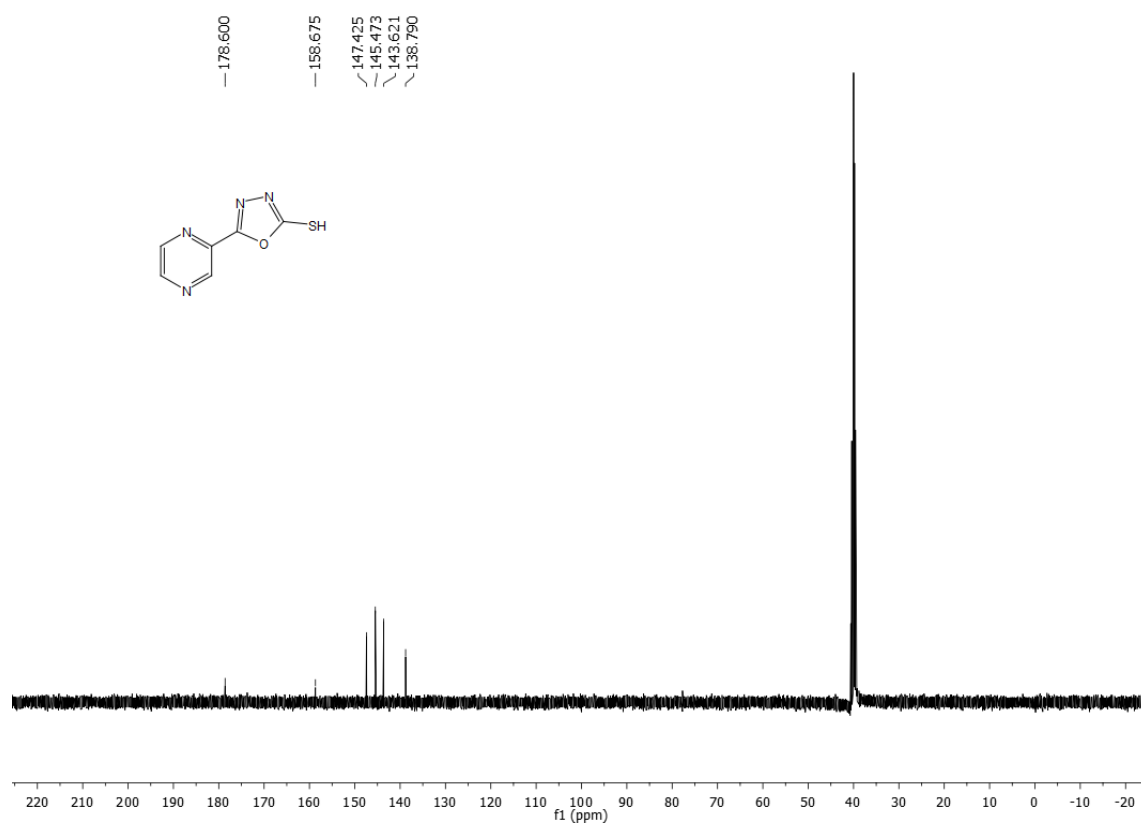
^{13}C NMR of compound **5** (100 MHz, CDCl_3):



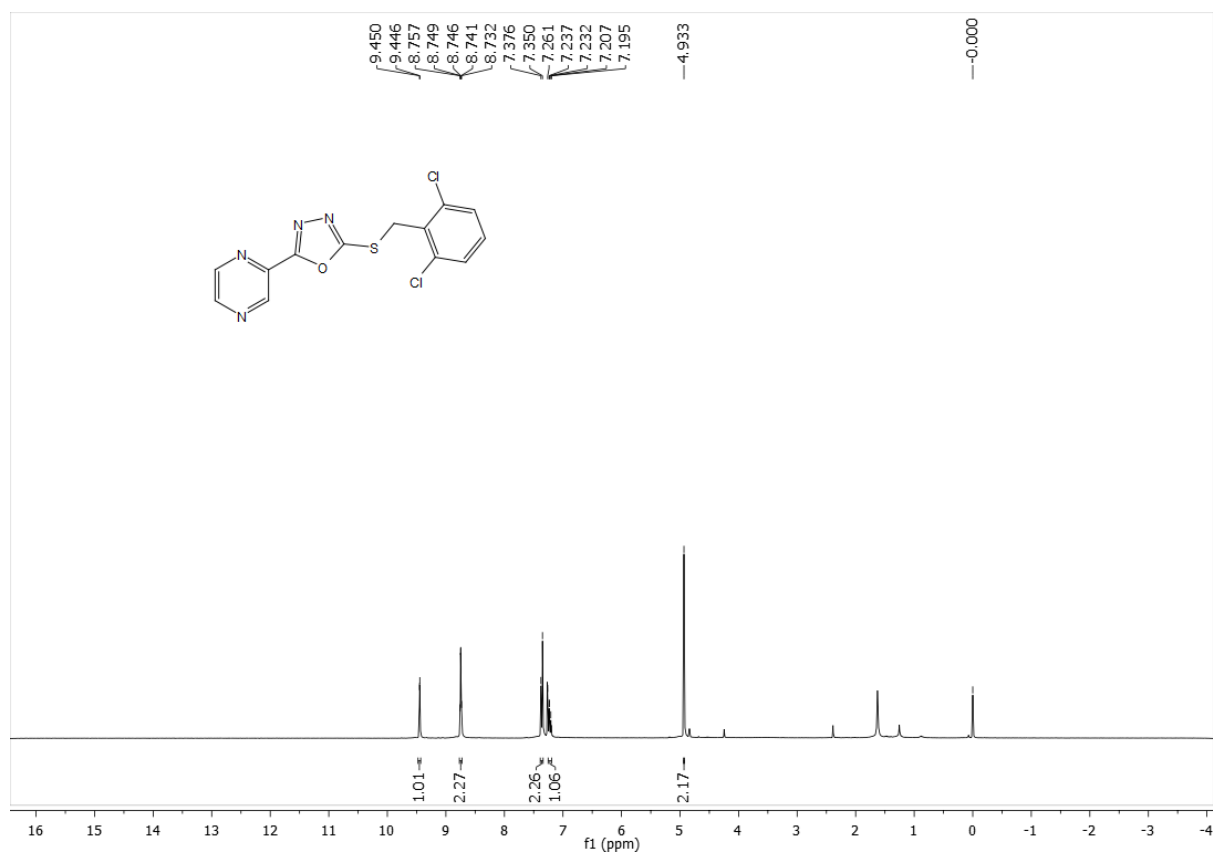
^1H NMR of compound **6** (400 MHz, d_6 -DMSO):



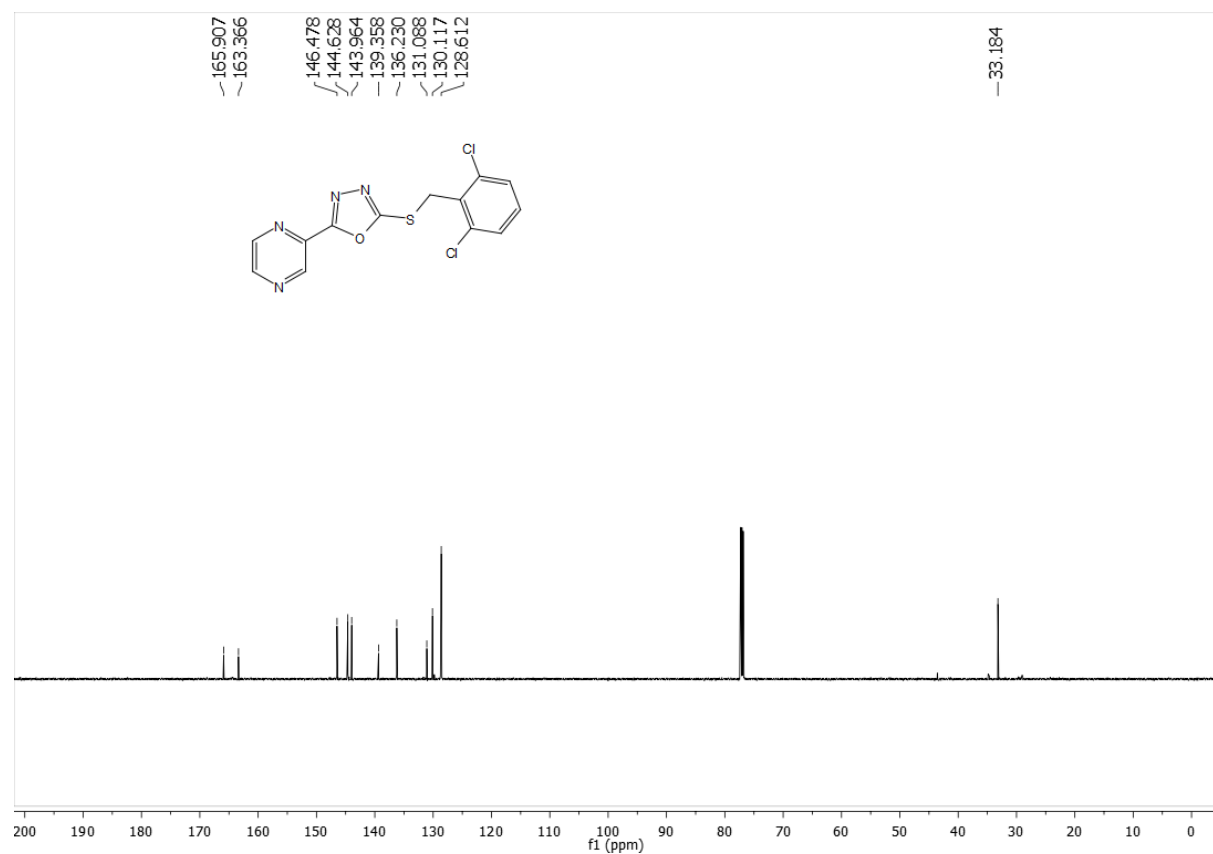
^{13}C NMR of compound **6** (100 MHz, d_6 -DMSO):



^1H NMR of compound **7** (300 MHz, CDCl_3):



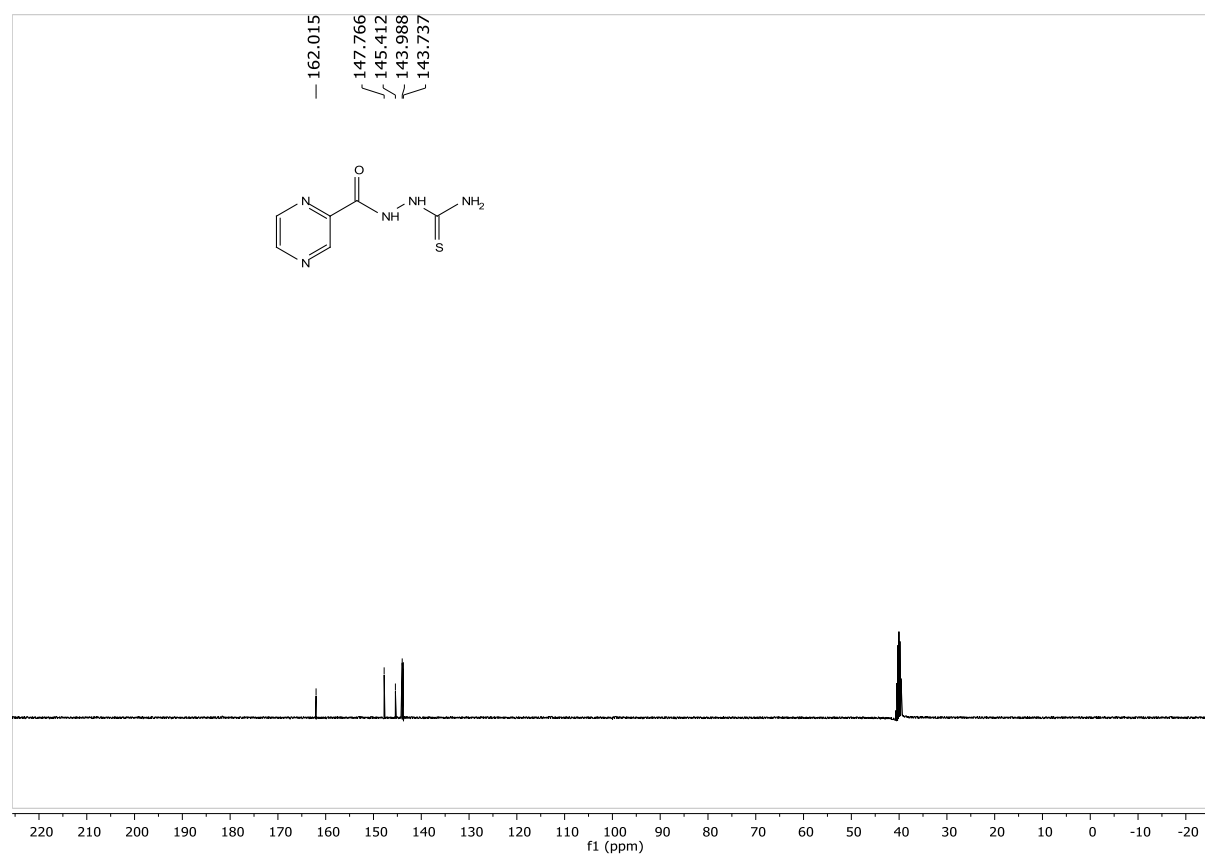
^{13}C NMR of compound **7** (75 MHz, CDCl_3):



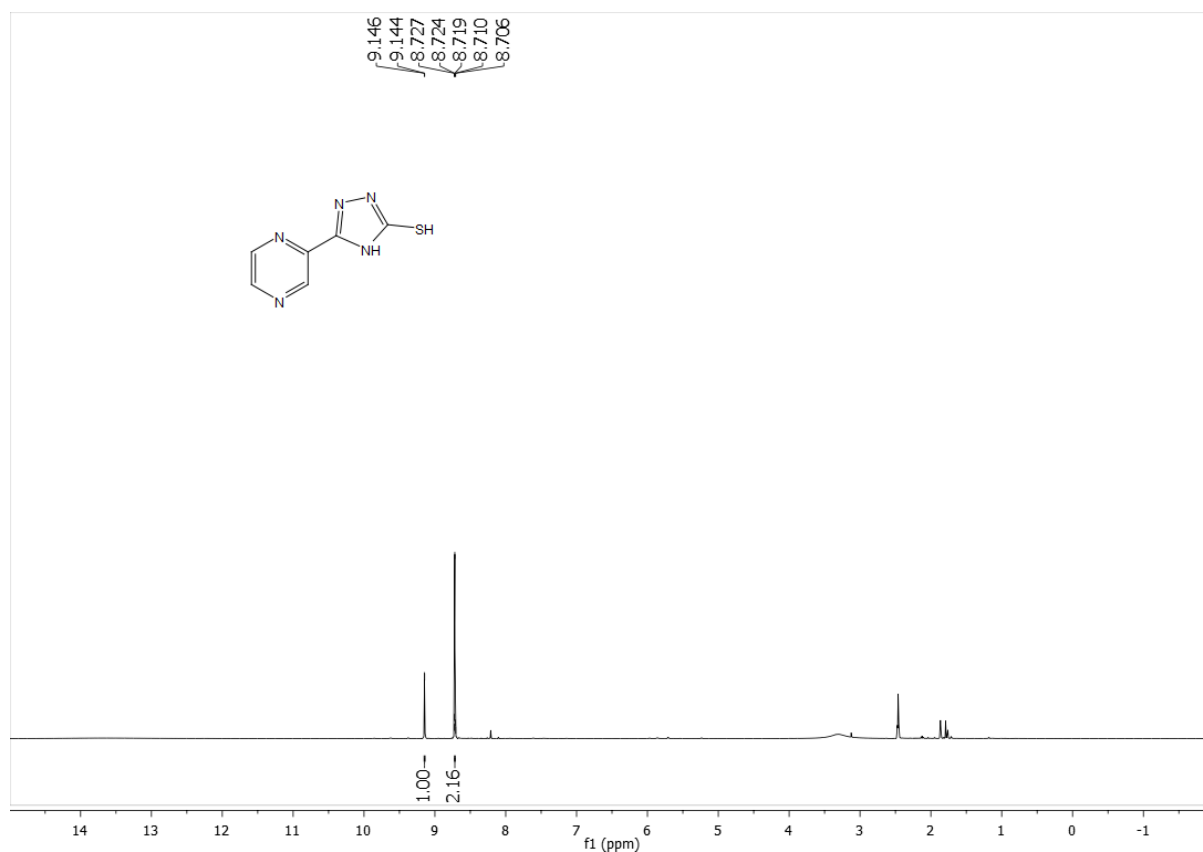
^1H NMR of compound **8** (400 MHz, d_6 -DMSO):



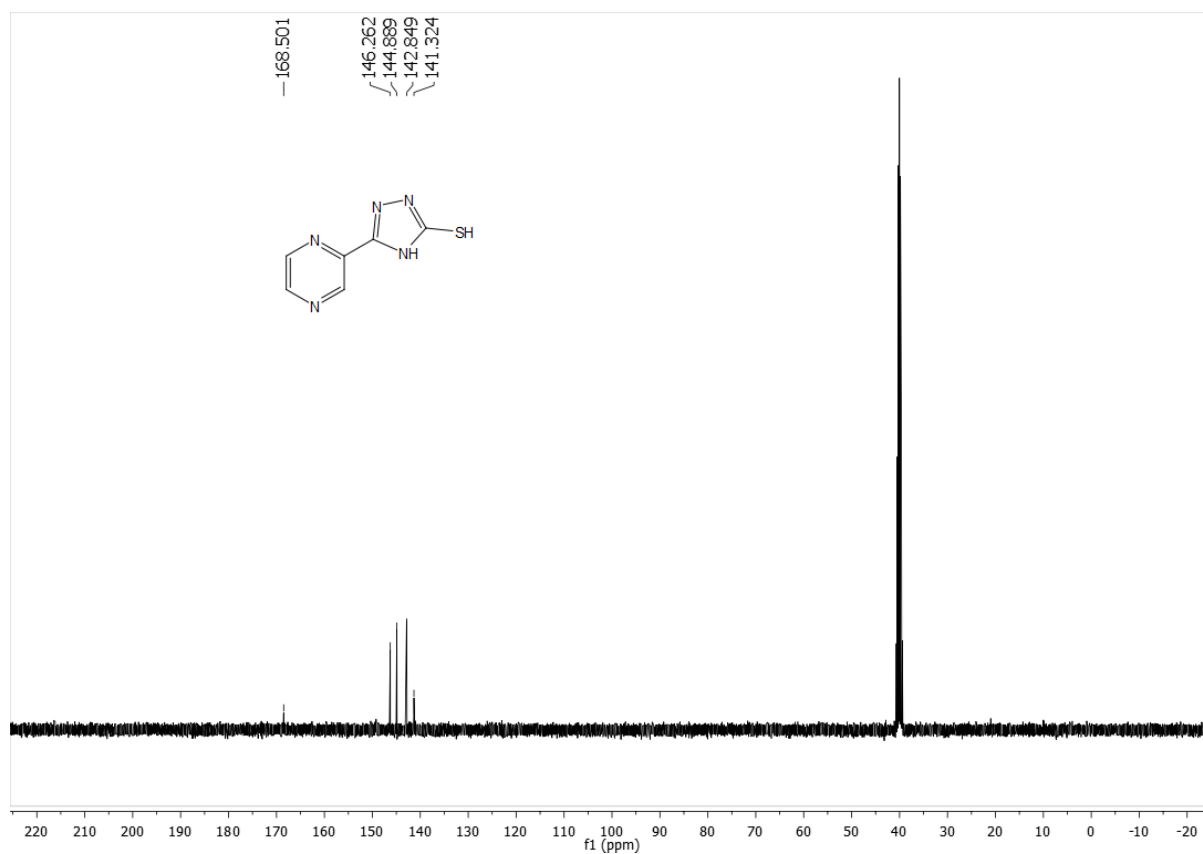
^{13}C NMR of compound **8** (75 MHz, d_6 -DMSO):



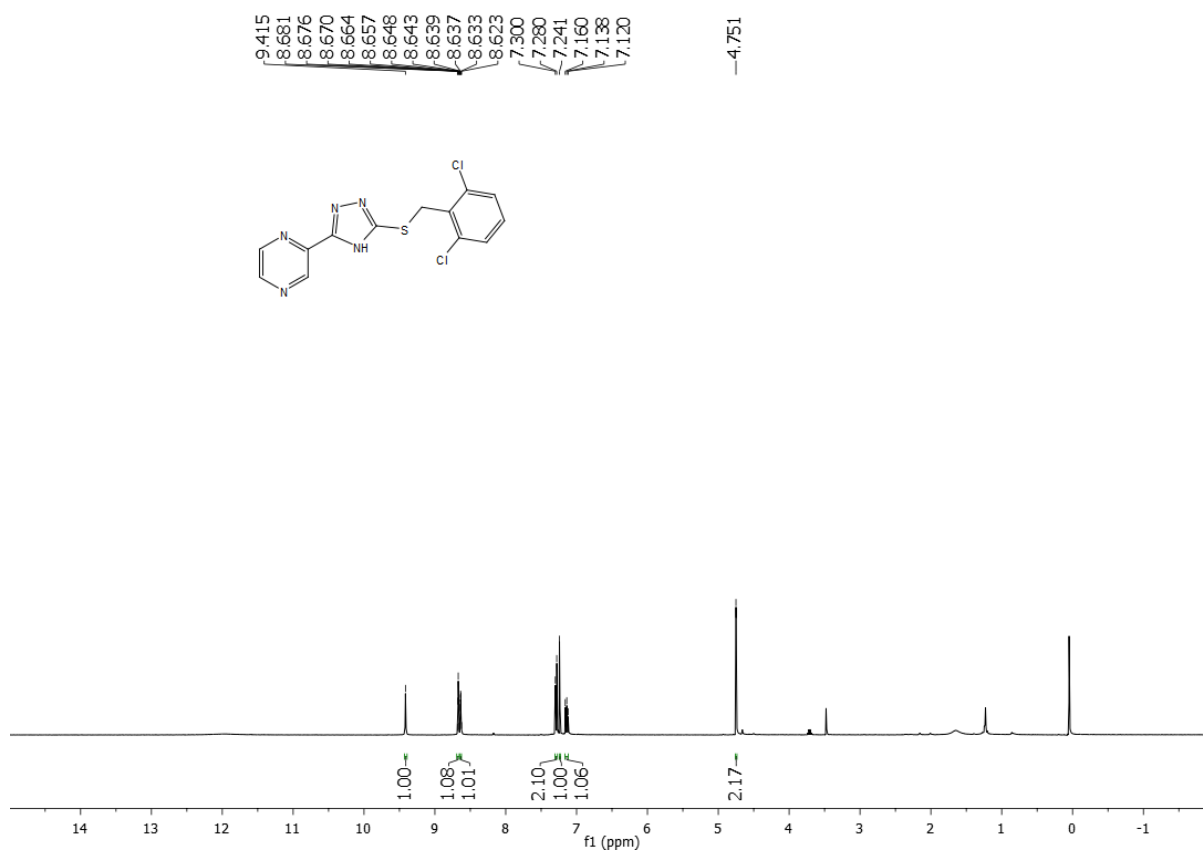
^1H NMR of compound **9** (400 MHz, d_6 -DMSO):



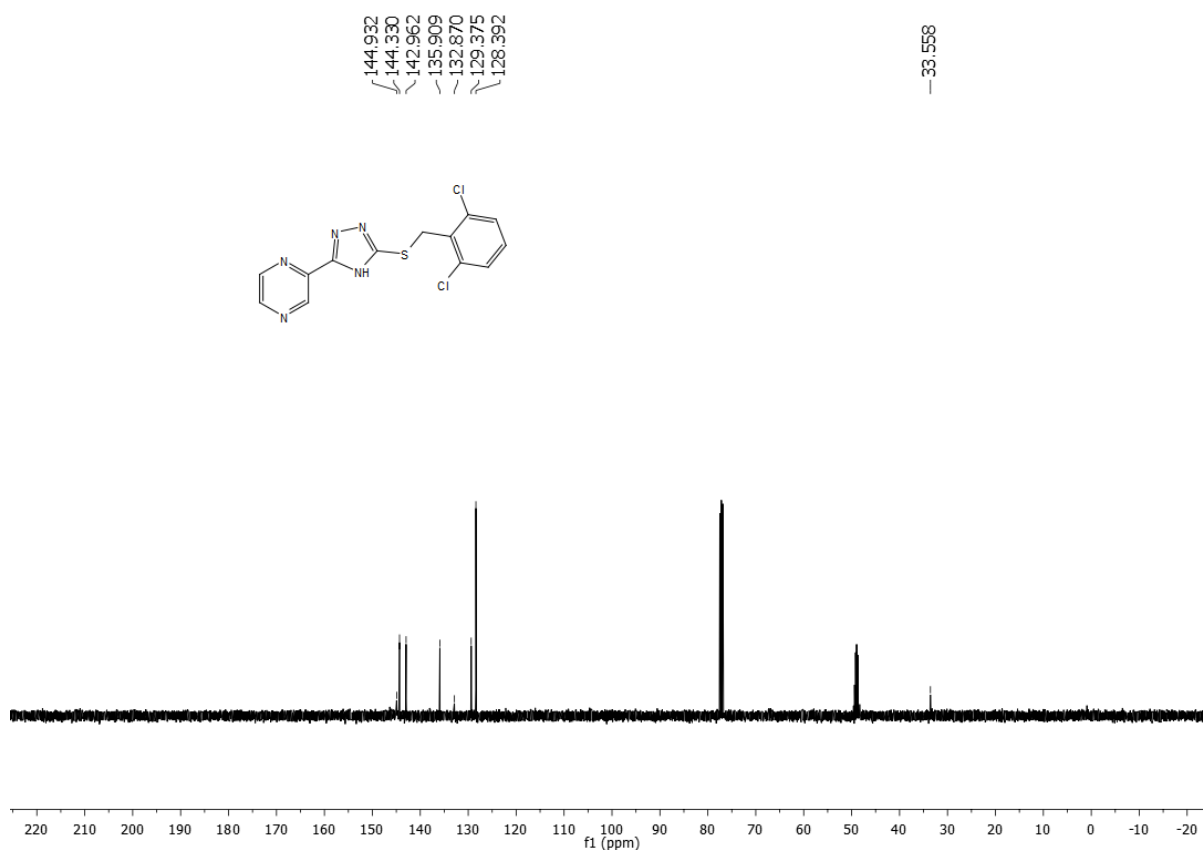
^{13}C NMR of compound **9** (100 MHz, d_6 -DMSO):



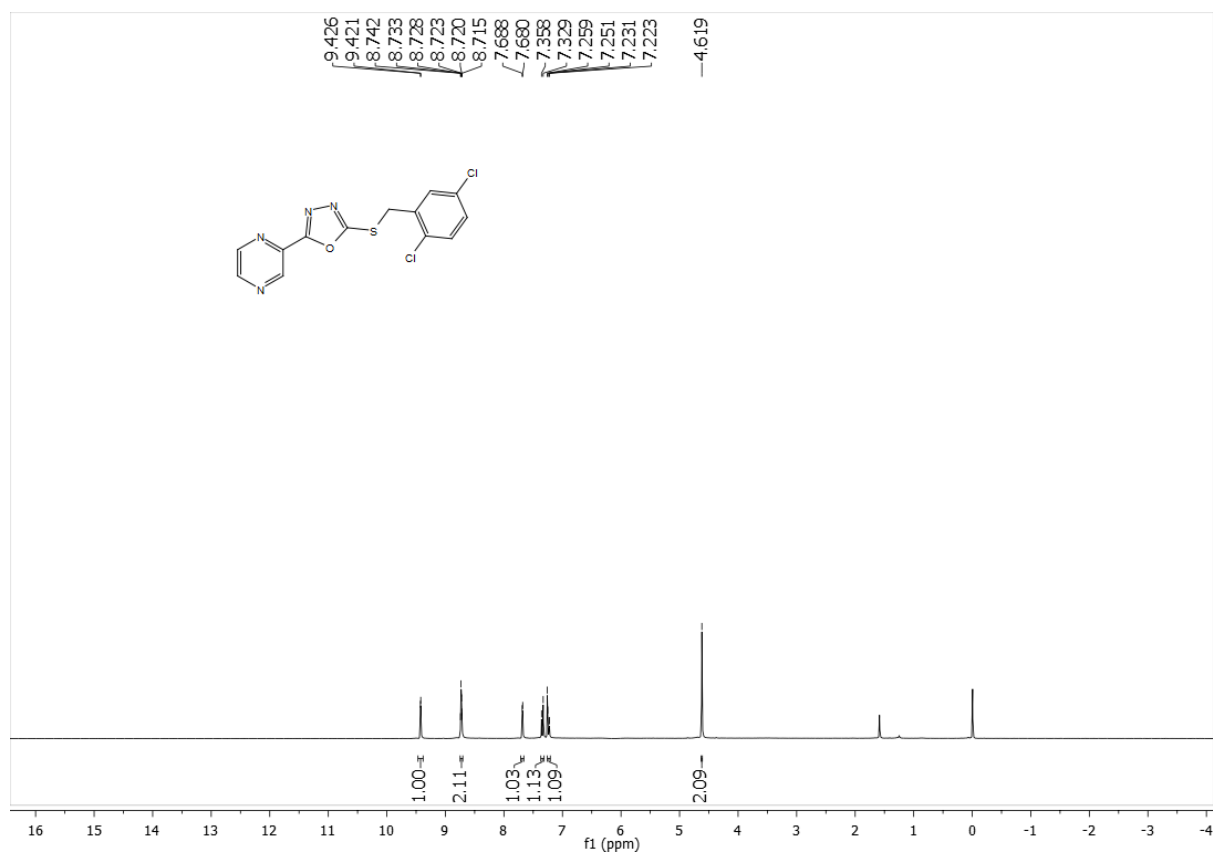
^1H NMR of compound **10** (400 MHz, CDCl_3):



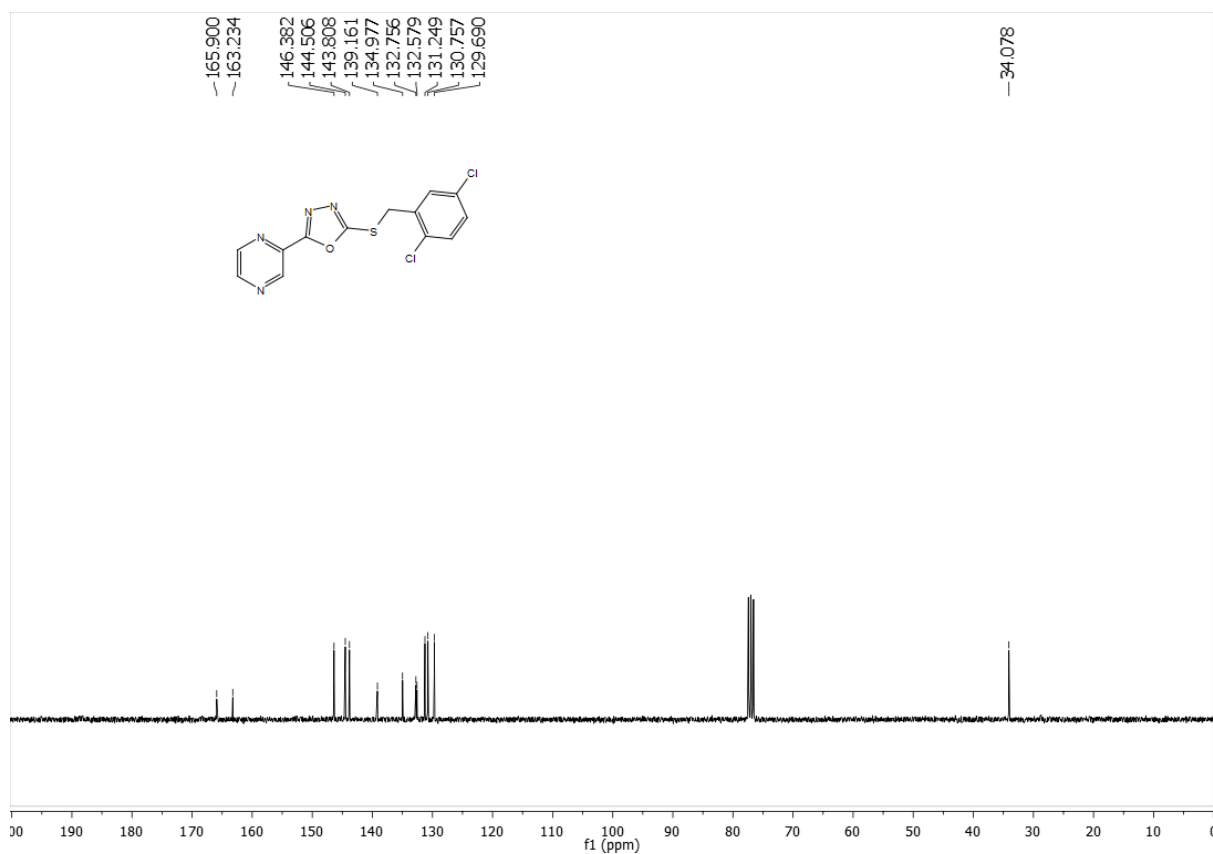
^{13}C NMR of compound **10** (100 MHz, CDCl_3):



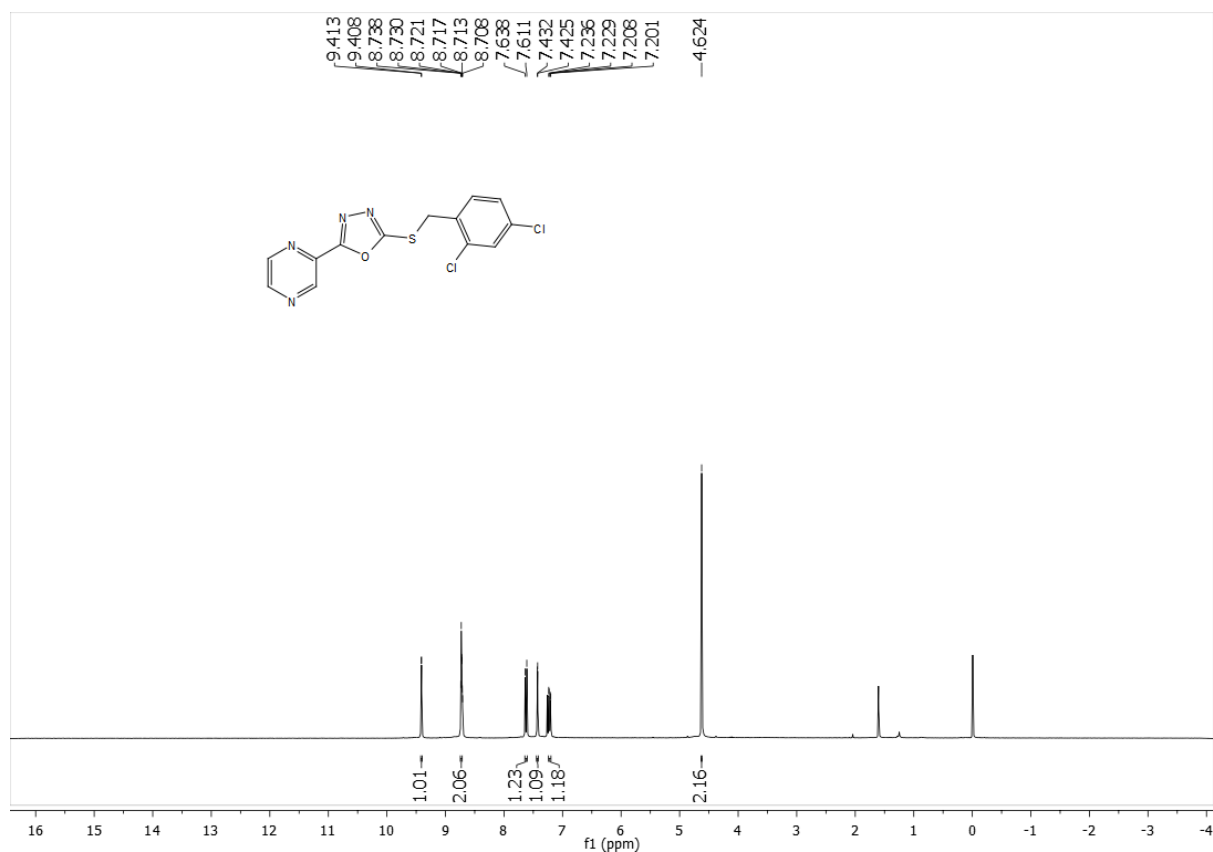
^1H NMR of compound **11** (300 MHz, CDCl_3):



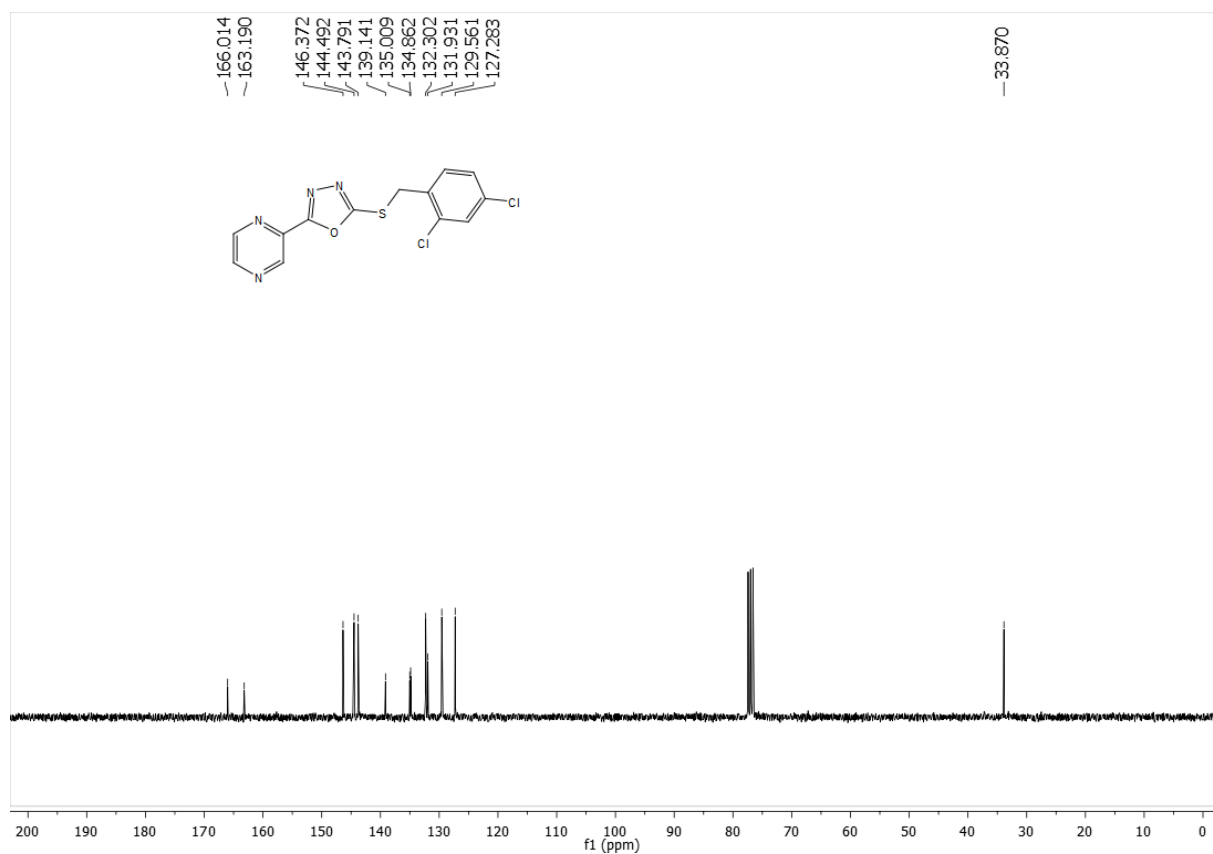
^{13}C NMR of compound **11** (75 MHz, CDCl_3):



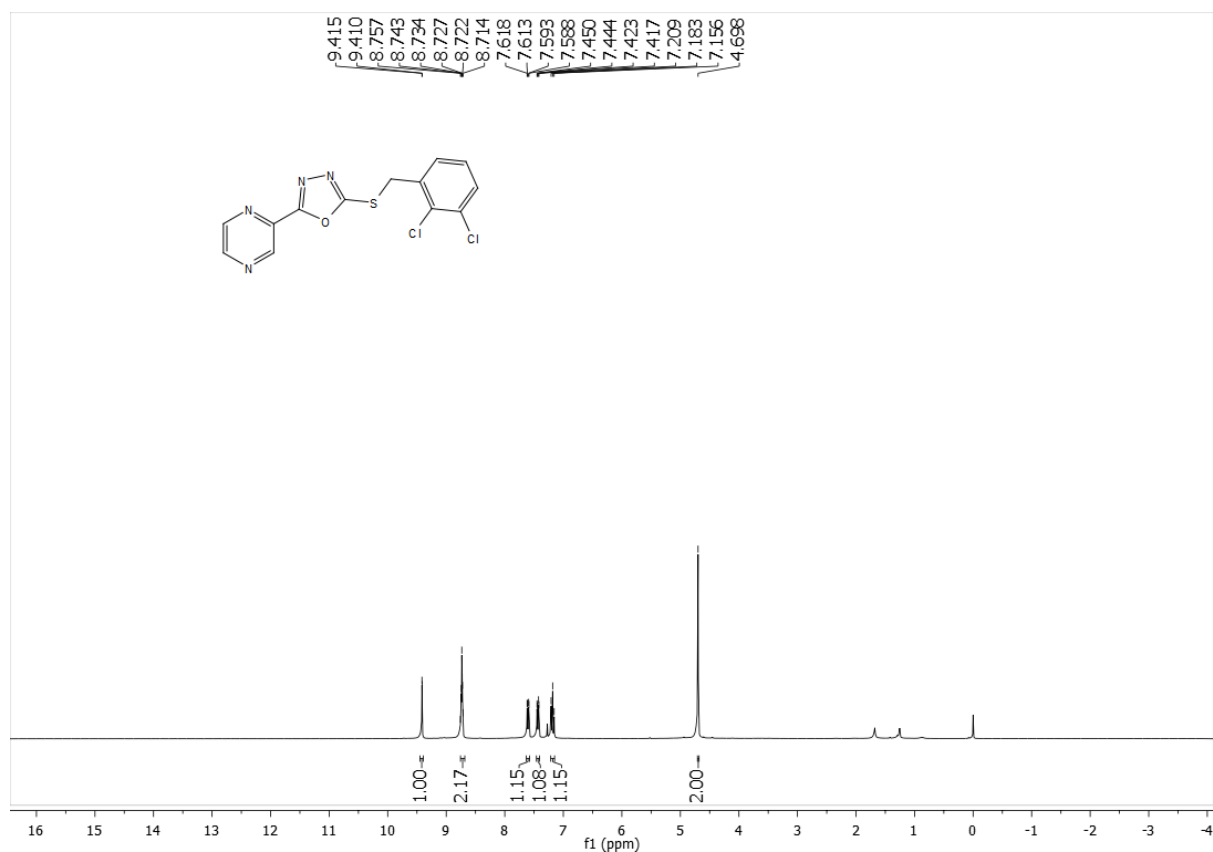
^1H NMR of compound **12** (300 MHz, CDCl_3):



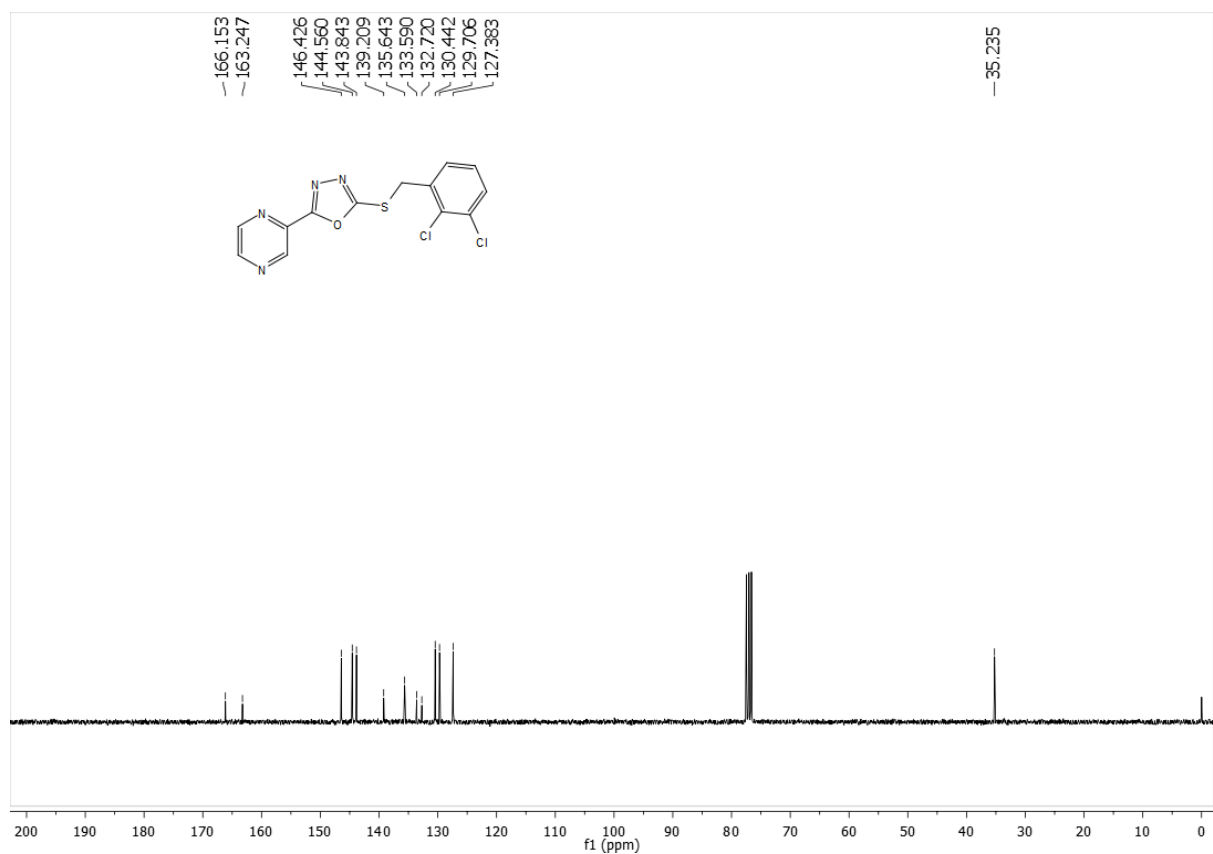
^{13}C NMR of compound **12** (75 MHz, CDCl_3):



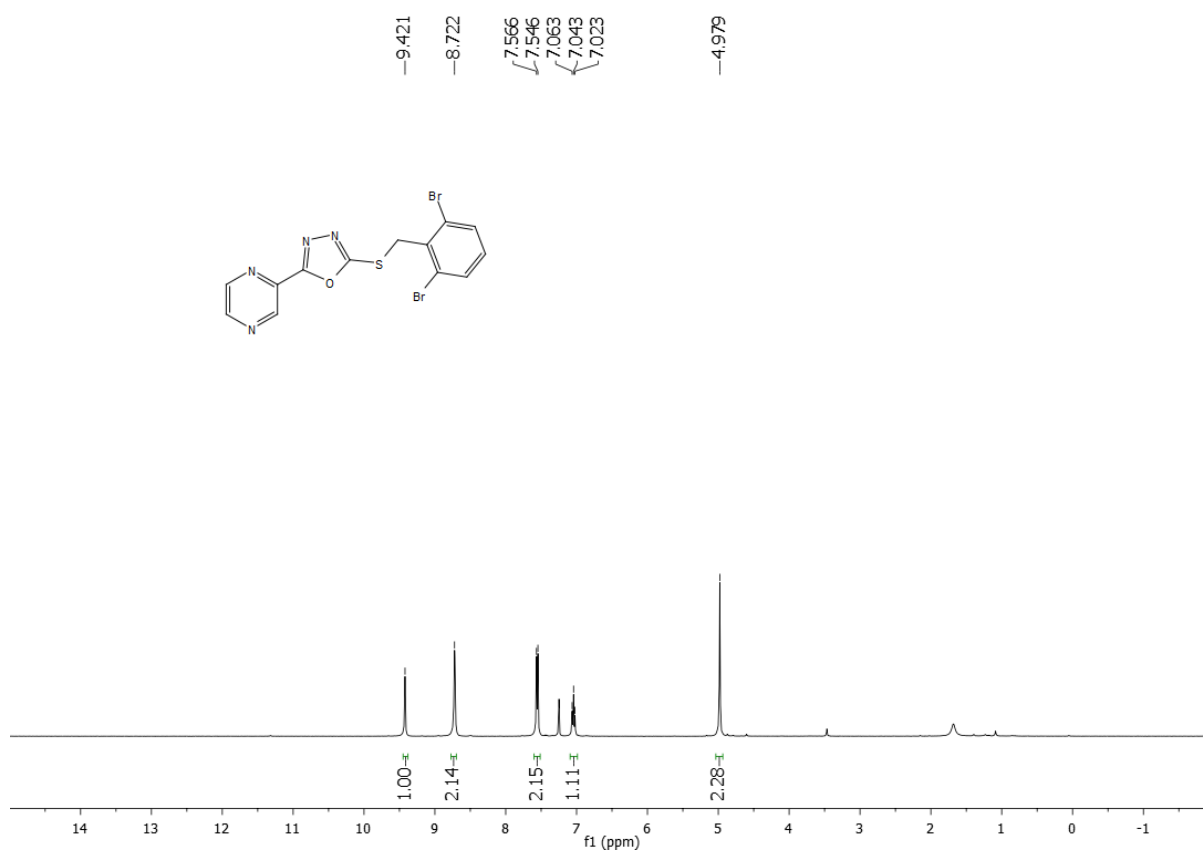
^1H NMR of compound **13** (300 MHz, CDCl_3):



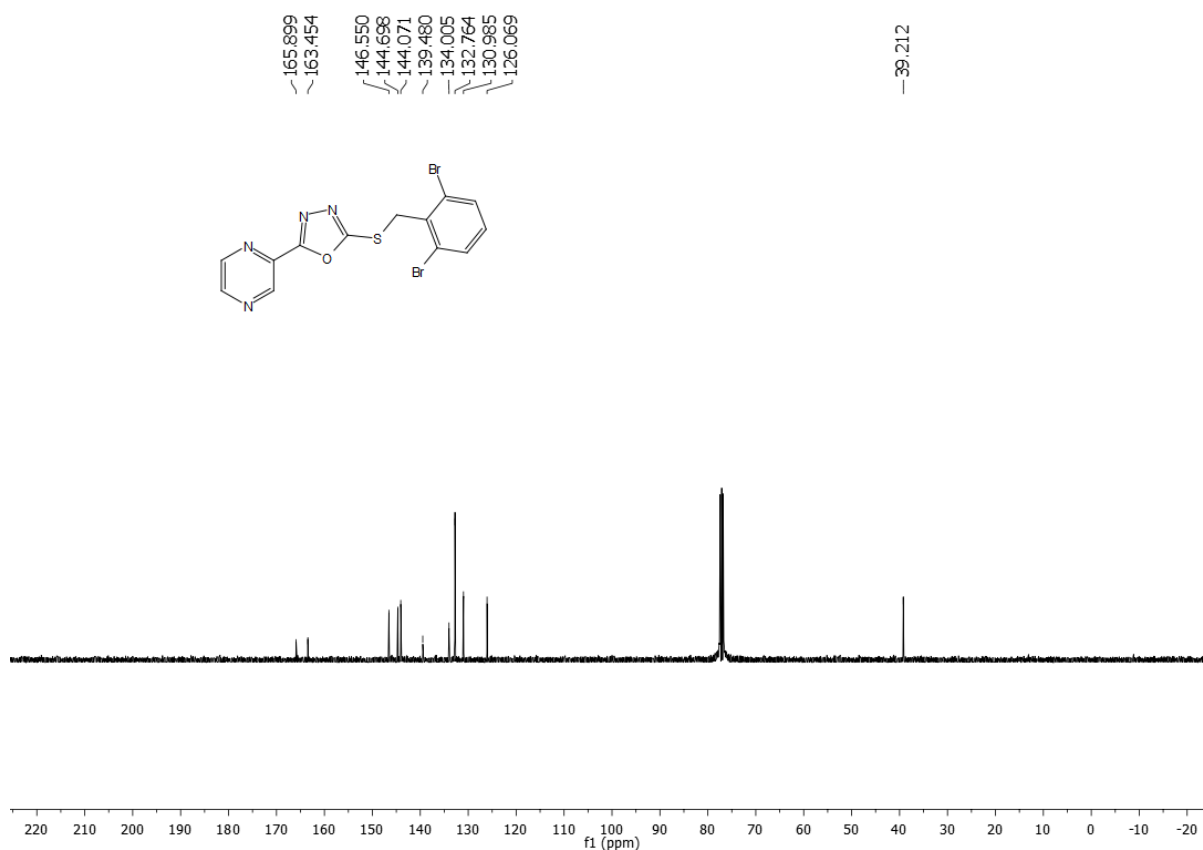
^{13}C NMR of compound **13** (75 MHz, CDCl_3):



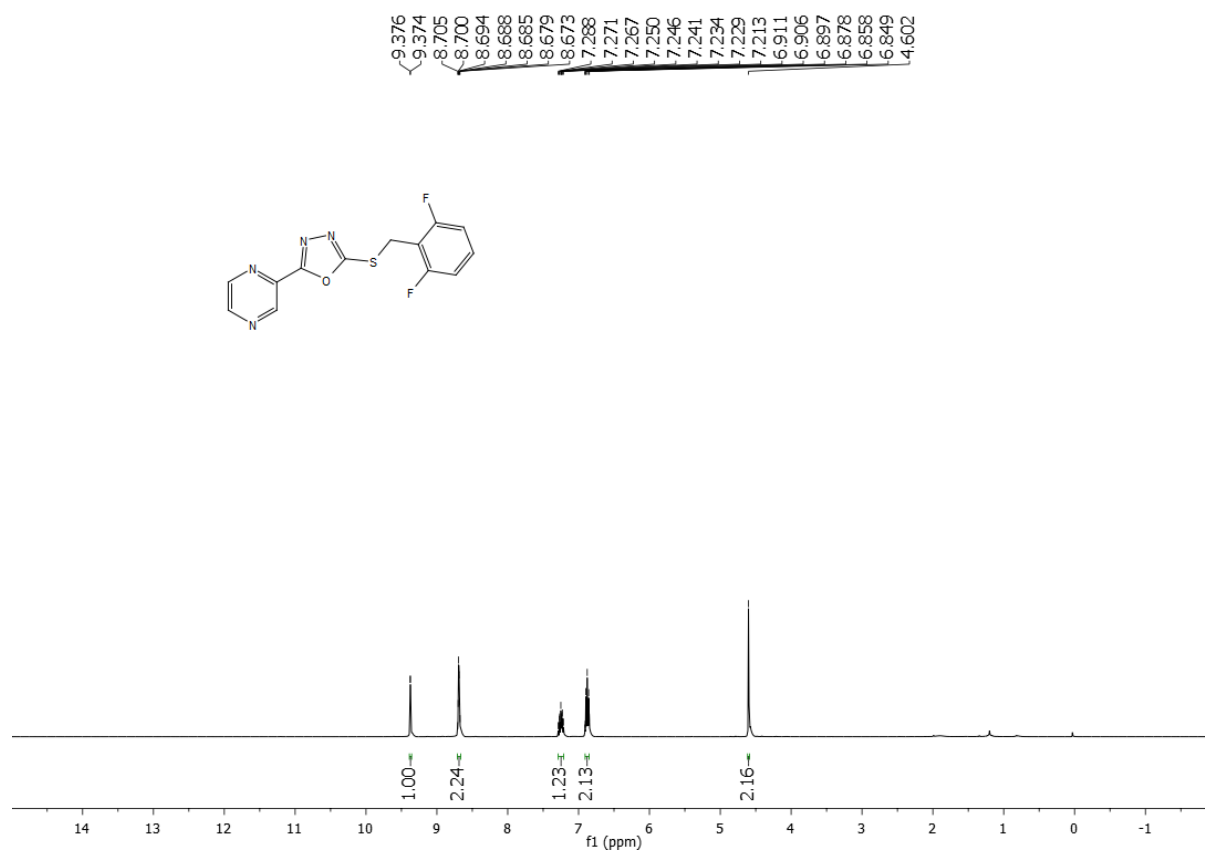
^1H NMR of compound **14** (400 MHz, CDCl_3):



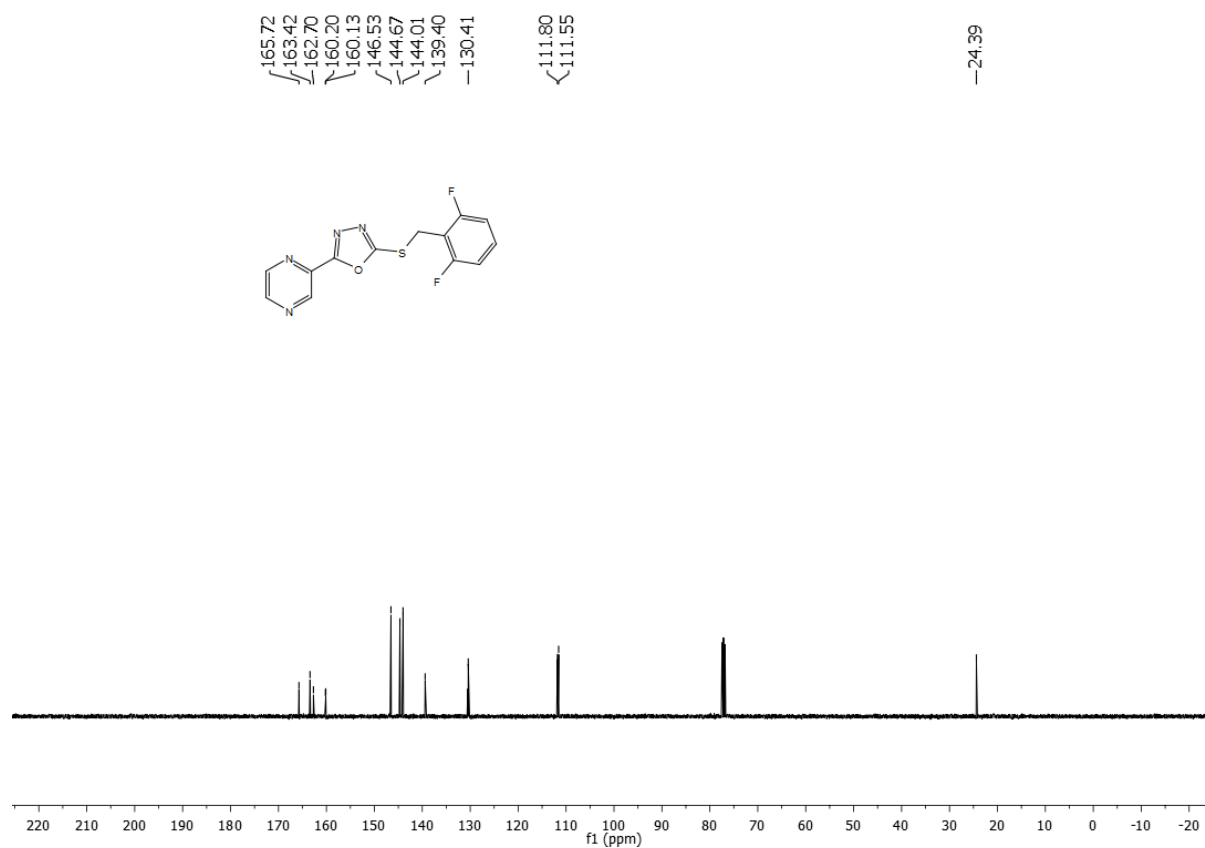
^{13}C NMR of compound **14** (100 MHz, CDCl_3):



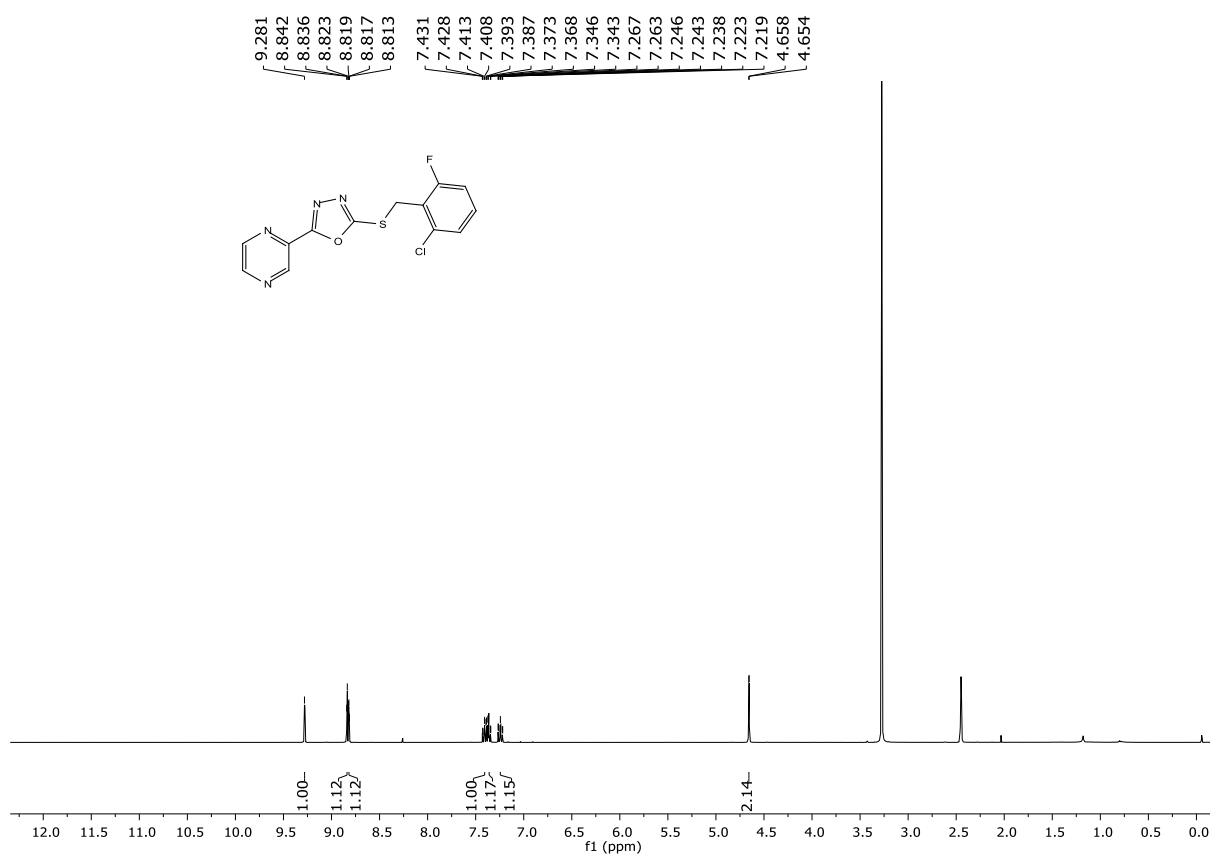
^1H NMR of compound **15** (400 MHz, CDCl_3):



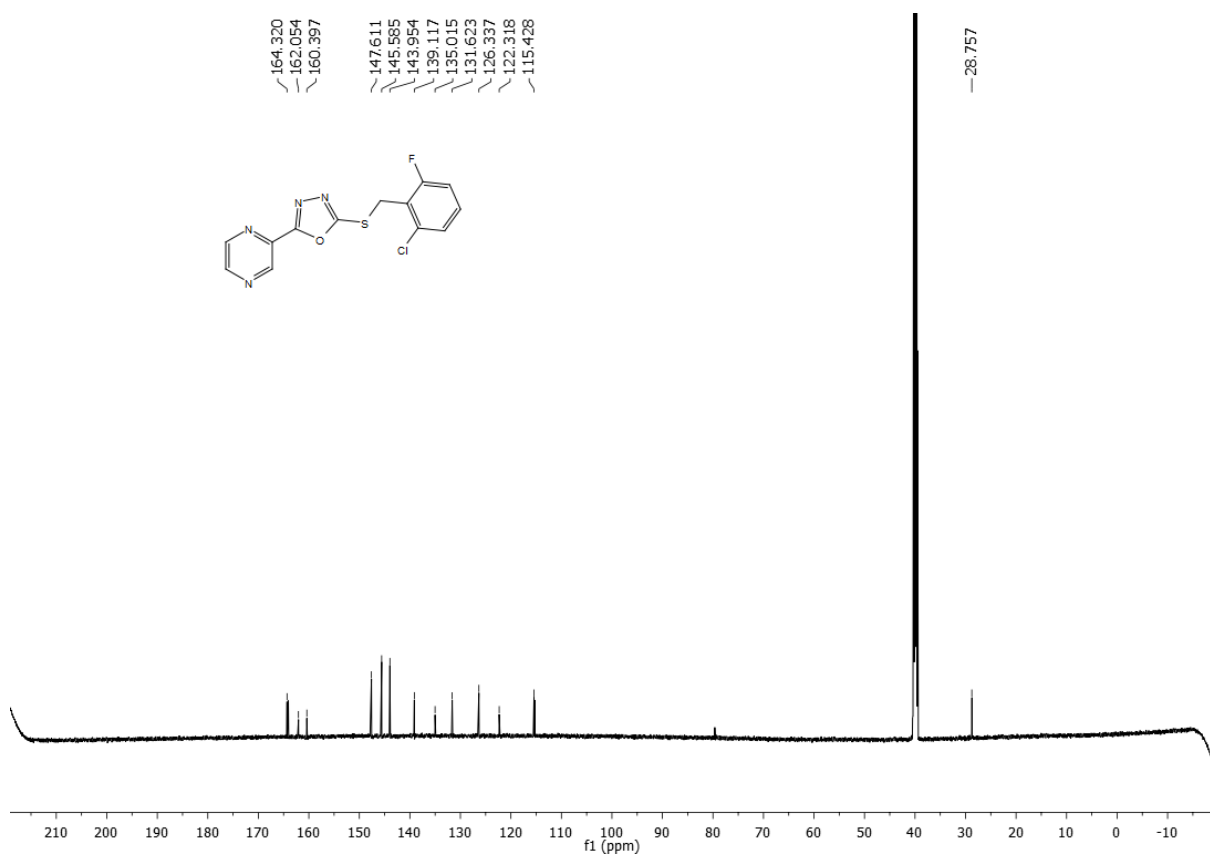
^{13}C NMR of compound **15** (100 MHz, CDCl_3):



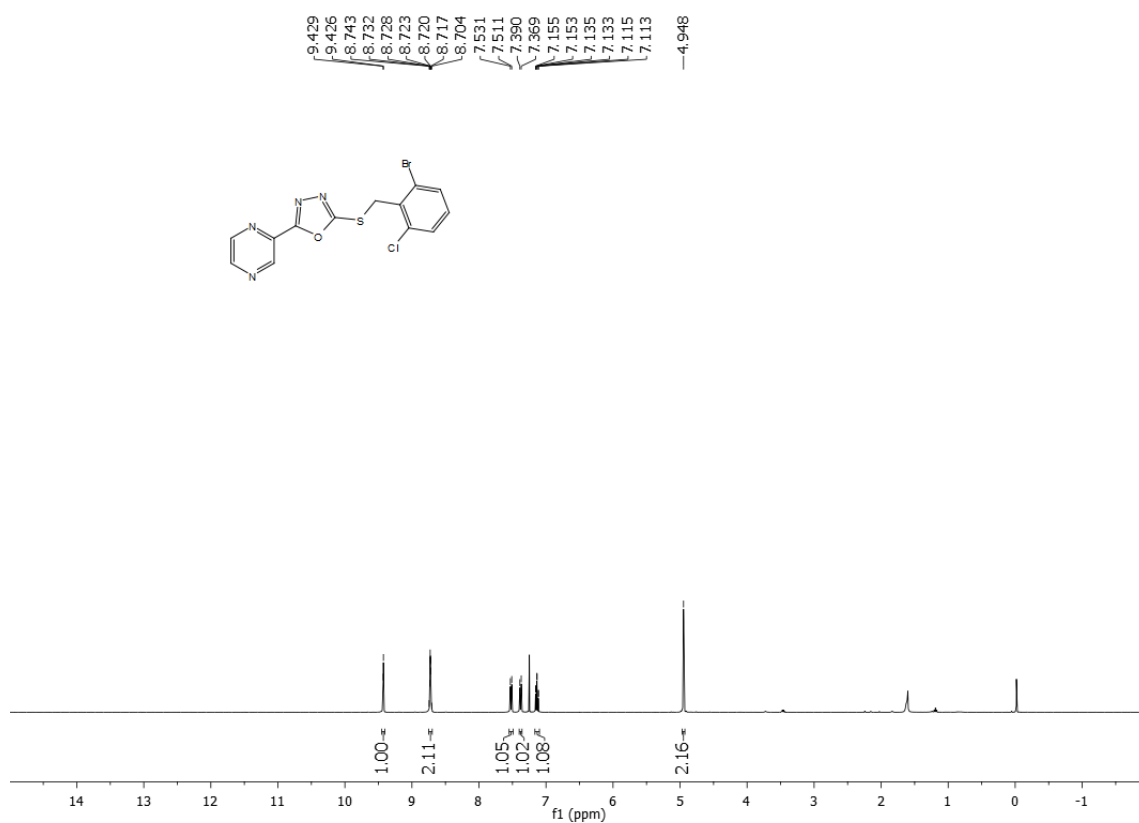
^1H NMR of compound **16** (400 MHz, d_6 -DMSO):



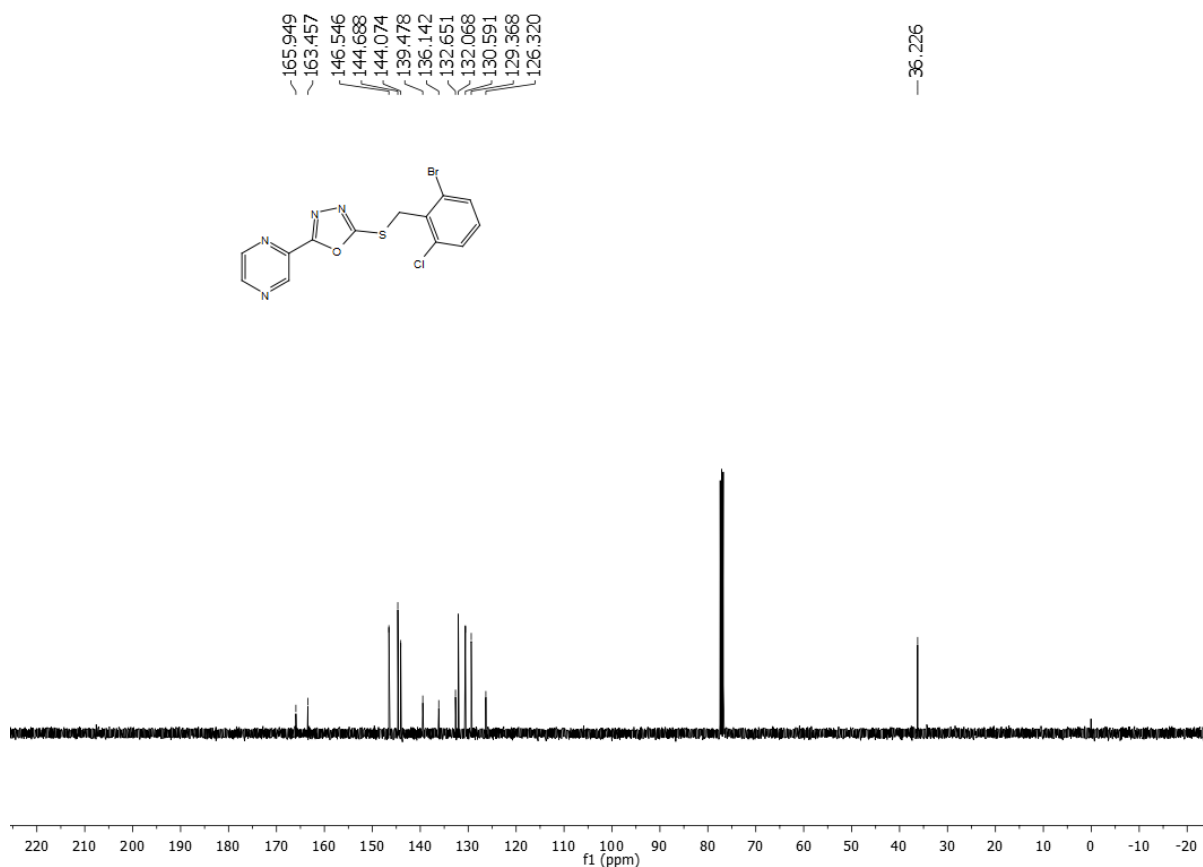
^{13}C NMR of compound **16** (151 MHz, d_6 -DMSO):



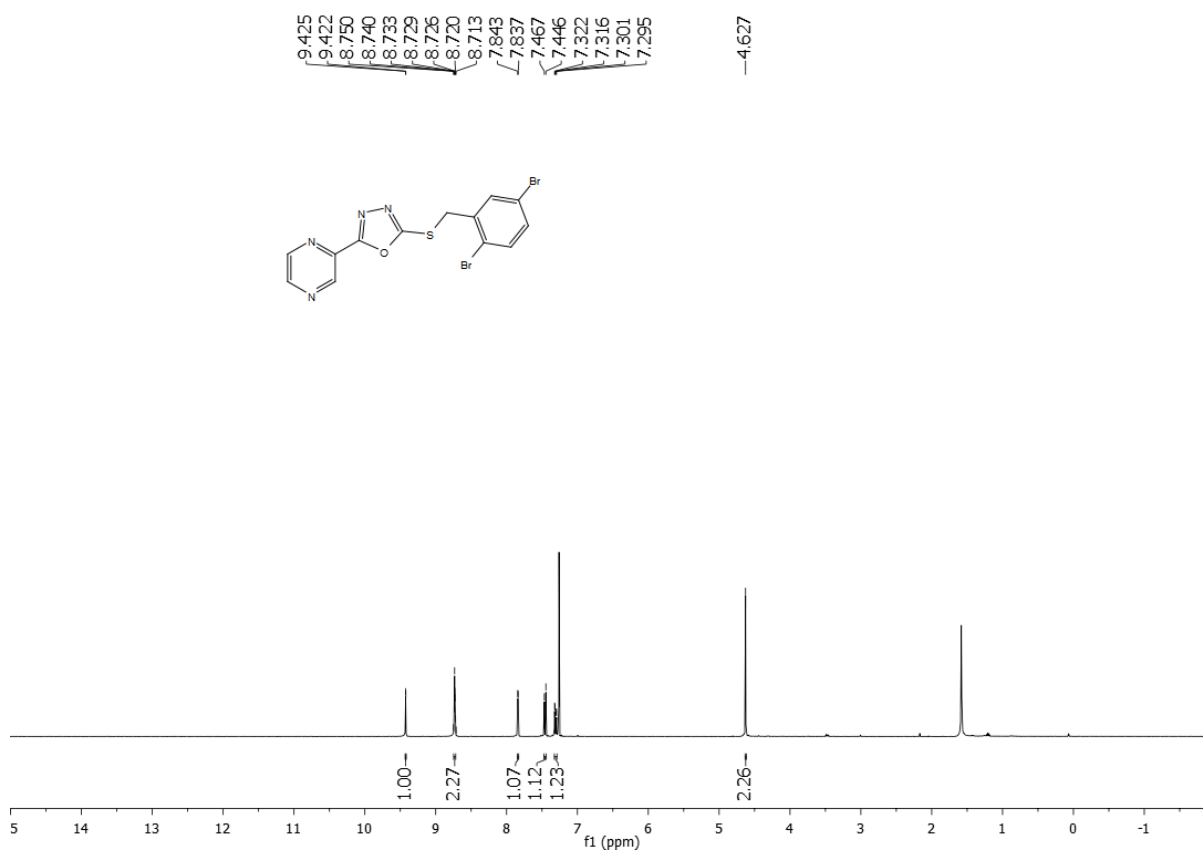
^1H NMR of compound **17** (400 MHz, CDCl_3):



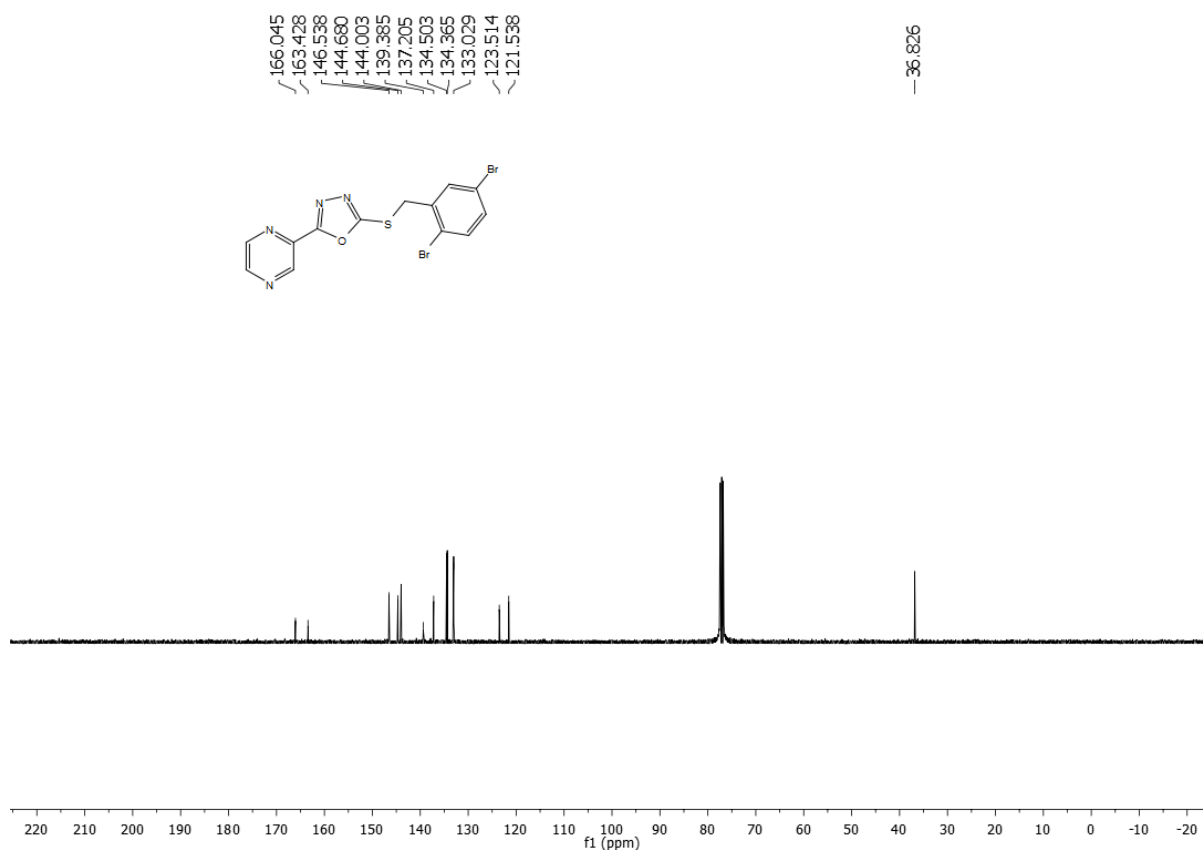
^{13}C NMR of compound **17** (100 MHz, CDCl_3):



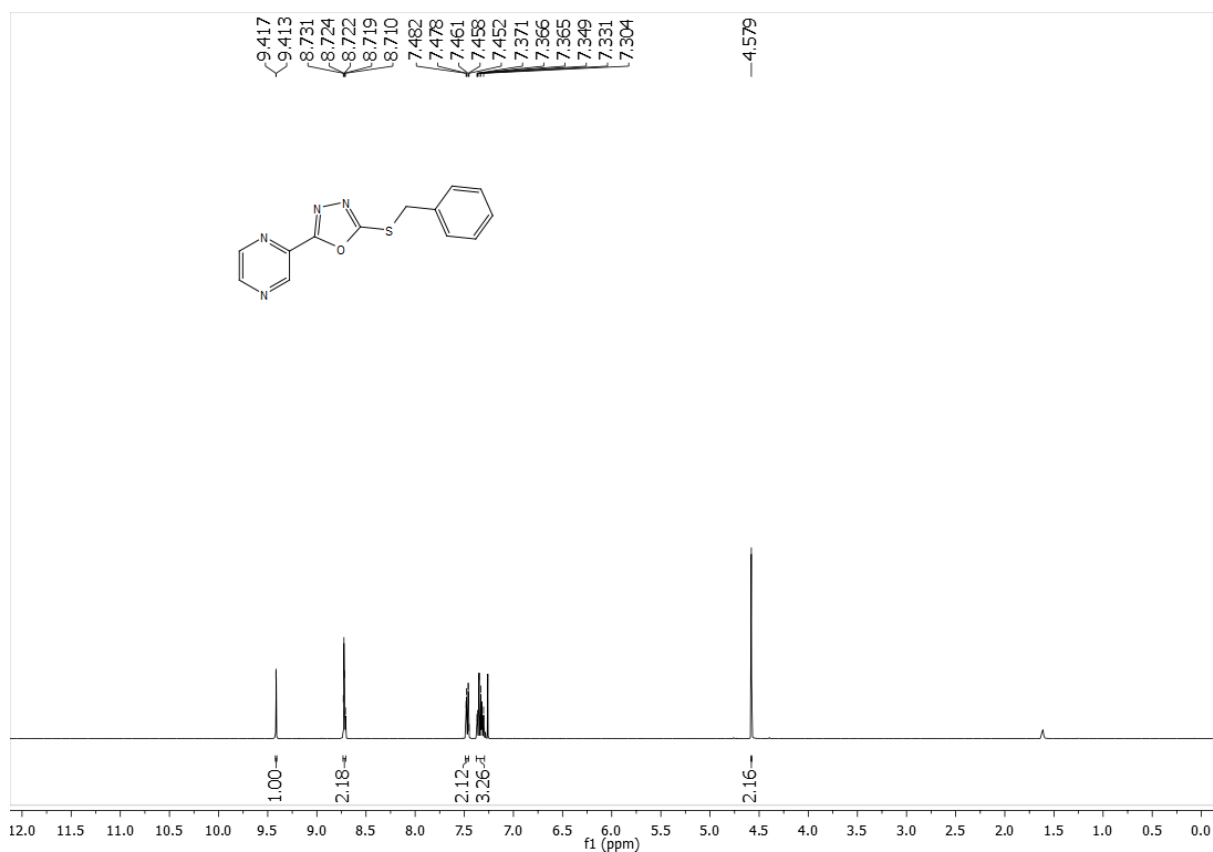
^1H NMR of compound **18** (300 MHz, CDCl_3):



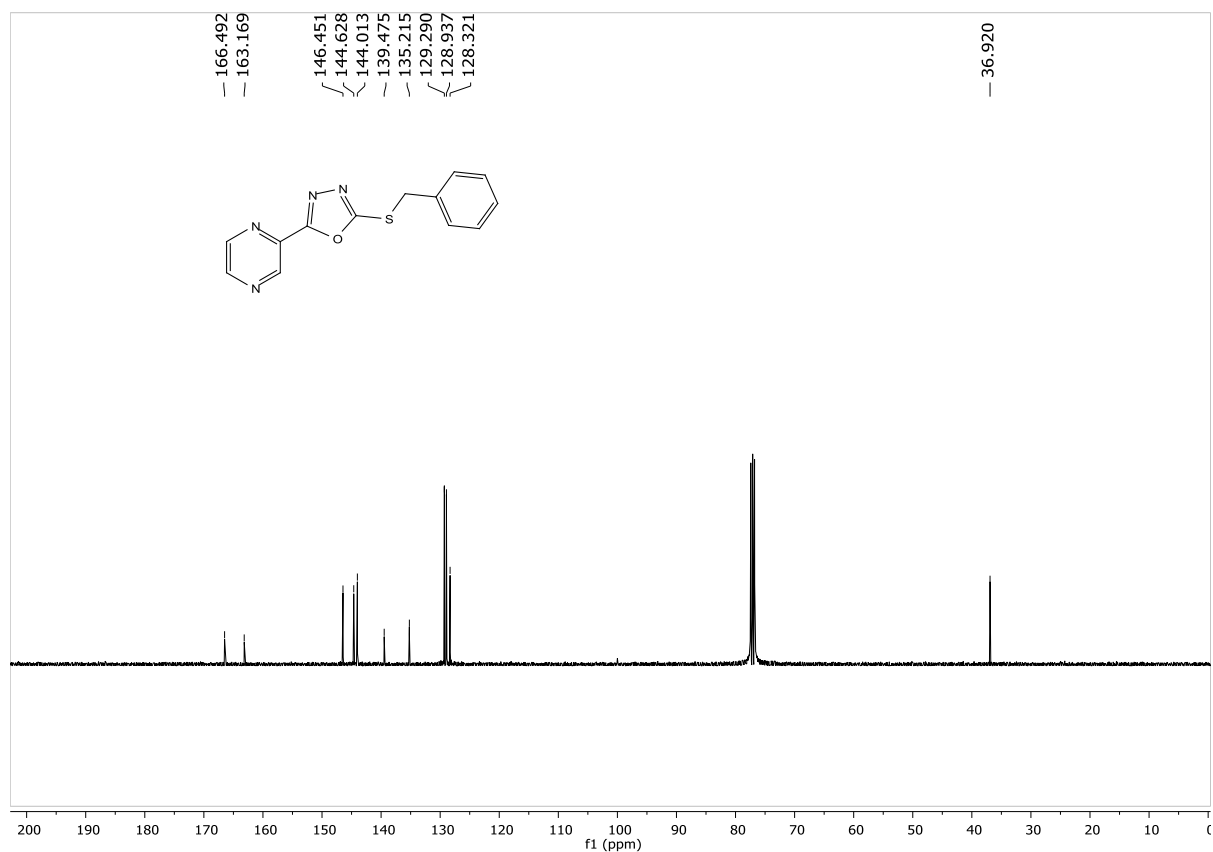
^{13}C NMR of compound **18** (75 MHz, CDCl_3):



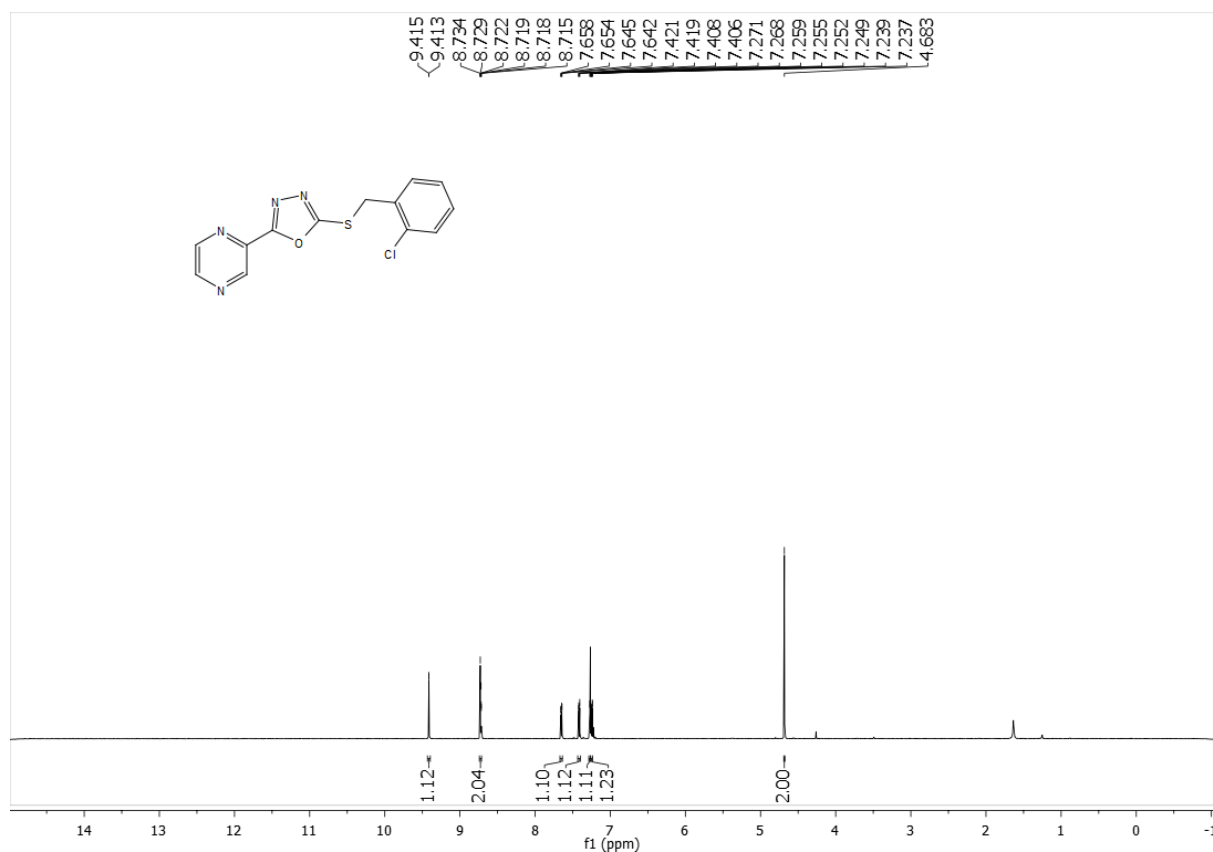
^1H NMR of compound **19** (400 MHz, CDCl_3):



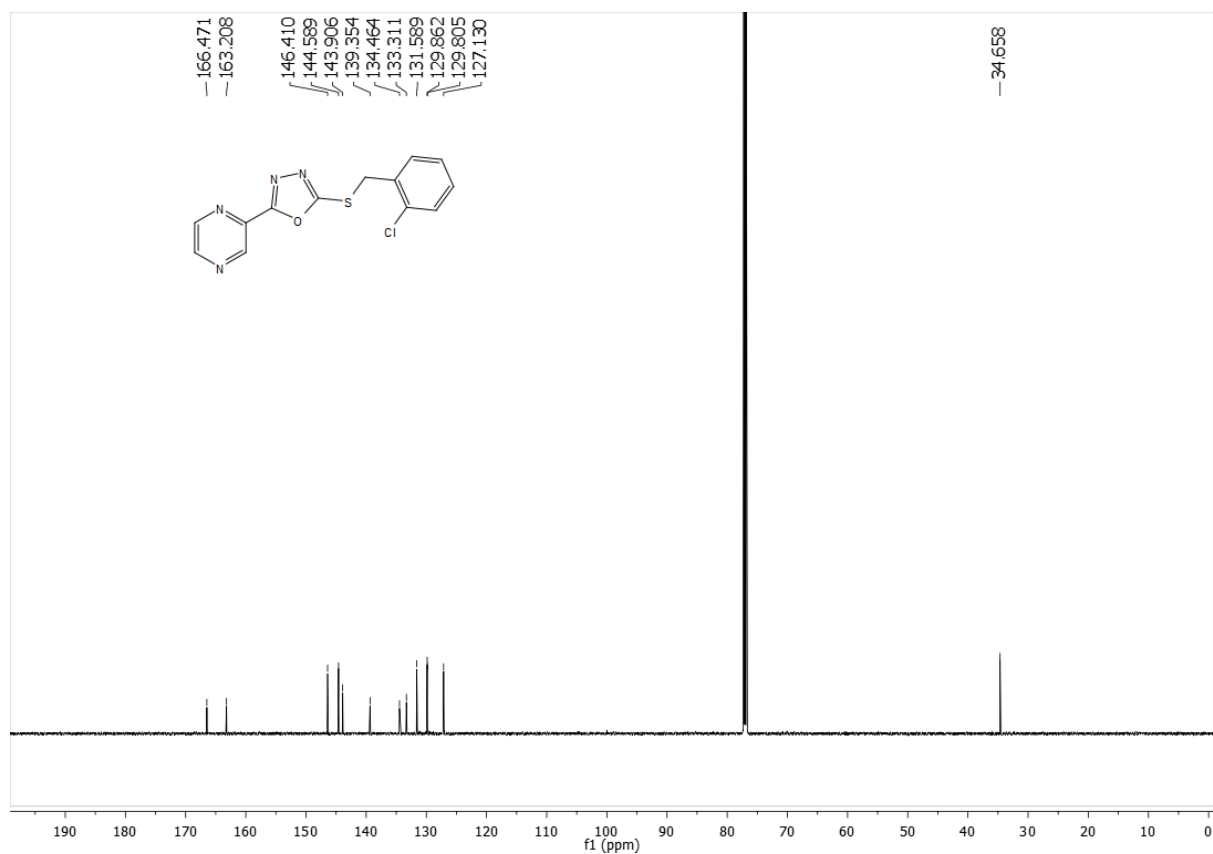
^{13}C NMR of compound **19** (100 MHz, CDCl_3):



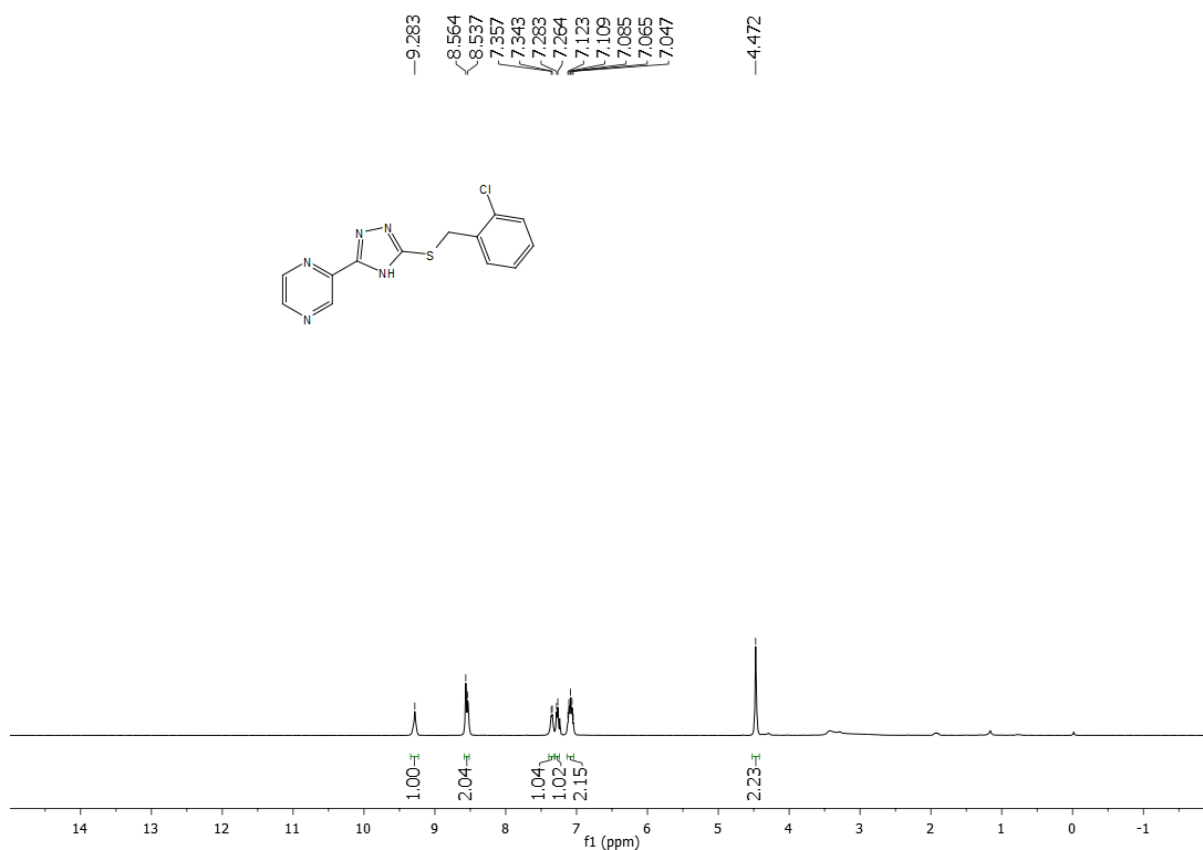
^1H NMR of compound **20** (600 MHz, CDCl_3):



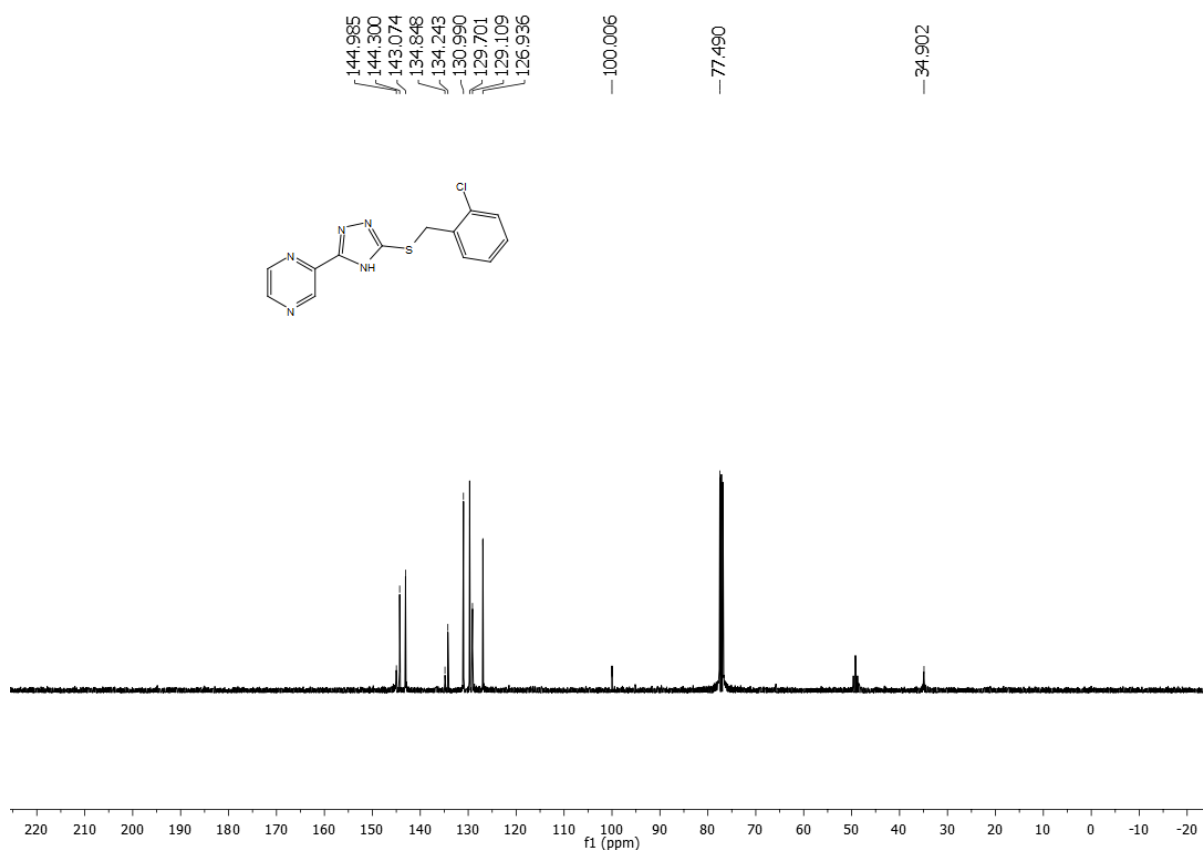
^{13}C NMR of compound **20** (150 MHz, CDCl_3):



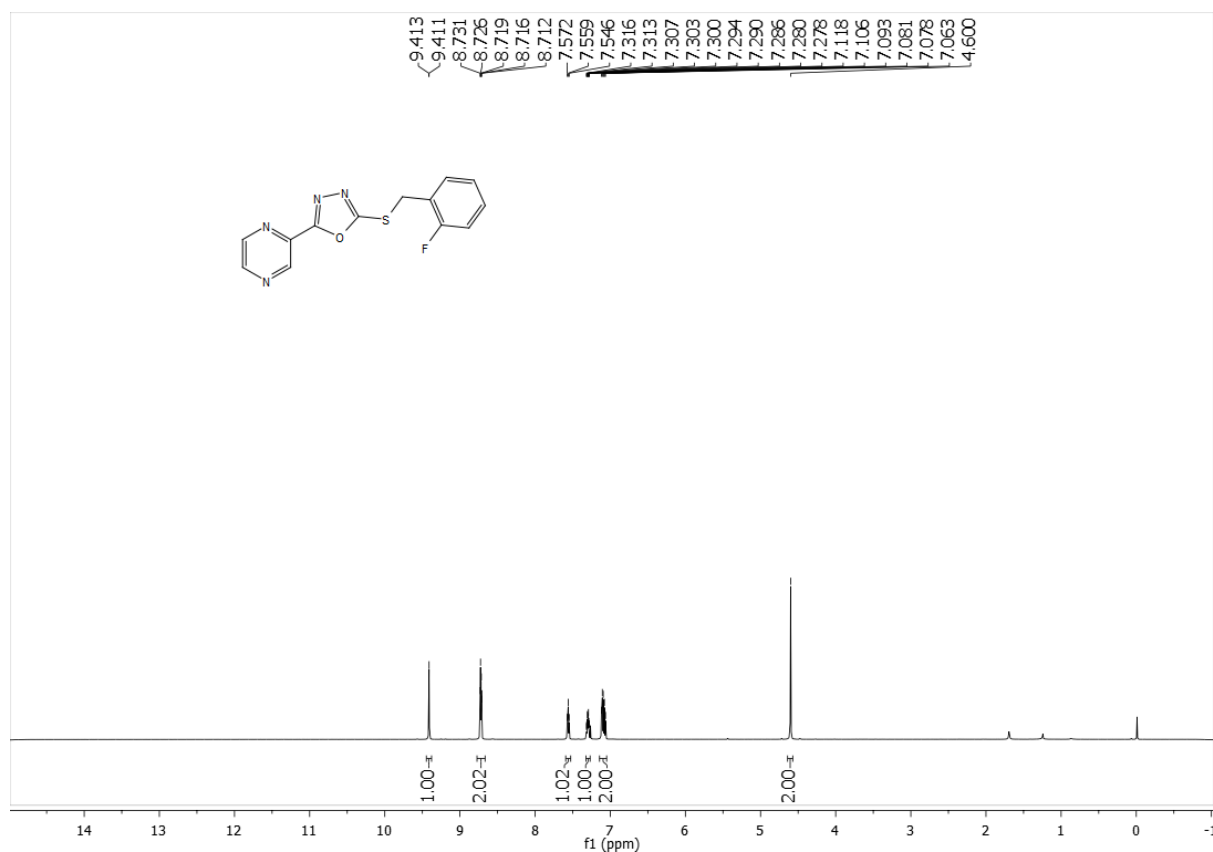
^1H NMR of compound **21** (400 MHz, CDCl_3):



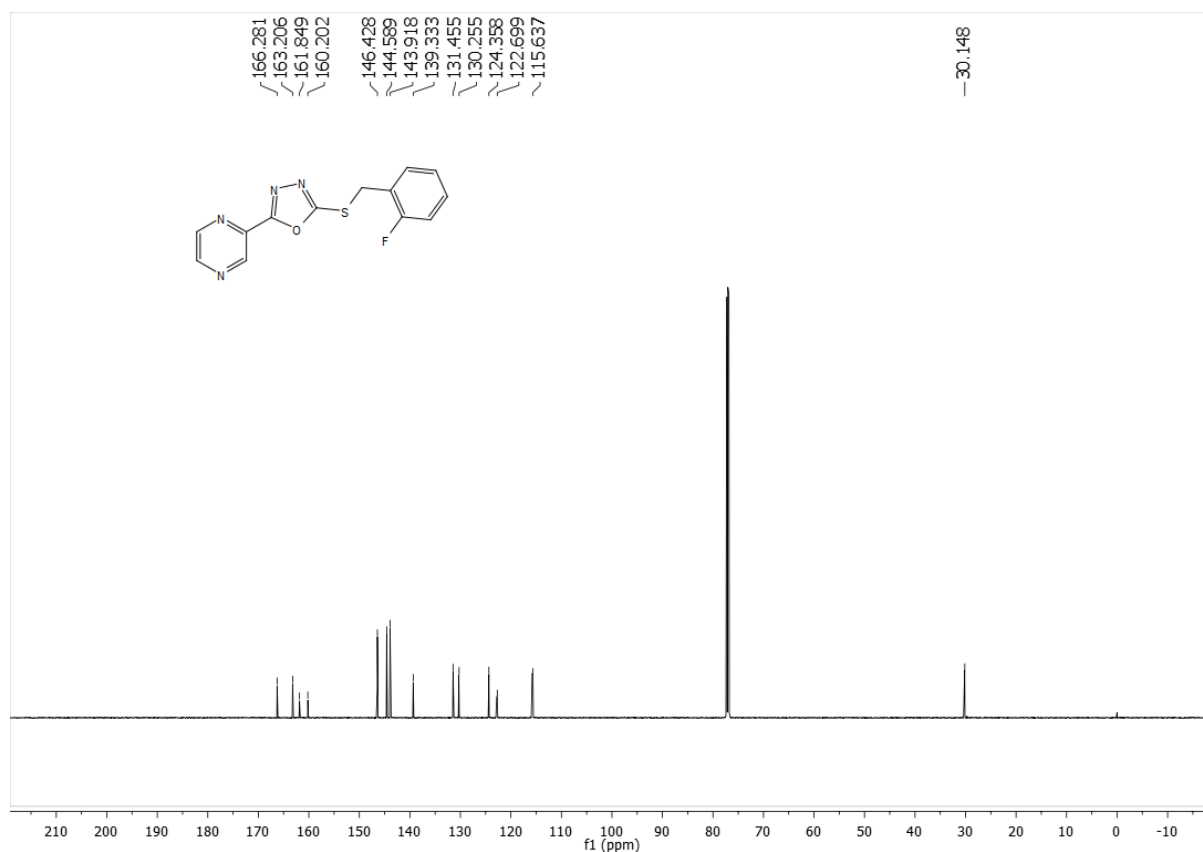
^{13}C NMR of compound **21** (100 MHz, CDCl_3):

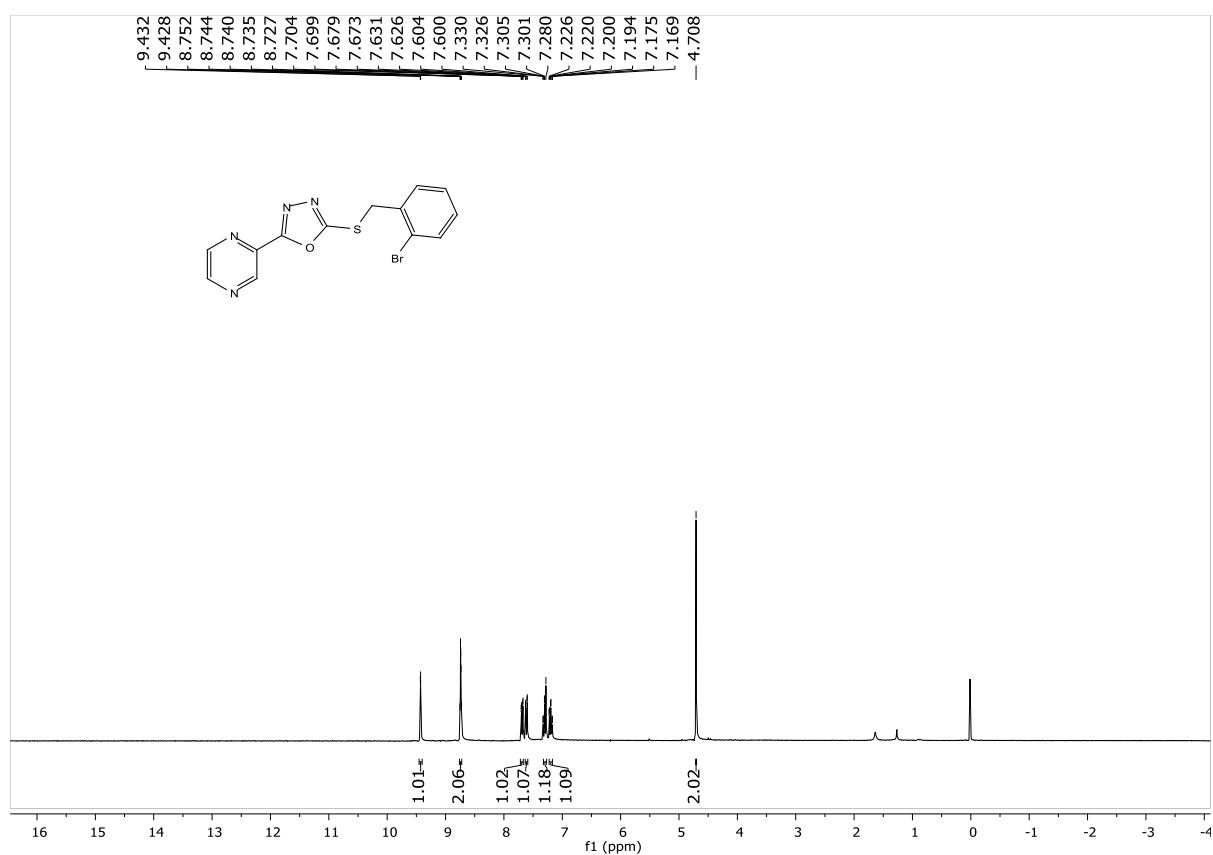
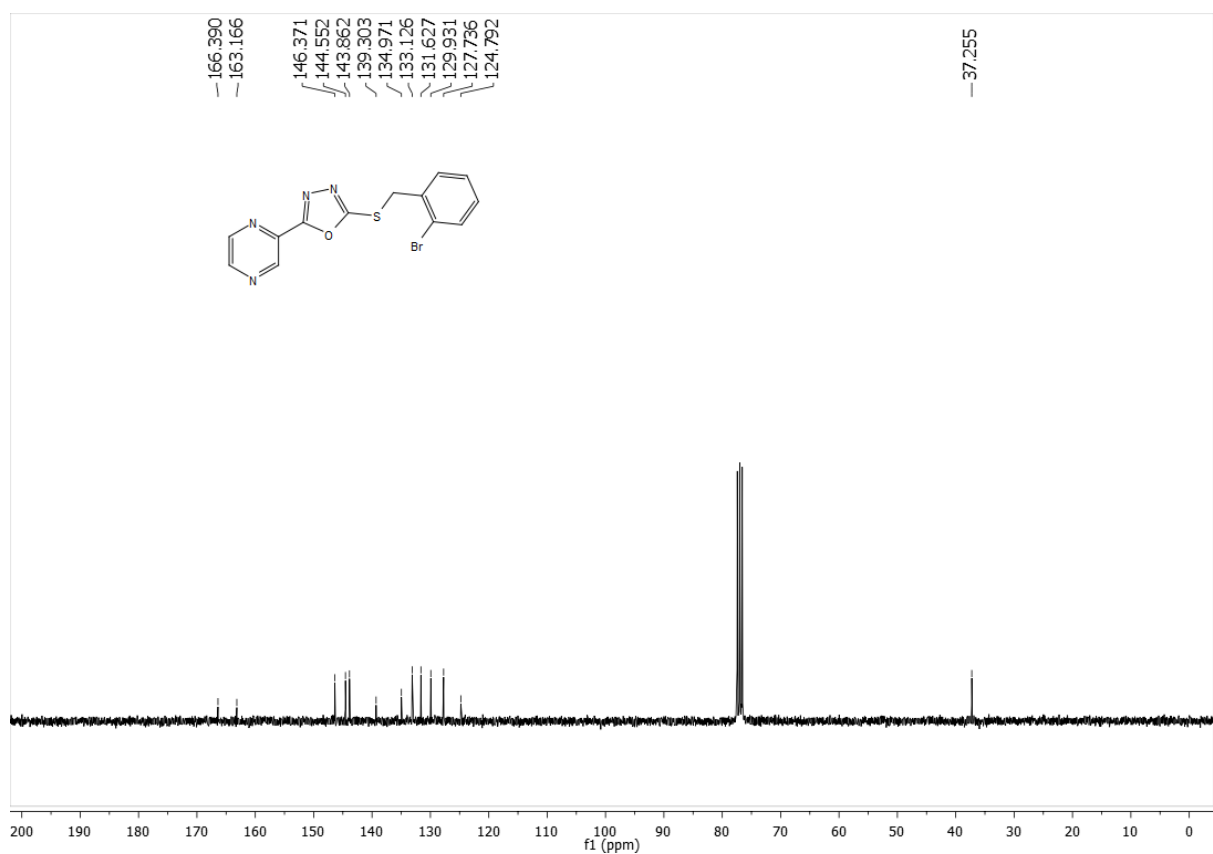


^1H NMR of compound **22** (600 MHz, CDCl_3):

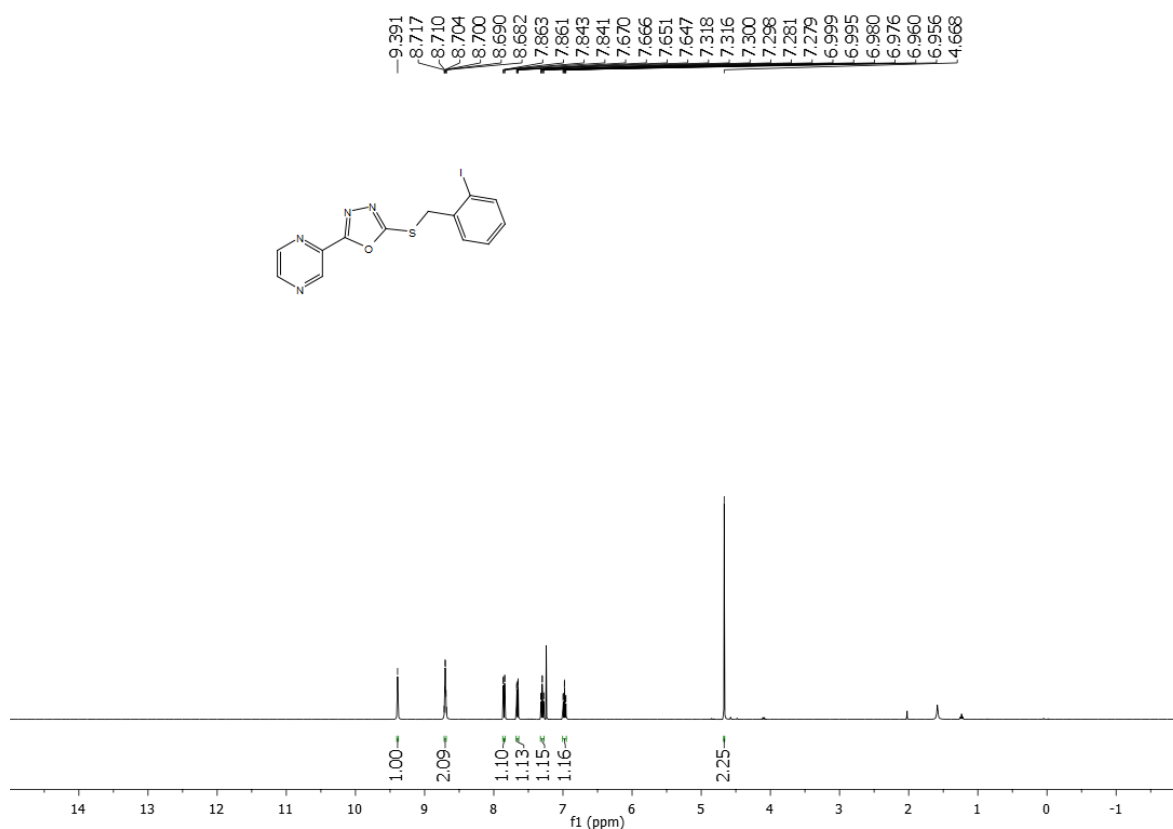


^{13}C NMR of compound **22** (150 MHz, CDCl_3):

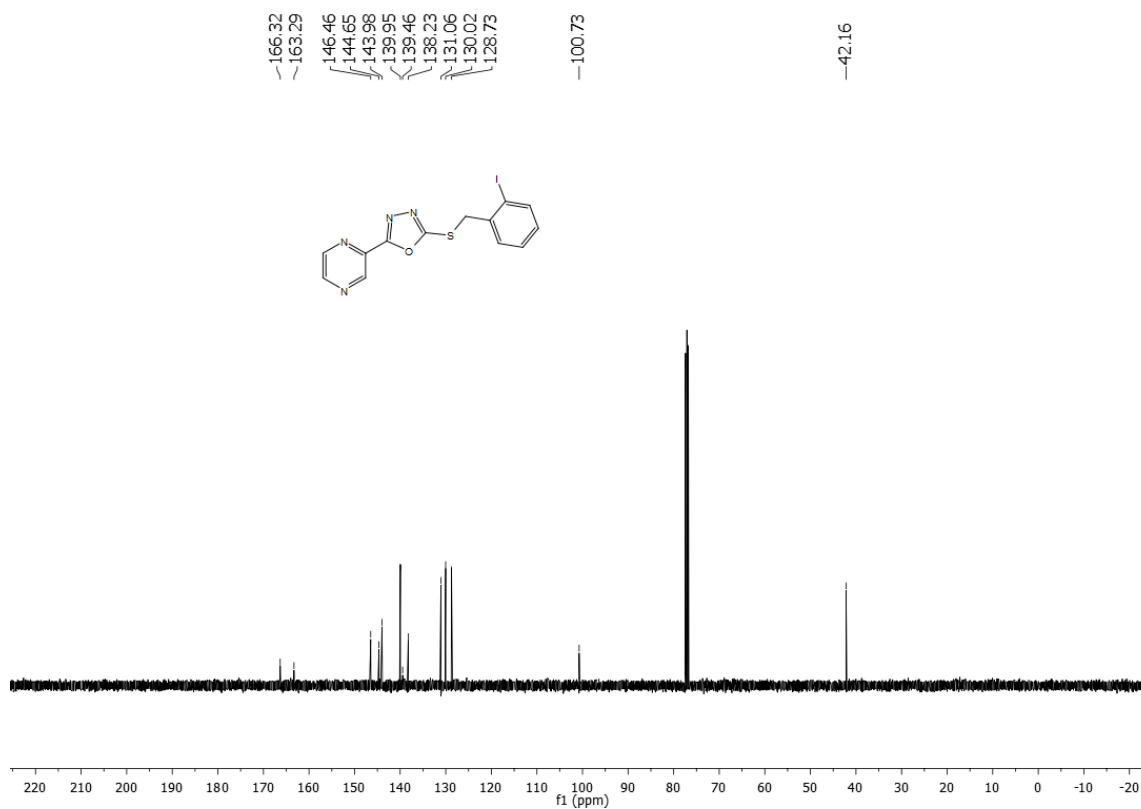


¹H NMR of compound **23** (300 MHz, CDCl₃):¹³C NMR of compound **23** (75 MHz, CDCl₃):

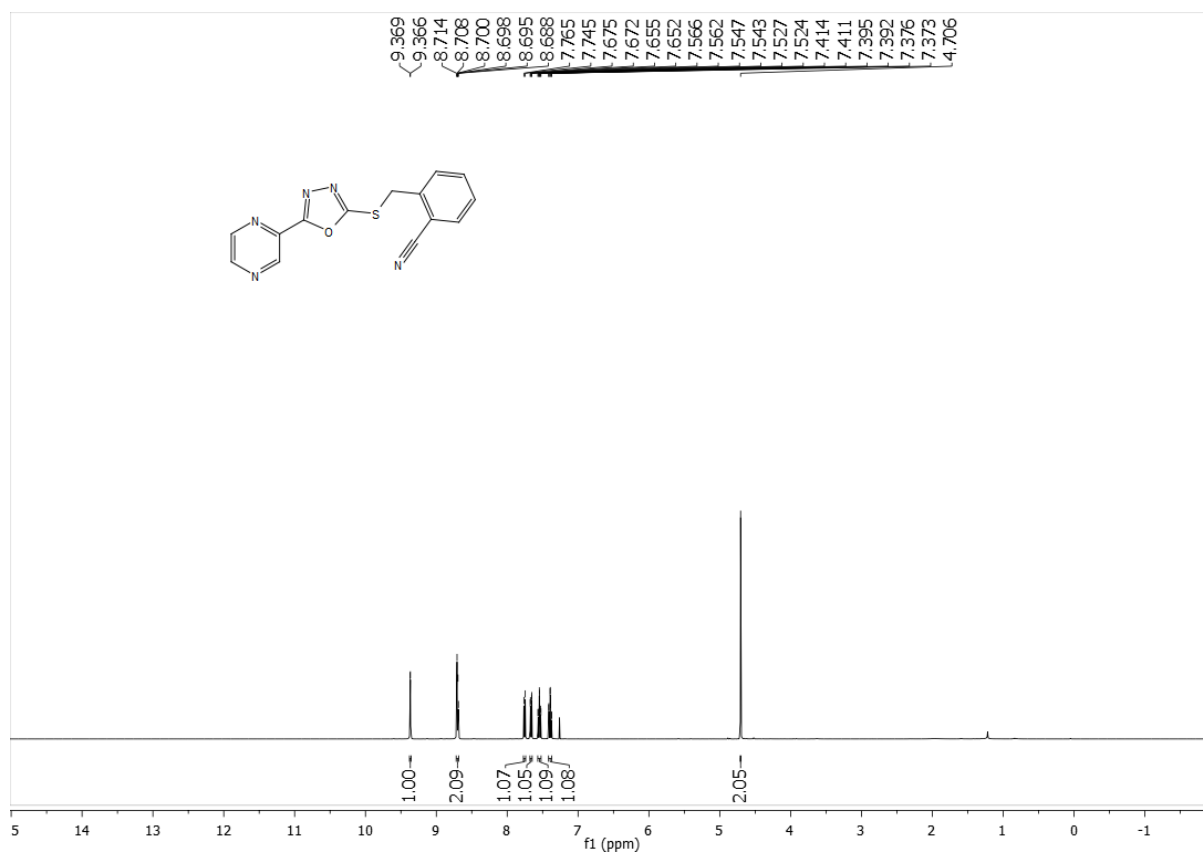
^1H NMR of compound **24** (400 MHz, CDCl_3):



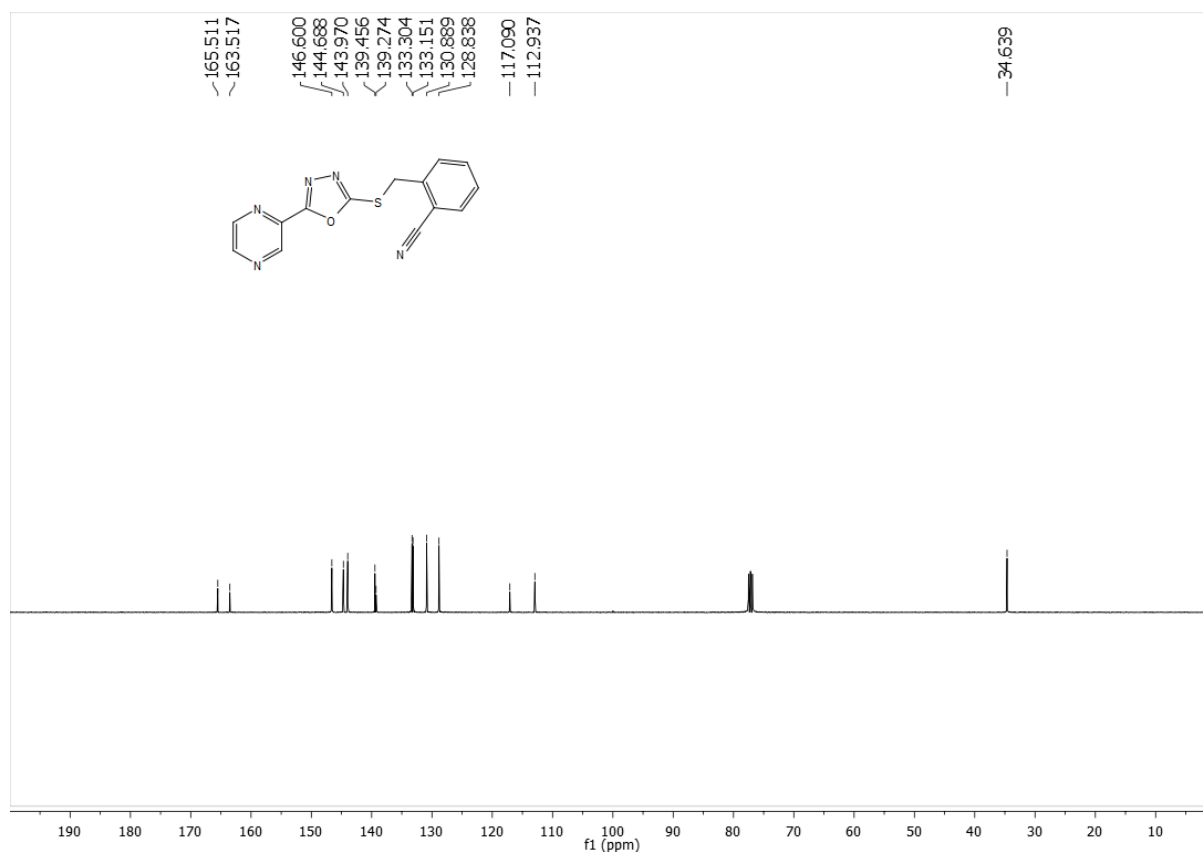
^{13}C NMR of compound **24** (100 MHz, CDCl_3):



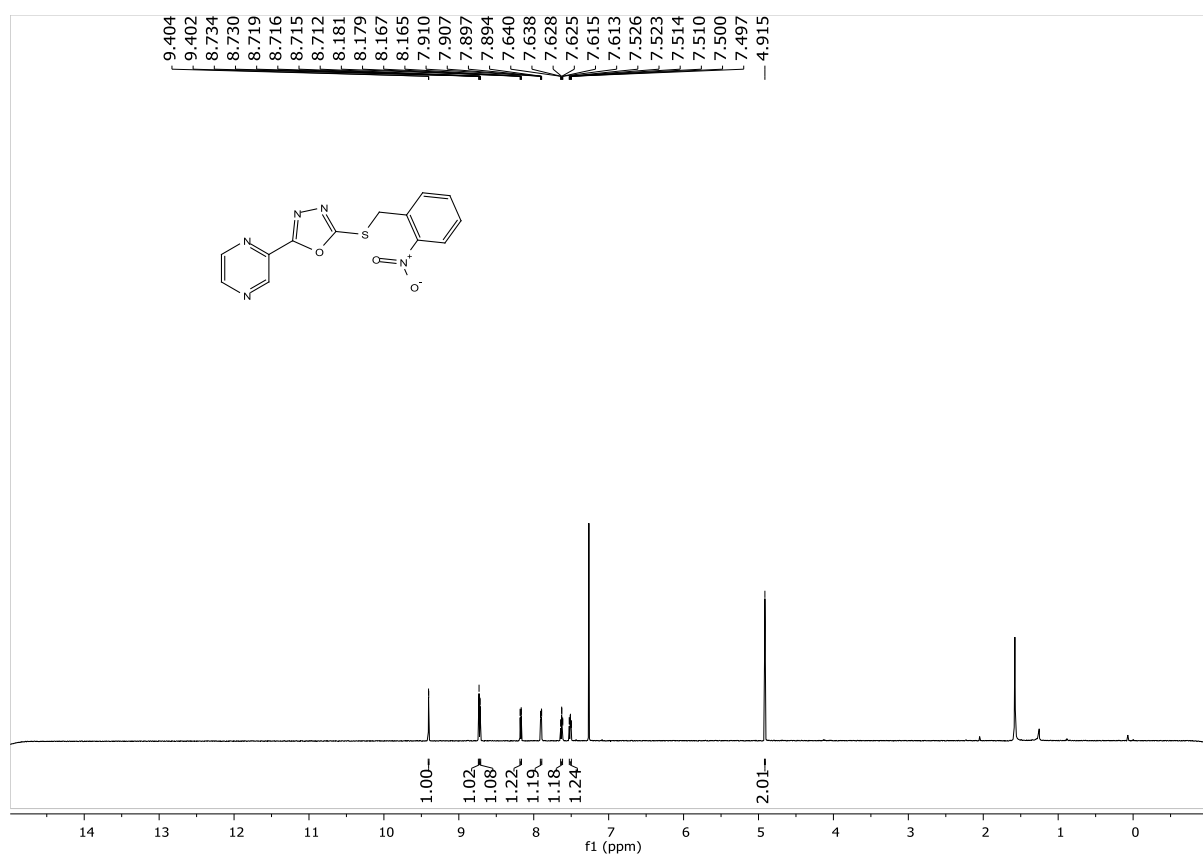
^1H NMR of compound **25** (400 MHz, CDCl_3):



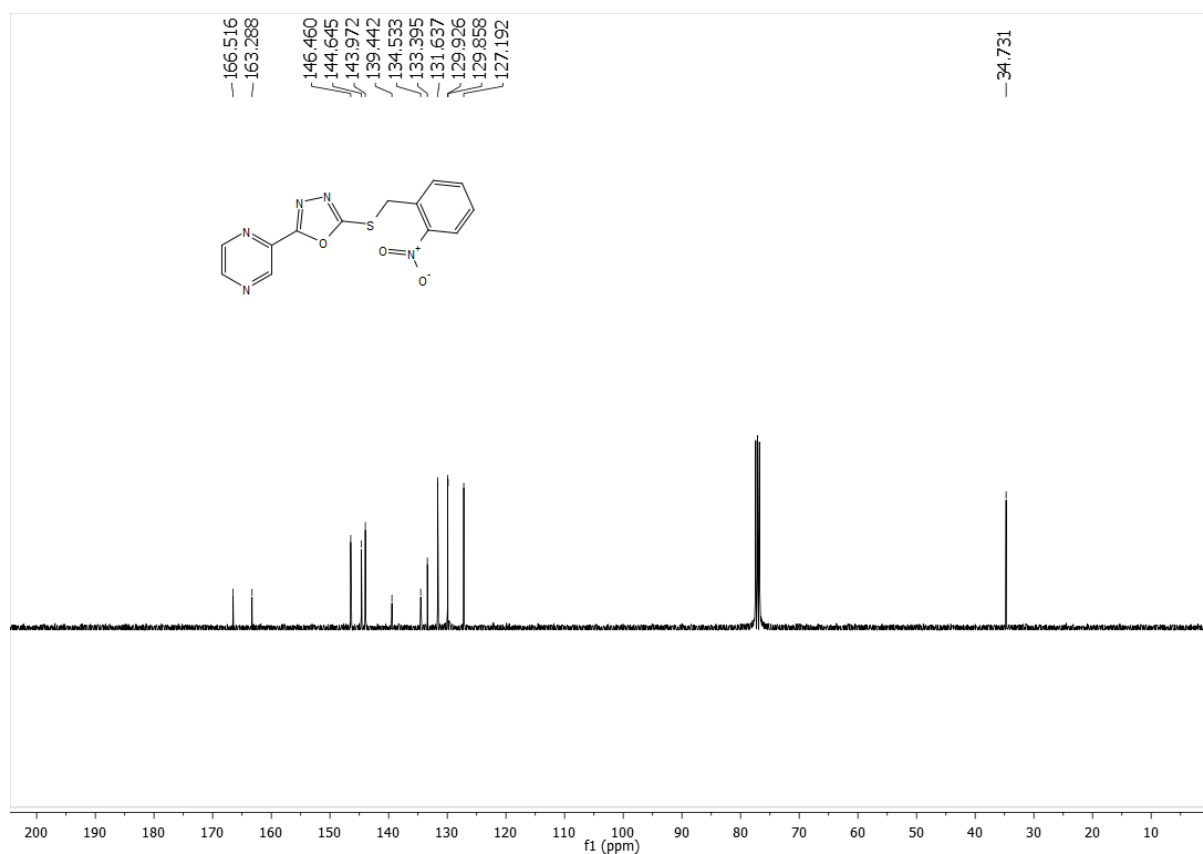
^{13}C NMR of compound **25** (100 MHz, CDCl_3):



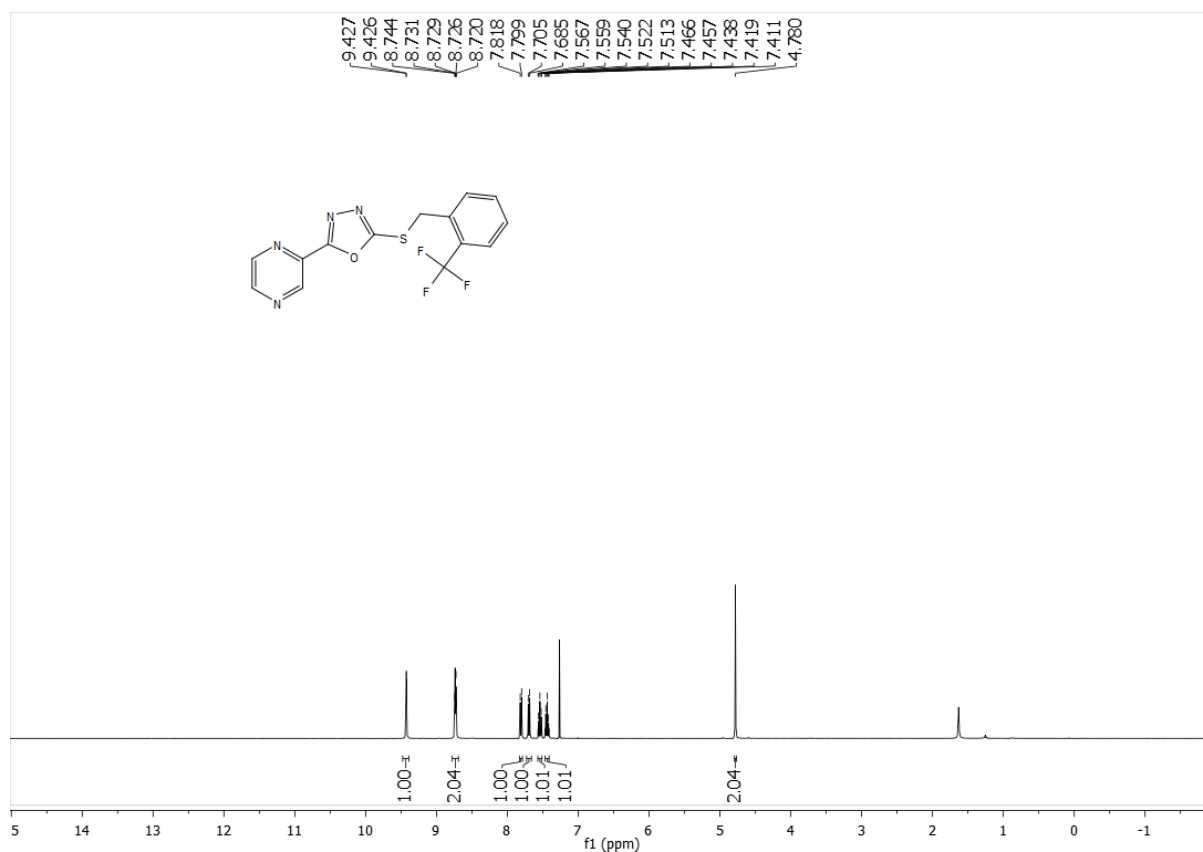
^1H NMR of compound **26** (600 MHz, CDCl_3):



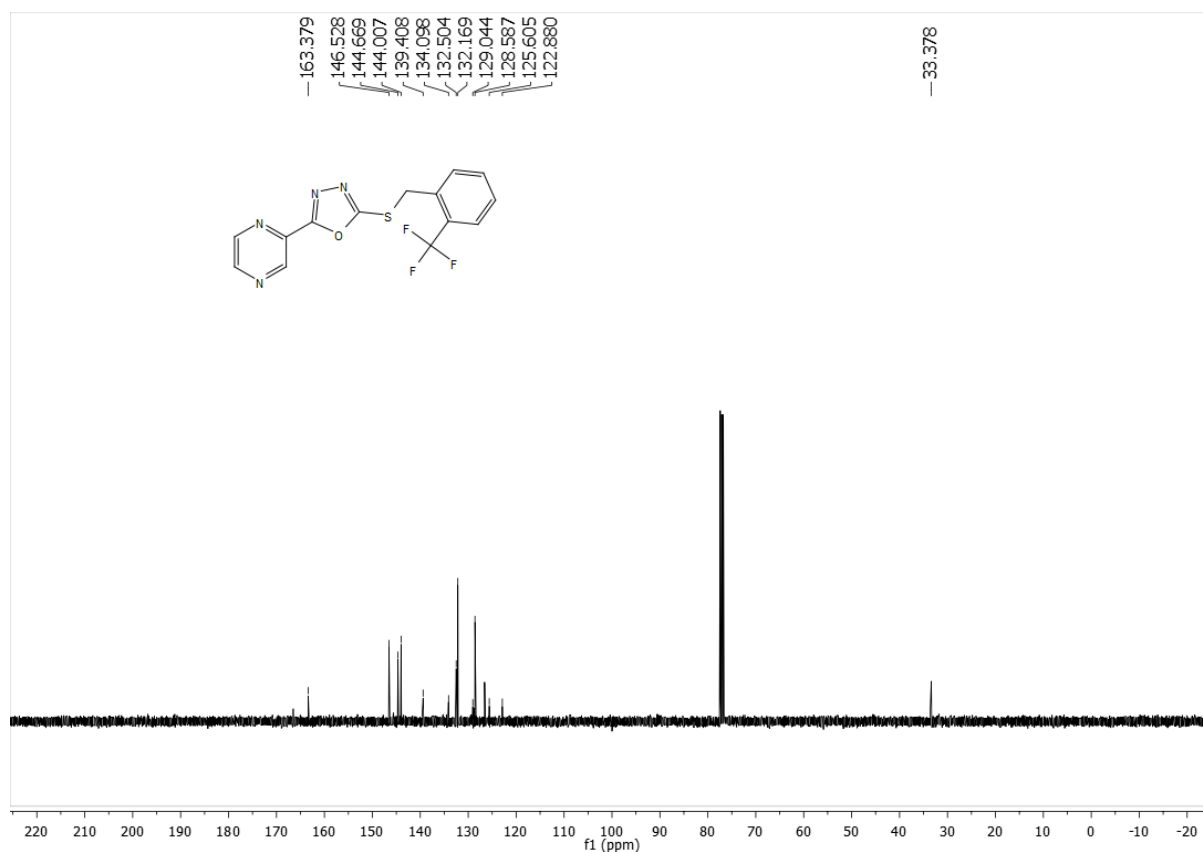
^{13}C NMR of compound **26** (100 MHz, CDCl_3):



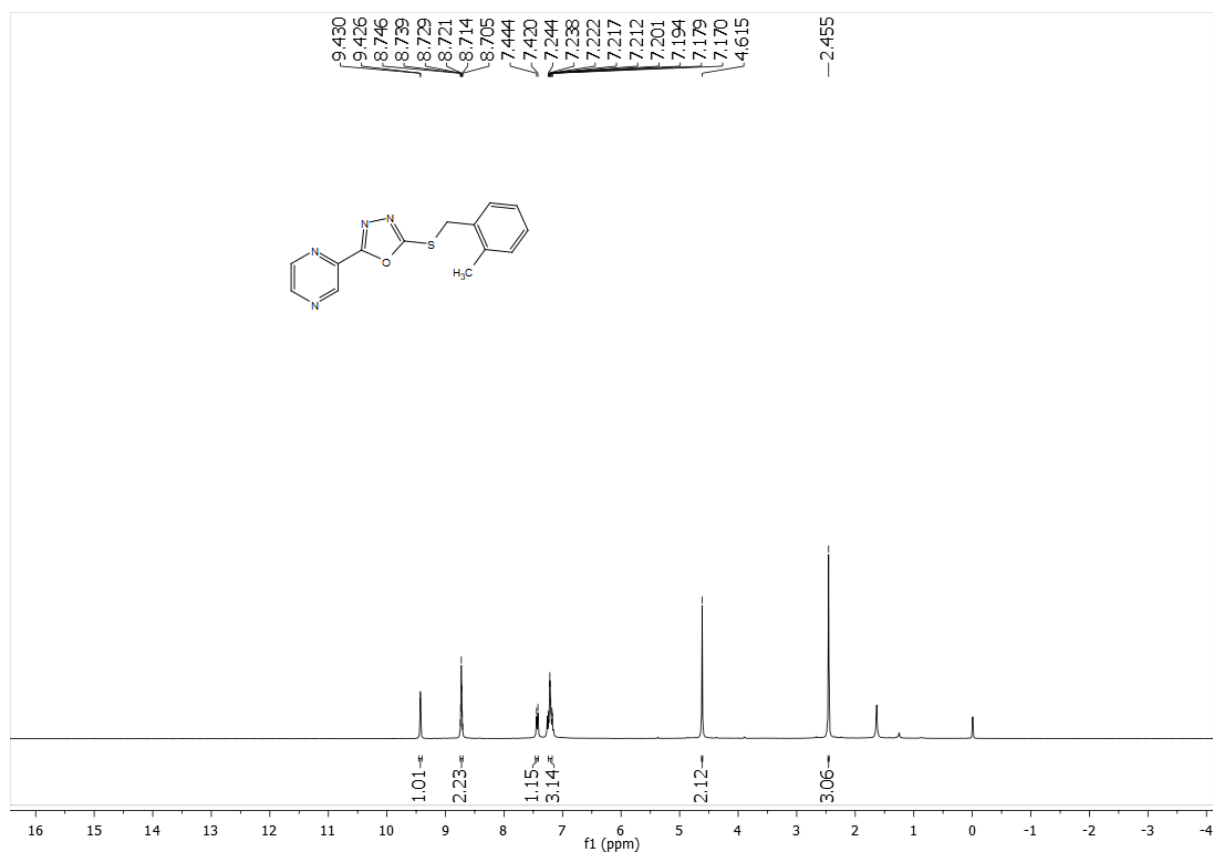
^1H NMR of compound **27** (400 MHz, CDCl_3):



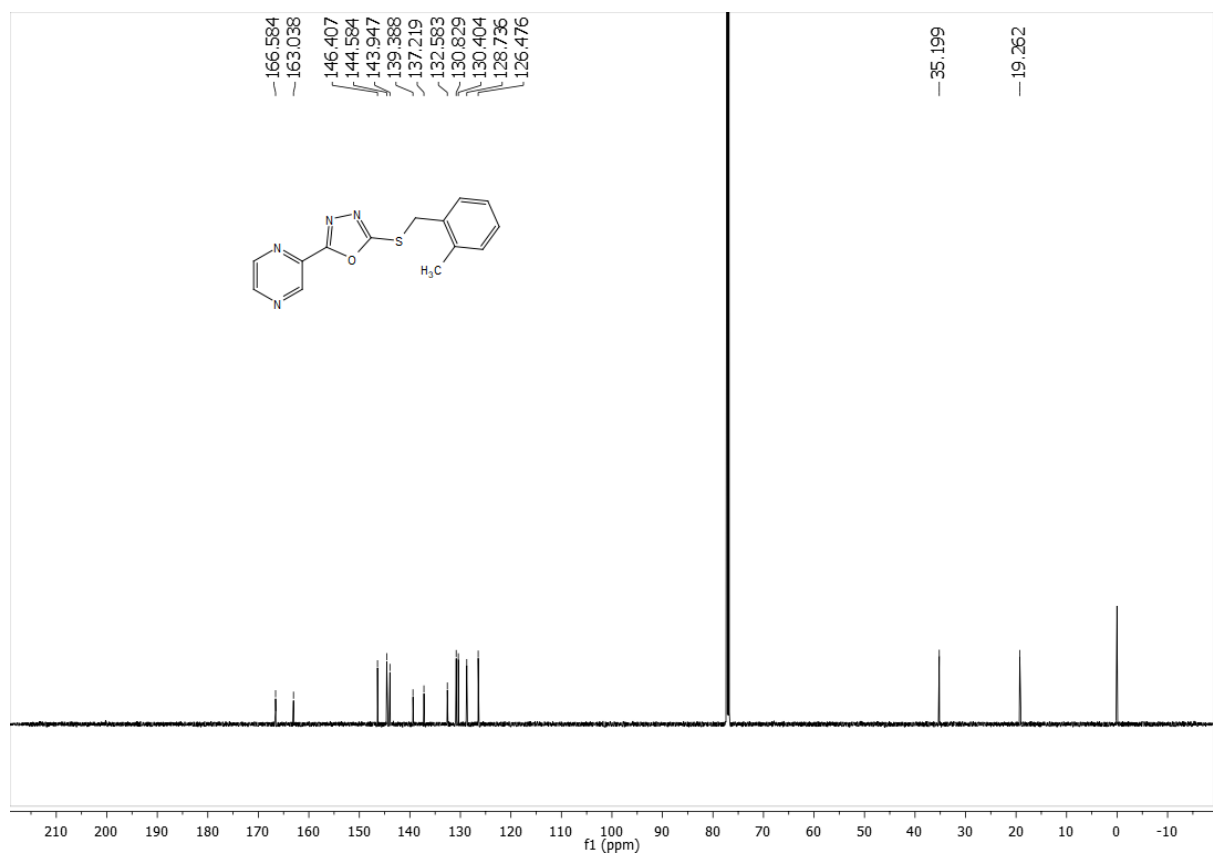
^{13}C NMR of compound **27** (100 MHz, CDCl_3):



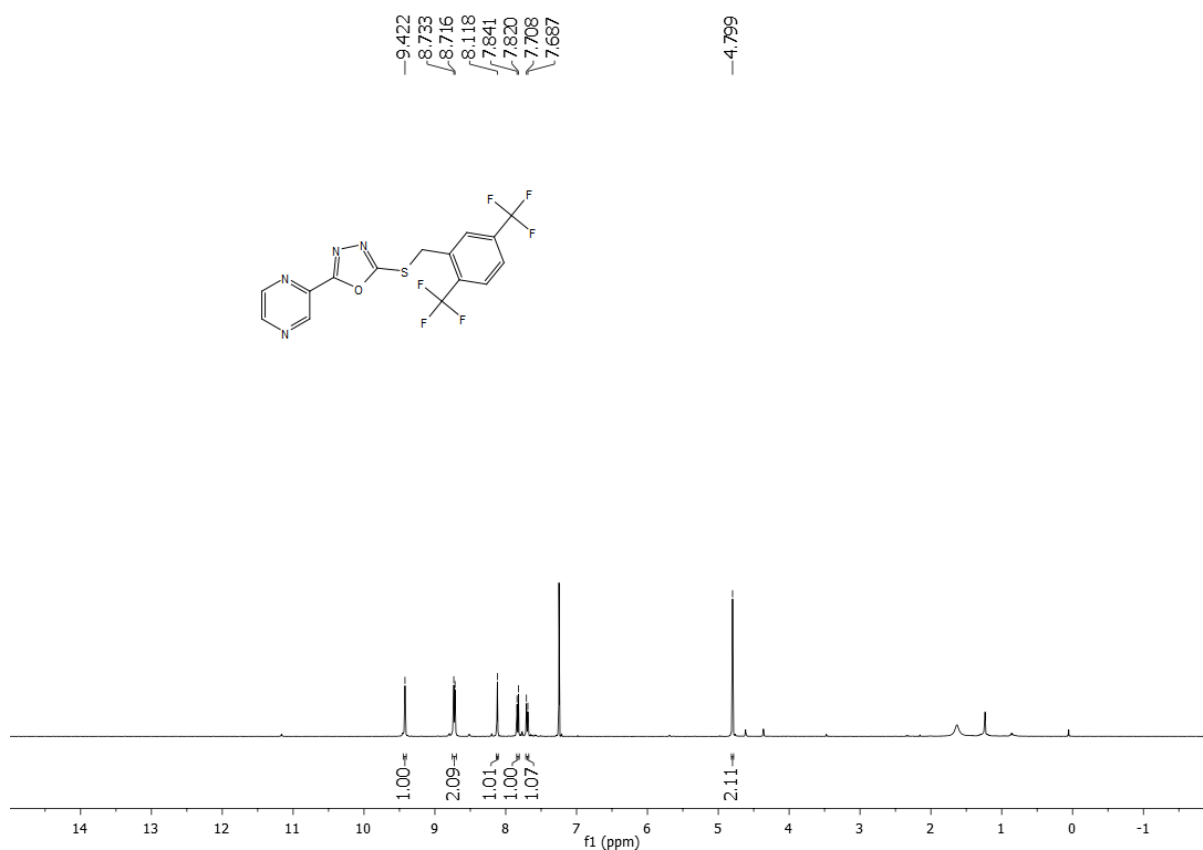
^1H NMR of compound **28** (300 MHz, CDCl_3):



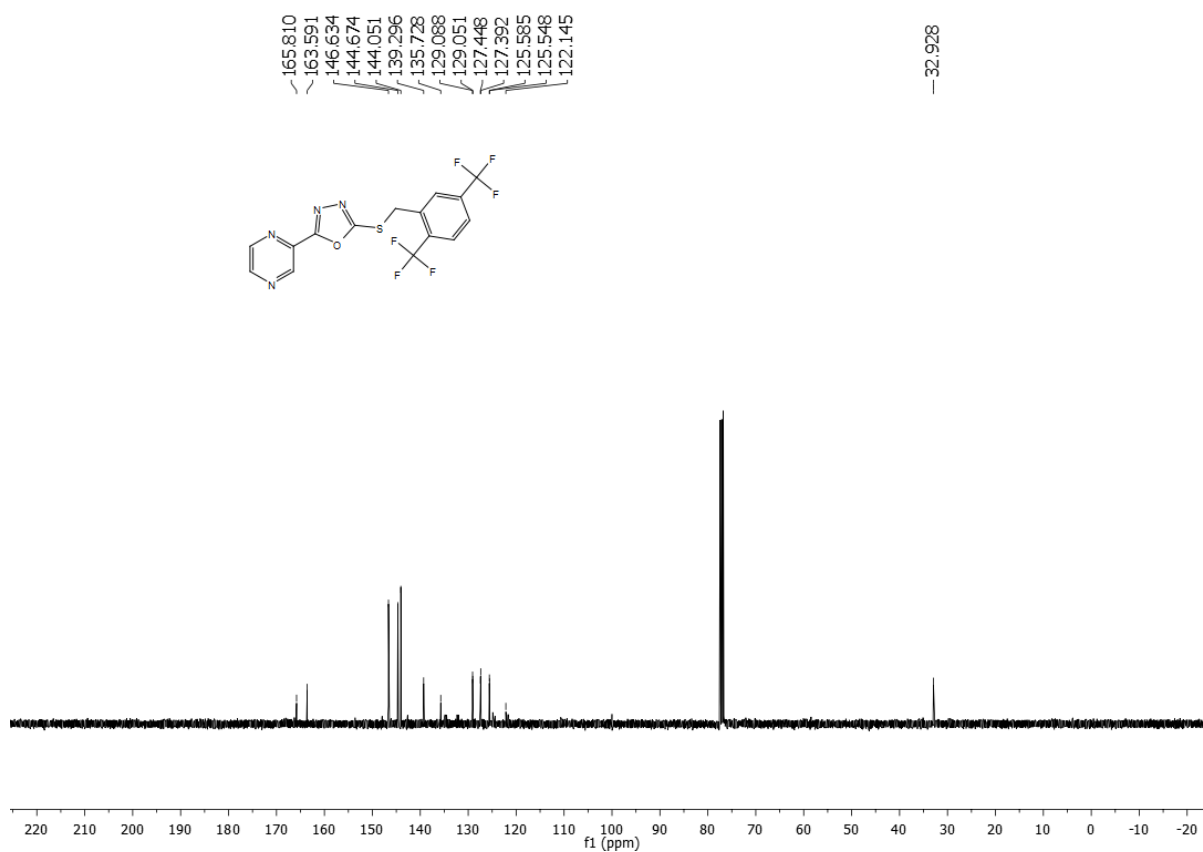
^{13}C NMR of compound **28** (150 MHz, CDCl_3):



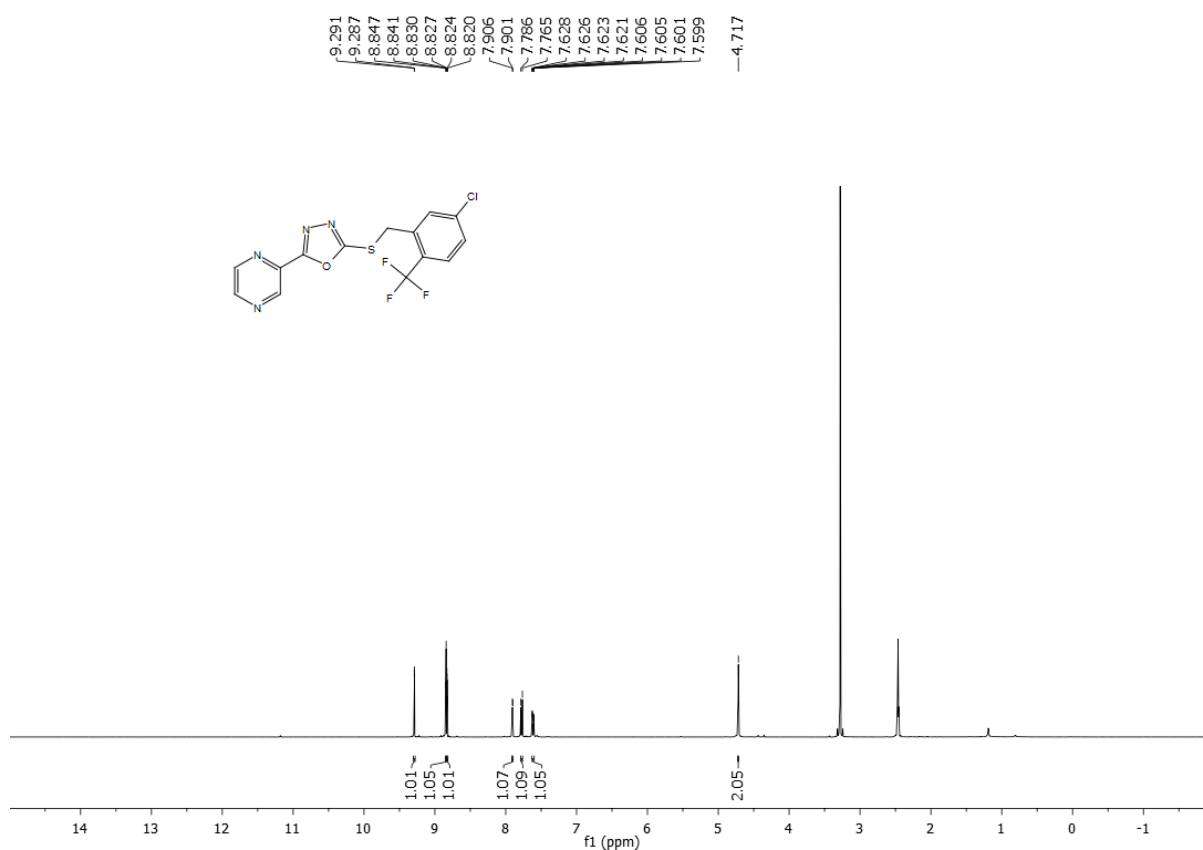
^1H NMR of compound **29** (400 MHz, CDCl_3):



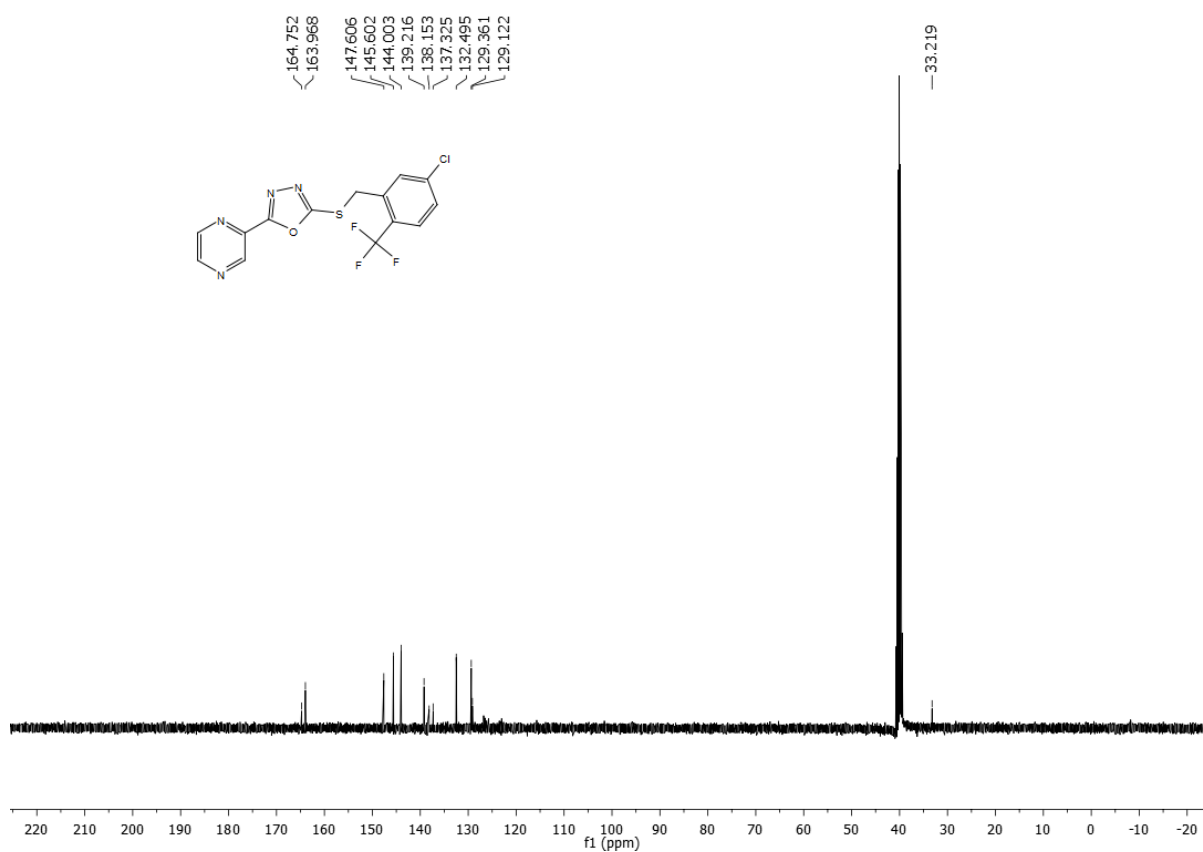
^{13}C NMR of compound **29** (100 MHz, CDCl_3):



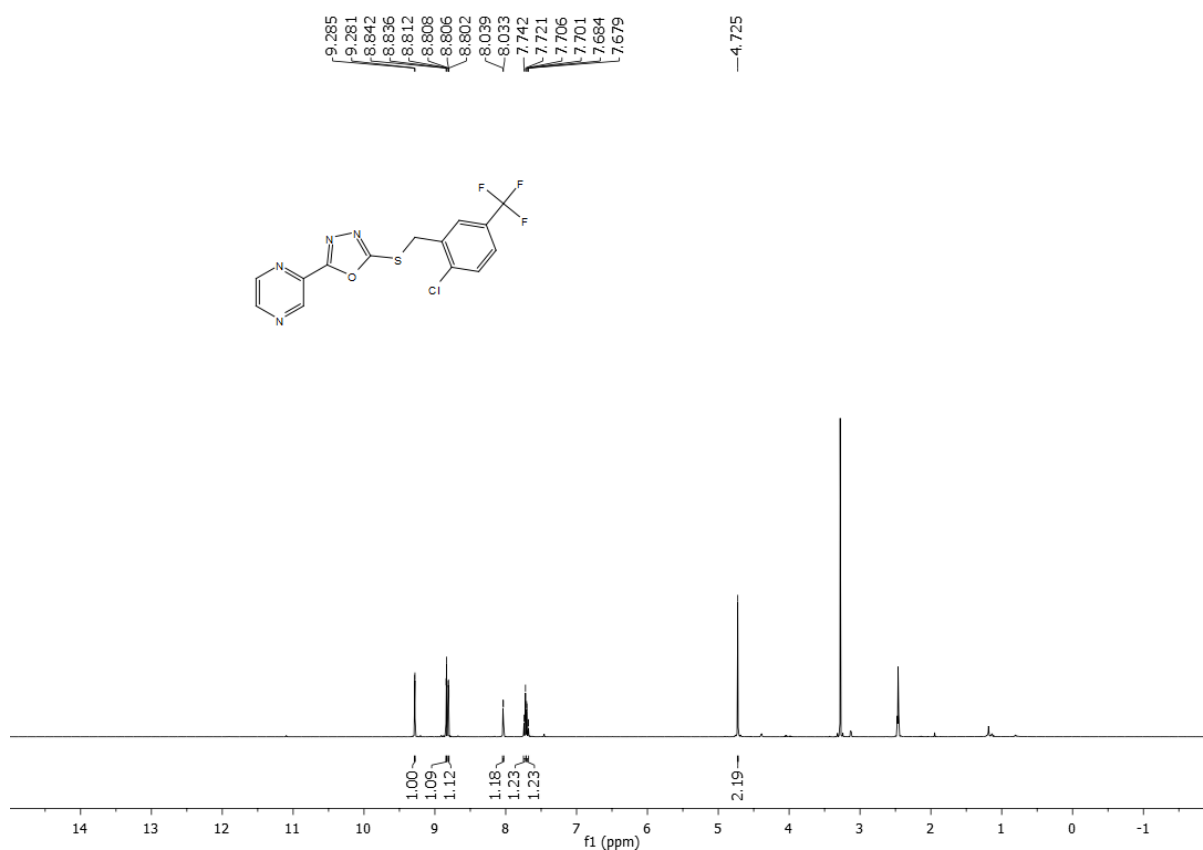
^1H NMR of compound **30** (400 MHz, d_6 -DMSO):



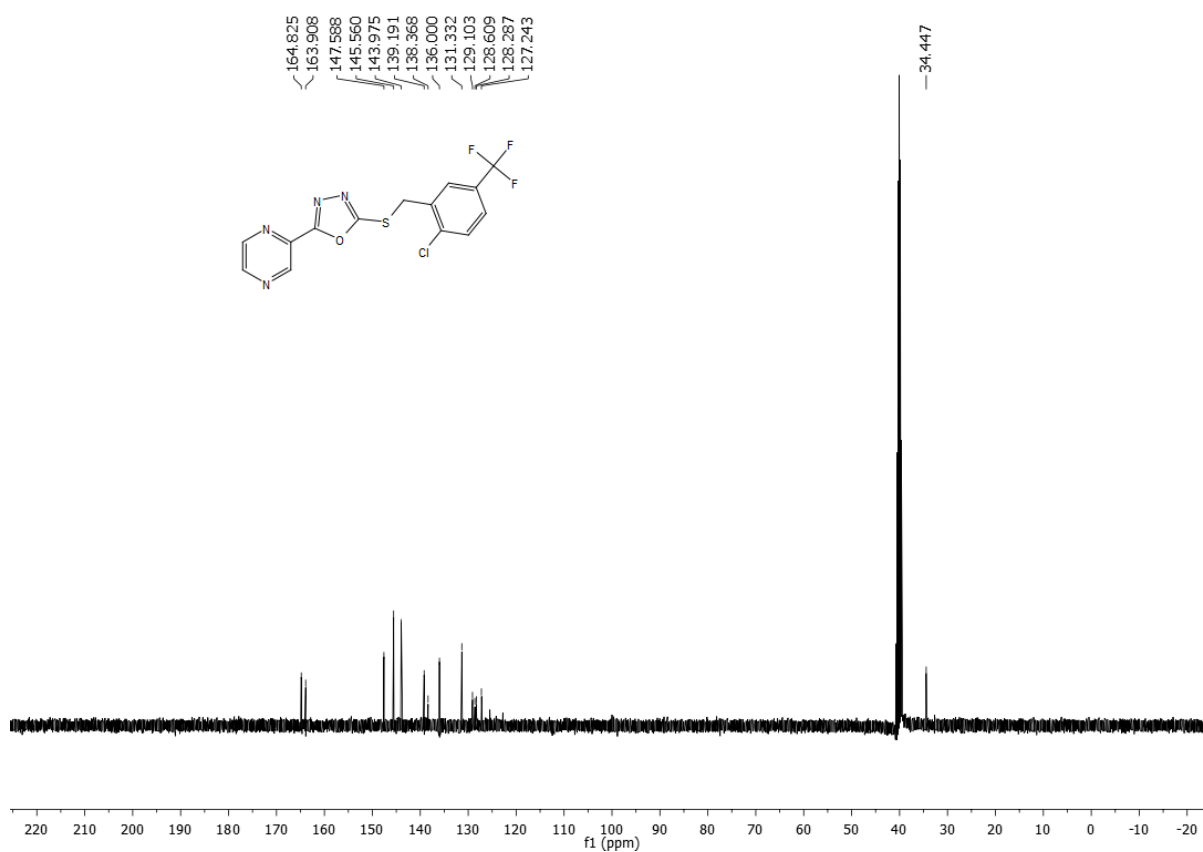
^{13}C NMR of compound **30** (100 MHz, d_6 -DMSO):



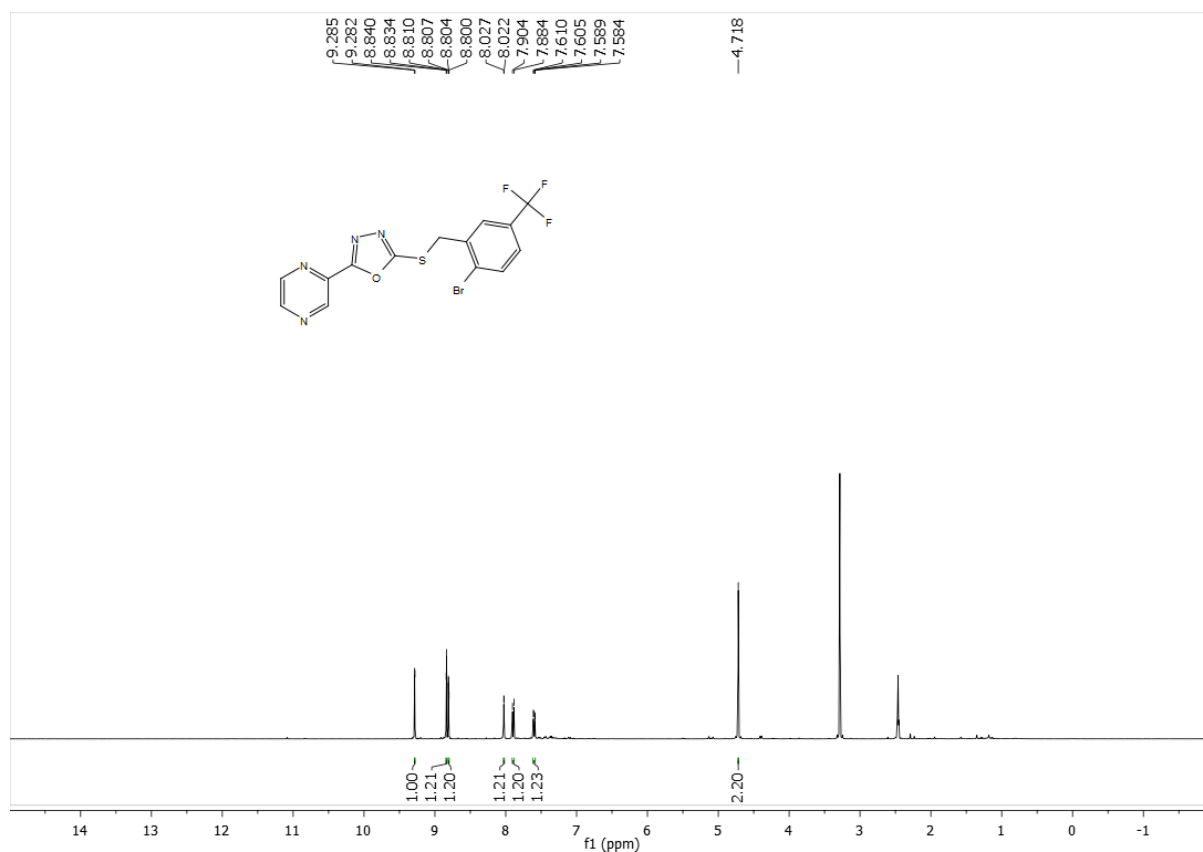
^1H NMR of compound **31** (400 MHz, d_6 -DMSO):



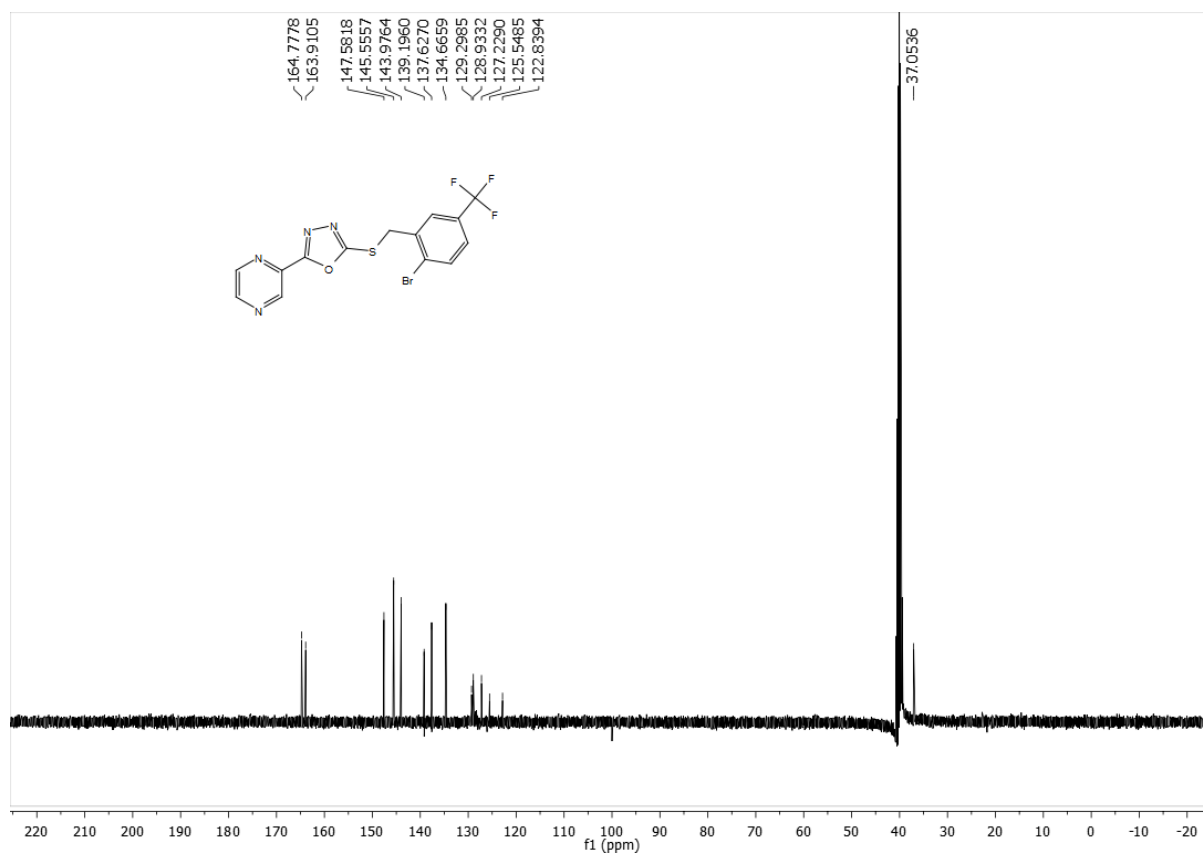
^{13}C NMR of compound **31** (100 MHz, d_6 -DMSO):



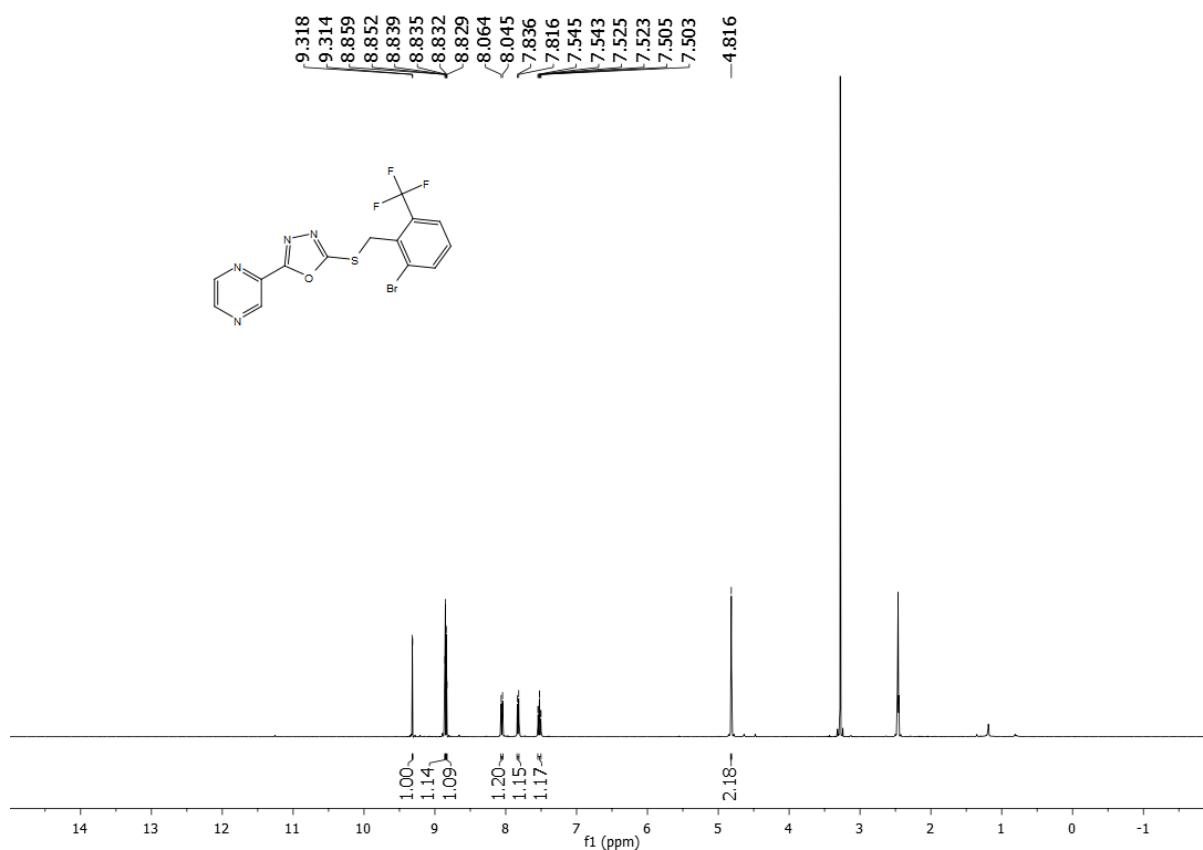
^1H NMR of compound **32** (400 MHz, d_6 -DMSO):



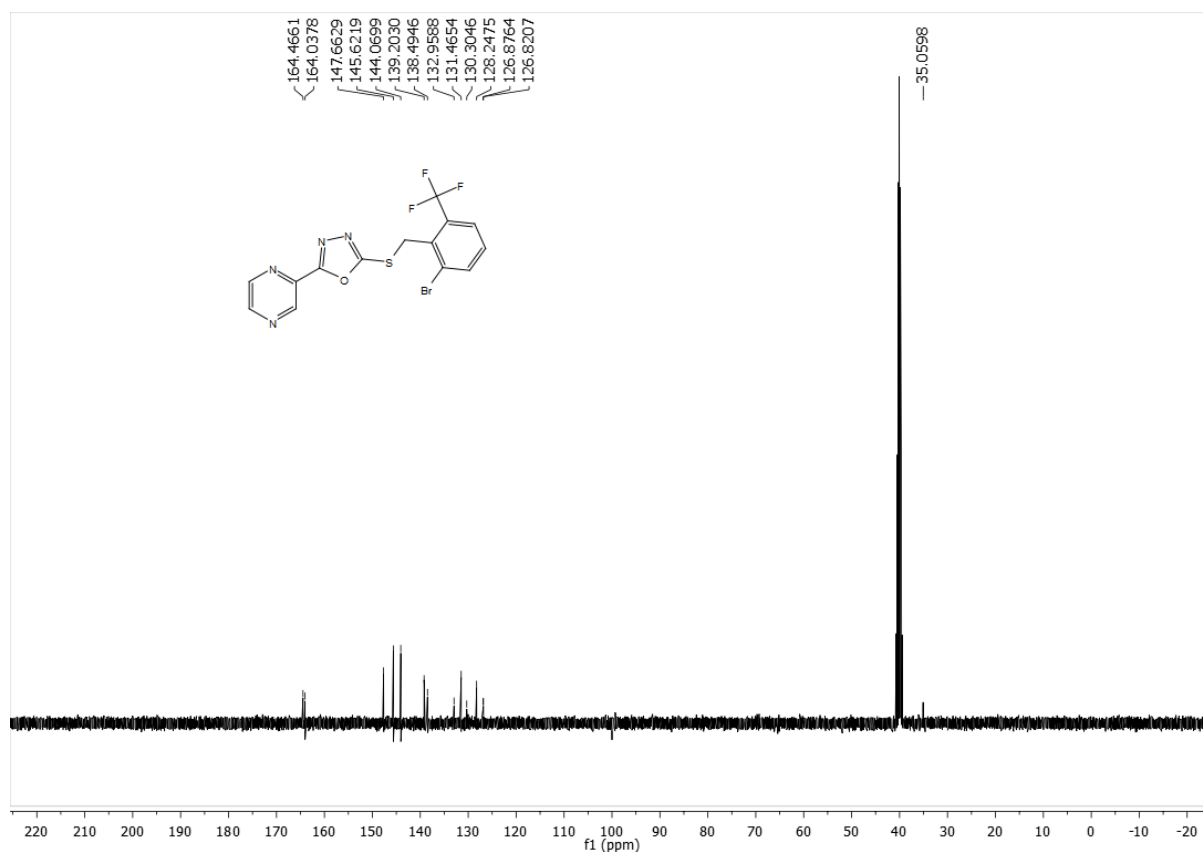
^{13}C NMR of compound **32** (100 MHz, d_6 -DMSO):



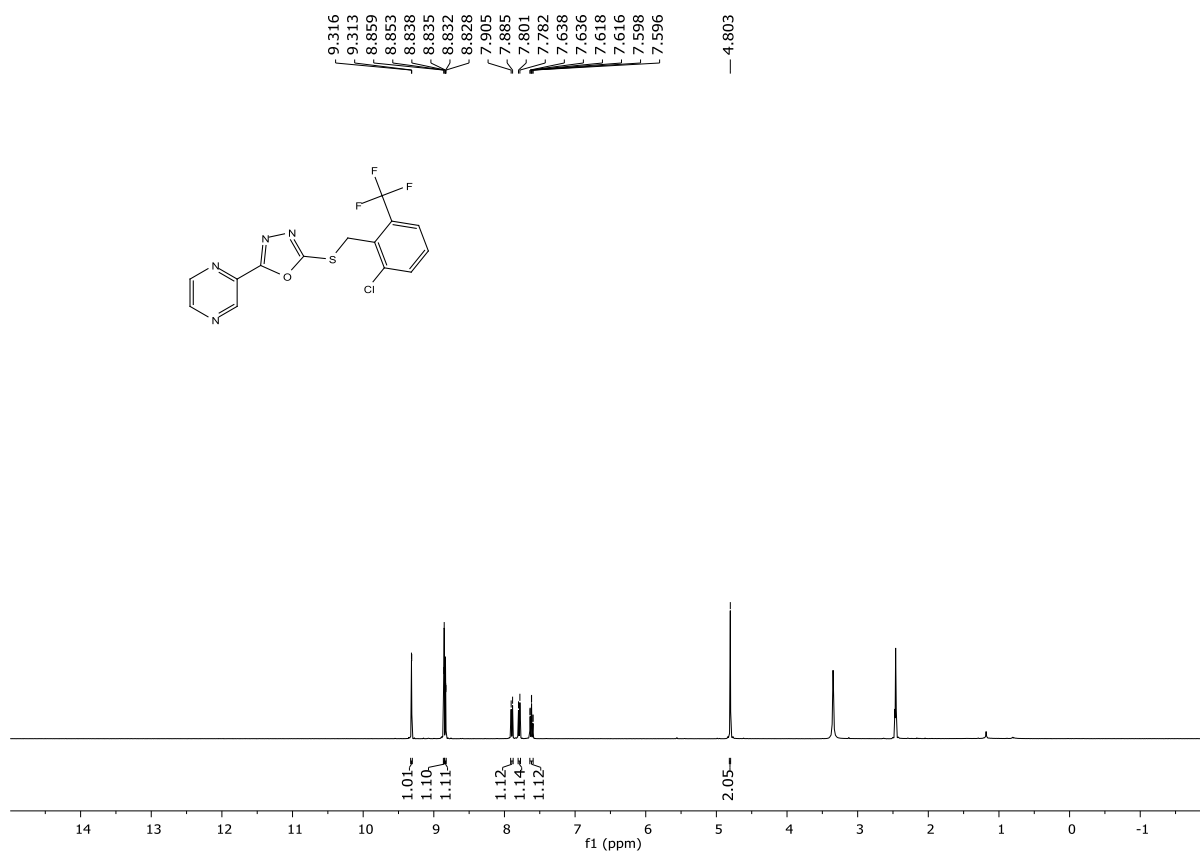
^1H NMR of compound **33** (400 MHz, d_6 -DMSO):



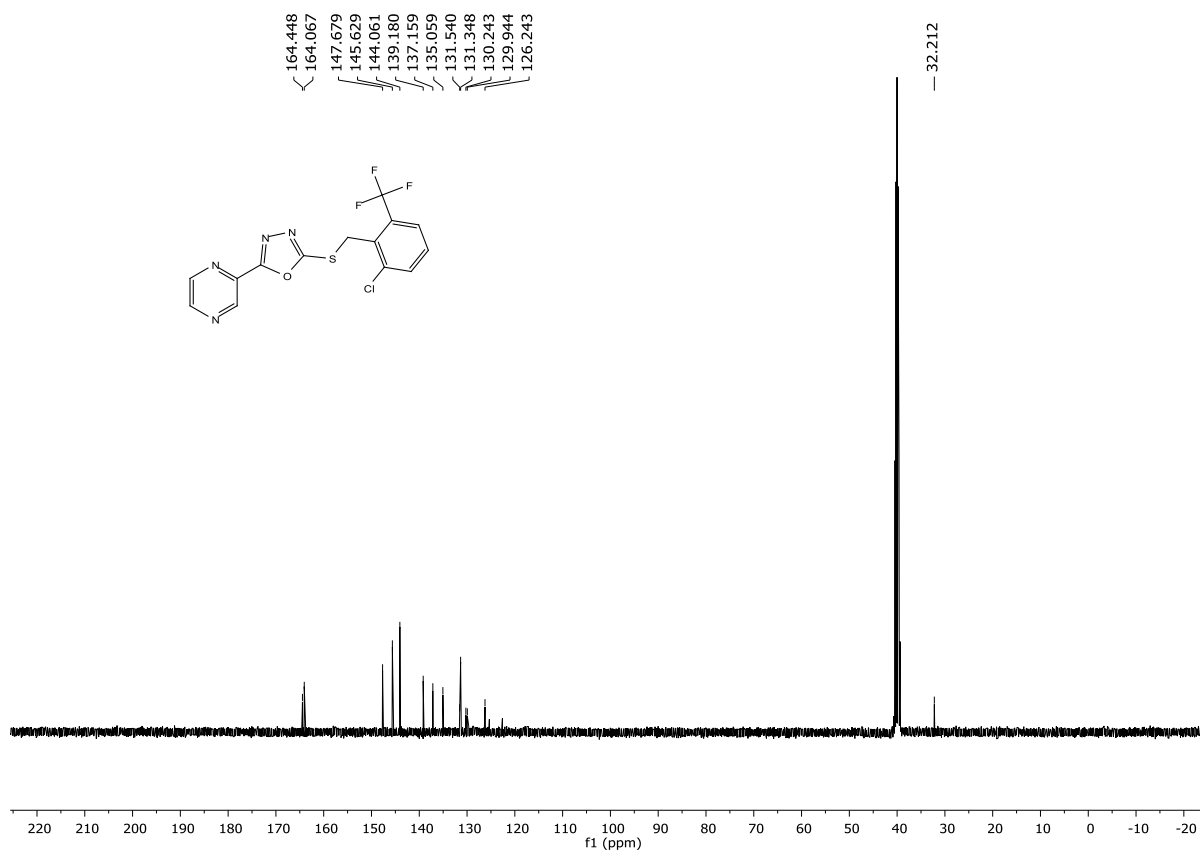
^{13}C NMR of compound **33** (100 MHz, d_6 -DMSO):



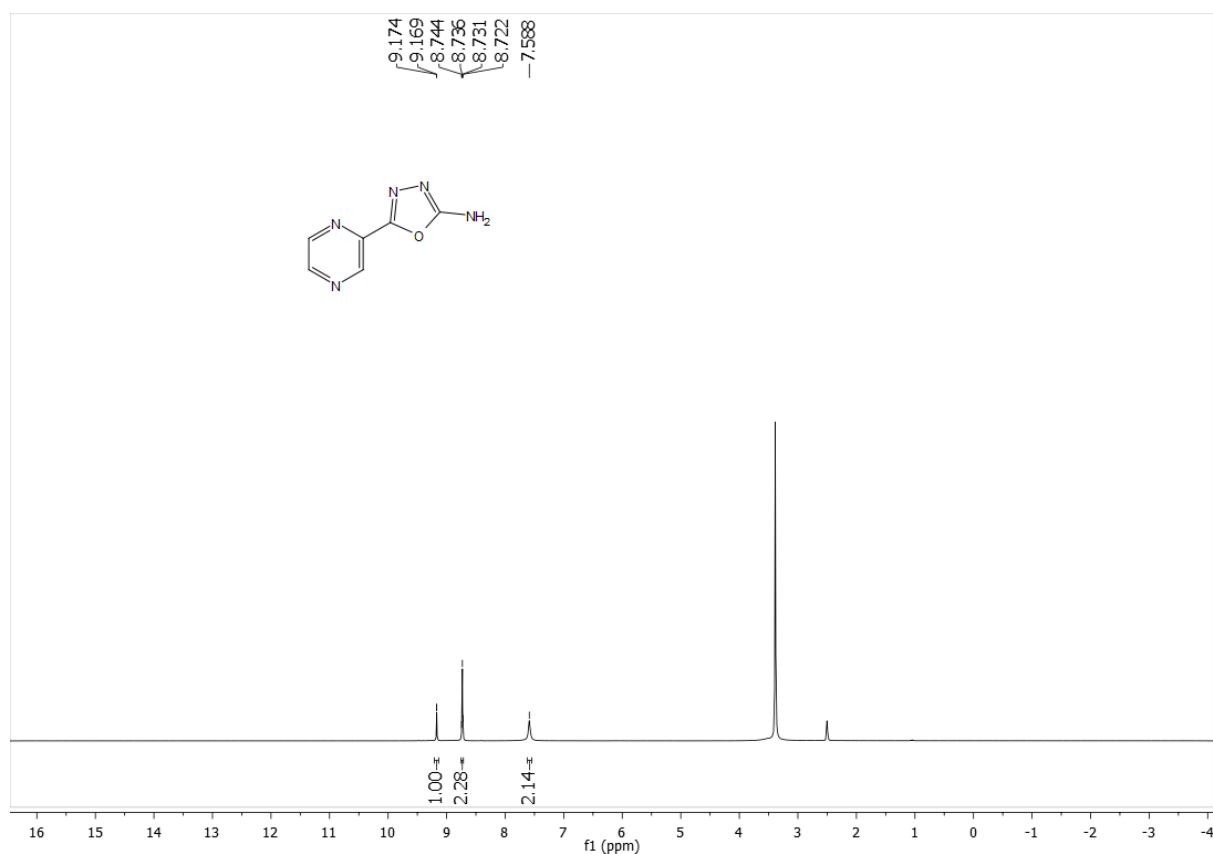
^1H NMR of compound **34** (400 MHz, d_6 -DMSO):



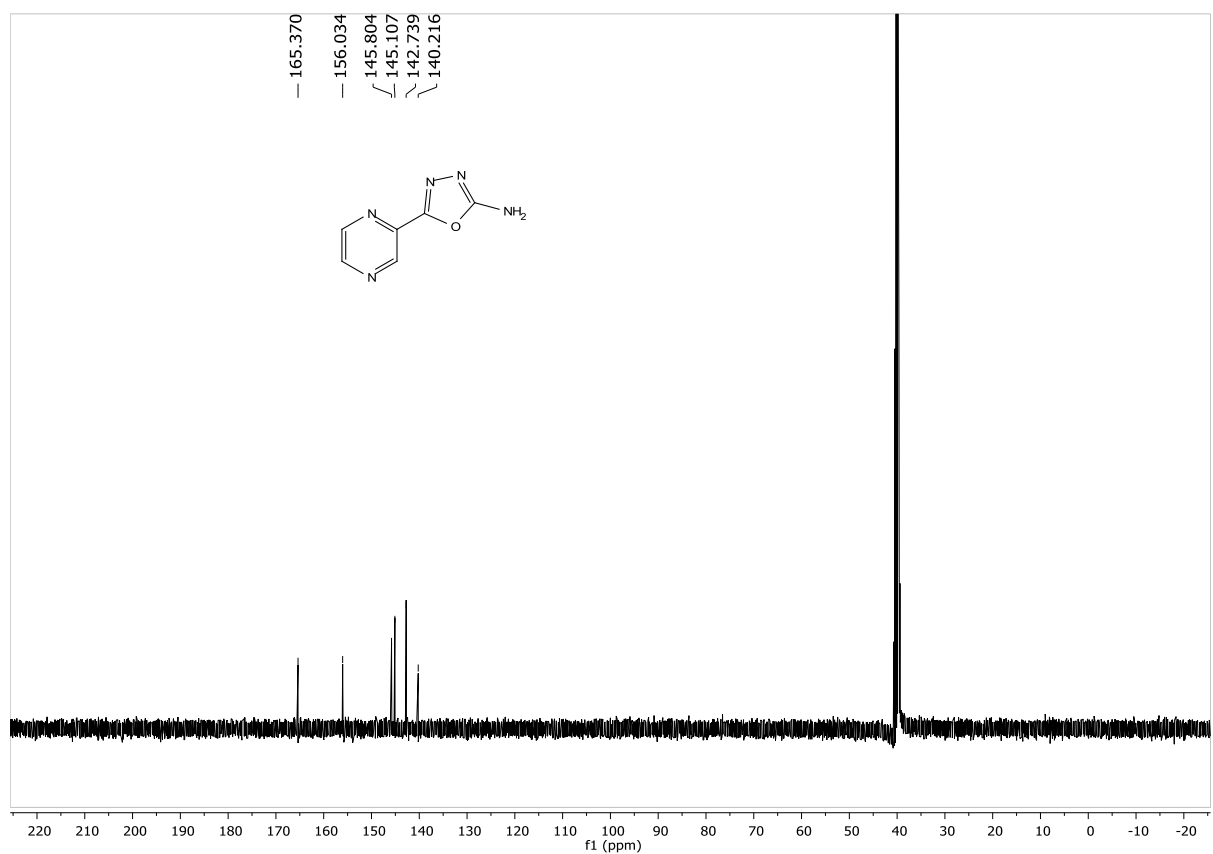
^{13}C NMR of compound **34** (100 MHz, d_6 -DMSO):



^1H NMR of compound **35** (300 MHz, d_6 -DMSO):



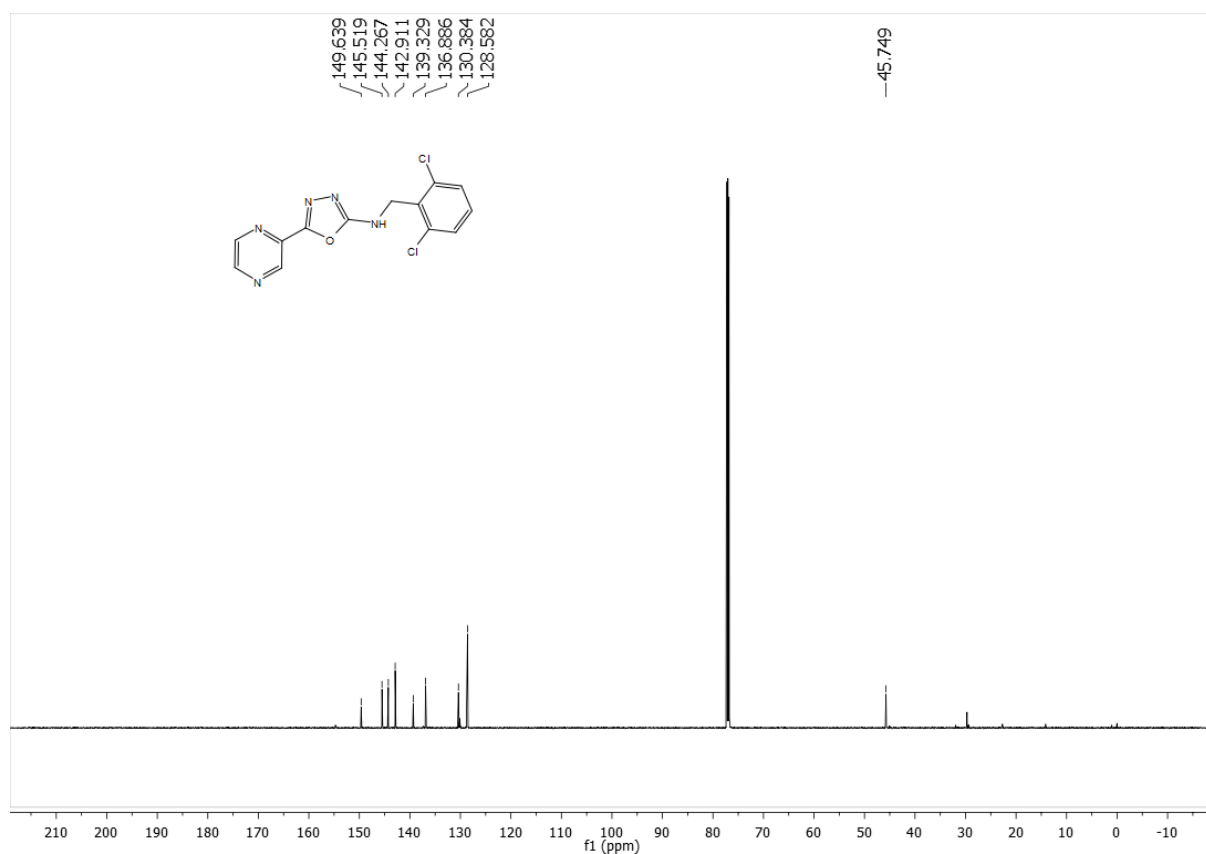
^{13}C NMR of compound **35** (75 MHz, d_6 -DMSO):



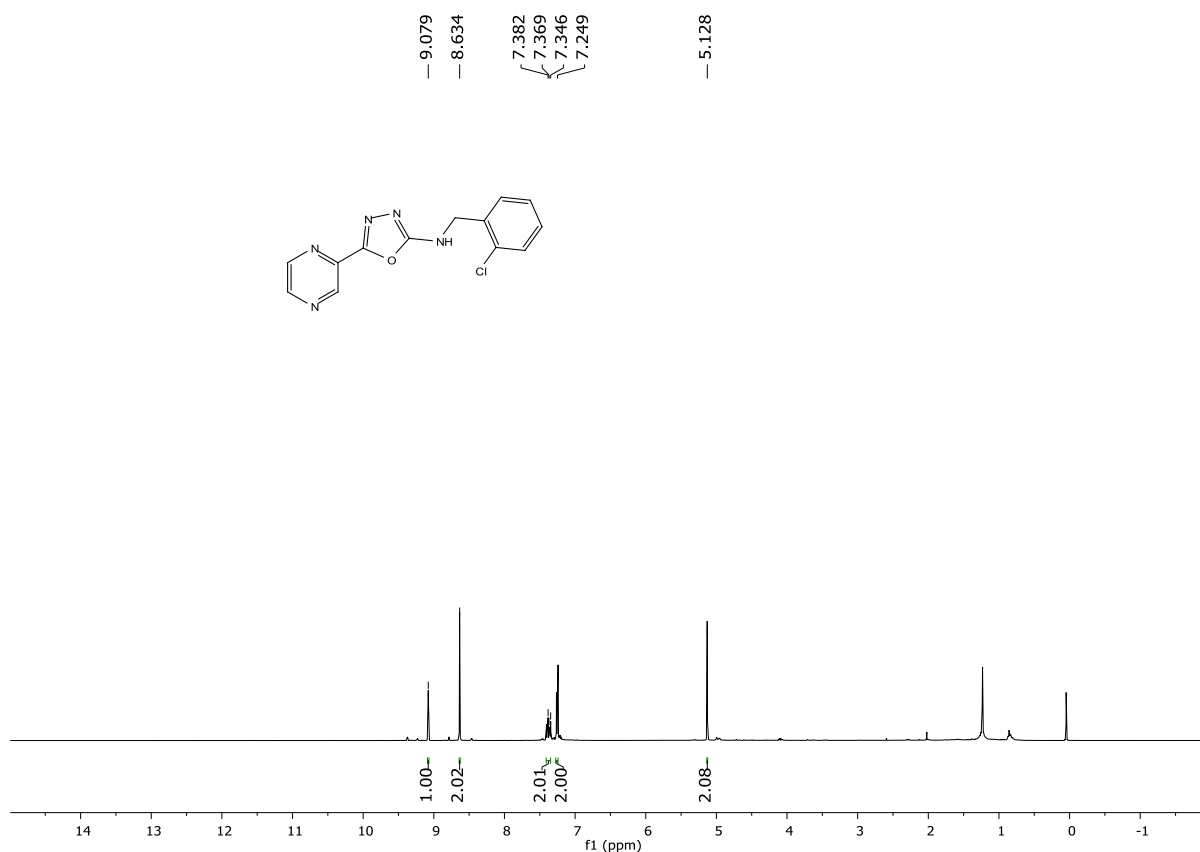
^1H NMR of compound **36** (400 MHz, CDCl_3):



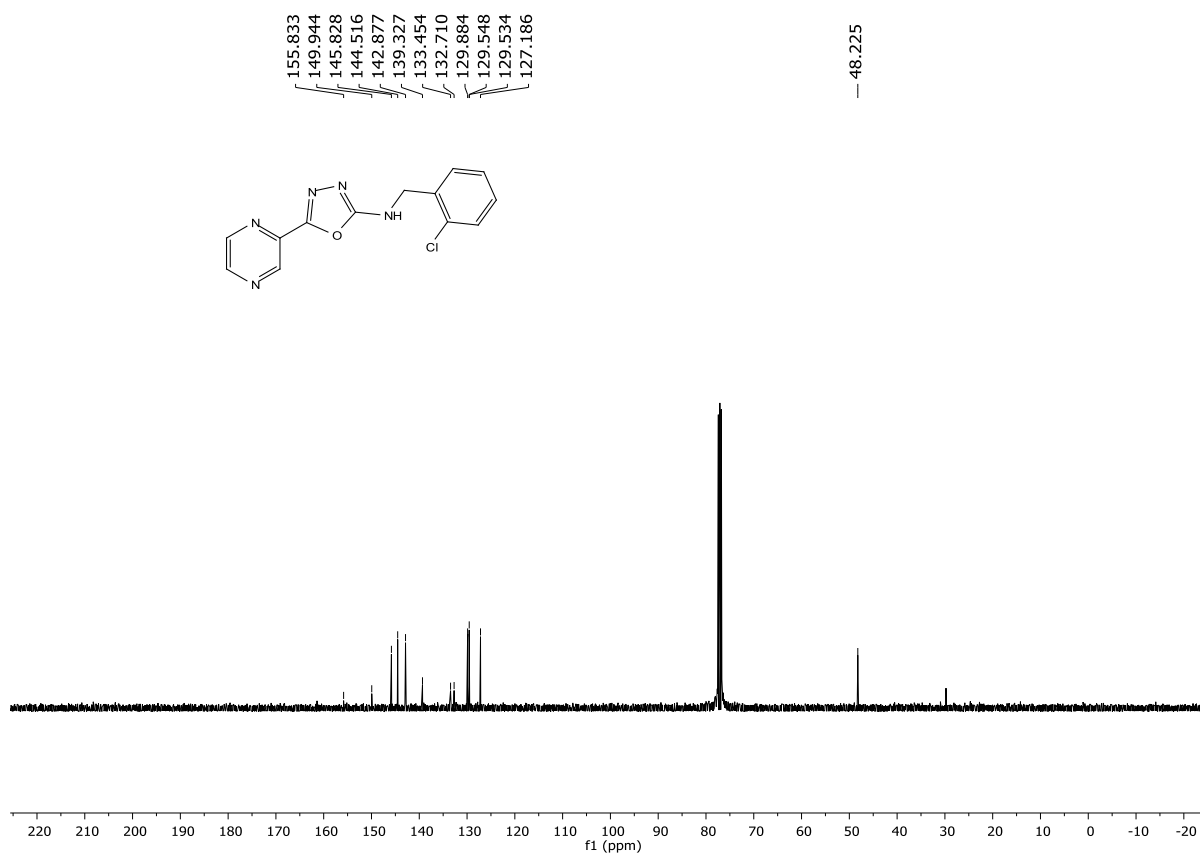
^{13}C NMR of compound **36** (100 MHz, CDCl_3):



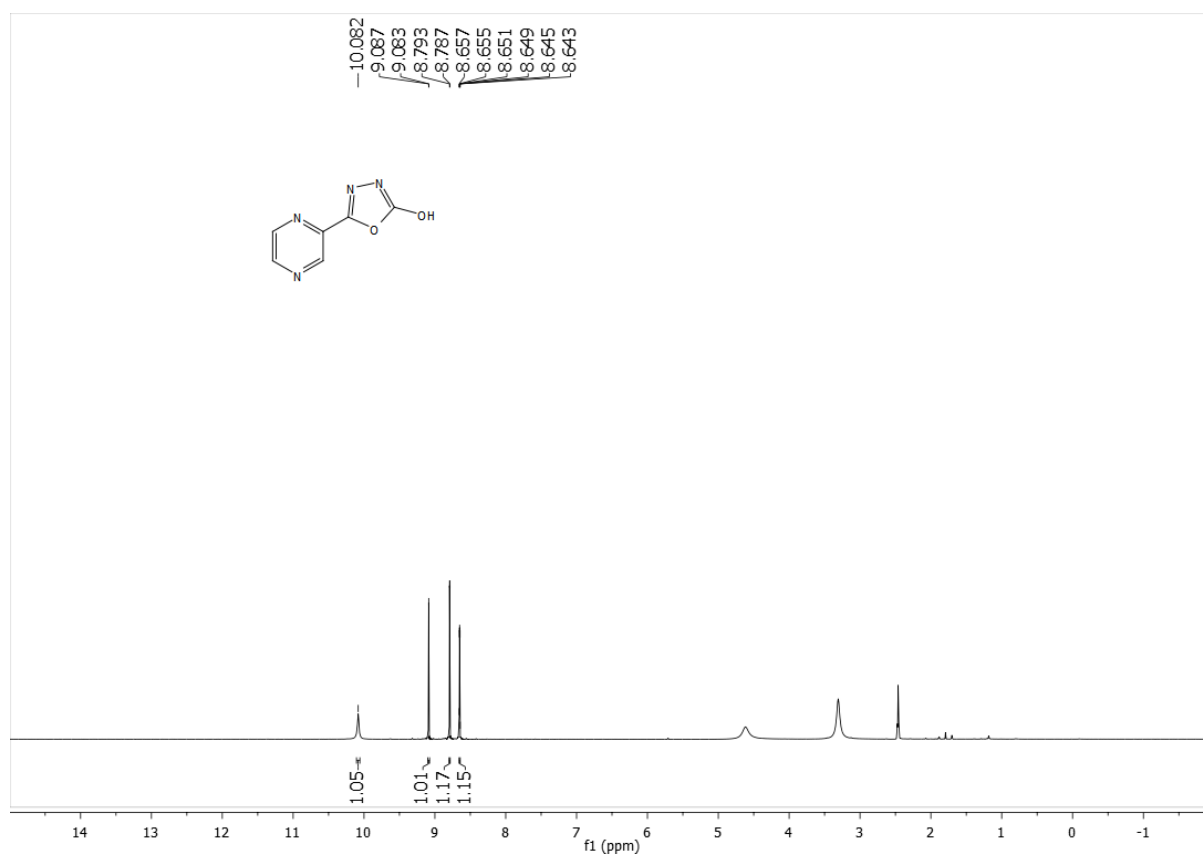
^1H NMR of compound **37** (400 MHz, CDCl_3):



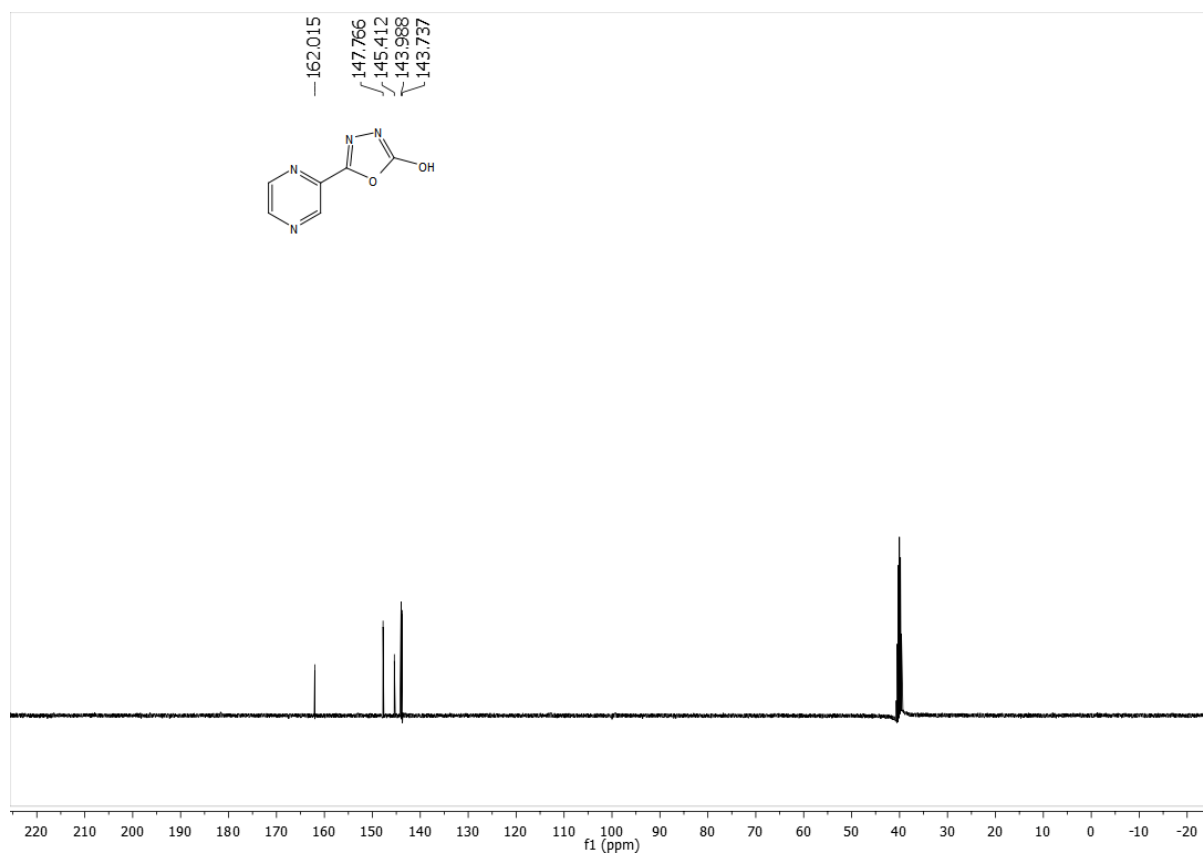
^{13}C NMR of compound **37** (100 MHz, CDCl_3):



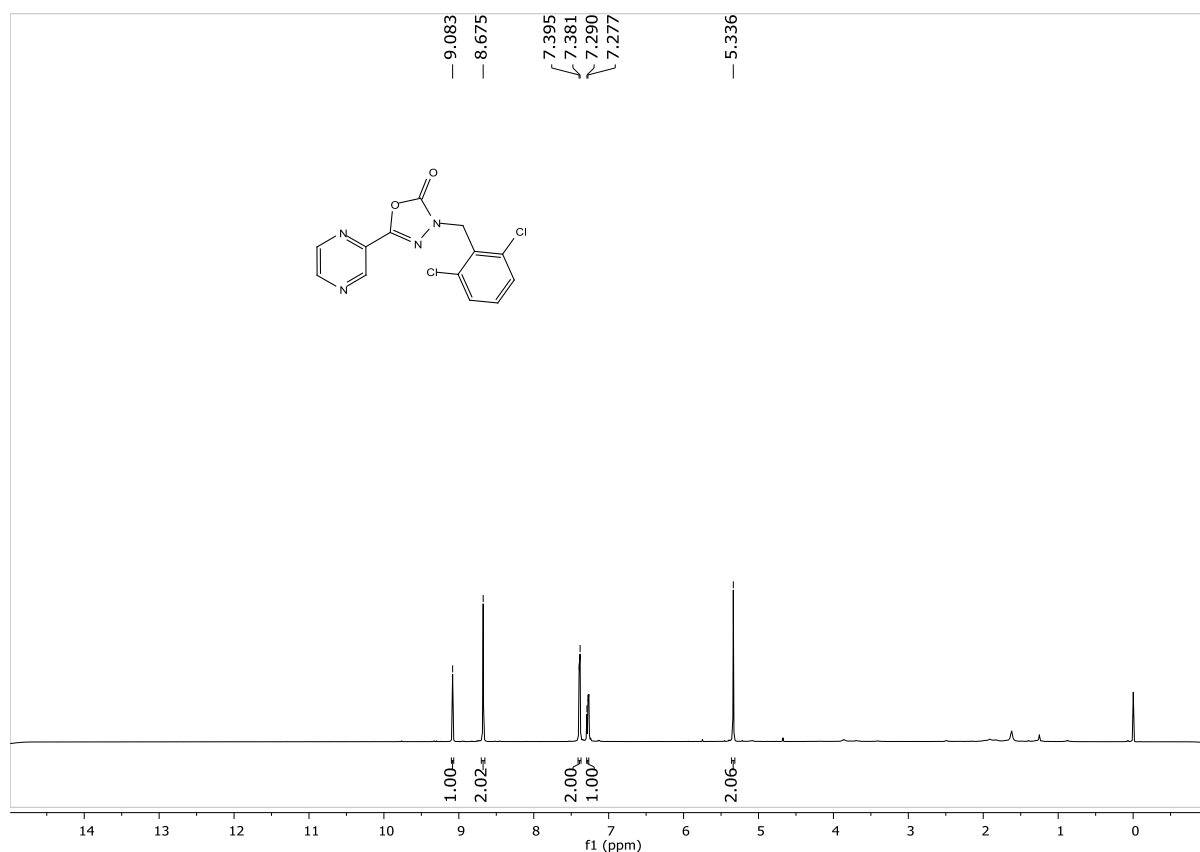
^1H NMR of compound **38** (400 MHz, d_6 -DMSO):



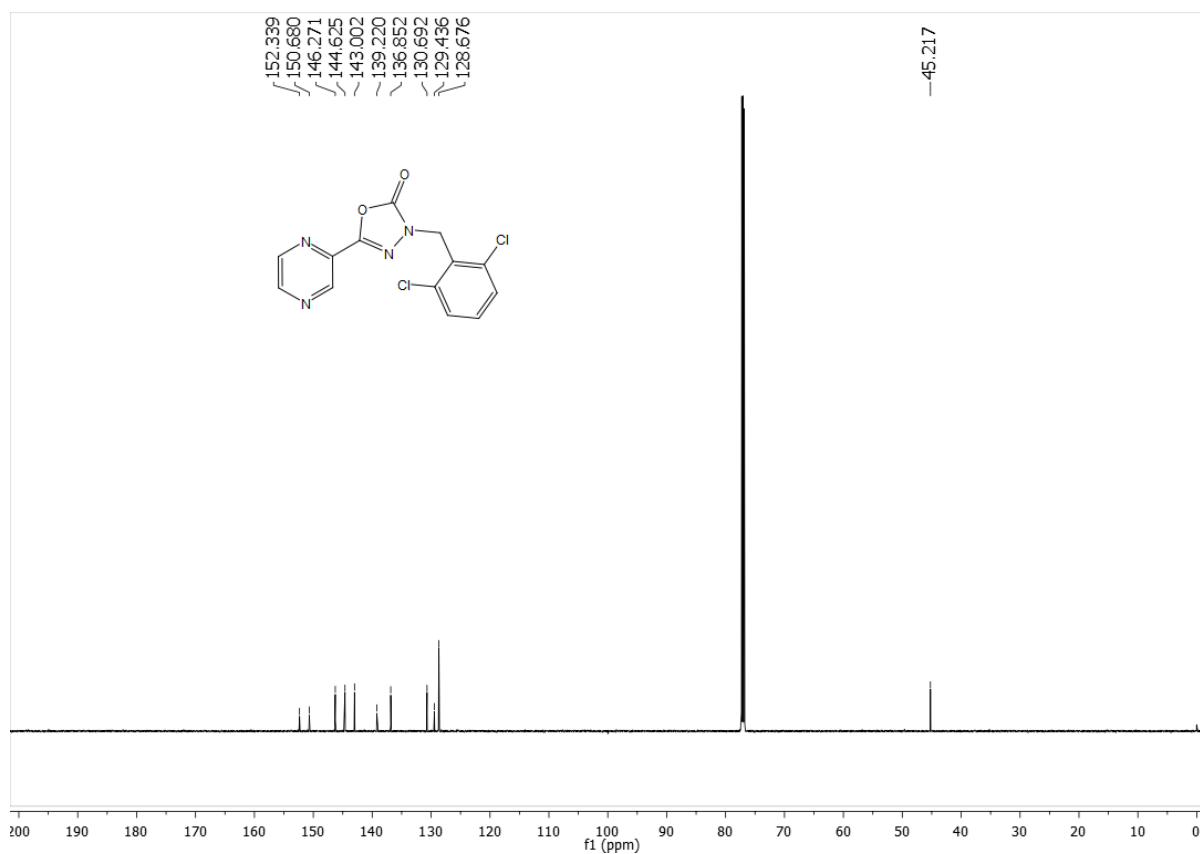
^{13}C NMR of compound **38** (100 MHz, d_6 -DMSO):



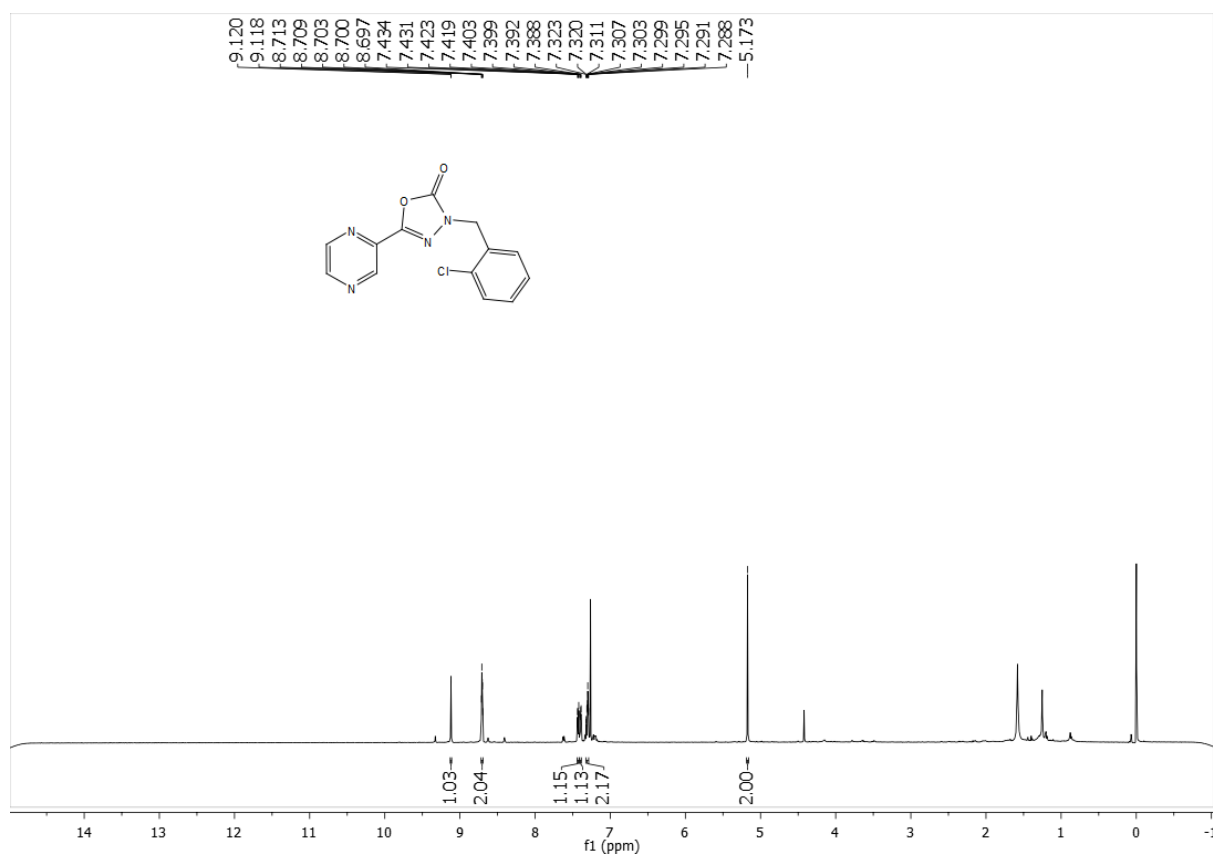
^1H NMR of compound **39** (600 MHz, CDCl_3):



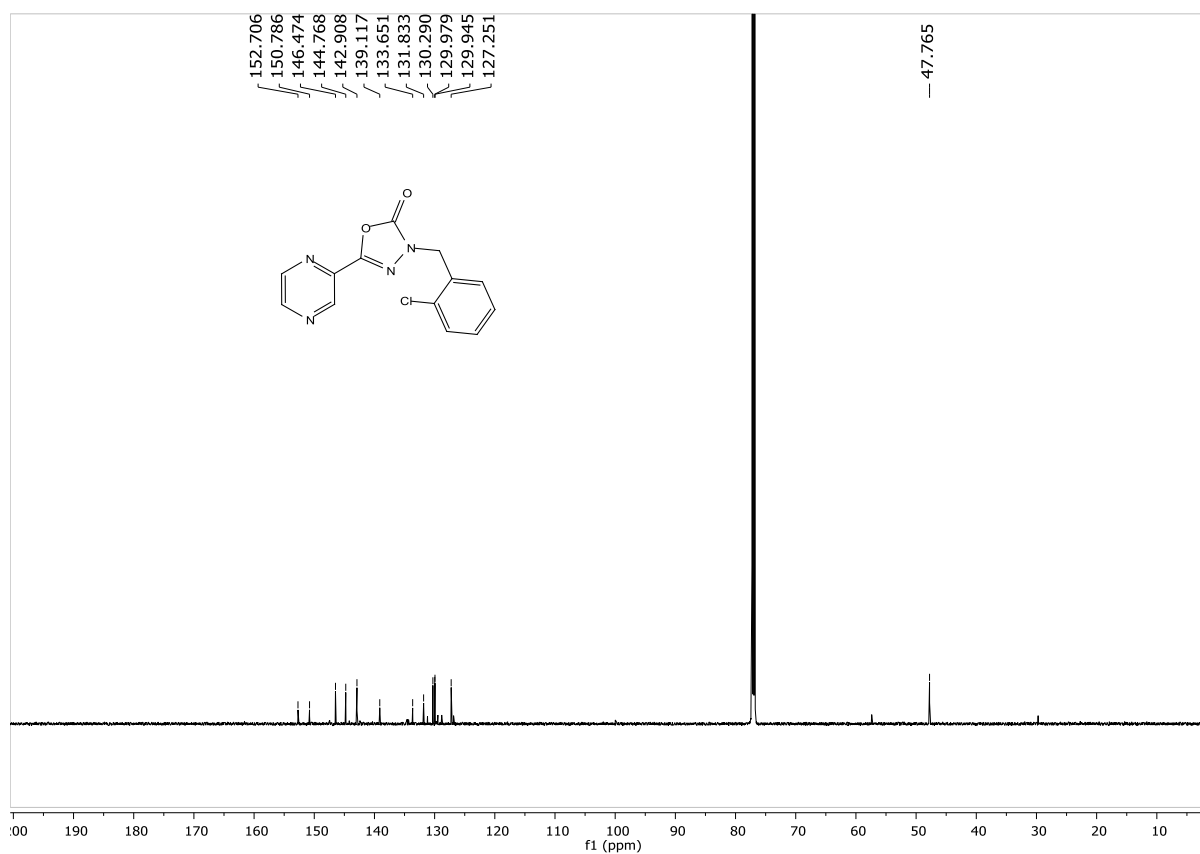
^{13}C NMR of compound **39** (150 MHz, CDCl_3):



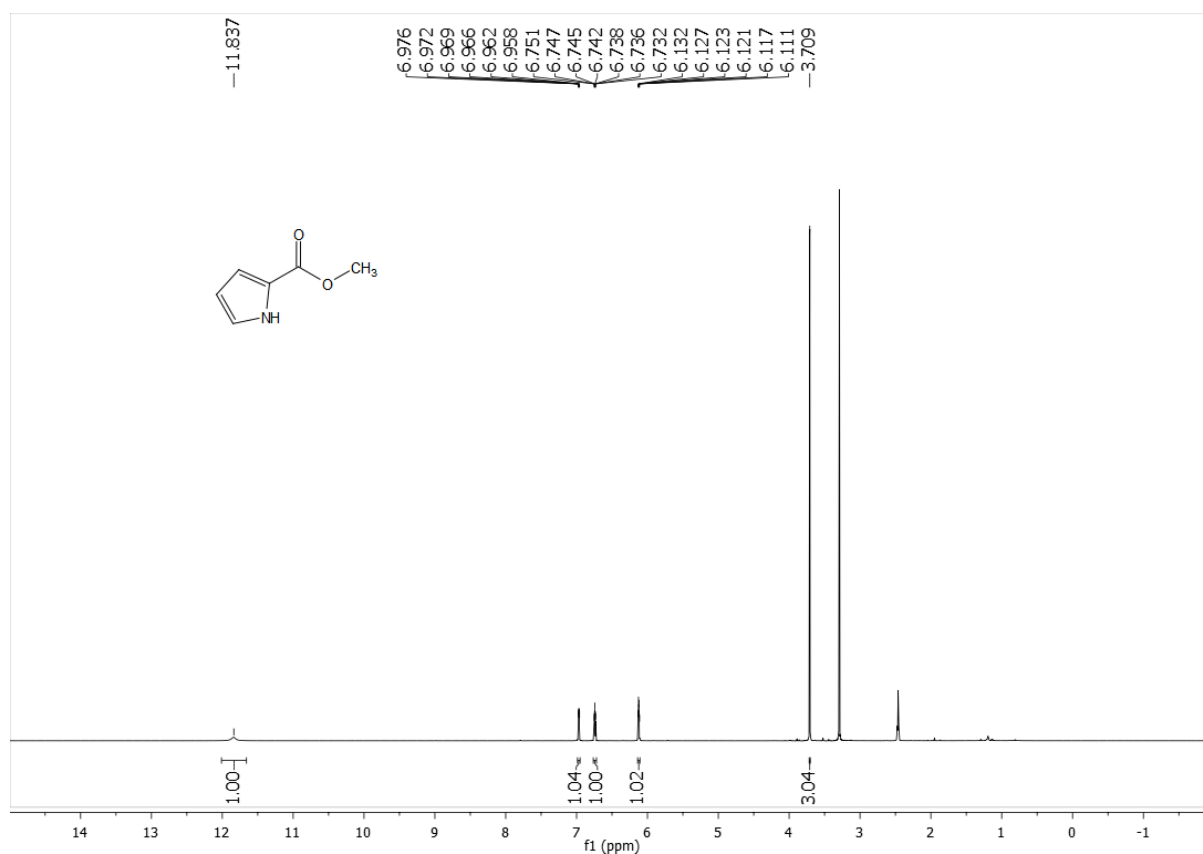
^1H NMR of compound **40** (600 MHz, CDCl_3):



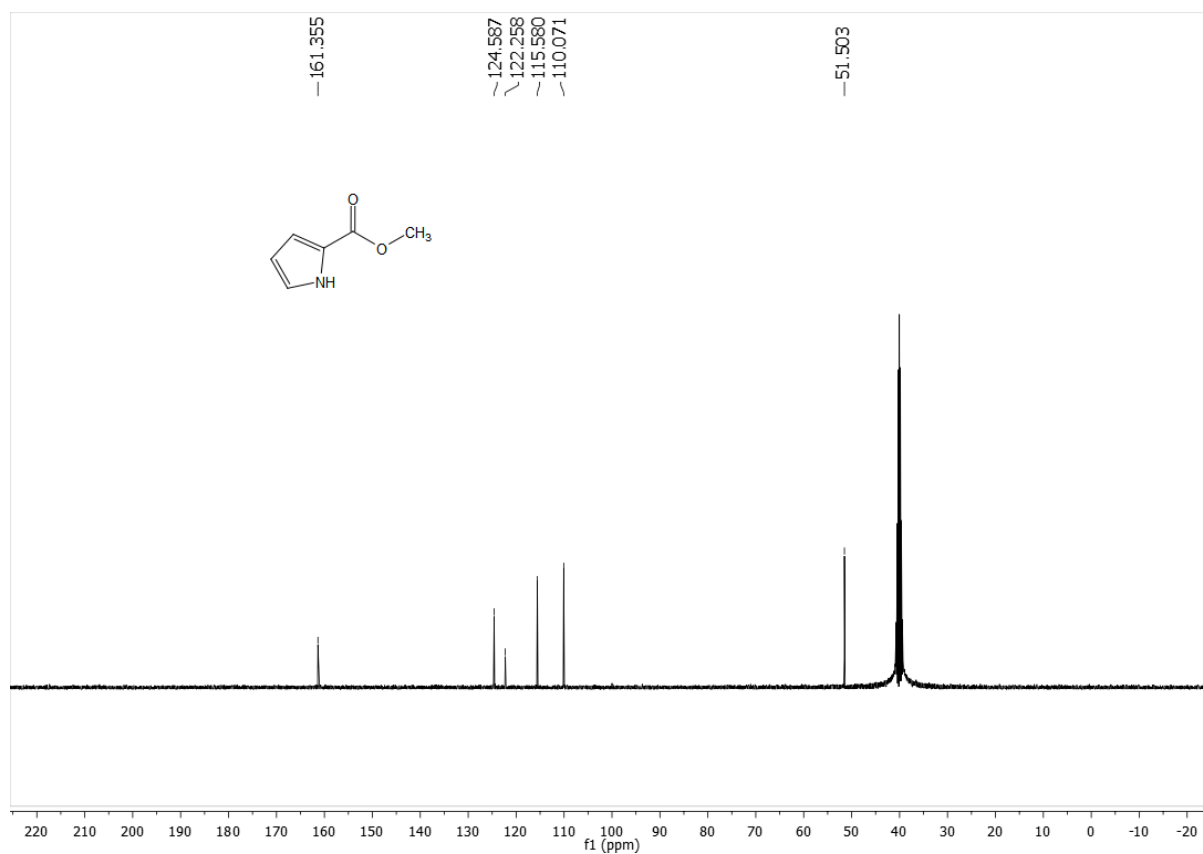
^{13}C NMR of compound **40** (150 MHz, CDCl_3):



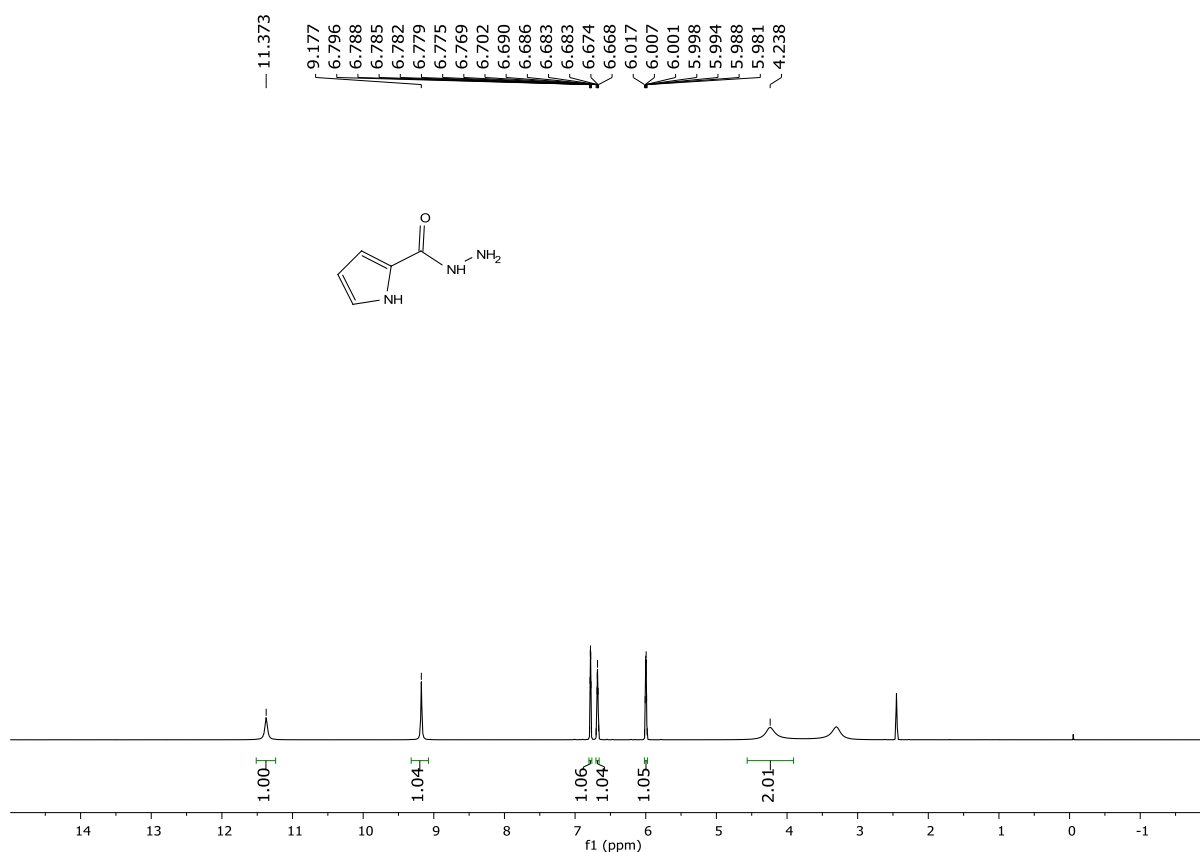
^1H NMR of compound **41** (600 MHz, d_6 -DMSO):



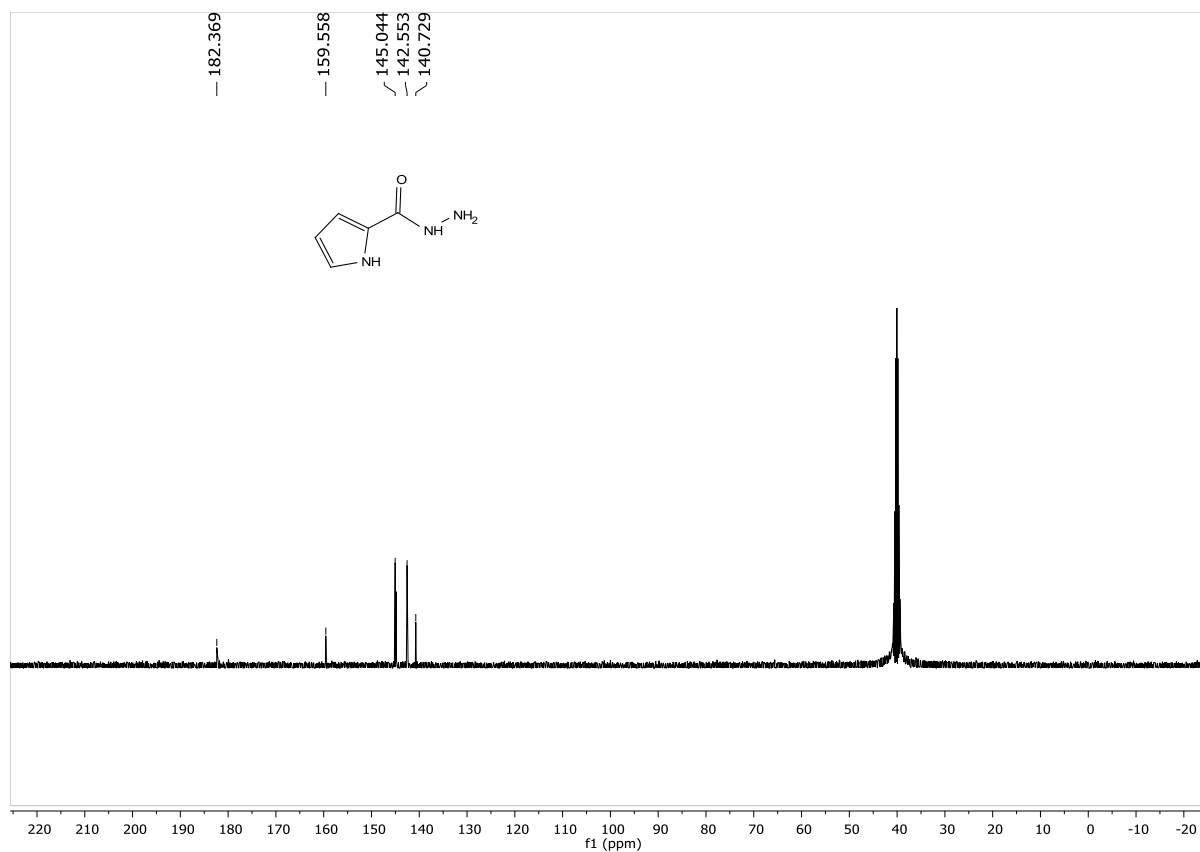
^{13}C NMR of compound **41** (100 MHz, d_6 -DMSO):



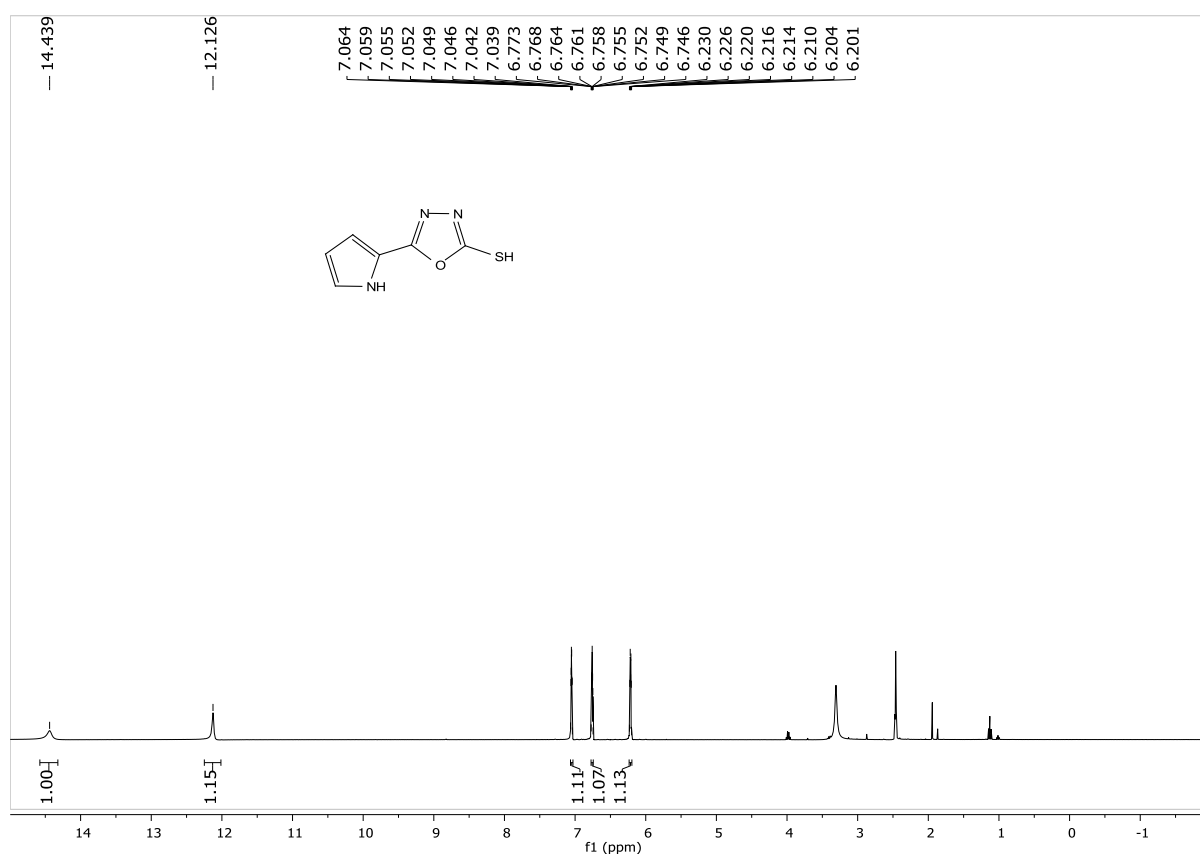
^1H NMR of compound **42** (400 MHz, d_6 -DMSO):



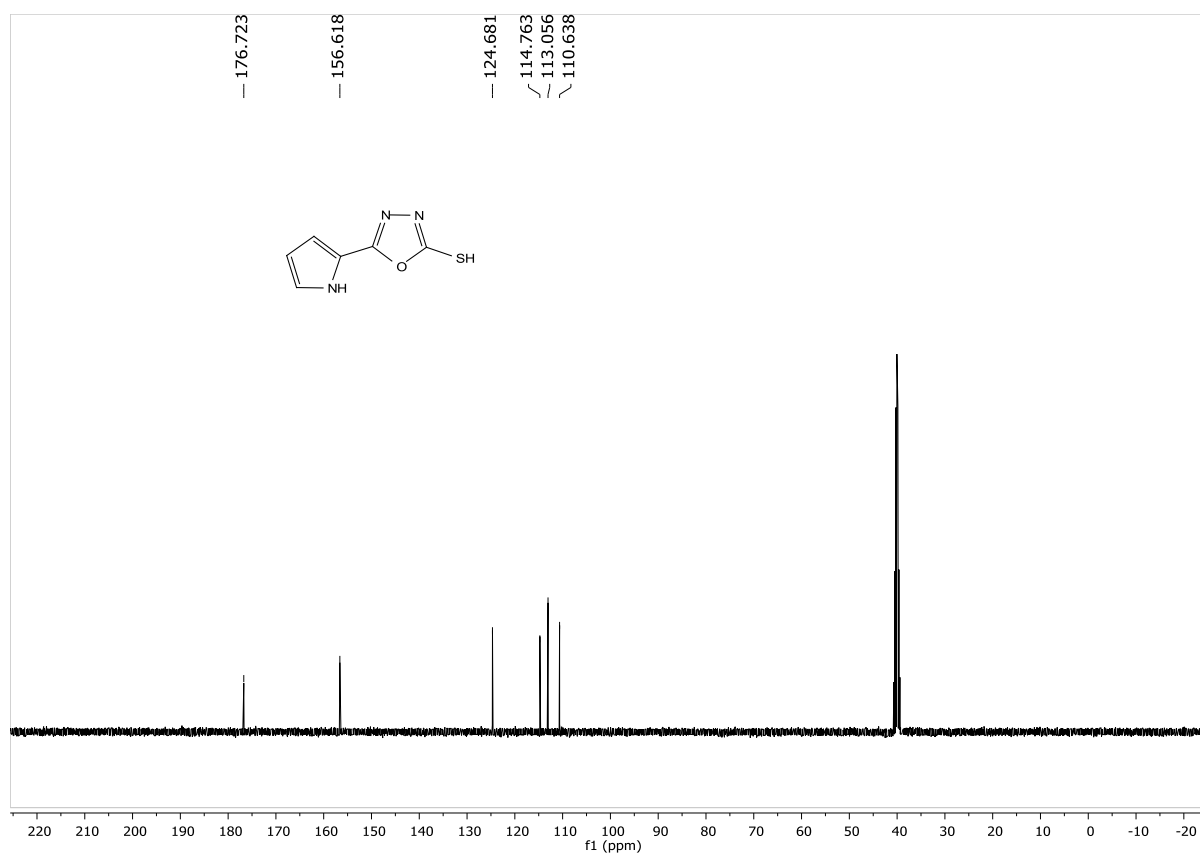
^{13}C NMR of compound **42** (100 MHz, d_6 -DMSO):



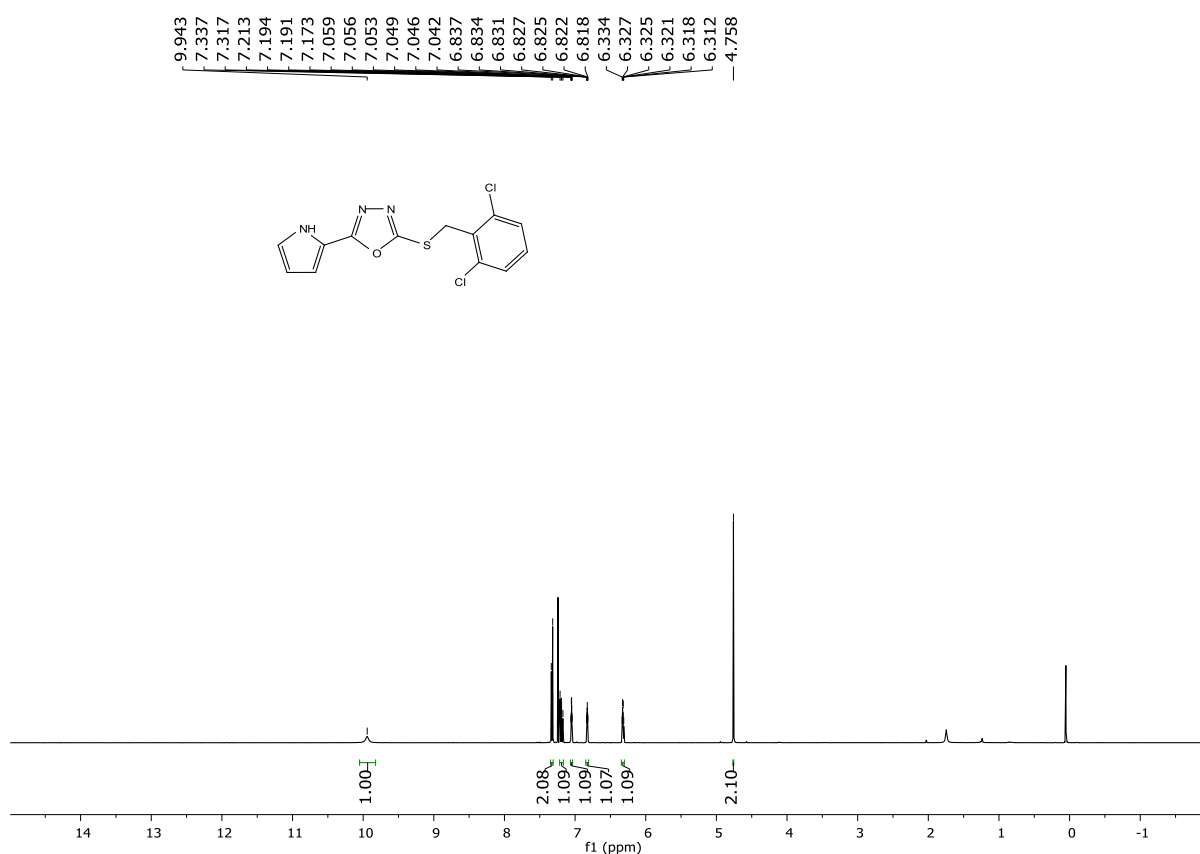
^1H NMR of compound **43** (400 MHz, d_6 -DMSO):



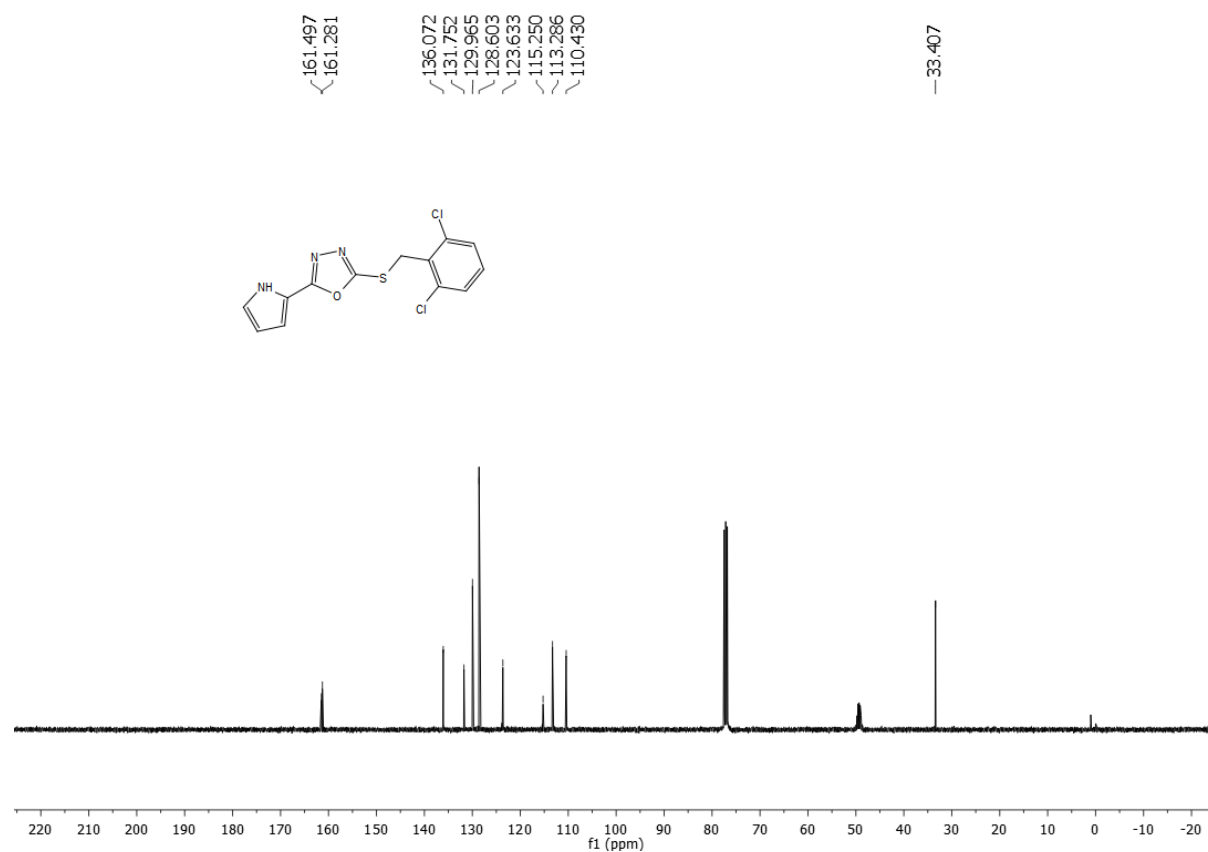
^{13}C NMR of compound **43** (100 MHz, d_6 -DMSO):



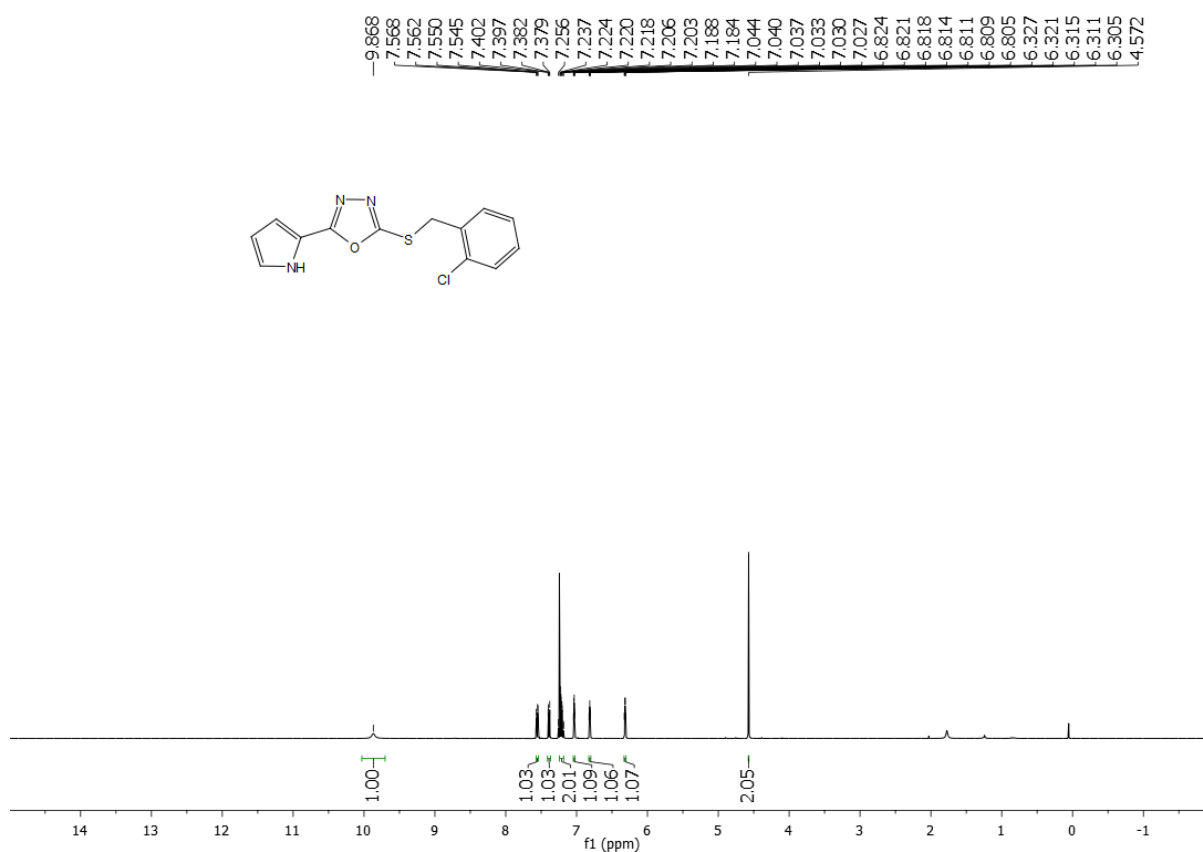
^1H NMR of compound **44** (600 MHz, CDCl_3):



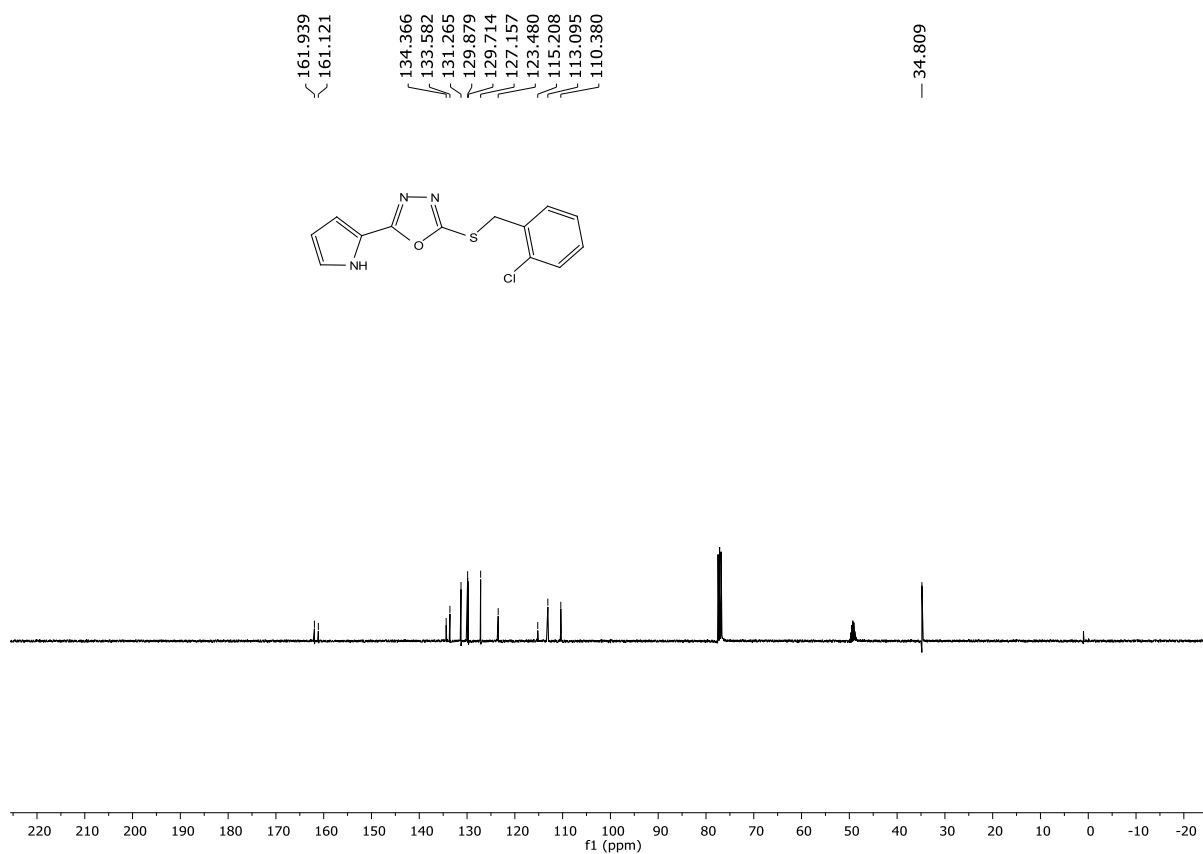
^{13}C NMR of compound **44** (150 MHz, CDCl_3):



^1H NMR of compound **45** (400 MHz, CDCl_3):



^{13}C NMR of compound **45** (100 MHz, CDCl_3):



LIST OF PUBLICATIONS

Journals

1. Exploring the Structural Attributes of Yoda1 for the Development of New-Generation Piezo1 Agonist Yaddle1 as a Vaccine Adjuvant Targeting Optimal T Cell Activation

Sunny Goon†, C. S. C. Liu†, U. G. Dastidar, B. Paul, S. Mukherjee, H. S. Sarkar, M. Desai, R. Jana, S. Pal, N. V. Sreedevi, D. Ganguly*, A. Talukdar* († equal first author)

DOI: <https://doi.org/10.1021/acs.jmedchem.4c00322>

Journal of Medicinal Chemistry, 2024, 67, 8225–8246.

2. Discovery and Development of Quinazolinones and Quinazolinones for Ameliorating Nonalcoholic Fatty Liver Disease (NAFLD) by Modulating COP1-ATGL Axis.

D. Sarkar†, S. Chowdhury†, Sunny Goon†, A. Sen†, U. G. Dastidar, M. A. Mondal, P. Chakrabarti, and A. Talukdar*. († equal first author)

DOI: <https://doi.org/10.1021/acs.jmedchem.3c01431>

Journal of Medicinal Chemistry, 2023, 66, 16728–16761.

3. Hit-to-lead optimization of 2-aminoquinazolines as anti-microbial agents against *Leishmania donovani*.

N. Das, J. Roy, B. Patra, E. Saunders, D. Sarkar, Sunny Goon, B. P. Sinha, S. Roy, S. Roy, J. Sarif, P. Bandopadhyay, S. Barik, S. Mukherjee, D. Ganguly*, A. Talukdar*

DOI: <https://doi.org/10.1016/j.ejmech.2024.116256>

European Journal of Medicinal Chemistry, 269 (2024) 116256.

4. Synthesis and characterization of new potent TLR7 antagonists based on analysis of the binding mode using biomolecular simulations

S. Pal, B. Paul, P. Bandopadhyay, N. Preethy, D. Sarkar, O. Rahaman, Sunny Goon, S. Roy, D. Ganguly*, A. Talukdar*

DOI: <https://doi.org/10.1016/j.ejmech.2020.112978>

European Journal of Medicinal Chemistry, 210 (2021) 112978.

5. Activity-guided development of potent and selective toll-like receptor 9 antagonists

B. Paul, O. Rahaman, S. Roy, S. Pal, S. Satish, A. Mukherjee, A. R. Ghosh, D. Raychaudhuri, R. Bhattacharya, Sunny Goon, D. Ganguly*, A. Talukdar*

DOI: <https://doi.org/10.1016/j.ejmech.2018.09.058>

European Journal of Medicinal Chemistry, 159 (2018) 187-205.

Review Articles

1. Topoisomerase I inhibitors: Challenges, progress and the road ahead

A. Talukdar*, B. Kundu*, D. Sarkar, Sunny Goon, M. A. Mondal.

DOI: <https://doi.org/10.1016/j.ejmech.2022.114304>

European Journal of Medicinal Chemistry, 236 (2022) 114304. (Impact Factor: 6.0)

Patent

1. Purine based small molecule modulators for PPAR γ in ameliorating non-alcoholic fatty liver disease: Preparation and Use thereof

A. Talukdar, P. Chakrabarti, Sunny Goon, D. Sarkar, S. K. Maity, A. D. Sharma, D. Bhattacharya, S. Pal, H. S. Sarkar.

Application number: 202311083005 *Date of Filing*: 05.12.2023

2. Small molecules for Adoptive T-cell Therapy (ACT) through activation of the mTOR signalling pathway, process for preparation thereof

A. Talukdar, S. Chatterjee, Sunny Goon, D. Sarkar, P. Ghosh, U. G. Dastidar, T. Ghosh.

Publication No. WO2024236589, *Application No.* PCT/IN2024/050437, *Filing Date*: 21.11.2024

3. A preparation of quinazolinones and use thereof

A. Talukdar, P. Chakrabarti, Sunny Goon, D. Sarkar, S. Chowdhury, A. Sen, U. G. Dastidar, B. Patra, I. Hoque

Publication No. WO2023119320, *Application No.* PCT/IN2022/051099, *Filing Date*: 29.06.2023.

4. Quinazolinones derivatives for treatment of non-alcoholic fatty liver disease, preparation and use thereof

A. Talukdar, P. Chakrabarti, Sunny Goon, D. Sarkar, S. Chowdhury, S. Das, N. Das, D. Sarkar.

Publication No. US20230357165, *Application No.* PCT/IN2021/050621, *Filing Date*: 09.11.2023.

CONFERENCES ATTENDED & ORAL/POSTER PRESENTATIONS

- **International Conference on “Current Trends in drug discovery techniques and diagnostics: Chemical Biology Approaches” (2024)**

Adichunchanagiri University, BG Nagara, Mandya, India. | POSTER PRESENTED |

- **Annual Convention of Chemists (ACC-2023)**

IIT-Delhi; New Delhi; India | POSTER PRESENTED |

- **ACS Spring 2023: Crossroads of Chemistry (2023)**

American Chemical Society, Indianapolis, Oral-Hybrid | ORAL PRESENTATION |

- **International Conference on Frontier Areas of Science and Technology (ICFAST-2022)**

University of Hyderabad; India | POSTER PRESENTED |

COPY OF PUBLICATIONS

Exploring the Structural Attributes of Yoda1 for the Development of New-Generation Piezo1 Agonist Yaddle1 as a Vaccine Adjuvant Targeting Optimal T Cell Activation

Published as part of Journal of Medicinal Chemistry *virtual special issue* “Medicinal Chemistry of Next Generation Vaccine Adjuvants”.

Sunny Goon, Chinky Shiu Chen Liu, Uddipta Ghosh Dastidar, Barnali Paul, Suravi Mukherjee, Himadri Sekhar Sarkar, Milie Desai, Rituparna Jana, Sourav Pal, Namala Venkata Sreedevi, Dipyaman Ganguly,* and Arindam Talukdar*



Cite This: *J. Med. Chem.* 2024, 67, 8225–8246



Read Online

ACCESS |



Metrics & More

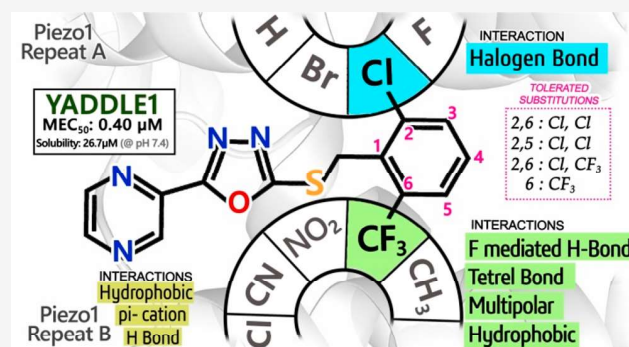


Article Recommendations



Supporting Information

ABSTRACT: Piezo1, a mechano-activated ion channel, has wide-ranging physiological and therapeutic implications, with the ongoing development of specific agonists unveiling cellular responses to mechanical stimuli. In our study, we systematically analyzed the chemical subunits in Piezo1 protein agonist Yoda1 to comprehend the structure–activity relationship and push forward next-generation agonist development. Preliminary screening assays for Piezo1 agonism were performed using the Piezo1-mCherry-transfected HEK293A cell line, keeping Yoda1 as a positive control. We introduce a novel Piezo1 agonist Yaddle1 (34, 0.40 μ M), featuring a trifluoromethyl group, with further exploration through in vitro studies and density functional theory calculations, emphasizing its tetrel interactions, to act as an ambidextrous wedge between the domains of Piezo1. In contrast to the poor solubility of the established agonist Yoda1, our results showed that the kinetic solubility of Yaddle1 ($26.72 \pm 1.8 \mu$ M at pH 7.4) is 10-fold better than that of Yoda1 ($1.22 \pm 0.11 \mu$ M at pH 7.4). Yaddle1 (34) induces Ca^{2+} influx in human CD4^{+} T cell, suggesting its potential as a vaccine adjuvant for enhanced T cell activation.



INTRODUCTION

Cellular fate and function are intricately regulated by physical cues from the external microenvironment.¹ The process of mechanotransduction comprises sensing of environment-specific mechanical cues at the cellular surface and converting them into meaningful biochemical signals that ultimately shape the biological response.² Piezo1 and Piezo2 proteins belong to a class of evolutionarily conserved mechanosensitive ion channels in vertebrates that respond to mechanical stimuli by allowing an influx of extracellular cations like Na^{+} and Ca^{2+} .³ Piezo1, being more widely expressed across various tissues and cell types, plays a central role in physiological processes like regulation of blood cell volume, stem cell and chondrocyte differentiation, epithelial-layer homeostasis, and regulation of vascular development and function by circulatory shear stress or blood pressure as well as immune response.⁴ Piezo1 deficiency causes several pathological conditions such as hereditary xerocytosis, arthrogryposis, lung inflation-induced sleep apnea, Gordon syndrome, and Marden–Walker syndrome.⁵ Piezo2, on the contrary, plays a crucial role in tactile sensation, nociception, and proprio-

ception.^{5,6} A force-triggered conformational change in the extracellular blades triggers gating of the central ion channel allowing passage of extracellular cations. Conformational remodeling at the surface blades is transmitted efficiently to the ion-conducting pore through the intracellular beams via a long-distance lever-like mechanism.^{7,8} Gating of this channel by mechanical stretching allows an influx of extracellular cations like Ca^{2+} .³ Increased cytosolic Ca^{2+} concentrations activate a number of calcium-dependent signaling pathways that affect cellular function. Due to their significant roles in extensive cellular processes, Piezo proteins are attractive pharmaceutical targets for physiological and therapeutic studies in diseased conditions. Because Piezo channels are mechanically gated,

Received: February 5, 2024

Revised: April 15, 2024

Accepted: April 22, 2024

Published: May 8, 2024



ACS Publications

© 2024 American Chemical Society

8225

<https://doi.org/10.1021/acs.jmedchem.4c00322>
J. Med. Chem. 2024, 67, 8225–8246

Discovery and Development of Quinazolinones and Quinazolinonediones for Ameliorating Nonalcoholic Fatty Liver Disease (NAFLD) by Modulating COP1-ATGL Axis

Dipayan Sarkar, Saheli Chowdhury, Sunny Goon, Abhishek Sen, Uddipta Ghosh Dastidar, Mohabul Alam Mondal, Partha Chakrabarti,* and Arindam Talukdar*

Cite This: *J. Med. Chem.* 2023, 66, 16728–16761

Read Online

ACCESS |



Metrics & More

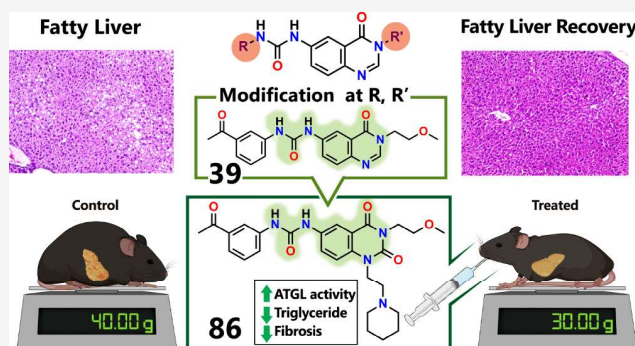


Article Recommendations



Supporting Information

ABSTRACT: E3 ubiquitin ligase, Constitutive Photomorphogenic 1 (COP1) regulates turnover of Adipose Triglyceride Lipase (ATGL), the rate-limiting lipolytic enzyme. Genetic perturbation in the COP1-ATGL axis disrupts lipid homeostasis, leading to liver steatosis. Using drug development strategies, we herein report quinazolinone and quinazolinonedione based modulators for COP1-ATGL axis. Systematic SAR studies and subsequent optimization were performed by incorporating relevant functional groups at the N1, N3, C5, and C6 positions of both scaffolds. Compounds' efficacy was evaluated by multiple biological assays and ADME profiling. The lead compound **86** could increase ATGL protein expression, reduce ATGL ubiquitination and COP1 autoubiquitination, and diminish lipid accumulation in hepatocytes in the nanomolar range. Oral administration of **86** abrogated triglyceride accumulation and resolved fibrosis in preclinical Nonalcoholic Fatty Liver Disease (NAFLD) model. The study thus establishes quinazolinonedione as a viable chemotype to therapeutically modulate the activity of COP1 and ATGL in relevant clinical contexts.



INTRODUCTION

Nonalcoholic fatty liver disease (NAFLD) is an emerging chronic liver disease and a manifestation of metabolic syndrome affecting 30% of the world population.^{1,2} This progressive disease initiates with gradual lipid accumulation in hepatocytes called nonalcoholic fatty liver (NAFL) or hepatosteatosis followed by an irreversible stage called nonalcoholic steatohepatitis (NASH), which is characterized by inflammation, hepatocytes ballooning, and hepatocellular death. NASH may progress to fibrosis or scarring that leads to liver cirrhosis.³ Although lifestyle modification and other supportive therapies can help in ameliorating NAFL, there are no FDA-approved drugs targeting NASH/NAFL pathogenesis.

At present, treatment strategies are mainly directed toward various targets that mediate hepatocyte dysregulation, inflammation, apoptosis, and oxidative stress. Extrahepatic targets whose roles are implicated in NASH like the microbiome, gut liver axis, and organs like muscle and adipose tissue are also being considered for designing therapeutic targets. Certain drugs are in clinical trials at various phases. Notably, elafibranor (PPAR- α/δ ligand), selonsertib (ASK-1 inhibitor), obeticholic acid, tropifexor, nidufexor (FXR agonist), cenicriviroc (CCR 2/5 inhibitor), and saroglitazar (PPAR- α/γ ligand) are in phase II/III clinical trials (Figure 1). All of these drugs aim at a much-advanced stage of fibrosis in

NASH. A few drugs like Aramchol (SCD-1 inhibitor), IMM-124E (Anti-LPS), MGL-3196 (THR- β agonist), NGM282 (FGF19 analogue), PF-05221304 (ACC inhibitor), etc., which are in phase II clinical trials aim at an improvement in liver fat and, therefore, target mainly the steatotic stage (Figure 1). Targeting the fibrotic stage in NASH may not always prove to be beneficial since mostly the stage is irreversible and much damage has already been inflicted on the liver with the deposition of collagen fibers and the beginning of scar tissue formation. NAFLD is a complex multifactorial disorder involving the interplay of several molecules and their associated signaling pathways. As is evident, the most prominent feature of NAFLD is the deposition of excessive TAG (triacylglycerol) in hepatocytes,⁴ and therefore, deregulation of enzymes responsible for controlling intracellular lipid turnover and homeostasis may play an important role in NAFLD.⁴ A pivotal enzyme associated with the intracellular

Received: August 4, 2023

Revised: October 31, 2023

Accepted: November 10, 2023

Published: December 15, 2023





Research paper

Hit-to-lead optimization of 2-aminoquinazolines as anti-microbial agents against *Leishmania donovani*

Nirmal Das^{a,1,2}, Jayasree Roy^{b,1}, Binita Patra^a, Eleanor Saunders^c, Dipika Sarkar^a, Sunny Goon^a, Bishnu Prasad Sinha^{b,2}, Shreya Roy^b, Swarnali Roy^a, Jafar Sarif^{b,2}, Purbita Bandopadhyay^{b,2}, Subhasis Barik^b, Suravi Mukherjee^b, Nicole McNamara^d, Swapna Varghese^d, Kaylene Simpson^e, Jonathan Baell^d, Malcolm McConville^c, Dipyaman Ganguly^{b,2,*}, Arindam Talukdar^{a,*,2}

^a Department of Organic and Medicinal Chemistry, CSIR—Indian Institute of Chemical Biology, 4 Raja S. C. Mullick Road, Kolkata 700032, West Bengal, India

^b IICB-Translational Research Unit of Excellence, Department of Cancer Biology and Inflammatory Disorders, CSIR—Indian Institute of Chemical Biology, CN6, Sector V, Salt Lake, Kolkata 700091, West Bengal, India

^c Department of Biochemistry and Pharmacology, Bio21 Institute of Molecular Science and Biotechnology (Bio21), University of Melbourne, Parkville, Victoria 3052, Australia

^d Medicinal Chemistry, Monash Institute of Pharmaceutical Sciences, Monash University (Parkville Campus), 381 Royal Parade, Parkville, Victoria 2052, Australia

^e Victorian Centre for Functional Genomics, Peter MacCallum Cancer Centre, 305 Grattan St, Melbourne, Victoria 3000, Australia

ARTICLE INFO

Handling Editor: Dr. Z Liu

Keywords:

Visceral leishmaniasis (VL)
Neglected tropical disease (NTD)
Guanidine linkage
Scaffold-hopping
Quinazoline
Hit-to-lead
Leishmania donovani
Metabolic stability

ABSTRACT

Visceral leishmaniasis is a potentially fatal disease caused by infection by the intracellular protist pathogens *Leishmania donovani* or *Leishmania infantum*. Present therapies are ineffective because of high costs, variable efficacy against different species, the requirement for hospitalization, toxicity and drug resistance. Detailed analysis of previously published hit molecules suggested a crucial role of 'guanidine' linkage for their efficacy against *L. donovani*. Here we report the design of 2-aminoquinazoline heterocycle as a basic pharmacophore-bearing guanidine linkage. The introduction of various groups and functionality at different positions of the quinazoline scaffold results in enhanced antiparasitic potency with modest host cell cytotoxicity using a physiologically relevant THP-1 transformed macrophage infection model. In terms of the ADME profile, the C7 position of quinazoline was identified as a guiding tool for designing better molecules. The good ADME profile of the compounds suggests that they merit further consideration as lead compounds for treating visceral leishmaniasis.

1. Introduction

Human leishmaniasis includes a spectrum of neglected tropical diseases (NTD), caused by 20 species of kinetoplastid protozoan parasites belonging to the genus *Leishmania*, which are transmitted by a variety of sandfly species [1–4]. These diseases are 'neglected', as they primarily affect some of the world's poorest communities and historically received much less attention from the pharmaceutical industries because of market size, precluding substantial return on investment [5]. The most serious form of human leishmaniasis is visceral leishmaniasis (VL,

Kala-azar) which occurs following the spread of the parasites to internal organs (spleen, liver, bone marrow) and is invariably lethal if not treated [1,6,7]. VL is generally caused by *Leishmania donovani* and *Leishmania infantum* [8,9]. It is transmitted to mammalian hosts by the bite of the female phlebotomine sandfly, *Phlebotomus argentipes* [8,10]. VL is second only to malaria, in terms of mortality and morbidity caused by protist infections, with an estimated ~1 million new cases of VL and 26,000 to 65,000 deaths each year worldwide [11,12]. Leishmaniasis is endemic in 88 countries across 5 continents affecting around 2 million people and representing a potential threat for more than 350 million

* Corresponding author.

** Corresponding author.

E-mail addresses: dipyaman@iicb.res.in (D. Ganguly), atalukdar@iicb.res.in (A. Talukdar).

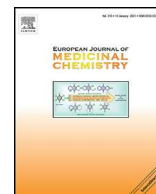
¹ These authors contributed equally to the study.

² Academy of Scientific and Innovative Research, Ghaziabad, 201002, India.



Contents lists available at ScienceDirect

European Journal of Medicinal Chemistry

journal homepage: <http://www.elsevier.com/locate/ejmech>

Research paper

Synthesis and characterization of new potent TLR7 antagonists based on analysis of the binding mode using biomolecular simulations



Sourav Pal^{a, c}, Barnali Paul^{a, 1}, Purbita Bandopadhyay^{b, c, 1}, Nagothy Preethy^{a, 1},
Dipika Sarkar^a, Oindrila Rahaman^b, Sunny Goon^a, Swarnali Roy^a, Dipyaman Ganguly^{b, *},
Arindam Talukdar^{a, **}

^a Department of Organic and Medicinal Chemistry, CSIR-Indian Institute of Chemical Biology, 4 Raja S. C. Mullick Road, Kolkata, 700032, WB, India^b IICB-Translational Research Unit of Excellence, Department of Cancer Biology and Inflammatory Disorders, CSIR-Indian Institute of Chemical Biology, CN6, Sector V, Salt Lake, Kolkata, 700091, WB, India^c Academy of Scientific and Innovative Research, Ghaziabad, 201002, India

ARTICLE INFO

Article history:

Received 25 January 2020

Received in revised form

21 October 2020

Accepted 26 October 2020

Available online 31 October 2020

Keywords:

Toll-like receptor 7

Antagonist

Molecular docking

Binding model

Molecular dynamics

Drug design

ABSTRACT

Aberrant activation of the endosomal Toll-like receptor 7 (TLR7) has been implicated in myriad auto-immune diseases and is an established therapeutic target in such conditions. Development of diverse TLR7 antagonists is mainly accomplished through random screening. To correlate human TLR7 (hTLR7) antagonistic activity with the structural features in different chemotypes, we derived a hypothetical binding model based on molecular docking analysis along with molecular dynamics (MD) simulations study. The binding hypothesis revealed different pockets, grooves and a central cavity where ligand-receptor interaction with specific residues through hydrophobic and hydrogen bond interactions take place, which correlate with TLR7 antagonistic activity thus paving the way for rational design using varied chemotypes. Based on the structural insight thus gained, TLR7 antagonists with quinazoline were designed to understand the effect of engagement of these pockets as well as boundaries of the chemical space associated with them. The newly synthesized most potent hTLR7 antagonist, i.e. compound **63**, showed IC₅₀ value of 1.03 ± 0.05 μM and was validated by performing primary assay in human plasmacytoid dendritic cells (pDC) (IC₅₀^{pDC}: 1.42 μM). The biological validation of the synthesized molecules was performed in TLR7-reporter HEK293 cells as well as in human plasmacytoid dendritic cells (pDCs). Our study provides a rational design approach thus facilitating further development of novel small molecule hTLR7 antagonists based on different chemical scaffolds.

© 2020 Elsevier Masson SAS. All rights reserved.

1. Introduction

Toll-like receptors (TLRs) are evolutionarily conserved pathogen-encoded molecular pattern identified receptors which play a critical role in the first line of defense against invading pathogens and is required to differentiate between self and non-self [1,2]. TLRs recognize pathogen-associated molecular patterns (PAMPs) present in pathogens [3,4]. Most TLR family members are expressed on the surface of different immune cell subsets, except for TLR3, TLR7, TLR8 and TLR9 which are localized on endosomal

membranes. These TLRs are capable of recognizing nucleic acids of both pathogenic as well as self-origin, in the endolysosomal compartments which have an acidic pH ranging from 5.5 to 6.5 [5]. In humans, the plasmacytoid dendritic cells and B lymphocytes are the only immune cells that express TLR7. Structurally, hTLR7 is composed of 1049 amino acids forming three different structural domains; a) type 1 integral membrane glycoprotein made of 27 consecutive leucine-rich repeat motifs (LRR), packed in between two terminal LRR modules named as LRRNT and LRRCT, in the horse-shoe shaped ectodomain region, which is actually responsible for ligand recognition [6]; b) cytoplasmic signaling domains are known as Toll/interleukin receptor (TIR) domain consisting of 150 conserved residues, which relays the downstream signaling to the next adaptor cascade molecules [7]; c) a single transmembrane helix that connects the extracellular LRR based ectodomain and the

* Corresponding author.

** Corresponding author.

E-mail address: atalukdar@iicb.res.in (A. Talukdar).¹ Authors contributed equally.



Contents lists available at ScienceDirect

European Journal of Medicinal Chemistry

journal homepage: <http://www.elsevier.com/locate/ejmech>

Research paper

Activity-guided development of potent and selective toll-like receptor 9 antagonists

Barnali Paul ^{a, c, 1}, Oindrila Rahaman ^{b, 1}, Swarnali Roy ^a, Sourav Pal ^a, Sohal Satish ^a, Ayan Mukherjee ^{a, c}, Amrit R. Ghosh ^b, Deblina Raychaudhuri ^b, Roopkatha Bhattacharya ^b, Sunny Goon ^a, Dipyaman Ganguly ^{b, **}, Arindam Talukdar ^{a, *}

^a Department of Organic and Medicinal Chemistry, CSIR-Indian Institute of Chemical Biology, 4 Raja S. C. Mullick Road, Kolkata, 700032, WB, India

^b IICB-Translational Research Unit of Excellence, Department of Cancer Biology and Inflammatory Disorders, CSIR-Indian Institute of Chemical Biology, CN6, Sector V, Salt Lake, Kolkata, 700091, WB, India

^c Academy of Scientific and Innovative Research, Kolkata, 700032, WB, India

ARTICLE INFO

Article history:

Received 23 July 2018

Received in revised form

24 September 2018

Accepted 24 September 2018

Available online 26 September 2018

Keywords:

TLR9

Inflammation

Antagonist

Drug design

Pharmacokinetics

ABSTRACT

TLR9 is one of the major innate immune receptors expressed in the endosomes of pDCs and B cells in humans. Aberrant TLR9 activation is implicated in several autoimmune and metabolic disorders as well as in sepsis, making this receptor an important therapeutic target, though specific TLR9 antagonists are yet to be available for clinical use. Here we elucidate the importance of specific physiochemical properties through substitution patterns in quinazoline scaffold to achieve potent hTLR9 inhibition at < 50 nM as well as > 600 fold selectivity against hTLR7, another closely related TLR that shares downstream signaling with TLR9 but plays distinct roles in physiology and pathology. Assays were performed using hPBMC and reporter cell lines. Favorable in vitro ADME profile, pharmacokinetics as well as validation in a clinically relevant in vivo TLR9-inhibition efficacy model in mice establish these novel TLR9-antagonists as candidate therapeutic agents in relevant clinical contexts.

© 2018 Elsevier Masson SAS. All rights reserved.

1. Introduction

Toll-like receptors (TLRs) are germline-encoded pattern recognition receptors critical for innate immunity in the body [1]. These innate receptors are involved in recognizing conserved pathogen-associated molecular patterns (PAMPs) and driving innate immune response in health and disease [2]. The group of TLRs (TLR7, TLR8 and TLR9) that are expressed in the endolysosomal compartment of immune cells are specialized for detecting nucleic acids of non-self origin which are acquired from phagocytosed microbes on their entry into the acidic (pH < 6.5) endolysosomal compartments [1,3,4]. TLR9 expression in humans is largely restricted to pDCs and B lymphocytes [5]. TLR9 identifies unmethylated 2-deoxyribo (cytidine-phosphate guanosine-CpG) DNA motifs, of both microbial and self-origin [6]. Interestingly, a great

number of studies over the past decade or so, including several by us, have shown that aberrant activation of TLR9 in response to self-nucleic acids are key pathogenetic events in a large number of autoimmune and metabolic disorders as well [7–13]. In addition, in the context of sepsis inadvertent hyper activation of TLR9 has been found to be a critical pathogenetic player [14].

The revelations about the aberrant activation of the endosomal TLR9 in autoimmune diseases such as psoriasis [7,8], systematic lupus erythematosus or SLE [9], Sjogren's syndrome, scleroderma [15], rheumatoid arthritis [16], type 1 diabetes [13], type 2 diabetes [12,17] also led to identification of TLR9 as a potential therapeutic target in these clinical contexts [14]. On activation, both TLR7 and TLR9, which are structurally very close as well as share the same immunocellular niche, initiate a common downstream signaling through recruitment of myeloid differentiation primary response 88 (MYD88) proteins to stimulate the transcription factors NF-κB and IRF7, followed by induction of inflammatory cytokines and type I interferons. Interestingly, in some diseases, such as in SLE, TLR7 and TLR9 are found to pursue conflicting roles during inflammation and downstream regulation [18–20]. Most notable inhibitor of all endosomal TLRs is hydroxychloroquine, a well-known antimalarial

* Corresponding author.

** Corresponding author.

E-mail addresses: dipyaman@iicb.res.in (D. Ganguly), atalukdar@iicb.res.in (A. Talukdar).¹ These authors contributed equally.



Topoisomerase I inhibitors: Challenges, progress and the road ahead

Arindam Talukdar ^{a, c, *}, Biswajit Kundu ^{a, **,}, Dipayan Sarkar ^{a, c,}, Sunny Goon ^{a, b,},
Mohabul Alam Mondal ^b

^a Department of Organic and Medicinal Chemistry, CSIR-Indian Institute of Chemical Biology, 4 Raja S. C. Mullick Road, Kolkata, 700032, WB, India

^b The Department of Chemistry, Jadavpur University, Kolkata, West Bengal, 700032, India

^c Academy of Scientific and Innovative Research, Ghaziabad, 201002, India

ARTICLE INFO

Article history:

Received 29 November 2021

Received in revised form

14 March 2022

Accepted 15 March 2022

Keywords:

Topoisomerase IB poisons

Natural source

Synthetic origin

Structure-activity relationship

Combination therapy

Antibody-drug conjugates

ABSTRACT

Topoisomerase IB (Top1), a subcategory of DNA topoisomerase enzymes is expressed much higher in several tumor cells. Therefore, modulating the activity of Top1 in tumor cells to prevent DNA replication and subsequent cell division made it an important drug target for anticancer therapy. FDA-approved camptothecin (CPT) derivatives topotecan and irinotecan exert anticancer activity through stabilization of enzyme-mediated DNA cleavage complex forming a ternary complex between DNA-Top1-drug. However, CPT derivatives suffer from several limitations which prompted interest in the development of 'non-camptothecin' Top1 poisons as anticancer agents.

This review aims to provide chronological development of different classes of Top1 poisons from both natural and synthetic sources through strategic structure-activity relationship (SAR) analysis with insight into the important structural features in different chemotypes that imparted Top1 inhibition along with the understanding of the structural basis of inhibition. This review also provides a snapshot of the application of Top1 poisons in various combination therapies in recent times. We believe such a comprehensive review is going to be beneficial for the medicinal chemistry community to design efficient drug development strategies using existing knowledge.

© 2022 Elsevier Masson SAS. All rights reserved.

Contents

1. Introduction	2
2. Type of topoisomerases	2
3. Mechanism of action of human DNA topoisomerase IB	2
4. Topoisomerase IB inhibition	3
4.1. Topoisomerase IB poisons	3
4.2. Topoisomerase IB catalytic inhibitor	4
4.3. Currently marketed topoisomerase IB poisons and clinical development status	4
5. Topoisomerase IB poisons from different origins	4
5.1. Topoisomerase IB poisons from natural sources	4
5.1.1. Camptothecin (CPT)	4
5.1.2. Evodiamine	8
5.1.3. Benzophenanthridine	9
5.1.4. Lamellarin	10
5.1.5. Luotonin A	12

* Corresponding author. Department of Organic and Medicinal Chemistry, CSIR-Indian Institute of Chemical Biology, 4 Raja S. C. Mullick Road, Kolkata, 700032, WB, India.

** Corresponding author.

E-mail addresses: atalukdar@iicb.res.in (A. Talukdar), biswakund123@gmail.com (B. Kundu).



US 20230357165A1

(19) **United States**(12) **Patent Application Publication**
Talukdar et al.(10) **Pub. No.: US 2023/0357165 A1**
(43) **Pub. Date: Nov. 9, 2023**(54) **QUINAZOLINONES DERIVATIVES FOR
TREATMENT OF NON-ALCOHOLIC FATTY
LIVER DISEASE, PREPARATION AND USE
THEREOF**(71) Applicant: **Council of Scientific and Industrial
Research, New Delhi (IN)**(72) Inventors: **Arindam Talukdar, Kolkata (IN);
Partha Chakrabarti, Kolkata (IN);
Dipayan Sarkar, Kolkata (IN); Saheli
Chowdhury, Kolkata (IN); Sunny
Goon, Kolkata (IN); Subrata Das,
Kolkata (IN); Nirmal Das, Kolkata
(IN); Dipika Sarkar, Kolkata (IN)**(21) Appl. No.: **18/013,681**(22) PCT Filed: **Jun. 25, 2021**(86) PCT No.: **PCT/IN2021/050621**

§ 371 (c)(1),

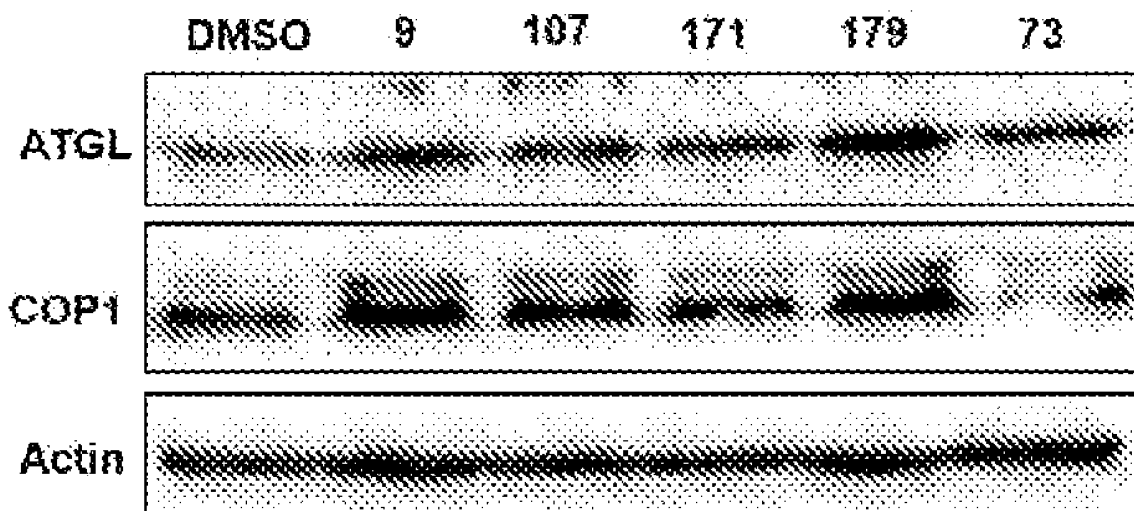
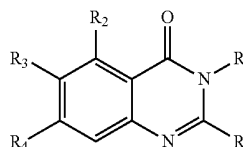
(2) Date: **Dec. 29, 2022**(30) **Foreign Application Priority Data**

Jun. 29, 2020 (IN) 202011027502

Publication Classification(51) **Int. Cl.**
C07D 239/91 (2006.01)
C07D 413/12 (2006.01)
C07D 401/04 (2006.01)
C07D 403/04 (2006.01)
(52) **U.S. Cl.**
CPC **C07D 239/91** (2013.01); **C07D 413/12**
(2013.01); **C07D 401/04** (2013.01); **C07D**
403/04 (2013.01)**ABSTRACT**

(57) Compounds having Structure I are provided for treating diseases and disorders for which inhibition or modulation of the Ubiquitin Ligase COP1 enzyme produces a physiologically beneficial response, in particular for the treatment of Non-Alcoholic Fatty Liver Disease (NAFLD). These compounds having Structure I are capable of increasing the level of adipose triglyceride lipase (ATGL). Also provided is the process of preparing compounds having Structure I.

Structure I



(12) INTERNATIONAL APPLICATION PUBLISHED UNDER THE PATENT COOPERATION TREATY (PCT)

(19) World Intellectual Property
Organization

International Bureau

(43) International Publication Date
29 June 2023 (29.06.2023)



(10) International Publication Number
WO 2023/119320 A1

(51) International Patent Classification:

C07D 239/96 (2006.01) C07D 487/04 (2006.01)
C07D 401/06 (2006.01)

(21) International Application Number:

PC1/IN2022/051099

(22) International Filing Date:

19 December 2022 (19.12.2022)

(25) Filing Language:

English

(26) Publication Language:

English

(30) Priority Data:

202111061087 25 December 2021 (25.12.2021) IN

(71) Applicant: **COUNCIL OF SCIENTIFIC AND INDUSTRIAL RESEARCH AN INDIAN REGISTERED BODY INCORPORATED UNDER THE REGN. OF SOC. ACT (ACT XXI OF 1860)** [IN/IN]; Anusandhan Bhawan, 2 Rafi Marg, New Delhi 110 001 (IN).

(72) Inventors: **TALUKDAR, Arindam**; Indian Institute of Chemical Biology, 4 Raja S.C. Mullick Road, Jadavpur, West Bengal, Kolkata 700032 (IN). **CHAKRABARTI, Partha**; Indian Institute of Chemical Biology, 4 Raja S.C. Mullick Road, Jadavpur, West Bengal, Kolkata 700032 (IN). **SARKAR, Dipayan**; Indian Institute of Chemical Biology, 4 Raja S.C. Mullick Road, Jadavpur, West Bengal, Kolkata 700032 (IN). **CHOWDHURY, Saheli**; Indian Institute of Chemical Biology, 4, Raja S.C. Mullick Road, Jadavpur, West Bengal, Kolkata 700032 (IN). **GOON, Sunny**; Indian Institute of Chemical Biology, 4, Raja S.C. Mullick Road, Jadavpur, West Bengal, Kolkata 700032 (IN). **SEN, Abhishek**; Indian Institute of Chemical Biology, 4, Raja S.C. Mullick Road, Jadavpur, West Bengal, Kolkata 700032 (IN). **GHOSH DASTIDAR, Uddipta**; Indian Institute of Chemical Biology, 4, Raja S.C. Mullick Road, Jadavpur, West Bengal, Kolkata 700032 (IN). **PATRA, Binita**; Indian Institute of Chemical Biology, 4, Raja S.C. Mullick Road, Jadavpur, West Bengal, Kolkata 700032 (IN). **HOQUE, Israful**; Indian Institute of Chemical Biology, 4, Raja S.C. Mullick Road, Jadavpur, West Bengal, Kolkata 700032 (IN).

(74) Agent: **LAKSHMIKUMARAN, Malathi** et al.; B6/10, Safdarjung Enclave, New Delhi 110029 (IN).

(81) Designated States (unless otherwise indicated, for every kind of national protection available): AE, AG, AL, AM, AO, AT, AU, AZ, BA, BB, BG, BH, BN, BR, BW, BY, BZ,

CA, CH, CL, CN, CO, CR, CU, CV, CZ, DE, DJ, DK, DM, DO, DZ, EC, EE, EG, ES, FI, GB, GD, GE, GH, GM, GT, HN, HR, HU, ID, IL, IN, IQ, IR, IS, IT, JM, JO, JP, KE, KG, KH, KN, KP, KR, KW, KZ, LA, LC, LK, LR, LS, LU, LY, MA, MD, MG, MK, MN, MW, MX, MY, MZ, NA, NG, NI, NO, NZ, OM, PA, PE, PG, PH, PL, PT, QA, RO, RS, RU, RW, SA, SC, SD, SE, SG, SK, SL, ST, SV, SY, TH, TJ, TM, TN, TR, TT, TZ, UA, UG, US, UZ, VC, VN, WS, ZA, ZM, ZW.

(84) Designated States (unless otherwise indicated, for every kind of regional protection available): ARIPO (BW, CV, GH, GM, KE, LR, LS, MW, MZ, NA, RW, SD, SL, ST, SZ, TJ, UG, ZM, ZW), Eurasian (AM, AZ, BY, KG, KZ, RU, TJ, TM), European (AL, AT, BE, BG, CH, CY, CZ, DE, DK, EE, ES, FI, FR, GB, GR, HR, HU, IE, IS, IT, LT, LU, LV, MC, ME, MK, MT, NL, NO, PL, PT, RO, RS, SE, SI, SK, SM, TR), OAPI (BF, BJ, CF, CG, CI, CM, GA, GN, GQ, GW, KM, ML, MR, NE, SN, TD, TG).

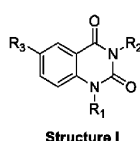
Declarations under Rule 4.17:

— of inventorship (Rule 4.17(iv))

Published:

— with international search report (Art. 21(3))
— with amended claims (Art. 19(1))
— in black and white; the international application as filed contained color or greyscale and is available for download from PATENTSCOPE

(54) Title: A PREPARATION OF QUINAZOLINEDIONES AND USE THEREOF



Structure I

(57) Abstract: The present invention described herein relates to a compound having Structure I for treating diseases and disorders for which inhibition or modulation of the Ubiquitin Ligase COP1 enzyme produces a physiologically beneficial response, in particular for the treatment of Non-Alcoholic Fatty Liver Disease (NAFLD). These compounds having Structure I are capable of increasing the level of adipose triglyceride lipase (ATGL). Also provided is the process of preparing compounds having Structure I.

WO 2023/119320 A1

(12) INTERNATIONAL APPLICATION PUBLISHED UNDER THE PATENT COOPERATION TREATY (PCT)

(19) World Intellectual Property
Organization
International Bureau

(43) International Publication Date
21 November 2024 (21.11.2024)



(10) International Publication Number
WO 2024/236589 A1

- (51) **International Patent Classification:**
C07D 43/32 (2006.01) C07D 473/34 (2006.01)
- (21) **International Application Number:**
PCT/IN2024/050437
- (22) **International Filing Date:**
24 April 2024 (24.04.2024)
- (25) **Filing Language:** English
- (26) **Publication Language:** English
- (30) **Priority Data:**
202311034981 18 May 2023 (18.05.2023) IN
- (71) **Applicant: COUNCIL OF SCIENTIFIC & INDUSTRIAL RESEARCH** [IN/IN]; Anusandhan Bhawan, 2 Rafi Marg, New Delhi 110001 (IN).
- (72) **Inventors: TALUKDAR, Arindam;** CSIR- Indian Institute of Chemical Biology, 4, Raja S.C. Mullick Road, Jadavpur, West Bengal, Kolkata 700032 (IN). **CHATTERJEE, Shilpak;** CSIR- Indian Institute of Chemical Biology, 4, Raja S.C. Mullick Road, Jadavpur, West Bengal, Kolkata 700032 (IN). **GOON, Sunny;** CSIR- Indian Institute of Chemical Biology, 4, Raja S.C. Mullick Road, Jadavpur, West Bengal, Kolkata 700032 (IN). **SARKAR, Dipika;** CSIR- Indian Institute of Chemical Biology, 4, Raja S.C. Mullick Road, Jadavpur, West Bengal, Kolkata 700032 (IN). **GHOSH, Puspendu;** CSIR- Indian Institute of Chemical Biology, 4, Raja S.C. Mullick Road, Jadavpur, West Bengal, Kolkata 700032 (IN). **DASTIDAR, Uddipta Ghosh;** CSIR- Indian Institute of Chemical Biology, 4, Raja S.C. Mullick Road, Jadavpur, West Bengal, Kolkata 700032 (IN). **GHOSH, Trisha;** CSIR- Indian Institute of Chemical Biology, 4, Raja S.C. Mullick Road, Jadavpur, West Bengal, Kolkata 700032 (IN).
- (74) **Agent: KOUL, Sunaina et al.;** Rahul Chaudhry & Partners, RCY House, C-235, Defence Colony, New Delhi 110024 (IN).
- (81) **Designated States** (unless otherwise indicated, for every kind of national protection available): AE, AG, AL, AM, AO, AT, AU, AZ, BA, BB, BG, BH, BN, BR, BW, BY, BZ, CA, CH, CL, CN, CO, CR, CU, CV, CZ, DE, DJ, DK, DM,

DO, DZ, EC, EE, EG, ES, FI, GB, GD, GE, GH, GM, GT, HN, HR, HU, ID, IL, IN, IQ, IR, IS, IT, JM, JO, JP, KE, KG, KH, KN, KP, KR, KW, KZ, LA, LC, LK, LR, LS, LU, LY, MA, MD, MG, MK, MN, MU, MW, MX, MY, MZ, NA, NG, NI, NO, NZ, OM, PA, PE, PG, PH, PI, PT, QA, RO, RS, RU, RW, SA, SC, SD, SE, SG, SK, SL, ST, SV, SY, TH, TJ, TM, TN, TR, TT, TZ, UA, UG, US, UZ, VC, VN, WS, ZA, ZM, ZW.

- (84) **Designated States** (unless otherwise indicated, for every kind of regional protection available): ARIPO (BW, CV, GH, GM, KE, LR, LS, MW, MZ, NA, RW, SC, SD, SL, ST, SZ, TZ, UG, ZM, ZW), Eurasian (AM, AZ, BY, KG, KZ, RU, TJ, TM), European (AL, AT, BE, BG, CH, CY, CZ, DE, DK, EE, ES, FI, FR, GB, GR, HR, HU, IE, IS, IT, LT, LU, LV, MC, ME, MK, MT, NL, NO, PL, PT, RO, RS, SE, SI, SK, SM, TR), OAPI (BF, BJ, CF, CG, CI, CM, GA, GN, GQ, GW, KM, ML, MR, NE, SN, TD, TG).

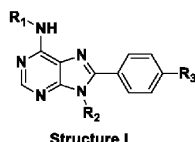
Declarations under Rule 4.17:

- as to applicant's entitlement to apply for and be granted a patent (Rule 4.17(ii))
- of inventorship (Rule 4.17(iv))

Published:

- with international search report (Art. 21(3))
- with amended claims and statement (Art. 19(1))

(54) **Title:** SMALL MOLECULES FOR ADOPTIVE T-CELL THERAPY (ACT) THROUGH ACTIVATION OF THE mTOR SIGNALING PATHWAY, PROCESS FOR PREPARATION THEREOF



(57) **Abstract:** The present invention relates to the preparation of 8-phenyl-purine-6-amino compounds with general structure I in free form or in acceptable salt form to identify small molecule activator of mTOR, which can be used to augment the effector function (IFN γ production) of T cells and hence heightened their antitumor response. More particularly, the invention relates to small molecules where R1, R2 and R3 are as defined in the description, capable of IFN γ production via mTOR activation pathway to elicit durable antitumor repose in the host. The invention describes strategies to generate T cells with high effector function, yet in a relatively short period of time so that a robust and durable anti-tumor response can be achieved in the host.